Astrophysics and Space Science Proceedings 47

Jacob Kleiman *Editor*

Protection of Materials and Structures from the Space Environment

ICPMSE-11

Springer

Astrophysics and Space Science Proceedings

Volume 47

More information about this series at http://www.springer.com/series/7395

Jacob Kleiman
Editor

Protection of Materials and Structures from the Space Environment

ICPMSE-11

Springer

Editor
Jacob Kleiman
Integrity Testing Laboratory Inc.
Markham, Ontario
Canada

ISSN 1570-6591 ISSN 1570-6605 (electronic)
Astrophysics and Space Science Proceedings
ISBN 978-3-319-19308-3 ISBN 978-3-319-19309-0 (eBook)
DOI 10.1007/978-3-319-19309-0

Library of Congress Control Number: 2017936676

Printed on acid-free paper

This Springer imprint is published by Springer Nature
The registered company is Springer International Publishing AG
The registered company address is: Gewerbestrasse 11, 6330 Cham, Switzerland

Preface

The collection of papers in this book was presented at the eleventh meeting of the International Conference on Protection of Materials from Space Environment—ICPMSE-11 held in Lijiang, China, in May of 2014. Since the first meeting in 1992, the ICPMSE conference has grown steadily, attracting a large number of engineers, scientists, researchers, and managers from industrial companies, scientific institutions, and government agencies in Canada, the USA, Asia, and Europe, thus becoming a true international event.

After the 10th ICPMSE meeting that has been held in Japan in 2011, the ICPMSE organizers were approached by Chinese scientists with an offer and an invitation to conduct the next meeting in China. After a series of consultations with the members of the organizing and program committees of the ICPMSE and discussions and meeting with our Chinese colleagues, a final decision was made to conduct the 11th ICPMSE meeting in China. The beautiful city of Lijiang was chosen as the venue for the meeting.

The 11th International Space Conference on "Protection of Materials from Space Environment" ICPMSE-11 organized by ITL Inc. (Integrity Testing Laboratory) and the Beijing Institute for Spacecraft Environment Engineering (BISEE) was held from 19 to 23 May 2014 in Lijiang, China. The Conference was sponsored by the Chinese Academy of Space Technologies (CAST) and a number of organizations. The goals of the meeting, as in previous years, were to facilitate exchanges between members of the various engineering disciplines involved in the development of space materials, including aspects such as environmental hazards of LEO, GEO, and Deep Space, ground-based qualification, and in-flight experiments and lessons learned from operational vehicles.

From being a duel-type space race between USSR and USA through the 1950s–1980s, with Europe joining it in the 1990s, the space exploration activities exploded in the 1990s with many countries like Japan, India, China, and others becoming major players in exploration of the space and the planets and comets.

In addition to the International Space Station that is fully functional by now with astronauts and cosmonauts servicing it and using for scientific and commercial

activities, other space laboratories like China's Tiangong 1, 2, and 3 were either launched already (Tiangong 1) or are being planned for launching in the next few years (Tiangong 2 and 3).

A number of ambitious space exploration programs were proposed that will see launching satellites to Moon orbits, landing on the Moon, and building Space Stations. The Mars exploration programs are also getting wider support and are gaining momentum. A common denominator to all activities of mankind in space is the safety of astronauts and cosmonauts and the reliability of the structures that are operating in conditions of space environment.

The influence of space environment on materials and structures will remain, therefore, a timely topic for years to come. Questions about thermal stability, resistance to radiation, resistance to combined effects of various space factors, etc., will continue to accumulate with the development of new materials and protective coatings.

As in past years, in addition to the traditional ICPMSE topics of protection of materials and structures from the atomic oxygen, VUV, and particle irradiation and thermal effects, topics covering micrometeoroids, space weather, and relevant protection issues for travel to Moon, Mars, other planets, and Deep Space exploration were added.

The 11th IPCMSE meeting, with a large majority of the over 150 papers being submitted by scientists from various Chinese space organizations, allowed offering to the Western scientists and engineers, working in the field of space environmental effects, a very rare glimpse into the work of numerous organizations in China in this area. Keeping in mind the increasing role that China is playing in the exploration of the space, we decided to use this unique opportunity and to publish most of the submitted papers in the proceedings. The delay in a timely publication of the proceedings was mainly due to the linguistic problems with editing of the proceedings.

ICPMSE-11 meeting covered a range of interdisciplinary topics concerning the protection of materials and structures in space. Its main objective is to continue the discussion on the effects of the aggressive Low Earth Orbit (LEO) as well as the GEO and Deep Space environments on materials and structures and to discuss ways predicting and reducing these for short- and long-term space missions. Over 150 contributions covering a wide range of topics on environmental issues were submitted with over 60 of them being published in these proceedings.

New generations of scientists in the last six decades were methodically studying the space environment and its effects on the materials. The coming generations of scientists will have to continue this work and tackle new challenges, continuing to build the wall of confidence allowing humans to continue the colonization of space. And we hope that ICPMSE-11 will be a small stone in that wall.

Markham, Canada
November, 2015

Organization

The 11th International Conference on "Protection of Materials and Structures from Space Environment" took place between 19 and 23 May 2014 in Lijiang, China

Chairmen:
Jacob Kleiman, ITL Inc., Canada
Liu Guoqing, Beijing Institute of Spacecraft Environment Engineering, China

Executive Chairman
Yao Jianting, Beijing Institute of Spacecraft Environment Engineering, China

Organizing Committee
Banks, Bruce A., NASA, USA
Briet, Richard, Centre National d'Etudes Spatiales (CNES), France
Cai Wei, State Key Laboratory on Space Materials and Environment, Harbin Institute of Technology, China
Duzellier Sophie, ONERA, France
Durin Christian, Centre National d'Etudes Spatiales (CNES), France Feng Weiquan, Beijing Institute of Spacecraft Environment Engineering, China
de Groh Kim K., NASA, USA
Edwards, David L., NASA, Huntsville, USA
Grossman, Eitan, Soreq NRC, Israel
Kimoto Yugo, JAXA, Japan
Minton, Timothy, Montana State University, USA
Nikanpour, Darius, Canadian Space Agency, Canada
Novikov, Lev S., Moscow State University, Russia
Roussel Jean-François, ONERA, France
Semprimoschnig Christopher O.A., European Space Agency, The Netherlands
Tagawa, Masahito, Kobe University, Japan
Van Eesbeek, Marc, European Space Agency, The Netherlands
Cao Yunzhen, Shanghai Institute of Ceramics, China

Yang Shengsheng, Lanzhou Institute of Physics, China

Program Committee
Cherniavsky, Anatoly. G., NPO Energia, Russia
Daly M., Space Engineering Department, York University, Canada
Golden, Johnny., Boeing, USA
Grigorievsky, Anatoly V., JSC Kompozit, Russia
Koontz, Steven, NASA, USA
Kim Daeweon, Seoul National University, Korea.
Remaury, Stephanie, Centre National d'Etudes Spatiales (CNES), France

Local Organizing Committee
Beijing Institute of Spacecraft Environment Engineering, China

Tao Tao
Yi Zhiqiang
Hu Songlin
Li Tianye

Acknowledgments

We would like to acknowledge the following for their generous support of the eleventh International Conference on Protection of Materials and Structures from Space Environment, ICPMSE-11, and the publication of these proceedings.

Sponsors:

- Chinese Academy of Space Technologies (CAST)
- Integrity Testing Laboratory Inc. (ITL)
- Beijing Institute for Spacecraft Environment Engineering (BISEE)

Cosponsors:
Beijing Aerospace Measurement & Control Technology Co., Ltd. (COSIC)\
National Key Laboratory of Material Behavior and Evaluation Technology in Space Environment (Harbin) (MBESE)
Procurement Department of China Academy of Space Technology (CASC)
Shenzhen Academy of Aerospace Technology (CASC)
Shenzhen Aerospace New Power Technology Ltd. (SANPT)

We are thankful to all sponsors and cosponsors without whose support the meeting would not be possible. We would also like to thank all members of the local Organizing Committee on whom the real burden of day-to-day organizational work fell. Special thanks go to our families and to many staff members of all sponsoring organizations that provided the level of understanding and support without which it would be impossible to put everything together.

Prof. Jacob Kleiman, Integrity Testing Laboratory, Inc.
Prof. Liu Guoqing, Beijing Institute of Spacecraft Environment Engineering, Chairmen-ICPMSE-11
Yao Jianting, Beijing Institute of Spacecraft Environment Engineering, Executive Chairman
November, 2015.

Contents

Protection of Materials and Structures from Space Environment—ICPMSE Proceedings Series: From Past to Present

Jacob Kleiman

Abstract A historical overview of the first ten meetings of the International Conference for Protection of Materials from Space Environment (ICPMSE) is presented. Through the published documents and pictures from personal archives the rich history of the meetings is illustrated. The collaborative links with ESA, CNES, ONERA and JAXA are described that helped to make the ICPMSE series of meeting a truly International event. The review is based on published ICPMSE proceedings as well as on personal archives of Prof. J. Kleiman who initiated the meeting in 1991.

Keywords ICPMSE • ISMSE • CNES • ONERA • JAXA • Kobe University • CSA

Introduction

This article presents an update of a paper presented by Dr. J. Kleiman at the 10th ICPMSE meeting in Okinawa, Japan [1]. It provides some additional details on the history of the ICPMSE meetings as well as the information on the last meeting conducted in Japan in 2011. Originally conceived as a brief overview in 2011, it will be updated as the meetings will continue to roll out.

Historical Overview

The initiation of ICPMSE meetings was triggered by the return of the Long Duration Exposure Facility (LDEF) satellite [2] that was brought back to Earth in 1989 from almost a 5-year stay in low Earth orbit (LEO). A number of successful

J. Kleiman (✉)
Integrity Testing Laboratory Inc., Markham, ON, Canada
e-mail: jkleiman@itlinc.com

J. Kleiman (ed.), *Protection of Materials and Structures from the Space Environment*, Astrophysics and Space Science Proceedings 47,
DOI 10.1007/978-3-319-19309-0_1

LDEF meetings in USA followed, where the results from exposure of numerous materials to LEO orbit environment were discussed. The UTIAS materials scientific team led by Prof. R.C. Tennyson, who was one of the principal investigators on the UTIAS LDEF Material's experiment team, participated actively and contributed to the LDEF meetings. When the LDEF meetings stopped, Dr. Kleiman, then a Research Scientist with the R&D Group of 3M Canada and an Adjunct Professor at the UTIAS, who worked closely with the space materials group at the UTIAS, soon realized that the North American space environment community is lacking a meeting place where the latest developments in new space materials, their behavior in LEO and other space environments, the results from ground based experiments and from flights can be shared and discussed. And that is how the first ICPMSE meeting was initiated in 1991.

Another, very instrumental factor in the initiation of the ICPMSE series of conferences was the Canadian Space Agency's Strategic Technologies for Automation and Robotics (STEAR) Program [3]. Through the STEAR Program, CSA promoted the advancement of strategic space technologies, including those contributing to the longevity of materials and structures in the space environment. As part of this effort, a program on development of new protective coatings was conducted during the period 1991–1995. The first ICPMSE meeting was devoted largely to the results of this STEAR program (Figs. 1, 2, 3 and 4).

With years, however, the meeting became a focal gathering point in North America for scientists, researchers, managers, students and academicians to discuss the latest developments in the area of interaction of materials and structures with the harsh space environment. Initially, the ICPMSE meetings were focused, mainly, on the effects of the low Earth orbit environment on materials. But with time it became clear that there is an intimate relationship between the various space environment factors and gradually, the scope of the meetings widened, including also the GEO and other environments. Also, following the worldwide space community plans for the colonization of the Moon and Mars, it was decided to add to the topics of the ICPMSE meetings the planetary and the interplanetary environments (Figs. 5, 6, 7 and 8).

Very soon, from being a North American event, the ICPMSE meetings became a truly international event, attracting scientists from Europe, Asia and other parts of the world. Being a biannual event, the ICPMSE meeting coincided in the year 2000 with another international meeting, the International Symposium on Materials in a Space Environment (ISMSE) that was organized since 1979 in Europe by CNES, ONERA and ESA every 3 years. A mutual decision was made by the ICPMSE and ISMSE organizers to conduct in such "coinciding" years both meetings jointly in Europe. First such joined meeting was conducted in the year 2000 in Arcachon

Fig. 1 The first meeting ICPMSE-1 in Toronto, Canada, 20–21 February, 1992. (**a**) Lunch arranged at the STEAR Program final projects exhibition; (**b**) participants of the ICPMSE-1; (**c**) Gary Pippin and Jacob Kleiman during the question period; (**d**) Prof. R. Tennyson explains the UTIAS LDEF experiment (seen on the table in front of him); (**e**) the front page of the proceedings and (**f**) the announcement brochure of the meeting

Fig. 2 The third meeting ICPMSE-3 in Toronto, Canada, 25–26 April, 1996. (**a**) The front page of the proceedings of the ICPMSE—3 [4]; (**b**) a group of participants from Russia, Israel, USA and Netherlands on a coffee break; (**c**) participants of the Ukrainian delegation at ICPMSE-3 with Canadian hosts; (**d**) round table panel of speakers after one of the sessions; (**e**) even lunches were used for discussions

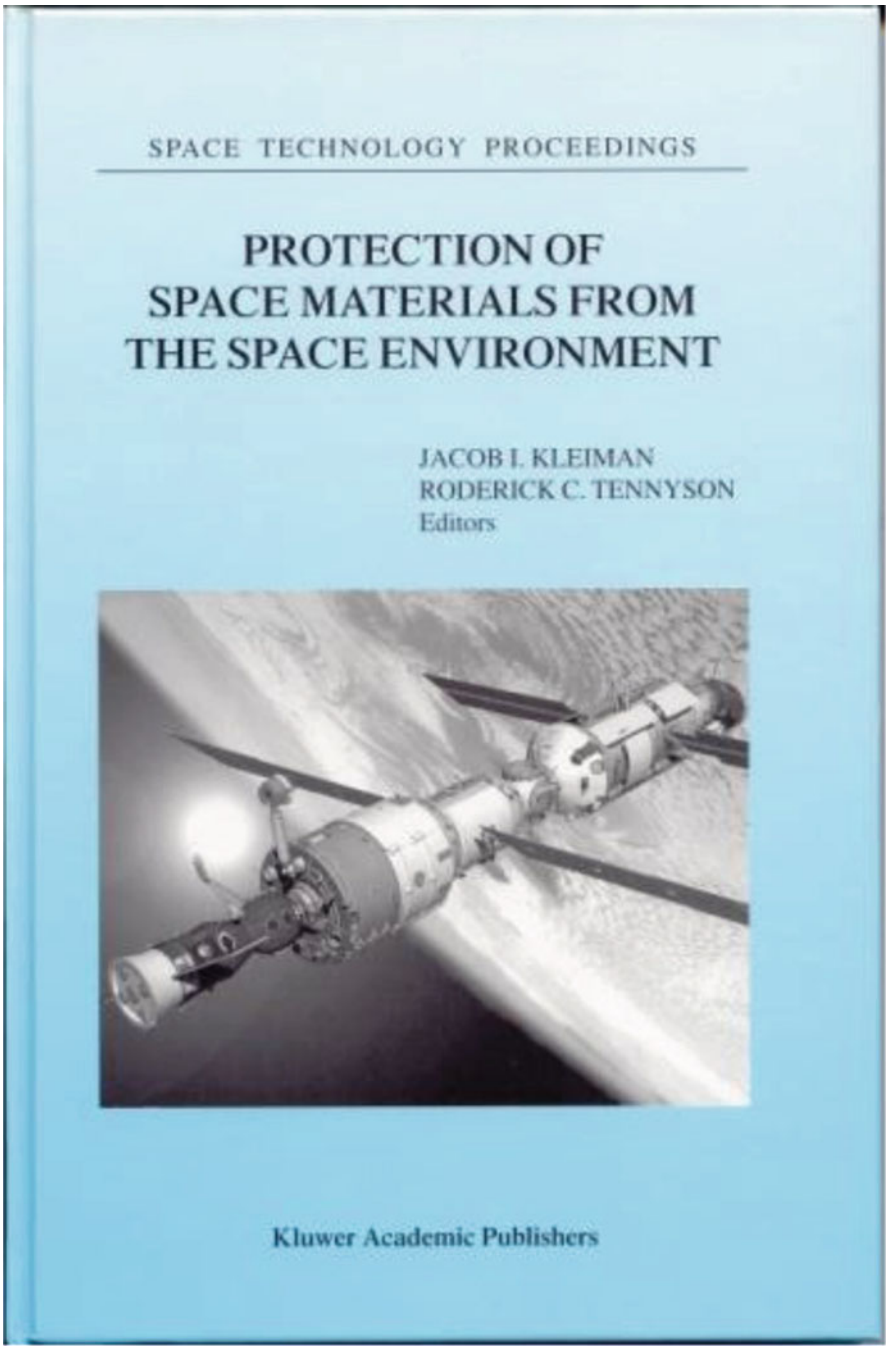

Fig. 3 The front page of the Proceedings of the ICPMSE—4: Toronto, Canada, 23–24 April, 1998, [5]

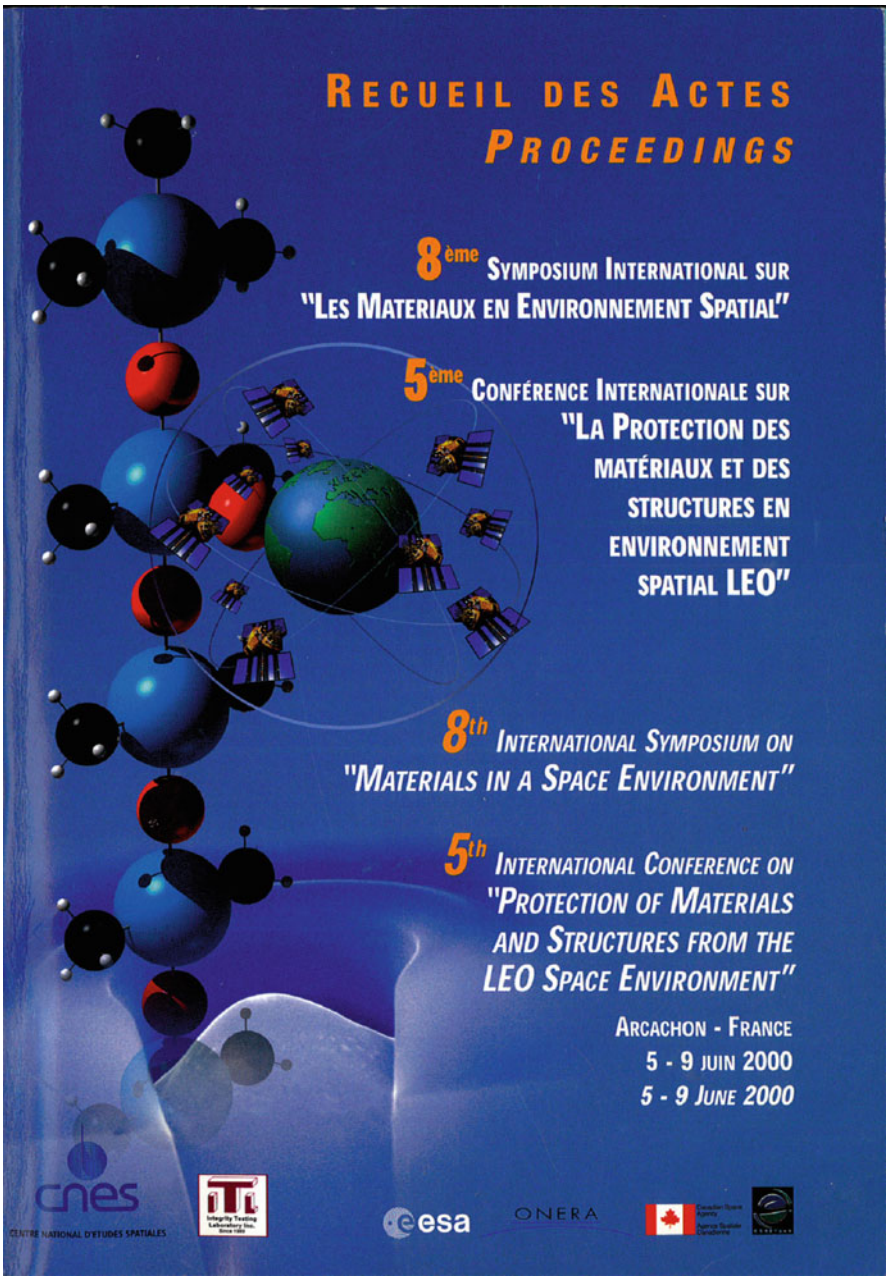

Fig. 4 Front page of ICPMSE–5 proceedings: Arcachon, France, 5–9 June, 2000, [6]

Fig. 5 The sixth meeting ICPMSE-6 in Toronto, Canada, May 10–13, 2004. (**a**) Members of the Russian delegation on a after-conference trip to Niagara Falls with ITL hosts; (**b**) conference dinner—a not to miss event at the meetings; (**c**) participants of the ICPMSE-6; (**d**) Bruce Banks delivers a talk at a session chaired by Tim Minton; (**e**) the front page of the proceedings of ICPMSE—6 [7]

Fig. 6 Special edition of JSR with selected papers from the ICPMSE-6 meeting, [8]

(ICPMSE-5/ISMSE-8). The next such meeting was in 2006 in Collioure, France (ICPMSE-8/ISMSE-10) (Figs. 9, 10, 11 and 12).

Starting from the 3rd ICPMSE meeting in 1998, Dr. Kleiman initiated the publishing of the Proceedings of the meetings as peer reviewed hard-cover books with such reputable publishing houses as Kluwer, Springer and the American Institute of Physics. In addition to such publications, the papers presented at the

Fig. 7 The seventh meeting ICPMSE-7 in Toronto, Canada, May 10–13, 2004. (**a**) The front page of the proceedings of the ICPMSE—7 [9]; (**b**) Dr. D. Edwards delivers the after dinner talk to an attentive audience; (**c**) cocktail hour before the dinner; (**d**) Dr. G. Pippin with American colleagues; (**e**) Dr. Z. Iskanderova in front of an improvised show of technical space literature that she organized during the meeting; (**f**) Prof. R. C. Tennyson (standing) and Prof. P. Hughes in a question period at the after dinner talk; (**g**) Russian guests with Prof. J. Kleiman on a tour of Edwards Gardens in Toronto

ICPMSE meetings were repeatedly published in special editions of such peer-reviewed journals as Journal of Spacecraft and Rockets and in High Performance Polymers.

Starting from 2008 it was decided to acknowledge at the meeting the distinguished scientists who contributed to the science and knowledge of the space environment interaction with materials and structures. And as a first, the retirement of two distinguished scientists, Prof. R.C. Tennyson and Dr. B. Banks was celebrated at the gala dinner of the ICPMSE-9 in Toronto.

With many countries joining the space community and actively contributing to the space environmental studies, it was the next logical step to extend the organizational effort of the ICPMSE meetings to other organizations and countries. In 2010 Japan expressed an interest to co-organize the next ICPMSE Meeting and conduct it in Japan. And the jubilee 10th ICPMSE meeting that was organized

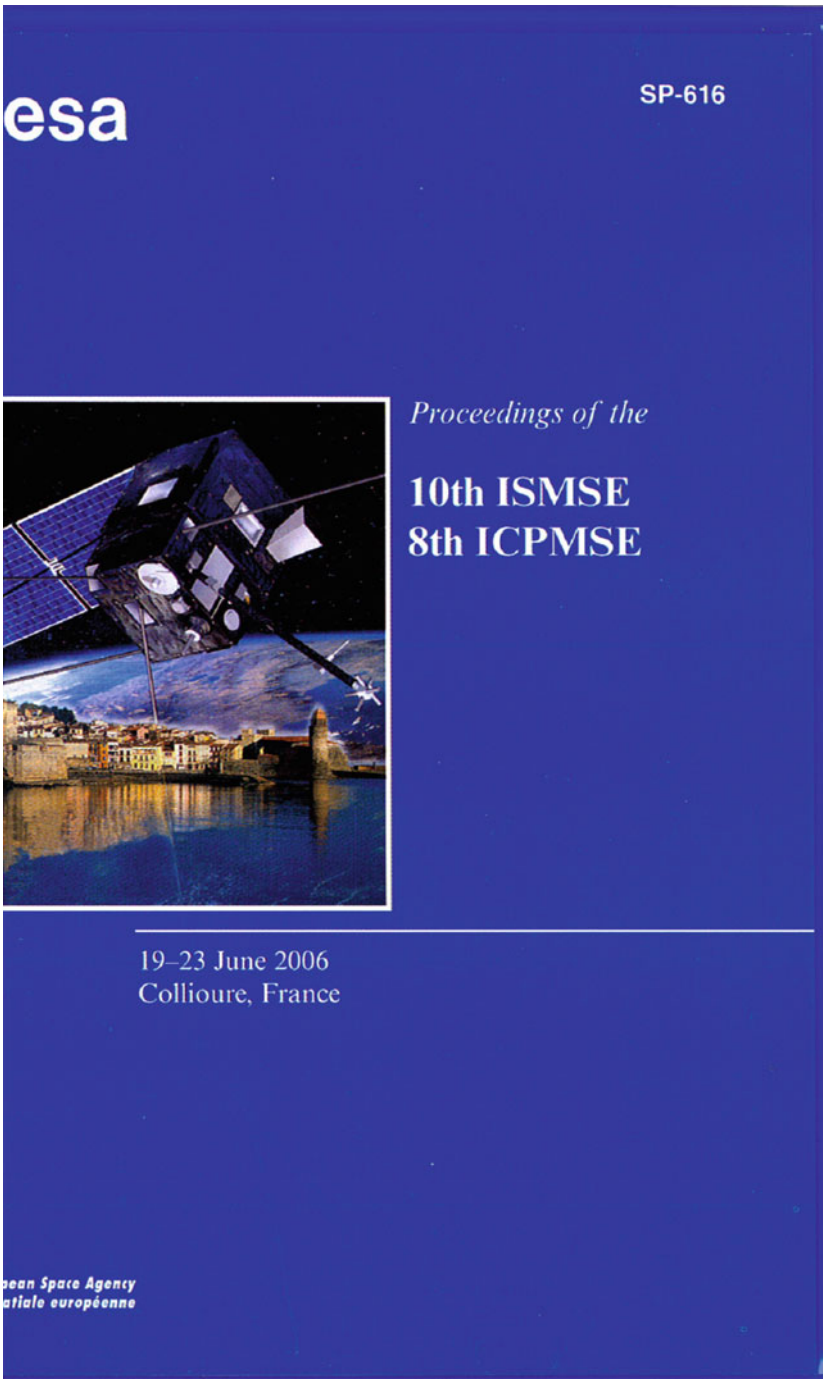

Fig. 8 The front page of the CD with the proceedings of ICPMSE—8: Collioure, France, 19–23 June, 2006, [10]

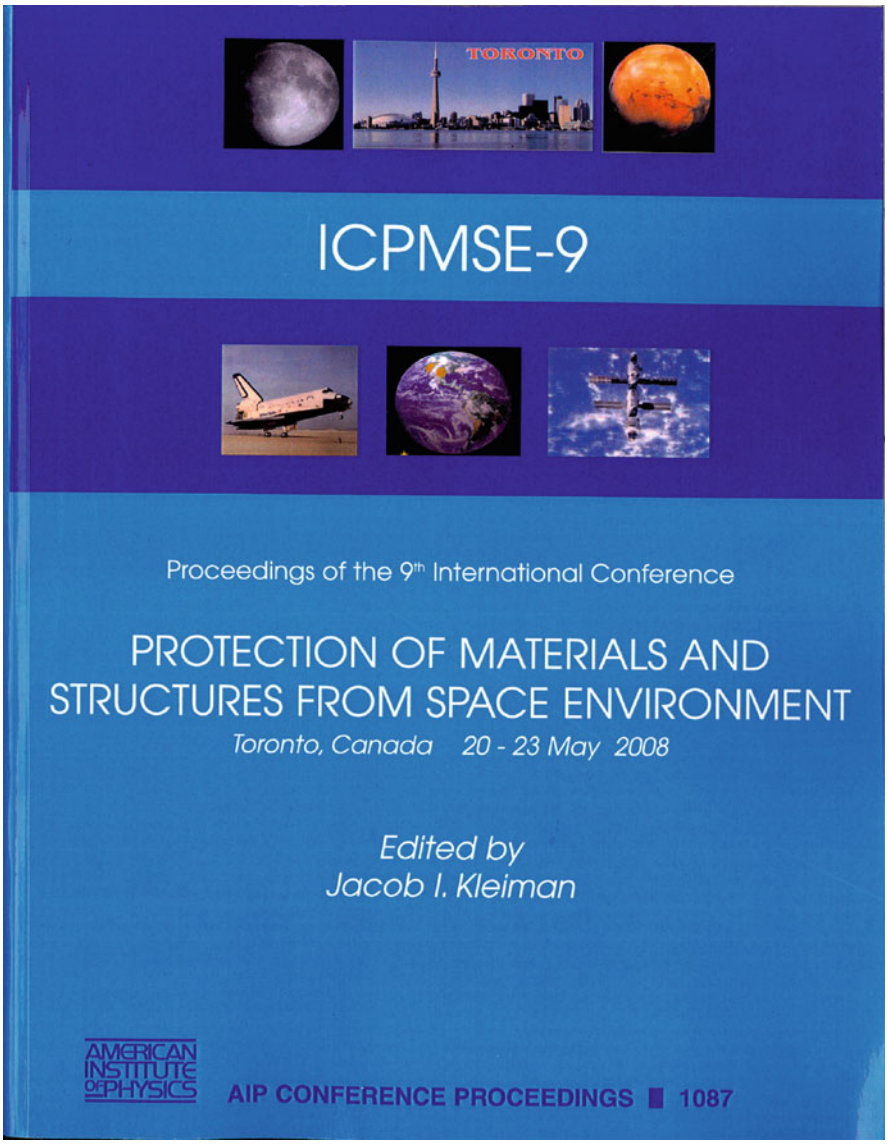

Fig. 9 The front page of the proceedings ICPMSE—9: Toronto, Canada, May 20–23, 2008, [11]

jointly by Canada and Japan took place between 12 and 17 June, 2011 in Okinawa, Japan. The success of the meeting encouraged continuing this policy and the next 11th ICPMSE meeting travelled to China where it was jointly organized by ITL and the Beijing Institute for Space Environmental Engineering (BISEE) in Lijiang on 13–19 June, 2014.

Fig. 10 Mementos from the ICPMSE-9 meeting. (**a**) Participants of the ICPMSE-9; (**b**) conference dinner—as usual, a not to miss event at the meetings; (**c**) and of course nothing can come close to a real Russian dance; (**d**) members of the USA delegation with J. Kleiman; (**e**) Canadian hosts proved that not only in France you can catch a glimpse of a real Can–Can dance; (**f**) members of the Korean delegation at lunch

One of the traditions of the ICPMSE meetings was to publish the proceedings as hard cover books. The images that are accompanying this write-up present some mementos from the past meetings and provide a brief account of the past meetings' Proceedings.

Fig. 11 The retirement of two distinguished scientists, Prof. R.C. Tennyson (*left*) and Dr. B. Banks (*centre*) was celebrated at the gala dinner of the ICPMSE-9 in Toronto. And as Bruce proved in the picture on the *right*, he can be funny too

Fig. 12 The tenth meeting ICPMSE-10J in Okinawa, Japan, June 12–17, 2011. (**a**) Group photo outside the Bankoku Shinryo-kan; (**b**) the cover page of the proceedings ICPMSE—10J [1]

References

1. Kleiman JI, Tagawa M, Kimoto Y (eds) (2013) Astrophysics and space science proceedings, vol 32. Protection of materials and structures from the space environment. In: Proceedings of the 10th international conference, ICPMSE-10J, Bankoku-Shinryokan, Okinawa, Japan, 12–17 June 2011. Springer
2. http://en.wikipedia.org/wiki/Long_Duration_Exposure_Facility
3. Francoeur JR (1992) The Canadian space agency, space station, strategic technologies for automation and robotics program technology development activity in protection of materials from the low Earth orbit space environment. In: Second LDEF post-retrieval symposium abstracts, NASA. Langley Research Center, 1 June 1992, p 128
4. Kleiman JI, Tennyson RC (eds) (1999) Space technology proceedings, vol 2. Protection of materials and structures from the low Earth orbit space environment. In: Proceedings of the

ICPMSE-3, third international conference, Toronto, Canada, 25–26 April 1996. Kluwer Academic Publishers. ISBN:0-7923-5540-7
5. Kleiman JI, Tennyson RC (eds) (2001) Space technology proceedings, vol 4. Protection of space materials from the space environment. In: Proceedings of the ICPMSE-4, fourth international conference, Toronto, Canada, 23–24 April 1998. Kluwer Academic Publishers. ISBN:0-7923-6981-5
6. Protection of space materials and structures from the LEO space environment. In: Proceedings of the ICPMSE-5, fifth international conference held in conjunction with the 8th international symposium on materials in a space environment, Arcachon, France, 5–9 June 2000. Available on CD only
7. Kleiman JI, Iskanderova Z (eds) (2003) Space technology proceedings, vol 5. Protection of materials and structures from space environment. In: Proceedings of the ICPMSE-6, sixth international conference, Toronto, Canada, 1–3 May 2002. Kluwer Academic Publishers. ISBN:1-4020-1690-5
8. Edwards D, Kleiman J (eds) (2004) Selected papers from the sixth international conference, ICPMSE-6, Toronto, Canada, 1–3 May 2002. J Spacecr Rockets 41(3):321–480. ISSN:0022-4650
9. Kleiman JI (ed) (2006) Space technology proceedings, vol 6. Protection of materials and structures from the space environment. In: Proceedings of the ICPMSE-7, seventh international conference, Toronto, Canada, 10–13 May 2004. Springer. ISBN:10 1-4020-4281-7 (HB)
10. Protection of materials and structures from the space environment. In: Proceedings of the ICPMSE-8, eighth international conference held in conjunction with the 10th international symposium on “Materials in a space environment”, Collioure, France, 19–23 June 2006. Available on CD only.
11. Kleiman JI (ed) (2009) Protection of materials and structures from space environment. In: Proceedings of the 9th international conference, ICPMSE-9, Toronto, Canada, 20–23 May 2008. AIP Conference Proceedings 1087. ISBN:978-0-7354-0619-3

Development of a Chromium Free Anticorrosion Primer

G. Sierra, S. Reymond, O. Guillaumon, S. Remaury, and P. Nabarra

Abstract MAPSIL® SILICo has been developed to substitute current chromium-based anticorrosion primers (Sierra, Cr free anticorrosion primers and treatments, 2012; Sierra, MAP management according European regulations for critical substances, 2013). This product complies with following launchers and satellites specifications:

1. Outgassing compliance with the ECSS-Q-70-02C standard for satellite materials (ESA, Thermal vacuum outgassing test for the screening of space materials, 2008);
2. Compliant behaviour towards space environment which includes UV, e−, p+ and γ irradiations on Earth;
3. Environmental tests behaviour: damp heat test and salt spray test;
4. Good adhesion on aluminum substrates (7075-T0, 6061-T6, 2024-T3) and steel substrates for launcher applications;
5. Compatibility with silicone and polyurethane paints used for satellites (SG121FD, PNC, MAP® AQ PU1…) and launchers (MAP® AQ STATIC, MAPSIL® AS…) (Remaury, White antistatic paint for launcher: MAP® AQ STATIC, CNES report, DCT-TV-TH-NT11-4384, 2011; Remaury, Black polyurethane waterborne non electrically conductive paint: MAP AQ PU1, CNES report, DCT-TV-TH-NT11-3938, 2011; Remaury, White antistatic coating for thermal protection of VEAG and ARIANE 5 launchers: MAPSIL® AS, CNES report, DCT-TV-TH-NT11-5588, 2011).

MAPSIL® SILICo has been developed in accordance with ISO 9001 and EN9100 standards ensuring quality of the products. This product is ITAR and EAR free as it is a co-development of a French company (MAP) and the French Space Agency (CNES).

G. Sierra (✉) • S. Reymond • O. Guillaumon
MAP, ZI—2 Rue Clément Ader, 09100 Pamiers, France
e-mail: g.sierra@map-coatings.com

S. Remaury (✉) • P. Nabarra
CNES, 18, Avenue Edouard Belin, 31401 Toulouse Cedex 9, France
e-mail: Stephanie.Remaury@cnes.fr

J. Kleiman (ed.), *Protection of Materials and Structures from the Space Environment*, Astrophysics and Space Science Proceedings 47,
DOI 10.1007/978-3-319-19309-0_2

Keywords Anticorrosion primer • Launcher • Satellite • MAPSIL® SILICo • MAPSIL® SILICo AS • REACh

Introduction

In order to reduce its impacts on human health and on environment, MAP has decided to develop alternative products to the current ones according to the REACh regulation. As far as the products are concerned, MAP has developed, case by case, since 2008, under CNES Research and Technology contracts, "Chromium free solutions", as alternative products to chromated primers.

MAPSIL® SILICo has been developed to substitute current chromium-based anticorrosion primers [1, 2]. This product complies with following launchers and satellites specifications:

1. Outgassing compliance with the ECSS-Q-70-02C standard for satellite materials [3];
2. Behaviour towards space environment which includes UV, e−, p + and γ irradiations on Earth;
3. Environmental tests behaviour: damp heat test and salt spray test;
4. Good adhesion on aluminum substrates (7075-T0, 6061-T6, 2024-T3) and steel substrates for launcher applications;
5. Compatibility with silicone and polyurethane paints used for satellites (SG121FD, PNC, MAP® AQ PU1...) and launchers (MAP® AQ STATIC, MAPSIL® AS...) [4–7].

Moreover, the following specific technical requirements were taken into account:

1. Room temperature curing and heat curing;
2. Only degreasing of the substrates—no use of pickling treatment for instance;
3. Spraying application;
4. Low thickness application, 2–4 μm for satellites and 8–15 μm for launchers applications;
5. Electrical conductivity of the substrate kept in low thickness application.

This paper presents, in the first part, the specifications of the anticorrosion protection for satellite and launchers applications. In the second part, the properties of MAPSIL® SILICo are presented. Finally, the qualification results obtained with MAPSIL® SILICo and MAPSIL® SILICo AS are presented.

Space Industry Requirements

Technical Specifications

As the satellite and launchers can be stored several weeks or months before launching, corrosion phenomena could occur on Earth. In order to prevent satellite parts and launchers from this potential issue, anticorrosion products are used before applying thermal control coatings for satellite and antistatic coatings for launchers.

For instance, on Ariane 5 launcher, polyurethane based antistatic coating MAP AERO STATIC B is applied on metallic and composite parts to provide antistatic protection. Before applying this coating and in order to provide anticorrosion protection MAP AERO WP and MAP AERO P primers are applied.

For satellite, and for the same reason as for launchers, chromated primers such as Phosmap 11 are applied on metallic parts before applying thermal control coatings such as SG121FD, PNC. . . Moreover, most of the aluminium alloys used are treated with Alodine 1200, which is a Cr^{VI} based surface treatment.

Regulatory Specifications

In the European Union, the REACh regulation (Registration, Evaluation, Authorization and restriction of Chemicals) is applicable since 2006. The REACh regulation tends to limit the use of hazardous substances in order to prevent human health and environment. The most critical substances such as Cr^{VI} will require authorization process. Since 2008, taking into account this regulation it has been decided to substitute Cr^{VI} based products. Since this date, most of the alternative products were developed and qualified in 2013. Indeed, the use of these substances will still be authorized until 2018.

MAPSIL® SILICO Specifications for Thin Film Substitution

Typical requirements of anticorrosion products for space uses are based upon (1) damp heat test and (2) salt spray test.

The damp heat test has been done following the ISO 6270 standard [8]. The main parameters of the test were as follows: (1) $T = 85\ ^{\circ}C$, (2) Relative humidity of 95 %, and (3) duration of 14 days. The conformance criteria were the following:

Corrosion: <5 pits for a 130×80 mm area;
Electrical resistance: <5 mW following ASTM D257-07 standard [9].

The salt spray test was done following the ISO 9227 NSS [10] and ASTM B117 [11] standards. The main parameters were as follows: (1) T = 35 °C and (2) NaCl concentration of 5 %. The conformance criteria were the following:

Corrosion: <5 pits for a 130 × 80 mm area;
Duration: 72 h minimum.

For both tests, the materials used were the aluminium alloys 7075-T0, 6061-T6 and 2024-T3. For the surface preparation we only used a degreasing step with isopropylic alcohol. All the samples were applied using spray gun pulverization with a surface mass of 1.5–3.0 g m^{-2} resulting in a thickness between 2 and 4 μm.

MAPSIL® SILICO Specifications for Thick Film Substitution

For thick film substitution (launcher uses), only salt spray test is required to evaluate the corrosion resistance. This test has been done following the same standards as previously mentioned. Only the conformance criteria changed, they are defined hereunder:

Corrosion: no damage over 3 mm on both sides of the cut (crossed cut);
Duration: more than 500 h for aluminium alloys and 168 h for steel;
Electrical resistance: no requirement.

The materials tested were the aluminium alloys 7075-T0, 6061-T6 and 2024-T3. The surface preparation consisted in degreasing the surface using isopropylic alcohol. All the samples were applied using spray gun pulverization with a surface mass of 3.0–6.0 g m^{-2} resulting in a thickness between 8 and 15 μm.

MAPSIL® SILICO Properties

The MAPSIL® SILICo anticorrosion primer is a poly-condensation silicone based product which curing cycle could be either obtained at room temperature (23 °C) or by accelerated heat curing (up to 100 °C). The MAPSIL® SILICo is a 2 component product composed of a base and a hardener. The mixing base/hardener weight ratio is 85/15. Standard curing cycle is obtained at room temperature during 48 h. The colour of the base is white, whereas the hardener is translucent. The density of the product is 1.13. Outgassing test has been carried out by INTESPACE laboratory. The RML has been measured at 0.52 % and the CVCM at 0.01 %.

This product is REACh compliant, ITAR and EAR free. Only degreasing of substrates is required. This product is applied by spray gun pulverization.

Table 1 Evolution of electrical surface resistivity versus surface treatment and corresponding thicknesses

Aluminium alloy	Surface treatment	Thickness (μm)	R_S (kΩ/□)
7075-T0	MAPSIL® SILICo	2	55
		8	80
2017-T4	Alodine	3	400

MAPSIL SILICO Qualification Results

Satellite Applications

For the anticorrosion evaluation, the results of damp heat test and the salt spray test were compliant: no defects were observed after respectively 14 days and 72 h.

The evolution of electrical surface resistivity versus thickness was also measured. The results are presented in Table 1.

Launchers Applications

The electrical surface resistance of the metallic substrate remains the same using MAPSIL® SILICo, even with thicknesses as thin as 8 μm. On the opposite, with the Alodine 1200 coating, the electrical surface resistance was ten times greater.

MAPSIL® SILICo meets the satellite requirements, therefore it could be an alternative to chromate based conversion coatings such as Alodine 1200. MAPSIL® SILICO has been CNES qualified with MAP® AQ PU1 thermal control coating and with MAPSIL® QS1123 ELEC LD, a silicone adhesive for OSR bonding.

MAPSIL® SILICo Results

For the anticorrosion evaluation, the salt spray test results were compliant, no defects were observed after more than 200 h depending on the substrate nature (Table 2).

Moreover, the MAPSIL® SILICo has been tested and qualified by CNES with both antistatic paints MAP® AQ STATIC and MAPSIL® AS.

Table 2 Duration of the salt spray test depending on the substrate nature

Substrate	Thickness (µm)	Duration (h)
2024-T3	42	>500
7075-T0	10	>1500
Steel	40	>200

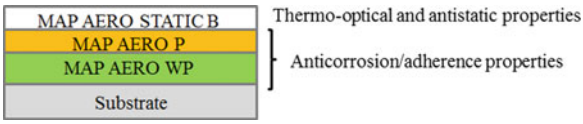

Fig. 1 Current whole system for launcher

Table 3 Evolution of thermo-optical properties and electrical surface resistance versus thickness

Thickness	22 µm	40 µm	52 µm
α_S	0.46	0.40	0.39
ε_{IR}	0.91	0.91	0.91
R_S (MΩ/□)	0.06	0.35	2.00

MAPSIL® SILICO AS Properties

Based upon the MAPSIL® SILICo formulation we have developed the MAPSIL® SILICO AS product which can ensure anticorrosion protection and provide antistatic properties. One product could replace the current whole system used (Fig.1).

To reach a good compromise between thermo-optical properties (α_S and ε_R), and antistatic behaviour (R_S), a minimum thickness of 40 µm is required (Table 3).

Conclusions

MAPSIL® SILICo was developed to provide a Chromium free, corrosion protection for light aluminum alloys and to be covered by thermal control coatings and antistatic paints. For launcher use, MAPSIL® SILICo applied as a thick layer (8–15 µm) provides a good corrosion resistance on aluminum alloys and steel. For satellite use and Alodine 1200 substitution, applied as a 2–4 µm thick layer MAPSIL® SILICo provides anticorrosion protection and electrical conductivity. This product has been already qualified by CNES with white antistatic coatings for launchers and thermal control coatings for satellites.

MAPSIL® SILICo AS has been developed for launcher use, to provide anticorrosion protection, antistatic and thermo-optical properties, to replace the current whole system (MAP AERO WP + MAP AERO P + MAP AERO STATIC B)

References

1. Sierra G (2012) Cr free anticorrosion primers and treatments. In: 3rd electronic materials and assembly processes for space, workshop, Genoa, Italy
2. Sierra G (2013) MAP management according European regulations for critical substances. In: NASA international workshop on environment and alternative energy 2013, Frascati, Italy
3. ESA (2008) Thermal vacuum outgassing test for the screening of space materials
4. Remaury S (2011) White antistatic paint for launcher: MAP® AQ STATIC, CNES report, DCT-TV-TH-NT11-4384
5. Remaury S (2011) Black polyurethane waterborne non electrically conductive paint: MAP AQ PU1, CNES report, DCT-TV-TH-NT11-3938
6. Remaury S (2011) White antistatic coating for thermal protection of VEAG and ARIANE 5 launchers: MAPSIL® AS, CNES report, DCT-TV-TH-NT11-5588
7. Remaury S (2013) Qualification of MAPSIL® QS1123 ELEC LD adhesive, CNES report, DCT-TV-TH 2013–2456
8. ISO 6270-2: 2005 standard, Paints and varneshes – determination of resistance to humidity
9. ASTM D257-07, Standard test methods for DC resistance or conductance of insulating materials
10. ISO 9227 NSS, 2006–07–15, Corrosion tests in artificial atmospheres – salt spray tests
11. ASTM B117-16, Book a standards 03. 02, Standard practice for operating salt spray (Fog) apparatus

Analysis of Materials' Specimens After Long-Term Exposure on ISS Surface in Komplast Experiment

S.K. Shaevich, N.G. Aleksandrov, A.E. Shumov, L.S. Novikov, V.N. Chernik, V.P. Petukhov, M.S. Samokhina, V.V. Sedov, I.A. Salnikova, D.J. Shindo, J.L. Golden, and M. Kravchenko

Abstract The article presents the first results obtained from the unique long-duration exposure experiment (12 years) on board of the International Space Station (ISS). The Komplast materials experiment was designed by the Khrunichev State Research and Production Space Center, together with other Russian scientific centers, and has been carried out since 1998. Eight Komplast panels with material samples and temperature sensors were located on the external surface of ISS Functional Cargo Block (FGB) module. In March 2011 two of eight panels were returned from ISS by Space Shuttle "Discovery". Post-flight investigations of specimens were carried out at Skobeltsyn Institute of Nuclear Physics, Lomonosov Moscow State University (SINP MSU) and at other Russian scientific institutes.

Keywords Spacecraft materials • Space environment • Long-duration exposure • Post-flight investigation

S.K. Shaevich • N.G. Aleksandrov • A.E. Shumov
Khrunichev State Research and Production Space Center (KhSC), Moscow, Russia

L.S. Novikov (✉) • V.N. Chernik • V.P. Petukhov • M.S. Samokhina
Lomonosov Moscow State University, Skobeltsyn Institute of Nuclear Physics, Moscow, Russia
e-mail: novikov@sinp.msu.ru

V.V. Sedov • I.A. Salnikova
Research Institute of Elastomeric Materials and Products, Moscow, Russia

D.J. Shindo
Materials and Processes Branch, NASA Johnson Space Center, Houston, TX, USA

J.L. Golden • M. Kravchenko
Boeing Research & Technology, Houston, TX, USA

J. Kleiman (ed.), *Protection of Materials and Structures from the Space Environment*, Astrophysics and Space Science Proceedings 47,
DOI 10.1007/978-3-319-19309-0_3

Introduction

The Komplast experiment, designed by the Khrunichev State Research and Production Space Center together with SINP MSU and other Russian scientific institutes, has been carried out since 1998. Its purpose was to study the effect of the low-Earth orbit (LEO) environment on samples of various spacecraft materials. Eight Komplast panels with material samples and sensors were located on the exterior surface of ISS Functional Cargo Block (FGB) module. The panels were delivered to orbit together with FGB on November 20, 1998.

Two of eight experiment panels (Panels 2 and 10) were retrieved during Russian extravehicular activity in February 2011 after 12 years of LEO exposure, and were subsequently returned to the Earth by Space Shuttle "Discovery" on the STS-133/ULF-5 mission on March 9, 2011.

Panel 2 contained polished samples to detect hard microparticles impacts, temperature sensor, several pieces of electrical cable, and samples of elastomeric and fluoroplastic materials. A temperature sensor, carbon composite and adhesive-bonded samples were placed on Panel 10.

So in this experiment, space environmental effects (SEE) on exposed specimens of various materials were studied in LEO as part of the ISS program.

The experiments similar to the Komplast experiment, in which specimens of spacecraft materials were exposed on the external surfaces of orbital stations for a given period of time, have been conducted on many occasions [1, 2]. The uniqueness of the Komplast experiment lies in its long duration of *in-situ* exposure of material specimens (12 years) on the FGB surface, significantly exceeding the exposure time of specimens in previous SEE experiments.

In this paper we present some results of *in-situ* measurements and post-flight laboratory tests of specimens that were exposed on the panels.

In-Flight Experiment

Figure 1 shows the FGB module with Komplast Panels 2 and 10 (marked with arrows) immediately after launch in 1998, and Fig. 2 shows closer views of these panels on the surface of the FGB in flight.

During all 12 years of flight the temperature of both Komplast panels was measured. Figure 3 shows an example of periodic changes in the temperature of Panel 2 due to the ISS rotation, and in Fig. 4 the maximum and minimum values of this panel temperature which were registries in 1999–2008 are presented. On Panel 2, the maximum and minimum temperatures recorded were +85 and −80 °C, on Panel 10 these values were +107 and −80 °C, correspondingly.

The total exposure to solar ultraviolet radiation was determined analysing the temperature dynamics and was estimated at 960 ± 200 kJ/cm^2, or $21{,}100 \pm 4400$ ESH (equivalent sun hours).

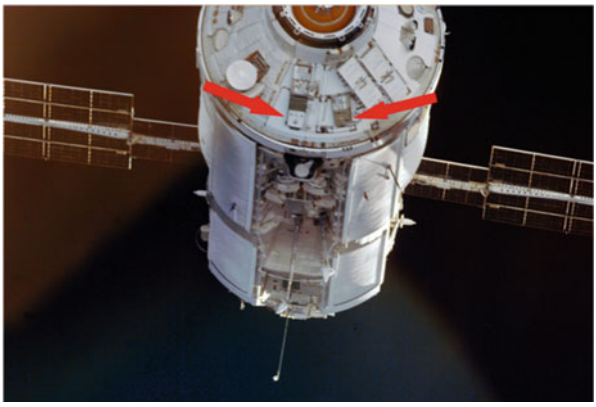

Fig. 1 FGB with mounted Komplast panels 2 and 10, 1998

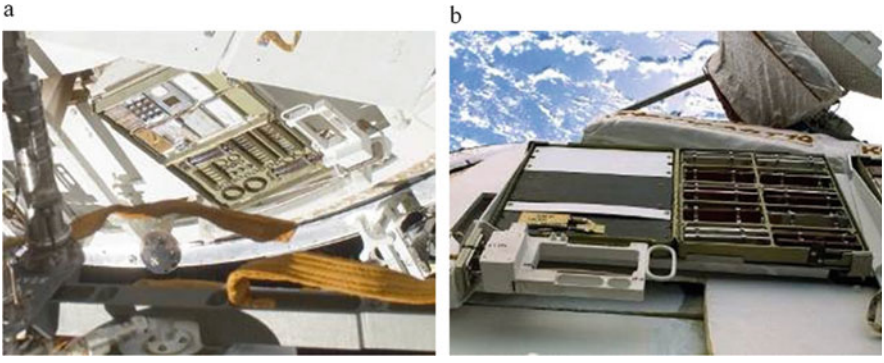

Fig. 2 Komplast Panel 2 (**a**) and Panel 10 (**b**) on the FGB surface

Atomic oxygen (AO) fluence was estimated approximately at 1.5×10^{21} atoms/cm^2. For this estimation the data on similar materials erosion under AO impact that had been obtained in previous experiments was used [2]. The fluence was evaluated for the entire 12-year period of panel exposure on the FGB and accounts for both the initial flight with random orientation and the modern flight period, during which the FGB end cone (on which Panels 2 and 10 were mounted) was not directly exposed to the ram AO.

During extravehicular activity Russian ISS astronauts removed two panels with samples from the FGB surface and put them into special container in vacuum before entering ISS. Inside this sealed container the panels were returned to Earth by Space Shuttle "Discovery".

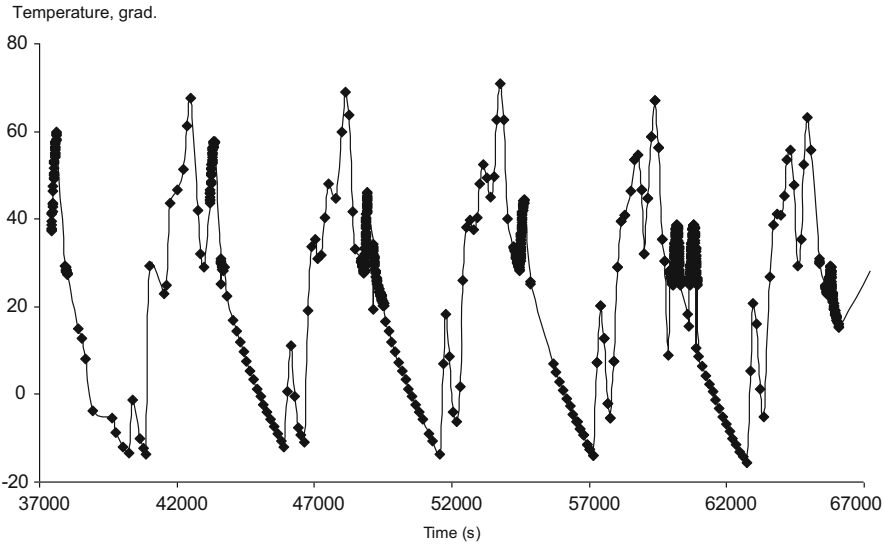

Fig. 3 Changes in the temperature (Degrees Celsius) of Panel 2 due to the ISS rotation around its axis, observed at 26.02.2000

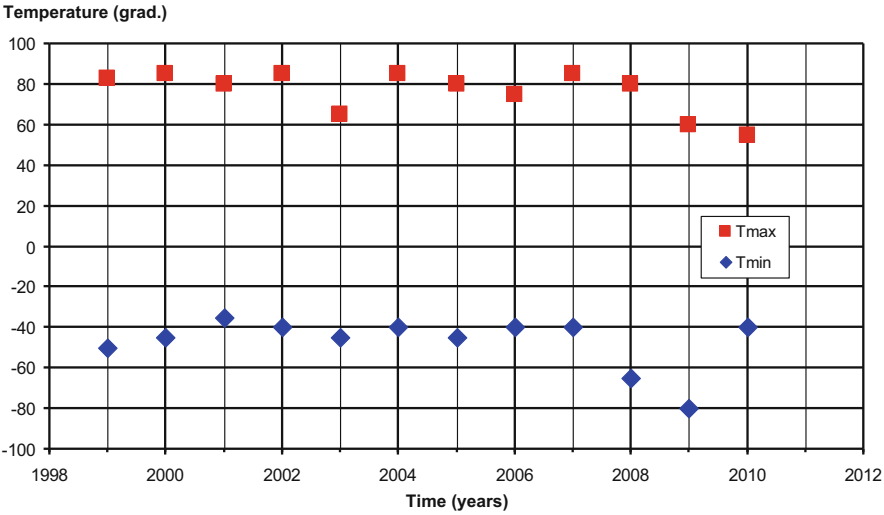

Fig. 4 Maximum and minimum values of Panel 2 temperatures in 1999–2008

Results of the Post-Flight Investigation

On July 12, 2011 in the special argon-filled chamber the container was opened, and the panels were retrieved from it and unfolded (Fig. 5).

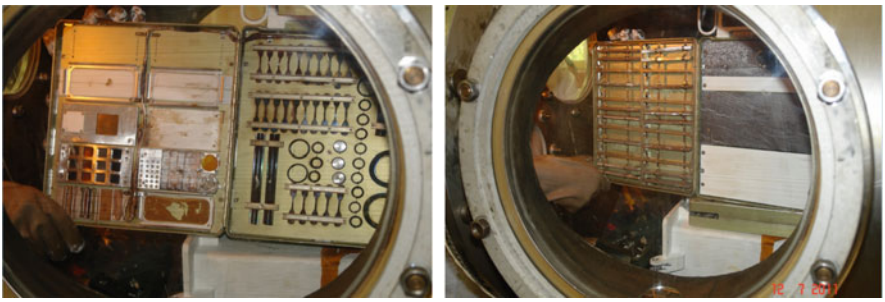

Fig. 5 The view of Panel 2 (*left*) and Panel 10 (*right*) through the window of the argon-filled chamber

The following specimens were set on the panels: Panel 2—rubber specimens, technical fabric and films, cable fragments, a microparticle sensor (12 polished samples), a temperature sensor; Panel 10—adhesive-bonded samples, carbon-reinforced plastics, Teflon specimens, and a temperature sensor.

The research performed included:

1. Surface investigation and measurements of mechanical parameters of samples;
2. Investigation of surface contamination;
3. Determination of quantity and size of craters on polished samples and the panel surface.

A distinctive feature of the conducted research was the additional ground-based irradiation of samples with oxygen plasma and 1–10 MeV electrons with fluences corresponding to 18 years of flight in order to forecast specimen radiation hardness and durability to AO impact in the case of extension of ISS operation time to 30 years. The electron irradiation was performed on SINP MSU linear high frequency accelerators [3], and the impact of atomic oxygen was simulated with SINP MSU magneto-plasma dynamic accelerator [4].

Elastomeric (Rubber) Specimens

Six types of rubber materials exposed to the LEO environment for 12 years on Komplast Panel 2 were investigated. Deformation, strength, and relaxation properties of rubber specimens were studied, and the sealing capability of rubber seal replicas was assessed.

As a result of the conducted research, it was determined:

1. After long-term exposure, exposed specimens retain their volume deformation and relaxation properties;

2. When exposed, rubber specimens are stretched by up to 50 %, structural failure and partial separation occurs in the surface layer (films forming on specimens under SEE) without volume failure for all exposed rubber types;
3. When studying sealing capability, a change was noted in the sealing mechanism of the forward-facing surface of seals: a transition occurs from diffuse-type leakage mode to contact one; i.e., the sealing capability of seals deteriorates after long-duration space exposure. In the same study, the retention of the sealing capability of shielded surfaces, protected from direct contact with the ambient environment, was observed.

The principal significant conclusion of the Komplast experiment regarding rubber material specimens is the localization of structural changes in the thin surface layer of exposed materials on surfaces unprotected to direct exposure to SEE. The localization of aging on a surface leads to the development of a lack of uniformity in exposed materials, the formation of surface films, their deformation, and failure.

The formation of rigid surface films explains the deceleration of processes in the volume of exposed materials, i.e., it causes rubber stabilization. Simultaneously, because of the rigid surface films, the sealing capability of openly exposed rubber deteriorates.

Another important conclusion from the experiment is the identification of the protective effect of different types of shielding (such as with specimen fasteners—Fig. 6).

Based on the kinetics of exposed specimen residual strain accumulation, the remaining time that rubber materials retain functionality was determined, confirming the feasibility of establishing an overall guaranteed operating life of rubber seals (when shielded on the FGB) of at least for 30 years.

Surface Contamination

Visible contamination spots on the surfaces of panels and material specimens were studied. Using X-ray fluorescence analysis (XRFA), the Rutherford backscattering (RBS) method and spectral X-ray microanalysis (SXRM) in combination with scanning electron microscopy (SEM), we studied the elemental composition and structure of contaminant spots on the panels [5].

It was found that the contamination occurred mainly in the form of deposition of the substances emitted from some specimens placed on the panels, primarily from rubber (elastomeric) samples. Figure 7a demonstrates several rubber samples in the form of shoulder blade that were mounted on Panel 2 (Fig. 5). One of specimens was removed from the panel, and it can be seen clearly that contamination films appeared around the rubber samples. The structure of the contamination film is shown in Fig. 7b.

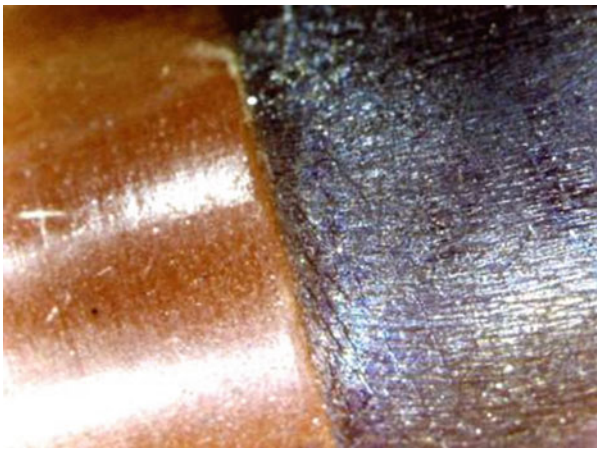

Fig. 6 Border between a rubber specimen surface shielded by a fastener (*left*) and an unprotected surface (*right*)

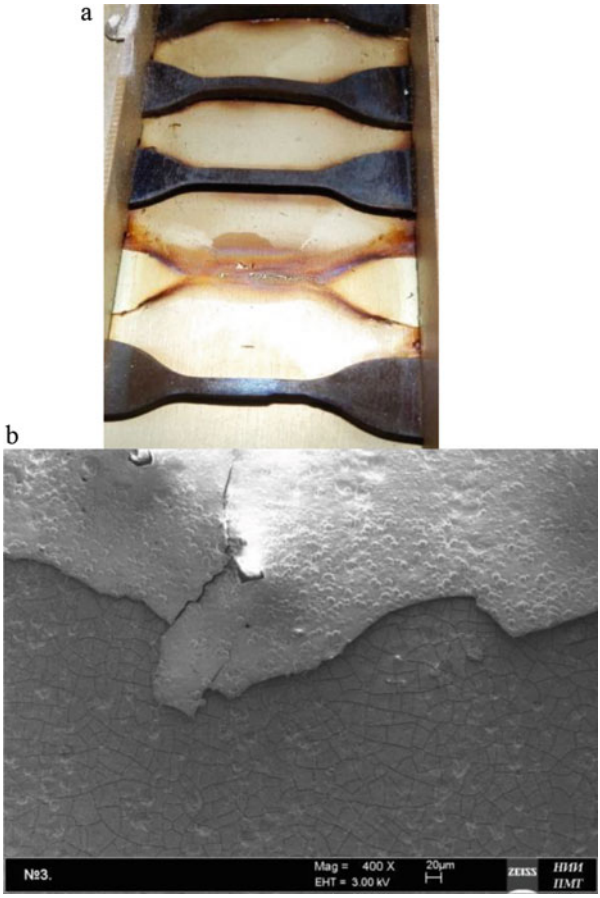

Fig. 7 (**a**) Specimens on Panel 2; (**b**) SEM image of the contamination film (*top*)

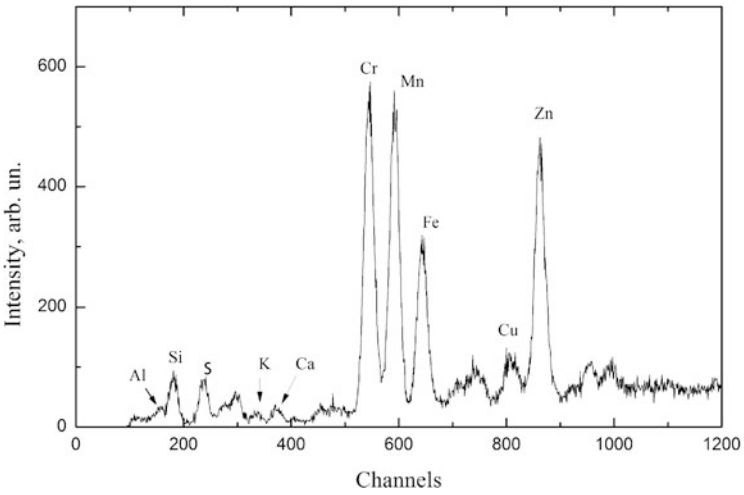

Fig. 8 X-rays spectrum of the contamination film

The XRFA spectrum of the contamination film near one of the specimens is shown in Fig. 8. It was found that peaks of Si, S, K, Ca, Fe и Zn correspond to the elemental composition of the rubber samples. The peaks of Al, Cr, Mn, Cu are associated with the material of the panel.

To receive the information on lighter elements in the contamination spots, the RBS analysis was used. With this method the significant content of carbon and oxygen in the contamination film was found. The similar data on the contamination elemental composition was obtained with the SXRM method. Thus, it was shown that the contamination spots contain elements from which the rubber or panels were made. The film depth was estimated to be ~5–7 μm.

Hard Particle Impact

To detect the impact of micrometeoroids and space debris with size 1–1000 μm, a special sensor containing polished samples of different materials (silicon, aluminum and copper alloys and titanium) was set on Panel 2. The microparticle sensor, after it was removed from the panel, is shown in two different views in Fig. 9.

For Komplast experiment, three polished specimens for each of four material had been prepared. The area of each sample was 1.96 cm^2, so the total area of all 12 samples was equal to 23.52 cm^2. After removing them from the panel, the surface of each sample was investigated with optical microscope and SEM.

Figure 10 shows SEM images of some craters found on Al, Cu and Si samples as well as an image of a low-velocity particle on Ti surface. The elemental analysis of this particle using the SXRM method suggested that it was composed mainly from

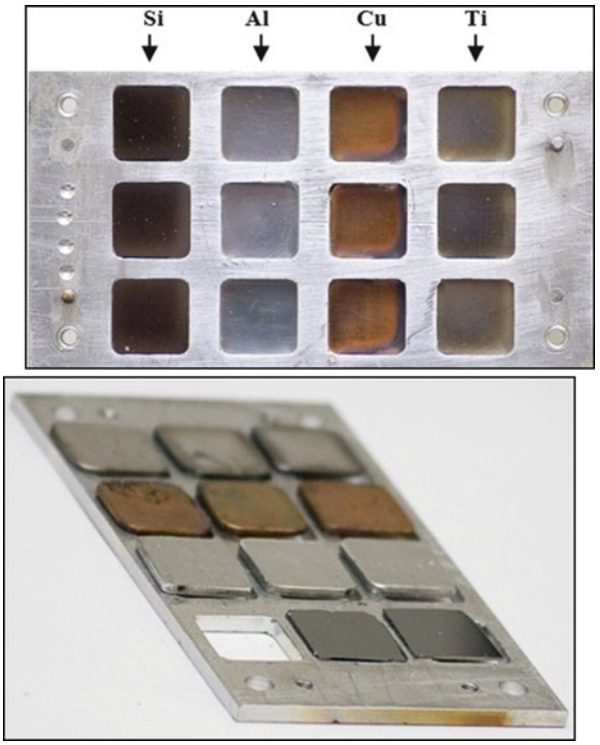

Fig. 9 The microparticle sensor after removing from Panel 2

CrO_x. Some other low-velocity particles consisting of SiO_2, ZnO, MnO_X, were found on the surfaces of the samples.

In addition to the study of the polished samples, the exposed to SEE surface of Panel 2 was examined as well. It consisted of Al alloy and had an area of 727.34 cm^2. Since its surface was not as smooth as the surface of the polished samples, only craters with sizes larger than ~35 μm were observed on the panel.

Figure 11 shows an average yearly cumulative microparticle flux, determined in the Komplast experiment, versus the diameter of particles. The flux was calculated based on both micrometeoroid and space debris impacts, and only on the data obtained from plastic metallic targets (Al and Cu polished samples and the Al alloy of the panel) were used. For the comparison, the total flux of space debris and micrometeoroids calculated with ORDEM2000 [6] and MASTER-2009 [7] models for the ISS orbit is given. For particles with diameter of 10–30 μm the difference between experimental and calculated data is about an order of magnitude, and for larger particles (50–500 μm) there is a good agreement of Komplast and model results.

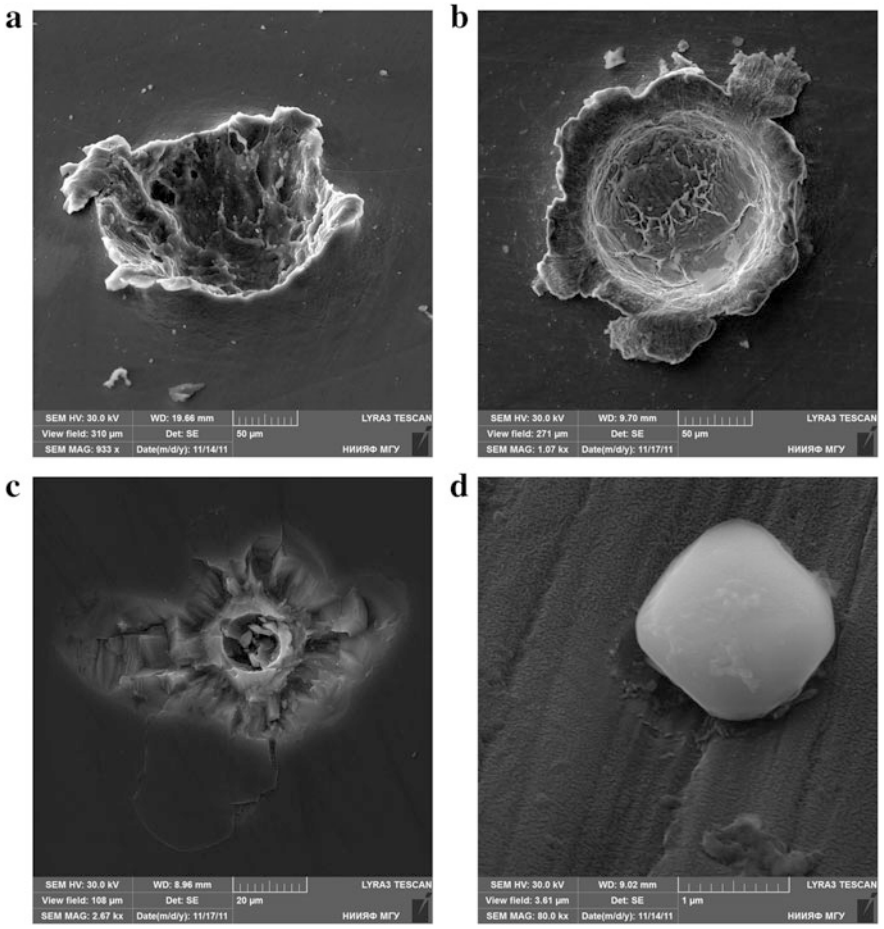

Fig. 10 Craters (**a**–**c**) and a particle (**d**) on the surface of polished samples

Conclusions

The measured temperatures that the panels experienced were in the range between −80 and +107 °C.

Most of the rubber samples preserved volumetric deformation and relaxation characteristics after 12 year exposure. The localization of structural changes in the thin surface layer of the exposed materials was determined.

The cumulative flux of micrometeoroids and space debris with diameter of 10–30 μm, obtained by analyzing the Komplast experimental data, differs by approximately one order of magnitude from the predictions of ORDEM2000 and MASTER-2009 for the ISS orbit. For larger particles (50–500 μm) there is a good agreement of Komplast and model results.

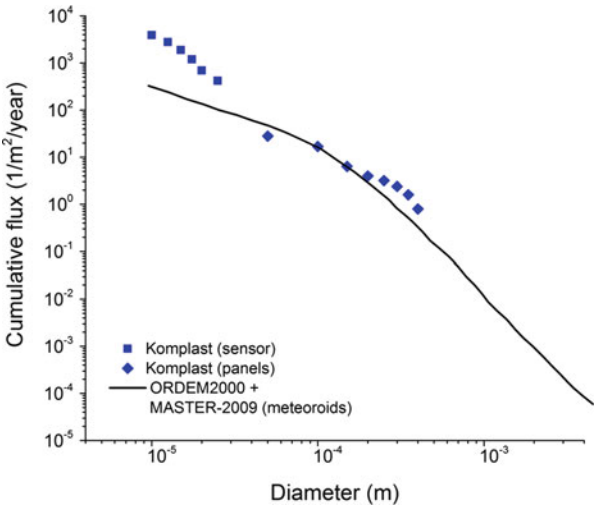

Fig. 11 Komplast cumulative microparticle flux (*squares* and *diamonds*) versus particle diameter compared with ORDEM2000 and MASTER 2009 model data (*line*)

In practical terms, the Komplast experiment contributed to the understanding of the processes, occurring in materials under the effect of outer space factors, and confirmation of the term of warranty for materials of FGB at long-term (30 years) of operation in the ISS orbit.

References

1. Golden JL, Koontz SL, Christiansen EL, Graves RF, Lorenz MJ, Alred JW, O'Rourke MJE (2009) Spacecraft materials in the space flight environment: international space station—May 2002 to May 2008. In: Kleiman JI (ed) Proceedings of the 9th international conference: protection of materials and structures from space environment, vol 1087. AIP Conference Proceedings, pp 3–29
2. Naumov SF, Borisov VA, Gorodetsky AA, Sokolova SP, Gerasimova TI, Kurilenok AO (2009) Study of materials and coatings on the spacecraft surfaces in the Salyut, MIR and ISS orbital stations: 1990–2008. In: Kleiman JI (ed) Proceedings of the 9th international conference: protection of materials and structures from space environment, vol 1087. AIP Conference Proceedings, pp 30–50
3. Chubarov OV, Alimov AS, Shvedunov VI (1997) A compact industrial CW LINAC. IEEE Trans Nucl Sci 44(3):1033–1036
4. Chernik VN, Novikov LS, Smirnova TN (2009) Ground-based atomic oxygen tests of pristine and protected polymeric threads. In: Kleiman JI (ed) Proceedings of the 9th international conference: protection of materials and structures from space environment, vol 1087. AIP Conference Proceedings, pp 107–116
5. Petukhov VP, Kulikauskas VS, Novikov LS, Petrov DV, Smirnova TN, Chernik VN, Shemukhin AA, Shumov AE (2014) Nuclear physical analysis of the contamination on the surface of a COMPLAST panel after 12 year exposure at the ISS. J Surf Invest X-Ray Synchrotron Neutron Tech 8(3):440–443
6. Liou J-C, Matney M, Anz-Meador PD, Kessler D, Jansen M, Theall JR (2002) The new NASA orbital debris engineering model ORDEM2000. In: NASA/TP-2002-210780, May
7. Flegel S et al (2011) MASTER-2009 final report. Institute of Aerospace Systems, June

Integrated Analysis of Radiation-Protective Thermal Control Coatings

S.V. Tokar, A.V. Grigorievsky, and L.V. Kiseleva

Abstract To prevent spacecraft astrionics failure, a radiation-resistant element base is employed along with protective screening to maximize operational lifetime and reliability while minimizing scale and mass specifications. The problem of protecting the element base from radiation thus amounts to that of selecting the most effective protective screen. It is therefore vital to develop a thermal control coating with providing extra protection from the harmful effects of the space environment's ionizing radiation for the element base, components and circuits of radio-electronic equipment.

The need to create such a coating is partly determined by the fact that modern spacecraft are increasingly using elements and astrionics components that are positioned on open platforms. In such circumstances, the use of thermal control coatings (TCC) with enhanced protective properties would be an effective means of providing additional ionizing cosmic radiation protection for astrionics elements. The effectiveness of this method is determined by the feasibility of applying a TCC of the necessary thickness on components of complex geometrical form, and by the possibility of regulating ionizing radiation linear energy loss by means of suitable fillers.

Keywords Thermal control coating • Radiation-protective coating • Astrionics

Introduction

In the course of operation, spacecraft astrionics is exposed to damaging space factors among which ionizing radiation (IR) including X-ray and solar gamma-ray, particles generated by solar (chromospheric) flares, solar wind, galactic and extragalactic cosmic rays, electrons/protons of radiation belts, neutron and alpha particles are the most dangerous ones.

S.V. Tokar (✉) • A.V. Grigorievsky • L.V. Kiseleva
JSC "Kompozit", 4, Pionerskaya St., 141070 Korolev, Moscow, Russia
e-mail: info@kompozit-mv.ru

J. Kleiman (ed.), *Protection of Materials and Structures from the Space Environment*, Astrophysics and Space Science Proceedings 47,
DOI 10.1007/978-3-319-19309-0_4

IR is one of the major factors restricting serviceability of electronics and spacecraft astrionics because dose and single effects caused by IR are the reason of up to 50 % of all qualified failures of spacecraft astrionics [1], although this percentage is virtually higher because degradation of materials is a booster for other types of failures.

Materials for electronics shielding shall have protective properties allowing to protect IC's or electronics against IR, mechanical strength, climatic strength, vacuum strength, chemical endurance to corrosive media with coatings and sealants, high electrostatic properties, thermal conductivity ensuring normal operation conditions for IC's and electronics, manufacturability during batch manufacturing, etc.

Presently applicable TCC were being developed only for maintaining thermal balance; however, followed by increased demands of spacecraft durability up to 10–15 years, radiation exposures to spacecraft astrionics have been raised sharply. Protection issues of spacecraft astrionics is currently solved through a variety of means, by raising resistance of the element base, accommodation of astrionics in the most secured locations of spacecraft (structural protection), establishment of additional protection for the most vulnerable electronics.

It is therefore vital to develop a TCC with the dual purpose of:

1. Maintaining the specified heat balance of spacecraft's systems within a given temperature range throughout its operative work-life;
2. Providing extra protection against harmful effects of the space environment's IR for the element base, components and circuits of electronics.

Experimental Results

Calculations of absorbed doses for different spacecraft orbits show that the major contribution in the doses comes from electron radiation. For instance, Table 1 gives calculated absorbed doses from electrons and protons for materials on external surfaces of spacecraft designed for 10.5-years service life at GSO.

It is seen that total absorbed dose is almost entirely identified by electron radiation.

Earlier it was shown [2] that average energy losses ΔE of monochromatic electrons passing through a layer of material with atomic number A and charge number Z are:

$$\Delta E(MeV) = 0.6\rho(Z/A)\Delta x/\beta^2 \quad (1)$$

where ρ—material density, g/cm^3; Δx—thickness of material layer in cm, $\beta = \upsilon/c$.

Since Z/A is approximately constant for different materials, then dE/dx in (1) is virtually dependent only on material density, ρ. Consequently, paths of electrons having given original energy E will be almost similar in different materials of the same density. Therefore, the higher the material density, the shorter the electron

Table 1 Absorbed doses from electrons of Earth radiation belts and protons of solar cosmic rays at GSO for10.5-years period depending on mass protection thickness of spherical screen

Protection thickness, g/cm^2	Absorbed dose, rad		
	Electrons	Protons	Total
0.00	3.56×10^8	3.87×10^5	3.57×10^8
0.01	2.98×10^8	3.23×10^5	2.99×10^8
0.10	6.09×10^7	6.36×10^4	6.10×10^7
1.00	8.03×10^4	7.17×10^3	9.22×10^4

path in it, and, subsequently, the smaller is the absorbed dose behind the protective screen.

According to experimental results and based on the above discussion, two enamel compositions were selected to prepare TCCs. The first one is composed of liquid lithium glass and pigment Bi_2O_3, it has the maximum density and designated as EKOM-RZP. The second composition is a previously developed TCC and designated as EKOM-ZhS-2.

Then, an integrated radiation protective TCC with two layers was composed:

- Bottom layer (composition EKOM-RZP) securing radiation protective properties of the coating (radiation reduction coefficient);
- Top layer (composition EKOM-ZhS-2) securing thermal and optical properties of the coating (absorptance α_s and emittance ε) and their low degradation in space environment.

Adhesion between the layers is provided by using the same binder, liquid lithium glass.

This two-layer coating was named as EKOM-RZ.

To study radiation protective properties of TCC samples were prepared of the coatings EKOM-RZ and EKOM-ZhS-2. Irradiation of the samples by electrons of different energies for a comparative evaluation of their radiation protective properties was performed in two stages:

- Irradiation by high-energy electrons (over 1 MeV);
- Irradiation by medium-energy electrons (100 keV–1 MeV).

Tests for finding reduction coefficients of electron radiation within the energy range 1.8–2.2 MeV were carried out by OAO "ENPO SPELS" using the U-31-33 electron accelerator. TCC layout in the tests is given in Fig. 1. Coatings were applied on A1 substrate—a 100 × 100 mm square plate and 600 μm thick.

Reduction of electron radiation by screen (samples) is determined as ratio of average values of detector groups 3 and 5 (Fig. 1)

$$K = D_3/D_5$$

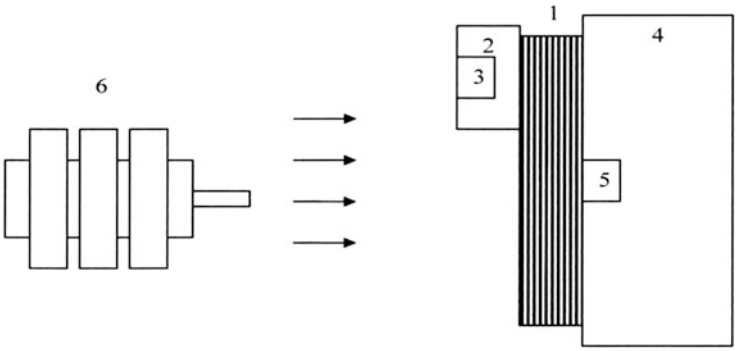

Fig. 1 Samples layout in tests. 1—samples package; 2, 4—container (aluminum); 3, 5—detectors; 6—electron accelerator

Table 2 Absorbed dose reduction coefficients of 1.86-MeV electrons in dependence on coating thickness

EKOM-RZ coating		EKOM-ZhS-2 coating	
TCC thickness, μm	Reduction coefficient	TCC thickness, μm	Reduction coefficient
541	2.95	660	1.16
901	13.8	1172	2.20
1418	273	1676	6.51
2118	972	2690	257
2786	1213	3227	1091

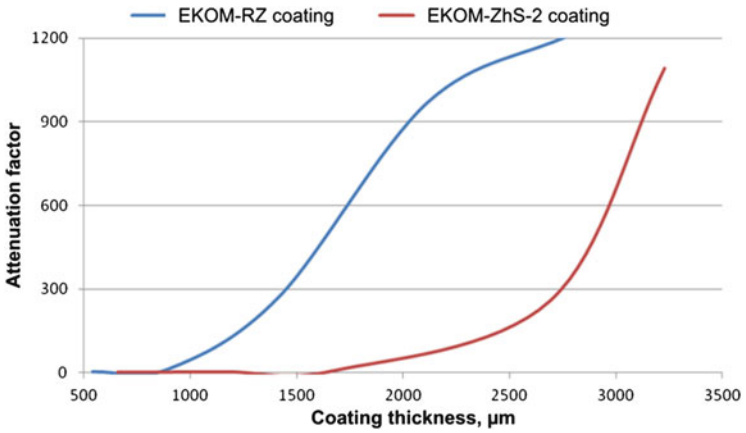

Fig. 2 Absorbed dose reduction coefficients of 1.86-MeV electrons versus EKOM-RZ and EKOM-ZhS-2 coating thicknesses

Table 2 and Fig. 2 give absorbed dose reduction coefficients of 1.86-MeV electrons for EKOM-RZ and EKOM-ZhS-2 coatings. For thickness up to 2 mm reduction of EKOM-RZ exceeds EKOM-ZhS-2 two–four times.

Results of Radiometric Tests and Calculations of Linear Absorption Coefficients of β-Particles by EKOM-RZ and EKOM ZhS-2 Coatings

It is known [3, 4] that electron/proton fluxes at radiation-dangerous orbits have a differential relationship against particles energy that ranges from a few kV to dozens of MV. Using a monochromatic electron flow we simulate only a part of the spectrum of electron radiation influencing the spacecraft.

The electron spectrum can be simulated only by β-radiation radioactive sources. Electrons and positrons generated in the process of radionuclide decay have continuous energy spectrum with maximum energy E_β and average energy $\approx 0.33\ E_\beta$ (Fig. 3).

The most part of β-radiation absorption curve is quite sufficiently described by exponential relationship:

$$N(x) = N(0)exp\,(-\mu x),$$

where, x—absorber thickness (g/cm^2), μ—mass absorption coefficient of β-particles (cm^2/g).

Point radioactive sources ^{90}Sr/^{90}Y (in equilibrium) and ^{36}Cl were used to study protective properties of EKOM-RZ and EKOM-ZhS-2 coatings for 1–2 MeV electrons. Radionuclides characteristics used for the study are summarized in Table 3.

Absorption capability of coatings was measured using the radiometer having SBT-7 self-quenching gas-discharge counter. The counter was screened against external radiation by a lead shield, internal walls of which were covered with aluminum in order to minimize back-scattering effect. The β-particle source and absorbers holder (retaining device) were fixed on a Plexiglas clamp stand. Source-

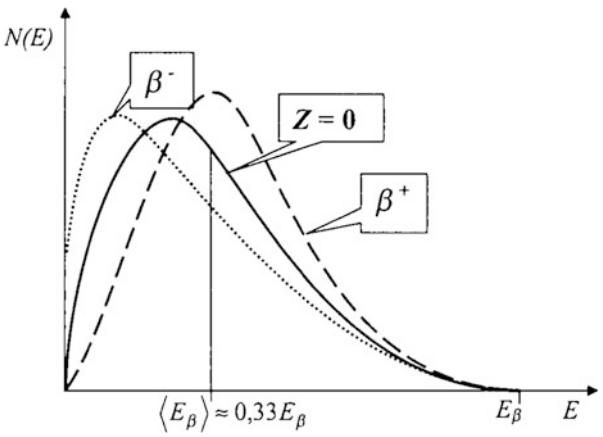

Fig. 3 Electrons/positrons energy spectrum generated in the course of β-decay (curve Z = 0—hypothetical spectrum that does not account for Coulomb interaction of particles with nucleus) [5]

Table 3 Summary of characteristics of radionuclides

Source	Half-life period	E_β, MeV
$^{90}Sr/^{90}Y$	28.6 years (^{90}Sr) 64.1 h (^{90}Y)	0.546 (^{90}Sr) 2.27 (^{90}Y)

Table 4 Counting rates of source $^{90}Sr/^{90}Y$ covered by plates with different coatings

Aluminum, source			EKOM-RZ			EKOM-ZhS-2		
d, μm	I, imp/s	$(I-I_\phi)$, imp/s	d, μm[a]	I, imp/s	(I-Iϕ), imp/s	d, μm[a]	I, imp/s	(I-Iϕ), imp/s
0	481.94	481.45	0	481.94	481.45	0	481.94	481.50
100	294.10	293.61	359	73.63	73.14	504	120.67	120.23
300	185.18	184.69	1056	10.05	9.56	1474	42.47	42.03
500	133.38	132.89	1758	1.26	0.77	2456	13.43	12.99

[a]w/o considering thickness of aluminum substrates

to-absorber and absorber-to-counter window distances were 2.5 cm. The pulses were counted using a scaling unit.

Background pulses were counted within 1000 s before and after source operation; background values were averaged when processing the results. The source pulses were counted with statistical error of 2.5 % at most.

To solve the task the following measurements were taken:

- Determination of counting rate of the source covered by aluminum plates without coating (1–5 plates);
- Determination of counting rate of the source covered by aluminum plates with EKOM-RZ;
- Determination of counting rate of the source covered by aluminum plates with EKOM-Zhs-2.

The thickness of aluminum plates was 100 μm in all measurements. Results of the measurements are presented in Table 4.

Attenuation curve represents dependence of particles counting rate on absorber thickness. As it is known, significant part of attenuation curve of β-particles (having continuous energy spectrum) is described by exponential relationship:

$$I := I_0 \cdot \exp[-(\mu \cdot d)] \tag{2}$$

In the case of $^{90}Sr/^{90}Y$ source that emits two groups of β-particles having different upper boundaries of partial spectra but the same contribution, this relationship will be as follows:

$$I := I_0 \cdot \left(\frac{1}{2} \cdot \exp(-\mu_{Sr} \cdot d) + \frac{1}{2} \cdot \exp(-\mu Y \cdot d)\right), \tag{3}$$

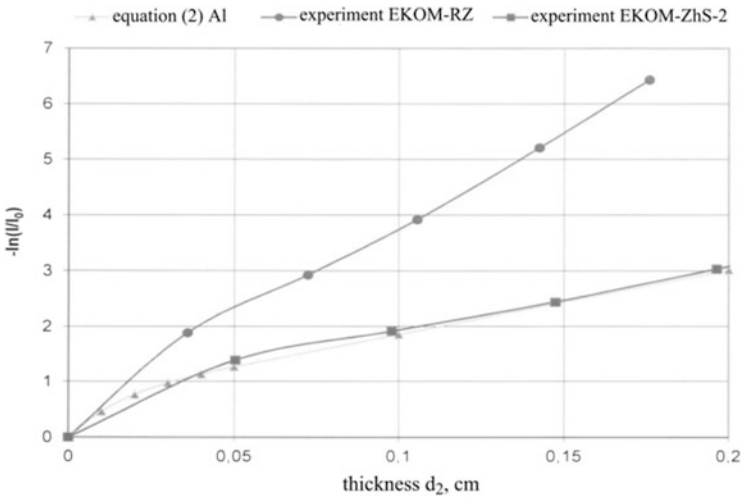

Fig. 4 Attenuation curves for Al, EKOM-RZ, and EKOM-ZhS-2

where μ_{Sr} and μ_Y are attributable to partial β-spectra ^{90}Sr and ^{90}Y respectively. In virtue of the fact that in general the absorber has a complex composition (aluminum + coating) Eq. (3) can be rewritten as follows:

$$I := I_0 \cdot \left(\frac{1}{2} \cdot \exp(-\mu_{Sr1} \cdot d_1 - \mu_{Sr2} \cdot d_2) + \frac{1}{2} \cdot \exp(-\mu Y1 \cdot d_1 - \mu Y2 \cdot d_2) \right), \quad (4)$$

where indexes 1 and 2 are related to aluminum and coating respectively. Thickness d_1 equals to 100 μm × number of aluminum substrates.

Transition to mass absorption coefficients is done through absorber mass density as follows:

$$\mu_m := \frac{\mu}{\rho} \quad (5)$$

Values of mass absorption coefficients of β-particles in aluminum are 37 and 4.3 for ^{90}Sr and ^{90}Y respectively. Obtained values are quite well matching theoretical results, according to which mass absorption coefficients of β-particles in aluminum (cm^2/g) are linked with upper boundary of β-spectrum (MeV) by:

$$\mu_m := \frac{15.5}{(E_\beta)^{1.41}} \quad (6)$$

Values calculated in accordance with (6) are equal to 36.4 (^{90}Sr) and 4.88 (^{90}Y). It is also known that experimental value μ_m for ^{90}Y is 4.7 cm^2/g [5].

Table 5 Linear and mass absorption coefficients of β-particles

Sample	^{90}Y	
	μ, cm^{-1}	μ_m, cm^2/g
Al	11.6	4.3
EKOM-ZhS-2	9.5	8.5
EKOM-RZ	28.3	10.1

Using experimentally measured values μ_{Sr1} and μ_{Y1} values of linear and mass absorption coefficients of β-particles of ^{90}Sr and ^{90}Y by EKOM-RZ and EKOM-ZhS-2 coatings were found by using the least square method.

All results are presented in Fig. 4 and Table 5.

Obtained results prove that EKOM-RZ has the most attenuation capability as compared to EKOM-ZhS-2 and aluminum. Linear absorption coefficient μ (cm^{-1}) of radiation protective coating EKOM-RZ for ^{90}Y source of electron radiation ($E_\beta = 2.27$ MeV) is 2.5 times more than coefficient μ (cm^{-1}) for EKOM-ZhS-2 and pure aluminum.

Conclusions

In this work a radiation protective TCC was developed with the following characteristics:

- Solar absorptance $As < 0.14$;
- Thermal emittance $\varepsilon > 0.91$;
- Total mass loss (TML) $< 0.75\,\%$;
- Volatile condensable materials, VCM $< 0.01\,\%$;
- Reduction of absorbed dose on GSO from 10 to 1000 times;
- GSO operating time ≥ 15 years.

Acknowledgments Authors express gratitude to G.A. Protopopov (OAO "NII KP") and A.B. Sazonov (D. Mendeleev UCTR) for calculations and tests.

References

1. Koons HC et al (1999) The impact of the space environment on space systems. Aerospace technical report TR-99 (1670-1, 1999)
2. Bete H, Ashkin UJ (1955) Passage of—particles through matter. In: Serge M (ed) Experimental nuclear physics
3. Vernov SN (1983) Model of space environment, vol 2, chapter 5. Moscow State University Publishing House, Moscow
4. RTM-2-K-83, GONTI-1 (1984) Test methods of thermal control coatings and assessing changes of their properties in operating conditions. RTM-2-K-83, GONTI-1, Korolev, Moscow Region (in Russian)
5. Sazonov AE et al (2005) Laboratory practicum on nuclear physics. Mendeleev University of Chemical Technology of Russia, Moscow

Space Environmental and Technical Performances of Organic Silicone Antistatic White Thermal Control Coating

Lei Hui, Lu Wu, Zeng Yibing, Luo Zhengping, Jin Ke, and Yin Yuchen

Abstract The space environmental and technical performances of the organic silicone antistatic white thermal control coatings were studied. The effects of combined irradiation with UV, electrons and protons, and with the UV and atomic oxygen on the change of solar absorptivity (αs) were studied in a space environment simulation facility. The experimental results show that the white thermal control coating is highly stable in the low-orbit space environment. It was found that after combined irradiation by 5000 ESH of UV, total electron doses of 2.0×10^{14} e/cm^2 and total proton doses of 5.0×10^{12} p/cm^2; combined irradiation by 5000 ESH of UV and atomic oxygen with a fluence 5.0×10^{21} atoms/cm^2 simultaneously, the solar absorptivity of these coatings changed very little. The effects of coating thickness on solar absorptivity and adhesion strength between the coatings and substrates were analyzed. The thermal cycling performances of the coatings on different kinds of substrates under temperature variation from −196 to +150 °C were investigated.

Keywords White thermal control coatings • Space environment • Technical performance

Introduction

White thermal control coatings that are composed of functional filler and resin, have low solar absorptivity (α_s) and high hemispherical emissivity (ε_H) and are used in the thermal protection of spacecraft surfaces [1–3]. Because of good thermal cycling and processing properties, the organic silicone white thermal control coatings could be sprayed easily on different kinds of substrate surfaces. When insulating coatings are exposed to space environment, an electric charge will accumulate at the coating surface as a result of bombardment by charged particles. A non-uniform distribution of the charging potential may cause discharge phenomena that could disturb the normal operation of electronic equipment. Combined

L. Hui (✉) • L. Wu • Z. Yibing • L. Zhengping • J. Ke • Y. Yuchen
Aerospace Research Institute of Materials & Processing Technology, Beijing 100076, China
e-mail: alexander_112@163.com

J. Kleiman (ed.), *Protection of Materials and Structures from the Space Environment*, Astrophysics and Space Science Proceedings 47,
DOI 10.1007/978-3-319-19309-0_5

exposure to space environment factors like long-term UV irradiation, protons, electrons, the thermal cycling affects the properties and the performance of coatings. It is necessary, therefore, for the flight safety to develop coatings that are affected as little as possible by these factors.

According to the thermal control requirements to the long-life satellites, based on the research of the acrylic antistatic thermal control coating (ACR-1), mixtures of the conductive zinc oxide and silicone rubber were used to prepare the organic silicon antistatic white thermal control coating. The effects of combined irradiation with UV, electrons and protons, and with the UV and atomic oxygen on the change of solar absorptivity (αs) were studied in a space environment simulation facility. The effects of coating thickness on solar absorptivity and adhesion strength between the coatings and substrates were analyzed. The thermal cycling performances of the coatings on different kinds of substrates under temperature variation from −196 to +150 °C were investigated.

Experiment

Raw Materials

The conductive zinc oxide, purified methyl silicone rubber, and curing agent were self-made. The solvent was purchased.

Preparation of the Coating Sample

The thermal control coatings were prepared by mixing conductive zinc oxide, silicone rubber and solvent in a ball milling system for 2–3 h. The coating samples were prepared by spraying them onto test panels and curing for 24 h at room temperature.

Performance Characterization

The solar absorptivity of the coating was measured on a Lamda950 spectrometer; emissivity was measured on a A/E radiometer; volume resistivity was measured by 6517B resistance meter; All test methods were conducted with reference to the GJB2505-2006 and GJB2704A-2006 standards.

Result and Discussion

Performances of Silicone White Thermal Control Coatings

Basic Performances of Coating

The thickness of the prepared silicone white thermal control coatings was about 150 μm. All basic parameters of the coating were measured and are shown in Table 1.

As can be seen from Table 1, the coating has low solar absorptivity and high emissivity. Also, it has the antistatic performance and good thermal cycling performance in space environment.

Combined Irradiation with UV and Atomic Oxygen

In the low-orbit space environment, the coating is influenced by the irradiation with UV, atomic oxygen, electrons, etc. In order to investigate the coating performance in low-orbit space environment, accelerated testing of the coating sample had been conducted for an equivalent of 8 years in orbit by combined irradiation with UV and atomic oxygen in a space environment simulator facility with in-situ measurements of the solar absorptivity. The maximum UV irradiation dose was 5000 ESH, acceleration ratio was about 4 times, UV irradiation spectrum was 200–400 nm. The total atomic oxygen fluence was 5×10^{21} atoms/cm^2 and the AO flux was 5×10^{15} atoms/cm$^2 \cdot$ s. The experimental results could be seen in Table 2.

As can be seen from Table 2, the in-situ measured solar absorptivity of the coating changed little after a combined irradiation by UV and atomic oxygen for 8 years in low-orbit space environment. The mass loss of the coating was 0.23 mg/cm^2. The reason for such loss is probably due to the combined action of UV radiation and atomic oxygen. The coating surface darkened and was damaged by the UV irradiation. However, the darkened coating surface was removed by the atomic oxygen, which kept the optical performance and lead to the mass loss of the coating.

Table 1 Basic parameters of the silicone white thermal control coating

Solar absorptivity (α_s)	Emissivity (ε_H)	Volume resistivity Ω cm	Mass loss	Collectable volatile condensed mass	100 times of thermal cycling under temperature from −196–150 °C
0.17	0.90	9×10^{10}	0.24 %	0.011 %	The coatings surface kept intact

Table 2 Experimental results of combined irradiation with atomic oxygen and UV

Atomic oxygen fluence (AO/cm^2)	UV irradiation time (ESH)	Equivalent time (year)	Absorptivity (Sample1)	Absorptivity (Sample2)
0	0	0	0.18	0.18
2.455×10^{19}	625	1	0.18	0.18
4.931×10^{19}	1250	2	0.18	0.18
7.397×10^{19}	1875	3	0.18	0.18
9.863×10^{19}	2500	4	0.18	0.18
1.233×10^{20}	3125	5	0.18	0.18
1.479×10^{20}	3750	6	0.18	0.18
1.726×10^{20}	4375	7	0.18	0.18
1.972×10^{20}	5000	8	0.18	0.18
5.0×10^{21}			0.18	0.19

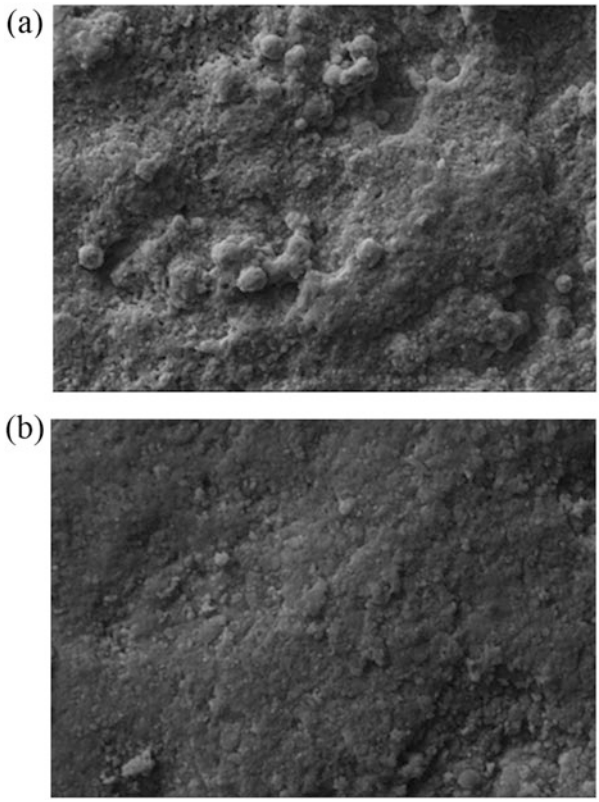

Fig. 1 SEM photographs of the coating (**a**) before combined irradiation by UV and atomic oxygen, (**b**) after combined irradiation by UV and atomic oxygen

Analyzing the appearance of the coating, it was established that after combined irradiation with UV and atomic oxygen, coatings glossiness decreased and a number of pits appeared on the surface (Fig. 1), also the roughness increased, suggesting that the polymer resin degraded and coatings mass was lost.

Combined Irradiation with UV, Protons and Electrons

To evaluate the influence of combined irradiation factors, the coating was exposed to UV, protons and electrons simultaneously for an equivalent 8 years of flight exposure with in-situ measurements of solar absorptivity. The UV irradiation dose was 5000ESH. The total electron dose was 2.0×10^{14} e/cm^2 and the total proton dose was 5.0×10^{12} p/cm^2. The summary of the experimental results is presented in Table 3.

As can be seen from Table 3, the in-situ measured solar absorptivity of the coating is increasing with exposure time to the combined irradiation by UV, protons and electrons. In the beginning of exposure the change rate of solar absorptance was high and it slowed down towards the end of the experiment. At the end, solar absorptivity of the coatings stabilized. After combined irradiation by UV, proton and electron for an equivalent 8 years of flight exposure, the change of in-situ measured absorptivity of the coating was 0.19.

Technical Performances of the Organic Silicone White Thermal Control Coating

The Effect of the Thickness on the Performances of the Coating

Several coating sample with different thickness were obtained using the same formulation design. The effect of the thickness on the performances of the coating was investigated. The experimental results are summarized in Table 4.

As can be seen from Table 4, with increasing coating thickness, the hemispherical emissivity and surface density of coating both increased but the solar absorptivity decreased. Starting from thickness of 120 μm, the optical performance of the coating did not change. Based on the conducted experiments the thickness of the coating was selected in the range 120–160 μm for optimum optical performance and decreased weight.

Effect of Surface Treatments on Coating Adhesion

According to the characteristics of the silicone white thermal control coating, in order to improve the adhesion between the coating and the substrate, a surface treatment agent should be sprayed onto the substrate surface firstly, then the coating could be sprayed. Based on the same coating formulation and spraying process, the effect of surface treatment agent on coating adhesion is demonstrated in Fig. 2.

As can be seen from Fig. 2, the surface treatment was important to improve the adhesion of silicone white thermal control coating. With no surface treatment the adhesion of the coating to the substrate was very poor (Fig. 2a). However, the

Table 3 Experimental results of combined irradiation with UV, proton and electron

Total electron dose (e/cm^2)	Total proton dose (p/cm^2)	UV irradiation dose (ESH)	Equivalent time (year)	Absorptivity (sample1)	Absorptivity (sample2)	Absorptivity (sample3)
0	0	0	0	0.20	0.20	0.20
2.5×10^{13}	6.25×10^{11}	625	1	0.25	0.30	0.25
5.0×10^{13}	1.25×10^{12}	1250	2	0.24	0.26	0.27
7.5×10^{13}	1.88×10^{12}	1875	3	0.33	0.35	0.34
1.0×10^{14}	2.50×10^{12}	2500	4	0.36	0.36	0.39
1.3×10^{14}	3.13×10^{12}	3125	5	0.38	0.38	0.38
1.5×10^{14}	3.75×10^{12}	3750	6	0.38	0.41	0.39
1.7×10^{14}	4.38×10^{12}	4375	7	0.37	0.38	0.37
2.0×10^{14}	5.0×10^{12}	5000	8	0.39	0.39	0.40

Table 4 The effect of the thickness on the performances of the coating

Thickness (μm)	40	80	120	160	200	300
Solar absorptivity (α_s)	0.26	0.21	0.17	0.16	0.16	0.15
Hemispherical emittance (ε_H)	0.87	0.89	0.90	0.90	0.91	0.90
Surface density (g/m^2)	135	226	298	396	512	790

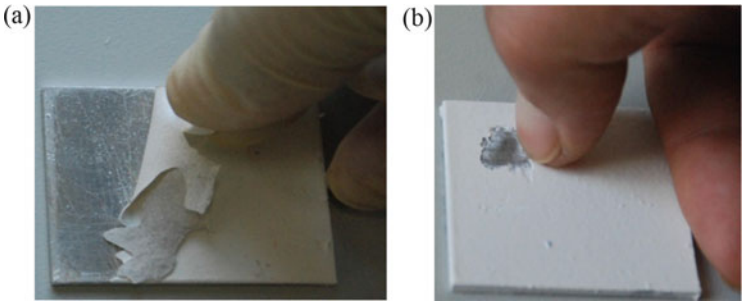

Fig. 2 Effect of surface treatment agent on coating adhesion. (**a**) Without surface treatments agent, (**b**) with surface treatments agent

coating could not be peeled even in condition of strong damage when the substrate surface treatment was applied.

Effect of Different Substrates on Thermal Cycling Performance of Coating

In order to validate adaptability between the silicone white thermal control coating and different kinds of substrates, thermal coatings with 150 μm thickness had been sprayed on a number of substrates such as FG4 ablative material for thermal protection, polyimide membranes, carbon fiber/epoxy and aluminum alloy and thermally cycled. Figure 3 shows the coated samples after 100 thermal cycles between −196 and +150 °C.

The results of thermal cycling testing indicated that the coating deposited on all samples withstood the thermal cycling very well, with no cracks or peeling. Such consistent behavior can be explained by favorable tensile strength and elongation at break parameters that could avoid the coating breakage caused by the expansion and contraction of substrate at different temperatures.

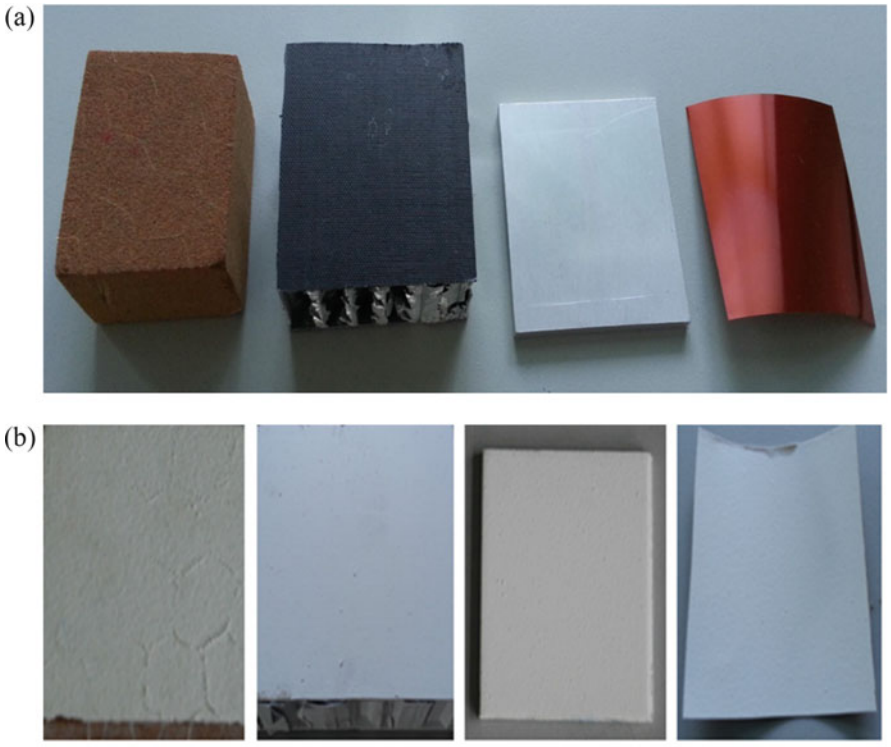

Fig. 3 The samples before and after the thermal cycling experiment: (**a**) different kinds of substrates, (**b**) the appearance of the coatings samples after thermal cycling experiment

Conclusions

1. An organic silicone antistatic white thermal control coating was developed with low solar absorptivity (α_s) and high emissivity (ε_H). An exposure of the coating to a combined irradiation with UV and atomic oxygen to an equivalent of 8 years in space had little effect on the change of solar absorptivity. After combined irradiation by UV, protons and electrons for an equivalent of 8 years of space exposure, the change of absorptivity of the coating is 0.19.
2. The coating thickness has an important influence on the solar absorptivity. For thicknesses >120 μm, the solar absorptivity changes very little. In order to optimize the optical performance of the coating and the weight, the thickness of the coating should be in the range of 120–160 μm.
3. The surface treatment processing improved the adhesion between the coatings and the substrate. The coatings met the requirement of thermal cycling performance with different kinds of substrates in space. Therefore, it could be applied widely in aerospace.

References

1. Ming GR (1991) Thermal control technology of satellite [M]. Aerospace Publishing House, Beijing, pp 162–165
2. Silverman (2009) LEO materials selection guide [M]. China Aerospace Publishing House, Beijing, pp 427–434
3. Zeng YB, Xiong CX, Wang H (2002) Space environmental and technical performances of antistatic white thermal control coatings [J]. Chinese Space Science and Technology 2:65–66

Space Environment Simulation Tests for Black Polyimide Film

Lei Wang and Yun-zhen Cao

Abstract Black polyimide film is electrically conductive with high solar absorptance and high infrared emittance. The material can be applied as satellite thermal control film to enhance radiative heat transfer and thereby help isothermalize the components of spacecraft. The film can be used in satellite optical devices and telescopes baffle systems to minimize reflection from stray light. In this paper the degradation of solar absorptance of black polyimide film under simulated space environment tests such as thermal cycling, ultraviolet irradiation, proton irradiation and electron irradiation are reported. The test results show that the black polyimide film has very good stability in simulated space environment.

Keywords Black polyimide film • Degradation • Solar absorptance • Irradiation test

Introduction

The purpose of thermal control system is to maintain all components of spacecraft within the allowable temperature limits in the space environments it is exposed to. Thermal control materials play a critical role in the thermal design of spacecraft through reflection of incident solar energy and emittance of infrared heat [1]. Solar absorptance (α_S) is a very important parameter for surface properties of spacecraft. It represents the extent of solar energy absorbed by spacecraft. The degradation is represented by the change of this parameter with the accumulated space environmental effect. Temperature increase of spacecraft at the end of a long term mission is mainly caused by the degradation of surface thermal control materials with a marked increase of its solar absorptance [2]. So maintaining the desired solar

L. Wang
Qian Xuesen Laboratory of Space Technology, Beijing 100094, China

Y.-z. Cao (✉)
The Key Laboratory of Inorganic Coating Materials, Shanghai Institute of Ceramics, Chinese Academy of Sciences, Shanghai 200050, China
e-mail: yzhcao@mail.sic.ac.cn

J. Kleiman (ed.), *Protection of Materials and Structures from the Space Environment*, Astrophysics and Space Science Proceedings 47,
DOI 10.1007/978-3-319-19309-0_6

absorptance for thermal control materials is crucial to assure the proper operating temperature of the spacecraft.

For a spacecraft flight on geostationary orbit, the spacecraft materials are subjected to the complicated space environmental effects, including high vacuum, severe thermal cycles, ultraviolet irradiation, electron radiations, proton radiations, etc. The exposure to the space environment results in spacecraft surface materials degradation due to the change of their chemical, optical, thermal, electrical and mechanical properties. The general result of these processes is an increase in materials' solar absorptance with little or no effect on infrared emittance [3]. The high vacuum, for example, induces outgassing of material volatile components that produces contamination on the surrounding surfaces. The solar ultraviolet irradiation can not only induce color center inside materials but also fix contaminant deposits via polymerization, which will cause the exposed surfaces darken over time and a marked change of their reflective properties. Thermal cycle of spacecraft surfaces that go into and out of the Earth's shadow frequently causes stress effects and, hence, an embrittlement of materials. Charged particles (electron, proton) penetrate into materials and contribute to the breakdown of polymeric chains causing the degradation of the thermal control materials [4–6].

Black polyimide film is electrically conductive film with high solar absorptance and high infrared emittance. The material can be applied as satellite thermal control film to enhance radiative heat transfer and thereby help isothermalize the compartment, also, the film can be used in satellite optical devices and telescopes baffle systems to minimize reflection from unwanted stray light. The selection of certain materials in thermal control system depends on the mission requirements, it is therefore necessary to forecast the degradation of thermal control coatings during service life in order to achieve and optimize the spacecraft thermal design. For this reason, a ground-based space environmental simulation test is carried out for black polyimide film in order to evaluate its long-term space environment stability.

In this paper we present results of experimental study of stability of black polyimide film exposed to the effects of simulated space environmental testing. Solar absorptance of the film before and after simulated space environmental testing was measured, the separate effects of thermal cycling, ultraviolet irradiation, proton and electron irradiation are discussed.

Test Conditions and Method

The black polyimide film samples were provided by Shanghai Institute of Ceramics, Chinese Academy of Sciences. The thickness of samples was 30 μm. For every single experiment, three samples 30 mm in diameter were mounted on the target for a simultaneous irradiation test. The solar absorptance for three samples was measured and the average value was taken as the solar absorptance (α_s) value of the material.

The irradiation tests were conducted in a space environmental simulator. The vacuum level in the test chamber was maintained at about 10^{-5} Pa during measurements. During the tests, the temperature of the samples was maintained at 298 ± 5 K by a temperature controller including a special sample stage, a liquid nitrogen screen and a thermal detector. The energy of protons was chosen as 90 keV and proton irradiation fluence was 1.08×10^{14} p/cm^2. The energy of electrons was chosen as 90 keV and electron irradiation fluence was 1.08×10^{15} e/cm^2. An ultraviolet, 5000 W xenon arc-discharge lamp was used with the spectral distribution in the ultraviolet being close to that of the sun. The spatial uniformity of the ultraviolet irradiation on the irradiated area was lower than $\pm 10\,\%$. The spectral reflectance of black polyimide film specimens in vacuum chamber was measured in-situ in the wavelength region of 250–2500 nm by a Lambda 950 Perkin-Elmer UV–VIS–NIR spectrometer, the solar absorptance was then calculated from spectral reflectance.

Results and Discussions

Ultraviolet Irradiation

The ultraviolet irradiation test conditions were as follows: a total dose of ultraviolet irradiation was 1386ESH, the acceleration factor was 3. Solar absorptance was measured during irradiation dose of 186ESH, 594ESH, 1002ESH, 1386ESH.

Solar absorptance values and its variation in the black polyimide film samples during the ultraviolet test are presented in Table 1. It can be seen from Table 1 that the solar absorptance of the black polyimide film remains very stable after ultraviolet irradiation. The biggest differences are found for samples at the beginning, the drop in solar absorptance for sample happens immediately after the initial exposure period. It may be due to some initial effects in the samples in vacuum. It remained stable for the rest of the test. The second drop in solar absorptance for samples happens at 1002ESH can be attributed to the error of measurement. The results show that the black polyimide film is very stable under ultraviolet irradiation environment.

Table 1 Solar absorptance of black polyimide samples after ultraviolet irradiation test

	After UV irradiation α_S	$\Delta\alpha_S$
0ESH	0.94	0.0
186ESH	0.95	0.01
594ESH	0.94	0.0
1002ESH	0.93	0.01
1386ESH	0.94	0.0

Proton Irradiation

The proton irradiation test conditions were as follows: the proton energy was 90 keV, proton irradiation fluence was 1.08×10^{14} p/cm^2.

The reflectance spectrum of sample under vacuum after the proton irradiation test is presented in Fig. 1. The solar absorptance degradation of the black polyimide film samples are shown in Fig. 2.

It can be seen from Figs. 1 and 2 that the solar absorptance of the black polyimide film is very stable.. After proton irradiation (1.08×10^{14} p/cm^2 of

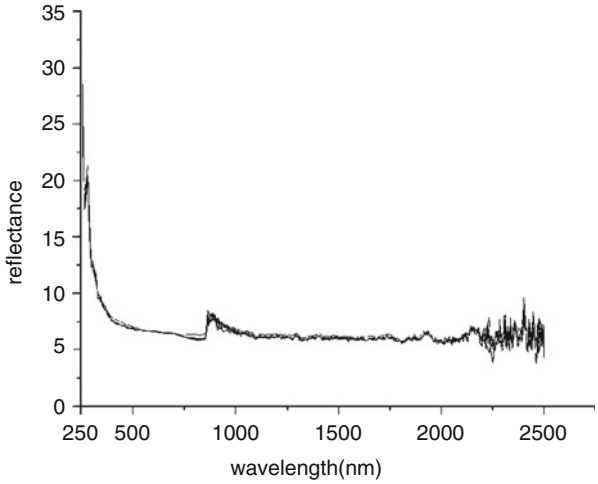

Fig. 1 Spectral reflectance of sample after proton irradiation

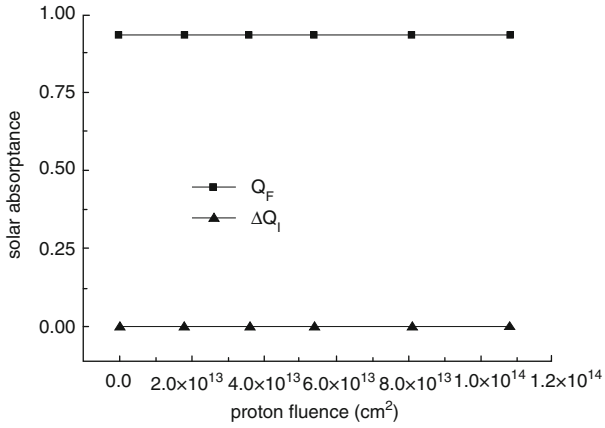

Fig. 2 Solar absorptance variation after proton irradiation test

90 keV), the change of solar absorptance is <0.02. The data presented in Figs. 1 and 2 confirmed the proton radiation stability of the black polyimide film.

Electron Irradiation

The electron irradiation test conditions were as follows: the electron energy was 90 keV, electron irradiation fluence was 1.08×10^{15} e/cm^2.

The reflectance spectrum of the sample under vacuum after electron irradiation test is illustrated in Fig. 3. The solar absorptance degradation of black polyimide film specimens is shown in Fig. 4.

As shown in the test results from Figs. 3 and 4, after electron irradiation (1.08×10^{15} e/cm^2 of 90 keV), the change of solar absorptance of sample is <0.02. The test results demonstrated that the black polyimide film degrades very little in simulated space environment.

Thermal Cycling

The thermal cycling test conditions were as follows: The samples were exposed to 100 thermal cycles in a temperature range between −196 and +120 °C, with a dwell time of 5 min at each temperature extreme.

The solar absorptance values of the samples after thermal cycling are presented in Table 2. It can be seen from Table 2 that after 100 thermal cycles (−196–120 °C) the change of solar absorptance is zero. Also, the film kept it original appearance without any cracks or defects on its surface.

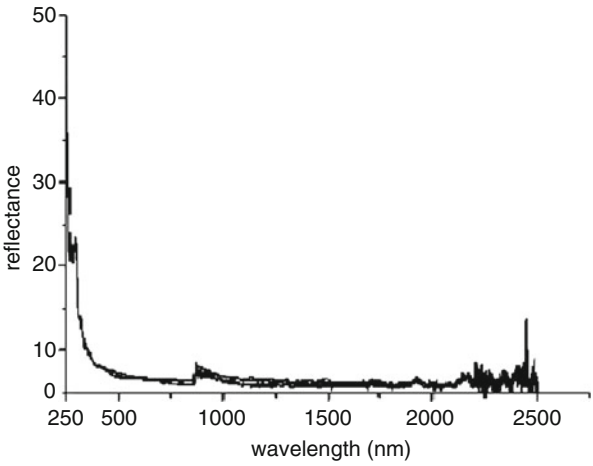

Fig. 3 Spectral reflectance of sample after electron irradiation

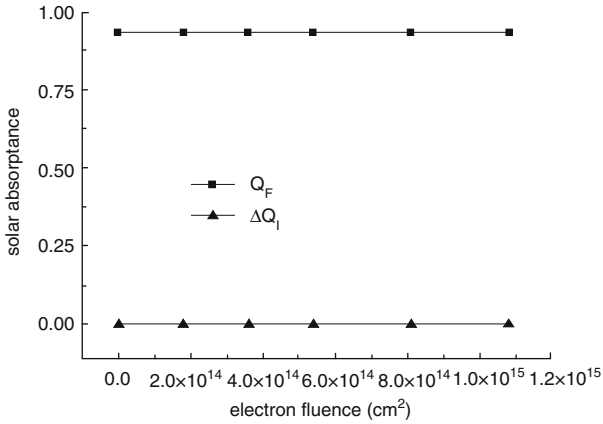

Fig. 4 Solar absorptance variation after electron irradiation

Table 2 The solar absorptance of black polyimide film after thermal cycle test

	Before thermal cycle	After thermal cycle	
Sample number	α_S	α_S'	$\Delta\alpha_S$
TC-1	0.94	0.94	0.0
TC-2	0.94	0.94	0.0
TC-3	0.94	0.94	0.0

Conclusions

The effects of simulated space environmental conditions on the black polyimide film have been studied. The results of solar absorptance measurements conducted after ultraviolet irradiation, electron and proton irradiation and thermal cycling indicate that black polyimide film is very stable, with the changes of solar absorptance after simulated space environmental effects being <0.02. The conducted analysis proved one more time that black polyimide film has very good space environmental stability.

References

1. Min G, Guo S (1998) Spacecraft thermal control technology. Science Press, Beijing
2. Feng W-q, Ding Y-g, Yan D-k et al (2007) Space combined environment simulation test on αS degradation of GEO spacecraft thermal control coatings. Spacecr Environ Eng 24(1):27–31
3. Gilmore DG (2002) Spacecraft thermal control handbook, vol I, Fundamental technologies, seconded. The Aerospace Corporation Press, El Segundo, CA
4. Troger L, Hunnefeld H, Nunes S et al (1997) Structural characterization of catalytically active metal nanoclusters in poly (amideimide) films with high metal loading. J Phys Chem B 101(8): 1279–1291

5. Fogdall LB, Leet SJ, Wilkinson MC et al (1999) Effects of electrons, protons, and ultraviolet radiation on spacecraft thermal control material. AIAA paper No. 99-3678. pp 1–9
6. Marco J, Bhojaraj H, Hulyal R (2003) Evaluation of thermal control materials degradation in simulated space environment. In: Proceedings of the 9th international symposium on materials in space environment. Noordwijk, Netherlands, 16–20 June

Analysis of the Performance of White Paint S781 in Space

Xu Tao, Chen Binbin, and Zhao Xiaoxiang

Abstract The performance of white paint S781 applied to the Fengyun-3 Satellite A and B in space is investigated in this paper. The solar absorptance of S781, including the degradation value in orbit in 5 years, are accumulated and analyzed by calculating the telemetry temperature data from the satellites. The result could provide the reference for other spacecrafts thermal design using the same white paint.

Keywords Thermal control coating • Satellite • Solar absorptance • In orbit • Degradation

Introduction

Fengyun-3 A (FY-3A) Satellite was functioning normally in orbit for over 5 years since it was launched from China Taiyuan Launch Base on May 27, 2008. The Fengyun-3 B (FY-3B) Satellite was functioning normally in orbit for over 2 years since it was launched on November 5, 2010. These two satellites were designed by Shanghai Institute of Satellite Engineering (SISE) using the three-axis-stabilized attitude control method. According to the design of satellite thermal control subsystem, a loop heat pipe (LHP) (B) radiator coated with white paint S781 was fixed on the satellite ram direction board by titanium alloy screws. A 15 mm glass steel heat insulation pad was used between them for heat insulation. The back, the profile and the edge of the board all were cladded with 15 multilayer insulation assemblies.

There are two application processes for the white paint S781. In one, the white paint F650 is used as the primer and in the other one, epoxy white paint is used as the primer. Then the S781 is sprayed on the primer. There are some differences in performance between these two coatings. In this paper, the F650 is used as the primer.

X. Tao (✉) • C. Binbin • Z. Xiaoxiang
Shanghai Institute of Satellite Engineering, Shanghai 200240, China
e-mail: tjumx@126.com

J. Kleiman (ed.), *Protection of Materials and Structures from the Space Environment*, Astrophysics and Space Science Proceedings 47,
DOI 10.1007/978-3-319-19309-0_7

Usually, thermal control coatings are affected in orbit by charged particles, ultraviolet radiation, high vacuum and the contaminant films that can deposit on almost all spacecraft surfaces [1–3]. The general result of these factors is an increase in solar absorptance that means high solar loads at end-of-life. In this paper the solar absorptance of the white paint S781 used in FY 3A and FY 3B is analyzed. The result could give a reference for other spacecrafts using the same white paint S781.

Telemetry Data Selection

Some telemetry thermistors were arranged on the ram direction surface of the LHP (B) radiator to obtain its temperature data during different periods of the satellite mission. The data showed that the LHP radiator temperature was constant for 3 or 4 min during sun light period, as shown in Fig. 1. The LHP (B) radiator temperature on December 1, 2012 is analyzed by building a mathematical model, as shown in Fig. 2. The trend of the simulation temperature is similar to the data from the telemetry results. At the same time, the result shows that the temperature near the wave crest is basically stable for a few minutes. Based on energy equilibrium, these data could be used to calculate the solar absorptance of the white paint S781.

A large amount of telemetry data have been obtained during the satellite operating in orbit for more than 5 years. The stable temperature data near the

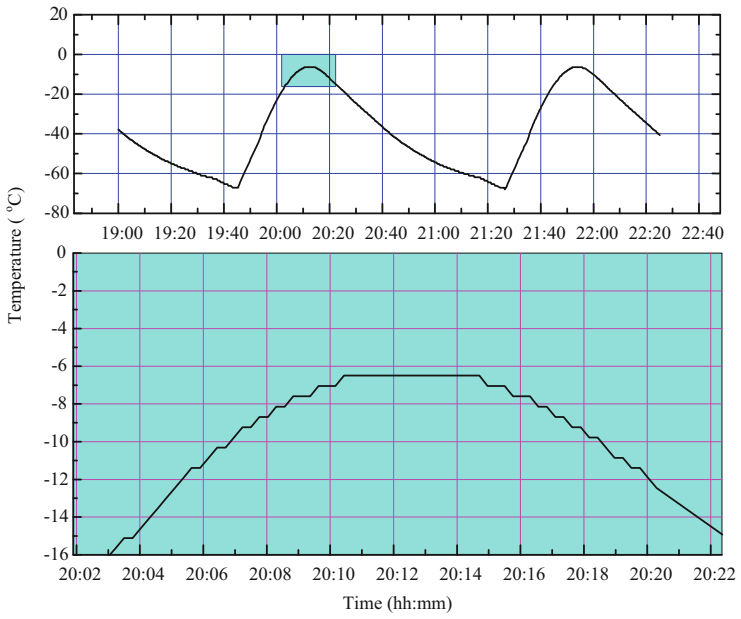

Fig. 1 Telemetry temperature curve of FY-3A on December 1, 2012

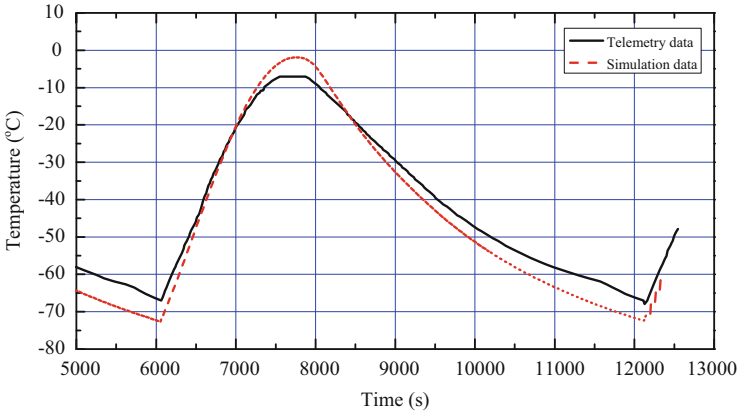

Fig. 2 Telemetry and simulation temperatures of FY-3A on December 1, 2012

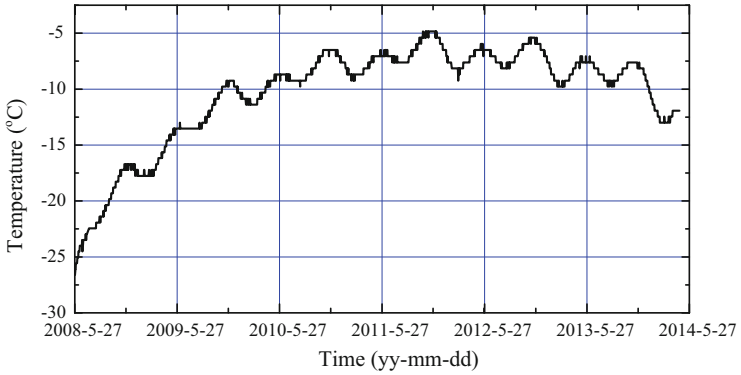

Fig. 3 The telemetry temperature curve of the LHP (B) radiator in FY-3A

wave crest was used for each of the selected days to prepare the telemetry temperature curve of the LHP (B) radiator, as shown in Fig. 3.

Thermal Analysis Methods

Thermal Equilibrium

The heat transfer between an object and the surroundings can be described usually by three main mechanisms, i.e., conduction, radiation and convection. Since the satellite is orbiting in space in high vacuum conditions, only heat conduction and radiation are considered, not including convection heat transfer. The 15 mm glass steel heat insulation pad is fixed by titanium alloy screw between the LHP

(B) radiator and the ram direction board to prevent heat conduction. The heat conduction between the pipe of LHP and the radiator can also be ignored, since the pipe is cladded by the multilayer insulation assemblies. As the LHP is shut down in orbit and the pipe is long enough, heat conduction between the LHP (B) radiator and the satellite through the pipe is also ignored.

Because the protuberances on the satellite are small, the heat radiation between the LHP (B) radiator and the protuberances of the satellite body is ignored. The board temperature is affected by the temperature of the LHP (B) radiator, if to ignore the heat leakage of the multilayer insulation assemblies. Then the board can be considered as an added heat capacity of the LHP (B) radiator. The heat radiation between the ram direction board and the radiator can be ignored.

When satellite orbits in space, it will be exposed to direct sunlight, sunlight reflected off Earth (Albedo) and infrared energy emitted from Earth (IR). Thermal equilibrium equation is expressed as

$$\alpha_S \varphi_1 S + \alpha_S \varphi_2 E_{r0} + \varepsilon_h \varphi_3 E_{i0} = \varepsilon_h \sigma T^4 \quad (1)$$

where S is the solar constant, which is selected according to WMO reference data, α_S is the solar absorptance of S781, φ_1 is the view factor from the sun to the LHP (B) radiator, φ_2 and φ_3 are view factors of Earth albedo and IR from the Earth to the LHP (B) radiator respectively, E_{r0} is the Earth albedo intensity and the average Earth reflectance is equal to 0.30, $E_{i0} = 220$ W/cm^2 is the average Earth IR intensity, $\varepsilon_h = 0.68$ is hemispherical infrared emittance of S781, $\sigma = 5.67 \times 10^{-8}$ W/m$^2 \cdot$K^4 is the Stefan–Boltzmann constant, T is the temperature of the LHP (B) radiator.

φ_1 and φ_2 Calculation

It is difficult to calculate φ_1 and φ_2. The position of the LHP (B) radiator, relative to the sun and the Earth, changes on different dates. This causes the steady temperature regime to appear at different times. But when the orbit beta angle β is kept constant, the duration intervals between the steady temperatures become fixed and the Earth shadow appearance doesn't change. The position of the LHP (B) radiator relative to the sun and the Earth is fixed, so the φ_1 and φ_2 could be calculated as a function of angle β. Figure 4 shows the φ_1 and φ_2 values at different β angles. Other values can be obtained by the interpolation method.

φ_3 Calculation

Due to the fixed position of the LHP (B) radiator relative to the Earth, the view factor φ_3 of Earth IR from the Earth to the radiator is constant. So the φ_3, equal to

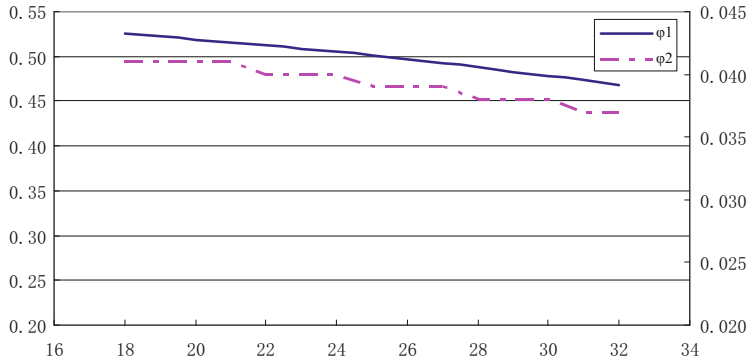

Fig. 4 Dependence of the view factors φ_1 and φ_2 on angle β

0.128, was calculated and obtained in this paper using thermal analysis software TMG.

Calculation of the Solar Absorptance of S781

Based on previous experience of irradiation testing of the thermal control coating, the hemispherical IR emissivity of the coating remains constant. According to the Eq. (1), the solar absorptance α_S can be expressed as

$$\alpha_S = \varepsilon_h\left(\sigma T^4 - \varphi_3 E_{i0}\right)/\left(\varphi_1 S + \varphi_2 E_{r0}\right) \tag{2}$$

The above obtained parameters, φ_1, φ_2 and φ_3, and the everyday stable temperatures of the LHP (B) radiator are substituted into Eq. (2) to gain the degradation curve of the solar absorptance of S781, as shown in Fig. 5.

Data Analysis and Results

Prime Variance Analysis

Figure 5 shows that at the initial stage, when satellite is launched into the orbit, the solar absorptance of S781 has already reached 0.21 which is larger than the terrestrial test value 0.17. Some factors are responsible for this phenomenon.

Firstly, when the solar absorptance is tested in terrestrial conditions, the source light is perpendicular to the surface of thermal control coating that means the test angle between the light and the surface is 90°. The sunlight in space, on the

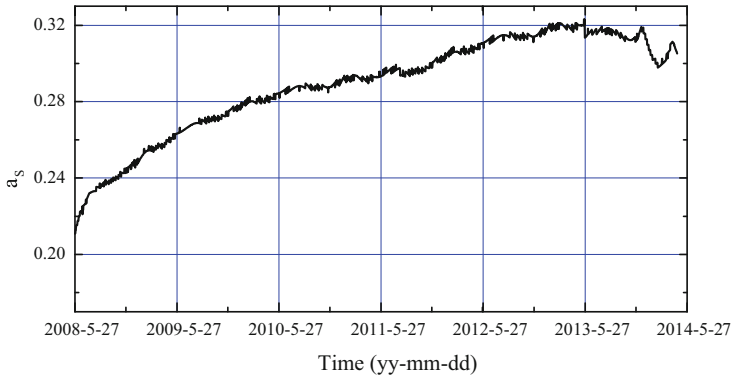

Fig. 5 The degradation curve of the solar absorptance α_S

other hand is not perpendicular to the surface of thermal control coating when the satellite orbits in space. So this will cause the difference of α_S between the terrestrial test value and the on-orbit value.

Secondly, the surface of thermal control coating is very clean, and, even if it will become contaminated in laboratory, will be cleaned for testing. In the pre-launch time the satellite may become contaminated by some dust and dirt, especially in the 2 h before it is launched. The environmental cleanliness around the satellite can't be controlled.

Thirdly, most of the satellite materials will start to outgas as the satellite orbits in high vacuum environment. Some condensable volatile substances may condense on the low temperature surfaces. As S781 is on the outmost surface of the satellite, its temperature is lower than other regions. The condensable volatile substances will condense on the surface of S781, which could raise its solar absorptance.

Fourth, the solar absorptance of S781 degrades seriously at the prime on-orbit stage. So the solar absorptance of S781 α_S tested in space is larger than the value tested on the ground.

Analysis on α_S Degradation

From the degradation curve of the solar absorptance α_S shown in Fig. 5, it is clear that in the early on-orbit stage it degrades seriously. For longer on-orbit duration, the degradation process of the solar absorptance α_S slows down. The average decrease of α_S is 0.05 in the first year and 0.02 in the previous 50 days. Subsequently, the decrease of α_S is 0.02 in the second year and 0.01 in every subsequent year.

The solar absorptance of S781 will not recover again after it degrades. But Fig. 5 shows that there is an obvious decrease in the data of the solar absorptance α_S in the third year. This phenomenon can be explained by two reasons. For one thing, the

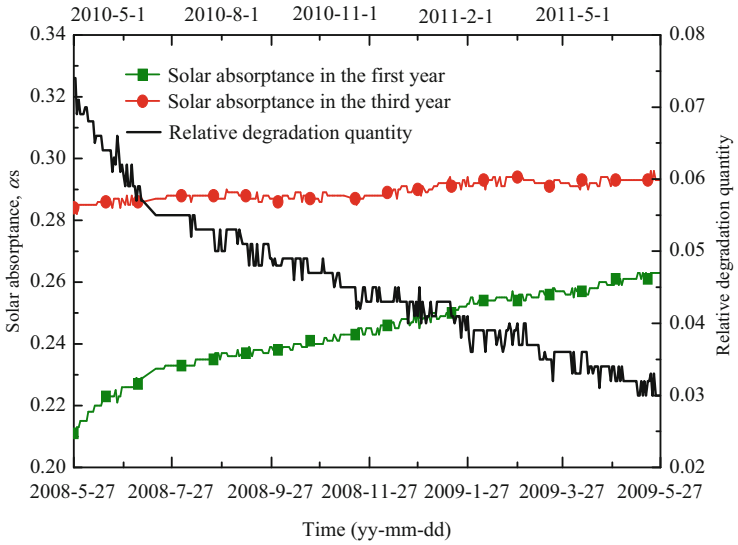

Fig. 6 A comparison between the solar absorptance degradation of the coating used in FY-3A in the first and third year

Earth infrared radiation intensity and the Earth albedo used in this paper are all selected as constant values, but in fact both of them are variable. For another, these two parameters including the Earth infrared radiation intensity and the Earth albedo also oscillate in the previous 2 years, but there influence is masked by the coating degradation. Thus, the influence of the Earth infrared radiation intensity and the Earth albedo becomes clearer with the coating degradation rate slowing down. For analyzing the coating degradation in the first year, the coating degradation data on the same date in the third year are compared with the data in the first year to decrease the influence of the variation of both earth infrared radiation intensity and the earth albedo on the coating degradation. The result shown in Fig. 6 indicates that the relative coating degradation rate decreases rapidly in the first 50 days of the on-orbit first year, then slows down in the following days.

The solar absorptance of S781 in FY-3B is calculated by the same method. Its degradation result is compared with the data of S781 in FY-3A on the same date, as shown in Fig. 7. The degradation trend of the solar absorptance of S781 in FY-3B is similar to that in FY-3A in the first 7 months. But the degradation quantity of α_s in the first 50 days is 0.03, which is larger than that in FY-3A.

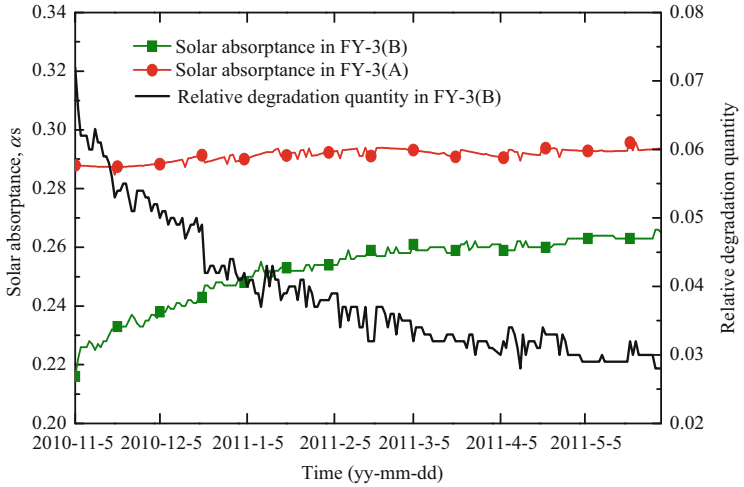

Fig. 7 Comparison of the solar absorptance degradation of the coating in FY-3A and B

Conclusions

The on-orbit solar absorptance degradation of the coating S781 was investigated by analyzing the telemetry data from FY-3A and B satellites. The solar absorptance of S781 degrades seriously in the first year, with most of the degradation occurring in the first 50 days in orbit. With an increase of the on-orbit time, the degradation rate gradually decreases, with final value of the solar absorptance of S781 staying at around 0.31.

The results of the above analysis suggest that the prime solar absorptance of S781 can use terrestrial test value 0.17. Considering keeping a suitable allowance for thermal design, a little large value is selected as the solar absorptance of S781 in the last on-orbit period. For instance, a value 0.28 can be selected as the solar absorptance after the first on-orbit year. And the solar absorptance increases 0.02 after each additional year.

References

1. Gilmore DG (2002) Spacecraft thermal control handbook, vol 1, 2nd edn, Fundamental technologies. The Aerospace Press, California
2. Min G (1991) Satellite thermal control technology. Aerospace Press, Beijing (In Chinese)
3. Min G (1998) Spacecraft thermal control, 2nd edn. Science Press, Beijing (In Chinese)

Wood-Based, Diamond-Like Carbon for Improved Resistance Against Atomic Oxygen

Takeshi Kajimoto, Toshimitsu Hata, Masahito Tagawa, Hirotsugu Kojima, and Hajime Hayakawa

Abstract Polyimide or fluorine polymer that are used as heat-control materials on structures in LEO and GEO orbits, if not protected from the atomic oxygen (AO) may be severely degraded by the formation of microcracks. Carbonized materials are suitable for use in low Earth orbit (LEO) as they have excellent mechanical strength, electrical insulation, and thermal conductivity. Carbonized wood, in the form of a Japanese lacquer composed of aromatic compounds derived from the urushi tree, could potentially be used as the outer surface material of spacecraft, provided however that its resistance against AO irradiation in LEO is sufficient. The main aim of this study, therefore, is to develop the requisite technology to impart erosion resistance against AO to the carbonized wood. Specifically, increased sp2 bonding in the Si-doped diamond-like carbon introduced here is shown providing effective resistance against AO-induced erosion.

Keywords Diamond-like carbon • Wood-based material • Atomic oxygen • Low earth orbit • Spacecraft

T. Kajimoto (✉)
Industrial Technology Center of Wakayama Prefecture, 60 Ogura, Wakayama, Japan
e-mail: kaji@wakayama-kg.jp

T. Hata • H. Kojima
Research Institute for Sustainable Humanosphere, Kyoto University, Gokasho, Uji, Kyoto, Japan

M. Tagawa
Graduate School of Engineering, Kobe University, 1-1 Rokodai-cho, Nada-ku, Kobe, Hyogo, Japan

H. Hayakawa
Japan Aerospace Exploration Agency, 3-1-1 Yoshinodai, Chuo-ku, Sagamihara-shi, Kanagawa, Japan

J. Kleiman (ed.), *Protection of Materials and Structures from the Space Environment*, Astrophysics and Space Science Proceedings 47,
DOI 10.1007/978-3-319-19309-0_8

Introduction

Highly reactive atomic oxygen (AO) is produced in the outer atmosphere of Earth by ultraviolet radiation reacting with molecular oxygen [1]. The surfaces of spacecraft in low Earth orbit (LEO; 200–700 km above the Earth) are susceptible to oxidation through ionization by ultraviolet radiation and reactions with AO. Interactions with AO and/or ultraviolet radiation lead to the rapid deterioration of the outer surface of spacecraft in LEO [2].

Polyimide or fluorine polymers that are usually employed as heat-control materials on the outer surface of spacecraft need to be protected against AO. For that reason they are coated by ceramic type of coatings. However, the protection provided by ceramic-coated polymers can be compromised by the formation of microcracks. The excellent mechanical strength, electrical insulation, and thermal conductivity provided by carbonized materials make them suitable alternatives for LEO protection [3]. Carbon materials, which are inflammable, light and robust are recognized as promising candidates for this purpose.

Previously, we carbonized organosolv lignin produced by cooking wood in L-lactic acid. We investigated its resistance to AO erosion in the presence of carbonized wood containing Si and found that aromatics in the carbonized wood played an important role in preventing damage from AO [4]. Urushi is traditionally used as paint and is extracted from the lacquer tree (*Toxicodendron vernicifluum*). Products coated with the lacquer are recognizable by an extremely durable and glossy finish. Our hypothesis is that carbonized urushi can also be used as an outer surface material for spacecraft.

In this study, we investigate the resistance to AO radiation of samples coated with diamond-like carbon (DLC) sputtered from a target of carbonized Urushi and Si. The erosion of the samples under AO was studied in order to identify the chemical reactions occurring between C, Si, and O in the DLC film. The DLC coat, composed of C, Si, and O was characterized by transmission electron microscopy electron energy-loss spectroscopy (TEM-EELS) and X-ray photoelectron spectroscopy (XPS) in order to reveal the mechanisms governing its resistance to erosion.

Experimental

Sample Preparation

Urushi was carbonized by heating up to 973 K at 4 K/min in a N_2 atmosphere, maintaining the temperature for 1 h, and then cooling to room temperature. Carbonized urushi and Si were mixed in a glove box to a 60:40 weight ratio. The mixtures were then sintered at 1173 K and at the mechanical pressure of 40 MPa for

15 min in vacuum. Thereby, sputtering targets 30 mm in diameter and about 2 mm thick were obtained of carbonized urushi with and without Si.

A layer of DLC was deposited on a Cu microgrid by DC magnetron sputtering using the prepared targets of the carbonized urushi with or without Si, in an Ar atmosphere under 20 Pa for 5–10 min.

AO-Exposure Experiments

All the samples were exposed to an AO beam generated by exciting molecular oxygen using a CO_2 laser beam (Fig. 1, wavelength: 10.6 μm; pulse energy: 5–7 J) [1]. The energy distribution of the AO beam was calculated as shown in Fig. 1. In this study, the average energy was about 5 eV and the flux was 2×10^{15} atoms/cm^2. This energy is equivalent to that of the AO in LEO. Samples were placed in the system with their pressed plane perpendicular to the AO beam.

Analysis

The DLC films deposited on 200-mesh Cu microgrids with holey carbon supported films were analyzed using a TEM-EELS (JEM2100F) before and after exposure to AO. The chemical state of the carbon in the DLC is reflected in the appearance, position, and intensity of the EELS peaks in the core-loss region of the spectra. The spectra have a smooth background, modeled here using a power-low curve, which was subtracted from beneath the carbon edge. The same DLC films on Cu microgrids were also analyzed by XPS (Shimadzu/KRATOS) using MgKα radiation.

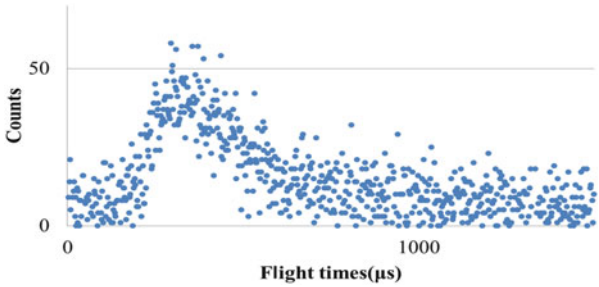

Fig. 1 Time-of-flight data for the AO beam generated by a CO_2 laser beam

Results and Discussion

TEM-EELS

Figure 2 shows TEM images after AO irradiation of DLC films on a Cu microgrid sputtered for 5 and 10 min. While the DLC film sputtered for 5 min is damaged in part by AO exposure, the one sputtered for 10 min remains intact. Using the setup described above, a sputtering time of 10 min is therefore necessary to form a DLC film resistant to AO exposure. Figure 3a and b show core-loss EELS spectra

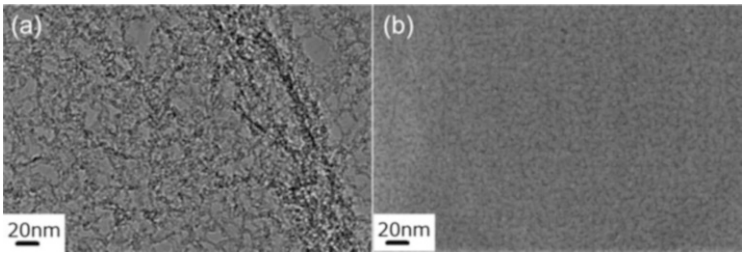

Fig. 2 Transmission electron micrographs taken after irradiation with atomic oxygen of diamond-like carbon films deposited on Cu microgrid substrates by sputtering for (**a**) 5 min and (**b**) 10 min

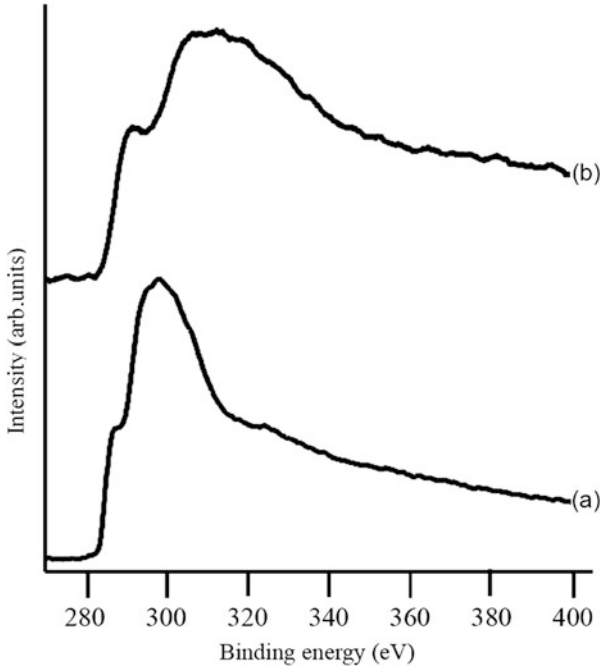

Fig. 3 C1s electron energy-loss spectra obtained (**a**) before and (**b**) after exposure to atomic oxygen of diamond-like carbon films sputtered for 5 min onto Cu microgrid substrates

obtained from DLC films sputtered for 5 min before and after exposure to AO, respectively. These reveal the chemical state and the concentration of the different elements in the DLC films.

The π^* feature at a binding energy of 285 eV is more sharply defined in Fig. 3b, while the broader spectral feature in Fig. 3a at 290–310 eV is typical of sp2-rich amorphous carbon [5]. This increase in the π^*/σ^* ratio implies that AO exposure enhances sp2 bonding in the DLC films.

XPS

Figure 4 shows C1s, O1s, and Si2p XPS spectra obtained from DLC films before and after AO exposure. The atomic concentration of each element is shown in Table 1 (note that Cu and Pd come from the background). The atomic concentration of SiOxCy increases by 1.2 % after AO irradiation, whereas the atomic concentration of C–O and C=O decreases. The change in the full width at half maximum of the C1s peaks from 1.9 to 1.6 eV after AO irradiation shows that the DLC films remain relatively free of oxidation after exposure. The increase in sp2 bonding in the DLC films mentioned above for the TEM-EELS results is supported by these XPS data. The original aromatic structure in urushi may be a contributing factor.

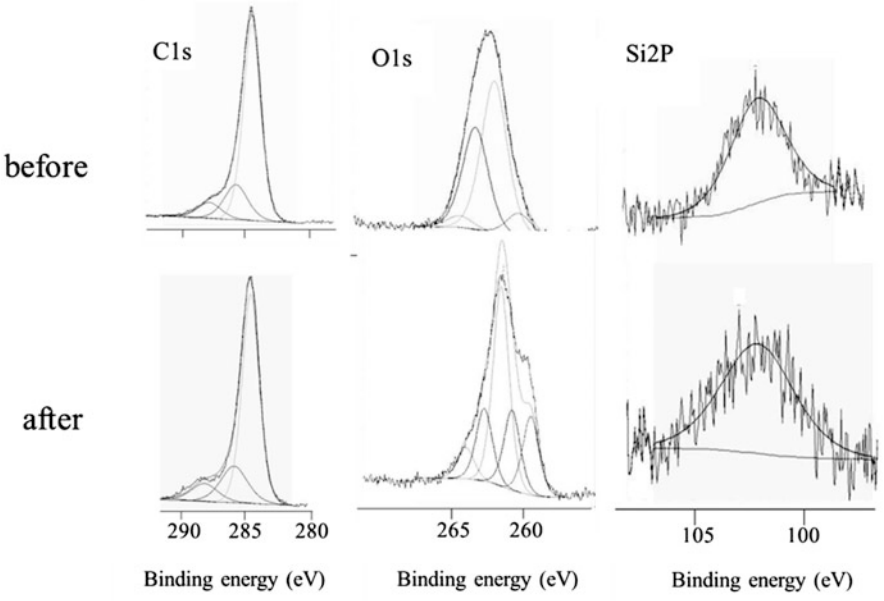

Fig. 4 X-ray photoelectron spectra obtained from diamond-like carbon films sputtered for 5 min onto Cu microgrid substrates before (*top*) and after (*bottom*) exposure to atomic oxygen

Table 1 Analysis with X-ray photoelectron spectroscopy on chemical bonds of diamond-like carbon films sputtered for 5 min onto Cu microgrid substrates before and after exposure to atomic oxygen

(at. %)													
Si 2p			C1s			O1s				Cu 2p			
						Binding energy (eV)							
	SiO_2	SiOxCy	C–C C–H	C–O C–OH	C=O	O–Cu	O=C	O–C	O_2–Si	Cu 2/3	Cu 1/2	Cu–O 2/3	Cu–O 1/2
	242	239.7	284.5	286	288	260.8	262.4	264	264.7	186.5	206.5	196.5	216.2
Before	1.3	0.7	5.34	8.5	11.3	4.2	0.6	14.1	1.3	0.2	0.1	2.7	1.6
After	0.1	1.9	47.0	4.0	9.8	2.7	19.0	7.5	0.1	3.3	1.7	1.4	1.3

Conclusions

DLC films obtained from carbonized urushi have been shown to successfully prevent AO-induced erosion. The formation of SiO_2 and increased sp2 bonding in the DLC films are the main protecting factors. The catalytic effect of Si–O on the formation of sp2 bonds may contribute furthermore to the prevention of damage from AO irradiation.

Acknowledgements This work was supported by KAKENHI (22251004), a Grant-in-Aid for Scientific Research (A) from the Japan Society for the Promotion of Science (JSPS) and a research grant for Mission Research from the Research Institute for Sustainable Humanosphere, Kyoto University.

References

1. Tagawa M (2001) Material degradation phenomena in low earth orbit space environment and their ground-based simulations. J Vac Soc Jpn 44(5):26–31
2. Yokota K, Ikeda K, Tagawa M, Okamoto A (2005) Erosion on polyimide and fluorinated polymers in combined low earth orbit space environment: simultaneous exposure effects of atomic oxygen and ultraviolet. High Temp Soc 31:318–323
3. Fujimoto K, Sato K, Shioya T, Seki N, Fujita K (2003) Degradation of materials by high-energy atomic oxygen. JSME Int J Ser A 46(3):283–289
4. Kajimoto T, Hata T, Tagawa M, Kojima H, Hayakawa H (2013) Resistance of silicon-containing carbonized lignin to atomic oxygen erosion. In: Protection of materials and structures from the space environment (Astrophysics and space science proceeding). Springer, Berlin, pp 541–546
5. Bruley J, Williams DB, Cuomo JJ, Pappas DP (1995) Quantitative near-edge structure analysis of diamond-like carbon in the electron microscope using a two-window method. J Microsc 180(1):22–32

Formation of E'γ Centers Under Electron Irradiation in Ultrapure Glass and Structural Relaxation

Chengyue Sun, Yiyong Wu, Haiying Xiao, Jianqun Yang, Jingdong Xiao, Yu Sui, Yi Wang, and Zhong Yi

Abstract The processes of defect formation and evolution in ultrapure glass under 1 MeV electron irradiation were investigated by the measurement of electron paramagnetic resonance (EPR) spectra and optical absorbance. The results show that the 1 MeV electron irradiation of the ultrapure glass can induce the formation of E'γ centers, and the structure of the E'γ center transform from E'γ(1) center to E'γ(2) center with the increasing irradiation fluence, and this variation also affects the defect optical absorption property in the material. During the room temperature aging process, the defects anneal process induces the recovery of the optical property of the ultrapure glass. It is worth to note that the defect structure varied during the ageing process, namely, the E'γ(2) center transform to E'γ(1) center, and the variation of the defect structure induced the no synchronous property between the defect anneal and the optical absorption recovery.

Keywords Electron irradiation • E'γ center • Defect structure transformation

C. Sun
Department of Physics, Center for Condensed Matter Science and Technology (CCMST), Harbin Institute of Technology, Harbin 150001, China

National Key Laboratory in Materials Behaviors and Evaluation Technology in Space Environments, Harbin Institute of Technology, Harbin 150001, People's Republic of China

Y. Wu (✉) • H. Xiao • J. Yang • J. Xiao
National Key Laboratory in Materials Behaviors and Evaluation Technology in Space Environments, Harbin Institute of Technology, Harbin 150001, People's Republic of China
e-mail: wuyiyong@hit.edu.cn

Y. Sui
Department of Physics, Center for Condensed Matter Science and Technology (CCMST), Harbin Institute of Technology, Harbin 150001, China

Y. Wang
Lanzhou Institute of Physics, Lanzhou 730000, People's Republic of China

Z. Yi
Beijing Institute of Spacecraft Environment Engineering, Beijing 100000, People's Republic of China

J. Kleiman (ed.), *Protection of Materials and Structures from the Space Environment*, Astrophysics and Space Science Proceedings 47,
DOI 10.1007/978-3-319-19309-0_9

Introduction

Amorphous SiO_2 (or silica) is widely used in various technological applications, in optics and in telecommunications. The presence of point defects can modify the physical properties of the material. They can give rise to electron paramagnetic resonance (EPR) signals and to optical absorption and photoluminescence emission bands [1–3]. Irradiation induced point defects in silica (a-SiO_2) are a topic of large interest in the characterization of this widely used material. For the amorphous silicon dioxide material, the *E*' centers are the most common defects which formed by the ionization irradiation. The investigations of the *E*' centers in amorphous silicon dioxide had continued for almost 60 years. The defects modify the physical properties of the material and limit its technological applications, such as, for instance, in microelectronics as an insulating layer of metal-oxide semiconductor devices or in optics, in fibers for light transmission, to name a few. It is, therefore, remains a challenge for solid state physics the further understanding of the structures and generation and the stability of defects in an amorphous material.

Irradiation on the amorphous silica material can induce the formation of the E'γ center, On the basis of the spectral features, a microscopic model was proposed for this defect that was tested in many experimental and theoretical studies. The model consists of a dangling bond of a threefold coordinated silicon atom with the unpaired electron in an approximately *sp*3 hybrid orbital: $O \equiv Si\bullet$ (the symbol $\equiv$ represents single bonds to three oxygen atoms and the symbol • stays for the unpaired electron) [1–4]. The origin of the E'γ center has been investigated and many types of precursors have been suggested, including intrinsic defect (the mono-vacancy of oxygen $O \equiv Si–Si \equiv O$ giving a charged E'γ by trapping a hole, $O \equiv Si\bullet + Si \equiv O$, and extrinsic), and the groups which would release the impurity, such as the $O \equiv Si\bullet + X$, where *X* is H or Cl. This variety of precursors can be used to explain the observation of complex kinetics of growth of the concentration of the E_γ' under irradiation. In the meantime, the microscopic structure of the environment of the $O \equiv Si\bullet$ also shows effect on the spectral features of the defects. It has been shown that that the EPR signal associated with E'γ centers undergoes line shape change during irradiation. The modifications are evidenced by two typical line shapes denominated as L1 and L2, one corresponding to a more axial and the other to a more orthorhombic *g* tensor, respectively, and they have been attributed to a structural variation in the center and also affect the position of the AO band.

In parallel with the investigation of defect formation process, the stability of the defect is also studied. Messina investigated the instability of E'γ centers in amorphous SiO_2 induced by γ irradiation (with the ionization dose range from 0.6 to 79 kGy) at room temperature and came to a conclusion that the annealing of the E'γ center is ascribed to the effect of the chemical reaction between the defect induced by irradiation and the diffusing molecule such as hydrogen, oxygen, or water [5]. It is also found that the irradiation dose affects the annealing rates of the sample, with the increasing irradiation dose the annealing rate decreases. Griscom studied the instability of E'γ centers in amorphous SiO_2 with the higher ionization dose

(27–4400 kGy), and the results show also that with the increasing irradiation dose the annealing rate decreases. It should be noted that for the sample with the dose of 4400 kGy, the defect population firstly increases in the initial stage of post storage and then decreases as the time goes by [6]. The evaluation of the E'γ center annealing process in the two above investigations is based on the evolution of the optical property of the glass.

The use of measurements of the variation of the optical absorption for evaluating the annealing of defects in the glass material is convenient and fast, but there are drawbacks in such measurements. Thus, for two types of defects with energy levels close to each other (for example the difference is <0.05 eV), the measurement of the optical absorption evolution cannot represent the variation of the specific defect accurately [7–9]. Compared to the measurement of the optical transmittance, the superiority of EPR analysis is that it can distinguish between the two types of defects in the silica material with energy levels close to each other. Zhang's investigation shows that there are two types of E'γ centers which can be formed in the glass, with the increasing of the irradiation ionization dose, the type of E'γ center transforms from $E'_{\gamma}(1)$ to $E'_{\gamma}(2)$ center, the marginal distinction between the two kinds of E'γ centers can be distinguished by the signal saturation property as a function of the EPR test power [10, 11]. His results also shows that with the increasing of the irradiation ionization dose, the type of E'γ center transforms from $E'_{\gamma}(1)$ to $E'_{\gamma}(2)$ center, in the meantime, the energy levels of the defects also change with the structure of the E'_{γ} center, and induce the variations of the macroscopic optical property. It is worth to note that the investigations on the E'_{γ} center mainly focus on the defect formation process, the defect structure property and the macroscopic optical property. Few researchers studied the stability of the E'_{γ} center and the structure transformation during the post storage, the evolution of defect population and the structure of the two types of E'_{γ} centers and the corresponding macroscopic optical behavior variations, and these parameters still need to be further investigated.

In this paper, the damage effects of 1 MeV electron irradiated ultrapure glass are investigated by the measurements of optical transmittance after the irradiation and during the post-irradiation storage. In the meantime, the electron paramagnetic resonance spectroscopy was also applied to study the formation and the evolution of the defects induced by 1 MeV electron irradiation in the super-pure glass. Both mechanisms influencing the defect evolution during the irradiation and the post storage will be discussed in this paper.

Experimental

In this work, the silica samples (provided by Beijing Zhong Cheng Quartz Glass Co., Ltd) with the purity of 99.9999 % and thickness of 100 μm were irradiated and investigated. The electron irradiation was carried out in an electron linear

accelerator (Technical Physics Institute of Heilongjiang Academy of Science, China). The electron energies and flux were set as 1 MeV and 5×10^{11} cm^{-2}, respectively.

The EPR measurements of the irradiated samples were carried out using a Bruker A200 spectrometer (Bruker Instrument, Germany). The spectrometer was operated at a microwave power of 0.93 mW, modulation of 1G, and a time constant of 40.96 s. The population of spins (free radicals) of the measured samples was obtained by the double numerical integration of the first derivative of the EPR spectra. The optical absorbance from 200 to 800 nm was measured by Perkin-Elmer Lamda 950UV-VIS-NIR spectrophotometer, with a resolution of 2 nm.

Results and Discussion

Defect Formation and Optical Degradation of Ultrapure Glass Under 1 MeV Electron Irradiation

A typical EPR spectrum obtained in materials irradiated with 1 MeV electrons at a fluence of 1×10^{15} cm^{-2} is shown in Fig. 1. As can be seen from Fig. 1, the upper scale relative to the g values has been obtained by fixing the first positive peak position of the E'γ center at $g1 = 2.00180$. We estimated the g2 and g3 principal values directly from the magnetic field positions indicated by vertical lines in Fig. 1. The obtained values, $g2 = 2.00063 \pm 0.00002$ and $g3 = 2.00036 \pm 0.00002$, are in quite good agreement with those corresponding to the maxima of the statistical distributions, $g2 = 2.0006$ and $g3 = 2.0003$, obtained by Griscom using a computer simulation of the experimental EPR spectrum. Figure 1b presents the evolution of E'_γ population as a function of irradiation fluence. It can be found that the population of the E'_γ increases with the irradiation fluence, it is worth to note that increase rate of the E'_γ defect in the initial stage of the electron irradiation, where the irradiation fluence is $<1 \times 10^{15}$ cm^{-2}, is higher than the one in the high irradiation fluence range (the fluence is more than 1×10^{15} cm^{-2}). The variation of the defect population increase rate can be ascribed to three aspects: the change of the irradiated material; the variation of the irradiation source and the transformation of the defects structure which formed during the irradiation. In this irradiation test, the irradiated sample is the super-pure glass, and the irradiation source is the 1 MeV electrons, both of them did not vary during irradiation test, thus, one can reach the conclusion that the variation of the defect population increase rate is induced by the transformation of the defects structure. The transformation process of the defects structure is also investigated.

Previous investigations show that there are two EPR line shapes of the E'γ center, arising from two slightly different microscopic structures. In Fig. 2, the normalized EPR spectra of the E'γ center with different irradiation fluence are superimposed. As shown, a modification of the E'γ center EPR line shape occurs on

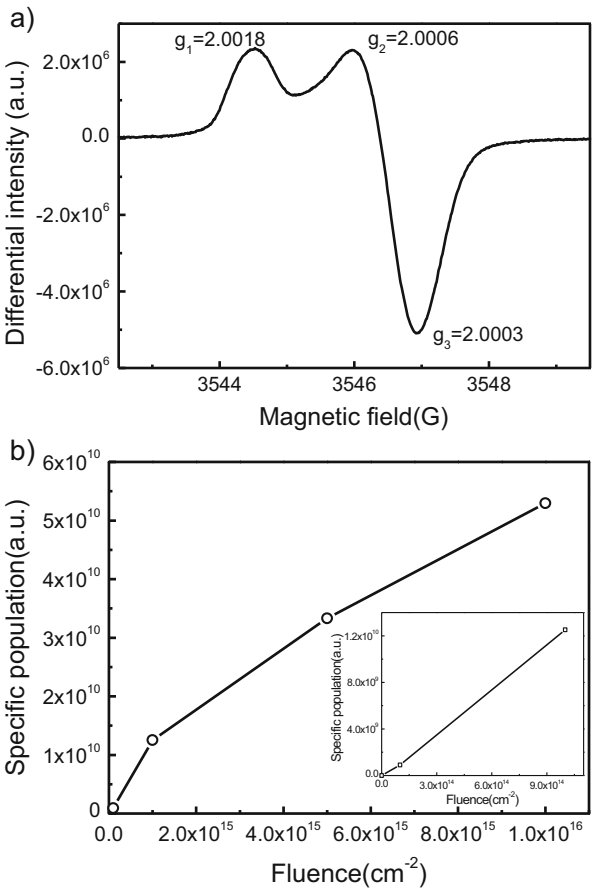

Fig. 1 EPR spectra of irradiated ultrapure glass with 1 MeV electrons and the free radical population increase with the irradiation fluence. (**a**) EPR spectra; (**b**) free radical population increase with the irradiation fluence

increasing the irradiation fluence, even though no specific feature attributable to the occurrence of this line shape change can be recognized in the growth curve of the defects concentration. The difference $\Delta g_{1,2} = g_1 - g_2$ varies from 0.00124 at a fluence of 1×10^{14} up to 0.00115 at 1×10^{16}. The variation of $\Delta g_{1,3} = g_1 - g_3$ is less pronounced on increasing fluence, changing from 0.00147 at a fluence of 1×10^{14} to 0.00142 at 1×10^{16}.

The investigation of EPR signals saturation properties as a function of microwave power is a powerful way to study the slight structure changes of the defect. Figure 3 shows the EPR signals saturation properties with microwave power of the E'_γ with low- and high-irradiation fluence. For convenience, symbols L1 and L2 have been adopted for the low- and high-dose EPR line shapes, respectively. It can be found that with the increasing irradiation fluence, the EPR signals' saturation curve transforms from L1 to L2, which means the defects structure varies with the increasing fluence. The defects structures which correspond to L1 and L2 EPR signals saturation curve are $E'_\gamma(1)$ center and $E'_\gamma(2)$ center, respectively.

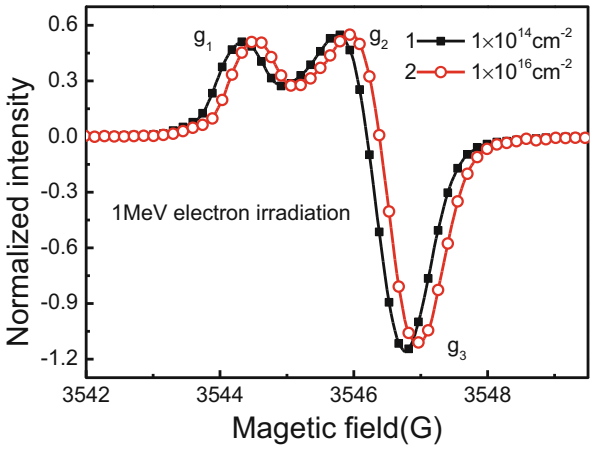

Fig. 2 The comparison of EPR differential spectra of 1 MeV electron irradiated ultrapure glass

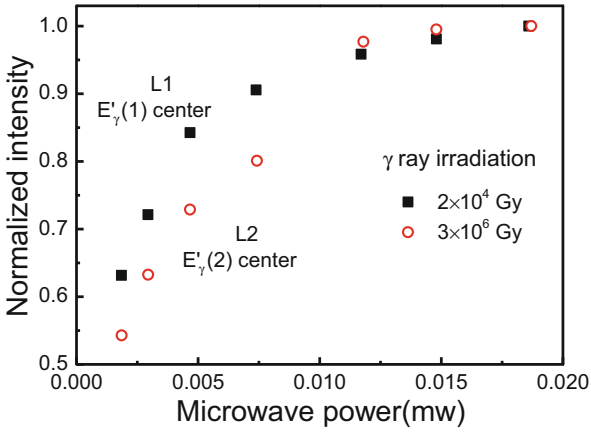

Fig. 3 FH-EPR signal intensity of E'$_\gamma$ center as a function of microwave power

Ionization effect of the 1 MeV electron and γ-ray irradiation in the ultrapure glass induces the formation of the E'$_\gamma$(1) center, with the increasing ionization dose, the E'$_\gamma$(1) center is further ionized, and all of these induce the formation of an electropositive state defect, namely the E'$_\gamma$(2) center. The formation process of E'$_\gamma$(2) center is shown in formula (1).

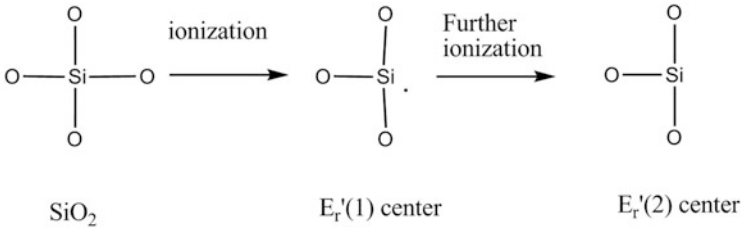

(1)

The irradiation with charged particles would induce the formation of color center in the glass and the degradation of the optical property of the glass material. Figure 4a shows the spectral transmittance variation with the increasing fluence in the super-pure glass under 1 MeV electron irradiation. It is understandable that spectral transmittance decreases with the increasing fluence, which is consistent with data reported in the literature. To determine the degraded tendencies, the corresponding differential spectra $\Delta T = T_{as\text{-}received} - T_{irrdiated}$ (where $T_{as\text{-}received}$ is the transmittance of the as-received glass and $T_{irrdiated}$ is the one after irradiation) of the irradiated super-pure glass were calculated, as shown in Fig 7b. It can be found that the differential absorbance increases with the increasing irradiation fluence.

The investigation of the defect structure evolution with the increasing ionization shows that the defects transform from E'$_\gamma$(1) to E'$_\gamma$(2) center. It is understandable that the variation of microscopic structure of the material certainly will induce the change of the macroscopic property.

The optical absorption properties of the E'$_\gamma$(1) and E'$_\gamma$(2) centers are also investigated. Figure 5 shows the normalized transmittance variation spectra ΔT with various irradiation fluence. It can be found that the peak position of the OA band that is associated with the E'γ centers shifts towards the lower energy with the increasing irradiation fluence, all of these is concomitant to the change of the EPR line shape from L1 to L2. Combining the data presented in Figs. 3 and 5, the peak position of the E'γ center OA band can be calculated. The peak position of E'$_\gamma$(1) OA band is centered at 5.83 ± 0.01 eV, at this moment, the defect exhibits the L1 EPR line shape, with the increasing irradiation fluence, the peak positions of E'$_\gamma$(2) OA band is located at 5.77 ± 0.01 eV, when the defect exhibits the L2 line shape [11]. The EPR and optical spectrum parameters of two types of E'$_\gamma$ centers are listed in Table 1.

The Room Temperature Aging of E'$_\gamma$ Center and the Corresponding Optical Property Recovery

It is known that the defects are in an unsteady state and during the annealing process the defect population would decrease with the storage time. The E'$_\gamma$ centers can be divided into two types, the stabilities of the two kinds of defects are investigated. Figure 6 presents the time evolution at room temperature of the defect population of

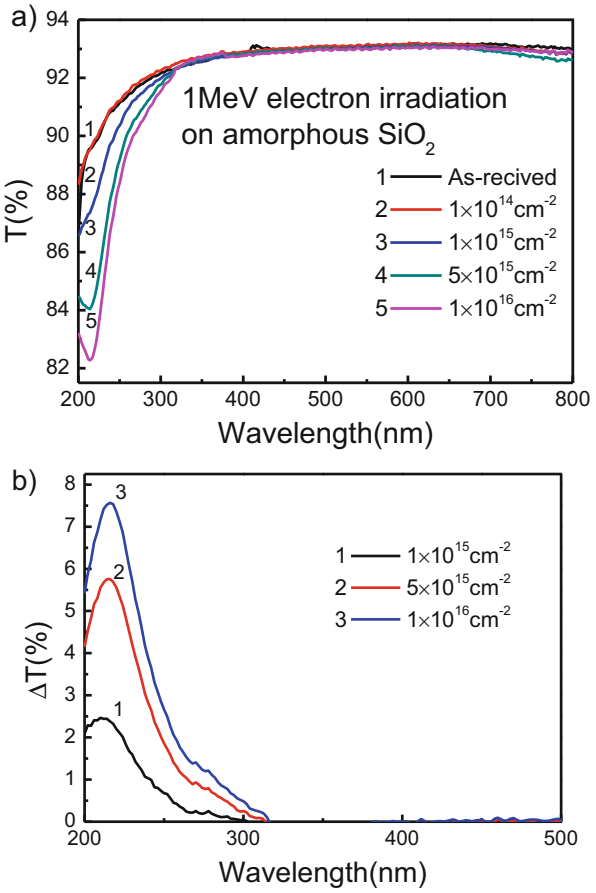

Fig. 4 Spectral transmittance and absorption spectrum of ultrapure glass after 1 MeV electron irradiation with various fluencies; (**a**) spectral transmittance; (**b**) absorption spectrum

E'$_\gamma$(1) center in the irradiated super-pure glass. One can see that the defect population decreases with the storage time. The evolution data can be mathematically fitted to an exponent, as shown below:

$$N_{electron} = A_{electron}\exp(-t/\tau_{electron}) + N_{electron-residual} \quad (2)$$

Where $N_{electron}$ is the experimental defect population, $A_{electron}$ is a constant related to the annealable defect population, $N_{electron\text{-}residual}$ is the residual specific free-radical population under the testing condition, $\tau_{radical}$ is the characteristic time constant (h), which is related to the recovery rate of the annealable defects induced by the recombination process.

The corresponding $A_{radical}$, $\tau_{radical}$ and $N_{residual}$ parameters are calculated and shown in Table 2. The $\tau_{radical}$ which represents the decrease rate of the E'$_\gamma$(1) center defect population is about 2.3 day.

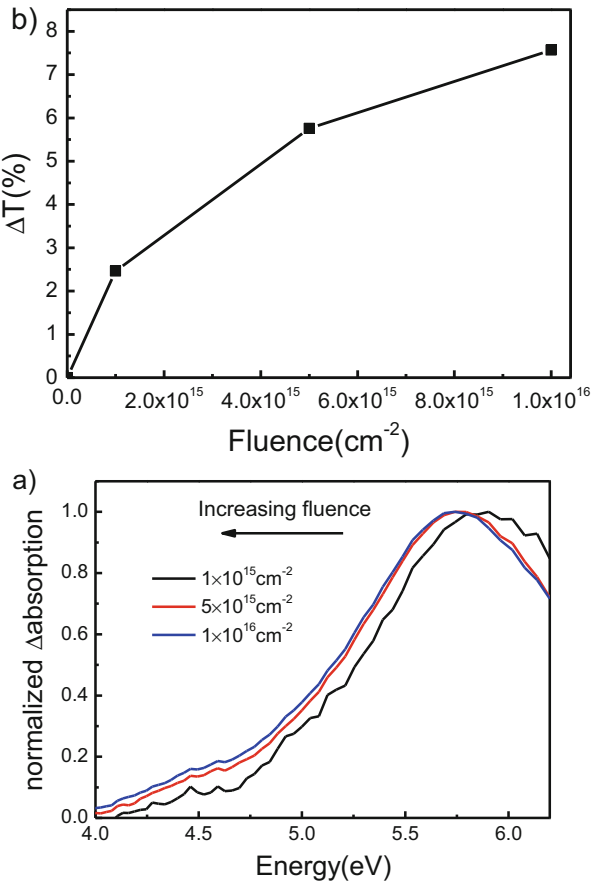

Fig. 5 Evolution of defect's energy level and the peak value of absorption spectrum with the irradiation fluence. (**a**) Defect's energy level evolution; (**b**) peak value of absorption spectrum evolution

Table 1 The EPR and optical spectrum parameters of two types of E'$_\gamma$ centers

	Type	$\Delta g_{1,2}$	$\Delta g_{1,3}$	Peak position of the OA band
E'$_\gamma$(1)	L1	$(1.24 \pm 0.02) \times 10^{-3}$	$(1.47 \pm 0.02) \times 10^{-3}$	5.83 eV ± 0.01
E'$_\gamma$(2)	L2	$(1.15 \pm 0.02) \times 10^{-3}$	$(1.42 \pm 0.02) \times 10^{-3}$	5.76 eV ± 0.01

The defect structure stability of the E'$_\gamma$(1) center is also investigated. Figure 7 shows the evolution of saturation with microwave power of the EPR signal of E'$_\gamma$(1) center during storage. One can see that during the post storage, there is almost no change of the saturation property of the E'$_\gamma$(1) center with EPR signal microwave power, which means that there is no significant variation of the E'$_\gamma$(1) center defect structure.

It is known that the defects formed under irradiation are responsible for the color centers in the material. The decrease of the defect population would induce the recovery of the optical property. The recovery processes of the 1 MeV electron irradiated ultrapure glass are also investigated. Figure 8 shows the recovery of the

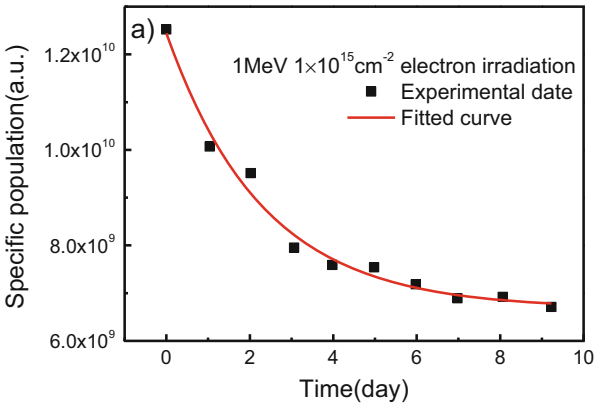

Fig. 6 Evolution of E'$_\gamma$(1) center population during the post storage

Table 2 The fitted parameters of free radical evolution in ionization irradiated ultrapure glass

Fluence	$A_{electron}$	$\tau_{electron}$ (day)	$N_{electron\text{-}residual}$	$A_{electron}/N_0$ (%)	$N_{electron\text{-}residual}/N_0$ (%)
1×10^{15} cm^{-2}	6.67×10^9	2.32	5.77×10^9	53.6	46.4

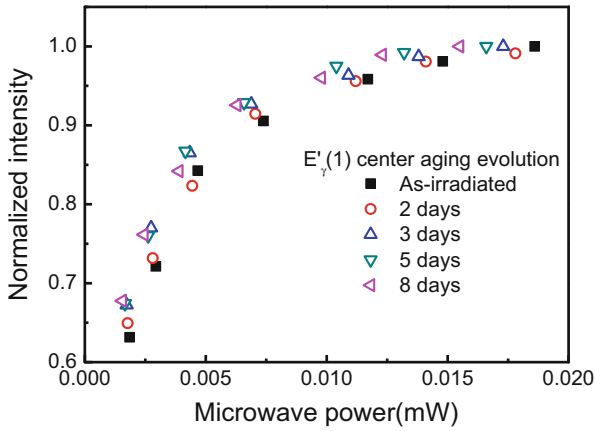

Fig. 7 Saturation with microwave power of the EPR signal of E'$_\gamma$(1) center during storage

ΔT at the wavelength of 212 nm that represents the variation of the top value of the absorption peak. It can be seen that the absorptance evolution shows features similar to those of the E'$_\gamma$(1) center defects during the post storage. Also, mathematical analysis of the data demonstrates that the absorptance evolution of the irradiated sample follows the same rules as for defect population, as shown in Eq. (3).

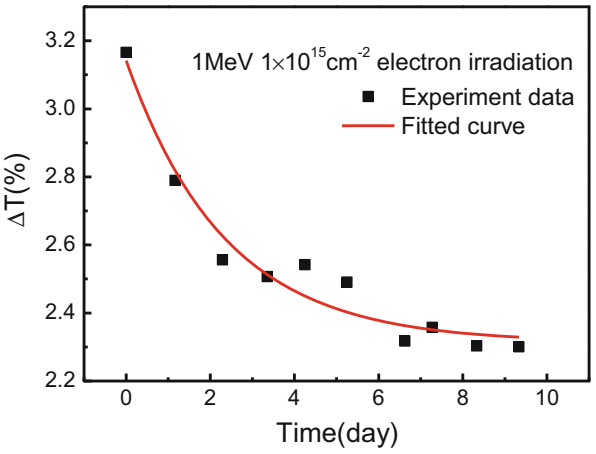

Fig. 8 Evolution of optical absorption peak value during the room temperature anneal under 1 MeV and 1×10^{15} cm^{-2} electron irradiation

Table 3 Fitted parameters of free-radical evolution in 1 MeV and 1×10^{15} cm^{-2} electron irradiated ultrapure glass

Fluence (cm^{-2})	$A_{electron}$	$\tau_{electron}$ (day)	$N_{electron\text{-}residual}$	$A_{electron}/N_0$ (%)	$N_{electron\text{-}residual}/N_0$ (%)
1×10^{16}	3.70×10^{10}	8.35	1.52×10^{10}	70.7	29.3

$$\Delta T_s = A_{optical}\exp\left(-t/\tau_{optical}\right) + \Delta T_{residual} \tag{3}$$

where $A_{optical}$, $\tau_{optical}$ (h), and $\Delta T_{residual}$ are constants related to the recoverable transmittance, characteristic time constant and the final optical transmittance degradation within the test time. The corresponding $A_{optical}$, $\tau_{optical}$ (h), and $\Delta T_{residual}$ parameters are calculated and shown in Table 3. When compared to the data presented in Table 1, one can find that the characteristic time constant τ_{defect} and $\tau_{optical}$ are almost the same. It can be suggested, therefore, that the recovery of the optical degradation with the wavelength of 212 nm is induced by the anneal of the E'$_\gamma$(1) center defects in the ultrapure glass.

The annealing process of the E'$_\gamma$(2) center is also investigated. Figure 9 presents the evolution of the defect population of E'$_\gamma$(2) center in the irradiated super-pure glass with changing anneal time at room temperature. It can be seen that the evolution mode of E'$_\gamma$(2) center defect population is different to the one of E'$_\gamma$(1) center. The distinctions between the anneal process of E'$_\gamma$(1) center and E'$_\gamma$(2) center can be represented by the defect evolution rate. The decrease rate of the E'$_\gamma$(2) center defect population is lower than that of the E'$_\gamma$(1) center, as shown in Fig. 9, and the fitted parameters are listed in Table 3. For the sample irradiated by 1 MeV electron with the fluence of 1×10^{16} cm^{-2}, though the defect population decrease process follows the exponential mode, as shown in Eq. (1), the characteristic time constant (h) is about 8.35 day which is much higher than that of the E'$_\gamma$(1) center evolution (2.32 day). It is worth to note that our investigation also

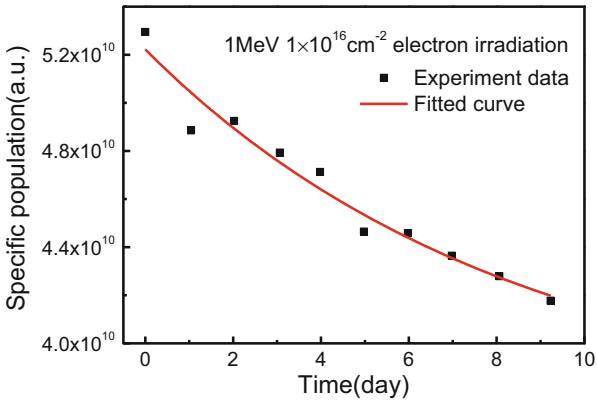

Fig. 9 Signal intensity evolution of E'$_\gamma$(2) type free radical during the post storage

established that for the sample with the high irradiation dose, in the initial stage of the anneal process, the defect population is increasing with the anneal time and then the defect population is decreasing as the time goes by (not shown here). The mechanism of defect population evolution will be discussed and published elsewhere.

The structure variation of E'$_\gamma$(2) center during the room temperature anneal process is also investigated. Figure 10 shows the evolution of the saturation property of the EPR signal of E'$_\gamma$(2) center as a function of microwave power during the anneal process. It can be found that saturation property changes of the EPR signal changes with the increasing anneal process, the line shape transforms from L2 to L1, which means that the during the anneal process, the E'$_\gamma$(2) center transforms into E'$_\gamma$(1) center. The mechanism of the transformation will be discussed in the following publications.

The optical property recovery process of the ultrapure glass with E'$_\gamma$(2) center defects are investigated, as shown in Fig. 11. One can find that the peak value of the transmittance differential is decreasing with the anneal time. The evolution follows the exponential mode, and the fitted parameters are shown in Table 4. When this data is compared to the evolution of the transmittance differential of the ultrapure glass sample with the E'$_\gamma$(1) center defects, it can be found that the characteristic time constant of sample with the E'$_\gamma$(2) center defects is lower than the one with E'$_\gamma$(1) center defects. The difference between the two characteristic time constants is induced by the variation of the defect evolution during the anneal process.

Previous investigations and our results have proved that there are two types of defects formed under 1 MeV electron irradiation. It is known that the evolution of the microscopic defects is the source of the variation of the macroscopic property, thus the key of the investigation on the optical property recovery is the anneal process of the two types of the E'$_\gamma$ center defects. For the E'$_\gamma$(1) center defect which formed in the low ionization dose range, during the anneal process, the anneal of the E'$_\gamma$(1) center is a thermodynamic process, and the recombination of the defect takes

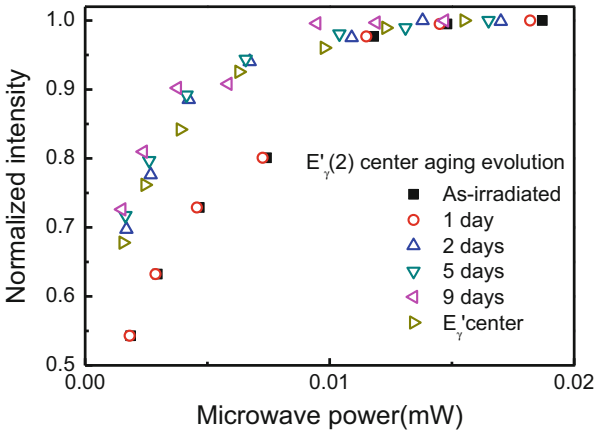

Fig. 10 Saturation with microwave power of the EPR signal of the E'$_\gamma$(2) center during post storage

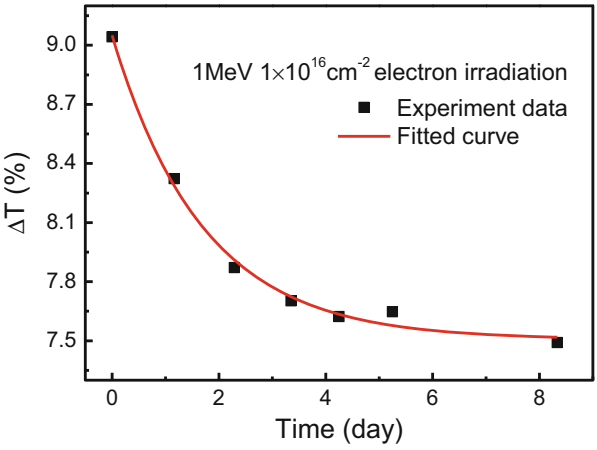

Fig. 11 Evolution of optical absorption peak value during the post storage with 1 MeV and 1×10^{16} cm^{-2} electron irradiation

Table 4 The fitted parameters of transmittance evolution of 1 MeV 1×10^{16} cm^{-2} electron irradiated ultrapure glass

Fluence (cm^{-2})	$A_{optical}$ (%)	$\tau_{optical}$ (day)	$\Delta T_{residual}$ (%)
1×10^{16}	1.54	1.71	7.51

effect, the structure of the defect does not change, which can be reflected by the saturation property of the EPR signal, as shown in Figs. 6 and 8. However, for the sample with the E'$_\gamma$(2) center, the situation is more complicated, during the anneal process, the transformation of the defect structure and the recombination of the defect both affect the population decrease [12].

It has been proven that the structure of E'$_\gamma$(2) center is similar to that of E'$_\gamma$(1) center, the difference between the two types of defects is that the ionization degree of E'$_\gamma$(2) is higher than that of E'$_\gamma$(1) center, and the scheme of E'$_\gamma$(2) is

shown in Eq. (1). The higher potential property of $E'_{\gamma}(2)$ provides the ability to capture the nearby electrons and to transform to $E'_{\gamma}(1)$ center, with the reaction process presented in Eq. (4). In annealing processes at room temperature, the electrons in the material vibrate in the equilibrium position. For strong potential effect, the electron can be captured by the $E'_{\gamma}(2)$ center, and this process can induce one $E'_{\gamma}(2)$ center transformation into two $E'_{\gamma}(1)$ centers that can be confirmed by the variation of the saturation property of the EPR signal during the anneal process (as shown in Fig. 10).

During the room anneal process, two factors contribute to the evolution of the total population of defects: one factor is the transformation of the $E'_{\gamma}(2)$ center, which can double the specific population of the defects, leading to the increase of the total defect population; the other factor is the anneal of the $E'_{\gamma}(1)$ center, which induces the decrease of the total defect population. The two factors both take effect on the population evolution during the room anneal process, and induce the decrease of the evolution rate, which can be presented by the variation of the characteristic time constants, namely the τ_{defect} of $E'_{\gamma}(2)$ center population evolution (8.35 day) and that of $E'_{\gamma}(1)$ center (2.33 day).

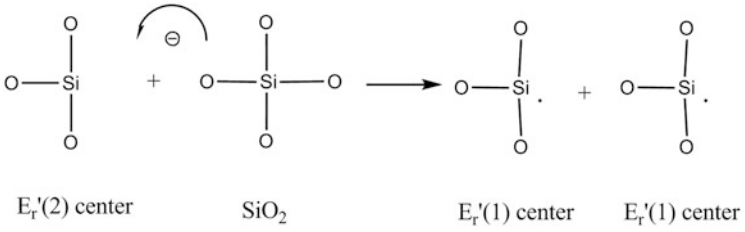

(4)

Conclusions

The damage process of ultrapure glass under 1 MeV electron irradiation was investigated by the electron paramagnetic resonance spectra and optical transmittance measurements. The results show that the electron irradiation induce the formation of E'_{γ} center, with the increasing fluence, the structure of the E'_{γ} center transforms from $E'_{\gamma}(1)$ to $E'_{\gamma}(2)$ center, and the formation of $E'_{\gamma}(2)$ center is the result of further ionization of $E'_{\gamma}(1)$ center. With the transformation of defect structure, the optical absorption energy level also vary, the optical absorption energy level decreases from 5.83 ± 0.01 eV [$E'_{\gamma}(1)$ center] to 5.77 ± 0.01 eV [$E'_{\gamma}(2)$ center]. The defects could be gradually annealed out and the optical property recovered during the room temperature storage. The defect population evolution follows an exponential mode, for the sample with the $E'_{\gamma}(1)$ centers, the defect anneal process is synchronous with the optical property recovery, namely the value of τ_{defect} which represents the anneal rate is consistent to that of $\tau_{optical}$ which represents the recovery rate of the optical absorption peak. During the room

temperature storage, one $E'_\gamma(2)$ center would transform into two $E'_\gamma(1)$ centers, and induce the decrease of the anneal rate of defect population and the inconsistent evolution rate between the defect anneal and the optical absorption recovery. The analysis on the transformation of defect structure can be used as another explanation to the increase of E'_γ centers anneal rate with the increasing ionization dose as shown in Zhang's investigation.

References

1. Srivastava SK, Ganesan K, Gangopadhyay P, Panigrahi BK, Nair KGM, Tyagi AK (2014) High energy ion irradiation induced surface patterning on a SiO_2 glass substrate. Nucl Inst Methods Phys Res Sect B 338:89–94
2. Zatsepin AF, Kaschieva S, Dmitriev SN, Buntov EA (2008) Characteristics of the electron-emission defects introduced in Si–SiO_2 structures by MeV electron irradiation. Nucl Inst Methods Phys Res Sect B 266(23):5027–5031
3. Skuja L, Kajihara K, Hirano M, Hosono H (2012) Oxygen-excess-related point defects in glassy/amorphous SiO2 and related materials. Nucl Inst Methods Phys Res Sect B 286:159–168
4. Mizutani T (1995) Compositional and structural modifications of amorphous SiO_2 by low-energy ion and neutral beam irradiation. J Non Cryst Solids 181(1–2):123–134
5. Alessi A, Agnello S, Sporea DG, Oproiu C, Brichard B, Gelardi FM (2010) Formation of optically active oxygen deficient centers in Ge-doped SiO_2 by γ- and β-ray irradiation. J Non Cryst Solids 356(4–5):275–280
6. Skuja L, Mizuguchi M, Hosono H, Kawazoe H (2000) The nature of the 4.8 eV optical absorption band induced by vacuum-ultraviolet irradiation of glassy SiO2. Nucl Inst Methods Phys Res Sect B 166–167:711–715
7. Nakagawa M, Okada M, Kawabata Y, Atobe K, Itoh H, Nakanishi S (1994) Defects in SiO2 crystals after neutron irradiations at 20 K and 360 K. Nucl Inst Methods Phys Res Sect B 91 (1–4):354–358
8. van Dillen T, Brongersma ML, Snoeks E, Polman A (1999) Activation energy spectra for annealing of ion irradiation induced defects in silica glasses. Nucl Inst Methods Phys Res Sect B 148(1–4):221–226
9. Cannas M, Agnello S, Boscaino R, Costa S, Gelardi FM (2002) Post-irradiation kinetics of UV laser induced defects in silica. Nucl Inst Methods Phys Res Sect B 191(1–4):401–405
10. Agnello S, Chiodini N, Paleari A, Parlato A (2007) Image centers induced by γ irradiation in sol–gel synthesized oxygen deficient amorphous silicon dioxide. J Non Cryst Solids 353 (5–7):573–576
11. Buscarino G, Agnello S (2007) Experimental evidence of image centers generation from oxygen vacancies in a-SiO_2. J Non Cryst Solids 353(5–7):577–580
12. Devine RAB, Grouillet A, Berlivet JY (1988) Temperature dependence of radiation induced defect creation in a-SiO2. Nucl Inst Methods Phys Res Sect B 32(1–4):307–310

Mechanism of Electron Radiation Induced Loss of the "Panda" Type Polarization-Maintaining Optical Fibers

Hai Liu and Hongbao Sun

Abstract Evolution and mechanism of the induced loss of the 1310 nm working-wavelength "Panda" type quartz PM fiber irradiated by the 1 MeV and 170 keV electrons respectively were experimentally investigated using electron accelerator. The results show that, fiber loss exhibits an exponential increase with increasing radiation fluence, which is higher under low-energy electrons than under high-energy electrons. The irradiated quartz fibers show an annealing effect. The restored loss of the fiber irradiated by high-energy electron is higher than that by low-energy electron. The radiation induced loss of quartz fiber has two mechanisms of Si–OH absorption and H_2 absorption. Under lower electron energy, the energy deposition of fiber core is in majority leading to more radiation defects forming while the loss is mainly controlled by Si–OH. In the case of the fiber subjected to high-energy electron radiation, the absorbed dose of fiber core is relatively low, which is dominated by H_2 absorption. Hydrogen that is involved in both mechanisms is generated by radiation induced degradation of polymer coating and diffuses into fiber core.

Keywords Polarization-maintaining optical fiber • Radiation effect • Induced optical loss • Infrared absorption • Si–OH defect

Introduction

Comparing with common mechanical gyroscope, the fiber optic gyroscope has an inbuilt advantage of navigation and positioning for spacecraft [1]. However, in the electron radiation environment, the fiber losses will be induced in fiber optic gyroscopes, influencing the positioning accuracy [2]. The radiation induced losses in fibers and the corresponding mechanisms were described and explored in many publications [3–5]. It is well known that the accumulation of radiation defects is an

H. Liu (✉) • H. Sun
School of Materials Science and Engineering, Harbin Institute of Technology, Harbin 150001, People's Republic of China
e-mail: hitliuhai@163.com

J. Kleiman (ed.), *Protection of Materials and Structures from the Space Environment*, Astrophysics and Space Science Proceedings 47,
DOI 10.1007/978-3-319-19309-0_10

intrinsic reason for the increase of the induced fiber loss. However, the unified conclusion about the type and formation mechanism of the radiation defect has been not established. It is generally thought that Si–OH and Ge–OH respectively generate strong absorption peaks around 1.38 and 1.415 μm. The absorption edges will affect optical transmission of the fibers working in the wavelengths of 1.31 and 1.55 μm. The absorption around 0.63 μm attributed to NBOHC defects results in the fiber loss for the fibers working at a wavelength of 0.85 μm [6, 7].

The behavior of optical fiber under radiation depends on the type and processing of the fiber. For the dehydrogenation treated quartz fiber, the source of H is a key for formation of –OH defect. It is believed that the hydrogen comes from the radiation degradation of the poly in coatings [8], which is related to the diffusion of hydrogen in fiber. There is no evidence for above theory due to difficulty in detection.

There is another unanswered theoretical question. Since these defects are thermodynamically stable at low temperature if the fiber loss is induced by Si–OH and Ge–OH [6], the distinct annealing effect of quartz fiber after radiation is inconsistent with that. It suggests that there are other mechanisms for the increase of the induced fiber loss besides radiation defects.

The present investigation aims to experimentally explore the new evidence for the mechanism of radiation-induced quartz fiber loss through appropriate analysis.

Experimental

The sample is a PMF1310 80-65/165 “Panda” type PM optic fiber supplied by China Wuhan Changfei Ltd. The fiber, 170 μm in diameter, consists of a fiber core (GeO_2 doping), 80 μm diameter cladding, a 23 μm diameter stressed zone (B_2O_3 doping), and a coating (PMMA). The working wavelength of the fiber is 1310 nm (1.31 μm).

The electron radiation tests were performed under 1 MeV and 170 keV on a DD1.2 type Dynamitron at Technical Physics Institute of Heilongjian Academy of Science and a Space Complex Radiation Simulator of Harbin Institute of Technology, respectively. The fiber loss was measured on a FPM-302 type light source and a FLS-302 optical power meter manufactured by EXFO Company, Canada.

EPR and FTIR techniques were employed to analyze the mechanism of fiber loss after radiation.

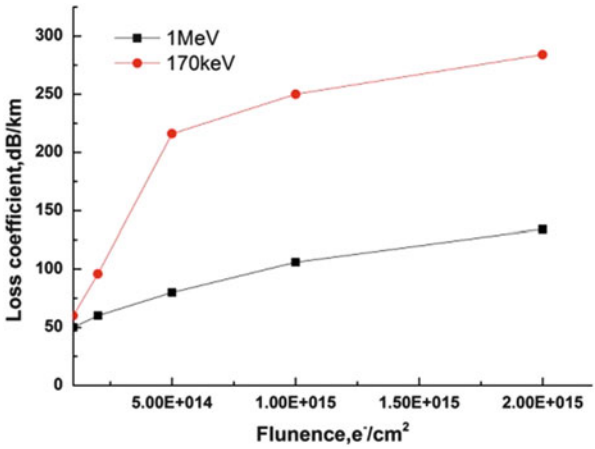

Fig. 1 Loss coefficient as a function of fluence under electron radiation

Results

Radiation Test

The relationship between the induced loss and radiation fluence for the "Panda" type PM optic fiber irradiated respectively by the 1 MeV and 170 keV electrons is shown in Fig. 1. It can be seen that the fiber loss increases with fluence. The increase of fiber loss is rapid at beginning of radiation and slows down after certain fluence. Under high-energy-electron radiation, the increase trend of fiber loss is slowing down when the fluence reaches 1×10^{12} cm^{-1}. Under the low-energy-electron radiation, the fiber loss keeps high growth rate even under 5×10^{14} cm^{-1} fluence. It indicates that the low-energy electrons have much higher radiation effect than the high-energy electrons. The maximum change in fiber loss is about 150 dB/km under the 1 MeV electron radiation, and more than 280 dB/km under the 170 keV electron radiation.

Annealing Test

The results of annealing test at room temperature for the fiber irradiated by the $2 \times 10^{15}/cm^2$ electrons are shown in Fig. 2. Figure 2a illustrates that distinct annealing effect occurs during the storage of the 1 MeV electron irradiated fiber at room temperature. The loss coefficient decreases from 135 to 95 dB/km within 25 min. Figure 2b shows that the annealing effect of the 170 keV electron irradiated fiber is weak with loss coefficient reduction of 15 dB/km within 350 min. With increasing annealing temperature, the loss efficient of the irradiated fiber is further reduced but unable to return to the value before radiation.

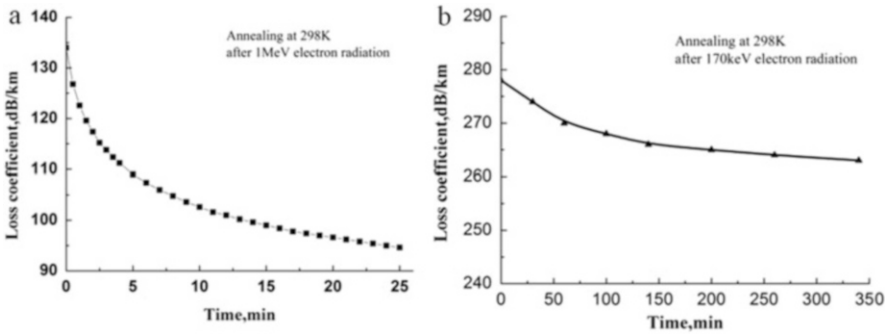

Fig. 2 Loss efficient of irradiated fiber as a function of annealing duration

Analysis of the Mechanism of Radiation Induced Loss of Quartz Fiber

Si–OH Defect Forming Mechanism

It was proposed in the literature that there are at least two steps in the formation of Si–OH during radiation. The first is the fracture of Si–O bonds in fiber core and formation of non-bridging-oxygen defects as shown below.

$$\equiv Si - O - Si \equiv \xrightarrow{\text{Radiation}} \equiv Si - O^{-} + \equiv Si^{+}$$

The second is the following reaction between non-bridging oxygen and hydrogen.

$$\equiv Si - O^{-} + \dot{H} \longrightarrow \equiv Si - OH$$

The first step has been verified by many researches. The EPR measurement was carried out on the irradiated and not irradiated fiber with results given in Fig. 3. Strong signal of E′ center is detected after radiation, which confirms the bond cleavage reactions of Si–O.

Figure 4 shows the FTIR result of the fiber irradiated with 170 keV electrons. The absorption peak attributing to OH is found at 3200–3800 cm^{-1}. Please note that the moisture absorption has little effect since no characteristic absorption peak of water around 1630 cm^{-1} is present in the spectra. The above results indicate that there is OH forming in the irradiated fiber, and also confirm the mentioned reaction of second step.

The next question is where the hydrogen comes from. The hydrogen-depleted treated fiber core is unable to provide enough hydrogen to sustain the reaction. Therefore, hydrogen can only come from outside of fiber core. The only possible hydrogen source in fiber is the organic cladding. There are a large number of methyl groups in the molecular structure of PMMA cladding. The C–H bond is easy to

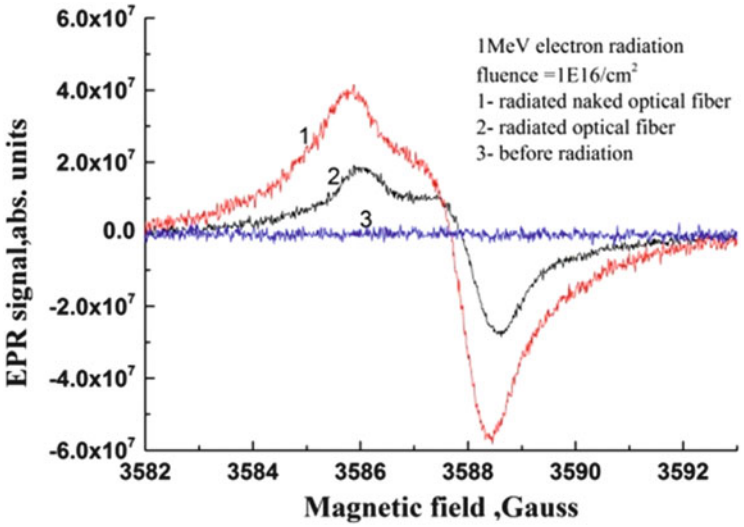

Fig. 3 EPR spectra of the fiber irradiated by 1 MeV electrons

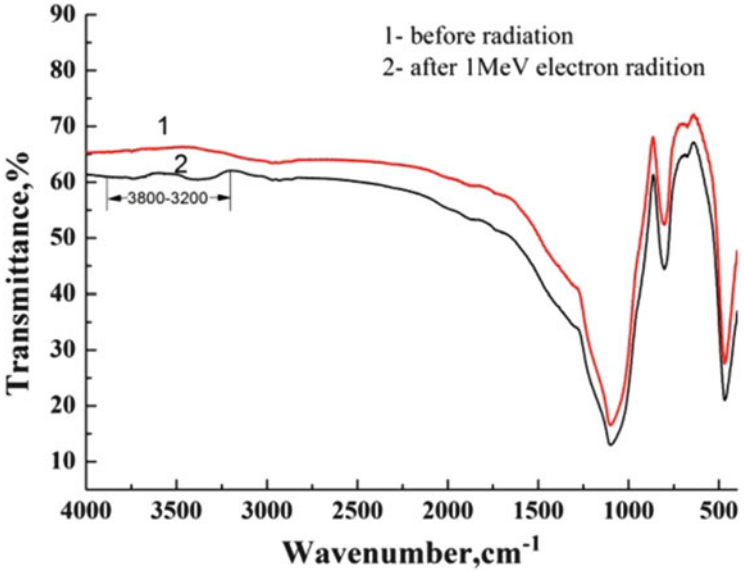

Fig. 4 FTIR spectra of the quartz fiber irradiated by 170 keV electrons

brake during radiation resulting in formation of hydrogen ions, as shown in Fig. 5. There is a possibility for the hydrogen to diffus into the fiber core if the concentration of the generated hydrogen ions is high enough.

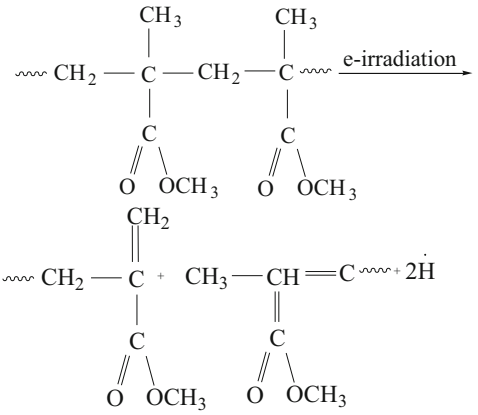

Fig. 5 Possible reaction in PMMA clad under electron radiation

Discussion on Mechanism of Hydrogen Absorption

It is known that Si–OH is a thermodynamically stable structure. If it is the unique mechanism for the increase of fiber loss at 1310 nm, it is hard to explain the annealing phenomenon of the fiber after the radiation. Some researchers found that the quartz fiber after H_2 treatment showed a significant increase of absorptions around 1245 and 1380 nm after the radiation leading to variation of loss spectrum in broad range. Meanwhile, the absorption around 1245 nm has distinct annealing effect, which confirms the H_2 absorption mechanism of quartz fiber [9].

It is proposed that the mechanism of combined H_2 and Si–OH absorption is a rational explanation for the induced loss of quartz fiber in the space radiation environment. Due to the difficulty in hydrogen detection, there is insufficient direct evidence of hydrogen absorption mechanism. It is difficult to describe quantitatively the effect level of hydrogen absorption on fiber loss. In this situation, the electron radiation induced damage of quartz fiber is characterized by data from energy analysis.

Figure 6 is the simulated energy loss of electron interaction with fiber obtained by COSINO software. The 1 MeV electron rang is much longer than fiber diameter while the absorbed dose of fiber is relatively low. By contrast, the 170 keV electron range is close to the fiber diameter with most energy deposited in the fiber core, resulting that the absorbed dose of fiber core and coating is higher than the case of high energy electron radiation. Within the fluence range of the present radiation test, the induced fiber loss does not achieve complete saturation, i.e., the radiation defects as absorbers have unsaturated concentration, implying that increase of absorbed dose leads to more defect formation, which is the reason for that radiation induced loss is higher under low-energy electrons than that under high-energy electrons. The EPR analysis of the electron irradiated fibers under two energy conditions shows that, the paramagnetic signal of the 170 keV electron irradiated fiber is distinctly higher than that of the 1 MeV irradiated, as shown in Fig. 7. It proves that the concentration of Si–OH that formed earlier, is increased with

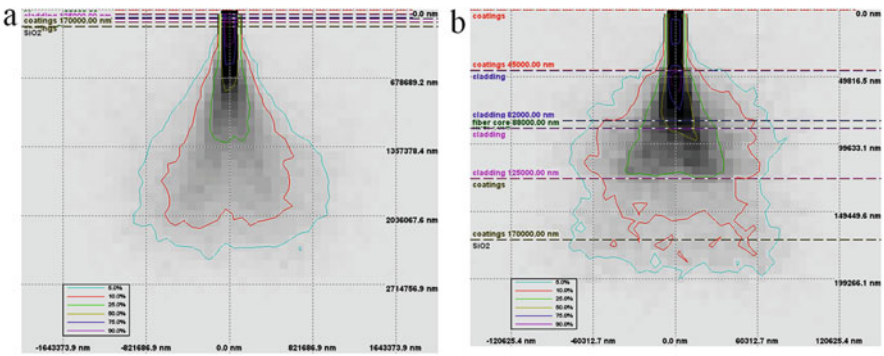

Fig. 6 Energy loss distribution of the injected electrons in optical fiber: (**a**) 170 keV electron; (**b**) 1 MeV electron

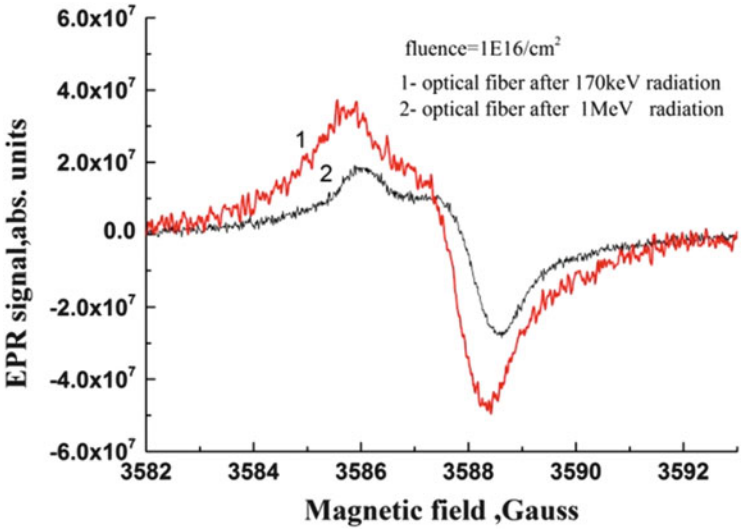

Fig. 7 EPR spectra of the irradiated fiber by electrons with different energy

increasing absorbed dose under low-energy electron radiation. Therefore, the induced loss is dominated by Si–OH mechanism under low-energy electrons radiation whereas it is controlled mainly by H_2 absorption under high-energy electrons radiation

Based on above analyses, the induced loss of quartz fiber is controlled by two mechanisms of Si–OH and H_2 absorption. The effect of each of the two mechanisms changes with the energy and the fluence of electrons. However, the prerequisite for above conclusion that the radiation induced degradation of the PMMA coating provides enough amount of H to the fiber core needs further investigation.

Conclusions

The electron-radiation induced loss of "Panda" type quartz PM fiber depends on the energy and fluence of electrons. The induced loss around the 1310 nm wavelength is controlled by two mechanisms of Si–OH and H_2 absorption. Under the same fluence, the fiber loss is dominated by the Si–OH absorption when the energy of electron radiation is lower and the absorbed dose of fiber is higher. The fiber loss is mainly controlled by the mechanism of H_2 absorption under higher-energy electron radiation.

References

1. Friebele EJ, Askins CG, Miller GA (2004) Optical fiber sensors for spacecraft: applications and challenges. The International Society for Optical Engineering, Denver, CO, pp 120–131
2. John S (1987) Strong localization of photons in certain disordered dielectric super lattices. Phys Rev Lett 58(23):2486–2489
3. Xu J, Zhao SH, Hou R, Yang SS, Zhang TP, Ni YH, Wu JL, Li YJ (2010) Gamma-ray radiation-induced damage to silicon single-mode fiber. Optik 121(21):1998–2000
4. Tomashuk AL, Golant KM, Dianov EM, Medvedkov OI, Plaksin OA, Stepanov VA, Stepanov PA, Demenkov PV, Chernov VM, Klyamkin SN (2000) Radiation-induced absorption and luminescencein specially hardened large-core silica optical fibers. IEEE Trans Nucl Sci 47(3): 693–698
5. Zhang H-C, Liu H, Xue H-J, Qiao W-Q, He S-Y (2012) Effects of 160 keV electron irradiation on the optical properties and microstructure of "Panda" type polarization-maintaining optical fibers. Opt Commun 285:4779–4784
6. Brichard B, Tomashuk AL, Bogatyrjov VA, Fernandez AF, Klyamkin SN, Girard S, Berghmans F (2007) Reduction of the radiation-induced absorption in hydrogenated pure silica core fibers irradiated in situ with gamma-rays. J Non Cryst Solids 353:466–472
7. Friebele EJ, Ginther RJ, Sigel GH (1974) Radiation protection of fiber optic materials: effects of oxidation and reduction. Appl Phys Lett 24:412–414
8. Deparis O, Griscom DL, Mégret P, Decréton M, Blondel M (1997) Influence of the cladding thickness on the evolution of the NBOHC band in optical fibers exposed to gamma radiations. J Non Cryst Solids 216(1997):124–128
9. Itoh H, Ohmori Y, Nakahara M (1986) Gamma-ray radiation effects on hydroxyl absorption increase in optical fibers. J Lightwave Technol LT-4(4):473

ASTM E1559 Comparative Testing of Low-Outgassing Silicone-Based MAP Thermal Control Coatings

Vitali Issoupov, Sergey Horodetsky, and Jacob Kleiman

Abstract Responding to the need for dynamic outgassing testing at high temperature, ITL Inc. has developed and built an Outgassing Test Facility that accommodates the set-ups for measuring the outgassing of materials according to the ASTM E1559 test method. This paper describes the design of the outgassing system, operation of its devices and components, and presents the test results obtained on several advanced conductive and non-conductive space thermal control paints and silicones by MAP Space Corporation (France).

Material outgassing tests were performed on four advanced silicone-based thermal control coatings recently developed by CNES/MAP, namely, the black PNC and mat white PCBE conductive silicone-based space paints, the white non-conductive silicone-based SG121FD paint, as well as the transparent MAPSIL® QS 1123 non-conductive silicone resin. A comparative evaluation and discussion of the outgassing test results per ASTM E1559 will be presented to prove that the MAP silicone paints do not cause contaminations on the sensitive optical coatings in the line-of-site direction by silicone-based contaminations during long-term operation in the Low Earth Orbit space environment.

Keywords Low earth orbit • Outgassing testing • Deposition kinetics • Total mass loss • Volatile condensable material

Introduction

Outgassing of organic materials can be described as a surface evaporation combined with diffusion for bulk contaminant species. These species can be either initially present components, or decomposition products. Contamination exists in many forms, e.g., particulates, chemical species, vapor condensation, corrosion, etc. Molecular contamination of materials in space due to outgassing poses a serious threat to sensitive devices, such as optics and thermal control surfaces [1].

V. Issoupov • S. Horodetsky • J. Kleiman (✉)
Integrity Testing Laboratory Inc., Markham, ON L3R 3R7, Canada
e-mail: jkleiman@itlinc.com

J. Kleiman (ed.), *Protection of Materials and Structures from the Space Environment*, Astrophysics and Space Science Proceedings 47,
DOI 10.1007/978-3-319-19309-0_11

Volatile condensable materials from silicone paints and silicones for space and high vacuum industries can contaminate optical surfaces, decreasing the long-term reliability of many systems on-board spacecraft. The ASTM E1559 Standard [2] helps predict the level of contamination, migration and deposition. The method is capable not only to evaluate the Volatile Condensable Materials (VCM) and Total Mass Loss (TML), but also to identify which species condense at different temperatures.

The ASTM E1559 method established as an improved version of the ASTM E595 tests materials over a wider range of temperatures and over a longer period of time. The ASTM E1559 test method characterizes the outgassing property of candidate materials and components in a controlled and repeatable way by measuring the amounts of outgassed products from the bulk of a material. Testing per ASTM E1559 is more expensive and time consuming, but offers much greater insight into the outgassing characteristics of a material through measuring the molecular deposition levels on three Quartz Crystal Microbalance sensors combined with a possibility to identify the volatile components of the material.

The ASTM E1559 test method has now been adopted in many programs for screening materials that are to be used in space applications. The present and future space-based systems with cooled optical and detection systems can be degraded or rendered inoperative by contaminant deposition. Contamination of thermal control surfaces and solar cell arrays can also result in a satellite thermal imbalance and a loss of solar cell efficiency. An example of how important ASTM E1559 testing is that presently all non-metallic materials to be flown on the International Space Station must undergo ASTM E1559 testing.

The TML and CVCM of materials have been tested per ASTM E1559 up to 125 °C by various organizations and companies across the US and Europe. In the previous years, ITL has developed and built three test facilities and developed the test procedure according to the ASTM E1559. The ASTM E1559 Outgassing Facility (OGF-2013) provides the means for the outgassing test of materials with the objective to select materials with low outgassing properties for spacecraft use and allows determining the following outgassing parameters: Total Mass Loss, Volatile Condensable Materials, and Outgassing Rate.

Experimental

The most up-to-date, self-contained OGF-2013 Outgassing Facility includes an oil-free pumping system, a set of three thermally controlled Quartz Crystal Microbalance (QCM) sensors, an effusion cell, and on inline SRS 300 RGA mass spectrometer [3]. As required per ASTM E1559, the outgassing and deposition rates can be measured continuously and the outgassing molecular components can be detected and identified. The 15 MHz Cryo-QCM sensors are set at various temperatures from 90 to 298 K for collecting the mass evolved. Prepared materials are subjected to environmental temperatures ranging from ambient to 398–573 K in

an effusion cell. The integrated effusion cell heater and temperature sensors are critical elements for the success of the test. Interlock chamber loading of the effusion cell and a transfer mechanism for inserting the cell into the main chamber offer an increased testing convenience and simplicity. The OGF-2013 facility is fully computer-controlled using a powerful proprietary COSIMOD™ software, thus all operations can be programmed to take place automatically.

The developed OGF-2013 facility is well suited to measure outgassing/deposition kinetics of volatiles released from materials, including adhesives, coatings, fabrics, grease, lubricants and liquids, to obtain both the static and the dynamic information about the total mass loss and the mass flux during transient thermal conditions.

The OGF-2013 Outgassing Facility features oil-free pumping with a scroll pump and two turbo pumps (77 L/s and 250 L/s) to obtain vacuum conditions better than 10^{-6} Torr and the test operation is made fully computer-controlled. The general view and different components of the OGF-2013 test facility are presented in Fig. 1.

Test ASTM E1559 uses a method that allows the total mass loss to be determined through the use of 3 Quartz Crystal Microbalances (QCMs) to be maintained at 90 K (−183 °C), 160 K (−113 °C), and 298 K (25 °C). The ASTM E1559 requires that the QCMs consist of two crystals (one for mass collection and one for reference) and that they have a sensitivity of at least 1×10^{-8} g/cm^2/Hz at 298 K (25 °C). This is typically accomplished with crystals that have natural frequencies

Fig. 1 Photograph showing the general view of the OGF-2013 outgassing facility developed and built by ITL for ASTM E1559 outgassing testing

of 10–15 MHz. The OGF-2013 facility uses QCMs with 15 MHz crystals that have a sensitivity of 1.73×10^{-9} g/cm^2/Hz. The crystals are 1.27 cm in diameter and optically polished and plated with gold [3]. The pair of crystals is designated as a sensor crystal and a reference crystal.

The effusion cell is a cylindrical container approximately 65 mm inside diameter by 50 mm deep, and is machined from stainless steel 304. The integrated heater ensures uniform temperature distribution throughout the inner cavity. The effusion cell has a detachable cover plate which allows for insertion of material samples. This lid has a cylindrical orifice of 3.0 mm in diameter by 3.0 mm long providing the appropriate flux distribution. The cell has an integral temperature sensor and heater, and control system which permits operating the cell from ambient to 398–573 K (125–300 °C) with a precision of 0.5 K or better. The effusion cell is positioned inside the test chamber at 150 mm from the surface of the sensing crystal in each QCM so that the center of the cell orifice exit plane coincides with the intersection point of the QCM axes. The cell orifice thus has the same view factor of 415.08 cm^2 to all QCMs.

The test chamber is evacuated to a vacuum level on the order of ~10^{-7} Torr before QCM cooling is commenced. The QCMs are maintained at approximately 298 K until the chamber liner and baffles have reached temperatures of less than approximately 75 K. At this point, the heaters to the QCMs are commanded to set point temperatures varying from 90 K for the coldest to as high as 298 K for the warmest. To provide low temperature, the QCM sensors are mounted at liquid nitrogen reservoirs. The QCMs are thermally shielded from each other to allow the temperatures to be independently controlled. Once these temperatures have become constant, outgassing data can be collected.

The effusion cell with the sample of the order of 10–20 g is and mounted in the interlock chamber (see Fig. 2). After the interlock chamber has been evacuated to a level of approximately 10^{-9} Torr, the gate valve is opened and the effusion cell is moved manually using the transfer mechanism shown in Fig. 1 to its location in the chamber so that the orifice is located at a distance of 150 mm from each of the QCM sensing crystals. Once the location has been established, the effusion cell temperature controller is set to the desired temperature, usually to 398 K (125 °C), and the QCM frequencies recorded as a function of time with a 1 min time period. The time required for completion of an outgassing test varies depending on the needs of the user. In many instances outgassing times of up to 5 days are used in order to determine the long-term outgassing rates.

Table 1 provides the main technical characteristics of the ASTM E1559 Outgassing Facility. This facility is now operational at Lanzhou Institute of Physics (China).

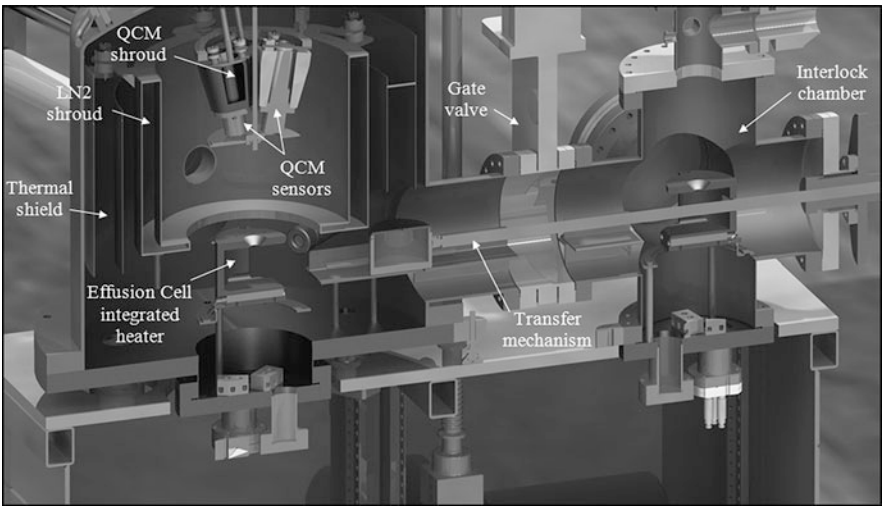

Fig. 2 Transferring the effusion cell from interlock chamber into ASTM E1559 test chamber

Table 1 Main technical parameters of the ASTM E1559 Outgassing Facility

	Parameter	Value
Vacuum system	Volume, m^3	~0.2
	Pumping speed (N_2), l/s	81/300
	Basic vacuum, Torr	$<10^{-9}$
ASTM E1559 test	QCM frequency, MHz	15
	Sensor sensitivity, g/cm^2 Hz	1.73×10^{-9}
	Sensors temperature, °C	−183/−113/+25
	Mass range, AMU	1–300
	– Outgassing and deposition kinetics testing – Measuring the TML, CVCM, and outgassing rate – QCM thermogravimetric analysis (QTGA)	

Results and Discussion

Material outgassing tests were performed per the ASTM E1559 test method on four advanced silicone-based thermal control coatings recently developed by CNES/MAP, namely, the black PNC and mat white PCBE conductive silicone-based space paints, the white non-conductive silicone-based SG121FD paint, as well as the transparent MAPSIL® QS 1123 non-conductive silicone resin [4].

The ASTM E1559 outgassing tests were performed with QCM temperatures at <90, 160, and 298 K. All samples were tested at an effusion cell temperature of 125 °C and the duration of each test was 72–120 h. Test data including the QCM frequencies and temperatures, as well as the reduced data (Total Mass Loss, Volatile Condensable Material, etc.) were stored as Excel data files. Test

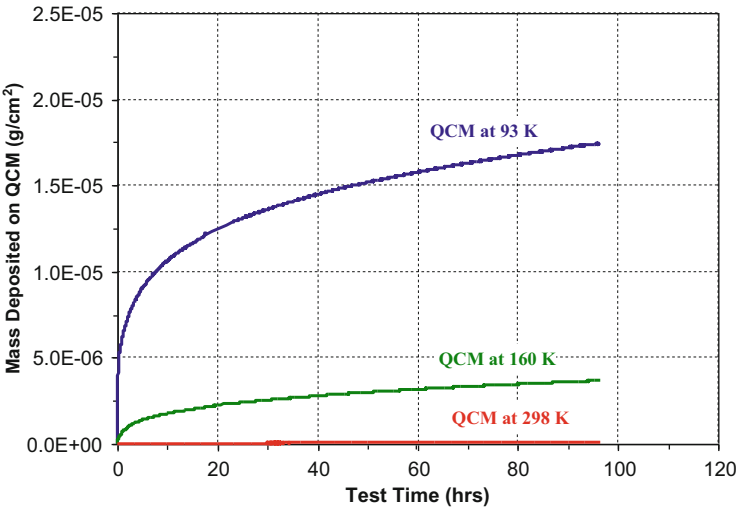

Fig. 3 Mass deposited on QCMs as a function of time during the isothermal outgassing test on Polyethylene beads at 398 K

information such as sample mass, sample dimensions, QCM type and sensitivity, apparatus view factors, and any exceptions to the ASTM method were also included.

Figure 3 shows the mass deposition data taken during the preliminary series of testing for Polyethylene beads. This material has been traditionally used for the ASTM E1559 Round-Robin test of outgassing test facilities worldwide [5]. The deposition data show a delta frequency varying between about 1930 and 2010 Hz and there is a good agreement of the outgassing results for this standard material with data obtained on other facilities for both TML and CVCM values (Figs. 4 and 5).

The standard physical properties of four silicone materials developed and produced by MAP with <0.1 % TML and 0.01 % CVCM are represented in Table 2. Based on property data, these silicone materials have no negative effects from the removal of low molecular weight species.

Figure 6 shows the TML during the isothermal outgassing test of low outgassing (PNC, PCBE) and ultra low outgassing (MAPSIL® QS 1123) silicones as a function of time over a 72–120 h period. The TML is obtained from mass deposition data on the coldest QCM sensor (<90 K). PNC and PCBE are black and white silicone conductive paints commonly used as thermal control coatings on spacecraft surfaces, while MAPSIL® QS 1123 is a transparent non-conductive coating used as encapsulating resin for electronic components, adhesive for glass on glass sticking, varnish for printed circuits (PCB), as well as for electrical insulation in space applications. The MAPSIL® QS 1123 silicone coating maintains an ultra low TML value, TML < 0.01 %, for the entirety of the test.

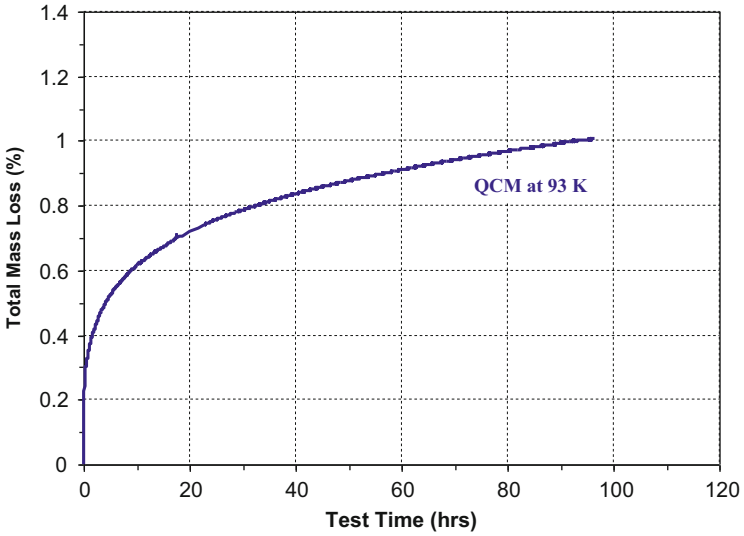

Fig. 4 Total mass loss from the sample as a function of time during the isothermal outgassing test on Polyethylene beads at 398 K

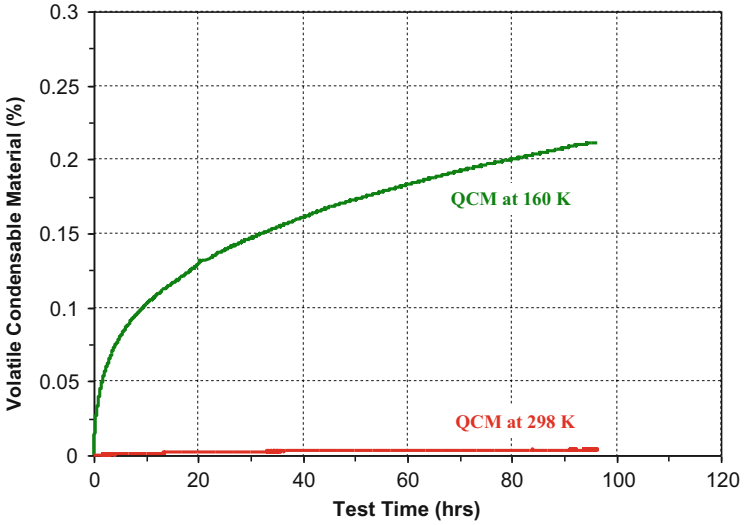

Fig. 5 Volatile condensable material for QCMs at 160 and 298 K as a function of time during the isothermal outgassing test on Polyethylene beads at 398 K

The percent of VCM that outgases from the MAP silicones as a function of time and condenses on the collector surface is plotted in Fig. 7. The VCM is obtained from mass deposition data on the QCM sensor at 160 K. The outgassing rates of the silicone materials are also analyzed from the isothermal outgassing test data as

Table 2 Standard physical properties of four MAP silicone materials

	PNC	PCBE	SG121FD	MAPSIL® QS 1123
Polymer matrix	Silicone	Silicone	Silicone	Two component silicone elastomer
Pigment	Carbon black	Metallic, Encap. ZnO	Metallic, Encap. ZnO	–
Solvent	Aromatic	Aromatic and aliphatic	Aromatic and aliphatic	–
Solar absorptance	0.98 ± 0.02	0.27 ± 0.04	0.20 ± 0.02	–
IR emittance	0.91 ± 0.03	0.88 ± 0.03	0.88 ± 0.03	–
Outgassing	In compliance with ECSS-Q-70-02A	In compliance with ECSS-Q-70-02A	In compliance with ECSS-Q-70-02A	TML < 0.1 % RML < 0.1 % CVCM < 0.01 %
Electrical surface resistance	$\leq 1 \times 10^6$ Ω/Sq.	≤ 1 kΩ/Sq.	$\geq 10^{12}$ Ω/Sq.	1.4×10^{11} Ω/Sq.

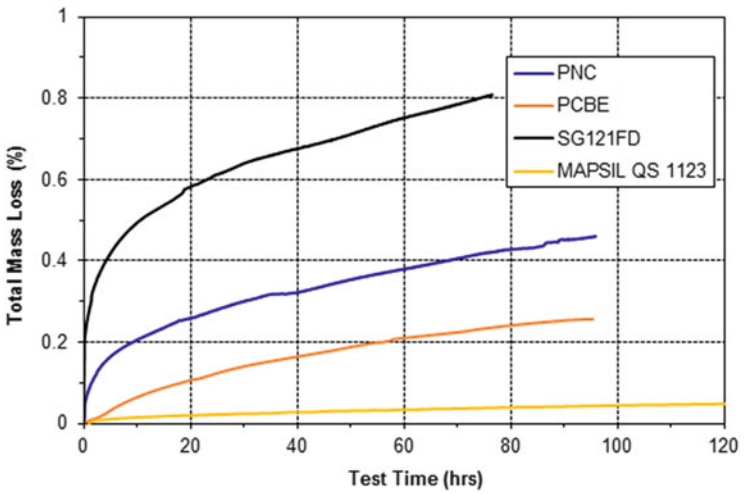

Fig. 6 Percent of total mass loss during isothermal outgassing test of low outgassing (PNC, PCBE) and ultra low outgassing (MAPSIL® QS 1123) silicones

shown in Fig. 8. For MAPSIL® QS 1123 the outgassing rate decreases 3 orders of magnitude, from 10^{-6} to 10^{-9}, within the first 7 days of testing, whereas the outgassing rate of the 3 other materials changes from 10^{-6} to 10^{-8}.

The outgassing kinetics show that the majority of the sample loss for all tested materials occurs in the first few hours of the test, then mass is lost at a steady rate for the remainder of the test. This indicates that there is a large initial burst of volatiles, most likely concentrated near the surface of the samples. The slow steady release

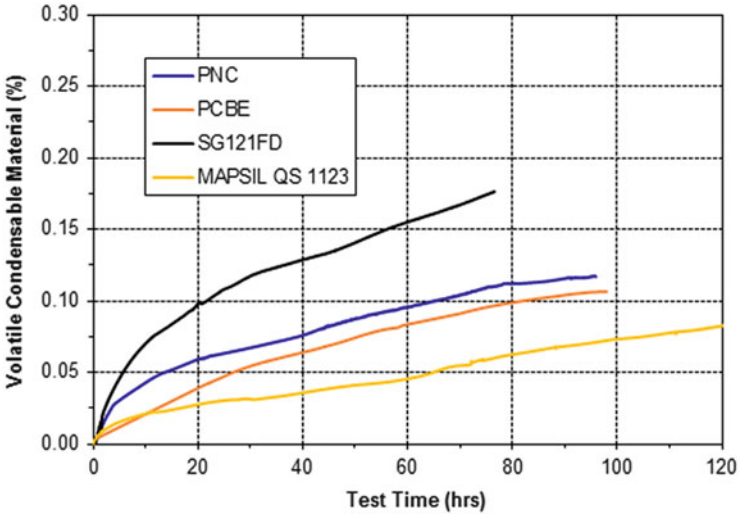

Fig. 7 Percent of volatile condensable material released as a function of time during isothermal outgassing test of low outgassing (PNC, PCBE) and ultra low outgassing (MAPSIL® QS 1123) silicones

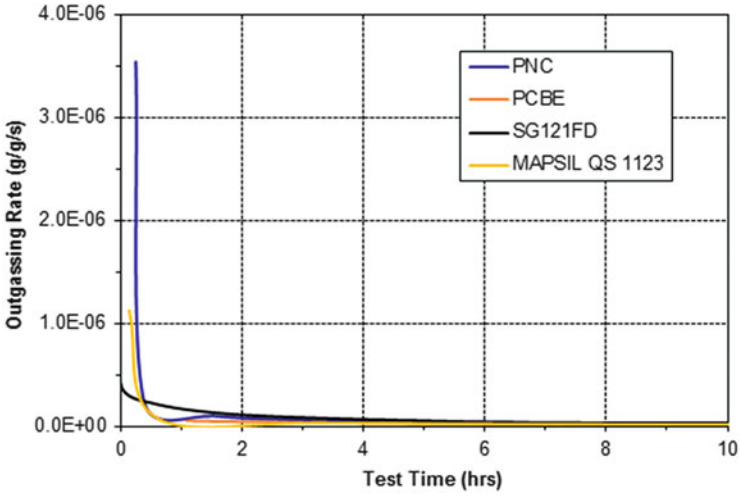

Fig. 8 Outgassing rate as a function of time during the isothermal outgassing test on MAP silicone materials

thereafter can be due to either a steady state diffusion of gaseous molecules distributed throughout the polymer matrix that migrate out of the material at a constant rate or the material can be reverting to reactants at a constant rate. Answering this question is the focus of future research.

At the conclusion of the isothermal outgassing test, the 80 K QCM is heated at increments of 1 K/min while the outgassed species that deposit on the surface evaporate from the crystal. As the temperature of the QCM increases, the evaporation rate of the species also increases until it reaches a peak. The slope of the leading edge is characteristic of the species being volatilized. Each species can then be identified using the *in-situ* mass spectrometer. The majority of outgassing species observed on the mass spectra for the four MAP materials tested could be identified as low molecular weight siloxanes with the Si–O–Si linkage.

Summary and Conclusions

Since the establishment of recent standardization testing, advances in formulating and processing have created a generation of silicones that have excellent performance in low vacuum environments and the outgassing phenomena causing contamination has been greatly diminished. It was observed that several silicone materials achieve much lower TML and CVCM values than the required ASTM E595 specifications. This paper considered the low and ultra low outgassing silicone materials developed and produced by MAP with TML and CVCM one-tenth the standard ASTM E595 specifications.

Testing per ASTM E1559 was performed using the OGF-2013 Outgassing Facility recently designed and built by ITL. A comparative evaluation and discussion of the outgassing test results per ASTM E1559 showed that the ultra low outgassing MAPSIL® QS 1123 silicone resin has the lowest TML, VCM, and Outgassing Rate values as compared to other MAP silicone materials, e.g., PNC, OCBE, and SG121FD. This study has also proved that the MAP silicone space coatings do not cause contaminations on the sensitive optical coatings in the line-of-site direction by silicone-based contaminations during long-term application in LEO.

Acknowledgements The authors would like to thank Dr. Stéphanie Remaury and Dr. Pascale Nabarra from CNES, France for providing the samples of MAP silicone materials.

References

1. Tribble AC (2003) The space environment: implementation for spacecraft design. Princeton University Press, Princeton, p 82
2. ASTM E1559-09, Standard test method for contamination outgassing characteristics of spacecraft materials
3. Kleiman J, Horodetsky S, Issoupov V (2011) Instrumentation for ground-based testing in simulated space and planetary conditions. In: Proceedings of the ICPMSE-10J meeting, Okinawa, Japan, 12–17 June

4. Guillaumon O, Remaury S, Nabarra P, Guigue-Joguet P (2009) Development of a new silicone adhesive for space use: MAPSIL® QS 1123. In: Proceedings of the 11th ISMSE meeting, Aix en Provence, France, 15–18 September
5. Wood BE (2007) NASA/CR-2007-214961, space environmental effects knowledgebase. Bob Wood Aerospace Consulting Services Inc., Tullahoma, TN

Dielectric Temperature Spectroscopy of Degraded Solar Cell Coverglass Due to Ground-Based Space Environmental Irradiation

Yu Chen, Lei Chen, Kazuhiro Toyoda, Mengu Cho, and Yonghong Cheng

Abstract Coverglasses are used to protect solar cells from damages caused by space environment irradiation. Damage to coverglasses from space irradiation, the electrostatic discharge and even the breakdown related to surface charging of coverglass are among the main reasons for malfunctioning of solar cells in space missions. This paper using dielectric temperature spectroscopy investigated the typical solar cell coverglasses that were exposed in ground-based simulators to space environments, such as thermal cycling, proton-beam irradiation, electron-beam irradiation, ultraviolet irradiation and their synergistic irradiation. The dielectric properties of coverglasses were measured using a broadband dielectric spectrometer with the frequency range from 0.1 Hz to 1 MHz at temperatures ranging from −140 to 120 °C. It was found that the dielectric constants of five kinds of irradiated coverglasses increase to different degrees at different temperatures compared with the virgin coverglass. And irradiation has little effect on the dielectric loss, DC conductivity and DC conductivity activation energy of coverglasses.

Keywords Solar cell coverglass • Ground-based space environmental irradiation • Dielectric spectroscopy • DC conductivity activation energy

Introduction

The space environment surrounding a spacecraft in orbit is extremely complex and dangerous that significantly affects the performance and reliability of spacecraft and even may cause different in-orbit failures of spacecraft [1, 2]. Coverglasses are

Y. Chen (✉) • L. Chen • Y. Cheng
State Key Laboratory of Electrical Insulation and Power Equipment, Xi'an Jiaotong University, Xi'an 710049, China
e-mail: chenyu@mail.xjtu.edu.cn

K. Toyoda • M. Cho
Laboratory of Spacecraft Environment Interaction Engineering, Kyushu Institute of Technology, Kitakyushu 804-8550, Japan

J. Kleiman (ed.), *Protection of Materials and Structures from the Space Environment*, Astrophysics and Space Science Proceedings 47,
DOI 10.1007/978-3-319-19309-0_12

used to protect solar cells on spacecraft from space irradiation and charged particles bombardment. The characteristics of the coverglasses will change over time, being exposed to the space irradiation factors, which will also affect the lifetime of solar cells. Therefore, studying the damage effects of space environment irradiation on coverglass is important in improving the reliability of solar cells and prolonging the lifetime of spacecraft.

Some investigations were focused on the damaging effects of space environment irradiation on spacecraft solar cells [3, 4]. Others mainly focused on the influences of space environment on secondary electron emission coefficient and photoelectron emission coefficient of space materials. For example, Kawakita et al. [5] investigated the total electron emission yield (TEEY) of CMG-100-AR coverglasses with and without 1 MeV E-beam or 50 keV P-beam irradiation. Miyake et al. [6] studied the TEEY of CMG-100-AR coverglasses with and without 500 keV E—beam or UV irradiation. In our previous work, we investigated the TEEY and photoelectron emission yield (PEY) of coverglasses exposed in ground-based simulators to space environmental factors [7, 8].

In order to prevent power system failure due to charging, some simulation tools have been developed for analysis of spacecraft charging. For example, NASCAP was the most widely used charging simulation tool until the end of the last decade [9]. Then came the next version, NASCAP-2K [10, 11], which was not available outside U.S. SPIS project in Europe [12], and MUSCAT in Japan [13] and so on. All these charging simulation tools need material properties such as conductivity, dielectric constant and so on to calculate the charging status of a satellite and obtain its' electric potential.

With the broadband dielectric spectrometer we can obtain information on the molecular structure, bound and mobile charges according to details of molecular system, mainly including: the dielectric constant, the dielectric loss tangent and conductivity. In this paper we used a dielectric spectrometer to investigate the dielectric temperature spectroscopy data of typical solar cell coverglasses which were exposed in ground-based simulators to such space environments as thermal cycling, proton-beam irradiation, electron-beam irradiation, ultraviolet irradiation and their synergistic irradiation. The dielectric temperature spectroscopy results of a virgin and five degraded samples is discussed.

Experimental

The solar cell coverglasses selected for testing are plate-shaped and belong to the family of borosilicate glasses. The coverglass CMG-100-AR uses 110 nm thick MgF_2 as front surface coating material and its substrate is doped with cerium, which has a stabilizing effect on controlling coverglass coloration by irradiation. The specification of CMG-100-AR coverglass is listed in Table 1.

The coverglasses were exposed to thermal cycling (T, 348 cycles, −160 °C ~110 °C), proton-beam irradiation (P, 50 keV), electron-beam irradiation

Table 1 Specification of CMG-100-AR coverglass

Sample	CMG-100-AR solar cell coverglass
Manufacture	Qioptiq Space Technology, UK
Front surface	110 nm thick MgF_2 coating
Substrate	100 μm thick CMG
Doping	Cerium doped
Min. transmission	359–400 nm, 83.5 %; 400–450 nm, 95.0 %
	450–900 nm, 97.0 %; 900–1800 nm, 96.5 %

Table 2 Irradiation conditions

Type	Thermal	P-beam	E-beam	UV
Specification	−160 to +110 °C	50 keV	500 keV	–
Condition	348 cycles	$7.8 \times 10^{19}/m^2$	$1.4 \times 10^{20}/m^2$	~4000 ESH
Flux	–	6.14×10^{16} $m^{-2}s^{-1}$, 1270 s	–[a]	–
Simulated time	~2.5 years in LEO	~15 years in GEO	~15 years in GEO	~166 ESD

[a]Step 1: 5.07×10^{14} $m^{-2}s^{-1}$, 138,100 s; Step 2: 1.96×10^{16} $m^{-2}s^{-1}$, 3580 s

(E, 500 keV), ultraviolet (UV) irradiation (~4000 ESH) and their synergistic irradiation (M) in the order of Virgin–T–P–E–UV to analyze the damage effects under the multiple-factors irradiation. All these irradiation treatments were conducted in Wakasa Energy Research Center, Takasaki Advanced Radiation Research Institute and Kyushu Institute of Technology. Details of irradiation conditions of coverglasses are listed in Table 2.

Concept 80 dielectric frequency spectrum system produced by Novocontrol company of Germany is used in the experiment to measure dielectric properties of coverglass with the frequency range from 0.1 Hz to 1 MHz at temperatures range from −140 to 120 °C.

Results and Discussion

Dielectric Constant

The data for dielectric constant, ε' of samples marked as Virgin, T, P, E, UV and M, respectively, at different temperatures are shown in Fig. 1. As can be seen from Fig. 1, the variation trend of ε' with frequency and temperature of six samples is the same and the main difference among samples is the measured values. The value of ε' monotonically increases with rising temperature, and it decreases when frequency increases. The specific relationship of ε' among six samples at three selected temperatures is shown in Fig. 2. It shows the value of ε' of six samples is

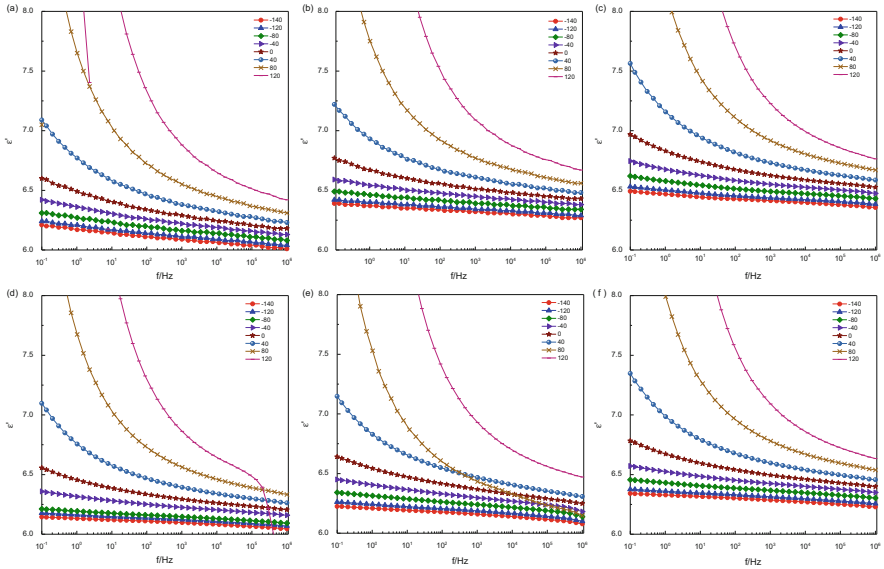

Fig. 1 Dielectric constant of coverglass. (**a**) Virgin; (**b**) T; (**c**) P; (**d**) E; (**e**) UV; (**f**) M

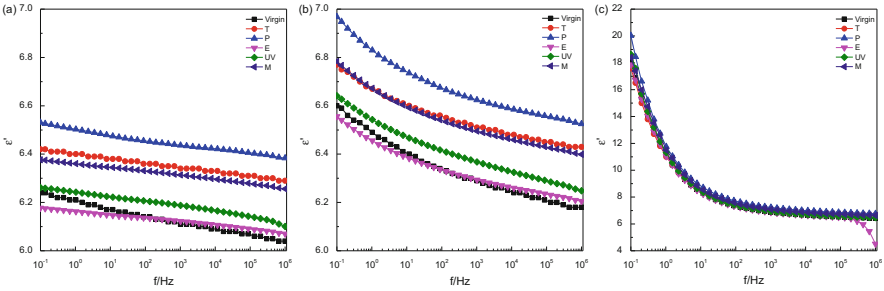

Fig. 2 Dielectric constant of coverglass. (**a**) −120 °C; (**b**) 0 °C; (**c**) 120 °C

related to the temperature. It can be found that when temperature is and below 0 °C, the order of the value of ε' is P > T > M > UV > Virgin > E from 0.1 to 100 Hz and P > T > M > UV > E > Virgin from 100 Hz to 1 MHz. But when temperature is 120 °C, the order is much more complicated. The results of dielectric constants of six kinds of samples at specific temperature and frequency are listed in Table 3.

Combining the data in Fig. 2 and Table 3, it can be found that the ε' of coverglass after being degraded is higher than that of virgin coverglass, and the ε' of coverglass irradiated with protons has the most obvious growth compared with that of other five degraded coverglasses. This behavior is related to the bond breaking of O–Si bond in some of Si–O–Si bonds in SiO_2 which leads to the formation of ODC (2) color center in the substrate of coverglass promoted by the strong ionization

Table 3 Dielectric constant of coverglasses

Temp	f (Hz)	Virgin	T	P	E	UV	M
−120 °C	0.1	6.24	6.42	6.53	6.18	6.26	6.38
	1	6.21	6.40	6.50	6.16	6.24	6.36
	10^3	6.11	6.34	6.44	6.12	6.19	6.31
	10^6	6.04	6.29	6.38	6.07	6.10	6.26
0 °C	0.1	6.60	6.77	6.97	6.56	6.64	6.78
	1	6.49	6.67	6.83	6.46	6.54	6.67
	10^3	6.29	6.51	6.62	6.29	6.37	6.49
	10^6	6.18	6.43	6.53	6.21	6.25	6.40
120 °C	0.1	18.10	17.60	20.03	17.86	18.62	18.41
	1	11.20	11.00	11.75	11.02	11.32	11.50
	10^3	6.88	7.09	7.23	6.86	6.93	7.09
	10^6	6.42	6.67	6.76	4.51	6.47	6.63

effect of proton-beam irradiation [14, 15]. This is because the average range of 50 keV proton-beam in coverglass is 515 nm, which is deeper than the thickness of MgF_2 anti-reflection coating (110 nm). Therefore, there are nearly no protons that deposit in the MgF_2 coating, most of the protons are deposited around the incident depth in CMG substrate and form holes created by the collision with atoms. The formation of holes leads to the increase of color center defects.

Dielectric Loss

The data of dielectric loss, *tanδ* of the six sample types marked as Virgin, T, P, E, UV and M, respectively, at different temperatures are shown in Fig. 3.

Figure 3 shows that when the frequency is low, the value of *tanδ* increases with the rise of temperature, and there are inconspicuous loss peaks at low temperature that move to higher frequency when temperature increases. These loss peaks at low frequency are related to interfacial polarization. When the frequency is high, two trends are observed. For sample P, E and UV, *tanδ* increases with the increase of frequency when it is below 0 °C, but when the temperature rises to 0 °C and even higher, *tanδ* decreases with the increase of frequency. However, for sample Virgin, T and M, *tanδ* doesn't increase when frequency increases at any temperature.

The relationship of *tanδ* among six samples at three different temperatures is shown in Fig. 4. It shows that the order of the value of *tanδ* of six coverglasses changes when frequency changes. It is found that there are loss peaks at −120 °C, but the peaks disappear at 0 and 120 °C.

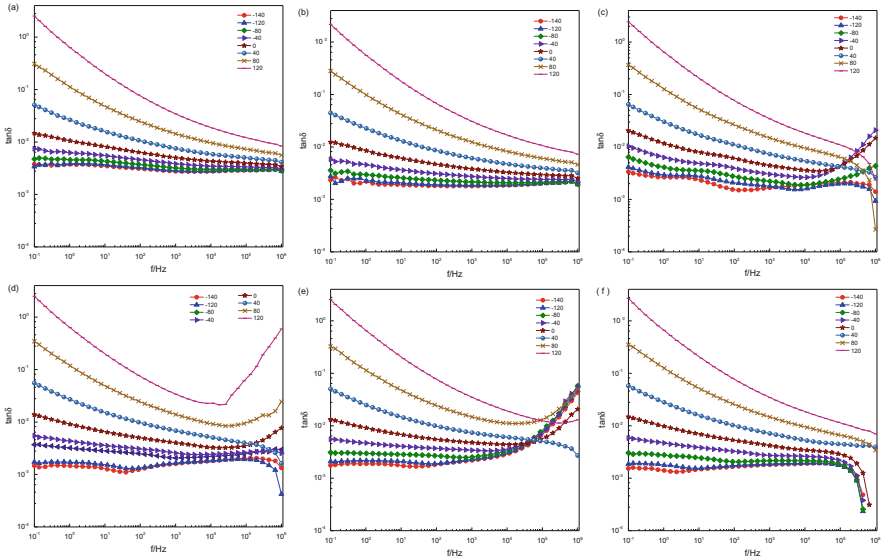

Fig. 3 Dielectric loss of coverglass. (**a**) Virgin; (**b**) T; (**c**) P; (**d**) E; (**e**) UV; (**f**) M

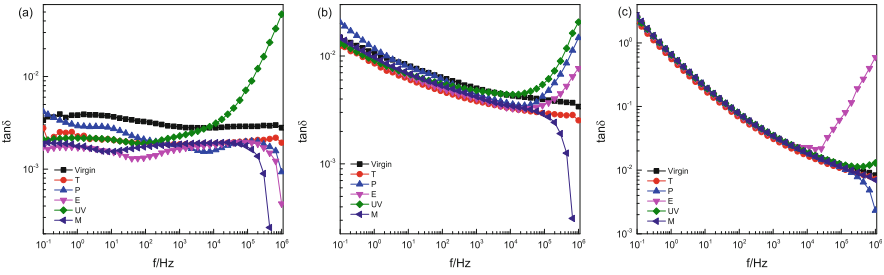

Fig. 4 Dielectric loss of coverglass. (**a**) −120 °C; (**b**) 0 °C; (**c**) 120 °C

Conductivity

The data for conductivity, σ' of samples marked as Virgin, T, P, E, UV and M, respectively, at different temperatures are shown in Fig. 5. It can be found that the variation trend of σ' with frequency and temperature of six samples is the same and it presents a characteristic of thermal activation. In the double logarithmic coordinates, with temperature rises to higher than 40 °C, σ' appears as a straight line with almost no change in its value at low frequency. This part is corresponding to the DC conductivity. And the value of σ' increases linearly with frequency increasing when frequency is high, this part is corresponding to relaxation conductivity. The specific relationship of the value of σ' among six samples at three temperatures is shown in Fig. 6.

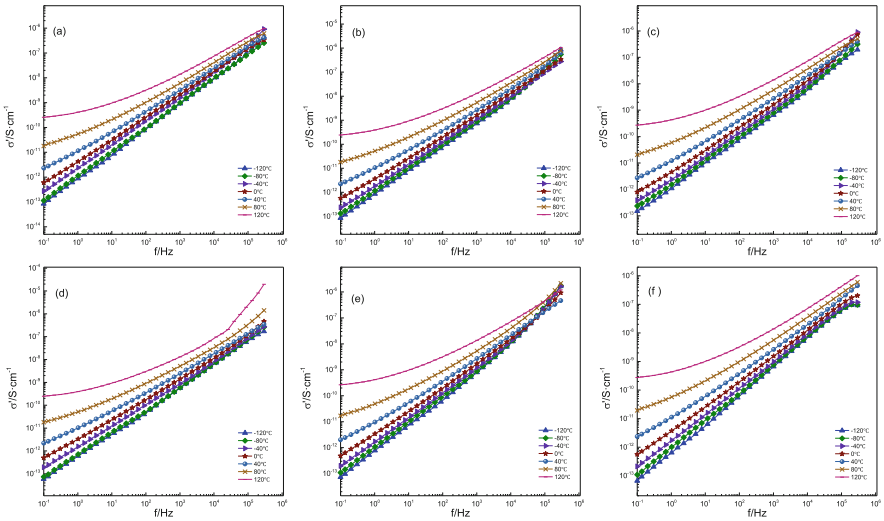

Fig. 5 Conductivity of coverglass. (**a**) Virgin; (**b**) T; (**c**) P; (**d**) E; (**e**) UV; (**f**) M

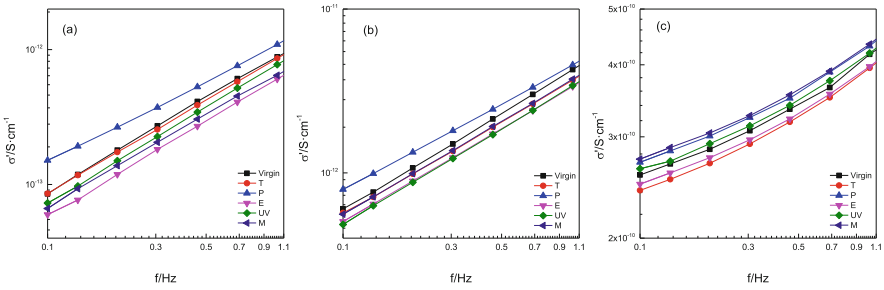

Fig. 6 Conductivity of coverglass. (**a**) −120 °C; (**b**) 0 °C; (**c**) 120 °C

When establishing the influence of the environmental treatments on the value of σ' in six samples, the order is P > Virgin > T > UV > M > E at −120 °C, P > Virgin > M > T > E > UV at 0 °C, and M > P > UV > Virgin > E > T at 120 °C. When considering the DC part of conductivity of samples, there is a relationship between conductivity and dielectric constant as follows:

$$\sigma'(\omega) = \omega\varepsilon_0\varepsilon''(\omega) = \sigma_{dc} + \frac{\varepsilon_0(\varepsilon_s - \varepsilon_\infty)\omega^2\tau}{1 + \omega^2\tau^2} \tag{1}$$

In Eq. (1), σ_{dc} represents DC conductivity, and the second term is the additional conductivity introduced by relaxation. When the frequency is very low, $\omega\tau << 1$, Eq. (1) can be simplified as:

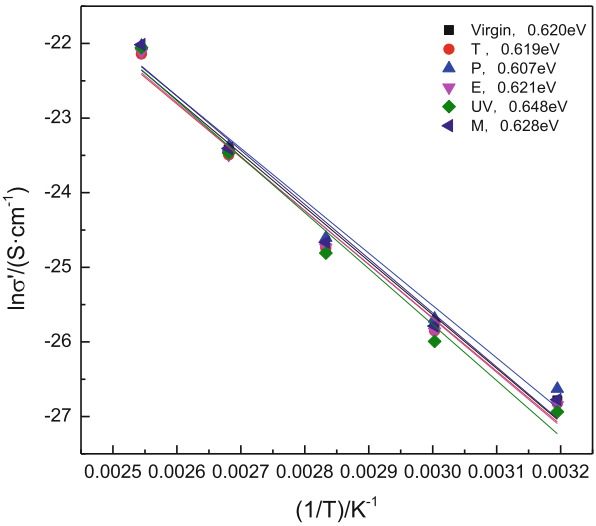

Fig. 7 DC conductivity activation energy of six coverglasses at low frequency

$$\sigma' \approx \sigma_{dc} \propto \exp\left(-\frac{u}{kT}\right) \tag{2}$$

Taking the derivative of both sides of Eq. (2), the following expression can be obtained:

$$ln\sigma' \propto \frac{1}{T} \tag{3}$$

Expression (3) is also established for distributed dielectric relaxation. Therefore, the DC conductivity activation energy u of coverglasses can be obtained from $ln\sigma' \sim 1/T$ by calculating. If we select the conductivity of six samples at 0.1 Hz with temperature ranging from 40 to 120 °C and plot the curve $ln\sigma' \sim 1/T$ we can obtain the curve and the calculated DC conductivity activation energy u as shown in Fig. 7.

It is found that the effects of irradiation treatments on DC conductivity activation energy of coverglasses are not obvious. The DC conductivity activation energy of six coverglasses is affected by the various environmental treatments in the following order P > Virgin > M > T > E > UV, which is the same as the order of influence on conductivity of six coverglasses at 0 °C.

Conclusions

1. The dielectric constants of five kinds of irradiated coverglasses increase to different degrees compared with the virgin coverglass, with the sample after proton-beam irradiation (P) having the greatest degree of growth. The growth of

dielectric constant is related to the formation of ODC(2) color centers in the substrate of the coverglass promoted by the strong ionization effect of proton-beam irradiation.
2. Different irradiation environments have different effects on dielectric loss, DC conductivity and DC conductivity activation energy of coverglasses, and the degree of the influence of dielectric spectrum is related to temperature.
3. The results we obtained can be used in the field of the analysis of spacecraft charging and spacecraft design.

Acknowledgements The authors acknowledge the funding by Japan Aerospace Exploration Agency, and the Specialized Research Fund for the Doctoral Program of Higher Education of China (No. 20120201120009), and China Postdoctoral Science Foundation (2013M532047). We also thank Qioptiq Space Technology, UK for the free coverglasses.

References

1. Lai ST (2011) Fundamentals of spacecraft charging: Spacecraft interactions with space plasmas. Princeton University Press
2. Pisacane VL (2008) The space environment and its effects on space systems. American Insititute of Aeronautics and Astronautics
3. Sun CY (2008) An investigation on the space charged particle environmental effects of the cover-glass for solar cell. Thesis, Harbin Institute of Technology
4. Jiang H (2008) Effects of electrons/protons irradiation in the optical properties of the cover glass and EPR invertigations of the irradiation-induced defects. Thesis, Harbin Institute of Technology
5. Kawakita S, Imaizumi M, Takahashi M, Matsuda S, Michizono S, Saito Y (2002) Influence of high energy electrons and protons on secondary electron emission of cover glasses for space solar cells. In: Proceedings of the 20th international symposium on discharges and electrical insulation in vacuum, Tours, France
6. Miyake H, Nitta K, Michizono S, Saito Y (2008) Secondary electron emission on degradation sample and development of new measurement system with low electron energy. In: Proceedings of the 23rd international symposium on discharges and electrical insulation in vacuum, Bucharest, Romania
7. Chen Y, Wu J, Okumura T, Takahashi M, Endo T, Iwata M, Toyoda K, Cho M (2013) Investigation on space environmental degradation effects of solar cell coverglass. IEEE Trans Plasma Sci 41(12):3471–3476
8. Chen Y, Maruyama A, Wu J, Toyoda K, Cho M (2012) Photoelectron emission yield measurement of insulator by vacuum ultraviolet light source and several narrow bandwidths filters. In: Proceedings of the 12th spacecraft charging technology conference, Kitakyushu, Japan
9. Katz I, Cassidy JJ, Mandell MJ, Schnuelle GW, Steen PG, Roche JC (1979) The capabilities of the NASA charging analyzer program. Spacecraft Charging Technology 2071:101–122
10. Mandell MJ, Davis VA, Cooke DL, Wheelock AT (2006) NASCAP-2K spacecraft charging code overview. IEEE Trans Plasma Sci 34(5):2084–2093
11. Davis VA, Mandell MJ, Gardner BM, Mikellides IG, Neergaard LF, Cokke DL, Mior J (2003) Validation of NASCAP-2K spacecraft environment interactions calculations. In: Proceedings of the 8th spacecraft charging technology conference, Huntsville, USA
12. Roussel JF, Rogier F, Volpert D, Forest J, Rousseau G, Hilgers A (2005) Spacecraft plasma interaction software (SPIS): numerical solvers—methods and architecture. In: Proceedings of the 9th spacecraft charging technology conference, Tsukuba, Japan

13. Muranaka T, Hosoda S, Kim JH, Hatta S, Ikeda K, Hamanaga T, Cho M, Usui H, Ueda HO, Koga K, Goka T (2008) Development of multi-utility spacecraft charging analysis tool (MUSCAT). IEEE Trans Plasma Sci 36(5):2336–2349
14. Skuja L (1998) Optically active oxygen-deficiency-related centers in amorphous silicon dioxide. J Non Cryst Solids 239(1):16–48
15. Blunt RF, Cohen MI (1967) Irradiation-induced color centers in magnesium fluoride. Phys Rev 153(3):1031

Measurement and Evaluation of the Atomic Oxygen Beam Parameters and Material Erosion

S. Horodetsky, V. Issoupov, V. Verba, and J. Kleiman

Abstract Atomic Oxygen fluxes are widely used for accelerated ground base testing of materials used for spacecraft. It is valuable to do this testing with Atomic Oxygen fluxes reaching realistic space environment values (oxygen atom velocity of 7 km/s). This testing is usually done with the help of a laser-detonation fast atomic oxygen (AO) source. Each beam usually contains Atomic Oxygen (90 %) as well as molecular oxygen and Ionic and Electronic Components which are produced during the generation of Atomic Oxygen. Molecular oxygen, under such residual pressures, is unlikely to contribute to physical/chemical changes of sample morphology. However, there is the possibility that the Ionic Component, given that it has the sufficient parameters, can significantly affect the sample morphology.

A study was conducted to determine the influence of the ionic component on the morphology of samples irradiated in the AO system. Based on the conducted experiments it was confirmed that the atomic oxygen beams produced by the laser-detonation fast atomic oxygen source, indeed, have an Ionic Component. The energy of the Ionic Component is approximately 7.25 eV and the current is approximately 3×10^{-7} A. It has been determined that the Ionic Component has no significant effect on sample morphology, which suggests that there is no need to suppress it.

Keywords LEO • Ionic component • Atomic oxygen

Introduction

The questions concerning the presence of an ionic component (IC) in Atomic Oxygen (AO) fluxes produced by laser-detonation fast AO sources as well as the effect of this component on physical-chemical properties of AO irradiated samples are described in various papers [1–3]. While in some papers the presence of the

S. Horodetsky • V. Issoupov • V. Verba • J. Kleiman (✉)
Integrity Testing Laboratory Inc., 80 Esna Park Drive, Units #7-9, Markham, ON L3R 2R7, Canada
e-mail: jkleiman@itlinc.com

J. Kleiman (ed.), *Protection of Materials and Structures from the Space Environment*, Astrophysics and Space Science Proceedings 47,
DOI 10.1007/978-3-319-19309-0_13

ionic component was not confirmed, in others the effects of IC on surface properties were described [2, 3]. The discrepancy of the results can be explained by the difference in the design and settings of the AO sources.

The goal of this paper is to demonstrate the presence of IC in AO beams created by an ITL Inc produced laser-detonation fast atomic oxygen source. This source is equipped with an IC suppressor. By comparing the spectra with and without the IC suppressor use, it can be determined whether IC exist in AO beams.

Experimental and Methodology

Methodology for Determination of the Ionic Component Energy with the Three Grid Energy Analyzer

For determining the presence of the IC, as well as calculating its energy, a Three Grid Energy Analyzer with flat grids was used. This type of analyzer was used due to its simple construction as well as good sensitivity and resolution [4]. The operating principle of the analyzer is in the creation of an electrostatic field which allows for the energy analysis of the flow of charged particles. To allow this a swiping saw tooth voltage (created by a sweep generator) is applied to the second grid. The first and third grids are grounded to allow for the creation of an equipotential space.

Another benefit of this type of analyzer is that it allows the analysis of positive as well as negative particles. This allows for the calibration of the analyzer using a simple electron source with variable energy.

The schematic of the Three Grid Energy Analyzer is shown in Fig. 1a and its image in Fig. 1b. On the schematic, the grids are represented by the dashed lines and the collector is represented by the wide solid line.

The signal is registered on the collector of the energy analyzer. It is analyzed with the help of a computer. An example of the first derivative of the signal over the voltage on the second grid (dI/dE) is shown in Fig. 2b. The differentiation of the signal is required for more accurate calculation of the energy of the charged particles.

Methodology for Three Grid Energy Analyzer Calibration with an Electron Gun

For determining the energy of IC, the energy analyzer was calibrated. This was done using an electron source with a variable energy beam. The energies of the electrons are determined as the difference of potentials between the filament and the sample. In this case, the sample was the collector of the energy analyzer. The

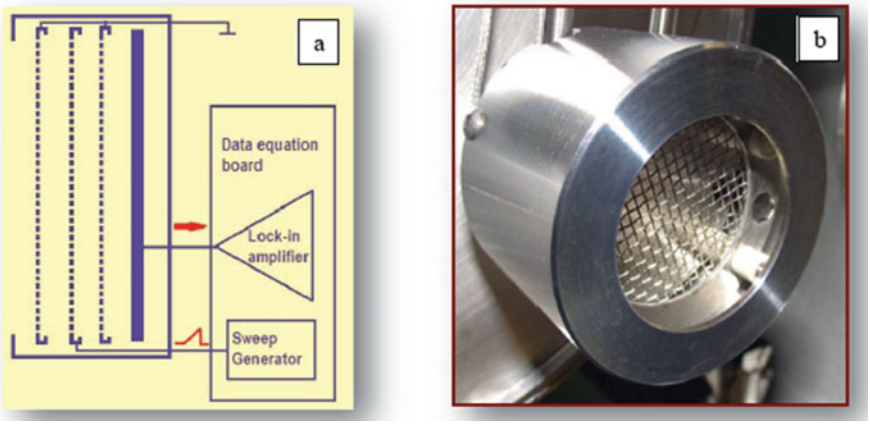

Fig. 1 Electronic schematic (**a**) and external appearance (**b**) of the three-grid energy analyzer

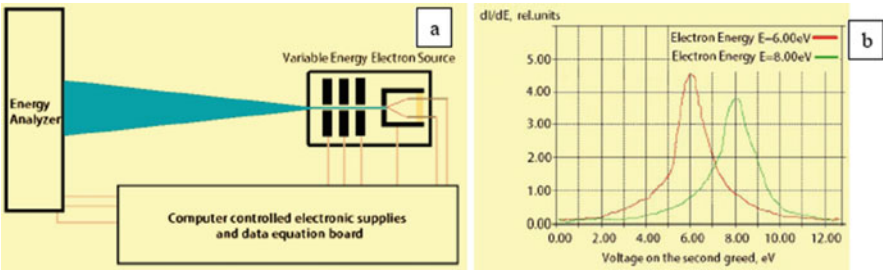

Fig. 2 Electronic schematic of the energy analyzer (**a**) and the collected distribution of the electrons with a primary beam of 6.00 and 8.00 eV (**b**)

electron energy (E_0) was changed over the range of 5–200 eV and the electric current was 1 μA.

The calibration involved the precise setup of the registering system of the Energy Analyzer using the value of E_0. An electronic schematic of this is demonstrated on Fig. 2a. The registered spectra, collected by the Electron Analyzer, with a primary beam of 6.00 and 8.00 eV are given in Fig. 2b

IC Suppressor

The IC suppressor installed on AO sources produced by ITL Inc, is based on electrostatic suppression of charged particles (both positive and negative) that are produced as a by-product of the AO source. A schematic of the suppressor is shown in Fig. 3a, and the image of the suppressor installed inside the AO chamber is shown in Fig. 3b.

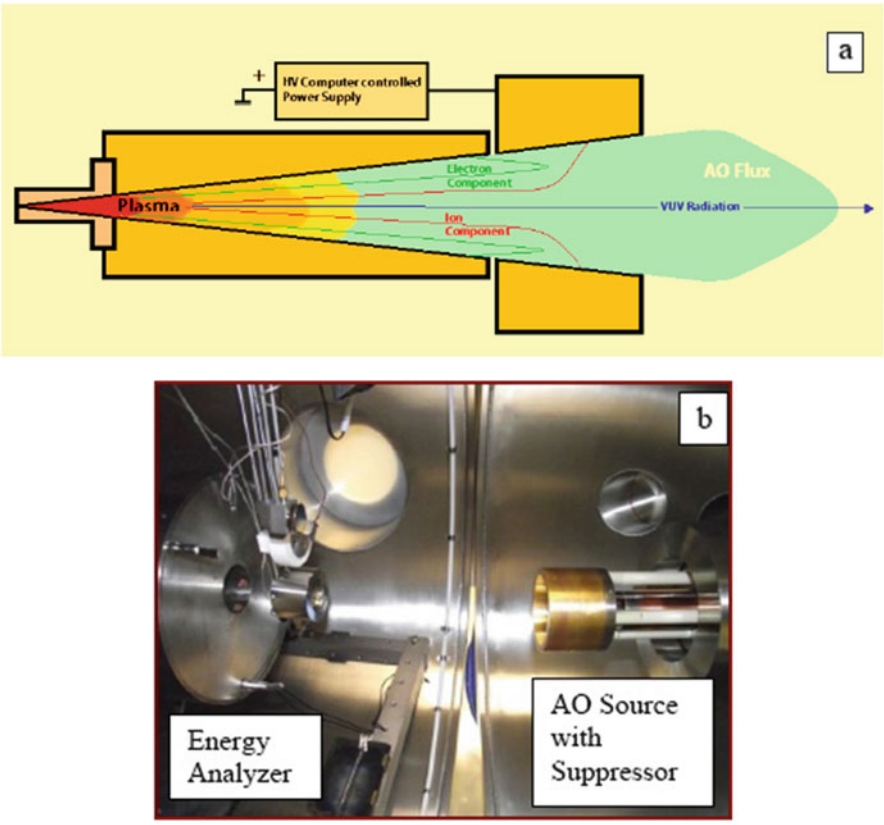

Fig. 3 Schematic view of the ion suppressor operation (**a**) and the AO simulator chamber with analytical equipment showing the installed ion suppressor and the energy analyzer (**b**)

The electrostatic potential on the suppressor is created using a regulated high DC negative voltage (0–15 keV) source. In this example the positive particles (which are equivalent to IC) are attracted to the suppressor and the negative particles are locked by the high voltage.

Results and Discussion

Using the described above methodology, a systematic study of the ionic component was done. In Fig. 4a, a specter is given of a working AO source with a disabled IC suppressor. On this specter there is an evident peak at 7 eV. The amplitude of this peak depends on the settings of the AO source (that is the delay time between injected oxygen pulses and the laser pulses) and can vary within 15 %.

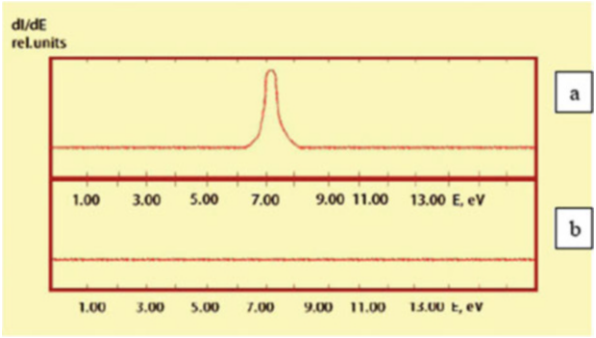

Fig. 4 Energy profile of the ionic component in the AO beam without the suppressor and with the suppressor (**b**)

Figure 4b shows a charged particles spectrum with the IC suppressor activated. As can be seen from Fig. 4, with the suppressor on, the signal at 7 eV disappears, demonstrating a complete suppression of IC. No IC peak was detected in the conducted ranges of 5–200 eV.

A more detailed study was done to determine the precise characteristics of IC. This experiment can be summarized in three parts:

Verification of the Ionic Nature of the Observed Effect

To verify whether the obtained peak (at 7 eV, when the IC suppressor is disabled) is ionic, it was necessary to measure the polarity of the registered signal. This was done using the schematic shown on Fig. 2a. During calibration the peak was negative—due to the registration of the negatively charged electrons. The active AO source has a positive peak, which demonstrates that the peak is ionic.

Determining the Characteristics (Energy and Current) of the IC Peak

To determine the energy of IC, the Three Grid Analyzer was used at following conditions: a sawtooth voltage (created by a sweep generator) was applied to the second grid with the first and third grid kept grounded to allow for the creation of an equipotential space. The signal received at the collector located after the third grid (see Fig. 2a) was processed and its derivative was obtained using a computer. The results of this test are shown in Fig. 5.

To determine the current of the IC, the Three Grid Energy Analyzer was used. The three grids and the collector were connected. The current was measured using a Data Acquisition Board (DAB). The current that was measured was 3×10^{-7} A, which was near the minimum sensitivity of the DAB.

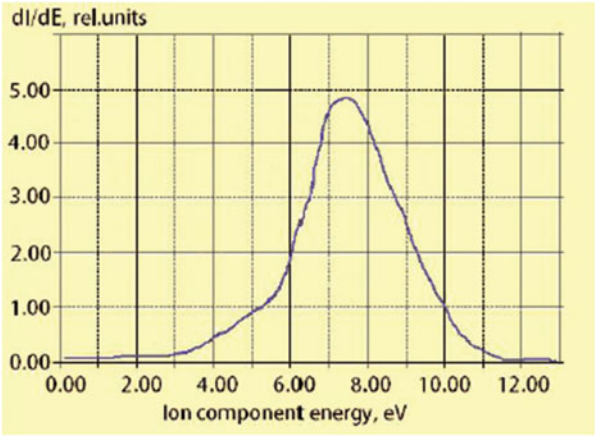

Fig. 5 Energy profile of the ionic component in the AO beam

As seen from this figure, the maximum of this IC peak is 7.25 eV. The full width at half maximum value is 1.50 eV.

Based on these numbers it can be concluded that the IC possesses very low energy and based on theoretical and experimental evidence, does not significantly contribute to any structural changes of the samples [5].

Determining the Effects of the Ionic Component on Sample Morphology

The results of an SEM analysis for AO-exposed Kapton Polyimide with and without an Ionic Component are provided in Fig. 6. The complete removal of the IC through the use of an IC Suppressor (Fig. 6a), does not significantly alter the morphology of the Kapton. When comparing AO-exposed Kapton sample with IC Suppression (Fig. 6a) to Kapton sample exposed to AO without IC Suppression (Fig. 6b), little difference in the morphology is found. These results offer evidence that the IC does not contribute to the structural changes of the samples (Fig. 6)

Summary and Conclusions

This paper provided a detailed overview of the properties of the ionic component that is present in the atomic oxygen beam produced by laser-detonation fast atomic oxygen (AO) source. The IC energy, current and effect on the surface erosion of Kapton were studied. The Ionic Component was analyzed using a Three Grid Energy Analyzer. The energy and the current of the IC were measured. To remove the IC from the beam of atomic oxygen an Ionic Suppressor was used. The

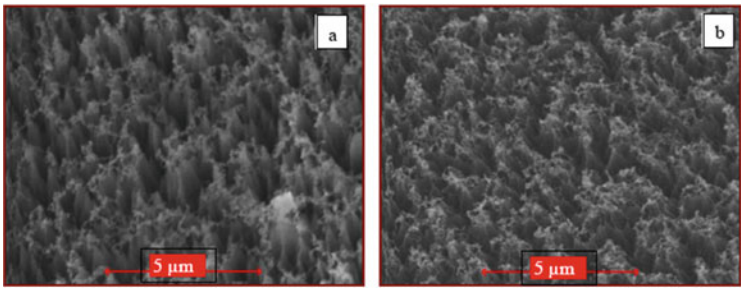

Fig. 6 SEM analysis of Kapton Polyimide AO-exposed with ion suppression (**a**) and without ion suppression (**b**)

Suppressor allowed to determine the existence of the Ionic Component, as well as to study the effects of the IC on the morphology of Kapton. The structure of the atomic oxygen exposed Kapton (with and without the Ionic Component) was studied using SEM.

The following conclusions can be made:

1. In Atomic Oxygen fluxes created by a laser-detonation fast atomic oxygen (AO) source, the Ionic Component (IC) is always present. The presence of the Ionic Component does not depend on the specific settings of the fast Atomic Oxygen source (the delay time between injected oxygen pulses and the laser pulses).
2. The energy of the IC is approximately 7.25 eV. The current of the IC is approximately 3×10^{-7} A.
3. The energy of the IC is insufficient to significantly alter the morphology of the exposed to AO beam samples. There is little difference in the morphology of samples exposed to Atomic Oxygen with and without the Ionic Component.
4. It is recommended to use laser-detonation fast atomic oxygen sources without any IC Suppression.

References

1. Banks BA, Rutledge SK, Paulsen PE, Stueber TJ (1989) Simulation of the low earth orbital atomic oxygen interaction with materials by means of an oxygen ion beam. NASA TM-101971
2. Caledonia GE (1989) Laboratory simulations of energetic atom interactions occurring in low earth orbit. In: Munts EO, Weaver DP, Campbell DH (eds) Rarefied gas dynamics: space-related studies, vol 116, Progress in astronautics and aeronautics. AIAA, Chicago, pp 129–142
3. Cazaubon B, Paillous A, Siffre J, Thomas R (1996) Five-electron-volt atomic oxygen pulsed-beam characterization by quadrupolar mass spectrometry. J Spacecr Rockets 33(6):870–876
4. Horodetsky S (1982) Energy analyzers for LEED/AES study of the solid surface. J Phys E Sci Instrum 13:1092
5. Horodetsky S (1992) Radiation-enhanced effects on the surface of metals and alloys, surface. Phys Chem Mech 2:113–129

The Effect of Small Concentrations of Nanopowders on the Radiation Stability of Lacquers

Chundong Li, V.V. Neshchimenko, and M.M. Mikhailov

Abstract The purpose of this research is to study the optical properties of the binders-lacquers based on organosilicon lacquers and epoxy resins modified by nanopowders ZrO_2, Al_2O_3, CeO_2, SiO_2, TiO_2 with concentration from 0.5 to 5 wt%, before and after proton irradiation $E_p = 100$ keV, $\Phi = 5 \times 10^{15}$ cm^{-2}. Analysis of the diffuse reflection spectra and calculation of the solar absorptance were performed. It was found that radiation stability of organosilicon lacquer is higher than of epoxy resins for both modified by nanopowders and not modified. It was established that the introduction of small concentrations (1–2 wt%) of nanopowders to binders based on organosilicon lacquer promotes decrease of their solar absorptance. Radiation stability of organosilicon lacquer ($\Delta a_S = 0.06$) modified by SiO_2 nanopowder ($\Delta a_S = 0.012$ for 1 wt%) is higher compared with other types of nanopowders ZrO_2, Al_2O_3, CeO_2, TiO_2 ($\Delta a_S = 0.024$, 0.026, 0.034, 0.04 accordingly for 1 wt%).

Keywords Nanopowders • Lacquers • Optical properties • Radiation stability • Proton irradiation

C. Li (✉)
Science and Technology on Material Performance Evaluating in Space Environment Laboratory, Harbin Institute of Technology, West Dazhi St., 150001 Harbin, China
e-mail: lichundong@aliyun.com

V.V. Neshchimenko
Science and Technology on Material Performance Evaluating in Space Environment Laboratory, Harbin Institute of Technology, West Dazhi St., 150001 Harbin, China

Space Materials Laboratory, Amur State University, Ignatyevskoe Shosse, 675027 Blagoveschensk, Russia

M.M. Mikhailov
Radiation and Space Materials Laboratory, Tomsk State University of Control Systems and Radio-Electronics, Lenina St., 634050 Tomsk, Russia

J. Kleiman (ed.), *Protection of Materials and Structures from the Space Environment*, Astrophysics and Space Science Proceedings 47,
DOI 10.1007/978-3-319-19309-0_14

Introduction

The impact of the space environment on spacecraft leads to changes in properties and performance of the external materials, especially to increase in solar absorptance of thermal control coatings (TCC). To a great extent it concerns white TCC of the class "solar reflectors", which include ceramic and enamel coating based on white pigments, polymer, and inorganic bonding agents. Among TCC of this class the paints based on organosilicon lacquers (OSL) and epoxy resins (ER) are used most frequently as the most stable to the exposure of charged particles and solar ultraviolet rays. However, a number of defects and absorption centers are formed in these pigments during a long-term spacecraft flight, which is enough to decrease the spectral reflectance (ρ) in the UV-, visible and near IR-regions of the spectrum, and increase the solar absorptance (a_s). Therefore it is an essential issue to develop techniques to improve photo- and radiation stability of TCC.

Experimental

The research was conducted using commercial ZrO_2, Al_2O_3, CeO_2, SiO_2, TiO_2 nanopowders of 99.8 % purity that were purchased from the Aladdin Chemical Company. The average particle size of the nanopowder was 40–50 nm.

Modification was carried out by addition of nanopowders to KO-859 organosilicon lacquer or ЭП-730 epoxy resins at concentrations of 0.5, 1, 2, 3, 5 wt% during sonication. Then modified lacquers were applied to aluminum substrate (АМГ-6) and dried at 50 °C temperature.

The investigated samples were irradiated with 100 keV protons to a fluence of 5×10^{15} cm^{-2} the flux was set as 1×10^{12} cm^{-2} s^{-1}. The vacuum in the irradiation chamber during the experiments was kept at 2.5×10^{-4} Pa. The reflective spectra of the samples were measured in a Perkin Elmer Lambda 950 spectrophotometer with a scanning rate of 5 nm/s. The value of solar absorptance of the samples was calculated in accordance with ASTM (E490 and E903-00a-96).

Results and Discussion

Figure 1A shows spectral reflectance of epoxy resin modified by different nanopowders at 5 wt%. As can be seen from Fig. 1a, the spectral reflectance in the entire spectral range for all samples is rather low, not exceeding 55 %. At the lower range of used nanopowder concentrations the values of ρ do not exceed the values obtained at 5 wt% concentration. In the region from 300 to 900 nm a 10–15 % increase of the reflectance is recorded compared with the initial lacquer with the introduction of CeO_2, ZrO_2 and TiO_2 nanopowders. For other

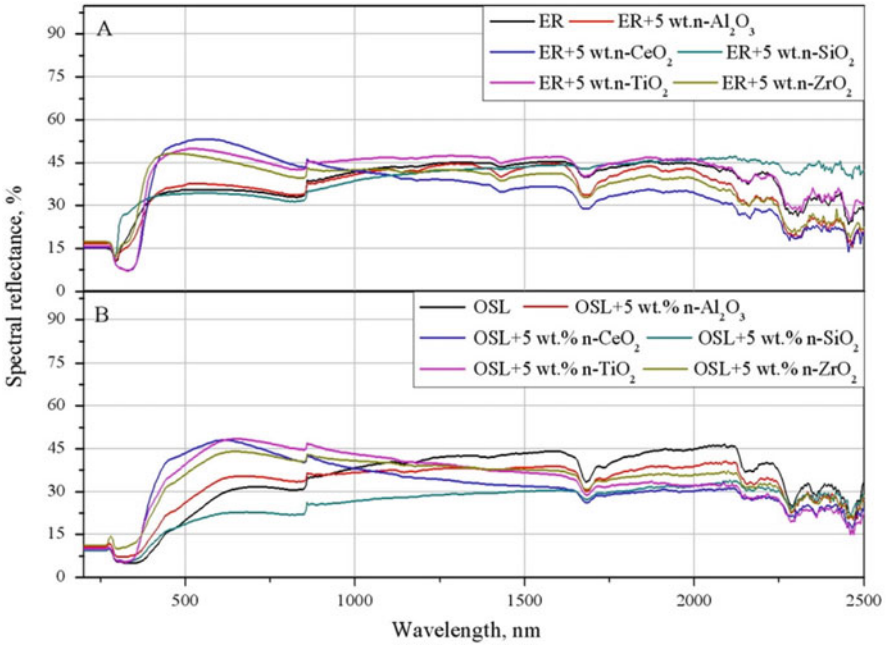

Fig. 1 Spectral reflectance of the epoxy resin (**a**) and organosilicon lacquer (**b**) modified by 5 wt% nanopowders

nanopowders, the values of ρ are close to the values of the initial lacquer. But in the near-IR region the reflectance of the modified samples increases in the order from samples with CeO_2 nanopowders to samples with SiO_2 nanopowders (which are characterized by shift of the edge of the main absorption to the UV region).

The reflectance spectra of the organosilicon lacquer samples modified by nanopowders (Fig. 1b) show significant differences in the value (ρ) for initial and modified lacquer. In the region from 300 to 900 nm the samples modified by SiO_2 nanopowders have the smallest value of diffuse reflectance, followed in ascending order by the unmodified sample and sample with Al_2O_3, ZrO_2, CeO_2 and TiO_2 nanopowders.

The reflectance of the samples was measured before and after the irradiation with protons. Figures 2a through 6a show the change in reflectance spectra ($\Delta\rho_\lambda$) obtained by subtracting the spectrum after irradiation ($\rho_{\lambda F}$) from the spectrum before irradiation ($\rho_{\lambda 0}$). As follows from Figs. 2a, 3a, 4a, 5a and 6a, the influence of protons on epoxy resin modified by various nanopowders for the most part leads to the formation of the continuous spectrum of induced absorption, with distinct maxima in the visible region at 4–3.8 and 3–2.5 eV. In most of the spectra a decrease in the intensity of the integral absorption band with the introduction of nanopowders is registered. As in the case of epoxy resin, the modification by

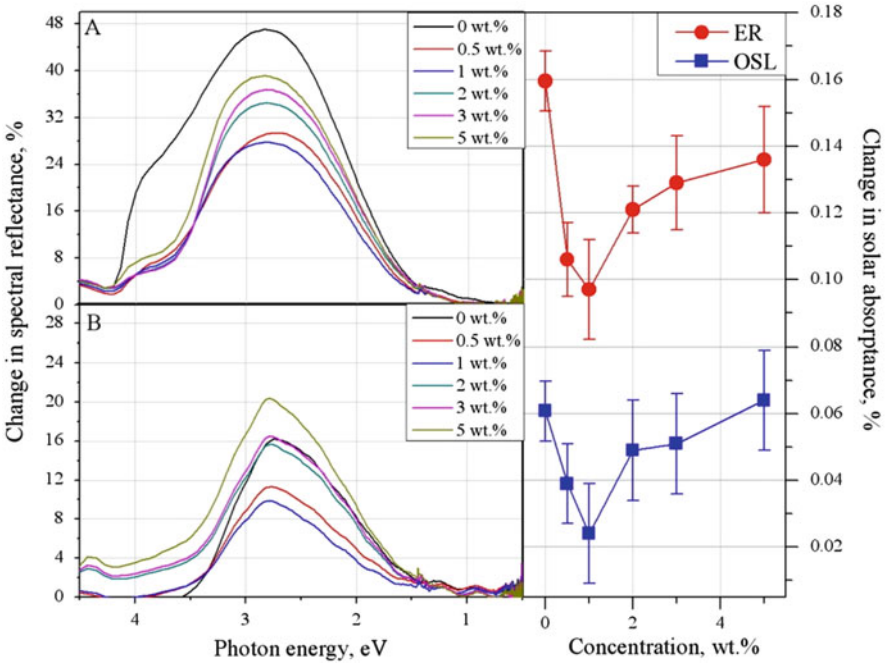

Fig. 2 Change in spectral reflectance of the epoxy resin (**a**) and organosilicon lacquer (**b**) modified by ZrO_2 nanopowders after proton irradiation ($E_p = 100$ $F = 5 \times 10^{15}$ cm^{-2}), their concentration dependence of change in solar absorptance (**c**)

nanopowders of organosilicon lacquer leads to reduced concentration of radiation-induced defects, but there are some differences.

As it follows from the change in spectral reflectance spectra (Figs. 2b, 3b, 4b, 5b and 6b), under the influence of proton irradiation onto the organosilicon lacquer, the integral absorption bands shift to the long-wave part of the spectrum and in the UV range the value of $\Delta\rho$ for samples modified by Al_2O_3, SiO_2, TiO_2 nanopowders has the opposite sign—observed an enlightenment effect.

From a comparison of the integrated intensity of samples based on organosilicon lacquer and the epoxy resin in the band that is registered near 2.9–2.5 eV it is clear that the smallest change in the optical properties by accelerated protons occurs for samples based on organosilicon lacquer, with their radiation stability being higher.

However, a negative impact was observed with the introduction of nanopowders to organosilicon lacquer, with typical concentrations of the TiO_2, CeO_2 and ZrO_2 nanopowders in the samples above 3 wt%.

Estimates of radiation stability of the lacquers were carried out by monitoring the changes in solar absorption that were calculated as $\Delta a_s = a_{s1} - a_{s0}$, where a_{s0}, a_{s1}—solar absorption before and after irradiation, respectively.

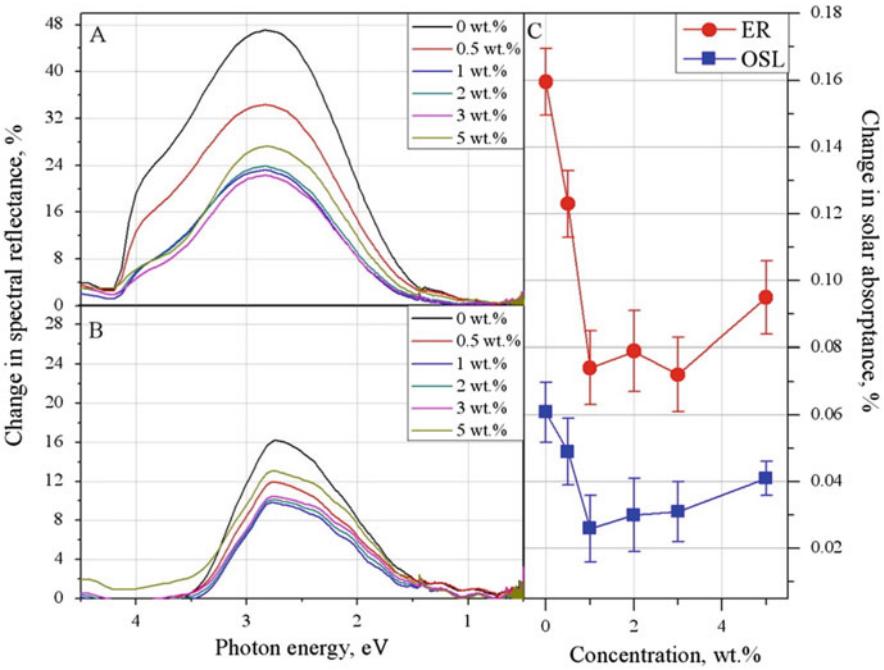

Fig. 3 Change in spectral reflectance of the epoxy resin (**a**) and organosilicon lacquer (**b**) modified by Al_2O_3 nanopowders after proton irradiation ($E_p = 100$ $F = 5 \times 10^{15}$ cm^{-2}), their concentration dependence of change in solar absorptance (**c**)

From the curves of the dependence of change in solar absorption on the concentration of the nanopowders (Figs. 2c, 3c, 4c, 5c and 6c) it can be suggested that the unmodified samples of epoxy resin ЭП-730 have the lowest radiation stability ($\Delta a_s = 0.16$). Addition of nanopowders at concentration of 1–2 wt% to the epoxy resin leads to increases of radiation stability: 24–39 % for ZrO_2, 50–53 % for Al_2O_3, 21–25 % for CeO_2, 40–43 % for SiO_2, 50–54 % for TiO_2. A further increase of nanopowders concentration leads to a decrease in radiation stability of the epoxy resin.

Radiation stability of unmodified organosilicon lacquer is higher than of the epoxy resin by 62 %, Δas is 0.06. Introduction of the nanopowders leads to increases radiation stability near a concentration of 1 wt%: 60 % for ZrO_2, 57 % for Al_2O_3, 42 % for CeO_2, 80 % for SiO_2, 34 % for TiO_2. For samples modified by 5 wt% of ZrO_2, TiO_2 and CeO_2 nanopowders the radiation stability decreases to −5, −26 and −34 %, respectively.

To explain the received patterns of changes in the optical properties after irradiation initial lacquers and lacquers modified by various oxides nanoparticles more research is needed. Presumably, two reasons may affect the increase in radiation stability of the epoxy resin and organosilicon lacquer modified by

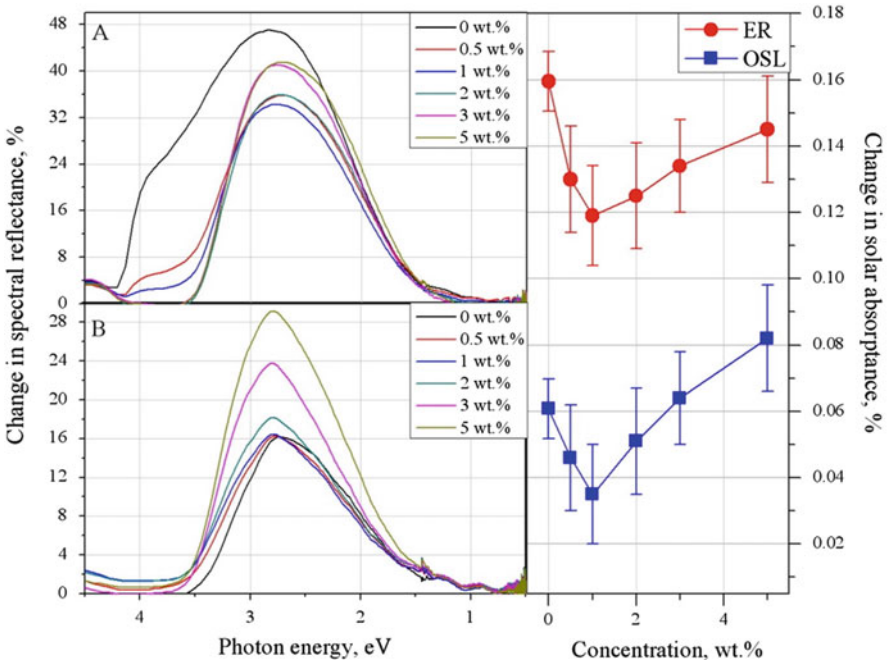

Fig. 4 Change in spectral reflectance of the epoxy resin (**a**) and organosilicon lacquer (**b**) modified by CeO_2 nanopowders after proton irradiation ($E_p = 100$ $F = 5 \times 10^{15}$ cm^{-2}), their concentration dependence of change in solar absorptance (**c**)

introduction of nanopowders. Firstly, cross-linking of oligomer chain ends with inorganic complexes (nanoparticles) which occur in the volume in three directions. That reduces the generation of broken chain under the action of accelerated protons which are often formed at the ends of $-CH_2-CH-CH_2$ glycidyl or $>C-C<$ epoxy groups for the epoxy resin and $-O-Si(CH_3)_2-$ polydialkylsiloxanes for organosilicon lacquer. Secondly nanoparticles in polymer matrices can act as the drains for electrons and holes, as well as the place of scattering polarons which are formed under the influence of radiation and localized on free radicals [1, 2].

To explain the found dependencies in the increase in radiation stability with the introduction of nanoparticles of various oxides (ZrO_2, Al_2O_3, CeO_2, SiO_2, TiO_2) into the binders lacquers it is necessary in our opinion to study their specific surface and the validity of these dependencies under other types of radiation exposure.

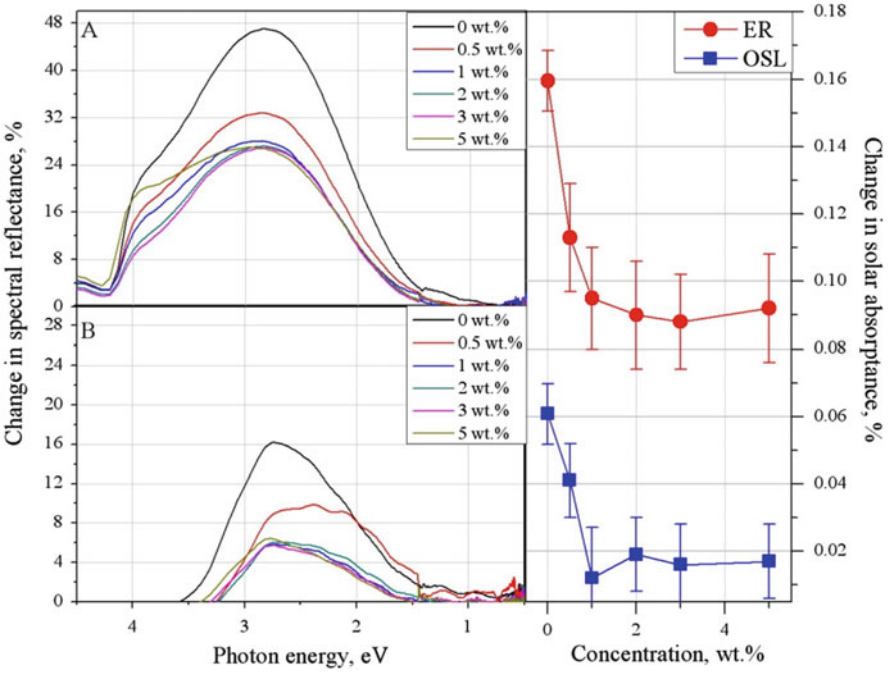

Fig. 5 Change in spectral reflectance of the epoxy resin (**a**) and organosilicon lacquer (**b**) modified by SiO_2 nanopowders after proton irradiation ($E_p = 100$ $F = 5 \times 10^{15}$ cm^{-2}), their concentration dependence of change in solar absorptance (**c**)

Conclusions

Studying the changes in solar absorption in samples of epoxy resin and organosilicon lacquer modified by a low concentration (1–2 wt%) of nanoparticles of ZrO_2, Al_2O_3, CeO_2, SiO_2, TiO_2.and irradiated with protons, the conditions for increasing radiation stability were found. A decrease in the solar absorption caused by decrease of the absorption bands intensity in the regions 4–3.8 and 3–2.5 eV for epoxy resin, and 2.9–2.5 eV for organosilicon lacquer was found. However, the mechanism of increasing radiation stability and the nature of the bands is unclear and require further studies.

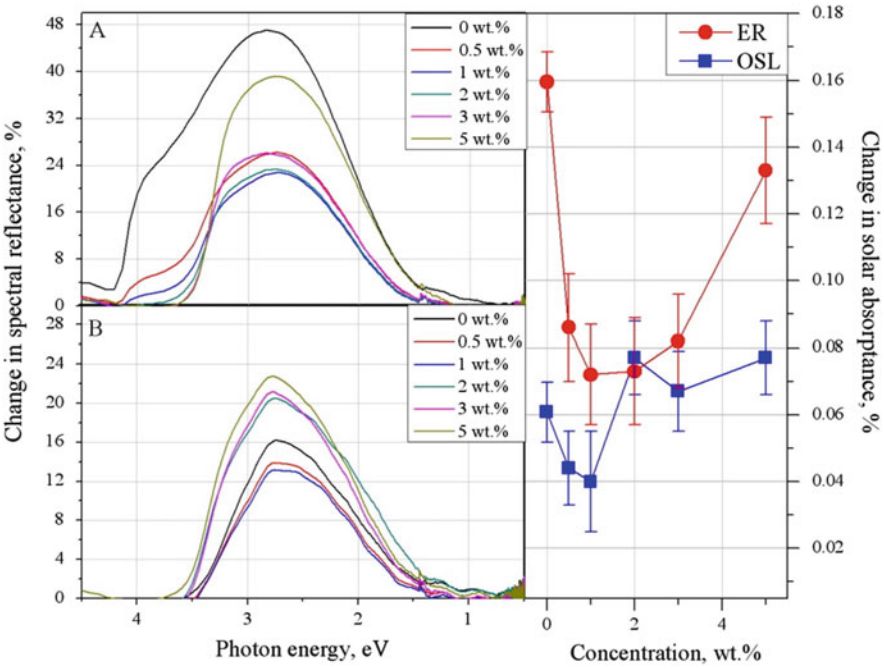

Fig. 6 Change in spectral reflectance of the epoxy resin (**a**) and organosilicon lacquer (**b**) modified by TiO_2 nanopowders after proton irradiation ($E_p = 100$ $F = 5 \times 10^{15}$ cm^{-2}), their concentration dependence of change in solar absorptance (**c**)

Acknowledgments We acknowledge support by Project No11275054 of the National Natural Science Foundation of China and by Project 2015DFR50400 of the International Science & Technology Cooperation Program of China.

References

1. Pope M, Swenberg HE (1999) Electronic processes in organic crystals and polymers. Oxford University Press, Oxford, p 1360
2. Vaisberg SE (1973) Reversible radiation effects in polymers. In: Kargin VA (ed) Radiation chemistry of polymers. Nauka, Moscow, p 376

Potential Space Applications of Nanomaterials

Lev S. Novikov and Ekaterina N. Voronina

Abstract This paper deals with physical fundamentals of nanomaterial structure and properties, their classification and the peculiarities of different classes, and the main potential applications of these materials in the next generation spacecraft. Some results of the experimental and mathematical simulation of the space environment influence on nanostructures are given.

Keywords Nanomaterials • Nanostructures • Nanocomposites • Spacecraft • Space environment • Durability

Introduction

Nanomaterials surpass traditional materials for space applications in many aspects due to their unique properties associated with nanoscale size of their constituents. This superiority in mechanical, thermal, electrical and optical properties will evidently inspire a wide range of applications in the next generation spacecraft intended for the long-term (~15–20 years) operation in near-Earth orbits and the automatic and manned interplanetary missions as well as in the construction of inhabited bases on the Moon.

Nanocomposites with nanoclays, nanotubes and various nanoparticles as fillers are one of the most promising materials for space applications. They may be used as light-weighted and strong structural materials as well as multi-functional and smart materials of general and specific applications, e.g., thermal stabilization, radiation shielding, electrostatic charge mitigation, protection from atomic oxygen influence and space debris impact, etc. Next-generation electronic components based on nanoelectronics, spintronics and photonics, as well as nanoelectromechanical systems, will provide great advantage over conventional microelectronics in performance, noise-immunity, energy consumption and heat emission.

L.S. Novikov (✉) • E.N. Voronina
Lomonosov Moscow State University, Skobeltsyn Institute of Nuclear Physics, Moscow, Russia
e-mail: novikov@sinp.msu.ru

J. Kleiman (ed.), *Protection of Materials and Structures from the Space Environment*, Astrophysics and Space Science Proceedings 47,
DOI 10.1007/978-3-319-19309-0_15

All these materials and components should be durable to most space environment factors and their effects. For the implementation of the nanomaterials and nanotechnologies in the spacecraft engineering it is necessary to develop next-generation ground-based facilities for studying the nanomaterials properties and behavior under the space conditions and to create physico-mathematical models describing properly the various space environment effects on the nanostructures.

This paper deals with the main potential applications of nanomaterials and nanotechnology in the next generation spacecraft for solving novel scientific and technological problems, and with methods of nanomaterials modeling and testing.

Nanomaterials and Nanostructures

The peculiar properties of nanomaterials are determined by the presence in their structure of nanoobjects—particles or grains, fibers, platelets, etc. with at least one linear dimension in nanoscale (size range from approximately 1–100 nm) [1, 2]. The lower boundary of this range approaches the size of atoms and molecules, but its upper one that separates nanoobjects from microobjects was set rather arbitrary. In general, it is not possible to associate unambiguously this upper boundary with any characteristic dimensional parameters that determine the material properties.

The strong influence of material nanostructure on its properties is caused by so called nanometer length scale effects which can be of classical and quantum nature. The nanoscale effects appear when the size of structural objects becomes comparable with a certain parameter of material which has a considerable influence on some physical-chemical processes in the matter and consequently on the material properties. A mean free path of charged particles, a diffusion length, etc. may be regarded as such parameters in the case of classical length scale effects, and for quantum ones its role is usually played by the de Broglie wavelength.

Another parameter of nanostructures called dimensionality, corresponds to the number of dimensions that lie within the nanometer range, and is used for analyzing the quantum confinement effects. According to this parameter, all objects may be divided into four groups [1, 3]:

3D-objects—bulk materials;
2D-objects—nanofilms, nanoplatlets;
1D-objects—nanofibers, nanotubes, nanorods, etc.;
0D-objects—nanoparticles, nanopores, nanocrystals, quantum dots, etc.

In a 3D-object electrons may move freely in all three dimensions. In a film whose width is comparable with the de Broglie wavelength (2D-object), electrons move without restrictions only in the film plane, but in the perpendicular direction they are in a deep potential well, that's why 2D-objects are usually called quantum wells. In 1D-objects, or quantum wires, two dimensions are comparable with the de Broglie wavelength. If the electron movement is limited in three directions, a

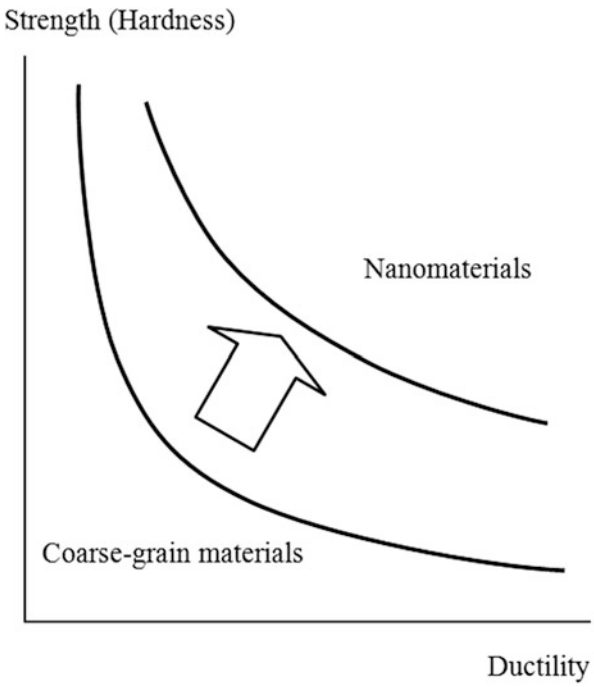

Fig. 1 Strength (hardness)/ductility ratios for bulk materials and nanomaterials

nanostructure becomes a 0D-object, or a quantum dot with discrete electronic states.

Due to nano-length scale effects, nano-structured materials acquire novel mechanical, thermal, electrical, magnetic and optical properties, which can surpass the properties of conventional bulk materials. Figure 1 demonstrates qualitatively that nanomaterials possess higher mechanical characteristics in comparison with conventional materials [4].

The creation of polymer nanocomposites with fillers of various shape and composition may play the pivotal role in spacecraft development and implementation of challenging space projects. Among possible fillers, the main attention is paid to carbon nanostructures: fullerenes, carbon nanotubes (CNT) and graphene that represent particular allotropic forms of carbon [5].

CNTs possess excellent mechanical characteristics. Because of low CNT density (1.3–1.4 g cm^{-3}), specific strength of the material, made of nanotubes, reaches record values. The electrical resistivity of individual single-walled CNTs has been measured under ballistic conductions to be as low as 10^{-6} Ω cm [6], CNT thermal conductivity is also very high: one of reported values is of ~3500 W m^{-1} K^{-1} [7].

Properties of graphene are unique in many respects. This material possesses very high strength and thermal conductivity which was measured to be (3–5) × 10^3 W m^{-1} K^{-1} [8]. Charge carrier mobility in perfect graphene reaches 10^5 cm V^{-1} s^{-1} at 300 K, and this value is much larger than in Si (~1.5 × 10^3 cm V^{-1} s^{-1}) [9]. Because

of such excellent electrical properties, graphene nano-ribbons (strips of a graphene monolayer with widths of several nanometers) are of special interest. Currently many researchers consider graphene nano-ribbons as the most promising substitute for silicon as a semiconducting material for nanoelectronics.

It should be noted that recently much attention is paid to nanoobjects of the similar structure, but of different composition. For instance, the investigations of nanotubes and sheets of hexagonal boron nitride are developed very rapidly. Boron nitride nanotubes (BNNTs), structural analogues of CNTs, attract much attention due to their excellent mechanical properties, high thermal stability and high resistance to oxidation, but as opposed to carbon nanostructures, BNNTs are electrical insulators with a wide band gap of ~5 eV [10].

Nanomaterial's Durability, Modeling and Testing

To estimate the possibilities of nanomaterial's space applications, it is very important to obtain the data concerning their durability to the impact of different space environment factors. If the durability of most conventional materials to the space environmental factors is investigated thoroughly, for nanomaterials such research is in its beginning.

A spacecraft is exposed in space to a wide range of space environmental factors: fluxes of high energy electrons and ions, cold and hot plasma, solar electromagnetic radiation, micrometeoroids and space debris, etc. [11]. Existing experimental and theoretical data demonstrate that nanomaterials responses to various space environment effects can differ substantially from those of conventional bulk spacecraft materials [12, 13].

The most important factor which reduces the reliability and lifetime of spacecraft equipment is the damaging impact of space radiation. Nano-structured materials can demonstrate higher radiation tolerance than conventional materials [14, 15]. When an electron or ion with the energy, typical for space radiation environment, interacts with a nanostructure, the energy transferred from the particle to it is only a small part of the projectile energy [16]. Therefore, only a small number of structural defects or additional charge carriers appear in a nanoscale object with the irradiation. The conditions of defects and charge migration in nanomaterials and in bulk materials differ substantially, too. The high stability of CNTs against forming and accumulating structural defects due to ionizing radiation may be explained by their ability to "heal" defects. The number of radiation defects is reduced also because a significant part of carbon atoms displaced from hexagonal lattice can be sputtered from the CNT without additional collisions with other atoms.

In nano-structured materials, due to the large number of grain boundaries, a distinct radiation resistance mechanism may exist. The grain boundaries and interfaces can capture interstitials and then release them into the lattice to destroy any vacancy that forms in the vicinity of the boundary [14]. Some nanoscale objects

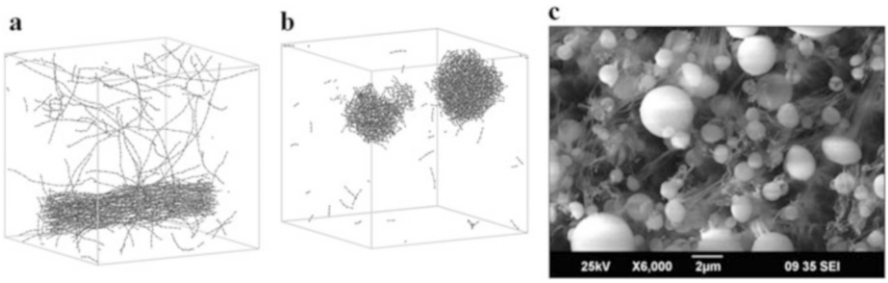

Fig. 2 (**a**, **b**) Examples of equilibrium structure of polymer composite with agglomerated nanotubes (**a**) and nanoparticles (**b**) obtained with DPD simulation. (**c**) SEM image of polymer nano-composite surface after AO exposure

including CNTs may play the role of grain boundaries as sinks for defects of all kinds. It should be noted that when a large number of defects is accumulating, the crystal structure of materials may be destroyed, so at high radiation doses the amorphization of nanostructures can be achieved [15, 16]. For polymer nanocomposites, the serious danger is the atomic oxygen that is the main component of Earth's atmosphere over the altitude range of 200–800 km and its interaction with the materials. Hyper-thermal (~5 eV) oxygen atoms can cause the erosion of polymer matrix and damage nano-fillers (e.g., carbon nanostructures) [12].

Therefore, detailed investigations of processes of space environment impact on nanostructures and nanomaterials via methods of both mathematical modeling and laboratory simulation are needed. For computer modeling it is necessary to apply and develop so called multi-scale simulation [17], and for experimental research the correct choice of regimes of ground-based tests for nanomaterials (types, energies, flux densities of radiation and emission applied, etc.) is of great importance.

Some results of computer simulation with dissipative particle dynamics method (DPD) of CNT and nanoparticles agglomerating into micro-sized objects within a polymer matrix are given in Fig. 2a–c shows such agglomerated objects observed in a polymer nano-composite after the atomic oxygen exposure [18]. It can be seen that these agglomerates protect underlying polymer chains and provide the decrease in mass loss of the composite material.

Potential Applications of Nanomaterials in Space

The necessity in broad applications of nanomaterials and nanotechnology in spacecraft design and construction in the near future is caused by the emerging changes in spacecraft design and usage.

All spacecraft may be considered as operating in some information systems because they either gather extensive information (e.g., on space environment conditions, the Earth's surface, etc.) or transfer a great amount of data. The new satellite system concept assumes the development of multi-satellite cluster systems,

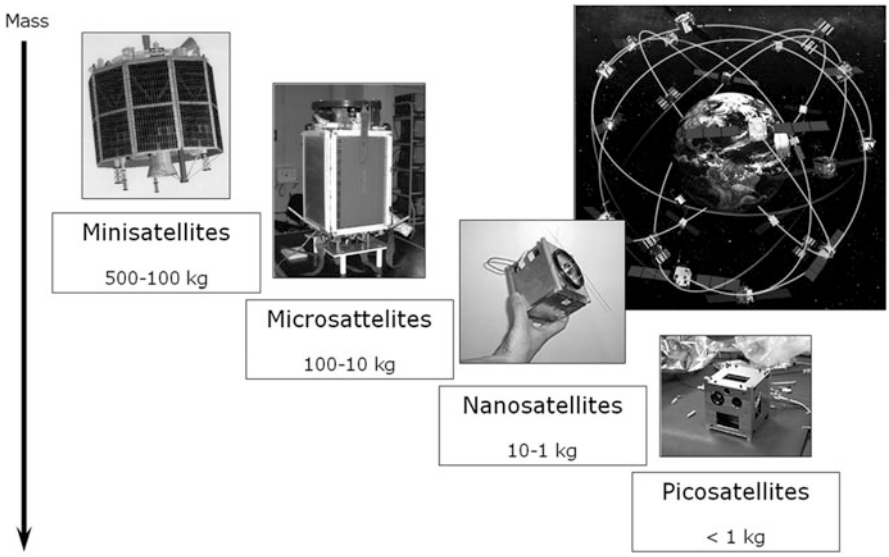

Fig. 3 Classification of small spacecraft

or satellite constellations [19], in which dozens of satellites on different orbits operate according to coordinated programs and share information not only with ground-based control centers but with each other.

Satellite constellation should include small-size lightweight satellites capable of executing most functions of conventional large and heavy-weight ones. The success of creation of such spacecraft is entirely determined by the level of applied technologies, the availability of new materials with required operating characteristics and the degree of miniaturization of electronic components used in spacecraft equipment. Therefore the realization and advance of this concept are in close connection with the progress in the field of nanotechnology. The classification of such spacecraft according to their mass is given on Fig. 3.

Along with creation of small satellites, nanomaterials and nanotechnologies will be widely applied in development of next-generation heavy satellites and manned spacecraft, in building so called 'space elevator', solar power space stations, as well as in implementation of the major space projects of the first half of twenty-first century: manned mission to Mars and inhabited bases on the Moon.

In recent years, in a number of countries, expert assessments were prepared in order to evaluate possibilities of nanomaterials and nanotechnology usage in spacecraft construction and operation and to outline the main directions of their applications. Some programs of the nanotechnology implementation into the space exploration, developed in the early 2000s [20, 21], provide the following main directions:

1. Multifunctional structural and functional materials, including smart materials;
2. Nanoelectronics components;

3. Materials and devices for power supply system of the spacecraft (energy storage, fuel cells, solar cells, etc.);
4. Spacecraft subsystems and payloads with nano-sensors, nanoelectromechanical systems, etc.;
5. Life support systems;
6. Futuristic projects which cannot be realized without the nanotechnologies.

According to NASA experts [22], nanotechnology can have a broad impact on space projects in aeronautics, planetary science, and space exploration owing to

Reduced vehicle mass.
Improved functionality and durability.
Enhanced power generation, storage and propulsion.
Improved astronaut health management.

In NASA Nanotechnology Roadmap [22], the great attention is paid to creation of light-weighted, ultra-strong, damage tolerant, multifunctional materials as well as smart-materials, including self repairing and self-diagnostic ones. Increasing levels of system design and integration is considered as a very important task to achieve enhanced efficiency of space technologies. The development of integrated complex systems for energy generation, storage and distribution, including highly efficient solar cells on quantum dots, ultra-capacitors, wires and cables network made of nanotubes, is of great significance. The very important research direction is the development of next-generation propulsion systems of different types. Nano-sensors of different kind and complexity (for temperature, pressure, humidity sensing, autonomous distributed sensors for chemical sensing, biosensors, etc.), spacecraft nanoelectronics, especially graphene based electronics, and various miniature instrumentation tools will play a crucial role in future space mission.

Polymer nanocomposites are considered in most cases as light-weighted multifunctional materials that can be used for solving different tasks. By varying the composition of matrixes and fillers one may impart distinctive properties to nanocomposites, so they may fit to a wide range of applications as structural and functional materials. In the short-term period light-weighted and strong nanocomposites will undoubtedly be used in spacecraft structural components due their advantages over conventional metals and ceramics. One of very important applications of nanocomposites is the development of multifunctional coatings to protect against hypervelocity impact and space radiation, to provide thermal shielding for the safe entry into atmosphere, to preserve spacecraft thermal regime during the flight, to impart required optical and electrical properties to spacecraft surface, etc. Polymer nanocomposites may be applied in radiation protection systems for interplanetary spacecraft and inhabited Lunar bases. To reduce the weight of protective radiation shields and the intensity of secondary radiation particles which are produced due to the interaction of space radiation particles with material atoms, it is effective to use the materials that consist of low-Z atoms. Thin conducting films made of nanocomposites and transparent network of CNT

can be applied to provide equipotential conditions on the spacecraft surface under space plasma charging conditions and to remove electrical charges from it.

Conclusions

1. In the near future nanomaterials and nanotechnologies will play a very important role in development and construction of next-generation spacecraft and in implementation of the major space missions.
2. Polymer nanocomposites with various nano-fillers, including carbon and boron nitride nanostructures can be applied as multifunctional spacecraft materials.
3. To investigate nanostructures and nanomaterials durability to the space environment impact it is necessary to develop rapidly special methods of mathematical simulation and ground-based testing.

References

1. Kelsall RW, Hamley IW, Geoghegan M (eds) (2005) Nanoscale science and technology. Wiley, New York, NY
2. ISO/TS: 27687 (2008) Nanotechnologies—terminology and definitions for nano-objects. http://www.iso.org/iso/catalogue_detail.htm?csnumber=51240
3. ISO/TS 80004-1 (2010) Nanotechnologies—vocabulary. http://www.iso.org/iso/home/store/catalogue_ics/catalogue_detail_ics.htm?csnumber=68058
4. Lyakishev NP, Alymov MI (2006) Structural nanomaterials. Nanotech Russia 1(2):71–81 (in Russian)
5. Gogotsi Y (ed) (2006) Carbon nanomaterials. Taylor & Francis Group, Oxford
6. Gao B, Chen YF, Fuhrer MS et al (2005) Four-point resistance of individual single-wall carbon nanotubes. Phys Rev Lett 95:196802
7. Pop E, Mann D, Wang Q et al (2006) Thermal conductance of an individual single-wall carbon nanotube above room temperature. Nano Lett 6(1):96–100
8. Ghosh S, Calizo I, Teweldebrhan D et al (2008) Extremely high thermal conductivity of graphene. Appl Phys Lett 92(15):151911
9. Neto AHC, Novoselov KS (2011) New directions in science and technology: two-dimensional crystals. Rep Prog Phys 74:082501
10. Golberg D, Bando Y, Tang C, Zhi C (2007) Boron nitride nanotubes. Adv Mater 19:2413–2432
11. Novikov LS (1999) Contemporary state of spacecraft/environment interaction research. Radiat Meas 30:661–667
12. Watson KA, Connell JW (2006) Polymer and carbon nanotube composites for space applications. In: Dai L (ed) Carbon nanotechnology: recent developments in chemistry, physics, materials science and device applications. Elsevier, Amsterdam, pp 676–698
13. Baur J, Silverman E (2007) Challenges and opportunities in multifunctional nano-composite structures for aerospace applications. MRS Bull 32:328
14. Ackland G (2010) Controlling radiation damage. Science 327:1587–1588
15. Andrievskii RA (2010) Effect of irradiation on the properties of nanomaterials. Phys Metals Metallogr 110(3):229–240

16. Krasheninnikov AV, Nordlund K (2010) Ion and electron irradiation-induced effects in nanostructured materials. J Appl Phys 107:071301
17. Mohanty S, Ross R (eds) (2008) Multiscale simulation methods for nanomaterials. Wiley, New York, NY
18. Voronina EN, Novikov LS, Chernik VN et al (2012) Mathematical and experimental simulation of impact of atomic oxygen of the Earth's upper atmosphere on nanostructures and polymer composites. Inorg Mater: Appl Res 3(2):95–101
19. Walker JG (1984) Satellite constellations. J Br Interplanet Soc 37:559–571
20. National Science and Technology Council (2004) Nanotechnology in space exploration. http://www.whitehouse.gov/files/docments/ostp/NSTC%20Reports/nni_space_exploration_rpt%202004.pdf
21. Ineke Malsch (ed) (2007) Nanotechnology in Aerospace 9th Nanoforum report. www.nanoforum.org. Accessed December 2014.
22. Meador MM et al (2010) NASA nanotechnology roadmap. Technology area 10. http://www.nasa.gov/pdf/501325main_TA10

Synergistic Effects in "Solar Reflectors" Thermal Control Coating Under GSO Simulated Conditions Exposure

M.M. Mikhailov and V.V. Neshchimenko

Abstract Synergistic effects in two types of "solar reflectors" thermal control coatings under conditions simulating geostationary orbit have been investigated by exposing them to separate and complex (simultaneous and continuous) irradiation by solar spectrum photons, electrons and protons. Energy and flux of protons and electrons were selected using a replacement model. This model based on replacement spectra of charged particles by monoenergetic beams during ground testing using the experimental fluence and energy dependences of the changes in solar absorptance. It has been found that the change in solar absorptance of complex irradiation is less than the sum of changes in solar absorptance due to the separate irradiation. Also, the additivity coefficient reaches up to 0.55 and depends on the type of coatings, acceleration and time of complex irradiation.

Keywords Synergistic effects • Complex irradiation • Thermal control coatings

Introduction

Among all effects of the space environment that lead to non-additive or synergistic effects when the sum of separate factors is not equal to a simultaneous/sequential action of same factors we select only combined effects from particles of different energy and charge and solar spectrum photons.

1. Complex action of electrons with different energies in their spectra range from 1 keV to 1.4 MeV on real orbits. No research was conducted covering this range. Previous researchers studied the impact of consistently monoenergetic beams of

M.M. Mikhailov (✉)
Radiation and Space Materials Laboratory, Tomsk State University of Control Systems and Radio-Electronics, Lenina St., 634050 Tomsk, Russia
e-mail: membrana2010@mail.ru

V.V. Neshchimenko (✉)
Space Materials Laboratory, Amur State University, Ignatyevskoe Shosse, 675027 Blagoveschensk, Russia
e-mail: v1ta1y@mail.ru

J. Kleiman (ed.), *Protection of Materials and Structures from the Space Environment*, Astrophysics and Space Science Proceedings 47,
DOI 10.1007/978-3-319-19309-0_16

electrons on materials in vacuum chambers, but they didn't imitate the whole spectrum of electrons. Under exposure to different energy electrons differences can arise in material of spacecrafts in interaction, mean free paths and types of radiation defects.

2. Complex action of protons with different energies in their spectra ranging from 1 keV to 300–400 MeV on real orbits. No research was conducted covering this range, as well.
3. Complex action of protons and electrons of different energies in wide spectra range from 1 keV to 300–400 MeV. Such effects haven't been studied before, neither as for effects in materials nor as to changes in their properties.
4. Complex action of electromagnetic solar irradiation (ESI) photons in ultraviolet, near-ultraviolet, visible, and infrared spectra regions. Such researches haven't held before. Previous researchers studied effects in materials after serial irradiation by VUV photons and photons within spectral regions from 200 to 3000 nm. The expected effects could be defined by different interaction mechanisms and differences among penetration depths of photons with energy from 0.4 eV to 10 keV.
5. Complex action of one charged particle's type and electromagnetic solar irradiation quanta's: electrons + ESI, protons + ESI. Such researches have been carried out only with low-energy photons, with the same energy as solar wind photons have (1–3 keV), the energy of electrons was about 10–100 keV. The expected effects could be defined by different interaction mechanisms and differences among penetration depths of photons and electrons.
6. Complex action of two types charged particles and electromagnetic solar irradiation quanta's: electrons + protons + EMR. Such researches have been carried out only with low-energy charged particles: the energy of protons was the same energy as solar wind protons (1–3 keV), the energy of electrons was about 10–15 keV. The expected effects could be defined by different interaction mechanisms and differences among penetration depths of photons and electrons.

The study of synergetic effects in such a wide range of conditions would let establishing the law of changes in material properties of spacecraft parts. This will increase the work reliability of structures and will lead to more accurate lifetime calculations. Moreover such knowledge will help us to invent new more efficient materials than we have today. In the early years of space exploration this problem was given great attention.

We should name the scientists, who made huge contributions into this field of science in 1970s: Fogdall, Gilligan, Cannaday, McCargo, Greenberg, Douglas, Brown, Kroes, Arvesen [1–8]. In Russia research of thermal control coatings degradation under the influence of both protons and electrons was'conducted in All-Union Institute of Aviation Materials by Barabashov and Bagatov [9, 10] and in Institute of Nuclear Physics (Tomsk Polytechnic Institute) by Mikhailov and Dvoretskiy [11–15]. Investigations devoted to impact of complex irradiation by protons and electrons on alkali-halide crystals and powders were carried out by Mikhailov и Ardushev [16, 17]. In their works the synergetic effects were

established, additive coefficients were calculated; their values were not equal to 1. Moreover the sum of effects, caused by two or three types of irradiation, sometimes was less than if it was one type.

The intensity of ESI, protons and electrons in such studies had random values, without associating them with real orbital spectra. That's why the obtained results were not very useful in practical applications.

Only in some works [11, 12] experiments imitated real orbit conditions. These results showed that thermal control coatings degradation, caused by simultaneous exposure to several irradiation sources, is less than when irradiated separately by each irradiation source in sequence. Taking these results into account, it is possible to decrease the thermal control radiator area and the weight of the whole spacecraft, making the overall cost of spacecraft and the launches cheaper.

The purposes of the present paper is analysis of optical properties of solar reflectors thermal controls coatings under the complex and separate action of electromagnetic solar irradiation, photons and electrons with same conditions of GSO.

Experiment and Method

Investigations were carried out on standard type TCC like TRSO-1 and TRSO-10 with zinc oxide (TRSO-1) and zinc ortatitanate (TRSO-10) as pigment powders, and potassium glass (TRSO-1 and TRSO-10) as binder.

Samples were prepared by coating deposition on 24 mm diameter aluminum substrates. The samples were positioned in the space environmental simulator "Spectrum" [18]. The vacuum in the chamber was 10^{-6}–10^{-7} Torr. Diffuse reflectance spectra were recorded *insitu* in the range from 250 to 2100 nm. Irradiation was carried out separately and simultaneously by electrons, protons and EMR. The reflectance spectra of samples irradiated by EMR were recorded after 10 h exposure. The registration of ρ_λ spectra in samples exposed to protons or electrons was performed at specified times for which the degradation kinetics have at least 5–6 dose points.

Determination of electron and proton fluxes with simultaneous irradiation was performed using the replacement method of the charged particles spectra in orbit by monoenergetic beams. The basis of this methodology is equal change in operating parameters (ΔP) of spectrum to monoenergetic beam [19, 20].

$$\Delta P\left(E_0, \varphi_{/\text{equivalent}}\right) = \Delta P \int_{E_1}^{E_2} \frac{d\varphi}{dE}\, dE \tag{1}$$

Solution to Eq. (1) is different for different operating parameters, depending on particle fluence ($F = \varphi \cdot t$) at constant energy. For the TRSO-1 and TRSO-10 irradiation tests this dependence follows a power law and is determined by the

equivalent flux ($\varphi_{equivalent}$). The action of φ at the chosen value of energy (E_0) leads to similar changes in the solar absorption a_s, as the action charged particles spectrum in orbit that is determined by

$$\varphi_{экв} = \frac{\int_{E_1}^{E_2} \alpha(E)^{\frac{1}{\beta(E)}} \frac{d\varphi}{dE} dE}{\alpha(E_0)^{\beta(E_0)}} \quad (2)$$

Values of equivalent electron ($\varphi_{equivalent}^{-}$) and proton ($\varphi_{equivalent}^{+}$) fluxes for each coating were calculated from the experimental curves $\Delta a_s = f(\Phi_{e-})$ and $\Delta a_s = f(\Phi_{p+})$ obtained in a wide range of energies $E_1 \div E_2$, selected for electrons as $5 \div 150$ keV and for protons as $0.5 \div 500$ keV [11, 21]. Calculated values of $\varphi_{equivalent}^{-}$ and $\varphi_{equivalent}^{+}$ at E_{oe-} and E_{op+} corresponded to acceleration of simultaneous irradiation χ_0, which is equal to one. To obtain large values of acceleration, the values χ_0 were multiplied by n, equivalent fluxes $\varphi_{equivalent}^{-}$ and $\varphi_{equivalent}^{+}$ were also increased by n times. EMR intensity in the first case is equal to one equivalent of solar radiation ($E'_s = 1$ ESR), in other cases, it has also been increased by n times. It was assumed that the degradation does not depend on accelerated tests in the range of values for the simultaneous irradiation [22].

Calculated values of the equivalent flux at selected energy of electrons and protons supported and controlled during at all times complex exposure. The duration of simultaneous or continuous irradiation by EMR, electrons and protons was selected between $0 \div 12$ h. During the exposures, after each hour the ρ_λ spectra were measured.

The solar absorption (a_s) is calculated from the following expression:

$$a_s = 1 - R_s = 1 - \frac{\int_{\lambda_1}^{\lambda_2} \rho_\lambda I_\lambda d\lambda}{\int_{\lambda_1}^{\lambda_2} I_\lambda d\lambda} \quad (3)$$

where R_s—solar reflectance; ρ_λ—spectral reflectance; I_λ—solar spectral intensity; $(\lambda_1 \div \lambda_2)$—range of wavelength form 220 to 2100 nm.

Results and Discussion

TRSO-1 Coating

This coating was irradiated simultaneously by EMR, electrons and protons at two acceleration values ($\chi = 1.5$ and $\chi = 5$) under conditions of simulated GSO (GEO orbit). To determine the equivalent fluxes of electrons and protons, experiments were conducted to study the changes in solar absorptance Δa_s depending on the electron and proton fluencies in the range $2{\cdot}10^{15} \div 5{\cdot}10^{16}$ cm^{-2} for energy values from 5 to 150 keV. Based on results from this study, using power functions $\Delta a_s = f(F_{e-})$ and $\Delta a_s = f(F_{p+})$, energy dependencies of $\varphi_{equivalent}{}^-$ and $\varphi_{equivalent}{}^+$ were obtained. From this dependence, the values of the equivalent flux during acceleration tests for the electron energy of 30 keV and a proton energy of 3 keV were determined as equal to one, i.e., nature conditions. Because the accelerated tests for three types of radiation were chosen at 1.5 and 5 equivalents of complex irradiation (eci), the values of the equivalent fluxes were increased respectively 1.5 and 5 times. For $\chi = 1{,}5$ it is: $\varphi_{equivalent}{}^- = 1.78 \times 10^9$ cm^{-2} s^{-1}, $\varphi_{equivalent}{}^+ = 1.04 \times 10^9$ cm^{-2} s^{-1}; for $\chi = 5$ $\varphi_{equivalent}{}^- = 5.93 \times 10^9$ cm^{-2} s^{-1}, $\varphi_{equivalent}{}^+ = 3.34 \times 10^9$ cm^{-2} s^{-1}. The kinetic dependencies of this coating's Δa_s, in separate and simultaneous irradiation by EMR, protons and electrons are shown in Fig. 1. Also shown are values Δa_s obtained by summing up the changes during separate irradiation.

The additivity coefficients were calculated, using the data from Fig. 1, as the ratio of change in solar absorptance of complex irradiation ($\Delta a_{s\Sigma}$) to the sum of the values obtained by separate irradiation:

$$K_{add} = \Delta a_{s\sum} / \left(\Delta a_{se-} + \Delta a_{sp+} + \Delta a_{sEMI}\right). \quad (4)$$

Table 1 shows the dependence of the additive coefficient on the simultaneous exposure time (ehsci) for two values of acceleration.

TRSO-10 Coating

This coating was irradiated simultaneously by EMR, electrons and protons at two acceleration value ($\chi = 3$ and $\chi = 8$) under conditions of simulated GSO (GEO). Similar to the TRSO-1 coating, we conducted experimental investigations aimed at determining the equivalent proton and electron fluxes providing similar effect on the GSO. For $\chi = 3$ conditions the following parameters were selected: $\varphi_{equivalent}{}^- = 2.1 \times 10^{10}$ cm^{-2} s^{-1}, $\varphi_{equivalent}{}^+ = 4.26 \times 10^{10}$ cm^{-2} s^{-1}; For $\chi = 8$ the following parameters were selected: $\varphi_{equivalent}{}^- = 5.6 \times 10^{10}$ cm^{-2} s^{-1} $\varphi_{equivalent}{}^+ = 1.14 \times 10^{11}$ cm^{-2} s^{-1}. The dose dependencies of Δa_s for separate and simultaneous irradiation of this coating by EMR, protons and electrons are shown in Fig. 2. Also shown are values of Δa_s obtained by summing up the changes for the separate irradiations.

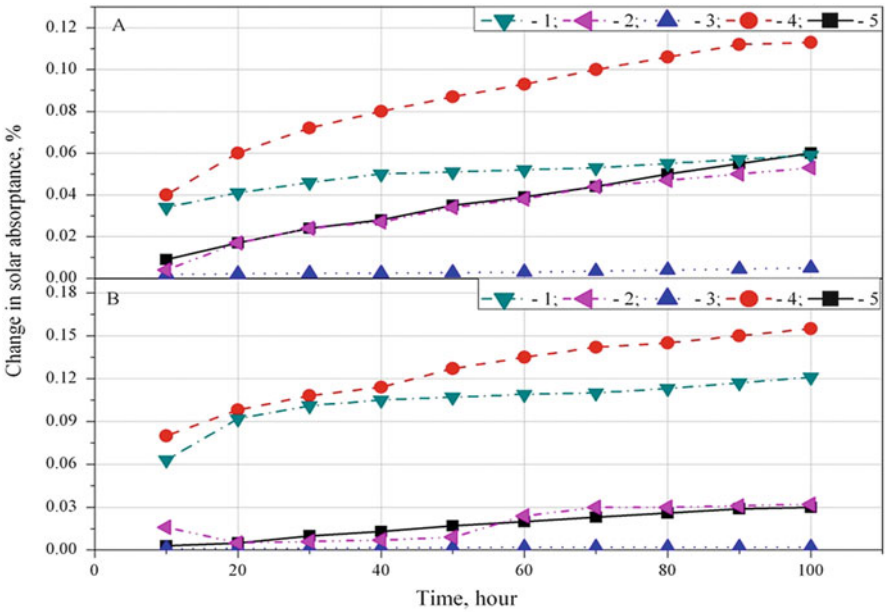

Fig. 1 The kinetic dependence of change in solar absorptance Δa_s of the coating TRSO-1 under electron irradiation (**1**) protons (**2**) EMR (**3**), the sum (**4**), and complex irradiation by electrons, protons and EMR with acceleration $\chi = 1.5$ (**a**) and 5 (**b**) at conditions simulated GSO (**5**)

Table 1 Time dependence (EHSCI—equivalent hours complex irradiation) of the additivity coefficients for simultaneous irradiation by EMR, protons and electrons of the TRSO-1 coating at conditions simulating GSO with acceleration of 1.5 and 5 eci (equivalent complex irradiation)

H, ehsci		10	20	30	40	50	60	70	80	90	100
χ, eci	1.5	0.24	0.28	0.33	0.36	0.38	0.42	0.45	0.49	0.53	0.55
	5	0.04	0.07	0.09	0.11	0.13	0.15	0.17	0.18	0.20	0.21

Table 2 shows the dependence of the additive coefficient on the simultaneous exposure time (ehsci) for two values of acceleration.

Analyzing the data shown in Figs. 1 and 2 and Tables 1 and 2 the following conclusions can be suggested:

- Additivity coefficient in all cases is not equal to one, it is significantly <1;
- Depending on the exposure time additivity coefficient is not constant. Usually the value increases and depends on the type of coatings and acceleration factor of tests.
- Additivity coefficient decreases with increasing acceleration of irradiation.

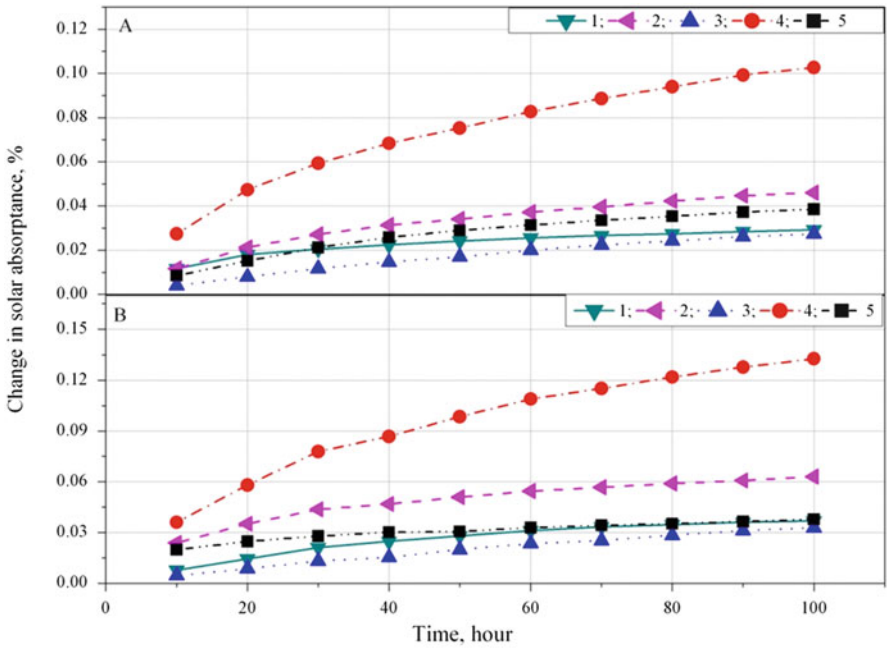

Fig. 2 The kinetic dependence of change in solar absorptance Δa_s of the coating TRSO-10 under electron irradiation (**1**) protons (**2**) EMR (**3**), the sum (**4**), and simultaneous irradiation by electrons, protons and EMR with acceleration $\chi = 3$ (**a**) and 8 (**b**) at conditions simulating the GSO (**5**)

Table 2 Time dependence of the coefficients additivity for complex irradiation by EMI, protons and electrons of the TRSO-10 coating at conditions simulated GSO with acceleration of 3 and 8 eci

H, ehsci		10	20	30	40	50	60	70	80	90	100
χ, eci	3	0.28	0.33	0.36	0.37	0.37	0.37	0.38	0.38	0.38	0.38
	8	0.17	0.23	0.25	0.27	0.28	0.28	0.29	0.29	0.29	0.29

Conclusions

Among factors affecting the additivity rules under simultaneous exposure to different radiation sources the following processes can be distinguished and should be taken into account:

1. Interaction of opposite charged accelerated particles (protons and electrons) in material surface.
2. Interaction of defects resulting in more complicated defects and their annihilation. The increase in the total concentration of defects while under simultaneous exposure, compared to separate exposures, increases the likelihood of their interaction and decreases their total concentration.

3. Charge formation in the free-path depth region after accelerated electrons and protons thermoisolation. Appearance of extra electromagnetic fields, direction and velocity changes of defects during their movements in these fields.
4. Self-organizing systems that lead, under the simultaneous exposure to several environmental factors, to a restructuring that increases their resistance to external influences, disproportional to resistance in an exposure to separate environmental factors.
5. The concentration of defects, generated by simultaneous action of different factors, is close to or higher than the concentration of atoms in the crystal lattice. In that case the interaction of particles from several radiation sources with one atom is possible that explains the smaller number of defects compared to situation with separate exposure conditions.

Given the diversity of defects formed during irradiation and in interactions with each other and a large number of factors that affect their concentration, to assess the contribution of each of these causes is difficult. But we can estimate the concentration of primary defects separately that form by the exposure to various types of radiation.

To estimate, we take zinc oxide pigment as an example. The range for electrons with an energy of 30 keV in zinc oxide is 3.5 μm. Calculations were carried out for GSO with accelerating factor of simultaneous exposure equal to one ($\chi = 1$), i.e., as for natural data. Equivalent electron flux $\varphi_{\text{equivalent}}{}^{-}$ with energy 30 keV for zinc oxide powder, imitating the GSO spectrum, according with the values of TRSO-1 coating based on ZnO can be taken as 1.0×10^9 cm^{-2} s^{-1}. So fluence of electrons during the year $F = 1.0 \times 10^9$ cm^{-2} s^{-1} $\times$ 3.1×10^7 s $= 3.1 \times 10^{16}$ cm^{-2}. In the irradiated layer with thickness of 3.5 μm, the volume density of electrons will be approximately 1×10^{20} cm^{-3} and at 30 keV the volume energy density of electrons is equal to 3×10^{24} eV cm^{-3}. With the band gap of zinc oxide of 3.3 eV, and the probability of electron–hole pairs formation equal to one, we have about 1×10^{24} pairs cm^{-3} of defects. Taking the concentration of atoms in the crystal lattice of zinc oxide as $N_{ZnO} = 4.21 \times 10^{22}$ cm^{-3} [23], shows that the number of defects formed by the primary ionization of electrons is more than 24 times higher than the number of atoms per unit volume of zinc oxide.

The depth of penetration of solar wind protons with 3 keV energy is about 0.5 μm. In this layer, the primary defect density under the complex action of electrons and EMP will be significantly greater than the 1×10^{24} cm^{-3}, and may exceed the concentration of atoms in the lattice a few dozen times. Therefore, the probability of interaction of electrons, protons and photons with atoms of the crystal lattice of zinc oxide can be reduced, resulting in unequal coefficient of additivity to one.

Acknowledgments We acknowledge support by the 15-13-10004 project of Russian science Foundation.

References

1. Brown RR et al (1969) Electron ultraviolet radiation effects in thermal control coating. Prog Astronaut Aeronaut Therm Des Princ Spacecr Entry 21:697–724
2. Gilligan JE (1967) The optical properties inducible in zinc oxide. Prog Astronaut Aeronaut 20:329–347
3. Fogdall LB, Cannaday SS, Brown RR (1970) Proton and electron effects on thermal control coatings. Final report to NASA/GSFC under contract NAS 5-11219
4. Kroes RL (1974) Heat exchange and thermal conditions of space systems. AIAA Paper 1971, № 829, pp 1–19
5. Streed ER (1967) An experimental study of the combined space environmental effects on a zinc-oxide/potassium silicate coatings. Prog Astronaut Aeronaut 20:237–264
6. Arvesen JC (1967) Spectral dependence of ultraviolet-induced degradation of coatings for spacecraft thermal control. Prog Astronaut Aeronaut 20:265–280
7. McCargo M, Greenberg SA, Douglas NJ (1969) A study of environmental effects upon particulate radiation-induced absorption bands in spacecraft thermal control coating pigments. Final report, Nas 2-4353, NASA Ames Research Center
8. Brown RR, Fogdall LB, Cannaday SS (1969) Elektron-ultraviolet radiation effects on thermal control coatings. Prog Astronaut Aeronaut 21:697–724
9. Barbashov EA, Bagatov VA, Kozin VI (1977) Influence of electron-proton irradiation in vacuum on optical properties of thermal control coatings. Space Mater Sci Technol 117–128 (In Russian) (Барбашов ЕА, Багатов ВА, Козин ВИ (1977) Влияние электронно-протонного облучения в вакууме на оптические свойства терморегулирующих покрытий. Космическое материаловедение и технология.// М.: Наука,1977, с. 117–128)
10. Barbashov EA, Bagatov VA, Kozin VI (1975) Changes in optical properties of thermal control coatings under joint and separate irradiation by electrons and protons. Space Mater Sci Technol 94–99 (in Russian) (Барбашов ЕА, Багатов ВА, Козин ВИ (1975) Изменение оптических свойств терморегулирующих покрытий при совместном и раздельном облучении протонами и электронами.// Космическое материаловедение и технология.// М.: Наука, с. 94–99)
11. Dvorecky MI, Mikhailov MM, Kosicin LG, Kuznecov BI (1982) Investigation of the reflectance spectra of white enamels irradiated jointly and separately by electrons, protons and UV. Space Mater Sci Technol Sci 100–106 (in Russian) (Дворецкий МИ, Михайлов ММ, Косицын ЛГ, Кузнецов БИ (1982) Исследование спектров отражения белой эмали, облученной раздельно и совместно электронами, протонами и ультрафиолетом. Космическая технология и материаловедение. М.: Наука, 1982.с. 100–106)
12. Mikhailov MM, Dvorecky MI (1991) Peculiarities in changes in the optical properties of zinc ortotitanate irradiated jointly and separately by electrons, protons and UV. Inorg Mater 27:2365–2369 (In Russian) (Михайлов ММ, Дворецкий МИ (1991) Особенности изменений оптических свойств ортотитаната цинка при раздельном и совместном облучении электронами, протонами и ультрафиолетовым светом. Неорганические материалы 27: 2365–2369)
13. Mikhailov MM, Dvorecky MI (1992) Peculiarities in changes in the optical properties of zinc ortotitanate irradiated separately and paired jointly electrons, protons and electromagnetic radiation. Inorg Mater 28:1431–1436 (In Russian) (Михайлов ММ, Дворецкий МИ (1992) Особенности изменений оптических свойств ортотитаната цинка при раздельном и совместном попарном облучении электронами, протонами и электромагнитным излучением. Неорганические материалы 28: 1431–1436)
14. Mikhailov MM, Dvorecky MI (1993) Nonadditivity in joint action of ultraviolet radiation, protons and electrons in the ZnO+ polymethylsiloxane. Inorg Mater 29:374–378 (In Russian) (Михайлов ММ, Дворецкий МИ (1993), Неаддитивность совместного действия

ультрафиолетового облучения, протонов и электронов на ZnO+ полиметилсилоксан. Неорганические материалы 29: 374–378)
15. Mikhailov MM, Dvorecky MI (1994) The methodology of predicting the performance of thermal control coating on spacecraft based on the results of ground tests. Inorg Mater 30:201–209 (In Russian) (Михайлов ММ, Дворецкий МИ (1994) Методика прогнозирования работоспособности терморегулирующих покрытий космических аппаратов по результатам наземных испытаний. Неорганические материалы 30: 201–209)
16. Mikhailov MM, Ardishev BM (1998) Accumulation of the F- and M-color centers in single crystals of KCl in combined irradiation by electrons and protons. Solid State Phys 40:2015–2018 (in Russian) (Михайлов ММ, Ардышев ВМ (1998) Накопление F- и М-центров окраски в монокристаллах KCl при комбинированном облучении электронами и протонами. Физика твердого тела 40: 2015–2018)
17. Mikhailov MM, Ardishev BM (1999) Synergistic effects in simultaneous irradiation of KCl powders with protons and electrons. Phys Chem Mater Process 3:9–12 (In Russian) (Михайлов ММ, Ардышев ВМ (1999) Синергетические эффекты при одновременном облучении порошков KCl протонами и электронами. Физика и химия обработки материалов 3: 9–12)
18. Kosicin LG, Mikhailov MM, Kuznecov BI, Dvorecky MI (1985) An instrument for studying the diffuse reflectance spectra and luminescence of solids in vacuo. Instrum Exp Tech 4:176–180 (In Russian) (Косицын ЛГ, Михайлов ММ, Кузнецов НЯ, Дворецкий МИ (1985) Установка для исследования спектров диффузного отражения и люминесценции твердых тел в вакууме. Приборы и техника эксперимента 4: 176–180)
19. Solov'yev GG (1979) Propagation of light in paint and varnish materials. NIITEChIM, p 42 (In Russian) (Соловьев ГГ (1979) Распространение света в лакокрасочных материалах. М.: НИИТЭХИМ, 42с.)
20. Vasil'yev VN, Dvorecky MI, Ignat'yev VN, Kosicin LG, Mikhailov MM, Solov'yev GG, Tenditnyi VA (1983) Simulation of complex influence of cosmic radiation on thermal control coatings. Model Space MGU 2(Ch. 13):375–393 (In Russian) (Васильев ВН, Дворецкий МИ, Игнатьев ВН, Косицын ЛГ, Михайлов ММ, Соловьев ГГ, Тендитный ВА (1983), Имитация комплексного воздействия космических излучений на терморегулирующие покрытия. Модель космоса. М.: МГУ. т. 2, гл. 13, с. 375–393)
21. Mikhailov MM (2000) Long-term forecasting of optical degradation of spacecraft thermal control coatings. Adv Mater 2:26–36 (In Russian) (Михайлов ММ (2000) Схема долгосрочного прогнозирования оптической деградации терморегулирующих покрытий космических аппаратов. Перспективные материалы 2:26–36)
22. Mikhailov MM, Dvorecky MI, Kosicin LG, Kuznecov BI (1982) The dependence of the solar radiation absorption coefficient of thermal control coatings on the intensity of UV radiation. Space Technol Mater Sci 100–106. Nauka (In Russian) (Михайлов ММ, Дворецкий МИ, Косицын ЛГ, Кузнецов БИ (1982), Исследование зависимости коэффициента поглощения солнечной радиации терморегулирующих покрытий от интенсивности ультрафиолетового излучения. Космическая технология и материаловедение. М.: Наука, с. 100–106)
23. Hirschwald W, Bonasewicz P, Ernst L, Grade M, Hofmann D, Krebs S, Littbarski R, Neumann G, Grunze M, Kolb D, Schulz HJ (1981) Zinc oxide. Properties and behaviour of the bulk, the solid/vacuum and solid/gas interface. Curr Topics Mater Sci 7:143–409

The REACH Regulation and the Space Activities

Ch. Durin, E. Laurent, and V. Cocheteau

Abstract The REACh regulation sets up, in the European Union, is a unique system of Registration, Evaluation and Authorisation of Chemical substances. The regulation applies not only to chemical substances in the strict sense, but also to any material, preparation (glue, paint), and article (constituent, adhesive tape). Besides the manufacturers and the importers of chemical substances, preparations and articles, all the down-users of these substances are concerned with the determination of the potential risk connected to the use of these products. Chemical substances which enter the composition of products regularly used for space applications may be present in the annexes of the regulation generating a risk of obsolescence in the shorter or longer term. This new risk could be later discovered in the development of a program and generate questioning of the qualifications. It would increase costs of re-qualifications and delays on the schedules. There is no unique solution but answers to be brought to every project according to its state of progress. This risk, in terms of sustainability of supply (stop of manufacturing a product), can also affect the performances planned for the application in case of formulation modification of the material and/or the use of a substitute. This article presents the internal tools developed by the CNES for a proactive approach of risk assessment in short, average and long term and the set-up of external networks (industrials and agencies) allowing the exchange of information and solutions.

Keywords Materials • Regulation • Obsolescence • REACh

C. Durin (✉) • E. Laurent
CNES, 18 avenue Edouard Belin, 31401 Toulouse Cedex 9, France
e-mail: christian.durin@cnes.fr; elisabeth.laurent@cnes.fr

V. Cocheteau
ALTEN, 6 Rue Ampère, 31670 Labège, France
e-mail: vanessa.cocheteau@cnes.fr

J. Kleiman (ed.), *Protection of Materials and Structures from the Space Environment*, Astrophysics and Space Science Proceedings 47,
DOI 10.1007/978-3-319-19309-0_17

Introduction

*R*egistration, *E*valuation, and *A*uthorisation of *Ch*emicals (REACH) applies to all chemicals imported or manufactured in the European Economic Area (EEA). The aim is to strengthen the knowledge on the risk of use of chemicals substances, raw materials or included in a preparation (glue, paint. . .), or an article (mechanical part, tape. . .) and to improve the protection of the human health and of the environment.

The regulation has come into force in Europe since June 1st, 2007. It is based on four procedures:

- *Registration*: Substances shall not be manufactured in the EEA or placed on the market unless they have been registered with the the *E*uropean *Ch*emicals *A*gency (ECHA). The registration of chemical substances is mandatory otherwise no EU market is possible for materials impacted.
- *Evaluation*: REACh shifts the responsibility for the demonstration of a safe use of chemicals from authorities to industries. The evaluation is the control tool of the ECHA. The registration file evaluation includes the examination of the tests proposals from the manufacturers and the importers and the recording conformity control.
- *Authorization*: Substances that are identified as *Su*bstance of *V*ery *H*igh *C*oncern (SVHC) may enter the authorisation procedure.
  The eligible list of substances in the authorization process is called candidate list. The SVHC identification to introduce into the candidate list is made twice a year. The prioritization result will issue partially from the *COm*munity *Ro*lling *Ac*tion *Pl*an (CORAP). Substances of the candidate list will be gradually included, allowing exception, in the annex XIV of the REACh regulation. Once included in that annex, they cannot be placed on the market or used after a date to be set (the so-called 'sunset' date) unless an authorisation is granted. Authorisations are only granted for a limited time and undergo periodic reviews. All not authorised uses have to be phased out.
- *Restriction*: the notion already exists in the past regulations before REACH. Certain uses of a Substance of Very High Concern will be forbidden (described in the Appendix XVII).

The decision to include a substance in one of the annexes of the regulation is taken by ECHA and the European Commission after opinion and consultation of member countries.

Chemical substances which enter the composition of products regularly used for space applications may be present in the annexes of the regulation generating a risk of obsolescence in the shorter, mid or longer term. This new risk could be late discovered in a program development and generate the qualifications questioning. It would increase the costs associated to re-qualifications and delays on the schedules. There is no unique solution but answers to be brought to every project according to its progress. This risk, in term of supply sustainability (stop of manufacturing a product) can also affect the performances aimed for the application in case of the material formulation modification and/or the use of a substitute.

That is why, the CNES set up internal tools for a proactive approach of risk assessment in short, average and long term while setting up external networks (industrials and agencies) allowing the information and solutions exchange. Indeed, this problem concerns all the actors of the space domain and can even find solutions in other technical domains (aeronautics, automobile)

The consequences of the REACh regulation and the small volume of the space market with regard to the chemical industry for example is going to make difficult the preservation of the "space exceptions". There is a rationalization of the number of chemical substances and thus of usable products. The main question is to identify, in our "niche" market, products technically essential and impacted by the REACh regulation.

REACh applies to every materials family in particular organic materials (paints, composite, glues), metallic materials (with chromium compounds for surface treatments for example) and even materials for the electronics.

Launchers, satellites, probes and inhabited structures are users of these risky materials. They have to take into account the regulations and find solutions to these obsolescence problems. Substances used on the CNES sites for ground applications are also concerned as well as that used during the implementation processes.

Risk Assessment

– At the national level.
  The CNES sets up a project group piloted by the Quality directory (IGQ) to answer to this new problem. This group leans on correspondents in every centre who have the responsibility of various activities susceptible to be confronted with the REACh regulation: projects, quality and the functioning of the centres. The various centres are represented with a different approach between launchers orbital systems for which an internal work is carried on to to take care of the REACh constraints directly. This group established contacts with the space and not space industrials.
– At the European level.
  The CNES participates to the working group "MPTB" *M*aterial/*P*rocess *T*echnical *B*oard gathering: ESA, Thales Alenia Space, AIRBUS Defence and space, RUAG, MAP, OHB, DLR and Heraklès. Joint actions on the REACh problem are proposed and piloted by the working group members [1].

The roles of these various groups are:

- To understand the regulation and its application in our activities.
- To inform the actors/users at CNES level.
- To inform the industrial actors in particular SME/SMI, laboratories.
- To measure the impact of the regulation on our products (risk assessment, early evaluation of risky substances for short term, mid-term and long term.
- To propose corrective actions that may include qualification of alternative technologies, development of alternatives, and preparation of relevant dossiers for REACH authorisation or exemption for space-related applications.

- To develop a Road Map.
- To make sure the traceability/archiving of the risks for materials/processes.

The identification of risky materials and processes is based on the following approach:

1. Set up of the materials list used in the satellite projects and launchers. The joint materials database of the MPTB WG contains currently about 1700 records.
2. Set up of the substances list included in these materials. The risk analysis required all materials to be split down into components based on their Materials Safety Data Sheet (MSDS). This list is called the space substances list.
3. Crosscheck the list of space substances with lists of substances identified as critical (from ECHA, national lists, non-governmental lists. . .).
   - Most imminent risks are evident for substances that appear in Annex XIV or are recommended for Annex XIV inclusion.
   - Mid-term risks may be considered for substances that have entered the candidate list or have been proposed as SVHC.
   - A very interesting reference database for establishment of potential long-term risks is the SIN (Substitute it Now) list. It is a Non-Governmental organisation (NGO) list for replacement of toxic substances.
4. Identification of critical materials for space projects: list of High Concern materials.
5. Risks prioritization using entries from other partners, other technical fields.
6. Action plan: roadmap, R&T studies for substitution, crossed tests campaign for delta qualification, discussion on plan test.

2014 Reach Status

– Short term impact:

Since 2012, Substances included in Annex XIV has increased: from 14 substances in 2012, 27 in 2013, it reaches 37 substances in 2014. Thanks to our crosscheck we have identified:

→ 11 space substances and 36 impacted space materials

The main impacted technological domain is:

– Surface treatments: anti-corrosion protections, adhesion primer, solvents, surfaces activation processes, cleaning agent.

Some examples are given:

Chromic acid (CAS number: 1333-82-0), sunset date in September 2017.

13 space materials are impacted in the field of surface treatment, for example Alodine ®1200 widely used for the aluminium alloys protection.

Strontium chromate (CAS number: 7789-06-2),

9 space materials are impacted in the field of surface preparation, for example, BR®127 used also for its activation properties.

→ **This inventory allowed us to confirm that the space domain is concerned with the REACh regulation in short term** [2]

– Mid-term impact.

The crosscheck is done with the Candidate List: (List of substances liable to be introduced in Annex XIV). 138 substances are identified by the process of authorization. ECHA aims at reaching 1000 substances before 2020. The result is:

→ **21 space substances and 58 space materials impacted**

Technological domains impacted in the mid-term are the following:

– Surface treatments,
– Lubricants (solvent),
– Inks,
– Polymers for PCB (solvents, resins) and adhesive systems (solvents, constituent of glues),
– Propulsion of satellites and launchers.

Some examples are given below:

Hydrazine (CAS number: 302-01-2) is a mono-ergol for the launchers and the satellites attitude control.

Diboron trioxide (CAS number 1303-86-2) used in Cho-term®1671, very used as thermal conductive elastomer for space application.

– M&P impacted in the long term.

The SIN list (NGO list) is used to anticipate substances susceptible to appear in the candidate list and finally in the Annex XIV.

→ **50 space substances and 180 space materials impacted**

The effects on the European space programs can be significant in terms of costly new products, process developments and space validation of alternative solutions. With the long life-cycle of space programs, there is a need to actively manage this risk taking into consideration the associated costs.

Risks Associated

Penal and Financial Risks

CNES as importer of certain raw materials and specific scientific equipments (from outside EU) has obligation of knowledge and communication (through the supply chain) of Candidate List substances present in more than 0.1 % in imported articles. Some penalties are statutory inside REACh regulation.

For every material and material involved in processes, we need to have:

- Technical data sheet and MSDS up to date, or
- Compliance letter from suppliers updated at each update of the Candidate List.

Obsolescence Risks of Qualified Materials, Processes and Technologies

This is the main risk concerning our products induced by the substances/materials disappearance of the European market.

The chosen proactive approach allows to anticipate at best the regulation evolutions and to try to give a more time to the projects to modify a design and/or validate/re-qualify materials and/or processes impacted.

Quality Risk: Decrease in Performances

This risk is difficult to deal with because we can find substitute but the properties could be lower than nominal materials. Another option is to face materials composition evolution without any change in the material name or in the MSDS file.

In our specific environment, lessons learned show that many anomalies or early ageing are due to materials/processes changes even in very small quantities.

Another risk is the non-space grade substitute. “Commercial” products are not specifically designed for our applications. Thus, we will need an effort (time and budget) to adapt them to our constraints.

Possible Actions

It is necessary to have a multi-approach strategy including compromise. Some general guidelines are given in the following paragraph.

- For new projects, we must take into account REACh Regulation from the project early development phases for example as early as conception (design) in order to save time and cost. It would be feasible if new approaches are considered for examples in manufacturing.
- Several solutions could be necessary to assure one function. Currently, for surface treatment, we are used to work with one product for all aluminum alloys. Tomorrow we could have to use two different substitutes for the same function on different types of aluminum alloys.
- We must support new processes without chemicals. Example: laser surface preparation in order to avoid chemical product for surface treatment.
- New manufacturing processes are stand up and must be an alternative way. For examples: additive layers manufacturing could reduce chemical in processes.
- We can change processes with the target to maintain performances but to reduce chemicals. One example is to replace solvents in paints by water.
- Some substitutions will have to be done but it will be a long process and it will demand budget and anticipation.
- The use of Authorization/exemption REACh procedure is not space dedicated. It is reserved to strategic Defense materials. For addressing such an issue, this needs budget, anticipation and common approach from users and suppliers.

Conclusions

REACH addresses the negative effects of chemicals to human health and environment. Through this innovative regulation, a progressive reduction of available materials and processes is expected. Impairment of quality and reliability or even loss of critical technologies through obsolescence of qualified materials and processes must be avoided. CNES and its European partners (MPTB WG) set up tools and methods to try to make a status of space activities situation and to answer the first requirements of the regulation. The results of the first activities show:

We are facing an evolution of the landscape of chemical substances. There is an important work to make on materials, on processes and technologies.

The effort to comply with REACh regulation is consequent now and at middle term. We must establish a long-term view, develop a risk matrix, and place appropriate actions for risk mitigation.

REACh is a new constraint in the current and future space developments. For the space actors, it implies anticipation and follow-up of the evolutions.

Communication/information and sharing results are essential to optimize and limit the costs relative to the studies of substitution/re-qualification of the M&P.

References

1. Rohr T, Bourrouilh C, Meurice D, McNair I, Tonon C, Cocheteau V, Combes H, Durin C, Laurent E, Burkhardt H, Cirone R, Contino MC, Ghidini T, Williamson J, Besson JM, Guillaumon O, Nowak M, Richter F, Becker T, Coello-Vera A, Allard P, Merillat S, Andre S, Lambert M, Triaud P, Moess E (2012) Impact of REACh legislation on European space programs. In: Proceedings of the12th international symposium on materials in the space environment
2. Laurent E, Durin Ch (2012) The consideration of the regulation REACh in the space activities. Actu Composant CNES N°38

Chinese Standard GJB 2502 for Test Methods of Spacecraft Thermal Control Coatings

Feng Weiquan

Abstract Spacecraft Thermal control materials such as various paints, OSR, Al-Kapton etc. need to be tested before they are used in spacecraft. Space environment such as electron, proton and UV factors etc. in Geosynchronous Orbit (GEO) or Low Earth Orbit (LEO) have severe degradation effects of solar absorptance, etc. The Chinese standard GJB2502 includes test methods of spacecraft thermal control coatings and covers the measurement of solar absorptance and emissivity, atomic oxygen test, ultraviolet test, electron and proton test, thermal cycle test, combined irradiation test, aero-dynamical environment test, etc. This paper introduces the process and main features of the standard such as test condition, test sample and test facility, etc..

Keywords Spacecraft • Thermal control coatings • Environment • Degradation • Simulation test • In-situ measurement • Space materials' test standard

Introduction

Spacecraft thermal control coatings are the most commonly used means of passive control of spacecraft temperature. Spacecraft temperature is an important factor for the satellite reliability and long-life performance. Space environments for thermal control coating application involve mainly vacuum, high and low temperature, electron irradiation, proton radiation, ultraviolet radiation, atomic oxygen, plasma, space debris and cosmic dust, and the harmful pollution induced by spacecraft. Under interaction with these environmental factors, thermal control coatings may develop a variety of degradation paths in thermal properties, optical properties, electrical properties, mechanical properties and vacuum characteristics etc., reduce the performance and service life, and even affect the operation of spacecraft.

F. Weiquan (✉)
Beijing Institute of Spacecraft Environment Engineering, P.O. Box 9832, Beijing 100029, China
e-mail: fengweiquan@aliyun.com

J. Kleiman (ed.), *Protection of Materials and Structures from the Space Environment*, Astrophysics and Space Science Proceedings 47,
DOI 10.1007/978-3-319-19309-0_18

Because thermal control coatings are exposed to the environment directly and the environmental conditions during life of spacecraft are very harsh, the thermal radiation performance degradation of thermal control coatings occurs generally on orbit. Various environmental tests and measurement for selection and quality control are very necessary. Standard test methods for thermal control coatings are important for the quality assurance of test. This paper introduces the forming process and the main contents of Chinese spacecraft thermal control coating test standard GJB2502-2006.

General Description

Chinese standards are divided into four levels: the national standard (GB, GJB), industry level standards, local standards and enterprise standards. GB is first letter for Chinese Pinyin of national standard. GJB is first letter for Chinese Pinyin of national military standard.

GJB is the requirements for Chinese military products in technology and management process, concept, procedure and method. Civilian products can use GJB standard if there are no similar GB standards. At present, GJB2502-2006 is the highest standard in China for test method of spacecraft thermal control coatings.

GJB 2502-2006 is a series of standards, which is divided into ten parts as follows: general [1], measurement of solar absorptance [2], measurement of emissivity [3], aerodynamic environment test [4], ultraviolet irradiation test in vacuum [5], proton irradiation test in vacuum [6], electron irradiation test in vacuum [7], thermal cycling test [8], atomic oxygen test [9], combined irradiation test [10]. There are two versions for GJB2502. The first version GJB 2502-1999 was released in 1999. The second version GJB2502-2006 was released in 2006.

The revision of GJB 2502-1999 was started in 2003. Compared with GJB2502-1999, the contents in GJB2502-2006 were significantly changed. Since it was ten years of using GJB2502-1999, Chinese space technologies had experienced much progress in application, materials, testing. Revision included adding atomic oxygen test, combined irradiation test, requiring in situ measurement for solar absorptance measurement during environment test, requiring testing in vacuum for electron and proton irradiation, increasing requirement for the dose-profile analysis for space and ground charged particles, paying much more attention to low-energy charged particle irradiation since it is more important for surface property degradation. During that time, application was expanded from satellite to manned spacecraft, space station, lunar probe, etc. GJB2502-2006 use new name with spacecraft instead of satellite. The life of satellites was extended for GEO communication satellites from the 8 to 15 years.

Table 1 GJB2502-2006 series standards list

No.	Standard name	Standard number
1	Test method for thermal control coatings of spacecraft part 1: general	GJB2502.1-2006
2	Test method for thermal control coatings of spacecraft part 2: measurement of solar absorptance	GJB2502.2-2006
3	Test method for thermal control coatings of spacecraft part 3: measurement of emissivity	GJB2502.3-2006
4	Test method for thermal control coatings of spacecraft part 4: aerodynamic environment test	GJB2502.4-2006
5	Test method for thermal control coatings of spacecraft part 5: ultraviolet irradiation test in vacuum	GJB2502.5-2006
6	Test method for thermal control coatings of spacecraft art 6: proton irradiation test in vacuum	GJB2502.6-2006
7	Test method for thermal control coatings of spacecraft part 7: electron irradiation test in vacuum	GJB2502.7 -2006
8	Test method for thermal control coatings of spacecraft part 8: thermal cycling test	GJB2502.8 -2006
9	Test method for thermal control coatings of spacecraft part 9: atomic oxygen test	GJB2502.9 -2006
10	Test method for thermal control coatings of spacecraft part 10: combined irradiation test	GJB2502.10 -2006

Main Features

General (GJB 2502.1-2206)

This part provides the spacecraft thermal control coating terminology, general requirements and test methods list. The terms include thermal control coatings, solar absorptance, reflectance, solar reflectance, emissivity, hemispherical emissivity, normal emissivity etc. General requirements to the laboratory environment, calibration for measurement instruments, general requirements for test records and reports. The environmental test rooms should be clean, with temperature between 15 and 35 °C, with relative humidity between 20 and 60 %, with room pressure of one atmosphere. Table 1 presents the list of standard tests outlined in GJB2502.

Measurement of Solar Absorptance (GJB 2502.2-2006)

This part specifies method requirements to solar absorptance measurements such as measurement instrument, specimens, procedures and data processing requirements. The main method is spectral reflectance measurement, in which a sample is placed on window of an integrating sphere of a spectral reflectance instrument. The wavelength is from 200 to 2600 nm covering most solar energy. After spectrum reflectance measurement, solar reflectance of samples is calculated by the following formula.

$$\rho_s = \frac{\sum_{i=1}^{n} \rho_{\lambda_i} ES(\lambda i) \Delta \lambda i}{\sum_{i=1}^{n} ES(\lambda i) \Delta \lambda_i} \tag{1}$$

where
ρ_s: solar reflectance of sample;
$\rho_{\lambda i}$: reflectance of samples at wavelength λ_i;
$E_S(\lambda_i)$: solar radiation intensity at wavelength λ_i (W/m^2—nm);
$\Delta\lambda_i$: wavelength interval (nm);
n: wavelength interval number, over 60.
Then solar absorptance of sample is calculated by:

$$\alpha_s = 1 - \rho_s. \tag{2}$$

where α_s: solar absorptance of sample.
There are other methods such as total radiation method which use solar simulator as a light source to measure solar reflectance of sample. Then solar absorptance is calculated by formula (2).

Measurement of Emissivity (GJB 2502.3-2006)
This part specifies method requirements to emissivity measurement such as measurement instrument, specimens, procedures and data processing requirements. Emissivity is defined as the ratio of sample thermal radiation emission and black body radiation with same temperature. There are two kinds of emissivity which are hemispherical emissivity and normal emissivity.
There are several emissivity measurement methods, such as calorimetry, reflection method, energy method and so on. The convenient method for hemispherical emissivity measurement is to use hemispherical reflectance method with radiation wavelength of 3–30 μm by a emission meter, which is also based on integrated sphere principle. Hemispherical reflectance is measured according to following formula:

$$\rho = \frac{I_D}{\sigma T_{IR}^4} \tag{3}$$

where
ρ: sample hemispherical reflectance;
T_{IR}: infrared radiation temperature (K);
I_D: energy density detected (W/m^2);
σ: Stefan Boltzmann constant, 5.67×10^{-8} [W/(m^{2}K^4)]

Hemispherical emissivity is

$$\varepsilon_h = 1 - \rho \tag{4}$$

where: ε_h—sample emissivity.

Aerodynamic Environment Test (GJB 2502.4-2006)

This part specifies requirements to aerodynamic environment testing such as test purpose, range and accuracy, principle, test equipment, test conditions, test specimens, test procedures and data processing requirements. There are two kinds of this test. One is the erosion test and another is the aerodynamic heating test for external thermal control coating when spacecraft returns to Earth.

In the erosion test method the wind tunnel test equipment for thermal control coatings is used to see if there are dynamic erosion effects. Evaluation of the damage to thermal control coating under wind is conducted by using Mach numbers from 2 to 7, and by adjusting the blow, air pressure and time.

Aerodynamic heating test method is using iodine tungsten lamp and other test equipment for gas aerodynamic heating environment simulation test, to check the damage to the thermal control coatings by temperature. The temperature is kept at <500 °C.

UV Irradiation Test in Vacuum (GJB 2502.5-2006)

This part specifies the requirements to UV irradiation testing in vacuum including the test purpose, principle, test equipment, test conditions, test specimens, test procedures and data processing requirements. Vacuum pressure background is not more than 1×10^{-3} Pa.

Near ultraviolet wavelength range is from 200 to 400 nm with form as close to solar near-UV as possible. The acceleration factor for Near-UV is less than 5. Irradiation flux is from 118 to 590 W/m^2. The irradiation uniformity is better than 85 %.

The far ultraviolet wavelength range is from 10 to 200 nm with form as close to solar Far-UV as possible. The acceleration factor for Far UV is <100. Irradiation flux for Far UV is from 0.1 to 10 W/m^2. The irradiance uniformity is better than 80 %.

Solar absorptance during test for all samples must be measured in situ. The sample temperature is controlled during irradiation in the range of -30 to +50 °C.

Proton Irradiation Test in Vacuum (GJB 2502.6-2006)

This part specifies the requirements tor proton irradiation testing of spacecraft thermal control coating in vacuum, including test purpose, principle, test equipment, test conditions, test specimens, test procedures and data processing requirements.

Vacuum chamber backgraound pressure is $<1 \times 10^{-3}$ Pa. Vacuum chamber has a cryogenic temperature shroud for contamination control. Vacuum system is based on low or no oil system, continuous no-load running 24 h before irradiation. Organic pollutants in the vacuum chamber is $<1 \times 10^{-7}$ g/cm^2.

Proton irradiation source is proton source or proton accelerator. The range of energy for proton source in general is from 10 to 60 keV. For proton accelerators, the energy is generally in the range 180 keV–6.8 MeV. The proton energy and current should be continuously adjustable. To ensure the purity of the beam with proton concetration of more than 95 %, a proton analyzer is used for proton accelerator. The irradiated area must be larger than the sample area. Proton beam uniformity on target is generally better than 30 %. Beam stability per hour on average is better than 5 %. Energy stability per hour is better than 0.1 %.

Solar absorptiance must be measured in situ. The sample temperature should be controlled. The sample number for each kind of thermal control coating is not less than 3. The sample temperature is generally in the range of −30 to +50 °C.

Electron Irradiation Test in Vacuum (GJB 2502.7)

This part specifies the requirements to electron irradiation testing of spacecraft thermal control coating in vacuum, including test purpose, principle, test equipment, test conditions, test specimens, test procedures and data processing requirements.

Vacuum chamber background pressure is $<1 \times 10^{-3}$ Pa. Vacuum chamber has a cryogenic temperature shroud for contamination control. Vacuum system belongs to low or oil-free system, continuous no-load running 24 h before irradiation. Organic pollutants in the vacuum chamber should be $<1 \times 10^{-7}$ g/cm^2.

Electron gun or electron accelerator is selected as irradiation source. The range of energy for electron gun in general is from 10 to 60 keV. For electron accelerator, the energy is generally in the range 180 keV–1 MeV. The electron energy and current are continuously adjustable. The irradiated area must be larger than the sample area. Electron beam uniformity on target is generally better than 20 %. Beam stability per hour on average is better than 5 %. Energy stability per hour is better than 0.1 %.

Solar absorptiance must be measured in situ. The sample temperature should be controlled in the range of −30 to +50 °C. The sample number for each kind of thermal control coating is not <3.

Thermal Cycling Test (GJB 2502.8-2006)

This part spesifies the requirements to thermal cycling testing such as test purpose, principle, test equipment, test conditions, test specimens, test procedures and data processe.

Thermal cycle facility consists of two temperature chambers, and can make the transfer of the specimen rapidly (within 10 s) from one chamber to another chamber. Sample transferring can be automatically or by hand.

For low temperature chamber, the humidity must be contoled to avoid a frosting on specimen. The temperature for high temperature chamber can be able to reach 200 °C. The temperaturefor high temperature chamber is able to reach the temperature of −160 °C. If methods is to immerse samples in liquid nitrogen, the temperature can reach −196 °C. The precision of temperature control is 2 °C. In general, high temperature is about 100 °C, low temperature is about −100 or −196 °C if using liquid nitrogen. Number of cycle is generally 100–300. Each kind of thermal control coating, the specimen number must be more than 3. Test atmosphere is nitrogen for low temperature chamber. Duration of one cycle is about 90 min. Duration for cold and hot stages are is about 15 min. The slope is larger than 10 °C/mn.

Atomic Oxygen Test (GJB 2502.9-2006)

This part specifies the requirements to atomic oxygen testing including the purpose, principle, equipment, conditions, procedures, sample, data processing and report.

Atomic oxygen kinetic energy is about 5 eV. The atomic oxygen flux density is from 1×10^{14}/(cm^2 s) to 1×10^{16}/(cm^2 s). Vacuum chamber should be oil-free. The uniformity of atomic oxygen flux density on sample target is better than 90 %. The angle between the atomic oxygen beam and the normal of sample surface is $<10°$. Oxygen ion flux density should be three orders less than the atomic oxygen flux density. The sample temperature is <80 °C. For each material, specimen number must be more than three. Sample mass loss and solar absorptance degradation, emissivity are measured after this environmental testing.

Combined Irradiation Test (GJB 2502.10-2006)

This standard part specifies the requirements to combined irradiation environment testing inlcuding the purpose, principle, test equipment, test conditions, test specimens, test procedures and data treatment. There are three irradiation factors, i.e., UV, proton and electron.

The requirements for vacuum, temperature, electron, proton and UV are same with requirements of single ultraviolet, electron and proton irradiation test. The angle between the electron, proton and UV irradiation and the normal direction of samples is $<30°$.

The electron, proton and UV are irradiated on samples together at the same time as possible. At least, the electron or proton are irradiated with UV together on samples at the same time. Electrons and protons can alternate their irradiation during that time. Their irradiation sequence is not required. Each material specimen number must be more than three. Solar absorptance degradation must be measured in situ.

Revision Suggestion

GJB2502-2006 standard has been used for 10 years. It plays an important role in quality control of spacecraft thermal control coatings in our country. However, some problems were found during applications. New applications and advanced technologies are developing rapidly during these years. The main revision contents of GJB2502-2006 are suggested as follows:

1. Test condition determination.
   Laboratory simulation experiment is the main means of environmental evaluation of thermal control coatings. Due to complicated space environments to be simulated, it is not possible to create in the laboratory the same environmental conditions as in orbit. Thus the conditions in the standard test method are very crucial. Real environment conditions determination, environmental effects determination and determination of the simulated environmental conditions based on equivalent condition effects are important to ensure that the ground tests, within a reasonable margin, are not seriously overdesigned or underdesigned.
2. Degradation prediction methods.
   The life of spacecraft is quite long and can easily reach 15 years. Degradation of properties of thermal control coating under the influence of space environment follows some routs in which, generally, it proceeds quickly at first, then slows down at later stages. Degradation models need to be established with test data and to be used to predict the degradation in time, which can greatly shorten the test time.
3. Surface electrical resistivity measurement.
   The surface electrical resistance of thermal control coating is more and more important for control of space surface charging of spacecraft. Surface charging of spacecraft especially in GEO results in ESD effects that can affect operation of spacecraft electronics. For that reason, the degradation of surface electrical resistivity need to be measured during tests.
4. Micro-debris impacting test method.
   Thermal control coatings suffer from a large number of impacts by micro debris and micrometeoroids that produce so called sand erosion effects on surface, and make the reduce the functional properties of affected materials. The resistance to micrometeoroid impact is an important problem in the design of spacecraft. While the micrometeoroids are very small, the number of impacts over for a long time can be substantial, cause surface damage. Hypervelocity impact testing should be conducted using simulated micro-debris on the thermal control coating used on the outer surfaces of the spacecraft.

Conclusions

The space environment factors and their effects like vacuum outgassing, particles and solar electromagnetic radiation, thermal cycling and atomic oxygen environment are affecting strongly the properties of spacecraft thermal control coatings. The development of GJB2502 standard has played an important role in ensuring the quality of thermal control coatings on spacecraft, strengthening the control process of spacecraft thermal control system and improving the quality and reliability of spacecraft. The ground simulation tests have been successfully applied to various types of spacecraft thermal control coatings. A number of recent new developments and advancements in test technology and testing methods require revision of GJB2052. The tight monitoring and control of anti-static requirements of spacecraft surfaces is necessary for thermal control coatings in GEO. The toxicity effects should be of much concern for coatings used in space station. Micro-debris effects have been considered for LEO spacecraft. Materials' outgassing has been a threat to the optical components of spacecraft and should be addressed.

References

1. GJB 2502.1-2006 (2007) Test method for thermal control coatings of spacecraft, part 1: general [S]
2. GJB 2502.2-2006 (2007) Test method for thermal control coatings of spacecraft, part 2: measurement of solar absorptance [S]
3. GJB 2502.3-2006 (2007) Test method for thermal control coatings of spacecraft, part 3: measurement of emissivity [S]
4. GJB 2502.3-2006 (2007) Test method for thermal control coatings of spacecraft, part 4: aerodynamic environment test [S]
5. GJB 2502.5-2006 (2007) Test method for thermal control coatings of spacecraft, part 5: ultraviolet irradiation test invacuum [S]
6. GJB 2502.6-2006 (2007) Test method for thermal control coatings of spacecraft, part 6: proton irradiation test in vacuum [S]
7. GJB 2502.7-2006 (2007) Test method for thermal control coatings of spacecraft, part 7: electron irradiation test in vacuum [S]
8. GJB 2502.8-2006 (2007) Test method for thermal control coatings of spacecraft, part 8: thermal cycling test [S]
9. GJB 2502.9-2006 (2007) Test method for thermal control coatings of spacecraft, part 9: atomic oxygen test [S]
10. GJB 2502.10-2006 (2007) Test method for thermal control coatings of spacecraft, part 10: combined irradiation test [S]

Biomimetic Gecko Micro/ Nano-Structures Adhesive Array for Space Application

Luojing Chen, Shanshan Du, Qiujie Lv, Mo Wang, and Danying Fu

Abstract The toe surface of the gecko has two elaborate hierarchica1 structures, micro-scale seta array and nano-scale spatula array, which result in the van der Waals force because of the realization of molecu1ar contact between the spatulas and contact surfaces. Because gecko adhesives rely on van der Waals force to create adhesion, they are fundamentally insensitive to temperature, pressure, and radiation. This makes them ideally suited for space applications. Key to this new capability, targets will not need special preparation; gecko adhesives can be used for capturing space objects like space debris. A tool with fixed gecko adhesives that can grip a variety of surfaces, both rigid and soft, without the need for careful planning, is needed to assure success. Gecko adhesive technology that mimics the ability of gecko to adhere to a target, will be a new way of on-orbit docking.

Firstly, the development of on-orbit docking technologies is discussed. The progress of domestic (Chinese) and foreign efforts made in this domain was summarized, including the attachment and detachment mechanisms of biomimetic gecko micro/nano-structures adhesive array and the fabrication methods. Then, various possible applications of the adhesive array in space are analyzed. Finally, the key technologies are proposed that aim at researching the adhesion and contact mechanism and design the parameters suitable for fabricating good capability biomimetic gecko micro-arrays.

Keywords Gecko adhesive • Van der Waals force • Micro/nano-array • Space application • Key technologies

Introduction

With the development of docking technologies, On-Orbit Servicing (OOS) is expected to play an increasingly important role in future space activities. Almost all OOS need to capture the object first, that is on-orbit docking. Usually, current

L. Chen (✉) • S. Du • Q. Lv • M. Wang • D. Fu
DFH Satellite Co. Ltd, Beijing, China
e-mail: lj.chen_5274@163.com

J. Kleiman (ed.), *Protection of Materials and Structures from the Space Environment*, Astrophysics and Space Science Proceedings 47,
DOI 10.1007/978-3-319-19309-0_19

on-orbit docking technology utilized robotic arms, which capture heads incorporating mechanical grippers, to grapple targets. These targets could provide reflectors/visual aids, a standard interface for capture, and a load path for joint vehicle control during mated operations. Moreover, they could ensure no velocity or impact to target during mating or separation. However, the damaged, malfunctioned satellites or space debris are already existing in orbit, as well as the satellites scheduled to be launched recently, are generally non-cooperative, such as neither any artificial patterns used for measurement, grappling fixtures for capturing, nor specially designed mechanisms for docking, are mounted on them. They have unknown tumble rates, unknown dynamics for extended structures, unknown condition of metal or structures to be used for grappling, Unknown propellant load and associated dynamics. The technology of gripping these targets is now a technical bottleneck hard to break. This paper intends to adopt the biomimetic gecko micro/nano-structures adhesive array as a new kind of capture load for on-orbit service, and explore the application of bionic adhesion materials in space.

Background

Geckos have an extraordinary ability which allow them to defy gravity by climbing vertical surfaces, for the adhesion is robust enough to function on unknown rough surfaces and also easily releasable on animal movement. It's demonstrated in 2000 by Autumn that gecko's special adhesion ability arises from the van der Walls interaction between the "hairy" system on the gecko foot and the contacted surface [1–5]. The toe surface of the gecko has two elaborate hierarchica1 structures, micro-scale seta array and nano-scale spatula array, which result in the van der Waals force because of the realization of molecu1ar contact between the spatulas and contacted surfaces (Fig. 1).

Since Autumn's paper published in Nature, gecko setae design and production is rapidly becoming a hot topic in the international arena. Inspired by the merits of the fine adhesive structure, gecko adhesives were first fabricated in 2003. In recent years, the development of physics, chemistry, MEMS processing technology

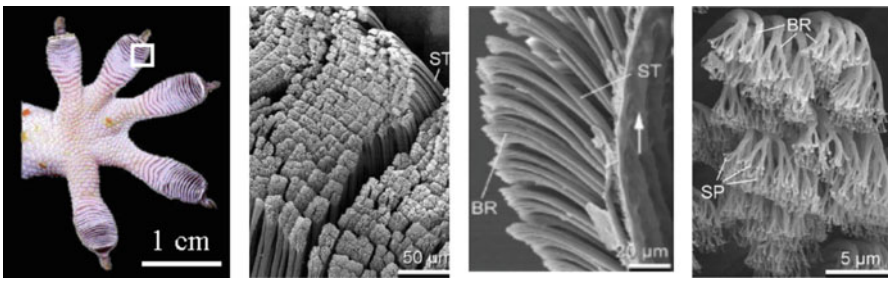

Fig. 1 The hierarchical structure of Tokay Gecko foot

promotes research of micro/nano polymer gecko adhesion array [6–16]. The research of biomimetic gecko adhesion array has culminated in preliminary results on the mechanism and in fabrication and testing [17–23].

Space Applications

Biomimetic gecko micro/nano-structures adhesive array has many capabilities, such as a large adhesion force, a good adaptive ability to rough surfaces, harmless to the contact surfaces, self-cleaning property, durability and reusability [24–26]. Because fibrillar adhesives rely on van der Waals forces to create adhesion, they are fundamentally insensitive to pressure, temperature and radiation. In comparison to approaches of magnets (which need ferrous surfaces) and suction cups (which requires a smooth surface and does not work in vacuum) for adhesion, biomimetic gecko adhesion is passive and has a compelling advantage to stick to nearly any surface in low pressure environments. Potentially, this type of adhesion would therefore be suitable for use in extraterrestrial environments as well as microgravity and vacuum environments, thus making them ideally suited for space applications where conventional pressure sensitive adhesives often fail due to evaporation, embrittlement, and other forms of material degradation common to natively tacky materials. Several emerging needs in Earth orbit require the adhesive ability to controllably stick and detach from the objects. Another advantage of the adhesive array is that it provides a method for capturing and controlling an unpredictably sized and shaped object. The object is not required to have any standard attachment points. This allows the present method to be used for recovering objects smaller than or larger than the adhesive capture head size. Also, objects having rough, smooth, or complex shapes may be recovered, including non man-made objects including space debris or asteroids. Various possible target applications, such as orbital debris clearance, rendezvous and docking, robotic inspection of reentry tiles, astronaut EVA, satellite servicing, and in space assembly, could all benefit from this type of adhesive [27]. These space applications are discussed below:

1. **Orbital Servicing** Biomimetic gecko micro/nano-structures adhesive array used for adhesive capture head could have capability of servicing multiple customers.
   - **Servicing/Repair** The adhesive capture head could allow grappling and gripping of satellites, cubesats, and react the forces of repair and retrieval, such as repositioning, life extension services, component swap-out and on-orbit assembly retrieval.
   - **Asset Inspection** The adhesive capture head could adhere to the exterior of an orbiting spacecraft to detect leaks and micrometeorite damage.
2. **Debris mitigation** The adhesive capture head could attach to, de-spin and de-orbit massive, tumbling, uncontrolled targets, such as retired satellites, NEOs and space rocks and tools lost during EVAs.

3. **Asteroids Sample Return** The adhesive capture head could controllably attach and detach from asteroids.

Traditional docking methods require the capturing mechanisms to accurately aim at the capturing position on the targets that brings rigorous demand of relative precision relative navigation and control for on-orbit servicer. Compared with the traditional methods (using multi-fingers, docking mechanism with apofogee kick motor, parallel jaw gripper, bolt hole gripper [28–34]), the method where biomimetic gecko micro/nano-structures adhesive array are used, would therefore be suitable for use in extraterrestrial environments as well as microgravity and vacuum environments. Such technology has many capabilities, such as providing the ability to recover objects faster than with mechanical grippers. The present method does not depend on the same degree of fine control as many types of mechanical grippers. By enlarging the area of adhesive array, it would reduce the high demands of stabilization and precision for attitude control of servicer. Yet another advantage of the present method is that it provides a method for capturing and controlling an object with unpredictable material, size and shape properties. The adhesive array can conform to the shape, topography, and/or texture of the object prior to the adhesive capture device making initial contact with the object. This method can tolerate much wider ranges of relative velocity and relative rates and may enable simpler rendezvous sensors. The adhesive array can be switched on or off quickly ($<$50 ms). The object is not required to have any standard attachment points. This allows the present technology to be used for recovering objects smaller than or larger than the capture head size. Also, objects having rough, smooth, or complex shapes may be recovered, including non man-made objects including space debris or asteroids.

Key Technologies

The Performance of the Adhesive Array in Space Environment

The space environment and the effects of its interaction with materials, i.e., thermal vacuum, thermal cycling, atomic oxygen erosion, ultraviolet radiation, charged particles irradiation, micrometeoroid and debris impacts, presents a substantial risk to space systems. The atomic oxygen erosion, ultraviolet radiation and charged particles irradiation in space have significant effects on the LEO space systems. They would severely erode many materials of the spacecraft surface, especially the serious damage effects of polymer materials, would affect the dimensional stability, physical properties and mechanical properties of these materials. For example, atomic oxygen reacts with many commonly used spacecraft materials resulting in degradation and mass erosion of exposed spacecraft surfaces. The ability of nanoscale materials that have high specific surface area and high reactivity to maintain stability in the harsh space environment is yet to be determined. As the biomimetic

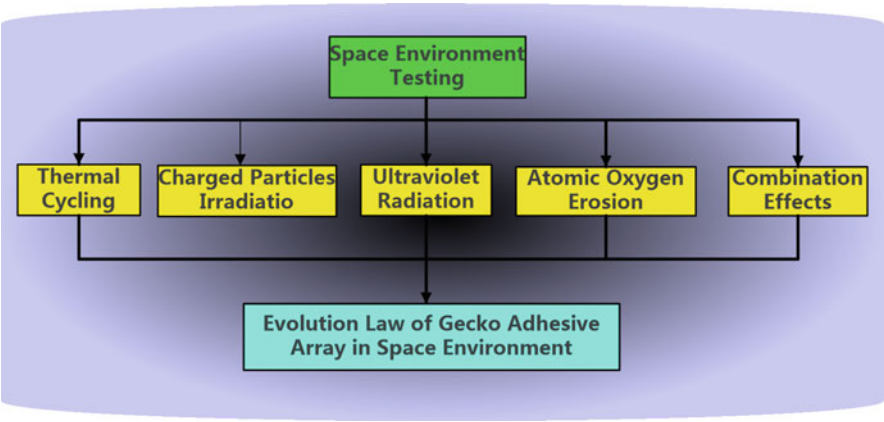

Fig. 2 Research on performance of the adhesive array in space environment

gecko micro/nano-structures adhesive array is directly exposed to the space environment, it is particularly vulnerable to damage. Currently, very little attention has been paid to the performance of the adhesive array in space environment, there are few results for the adhesion mechanism. The project aims to study how the performance of the adhesive array changes in the space environment, as well as the evolution mechanism and enlistment life (research roadmap is shown in Fig. 2).

Choice of Adhesion Position on Spacecraft or Satellite

Based on the non-specific adhesion characteristics and flexibility of the biomimetic materials, the capture tool with the installed biomimetic gecko micro/nano-structured adhesive arrays could attach to the space object surface with a small preload. Instead of targeting a specific hard point on an object for grappling, adhesive array enables the grappling at almost any surfaces on the space objects, including flat plates like solar panels, radiators, and other structures, curved surfaces like fuel tanks and tubing, and even flexible surfaces like Multi-Layer Insulation blankets (MLI).

Considering the factors affecting reliable adhesion, such as shape features, movement characteristics, surface materials, structural strength and mass of space target, as well as impact velocity when adhering, the best adhesion position on the target would be obtained. These factors need to be considered and are discussed below.

Shape Characteristics of Adhesion Target The first factor is the shape characteristics of the target surface at the point of adhesion, especially its surface matching degree. For example, for an arc-shaped position, such as parabolic antenna or marmon ring, the adhesion array should be arc shaped. Furthermore,

the less is the surface roughness at the adhesion position, the better adhesion effect can be achieved.

Adhesion Position Can Be Reached Because a load has to be applied to the gecko micro/nano-structured adhesive arrays to attach them to the space object, the adhesion position should not be obstructed.

Stiffness and Strength The target surface at the gecko attachment position needs to meet the requirements of stiffness and strength when the adhesion load is applied to attach the gecko array, and can satisfy the stress requirements of the adhesion operation at the same time.

Security Requirement In selecting the positioning of the gecko micro/nano-structured adhesive arrays, the areas of contact with the target should be positioned away from the engine plume range to avoid contamination and possible damage to the arrays. The forces and torques induced by the plume would affect the performance of the gecko micro/nano-structured adhesive arrays.

Evaluation Method of Adhesion Position on Spacecraft or Satellite

Due to large differences between the space environment conditions and the terrestrial conditions, the aging mechanisms are absolutely different. The vacuum causes sublimation and outgassing, with some materials affected more than the others. The vacuum outgassing and atomic oxygen erosion products of polymer materials are the major sources of molecular contamination in low Earth orbit (LEO) space environment. The subsequent condensation of the sublimed vapor on cold surfaces can cause short circuits in electrical parts and reduced optical performance. The vacuum evaporation, sublimation and decomposition of materials are major factors leading to performance degradation. Proper material selection and venting is needed to reduce or avoid deterioration in performance. Any material can be used in space as long as the volatile content is $<0.1\,\%$ and the total mass loss in space is $<1\,\%$.

How to evaluate the adhesive performance of the biomimetic gecko micro/nano-structures adhesive array in terrestrial conditions and how to prolong its reliability and life are important problems. Some typical materials used in spacecraft or satellite designs were selected for adhesion samples. The effects of the outgassing volume and rate under different low-pressure conditions were studied (research roadmap is shown in Fig. 3). The solar panels, radiators, marmon ring, parabolic reflection antenna, fuel tanks, and MLI were initially studied and the possible adhesion positions preliminary selected. In accordance with the roadmap, by measuring the adhesion performance on various spacecraft surfaces (variety of materials, surface morphologies and roughness), appropriate testing and evaluation methods of selecting the adhesion position on various potential targets for gecko

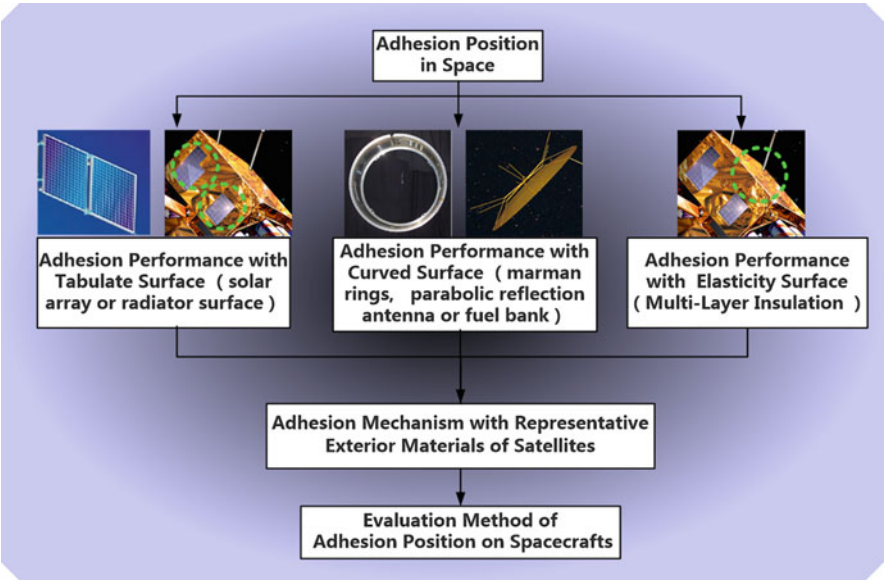

Fig. 3 Roadmap of research on adhesion mechanism of the adhesive array to different targets in space environment

arrays adhesion will be identified that will help revealing the internal mechanisms and the key factors influencing the adhesion performance in space environment.

The adhesion performance between the biomimetic gecko micro/nano-structures adhesive array and adhesion samples in thermal vacuum environment will be conducted in an experimental apparatus consisting of a thermal vacuum chamber providing vacuum conditions and temperature from −100 to +130 °C, a two-dimensional force sensor test system, a data acquisition, a control system, a regulated power supply, a thermal control system and a test sample. The testing would verify the adhesive's performance in Earth-orbit like conditions. A schematic diagram of the test setup is shown in Fig. 4.

Adhesion Device Design

The adhesion device includes a control system, an adhesive capture head and an expandable sleeve. For the typical mode of OOS, such as capturing the decommissioned or malfunctioned satellites, the design of adhesion device should satisfy the requirements of different adhesion targets and variety of service functions. These requirements are discussed below:

1. The sleeve of the adhesion device should be expandable and retractable between the fixed and free end.

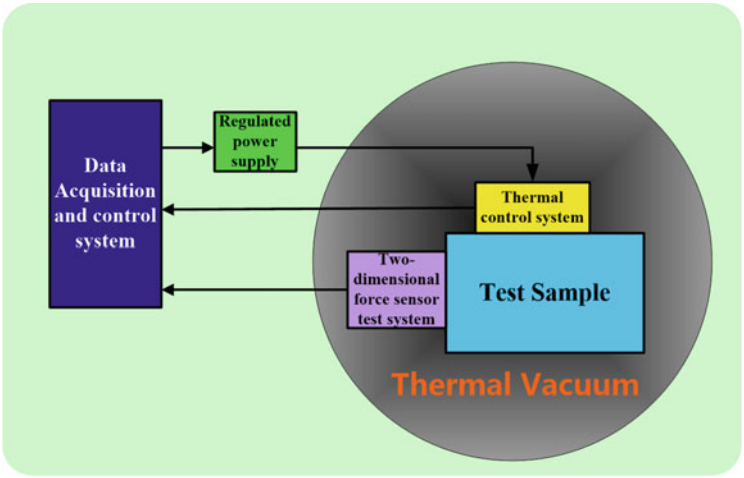

Fig. 4 Adhesion performance experimental apparatus

2. The control system should be able to move the adhesive capture head closer to the target if it determines that the adhesive capture head is not close enough to the object to capture it.
3. The control system should be able to minimize the relative velocity between the adhesive capture head and the target, if the adhesive capture head is close enough to the object.
4. The control system should be able to move the target after its motion has been arrested.
5. The adhesive capture head should be able to capture and control an unpredictably sized and shaped object. It provides a method to conform to the shape, topography, and/or texture of the object prior to the adhesion device making initial contact with the object.
6. The adhesion device should minimize likelihood of damage to sensitive outer coverings or electronics on recoverable payloads of the object.
7. The operation of adhesion device should also minimize the impact to the object and servicer in the capture and departure process, to keep the attitude stabilization of them.

Conclusions

The potential advantages of biomimetic gecko micro/nano-structures adhesive arrays and the particular problems of this material in space have been discussed. Among its applications, the satellite servicing (refueling, repairing, or upgrading) is seen as a promising application that will allow extending the life of large, high-priced existing and future satellites.

The initiated study is designed to understand how the performance of the adhesive array changes in space environment, including its evolution mechanism and enlistment life. By investigating the adhesion performance of gecko style arrays on various spacecraft surfaces, we will establish the test and evaluation method for selecting the appropriate adhesion position on the targets. Such studies will allow revealing the internal mechanisms and the key factors influencing the adhesion performance in the space environment. The results will help to establish an academic and technical base for developing on-orbit servicing stations based on the biomimetic gecko micro/nano-structures arrays. The results of this study can be also applied to new applications of the biomimetic technology to solve problems in space environment and help to improve the development of inter-disciplinary approaches in space science, materials science, nanotechnology and manufacturing science.

References

1. Autumn K, Chang WP, Hsieh T et al (2000) Adhesion force of a single gecko foot-hair [J]. Nature 405(8):681–684
2. Autumn K, Peattie AM (2002) Mechanisms of adhesion in geckos [J]. Integr Comp Biol 42 (6):1081–1090
3. Johnson K, Kendall K, Roberts A (1971) Surface energy and the contact of elastic solids [J]. Proc R Soc Lond 324(1558):301–313
4. Persson BNJ (2003) On the mechanism of adhesion in biological systems [J]. J Chem Phys 118 (16):22
5. Autumn K, Gravish N (2008) Gecko adhesion: evolutionary nanotechnology [J]. Philos Trans R Soc 366(11):1575–1590
6. Kwak J-S, Kim T-W (2010) A review of adhesion and friction models for gecko feet [J]. Int J Precis Eng Manuf 11(1):171–186
7. Schubert B, Lee J, Majidi C et al (2008) Sliding-induced adhesion of stiff polymer microfibre arrays II, macroscale behaviour. J R Soc Interface 5:845–853
8. Aksak B, Murphy MP, Sitti M (2007) Adhesion of biologically inspired vertical and angled polymer microfiber arrays. Lanqmuir 23:3322–3332
9. Jeong HE, Kwak MK, Suh KY (2010) Stretchable, adhesion-tunable dry adhesive by surface wrinkling. Langmuir 26(4):2223–2226
10. Geim AK, Dubonos SV, Grigoriev V et al (2003) Microfabricated adhesive mimicking gecko foot hair. Nat Mater 2:461–463
11. Dan S, Brendan F (2012) Robust large-area synthetic dry adhesives. J Adhes Sci Technol 693802:1–17
12. Jeong HE, Kahp Y (2009) Nano hairs and nanotubes, efficient structural elements for gecko-inspired artificial dry adhesives. Nano Today 4(4):335–346
13. Qu LT, Dai LM, Stone M (2008) Carbon nanotube arrays with strong shear binding-on and easy normal lifting-off. Science 2008(322):238–242
14. He Q, Yu M, Ding Y (2012) Synthesis and characterization of multiwalled carbon nanotube/IPMC actuator for imitating locomotion of gecko's toes, electroactive polymer actuators and devices (EAPAD). Proc SPIE 8340(83401M):1–8
15. Liu K, Jiang L (2011) Bio-inspired design of multiscale structures for function integration. Nano Today 6:155–175

16. Liu K, Du J, Wu J, Jiang L (2012) Superhydrophobic gecko feet with high adhesive forces towards water and their bio-inspired materials. Nanoscale 4(7):68–72
17. Huber G, Gorb SN, Spolenak R et al (2005) Resolving the nanoscale adhesion of individual gecko spatulae by atomic force microscopy. Biol Lett 1(1):2–4
18. Varenberg M, Pugno NM, Gorb SN (2010) Spatulate structures in biological fibrillar adhesion. Soft Matter 6(14):3269–3272
19. Peng ZL, Chen SH, Soh AK (2010) Peeling behavior of a bioinspired nano-film on a substrate. Int J Solids Struct 47(14–15):1952–1960
20. Peng ZL, Chen SH (2011) Effects of surface roughness and film thickness on the adhesion of a bioinspired nanofilm. Phys Rev E 83(5):051915
21. Li Y, Zhang H, Xu G et al (2013) Adhesion performance of gecko-inspired flexible carbon nanotubes dry adhesive. In: Proceedings of SPIE 8686, Bioinspiration, biomimetics, and bioreplication, 86860S, pp 1–11
22. Birkmeyer P, Andrew GG, Fearing RS (2012) Dynamic climbing of near-vertical smooth surfaces [C]. In: 2012 IEEE/RSJ international conference on intelligent robots and systems, 7–12 October. pp 286–292
23. Mark Cutkosky. Stickybot, [EB/OL]. http://bdml.Stanford.edu/twiki/bin/view/Ris-e/Stickybot. 12 Feb 2014
24. Autumn K, Majidi C, Groff RE et al (2006) Effective elastic modulus of isolated gecko setal arrays. J Exp Biol 209(18):3558–3568
25. Autumn K, Hansen W (2006) Ultrahydrophobicity indicates a non-adhesive default state in gecko setae. J Comp Physiol A 192(11):1205–1212
26. Gao HJ, Yao HM (2004) Shape insensitive optimal adhesion of nanoscale fibrillar structures. Proc Natl Acad USA 101(21):7851–7856
27. Kaiser C, Sjoberg F (2004) SMART-OLEV—an orbital life extension vehicle for servicing commercial spacecrafts in GEO. Acta Astronaut 2008(63):400–410
28. Hirzinger G, Landzettel K, Brunner B et al (2004) DLR's robotics technologies for on-orbit servicing. Adv Robot 18(2):139–174
29. Hirzinger G, Brunner B, Landzettel K et al (2003) Space robotics DLR's telerobotic concepts, lightweight arms and articulated hands. Auton Robot 14(2/3):127–145
30. Bosse AB, Barnds WJ, Brown MA et al (2004) SUMO: spacecraft for the universal modification of orbits. Proc SPIE 5419:36–46
31. Obermark J, Creamer G, Kelm BE et al (2007) SUMO/FREND: vision system for autonomous satellite grapple. Proc SPIE 6555(65550Y):1–11
32. Bosse A, Barnds WJ, Brown MA et al (2005) SUMO: spacecraft for the universal modification of orbits. Proc SPIE 5419:36–46
33. Creamer NG, Arnold SP, Butcher ST et al (2006) Laboratory demonstration of a prototype geosynchronous servicing spacecraft. NRL review. In: Space research and satellite technology, pp 1–3
34. Iannotta B (2006) SUMO. Aerosp Am 2006(2):26–30

Polymer Surface Modification for Space Applications

J.I. Kleiman

Abstract Many polymers, paints and organic-based materials exposed to space environment undergo dramatic changes and irreversible degradation of physical and functional characteristics. A number of protective schemes are used to reduce the effects of space environment among which protective coatings, mechanical metal foil wrapping or cladding, specially synthesized bulk materials can be mentioned. However, protection of such materials in space still remains a major challenge, especially for future long duration exploration missions or permanent space stations. In addition to the traditional approaches, surface modification processes are used increasingly to protect or to impair new properties to polymers, paints and other organic-based materials.

A brief overview of surface modification processes developed at ITL for space materials is presented in this paper. The developed processes helped to change the surface properties of treated materials thus protecting them from the hazards of low Earth orbit (LEO) and Geostationary orbit (GEO) environments or impairing new functional properties to space materials used in LEO/GEO.

Keywords Surface modification • Space environment • Low earth orbit • Photosil™ • Implantox™ • Carbosurf™

Introduction

Among the major problems encountered by polymer materials, paints, graphite and polymer-based composites in LEO and GEO space environments one can mention erosion of materials in LEO due to the atomic oxygen effects, change in such functional characteristics like thermal optical properties, surface charging and space equipment performance degradation of high-voltage solar arrays due to arcing in GEO and secondary arcs on solar generators and a number of other problems in long-term modern antennae performance in GEO.

J.I. Kleiman (✉)
Integrity Testing Laboratory, Inc., Markham, ON, Canada
e-mail: jkleiman@itlinc.com

J. Kleiman (ed.), *Protection of Materials and Structures from the Space Environment*, Astrophysics and Space Science Proceedings 47,
DOI 10.1007/978-3-319-19309-0_20

Figure 1 provides compelling evidence of the effects of low Earth orbit on such tough materials as carbon fiber-epoxy composite materials.

Higher energy erosion processes, such as physical sputtering, are well understood for polymers. Chemical reactions of polymer oxidation at thermal energies, including those by thermal atomic oxygen, are also well understood, yet only a few attempts have been made to study the basic aspects of the accelerated mechanism of polymer erosion by energetic neutral beams [1, 2], (Fig. 2).

In general, the cost of developing new polymer materials and paints for use in space is very high, because of constraints on bulk optical, thermal and mechanical properties. Presently a number of different technological solutions are offered to solve the problems discussed above [3–7] (see also the references therein).

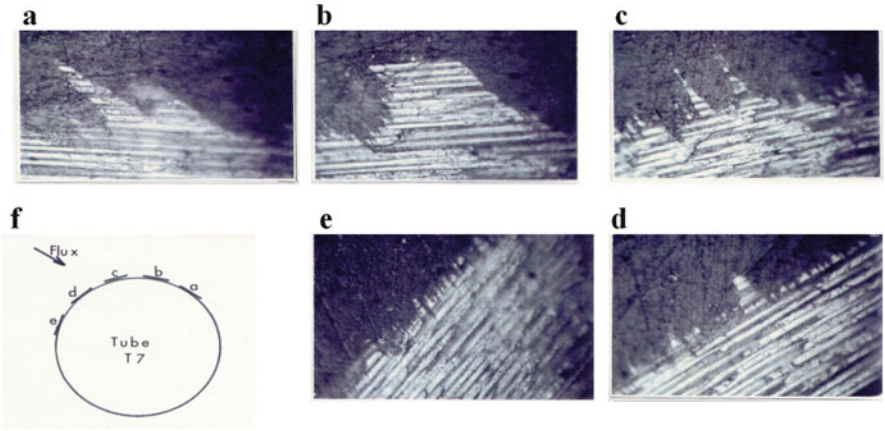

Fig. 1 Optical microscopy analysis of a cross-sectioned carbon fiber-epoxy 4-ply composite material tube (~50 mm in diameter) exposed to the LEO environment for ~4.5 years on the LDEF satellite. Images in (**a**) through (**e**) show the state of eroded surface on the composite tube sample. (**f**) Schematically presents the locations of the above regions on the tube in relation to the incoming atomic oxygen flux (the direction of the incoming flux is marked with an *arrow*)

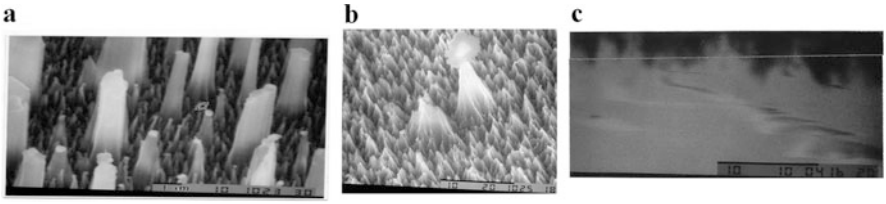

Fig. 2 Scanning electron microscopy (SEM) analysis of polymer surfaces exposed to fast atomic oxygen (FAO) fluxes in a low Earth orbit simulator and to ion beams. (**a**) SEM image (secondary electrons) of a PE polymer exposed to a FAO flux of ~$4 \cdot 10^{15}$ at/cm^2 for 6 h; (**b**) SEM image (secondary electrons) of a Kapton HN polymer exposed to a FAO flux of ~$4 \cdot 10^{15}$ at/cm^2 for 6 h; (**c**) cross-sectional SEM image (secondary electrons) of a Teflon polymer exposed to a Krypton gas flux in an ion-beam vacuum system for 8 h

Protection is provided by metals or by stable inorganic compounds (mostly by oxides or oxide-based surface structures). Oxide coatings are often deposited by one of a few advanced deposition techniques [8]. Also, specially selected or synthesized materials are used that are able to form oxide(s)-based compounds in a top surface layer under aggressive oxidative environments due to surface conversion processes [3, 5, 8–13].

In special cases, mechanical protection by metal foil wrapping or cladding may be used. In addition to structural stability, preservation of important functional properties, such as optical, thermal-optical, electrical, etc. is often required. Deposition of advanced protective coatings, surface modification of materials, development of modern thermal control paint systems, synthesis of special silicones or other polymers with improved resistance to LEO/GEO environment are the major trends for protection.

An extensive review on surface modification technologies developed for protection of materials from the space environment and for impairing new functional properties to them in different space environments was published in 2010 [14]. The present paper will review briefly the work on surface modification technologies that were developed at ITL either to protect the basic properties of the materials [14–24] or to change them in a desirable way, without altering the bulk properties.

Surface Modification Processes Developed at ITL

A number of surface modification processes were developed in the last 15 years at ITL for protection of materials, films and structures from LEO environmental factors, and to change or impair new functional properties to the treated surfaces.

Surface Modification Processes for Protection in LEO

Protective coatings of oxides, such as silicon and aluminum oxides, deposited on the surface of polymers or composites provide improved erosion resistance in LEO environment. However, the thin oxide coatings when exposed to thermal cycling in the LEO space environment develop cracks and/or spalling, mostly because of interfacial stresses and differences in thermal expansion coefficients between the coatings and polymers they supposed to protect. These destructive processes leave the underlying polymeric material exposed to FAO, thus causing extensive surface erosion. High-quality protection of polymer-based materials in LEO, therefore, remains a major challenge, especially for future long-duration missions or deployed space stations.

Surface modification processes designed for protection of materials from the harsh space environment factors were developed as a complimentary to coatings

approach that in many cases are lacking the deficiencies of the coating approaches. Two surface modification processes, one taking a "chemical route" [7] with the other following the "physical route" [15] were developed by ITL for protecting the polymer materials from erosion by atomic oxygen in LEO.

In the chemical approach, the surface modification of space-approved, commonly used polymer-based materials, paints and CFRP composites enriched their top surface layers with specially selected elements that are able to form stable protective oxides or oxide-based protective surface structures in oxidative environments that allowed preventing erosion and etching in LEO and in other severe oxidative environments.

The Photosil™ process is based on a silylation reaction and allows Si to be incorporated into the sub-surface region of the originally treated material. As a result of the Photosil™ process, a newly developed organic structure containing silicon, carbon, and oxygen atoms bonded in a complex configuration is formed that stops the destruction of the polymers and thermal control paints in different oxidizing environments. The depth of the silylated region and the chemical composition of the treated regions were established by XPS and SIMS depth profile analyses. It was confirmed that the silicon atoms penetrated to a depth of at least 0.5 μm.

In essence, the process involves three major steps: UV/air pre-treatment (activation) of the material, actual silylation, and UV/air post-treatment (stabilization) of the modified material.

The XPS analysis of a number of treated polymers and thermal control paints as well as a lacing tape indicated that considerable changes occurred in the treated regions. The high resolution spectrum of the C1s region contained a new peak at 283.2 eV that may be indicative of a Si–C bonding in a carbide structure. The ratios between Si, C, and O are characteristic for each material and depend on the chemical structure of the original polymer. The XPS data for the thermal control paints indicated a sharp increase in silicon and oxygen contents in the outer portion of the surface region with a decrease in carbon content and a nearly total disappearance of nitrogen, as a result of Photosil™ treatment. These results verified the incorporation of silicon-containing groups and confirm the modification of the sub-surface region of the original paint material.

No mass loss or morphology changes were evident for the Photosil™ treated polymer samples after FAO testing. Moreover, the XPS surface content of samples before and after the FAO testing was practically the same for all analysed samples. The FAO test results for the other Photosil™ treated samples showed that the erosion yields were about two orders of magnitude lower than the erosion yield of untreated polymer samples. Figure 3 provides an example of a lacing tape product used on the ISS that was treated by Photosil and exposed to a FAO beam.

Thermal optical characteristics of pristine, Photosil™-treated, and Photosil/FAO-tested polyurethane-based paints were also evaluated before and after surface treatment and FAO testing. All paints after surface treatment have maintained their original thermal optical properties, even after FAO exposure. Both solar absorptance and thermal emittance values remained essentially unchanged within the

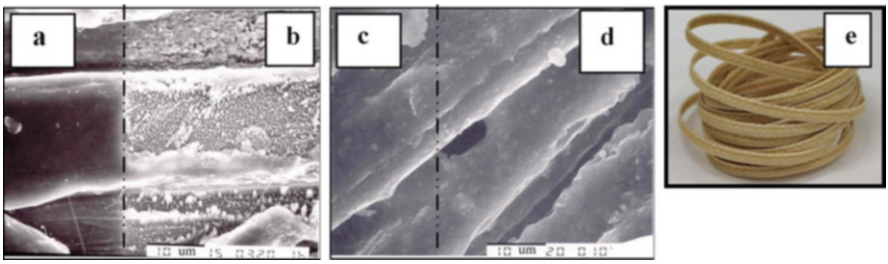

Fig. 3 SEM micrograph of lacing tape exposed to oxygen plasma (Effective Fluence ~$2 \cdot 10^{20}$ atoms/cm^2) before and after Photosil™ treatment. Magnification 2000×. (**a**) Untreated surface, masked section. (**b**) Untreated surface, exposed section. (**c**) Treated surface, masked section; (**d**) treated surface, exposed section. The *black line* separates the masked and unmasked regions on the surface. (**e**) General view of the lacing tape. The aromatic polyamide (Nomex) flat braided lacing tape impregnated with a synthetic resin is suitable for use with electrical wire harness assemblies

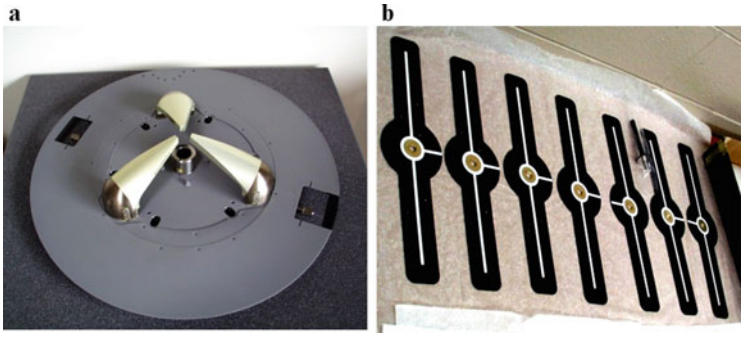

Fig. 4 Examples of space hardware treated by the Photosil™ process. (**a**) The grapple fixture. It is attached to a satellite or payload for the end effector of the Remote Manipulator System (RMS) robot arm to grasp it and maneuver it. The grapple fixture is painted with polyurethane-based *gray* (Aeroglaze® A276:Z306) and *black* (Aeroglaze® Z306) paints. (**b**) Optical target plate/rod. The assembly is used as a visual alignment aid to assist in positioning the RMS robot arm end effector over the grapple spike for capture. The visual cues of the target and rod are painted with *black* (Aeroglaze® Z306) paint with *white* (Aeroglaze® A276) markings

experimental uncertainty ($\alpha = \pm 0.02$ and $\varepsilon = \pm 0.01$). A slight increase of the thermal emittance of the untreated samples after AO exposure was noticed that might be due to roughening of the surface by non-uniform erosion of the paint.

Currently, the Photosil™ technology is used to protect painted external components of NASA's Canadarm2 systems [19]. Photosil™ has been used, as well, to treat painted external components of the Special Purpose Dexterous Manipulator (SPDM), a sophisticated evolution of the Canadarm installed onboard the International Space Station [19]. Figure 4 shows some space hardware that was treated by the Photosil™ process.

Another surface modification process based on high energy ion beam sources was developed to modify space-bound materials in order to provide new protective properties to their surfaces. A method of surface modification of advanced polymers, graphite and carbon-based composites named Implantox™ and based on high-dose ion implantation with Si, Al, Si + Al, Si + B, Si + Al + B, Y, Sm, Gd and special oxidative post-treatment was developed and patented in 1997 [16, 20–23]. The developed technology allowed increasing dramatically the erosion and oxidation resistance of polymer-based materials together with substantial improvements in mechanical, electrical, and optical properties.

In the Implantox™ process, a high-dose single or binary ion implantation of metals or semi-metals is performed into polymers that when combined with a special following post-treatment produces a graded oxide(s)-based surface layer, with a variable degree of carbonization, chemically bonded to the original polymer, and highly resistant to erosion and oxidation. Based on computer simulation and experimental studies, the implantation energy range required to produce a 50–100 nm thick, modified, protective oxide-based layer in most of the treated materials was determined to be 20–50 keV and the required ion dose range was found to be 10^{16}–10^{17} ions/cm^2 [15, 20]. The types of oxides, the degree of surface carbonization, i.e., the surface content of oxide(s)-based structures and the amount of carbonized (graphitized) phases in the modified surface layers can be varied and controlled in a wide range of parameters. Various surface-sensitive properties of the modified layers, such as mechanical, optical, electrical, etc. can be tailored and controlled by the conditions of ion implantation and following oxidative post-treatment. It was confirmed in a number of studies that surface treatment by Implantox™:

- Protects polymers and composites from space environment in low Earth orbits,
- Increases the oxidation resistance in highly oxidative environments, such as atomic oxygen, ozone, oxygen plasmas,
- Improves the durability of polymeric materials and coatings,
- Allows to tailor the degree of hydrophobicity and hydrophilicity.
- Allows tailoring of optical and thermal-optical surface properties, including refraction, reflection, color, and degree of transparency.

It is important to notice that Implantox™ as well as the Photosil™ processes are not coating processes. During the Implantox™ process, the surface layers of the treated material are modified. Because of this new protection philosophy, problems of adhesion, thermal mismatch and change in dimensions disappear. Virtually all hydrocarbon polymers, carbon and CFRP composites can be modified by Implantox™ that is a non-thermal process, allowing, thus, for low melting temperature materials to be treated. Since this surface treatment technology is based on ion-implantation in vacuum, it is absolutely clean and environmentally friendly. No hazardous materials are used or released in this process.

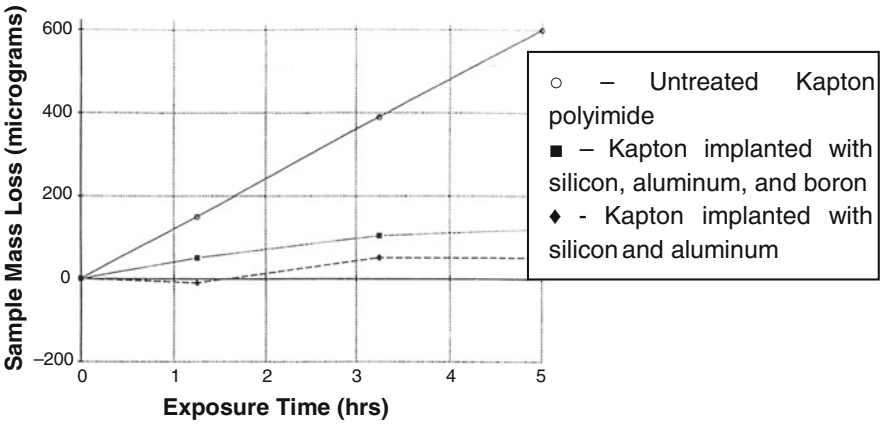

Fig. 5 Kinetic plots of mass loss of Kapton polyimide, implanted with silicon and aluminum (*diamonds*); with silicon, aluminum and boron (*squares*) and of an untreated sample (*circles*) under fast atomic oxygen and vacuum ultraviolet irradiation exposure. Notice that mass loss in both implanted samples stopped shortly after the start of the experiment, indicating that full surface stabilization and protection were achieved

The kinetics of mass loss upon exposure to FAO flux during the conversion and surface stabilization stages presents a clear indication of the development of erosion resistant, protective surface layer (Fig. 5).

The stabilization and protection effects in Implantox-treated materials can be explained by examining the surface content of the implanted materials after FAO testing. A certain amount of carbon was removed from the surface of every material in the interaction with FAO. The stoichiometry of the surfaces suggested that protective, oxide-based layers were developed during the conversion processes. This suggestion was fully confirmed by high-resolution XPS which showed the formation of implanted metals = oxides at the surface as illustrated in Table 1

High quality protection by Implantox^{TM} is clearly illustrated in Fig. 6 where two samples of Kapton and Mylar polymers are shown after an exposure for 1 year in open space to FAO as part of the NASA Materials on International Space Station Experiment (MISSE).

Figure 7 presents the results from a high resolution XPS analysis of Kapton and Mylar samples treated by Implantox and exposed to LEO environment. As can be seen from Fig. 7, the implanted Si underwent a full conversion to a SiO_2.

The major appeal of the ion implantation approach over conventional inorganic coatings is that the difficulties associated with brittleness, mismatch of coefficients of thermal expansion, and change in surface morphology are mitigated by creation of a graded surface modified region.

Table 1 XPS data for surface composition of implanted polymers after FAO testing

Implanted ions	Concentration of elements detected by XPS (at %)				
	C	O	Si	Al	Other
	Kapton				
Si	17.0	54.0	29.0	–	–
Si–B	24.0	46.0	30.0	–	–
Si–Al	30.5	45.6	5.4	17.5	0.9
Si–Al–B	30.7	44.6	6.4	17.1	1.4
	PEEK				
Si	41.2	39.7	19.1	–	–
Si–Al	37.4	41.0	5.6	13.1	2.8
	Mylar				
Si–Al	43.3	37.8	5.1	12.2	1.6
Si–Al–B	36.3	42.4	5.3	14.1	1.9
	Graphite				
Si	40.0	41.90	16.6	–	1.5
Si–B	38	44.1	15.6	–	2.0

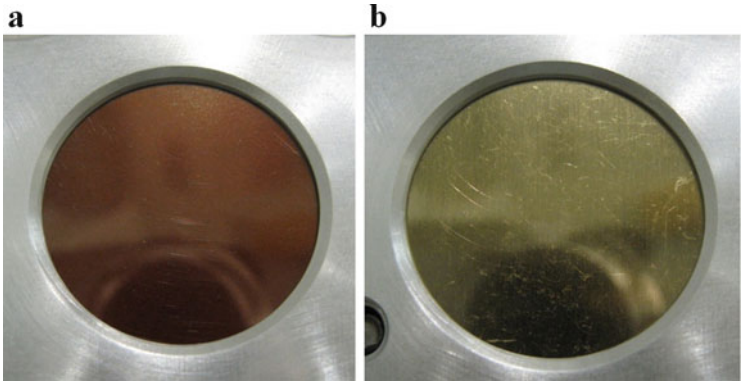

Fig. 6 Kapton HN (**a**) and Mylar (**b**) implanted with Si + B atoms and exposed in open space on the International Space Station to LEO environment in a Materials Flight Experiment MISSE-2 for 1 year. AO fluence ~$5{\cdot}10^{20}$ cm^{-2}. Notice no morphology change—clear glossy appearance. The samples did not experience any mass loss, even a slight mass gain

Surface Modification Processes for Impairing New Functional Properties

Surface modification of polymers could be used not only for protection of materials from various space factors but for impairing new properties as well. In this area of research the use of ion beams has proven to be very successful [25–29].

A **surface** modification **texturing process, Surftex™** was developed at ITL that changes the appearance of the surface in a controlled manner from a metallic-

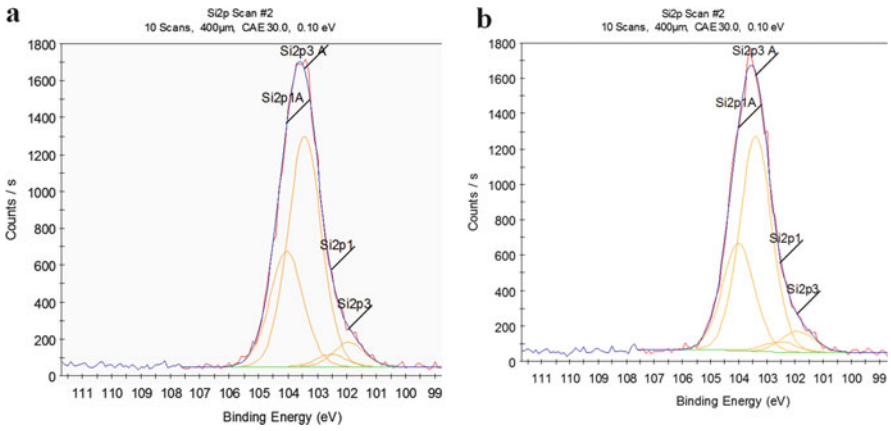

Fig. 7 High resolution XPS data for Si obtained from the samples of Implantox-treated and LEO exposed Kapton (**a**) and Mylar (**b**)

like and shiny to complete milky-white appearance. The developed surface texturing process is based on ion-beam bombardment of the surface with noble gases. As a result of such treatment, the specularity of the treated surfaces can be reduced dramatically, with the surface morphology changing from metallic-like and shiny to complete milky, white appearance.

The developed process was applied to Teflon thermal protection coverings silver-coated on the back [25–27] that were used to cover the camera and light equipment on the International Space Station using an adhesive.

Figure 8 shows the total and diffuse reflectance of a 127 µm thick Silver/Teflon sample after its surface was treated with Krypton ions. As can be seen from Fig. 8, most of the light was reflected as diffused, with the diffused reflectance almost equalling the total reflectance. The developed treatment allowed reducing dramatically the specularity of Silver-Teflon thermal control films, without significantly affecting their thermal optical properties.

The surface treatment allowed developing a cone or spike-like surface morphology thus increasing dramatically the diffuse reflectance of the surface (see Figs. 8 and 2c). The space hardware covered with the textured Silver-Teflon is used on the ISS in open space routinely and an example of a camera that was exposed to the open space environment between June 2002 and June 2006 and brought back to MDA around November 2006 is shown in Fig. 9.

Charge Dissipative Ion-beam Treatment Process Carbosurf™

A surface modification technology (tentatively named Carbosurf™) that was developed to achieve charge dissipative properties on the surface of polymers is based on the controlled carbonization of the surface layer of thin polymer films

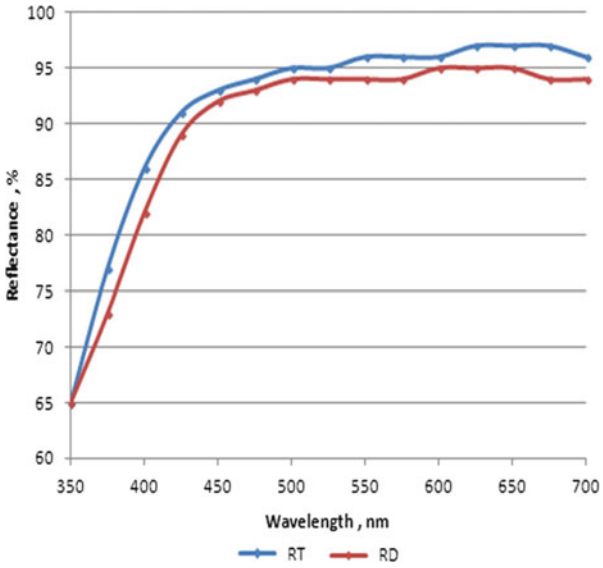

Fig. 8 Total (R_T) and diffuse (R_D) reflectance measurements for a Ag/Teflon sample after an exposure to a Krypton gas ion-beam

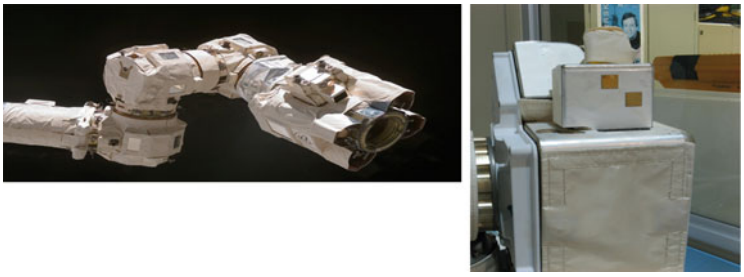

Fig. 9 Visual appearance of the camera CLPA S/N 206 (TVC S/N209) in space installed on MBS of the ISS (*left*) and after delivery in November of 2006 to MDA (*right*) (stored in a clean room at MDA)

[28, 29]. Temperature stable surface resistivity (SR) in the charge dissipative range, from ~2 MΩ/sq up to 150 MΩ/sq, has been achieved on hydrocarbon and partially fluorinated poly-imides due to surface carbonization using specially selected ion beam treatment conditions. The created surface resistivity can be tailored to the desired values for particular applications on a variety of space polymer films. The Carbosurf™ treatment is performed using ion beams of back gases, without affecting the mechanical and any other properties of the polymeric material underneath, and may be scaled-up using industrial high-intensity ion beams.

The main advantage of surface carbonization over technologies currently available is a low temperature dependence of the achieved surface resistivity and

Table 2 Surface resistivity of thin (1 mil) polymer films after moderate energy ion beam treatments by various ions at room temperature

	Surface resistivity at room temperature, ρ (Ohm/sq.)		
Materials/Surface treatment	Xe^+	Ar + (I)	Ar^+ (II)
CP 1 White	0.75×10^7	2.5×10^8	1.3×10^7
CP 1	0.6×10^7	5×10^8	1.3×10^7
Kapton HN	1.5×10^7	5×10^{10}	3×10^9

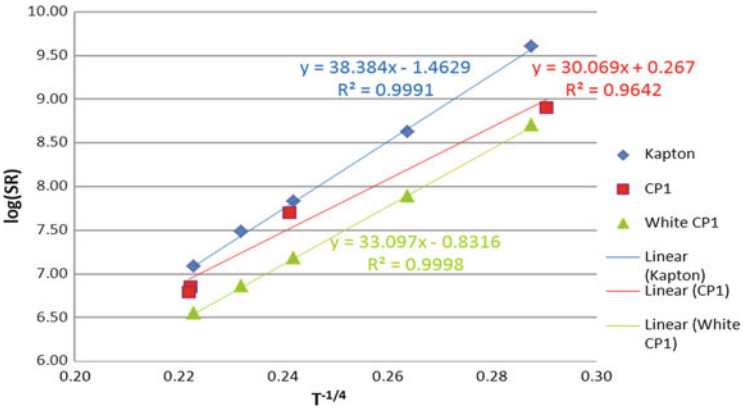

Fig. 10 Semi-log graphs of the $T^{-1/4}$ temperature dependence of the surface resistivity of various polyimide samples with different Carbosurf treatments. It is an indication of variable range hopping conductivity mechanism in the thin Carbosurf-treated surface layer of polymers

Table 3 Summary of charge dissipative properties and RF losses of treated by Carbosurf™ Kapton100HN polymer film (the last raw for Ge/KaptonHN is given for comparison)

Material	Treatment	SR (Ω/sq)	SR (Ω/sq) GEO tested	Ku band insertion loss (dB)	Ku band return loss (dB)
Kapton100HN	Pristine	$>10^{12}$	$\sim 10^{11}$	0.015–0.020	30–31
Kapton100HN	Carbosurf™	$(13–25) \times 10^6$	18×10^6	0.015	31
Ge/KaptonHN	Deposition of Ge (1000 Å)	5×10^7	1.3×10^8	0.015	30

excellent RF performance. Table 2 and Fig. 10 present the results of measurements of SR behavior at room temperature (Table 2) and with temperature varying in the range from −150 to +150 °C (Fig. 10) for two treated polymers, namely, CP1 treated by Ar^+ ion beam and Kapton HN exposed to Kr^+ ion beam [28]. It is clear from Fig. 10 that the temperature dependence is quite slow and at low temperatures the ion beam treated samples still keep the surface resistivity in the appropriate range of values.

The other important feature of the Carbosurf™-treated materials, i.e., their full RF permeability is demonstrated in Table 3. The significant distinction of the

developed surface carbonization technology from deposition of semi-conductive coatings is that the Carbosurf™ treatment is "graded" into the material thus eliminating any sharp interfaces that could be a weak point of the alternate coatings' technologies.

Charge dissipation and RF transmittance of Carbosurf™ treated polymers provide a broad range of required SR values in a very thin top surface layer, without any influence on the rest of material and on RF transmittance. By tuning the process parameters, it is possible to obtain surface resistivity changes in a range over 5 orders of magnitude, as well as variable thermal optical properties with a weak temperature dependence of surface resistivity at low temperatures and no RF losses in the treated materials.

Conclusions

Surface modification technologies present a viable alternative for protection and impairment of new functional properties to polymers, paints and other carbon-based materials and structures used in space. Surface modification processes have been developed at ITL to provide an alternative solution to the problems caused by different space environment factors to polymer-based materials, composites and paints used in LEO/GEO spacecrafts. The developed processes allow to drastically reducing the atomic oxygen erosion by creating a self-healing protective layer that allows, in turn, protecting the major functional properties like the thermal optical properties.

Ion-beam based surface modification treatments also allowed to impair new functional properties to surfaces like reduced glare or increased surface conductivity that extended the use of traditional space materials in space applications. The material science field is developing at a tremendous paste. Nanotechnology is the buzz word of the twenty-first century. All topics discussed in this short review are greatly influenced already by the new nanomaterials and associated with them new technological processes and solutions. It is not hard to envision that most of the technological approaches including deposition processes, surface modification processes, bulk material technologies, etc. will undergo dramatic changes and improvements in the near future with many such developments already well under way.

While there certainly will be a "delay" for the new solutions to get from the "drawing boards" and laboratories into the actual production and acceptance by the space industry, we should expect a very exciting time ahead of us, where these approaches will be discussed, criticized and either accepted or rejected in the upcoming professional meetings, publications, etc.

Acknowledgments The author would like to thank his co-workers, Dr. Z. Iskanderova and Dr. Y. Gudimenko for their devotion to the topic and many years of hard work at ITL that they put into the conceiving and development of these processes. Special thanks are due to Prof.

R.C. Tennyson who envisaged the importance of the surface modification approach and was mostly instrumental in the first steps undertaken at UTIAS in this field. Finely my thanks are due to all my colleagues who participated in the work during the past years that lead to the development and applications of the surface modification technologies at ITL.

References

1. Minton TK, Seale JW, Garton DJ, Frandsen AK (2001) Dynamics of atomic-oxygen degradation of materials. In: Kleiman JI, Tennyson RC (eds) Space technology proceedings, vol 4. Proceedings of ICPMSE-4 "Protection of space materials from space environment", Toronto, April 23–24, 1998. Kluwer Academic Publishers, pp 15–31
2. Pascual RZ, Schatz GC, Garton DJ (1995) A direct trajectory dynamics investigation of fast O^+ alkane reactions. In: Kleiman JI, Iskanderova ZI (eds) (2003) Space technology proceedings, vol 5. Proceedings of ICPMSE-6, "Protection of materials and structures from the space environment", Toronto, May 1–3, 2002. Kluwer Academic Publishers, pp 537–541
3. Reddy MR (1995) Review: effect of low earth orbit atomic oxygen on spacecraft materials. J Mater Sci 30:281–307
4. Kleiman JI, Iskanderova ZA, Perez FJ, Tennyson RC (1995) Protective coatings for LEO environments in spacecraft applications. Surf Coat Technol 76/77:827–834
5. Packirisamy S, Schwam D, Lite MH (1995) Review: atomic oxygen resistant coatings for low earth orbit space structures. J Mater Sci 30:308–320
6. Kleiman JI (2005) Surface modification of polymers, paints and composite materials used in the low earth orbit space environment. In: Chipara M, Edwards DL, Benson RS, Phillips Sh (eds) Materials for space applications. Mater. Res. Soc. Symp. Proc. 851, Warrendale, PA, 2005, paper NN8.6
7. Goudimenko Y, Kleiman JI, Cool GR, Iskanderova Z, Tennyson RC (1999) Modification of subsurface region of polymers and carbon-based materials. US Patent 5,948,484, 7 Sept
8. Gissler EW, Jehn HA (1992) Advanced techniques for surface engineering. Kluwer Academic Publisher, Dordrecht
9. Connell JW (2000) The effect of low earth orbit atomic oxygen exposure on phenylphosphine oxide-containing polymers. High Perf Polym 12(2000):43–52
10. Shepp A, Haghighat R, Lennhoff J, Schuler P, Connell J, Clark TS, Vaughn J, Swiener J (1999) TOR and COR AO-VUV resistant polymers for space. In: Kleiman JI, Tennyson RC (eds) Space technology proceedings, vol 4. Proceedings of ICPMSE-4 "Protection of space materials from space environment", Toronto, 23–24 April, 1998. Kluwer Academic Publishers, pp 235–254
11. Schuler P, Mojazza HB, Haghighat R (2000) Atomic oxygen resistant films for multi-layer insulation. High Perf Polym 12(2000):113–123
12. Vilgor I (1987) Synthesis and characterization of atomic oxygen resistant poly(siloxane-imide) coatings. In: Lee L-H (ed) Adhesives, sealants, and coatings for harsh environments. Plenum Press, New York, NY, pp 249–264
13. Oldham S, Elias WE, Bigus SJ, Lan TSY (1993) Aromatic silane polymer coating. US Patent 4,874,643, Oct 1989.
14. Kleiman JI (2010) Surface modification technologies for durable space polymers. MRS Bull 35(01):55–65
15. Iskanderova Z, Kleiman JI, Goudimenko Y, Cool GR, Tennyson RC (1997) Surface modification of polymer and carbon-based materials by ion implantation and oxidative conversion. US Patent 5,683,757, 4 Nov
16. Goudimenko Y, Iskanderova Z, Kleiman J, Cool GR, Morison D, Tennyson RC (1997) Erosion protection of polymer materials in space. In: Proceedings of 7th international symposium, "Materials in space environment", Toulouse, France. pp 403–410

17. Kleiman JI, Iskanderova ZA, Gudimenko YI, Morison WD, Tennyson RC (1999) Polymers and composites in the low earth orbit space environment: interaction and protection. Can Aeronaut Space J 45(2):148–160
18. Gudimenko Y, Ng R, Kleiman J, Iskanderova Z, Hughes PC, Tennyson RC, Milligan D (2002) Photosil™ surface modification treatment of polymer-based space materials and external space components. In: Kleiman J, Iskanderova Z (eds) Proceedings of the 6th international conference on protection of materials and structures from space environment—ICPMSE-6, Toronto, 1–3 May. pp 419–434
19. Kleiman J, Iskanderova Z, Tennyson RC (1998) Ion implantation protects surfaces. Adv Mater Process 26–30, April
20. Iskanderova Z, Kleiman JI, Gudimenko Y, Morison WD, Tennyson RC (1999) Surface modification of polymer-based materials by ion implantation—a new approach for protection in LEO. In: Kleiman JI, Tennyson RC (eds) Space technology proceedings, vol 4. Proceedings of ICPMSE-4 "Protection of space materials from space environment", Toronto, 23–24 April, 1998. Kluwer Academic Publishers, pp 243–252
21. Iskanderova Z, Kleiman J, Gudimenko Y, Morison WD, Tennyson RC (1997) Improvement of oxidation and erosion resistance of polymers and composites in space environment by ion implantation. Nucl Instrum Methods Phys Res B127/128:702–709
22. Iskanderova Z, Kleiman J, Morison WD, Tennyson RC (1998) Erosion resistance and durability improvement of polymers and composites in space environment by ion implantation. Mater Chem Phys 54:91–97
23. Gudimenko Y, Ng R, Kleiman JI, Iskanderova ZA, Tennyson RC, Hughes PC, Milligan D, Grigorevski A, Shuiski M, Kiseleva L, Edwards D, Finckenor M (2003) Enhancement of surface durability of space materials and structures in LEO environment. In: Proceedings of the 9th international symposium on materials in a space environment, Noordwijk, The Netherlands, 16–20 June 2003 (ESA SP-540, September 2003). pp 95–106
24. Iskanderova Z, Kleiman J, Mojazza B, Sutton M (1993) Erosion protection and surface conductivity enhancement of TOR polymers by Implantox™ Technology. In: Proceedings of the 9th symposium on materials in a space environment, Noordwijk, The Netherlands, 16–20 June 1993. pp 473–478
25. Kleiman JI, Popov O, Tong A, Molenda D (1999) Development of high diffuse reflectance surfaces on teflon. In: Proceedings of the ICPMSE-3 conference, 25–26 April 1996. Kluwer Academic Publishers, pp 167–177
26. Kleiman JI, Gudimenko Y (1997) Reduced glare, high diffuse reflectance teflon surfaces for improved performance of video cameras on Canadian MSS For SS alpha. In: The 7-th international symposium on materials in a space environment, 16–20 June, ENSAE-SUPAERO, Toulouse, France. pp 419–425
27. Kleiman JI, Iskanderova Z, Antoniazzi J (2009) Long term flight performance of high diffuse reflectance Ag/Teflon coverings flown on Canadian mobile servicing station, MSS. In: Proceedings of the ISMSE-11 symposium, Aix-en-Provence, France, 15–18 September 2009 (available on CD)
28. Iskanderova Z, Kleiman JI, Issoupov V, Bussieres F (2009) CARBOSURF™ surface modification technology for charge dissipative and radio-transparent GEO durable space polymers. In: Kleiman JI (ed) Proceedings of the 9th international conference "Protection of materials and structures from space environment", vol 1087, Toronto, Canada, 20–23 May 2008. AIP Conference Proceedings, pp 588–599
29. Iskanderova Z, Kleiman J, Bussieres F, Grigorevskiy A, Sodhi R (2013) Ion beam treatments for enhancement of surface conductivity and durability of space polymers: results, analysis, mechanisms. In: Kleiman JI, Tagawa M, Kimoto Y (eds) Astrophysics and space science proceedings, vol 32. Proceedings of the 10th international conference, ICPMSE-10J, Bankoku-Shinryokan, Okinawa, Japan, 12–17 June 2011. Springer, pp 317–325

Development of a Silicone Adhesive for OSR Bonding

G. Sierra, O. Guillaumon, D. Sacramento, S. Remaury, and P. Nabarra

Abstract Optical solar reflectors (OSR) are used for the thermal control of spacecraft on the sun-facing sides of satellites. The operating principle is based on the reflection from incoming solar radiation while simultaneously radiating internally-generated heat. OSR are small specific glasses ($40 \times 40 \times 0.1$ mm) surface of which has been treated in order to obtain maximum reflectance of sun irradiation. In some cases, these OSR are manually bonded onto panels and the bonding appears as a time-consuming step in the satellite production because it comes at the end of the production of some structural panels, which are often on the critical path.

In order to improve OSR bonding process, a specific silicone adhesive, called MAPSIL® QS 1123 ELEC LD has been developed, ensuring: relatively small viscosity, long working-time, electrical conductivity and self-adhesion on OSR (Sierra, Development of a specific OSR automated bonding process, 2012). This adhesive has been developed with the following specifications:

1. Development of a silicone based adhesive, mostly used due to its ability to be used in a wide temperature range;
2. Outgassing compliance with the ECSS-Q-70-02C standard (ESA, Thermal vacuum outgassing test for the screening of space materials, 2008);
3. Behaviour towards the space environment which includes UV, e−, p+ and γ irradiation factors. These tests are validated by specific irradiation testing on Earth and/or space, using correlations between duration and irradiation;
4. Have good electrical conductivity in order to avoid electrostatic discharges;
5. Have good thermal conductivity to ensure a good thermal transfer between the satellite and the lightweight panels;
6. Density should be as low as possible to limit the total weight of the OSR—adhesive system to improve the global performance of the satellite;
7. No use of adhesion primer on aluminium substrates and OSR;

G. Sierra (✉) • O. Guillaumon • D. Sacramento
MAP, ZI—2 Rue Clément Ader, 09100 Pamiers, France
e-mail: g.sierra@map-coatings.com

S. Remaury (✉) • P. Nabarra
CNES, 18, Avenue Edouard Belin, 31401 Toulouse Cedex 9, France
e-mail: Stephanie.Remaury@cnes.fr

J. Kleiman (ed.), *Protection of Materials and Structures from the Space Environment*, Astrophysics and Space Science Proceedings 47,
DOI 10.1007/978-3-319-19309-0_21

8. Good adhesion between aluminium substrates and OSR after thermal cycling under vacuum (−70 to 90 °C), and after damp heat test (50 °C at 95 % of relative humidity).

Moreover, MAPSIL® QS 1123 ELEC LD has been developed in accordance with ISO 9001 and EN9100 standards ensuring quality of the products and it is ITAR and EAR free as it is a co-development of a French company (MAP) and the French Space Agency (CNES).

Keywords Optical solar reflectors • Silicone adhesive • MAPSIL • Self-adhesion • Bonding process

Introduction

In the current time-consuming manual bonding processes of the OSR on the lightweight panels some critical steps exist. Firstly, due to the silicone adhesives presently used, the use of an adhesion primer is mandatory to reach a good adhesion between the OSR and the panels. Secondly, current adhesives have limited working time interval of about 15 min in which the numerous operations like base/hardener weighing, mixing and outgassing must be finished.

As the application of the primer on each OSR is a time-consuming step, removing the use of an adhesion primer could be an interesting advantage. In order to improve the current bonding processes of the OSR on the lightweight panels, a new adhesive has been developed [1].

This paper presents, in the first part, the specifications of the new silicone adhesive. In the second part, the silicone adhesive development is presented, focusing on its intrinsic properties (mechanical, rheological, electrical and thermal). Finally, the performance results of the bonded OSR on specimen with MAPSIL® QS1123 ELEC LD are presented.

Adhesive Specifications

To bond the OSR on the lightweight panels, silicone adhesives are mostly used due to their ability to be used in a wide temperature range. The main property of the space adhesives is the outgassing property that must comply with the ECSS-Q-70-02C standard [2] that stipulates that the recovered mass loss (RML) must be $<1.0\,\%$ and that the collected volatile condensable material (CVCM) must be $<0.1\,\%$. The resistance to the space environment must also be verified which includes exposures to UV, e−, p+ and γ irradiation.

In addition to these general specifications relevant to all space materials, specific properties related to the OSR use are required. Firstly, in order to avoid electrostatic discharges, an electrically conductive adhesive is required. Secondly, to ensure a

good thermal transfer between the satellite and the lightweight panels the adhesive must have an adequate thermal conductivity. The adhesive density should be as low as possible to limit the total weight of the OSR—adhesive system. Regarding the performance of the adhesive, good adhesion on aluminium substrates and OSR is also required. The approach of not having an adhesion primer at all could be an interesting opportunity to simplify the bonding process. The good adhesion between aluminium substrates and OSR must be validated in the wide temperature range used for the OSR, −70 to 90 °C.

Silicone Adhesive Development

On the basis of the general and particular specifications, it was decided to develop a specific product based on the MAPSIL® QS1123 technology [3–5]. In fact, this adhesive complies with all space specifications (outgassing, irradiation life) and has been already qualified [6–10].

General Properties

The MAPSIL® QS 1123 ELEC LD silicone adhesive has been developed on the basis of the MAPSIL® QS1123 technology.

This product has been developed on the poly-addition technology with its curing cycle performed either at room temperature (23 °C) or accelerated by heat curing (up to 100 °C). The MAPSIL® QS 1123 ELEC LD is a 2 component product consisting of a base and a hardener. The mixing base/hardener weight ratio is 100/10. Standard curing cycle is obtained at room temperature during 1 week. The colour of the base is blue–grey, whereas the hardener is whitish. The density of the product is 1.17. Outgassing test has been carried out by INTA laboratory. The RML has been measured at 0.27 % and the CVCM at 0.04 % [11].

Rheological Properties

The viscosity of the base is of 75 Pa s and for the hardener it is 2.5 Pa s. A high viscosity has been chosen to facilitate the stability of the OSR during the bonding process but also to allow vertical bonding. The pot-life of the MAPSIL® QS 1123 ELEC LD is around 125 min at 23 °C. This relatively long pot life ensures long working time with the same mixture.

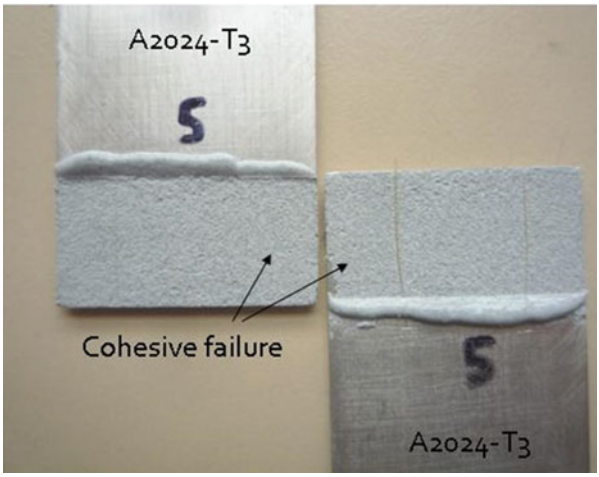

Fig. 1 Failure faces of 2024-T3 specimens

Mechanical Properties

Mechanical properties were characterized at 23 °C and for a curing cycle of 1 week at 23 °C. The hardness is 74 Shore A. Tensile strength is around 3.1 MPa with 80 % elongation. The Young modulus of the adhesive has been measured by DMA. A value of 7.1 MPa has been obtained at a frequency of 1 Hz.

Tensile-shear tests have been carried out following the ISO 4587 2003 standard [12] using 2024-T3 specimens ($105 \times 25 \times 1.6$ mm) and a single lap joint of 12.5×25 mm area. The MAPSIL® QS 1123 ELEC LD composition has been developed in order to remove the use of an adhesion primer. In these conditions the tensile-shear strength is 2.5 MPa. All the failures occurred via a cohesive mode demonstrating the good quality of the bonding (Fig. 1).

Electrical and Thermal Properties

Electrical properties were measured at 23 °C on 500 µm thick film. An electrical volume resistivity of $1.17 \times 10^4\,\Omega$ cm has been measured following the ASTM D257-99 standard. Following the same standard an electrical surface resistance of $3 \times 10^5\,\Omega$/sq has been measured. The electrical conductivity of the MAPSIL® QS 1123 ELEC LD, characterized by the volume resistivity but also by the surface resistance, prevents it from electrostatic discharges.

In order to check the behaviour of a representative test assembly (2024-T3—MAPSIL® QS 1123 ELEC LD—OSR), ESD tests were carried out and validated by ONERA laboratory [6].

The thermal conductivity has been measured using the Guarded-Hot-Plate method at 23 °C under vacuum within CNES facility. The measured value,

$\lambda = 0.36\ W\ m^{-1}\ K^{-1}$ is higher than that of the MAPSIL® QS1123 ($\lambda = 0.16\ W\ m^{-1}\ K^{-1}$) which means that the developed adhesive is quite a good thermal conductor.

Ageing Tests

The mechanical properties have been evaluated after ageing tests. Firstly, we carried out damp heat test (7 days at 50 °C and 95 % of relative humidity) and then thermal cycling tests (100 cycles from −70 to 90 °C).

A slight increase in the tensile-shear strength from 2.5 MPa at the initial stage to 3.4 MPa after ageing has been observed whereas the failure faces remain the same, showing a cohesive failure (as shown in Fig. 1).

OSR Bonding Results

OSR's were bonded on metallic and glass samples in order to check the quality of the bonding.

The inspection of the glass samples on the front side (Fig. 2a) and on the back side (Fig. 2b) shows that the adhesive is homogeneously spread on the whole surface. Moreover, the examination of the rear side does not show bubbles, confirming a good reliability and robustness of the bonding process.

We also measured the thickness of the adhesive to be <0.2 mm. Several measurements were done on many samples proving that the adhesive thickness was mastered using this bonding process.

An OSR bonded 2024-T3 aluminium specimen is presented in Fig. 3. Nine OSR's have been bonded on the substrate. Thicknesses of <0.2 mm and joint gaps <0.2 mm between OSR's were measured, showing good accuracy in OSR positioning.

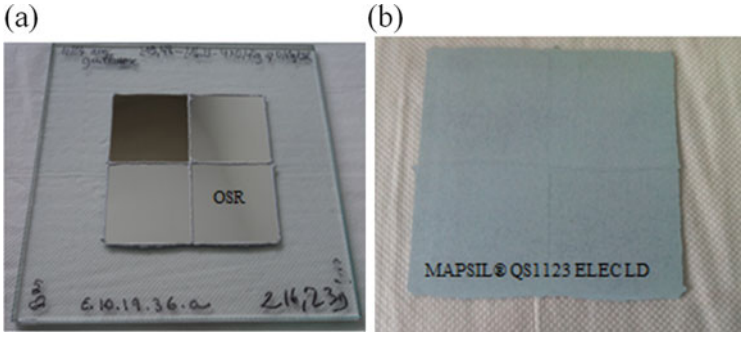

Fig. 2 OSR bonded on glass substrate. (**a**) Front side and (**b**) back side

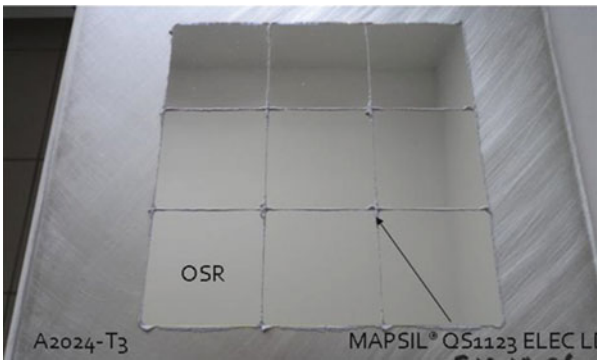

Fig. 3 Validation specimen of MAPSIL® QS1123 ELEC LD bonded OSR

The OSR adhesion to the substrate has been validated by successive peeling tests using growing adhesion strength scotch tapes. Ageing tests were also carried out on such specimens [13]:

- Damp heat test (1 week under 95 % Relative Humidity and 50 °C);
- Thermal cycling test (100 cycles between −70 to 90 °C).

Conclusions

In order to improve the current process of OSR bonding, a specific silicone adhesive has been developed based on the MAPSIL® QS 1123 technology, called MAPSIL® QS 1123 ELEC LD. This new formulation is based on a silicone polyaddition curing which ensures good mechanical properties, curing modulation and low outgassing rate. In addition, this new adhesive is electrically and thermally conductive; it has a low density and very good tensile-shear strength properties. One interesting property of this adhesive is its ability to be used without adhesion primer on OSR and aluminium substrates allowing time-saving on the global bonding process of the OSR.

References

1. Sierra G (2012) Development of a specific OSR automated bonding process. In: Proceedings of 12th international symposium on “Materials in the space environment”, Noordwijk
2. ESA (2008) Thermal vacuum outgassing test for the screening of space materials. ECSS-Q-ST-70-02C
3. Guillaumon O, Remaury S, Guigue P (2008) Development of an ITAR free silicone adhesive for space use: MAPSIL® QS 1123. In: 9th ICPMSE, Toronto, Canada
4. Marco J, Remaury S, Tonon C (2009) Eight years GEO ground testing of thermal control coatings. In: 11th ISMSE, Aix-en-Provence, France

5. Guillaumon O, Remaury S, Nabarra P, Guigue P, Combes H (2009) Development of a new silicone adhesive for space use: MAPSIL® QS 1123. In: 11th ISMSE, Aix-en-Provence, France
6. Remaury S (2011) ESD test results of silicone adhesives on OSR assemblies. CNES report DCT/TV/TH/NT11-8705
7. Remaury S (2010) Eight years GEO ground testing of thermal control coatings. CNES report DCT/TV/TH/NT10-1267
8. Remaury S (2009) Qualification report—MAPSIL® QS1123 silicone resin. CNES report DCT/TV/TH/09-14628
9. Remaury S (2011) Thermal conductivity measurement of MAPSIL® QS1123. CNES report DCT/TV/TH/NT09-6039
10. Levan L, Rohr T, Van Eesbeek M (2009) MAPSIL® QS1123 material investigation. ESA report N°5880
11. Herrera Hernandez A (2011) Outgassing test report DMAV1118
12. ISO 4587: 2003 Adhesives—determination of tensile lap-shear strength of rigid-to-rigid bonded assemblies. AFNOR standard
13. MAPSIL® QS 1123 ELEC LD (2013) CNES qualification report DCT-TV-TH 2013-2456

Surface Modification of Flat Cable Conductors to Prevent Surface Charging

Z. Iskanderova, J. Kleiman, C. Noemayr, and C. Zimmerman

Abstract A method of making charge dissipative both surfaces of Flexible Cable Connectors (FCCs), used for Solar Arrays in GEO, by specially developed ion beam surface treatment is described in this study. FCC's made of dielectric space polymer Kapton100HN with shaped/grooved surfaces and back surfaces containing embedded inorganic particles have been made charge dissipative, with required values of surface resistivity and in a wide space-defined temperature range. The method comprises controllably carbonizing the surface of the polymer-based material in a vacuum environment with simultaneous surface renewal, by bombarding the surface with an ion beam from a linear gaseous high-current technological ion beam source of back gas with added required amount of a carbonaceous gas for simultaneous carbonized surface renewal in a dynamic way. Surface resistivity values of ~10 MΩ/square at room temperature were achieved. The treated FCCs kept the surface charge dissipation properties at least in the space-related temperature range of ±150 °C, have been shown to be resistant to thermal cycling, being durable, radiation resistant and surface charge dissipative in imitated GEO environment for at least 15 years of GEO space equivalent, with the influence on the final thermal optical properties almost the same as on original FCCs surfaces.

Keywords Flexible cable connectors • Ion beam surface treatment • Surface resistivity • Charge dissipative • Carbonized surface • GEO environment • Thermal optical

Z. Iskanderova • J. Kleiman (✉)
Integrity Testing Laboratory Inc., 80 Esna Park Drive, #7-9, Markham, ON, Canada
e-mail: jkleiman@itlinc.com

C. Noemayr • C. Zimmerman
Airbus Aerospace, Materials, Mechanical Parts and Processes, APQ42, Munich 81663, Germany

J. Kleiman (ed.), *Protection of Materials and Structures from the Space Environment*, Astrophysics and Space Science Proceedings 47,
DOI 10.1007/978-3-319-19309-0_22

Introduction

A project was conducted to prevent a particular space product Flexible Cable Connectors (FCC's) from space charging effects during long-term modern space missions in GEO. The FCC's are used for solar arrays in GEO orbits and come in different sizes and shapes. They are manufactured based on DuPont Pyralux LF1010 that basically consists of a Pyralux LF1010 copper clad laminate and same type coverlay, i.e., Kapton100HN (1 mil) films, joined together by a special acrylic adhesive with thin copper strips pressed in between them at processing stages [1]. As can be seen from Fig. 1 that presents a portion of an FCC, the polymeric surfaces of FCCs are not plain thin films, but look "grooved" due to the manufacturing technology. The goal of the project was to impair charge dissipative properties to both sides of FCC's, with surface resistivity (SR) ~10 MΩ/sq, and maintain their durability in GEO for ~15 years.

Front and Back Surfaces of the FCCs Units

In the very beginning of the project an unexpected difference in appearance between the front and the back surfaces of all FCCs has been identified (Fig. 2a, b). It was found, using optical and scanning electron microscopy that the front shiny side had a

Fig. 1 Optical image of a portion of the FCC demonstrating the grooved nature of its surface

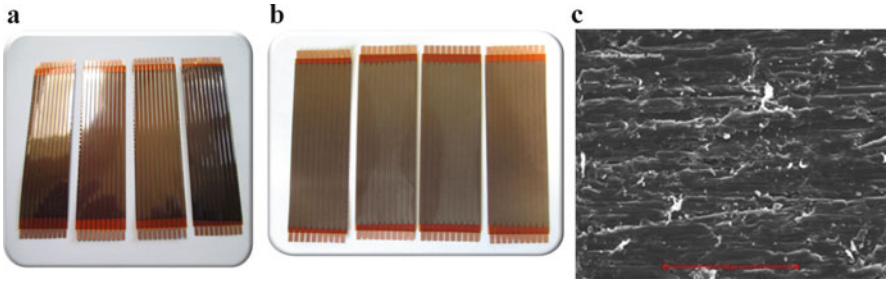

Fig. 2 Images of a number of FCCs demonstrating the shiny smooth appearance of the front side (**a**) and the matt, rough appearance of their back side (**b**). Surface morphology of the back side is shown in greater details in the scanning electron microscopy image in (**c**)

featureless, smooth surface, similar to a regular Kapton, while the matt back side, when analyzed at higher magnifications, demonstrated a highly developed surface morphology/roughness and significant contamination with small particles [1].

The back surface of the FCCs was found to be strongly eroded and contaminated (Fig. 2c). It was clarified with the FCCs manufacturer that the back surface was treated with water slurry containing tiny pumice particles under pressure (to enhance the bonding of copper stripes with an adhesive during FCCs' manufacturing). As a result of this treatment, the Kapton100HN back surface was eroded, with a significant amount of tiny pumice particles incorporated into the surface.

Pumice represents a regolith that is a volcanic rock with high concentrations of silica that has the chemical formula SiO_2. High amount of silica, together with some additional metal oxides, gives pumice usually its light-gray color.

The grayish color of the back surfaces, with various degree of darkness, is defined by the amount of pumice particles incorporated into the back surface of Kapton100HN that, according to the process diagram, is contaminated and eroded twice during the manufacturing process. This specifics, as well as the "grooved" character of both FCCs surfaces was causing problems, when the ion beam treatment process Carbosurf [2–4] developed for making space polymer films surfaces charge dissipative, was applied for FCCs.

Experimental Studies

Surface Analysis of FCCs: Back and Front Surfaces

A number of surface analytical techniques, such as SEM/EDS and XPS were used before and after various surface treatments and GEO imitation testing. In addition, such functional properties as surface resistivity and thermal optical properties have been also used in this study, using the devices and facilities, described in [2–4].

Ion Beam Surface Treatment of FCCs for Charge Dissipation

A special sophisticated version of ion bombardment with simultaneous surface renewal was developed and applied in this work for the treatment of both front and back surfaces of the FCCs units. The technological specifics of the process are based on a general approach, previously developed, patented, and studied in [5–7], in combination with the innovative Carbosurf ion-beam treatment of thin space polymer films, described in [2–4]. In all experiments, the FCCs have been taped over their edges to the surface of a rotating drum with a KaptonHN adhesive tape that covered in a proper way the external Cu contacts. The drum was placed inside a high-vacuum chamber with a liner-type gaseous high-power technological ion beam.

Since Kapton polyimide normally contains a significant amount of absorbed water vapor, special attention was paid to the outgassing procedure. High vacuum Carbosurf^{TM} treatment can be easily disrupted by the presence in the vacuum chamber of minor amounts of moisture due to samples dehydration and outgassing of trapped air bubbles. Each ion beam treatment run was conducted following a timely high vacuum outgassing stage, where the FCCs temperature was kept around 35 °C. During the ion beam treatment significant limitations appeared due to both temperature limitation caused by the sensitivity of the adhesive used for FCCs manufacturing, and due to drastic difference of the sputtering rate of the organics and lower rate of inorganic pumice inclusions on the back sides.

A very special approach was found, that allowed for successful ion beam surface treatment of both front and back sides of FCCs. This treatment, when performed at so called “surface renewal” [5] conditions, consisted of adding a pre-defined amount of carbonaceous gas to the ion beam source, in order to compensate surface sputtering caused by the ion beam. This approach allowed modifying both the front and the back side surfaces for surface carbonization, with very successful results and long-term stability at storage, i.e., long-time shelf life.

After one run, the SR was measured using a special SR probe unit following the procedure described in [8] and, if the achieved SR value was acceptable, the same FCCs have been taped back to the drum with the other side facing the ion beam, and the run was repeated, without influencing the results achieved on the already treated surface. The best treatment conditions have been found as a result of numerous TRIM software calculations and experimental trials [1].

Surface Resistivity of FCCs After Ion Beam Treatment

Comparative surface analysis of morphology and elemental composition has been performed on front and back surfaces of a number of FCCs in “as received” condition and after the treatment, as described above, using optical microscopy and SEM/EDS. It was shown that the front side of the treated FCC unit remains

shiny and the back surface appears matt, and the developed ion-beam treatment did not influence the surface morphology of the front surface, with both sides becoming darker in appearance.

The results of SR measurements on the front side averaged around 10 MΩ/sq for short units and ~8 MΩ/sq for long units, while the back-side values averaged around 18 MΩ/sq for both short and long FCCs, in full agreement with the values derived from the best results of experimental trials. In order to have enough ion beam treated FCCs for an extended Program of Space Specification, 50 short and long FCC units have been treated on both sides at the best treatment conditions.

Statistical values had been calculated for SR data on the FCC units for all 50 treated FCCs, separately for short and long units. Short and long FCC units' data had been statistically evaluated separately, since one SR measurement has been conducted on short units and three measurements on long ones. Average values and standard deviations had been calculated for the entire set of 33 short units and 17 long ones.

The average SR values for the front surfaces of all treated long and short FCC have been found to fall between 7.4 and 9.6 MΩ/sq, that are even lower than the 10 MΩ/sq, initially required at the beginning of this work.

The average SR values measured for the back surfaces were between 13.3 and 21.0 MΩ/sq. It is obvious, that the average SR values achieved for the back surfaces are approximately twice higher when compared to the corresponding averages of the front side. Although, while the differences between the smooth front and rough back surfaces, contaminated to various degrees (see Fig. 2b), could not be completely eliminated, it was possible to minimize their influence on the treatment results. This achievement should be considered as an exceptionally good outcome of the developed innovative treatment technology.

The calculated average values demonstrated exceptional stability of the measured SR values that deviated $<2\,\%$ of the initial values following at least 1 month of storage, and later extended up to 2–2.5 years of storage in laboratory conditions. We attribute these minor discrepancies just to the measurement accuracy of the SR values by the used contact method.

The developed technology allowed us to convert the electrically insulating FCCs' surfaces to fully charge dissipative ones, with time invariant surface resistivity properties stable in laboratory storage conditions. The results of long-term ground-based GEO imitating testing of the treated FCCs are presented in the next chapter.

GEO Simulation FCC Testing

Nonmetallic materials used in space systems are affected by electrons and protons in a broad energy interval, electromagnetic solar radiation (both the near and the far ultraviolet radiation), and X-ray radiation. The response of nonmetallic materials to

radiation depends on the type of radiation and its energy that defines the ionization losses density, and the radiation response of materials depends on these losses.

A range of GEO-imitating testing procedures have been practically used for a number of years by NASA, European Space Agency and Russian space professionals. However, a significant effort had been made for the last 12–15 years to develop an International Standard that finally resulted in publication of the latest version of "Space systems–Space environment—Simulation guidelines for radiation exposure of non-metallic materials" in 2010 [9].

GEO Imitating Testing Approach

Treated and original FCC units had been exposed to GEO-imitating environment using a unique testing facility. The GEO simulation facility was designed for studying physical–chemical properties of materials and coatings under separate and combined action of space factors that may influence the materials in GEO. Those factors to consider are vacuum as low as 10^{-5} Pa, electrons and protons with energies up to 50 keV, solar electromagnetic radiation up to 10 SEE (solar exposure equivalent) and temperature in the range of ±150 °C [3,4,8,10].

The sample holder table, 10 cm by 10 cm in size, is attached to a water cooled base, maintaining the temperature of tested samples mostly around 20 °C. Depending on the actual expected GEO exposure time, and the selected acceleration factor, the longevity of GEO simulation experiment can be defined by the computerized system for measurement, control, and monitoring. Functional properties of the tested materials are evaluated before and after the completion of testing using appropriate testing methodology, devices and measurement units in order to evaluate the effects of radiation exposure. Thermal-optical properties (such as solar absorptance and thermal emittance) are normally measured, as well as electrophysical characteristics such as surface and volume resistivity, if required.

Every set of FCC units had been placed in a special custom-made sample holder (as shown in Fig. 3) and subjected to combined irradiation consisting of protons, electrons and ultra-violet light. The first set of three FCC units had been subjected to 33 h of combined $p^+ + e^- + UV$ irradiation, with proton energy $E_p = 20$ keV, current density equal to $J_p = 5 \times 10^{11}$ s^{-1} cm^{-2}, electrons energy $E_e = 40$ keV, current density of $J_e = 5 \times 10^{11}$ s^{-1} cm^{-2} and with simultaneous UV exposure. The selected conditions correspond to a total proton fluence equal to $F_p = 6 \times 10^{16}$ cm^{-2} that roughly corresponds to 15 years of equivalent GEO exposure. Due to well-known limitations, accepted by the space materials community, the UV exposure was selected at 2 times the intensity of solar light. Temperature of the samples was kept around 52 °C during testing experiments.

Pictures of the tested samples had been acquired and surface resistivity measurements performed after intermediate timing of ~4 years, and then after final 15 years of space equivalent GEO exposure. Figure 3 shows the results of the intermediate and the final appearance of the samples. Apparent visual differences

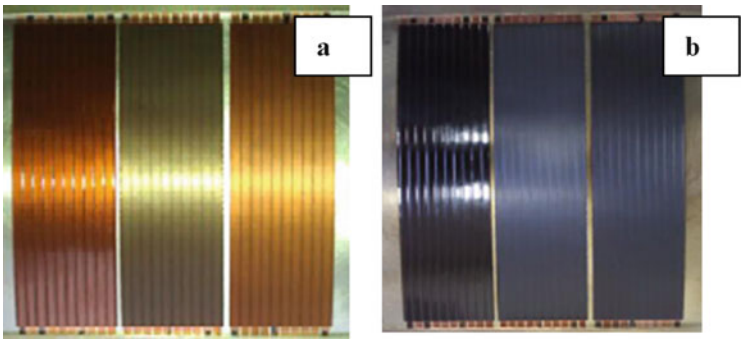

Fig. 3 FCC samples exposed to a GEO environment for ~4 (**a**) and 15 (**b**) space equivalent years

(the degrees of darkening) demonstrate the increasing effect of simulated GEO radiation on the surfaces of tested FCC units. It is obvious that both sides of pristine and ion-beam treated samples, exposed to GEO-simulating environment, become darker after 4 years, and finally strongly blackened after 15 years. The images in Fig. 3 clearly illustrate the visual differences between the front and back surfaces of tested FCC units—the front side of exposed FCCs looked almost black, but remained glossy, while back surface looked dark grey-blackish, bur remained matt.

The changes in quantitative characteristics of the ion-beam treated and GEO-tested units, such as surface resistivity and thermal optical properties, are discussed in details below.

Results and Discussion

Influence of GEO Environment on Thermal Optical Characteristics

Solar reflectance spectra have been measured for few treated and all tested FCCs, and solar absorptance values α have been calculated, based on these measurements.

The results for a pristine FCC sample #2, labelled 2Б for front glossy side and 2M for back matt side, are presented in Fig. 4, and the spectra and α values for both glossy front (1B) and matt back (1M) surfaces of an ion beam treated sample #1 are presented in Fig. 5.

From the comparison of the results, presented in Figs. 4 and 5, it is obvious, that the solar reflectance is always less on the darker back side, and the ion-beam treatment significantly decreased the solar reflectance, i.e., increase the solar absorptance, on both front and back sides, influencing the back surface comparatively more than the front one. It is clearly seen that the ion-beam treatment reduced the reflectance in both visible and near infrared spectral regions. The thermal emittance measurement results did show insignificant change of ε on both surfaces

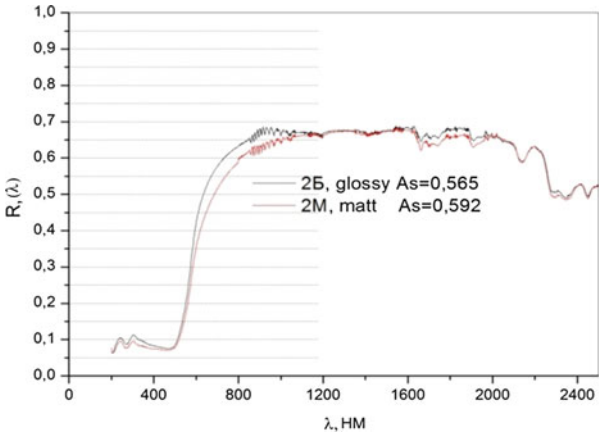

Fig. 4 Solar reflectance spectra and solar absorptance values for glossy front (2B) and matt back (2M) sides of the pristine FCC sample #2

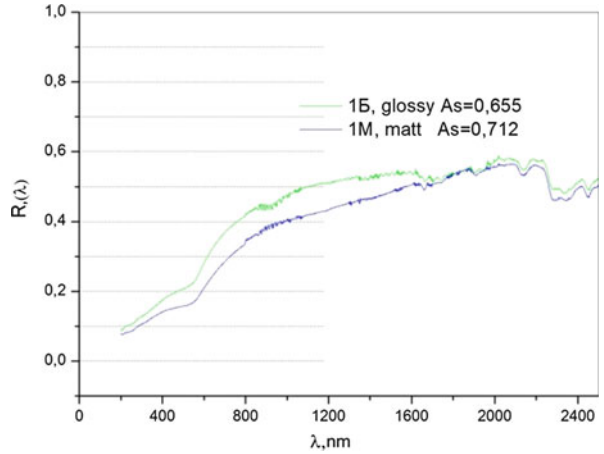

Fig. 5 Solar reflectance spectra and solar absorptance values for glossy front (1B) and matt back (1M) surfaces of an ion-beam treated FCC (sample #1)

due to ion-beam treatment, and all these thermal optical results are presented in Table 1.

It is easy to derive, that the change in solar absorptance due to the performed ion-beam treatment for front FCC surface is around $\Delta\alpha_s = 0.09$, and for the back surface it is around $\Delta\alpha_s = 0.12$. The thermal emittance measurements did not show any measurable change after ion-beam treatment. Similar trends and even close numerical values have been shown in [2–4] after the ion-beam treatment of Kapton100HN thin film.

It was very important to define the final thermal optical properties for both front and back surfaces of pristine and ion-beam treated FCCs (Fig. 6), in order to provide the forecast of their potential end-of-life (EOL) properties after 15 years in GEO space environment. The solar absorptance on the exposed pristine and treated surfaces increased in both visible and infrared areas, coming to $\alpha_{front} \approx 0.79$ for front of a pristine sample (#1) and to $\alpha_{back} \approx 0.82$ for the back of a pristine

Table 1 Thermal optical characteristics of ion-beam treated (#1) and pristine (#2) FCCs (before GEO imitating testing)

#	1Б	1М	2Б	2М
Side	Glossy (front)	Matt (back)	Glossy (Front)	Matt (back)
α_s	0.655	0.712	0.565	0.592
ε	0.82	0.83	0.83	0.83

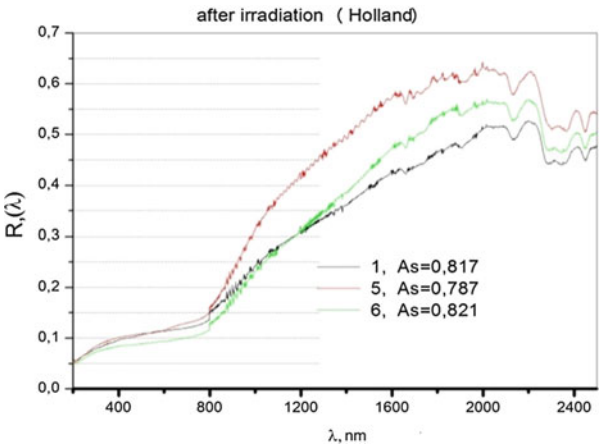

Fig. 6 Solar reflectance spectra and solar absorptance values for the first set of FCCs as a result of GEO testing at 15 years GEO space equivalent

sample (sample #5) and $\alpha_{back} \approx 0.82$ for the back surface of an ion beam treated FCC (sample #6) due to long-term GEO-simulated exposure. Thermal emittance measurements showed insignificant changes, with the thermal emittance remaining around $\varepsilon = 0.80 \pm 0.02$.

It is clear, that for ion-beam treated sample the solar reflectance dropped also in both visible and infrared areas and the solar absorptance increased up to almost the same values for front and back surfaces, as for pristine GEO tested FCCs! Thermal emittance changed insignificantly, remaining around $\varepsilon = 0.80 \pm 0.02$. The thermal optical characteristics, measured in this study, are collected and presented in Table 2.

A conclusion can be made, that the developed ion-beam treatment does increase the solar absorptance of the treated FCCs surfaces; however, it practically almost does not have an influence on the final thermal optical characteristics of the FCCs after 15 years in GEO space environment! The darkening effects in pristine and ion-beam treated surfaces and the change of the thermal optical characteristics are almost equally strongly pronounced on both sides of pristine and ion-beam treated FCCs.

It is important to note that the 50 treated FCCs, mentioned above, have been used to establish and successfully accomplish an extended Program of Space Specification that included a variety of tests, required for certification of the treated Flexible Cable Conductors for Solar Arrays in long-term GEO environment applications. The results will be presented in additional publication(s).

Table 2 Thermal optical characteristics of a pristine, ion-beam treated, and GEO tested FCC samples from the first set

Sample ID	Side	Solar absorptance α	Thermal emittance ε	α/ε
Pristine	Front	0.565	0.81	0.70
	Back	0.592	0.80–0.81	0.74
Ion-beam treated	Front	0.691–0.695	0.79–0.80	≤0.88
	Back	0.712–0.714	0.80	≤0.89
GEO-tested	Front	0.787	0.78–0.82	1.01
	Back	0.817–0.821	0.79–0.81	≤1.04

For all GEO simulating tested pristine FCCs, after both 4 and 15 years GEO space exposure equivalents, the SR values of the front and the back surfaces exceeded 10^5 MΩ/sq, or 10^{11} Ω/sq, i.e., remained fully insulating. For the second tested set, a decrease in measured SR values was indicated on all ion-beam treated samples after 15 years GEO space equivalent ground-based testing. Since the processing of results of GEO simulation effects on surface resistivity was not finished at the time of this paper preparation, the full results will be published elsewhere..

Conclusions

An innovative ion-beam treatment process with simultaneous surface renewal (IB/SSR) was developed at ITL and successfully used for treatment of both sides of space-bound FCCs. The results of SR measurements of the front FCC sides averaged around 10 MΩ/sq for short FCC units and around 8 MΩ/sq for long units. The SR values for back sides averaged around 18 MΩ/sq for both short and long FCCs. These values remained unchanged during ~1 month storage of the treated FCCs at lab conditions, and after a following 2–2.5 year's storage. Extended long-term ground-based GEO environment simulation testing experiments (15 years space equivalent) that involved simultaneous exposure to all three GEO environmental factors, i.e., protons, electrons, and UV have been performed on two specially selected FCC sets. These sets included pristine and IB/SSR-treated FCCs, and radiation exposure was done for both front and back FCC surfaces. It was demonstrated that the surface conductivity obtained on the insulating space polymer films is almost insensitive to space radiation during the 15 years in GEO. It was also shown that the long-term influence of GEO radiation on thermal optical characteristics of both FCCs sides does not significantly differ for pristine and ion-beam treated samples.

References

1. Iskanderova Z, Kleiman J (2011) Ion-beam treatment technology for space FCC's to provide charge dissipative surfaces resistant to GEO environment. Final report to airbus defence and space, contract G30/4509250924, ITL—020911-11021
2. Kleiman JI, Iskanderova Z, Issoupov V, Bussieres F (2008) CARBOSURF™—surface modification technology for charge dissipative and RF-transparent GEO durable space polymers. In: Proceedings of the 9-th international conference "Protection of materials and structures from space environment", Canada. pp 588–599
3. Iskanderova Z, Kleiman J, Bussieres F, US Patent No. 9,174,396 B2, Nov 3, 2015
4. Kleiman JI, Iskanderova Z, Bussieres F, Grigorevskiy A, Sodhi R (2013) Ion-beam treatment for enhancement of durability and surface conductivity of space polymers: results, analysis, mechanisms. In: Kleiman J, Tagawa M, Kimoto Y (eds) Protection of materials and structures from the space environment, Astrophysics and space science proceedings 32. Springer, Berlin, pp 317–326
5. Arifov UF, Iskanderova ZA, Radzhabov TD (1975) Method of multilayered structures formation by simultaneous or alternating films deposition and ion bombardment. Patent of USSR, # 471631, 25 May 1975 (In Russian) (*Арифов* UF,. *Искандерова* ZA, *Раджабов* TD (1975) *Способ получения многослойных структур*, Патент СССР №471931, 25.05.1975)
6. Iskanderova ZA, Radjabov TD, Arutunova EO, Rakhimova GR (1985) Thin film simultaneous deposition on membrane surface for permeability increase of gas being implanted (theoretical consideration). Vacuum 35(1):5–8
7. Iskanderova ZA, Radjabov TD, Leiderman RYu, Tukfatullin FK (1988) A model of a combined film deposition and ion bombardment for coatings formation. In: Proceedings of MRS fall meeting, vol 128
8. International Standard ISO 15856:2010(E), Space systems–space environment—simulation guidelines for radiation exposure of non-metallic materials
9. ASTM Standard D257-99, Standard test methods for DC resistance or conductance of insulating materials. V.15.03
10. Smirnov IA (2006) Radiation-induced conductivity of polymers at long-time radiation exposure). PhD Thesis, Russia (In Russian) (Смирнов, Игорь Александрович (2006) Радиационная электропроводность полимеров при длительном облучении)

Research of Contamination Prevention in the Whole Process of Lunar Samples Transfer

Danming Li, Qipeng Wu, Xiaojing Sun, and Guangliang Zhang

Abstract According to the China's lunar exploration program, in its third phase lunar samples will be collected and returned to Earth. An extensive research was conducted on the contamination prevention measures and the development of the requirements for protection and contamination prevention of lunar samples in the course of opening the samples' packaging device after its return to Earth, transfer and storage of the samples, preparation and analysis of the samples and so on. At the same time, we present a design concept of the most important ground facility for opening the device and re-packaging the samples in Lunar Sample's Preservation and Processing Laboratory. Analysis and calculating of the key technical index of the environment requirements for contamination prevention were also accomplished.

Keywords Lunar samples protection • Contamination prevention • Lunar exploration

Introduction

One of the important tasks of lunar exploration is to collect the moon soil and rock samples on the surface of the moon, to seal them in good condition and to bring them back to Earth for further scientific research. According to the China's lunar exploration program, this goal will be achieved by collecting the lunar samples

D. Li (✉)
Lanzhou Institute of Physics, Lanzhou 730000, China

Science and Technology on Material Performance Evaluating in Space Environment Laboratory, Lanzhou, China
e-mail: lidanming@sina.com

Q. Wu • X. Sun
Lanzhou Institute of Physics, Lanzhou 730000, China

G. Zhang
National Astronomical Observatory, Chinese Academy of Sciences, Beijing, China

J. Kleiman (ed.), *Protection of Materials and Structures from the Space Environment*, Astrophysics and Space Science Proceedings 47,
DOI 10.1007/978-3-319-19309-0_23

automatically in unmanned expedition conditions and taking them back to Earth before or after 2017 [1].

The lunar environment includes high vacuum and high temperature conditions. The lunar samples to be collected from the surface of the Moon were exposed to the lunar environment conditions for billions of years. In order to guarantee that their scientific value would not be affected after being collected and returned to Earth, the lunar samples must be preserved under special conditions, to avoid the exposure to any living organisms on Earth, water, oxidation conditions and so on, so as to keep the samples in original state. Once the sample is exposed to the Earth's atmosphere, it would react with the air. For example, superfine elemental metallic iron in lunar samples would react with oxygen and produce rust; glass and minerals could combine with the water in the air to form clay [2]. So a specially equipped laboratory must be designed for preservation and processing of the lunar samples that will be ready to accept them upon return to Earth to ensure that the samples are protected from the contamination effects of Earth environment. The laboratory conditions will allow for processing, storage and research the lunar samples in their original state. The construction principles of such laboratory may refer to the world's leading sample preservation and processing laboratories such as the Apollo lunar samples laboratory, the Meteorites processing laboratory [3], etc. with an example shown in Fig. 1.

Contamination Prevention Measures

In order to successfully accomplish the third phase of China's lunar exploration program the following tasks need to be accomplished:

1. Collect the lunar samples and seal them on the surface of the moon automatically in a contamination-free, nondestructive way and without affecting their structure.
2. Return the lunar samples safely back to Earth.
3. Open the sample's container and keep them in a contamination-free environment. Ensure that the samples are not affected or modified by preventing any possible destructive and degenerative applications.

The amount of the lunar samples that will be collected in China's lunar exploration program is expected to be very small, making them extremely precious and with an immeasurable value. In order to ensure they are not affected by various factors after collecting and before returning to Earth and to keep the samples in their original state, with all their chemical and physical properties preserved to the greatest extent possible, they should be sealed in a specially designed device which has extremely low leakage rate. It's required that the leakage rate of the automatic packaging and sealing device (as shown in Fig. 3) should be less than 5×10^{-11}Pa·m^3/s. After being returned to Earth, the packaging and sealing device with the lunar samples must be transferred, unlocked and stored in a contamination-

Fig. 1 A corner of the meteorite processing laboratory in USA

free environment. A scientific, strict, complete workflow must, therefore, be developed to make sure that all contamination factors are strictly controlled under the specified level.

Workflow of the Lunar Samples' Ground Application System

After the lunar samples being returned to the Earth, we would start the whole ground processing workflow which is mainly divided into six stages. The main work contents included in each stage are as follows:

1. Samples handover and transshipment: remove the lunar samples' packaging and sealing device in complete packaging from the lunar module and put it in the special transport box. The box will be placed on a special car, delivered to the ground application facility and transferred to the sample preservation and processing laboratory.
2. Opening of the automatic packaging and sealing device: After the device was transferred to the lunar sample's preservation and processing laboratory, it would be opened there and the lunar samples will be re-packaged. In next step, all of the samples would be collected.
3. The samples description and separation: After being unpackaged, the lunar samples would be roughly separated, and each part would be described and packed into various bags in the same facility.

4. The samples storage: After being roughly separated, the samples would be put in the storage area, waiting for further careful separation, handling, preparation and analysis.
5. The samples preparation: Initial description of the samples' characteristics will include particle size evaluation using a microscope. The samples will be stored in different nitrogen-filled cabinets for following preparation steps such as grinding, cutting, molding, etc.
6. Analysis of the samples: The analysis will include evaluation of samples' physical properties, chemical composition and structure.

The Contamination Protection Requirements during Ground Processing and the Relevant Main Facilities

It's required to maintain strict protective measures against contamination during the whole process of lunar samples being processed and stored on the ground [4]. At the stage when the samples are stored in cabinets filled with high purity nitrogen, the humidity and oxygen concentrations must be controlled. It's required that the oxygen concentration will be less than 20mol per million mole of nitrogen, and the water concentration be less than 50mol, with the requirements to the cleanliness level of the internal environment of the operating cabinet be higher than level 100. So the relevant facilities used in the ground processing of lunar samples must be equipped with clean rooms and have supplies of high purity nitrogen and clean vacuum environments.

The main facilities and devices to be used in the whole process on the ground must consist of:

1. Samples' transfer facility in a special truck equipped for transfer and transport of the lunar samples' packaging and sealing device. A vacuum system set on the truck is needed;
2. Facility for opening the device and re-packaging of the samples;
3. Samples storage cabinets;
4. Samples' boxes and transfer cases;
5. Nitrogen-filled cabinet and internal operation platform;
6. Samples' packaging facility;
7. High purity nitrogen gas supply facility, etc.

The Requirements for Selection and Control of Materials Used in the Facilities

The materials in the storage and processing facilities could release substances potentially contaminating the lunar samples. The external pollutants may penetrate the wall material of the laboratory, especially water and oxygen molecules. So the

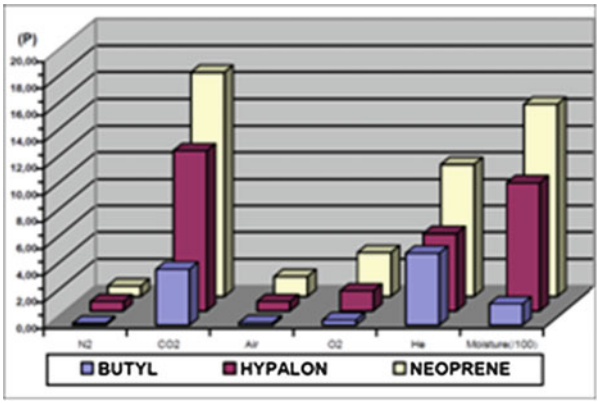

Fig. 2 The bar diagram of gas permeability for three types of glove materials for vacuum use

selection of materials needs to be controlled strictly. The principles for material selection are as follows:

1. They should have low vacuum outgassing rates;
2. They should have lower water, oxygen and organic matter release rates;
3. They should have lower adsorption characteristics;
4. High ability of prevention for water and oxygen penetration.

For example, in the choice of materials of the operating gloves, we need to study and evaluate the gas permeability of materials, as shown in Fig. 2.

The Design Concept of the Ground Facility for Opening the Lunar Samples' Packaging Device and Re-packaging the Samples

As mentioned before, the leak rate of the automatic packaging and sealing device should be less than 5×10^{-11} Pa·m^3/s. To prevent higher leak rates, the device was designed and built employing extremely delicate mechanical structural and sealing technology concepts. Because the whole process of packaging and sealing lunar samples should be done automatically on the moon, it implies that the device by itself is an extremely complicated vacuum system. That greatly increases the difficulty of the design of the ground facility for opening the device. The questions of how to open the device with the lunar samples while keeping them in the original state, and how to transfer the unsealed lunar samples to other devices and facilities where they will be processed or stored under the condition of vacuum or high purity nitrogen environment, are very complicated and difficult to tackle. Therefore, the facility for opening the device and re-package the samples is a very important ground application facility. This paper focuses on the design of this facility.

Fig. 3 The automatic packaging and sealing device for transportation of lunar samples developed by Lanzhou Institute of Physics

In recent years, the Lanzhou Institute of Physics has investigated and developed the lunar samples' automatic packaging and sealing device. The device adopts vacuum sealing technology, which contains the collected lunar samples under the condition of ultra-high vacuum environment on the moon. It is designed to keep the lunar samples in the original vacuum environment. The device is shown in Fig. 3.

Our research group has also successfully developed the facility for storing and handling the lunar samples upon their delivery to Earth. The facility can maintain a certain environment for contamination prevention, and it is shown in Fig. 4. Based on part of its design concept, recently we have designed the structure of the ground facility for opening the lunar samples' automatic packaging and sealing device and re-package the samples, as shown in Fig. 5. In the mean time we have studied the key mechanical mechanisms for opening. All of the design would meet the requirements of opening the lunar samples' device and re-packaging the samples without being polluted by the terrestrial environment, analyzing the gases released from the lunar samples in-situ, separating, packaging and transferring the unsealed samples.

Analysis of the Key Environment Technical Index for Every Contamination Prevention Facility

In the condition of normal atmospheric pressure (1atm), the molecular number N_A (Avogadro's constant) of any gas in 1mol is 6.022×10^{23}, the molecular number n_0 of any gas in 1 m^3 is 2.687×10^{25} (Loschmidt constant). Under normal temperature, the molecular number of nitrogen at a pressure of 1 atmosphere is:

Fig. 4 The device for storing and handling back samples, which could maintain a certain environment for contamination prevention

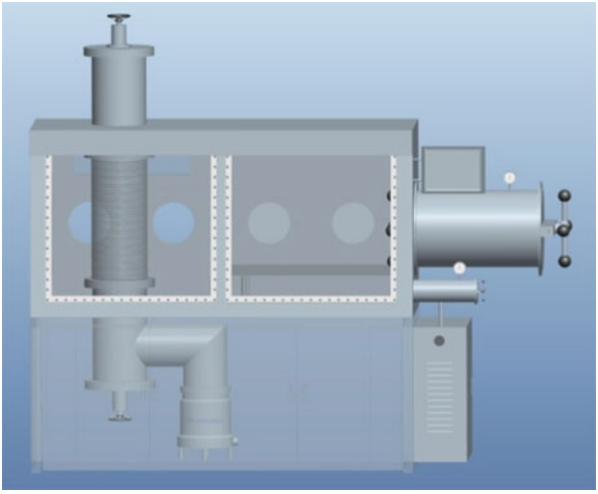

Fig. 5 The structure of the ground facility for opening the packaging and sealing device with lunar samples and re-packaging the samples

$$n_{N2} = 2.687 \times 10^{25}/\mathrm{m}^3 = 0.446 \times 10^2 \mathrm{mol} \cdot \mathrm{m}^{-3} \quad (1)$$

Assuming that the content of water vapor in the high purity nitrogen is 50 ppm, and oxygen is 20 ppm, the corresponding molecular number of water vapor and oxygen are:

$$n_{H2O} = 0.446 \times 10^2 \,\text{mol} \cdot \text{m}^{-3} \times 5 \times 10^{-5} = 2.23 \times 10^{-3} \,\text{mol} \cdot \text{m}^{-3} \quad (2)$$

$$n_{O2} = 0.446 \times 10^2 \,\text{mol} \cdot \text{m}^{-3} \times 2 \times 10^{-5} = 8.92 \times 10^{-4} \,\text{mol} \cdot \text{m}^{-3} \quad (3)$$

Accordingly, the molecular number of oxygen per unit volume in vacuum environment should be less than 8.92×10^{-4}mol·m^{-3}. Volume percentage of oxygen in atmosphere is 21%, so the molecular number percentage of oxygen in the condition of normal atmospheric pressure is 21%. Ignoring the calculation error which was brought by selective extraction of the vacuum pump at mid-high vacuum range for different gases, and considering the existence of water vapor molecules, it could be thought that under this condition the maximum molecular number percentage of oxygen is 21% (calculations below is based on this value).

According to the gas pressure formula:

$$p = n \cdot k \cdot T \quad (4)$$

p—pressure of the gas, [Pa];
n—density of the gas, [m^{-3}];
k—Boltzmann's constant, 1.38×10^{-23} J/K;
T—thermodynamic gas temperature, [K].

Aiming at a series of typical vacuum pressure, we have calculated the total molecular number of gases and the molecular number of oxygen per unit volume, which are shown in Table 1.

Considering the gas leakage rate of the vacuum chamber where the lunar samples will be unpacked, outgassing of various materials and the high reliability requirements of the lunar exploration plan, we choose the pumping system to consist of the main turbo molecular pump and the front pump a dry mechanical vacuum pump. The limit pressure of the dry vacuum pump is generally 0.1Pa~10Pa, backing pressure of the turbo molecular pump is 10^{-1} Pa, and the limit pressure of the turbo molecular pump is less than 10^{-8} Pa. Based on the calculation of possible gas load, this configuration could ensure that the pressure in the vacuum chamber is less than 5×10^{-2} pa, so the maximum molecular number of oxygen is 4.2×10^{-6} mol·m^{-3}, which completely meet the requirement that the molecule number of oxygen is less than 8.92×10^{-4}mol·m^{-3}(see formula (3)).

In addition, it is also required that the molecular number of water vapor in the vacuum environment per unit volume is less than 2.23×10^{-3} mol·m^{-3} (see formula (2)). Because water vapor is difficult to pump out from the vacuum chamber compared with other gases, it should be specially taken into consideration. If the work pressure in the vacuum chamber for unpacking the lunar samples is at about 5×10^{-2}pa, then according to the experience, the gases in the container are mainly nitrogen, water vapor, carbon dioxide and oxygen, whereby the proportion of water vapor is about 20%. So it could be calculated that the partial pressure of water vapor is 1×10^{-2} Pa.

Table 1 The total molecular number of gases and the molecular number of oxygen per unit volume under different vacuum pressure

Vacuum pressure (Pa)	10	1	1×10^{-1}	5×10^{-2}	1×10^{-2}
The total molecular number of gases per unit volume in vacuum ($mol\cdot m^{-3}$)	4.0×10^{-3}	4.0×10^{-4}	4.0×10^{-5}	2.0×10^{-5}	4.0×10^{-6}
The molecular number of oxygen per unit volume in vacuum ($mol\cdot m^{-3}$)	8.4×10^{-4}	8.4×10^{-5}	8.4×10^{-6}	4.2×10^{-6}	8.4×10^{-7}

According to the formula (4), it could be calculated that the molecular number of water vapor is 4×10^{-6} $mol\cdot m^{-3}$, when the work pressure in the unsealing vacuum chamber is 5×10^{-2} pa, which meets the requirement that the molecular number of water vapor should be less than 2.23×10^{-3} $mol\cdot m^{-3}$.

Summary

Because the collection and returning of the lunar samples are extremely difficult and high cost tasks, the samples are very precious. In order to ensure that the lunar samples are processed, stored, and researched in their original state, careful planning of whole process is required, including all stages of transportation, opening, storage, protection and control of contamination.

Based on the basic research conducted in these areas a plan for the design and construction of a special laboratory was developed for achieving and maintain environment in which the lunar samples could be stored and processed. With the related planning and national investment, we confidently can finish the construction of the laboratory for preservation and processing the lunar samples on time.

References

1. Peijian Y, Ke P (2006) Deep space detection and the outlook of explorations of China [J]. Chin J Eng Sci 8(10):212–215
2. White DR, Lyndon B (1976) Apollo experience report—lunar samples processing in the receiving laboratory high vacuum complex. Johnson Space Center, NASA, Houston
3. Mangus S, Larsen W (2004) Lunar receiving Laboratory Project History. NASA, Houston
4. Sears D, Allen C, Britt D, Brownlee D et al (2004) The Hera mission: multiple near-Earth asteroid samples return. Adv Space Res 34:2270–2275

The Research of Lunar Dust Environment Influence and Design of a Simulation System

Man Li, Dongbo Tian, Zhihao Wang, Yu Bai, Yu Li, and Qiang Yu

Abstract Lunar dust plays an important part in Lunar Exploration Program. It could influence normal operation of thermal control materials, optical cameras, optical sensors and other aircraft components and even seriously damage the solar arrays electrical generation by reducing their working efficiency. In this paper, a review of the lunar dust environment interaction with materials affecting thermal control system faults, seal failures, material wear, mechanisms' failure, and electrostatic effects are discussed. It summarizes lunar dust characteristics including particle size distribution, density, chemical composition, abrasion, adhesion, cohesion. At last, it summarizes the problems associated with lunar dust suspension caused by lunar rover operation. The results of this research are important in future lunar exploration missions and in development efficient space material protection technologies.

Keywords Lunar dust • Environment influence • Lunar dust characteristic • Simulation system

Introduction

Apollo 17 astronaut Harrison Schmitt said at a lunar simulation workshop in 2005 that "Dust is the number one environmental problem on the moon" [1]. After only hours on the lunar surface, the Apollo astronauts observed that lunar dust was the source of certain aggravating operational problems. They reported that it had the capacity to get everywhere. The O-ring seals of their suit gloves and helmets became "bogged down with dust," and dust interfered with their mechanical pulleys and zippers [2].

M. Li (✉) • D. Tian • Z. Wang • Y. Bai • Y. Li • Q. Yu
National Key Laboratory of Science and Technology on Reliability And Environmental Engineering, Beijing Institute of Spacecrafts Environment Engineering (BISEE), Beijing, China
e-mail: liman8319@126.com

J. Kleiman (ed.), *Protection of Materials and Structures from the Space Environment*, Astrophysics and Space Science Proceedings 47,
DOI 10.1007/978-3-319-19309-0_24

Lunar Dust Environment Influence

Contamination on Material Surfaces

Lunar dust particles quickly adhere to all kinds of surfaces with which they come into contact, including the boots and gloves of astronauts, radiators, solar panels, etc. and, after adhering to such surfaces, these particles cannot be removed easily. The adhesive force of lunar dust to a metal surface (e.g., aluminum) is, generally, 200 ~ 300 Pa and for metal painted surfaces it can reach values around 1000 Pa.

The lunar dust can contaminate thermal control surfaces, cause changes in solar absorptivity and thermal emissivity, and lead to faults in the temperature control system. For example, the solar cell arrays are among the components that are most easily influenced by lunar dust. During the tasks carried out on Apollo 11, the surface of the cable which was connected to the television camera was covered by lunar dust, making it impossible to see it and, on several occasions, causing astronauts to trip and stumble. During the tasks carried out on Apollo 12, lunar dust settled on optical lenses and affected seriously their performance.

Thermal Control System Faults

If lunar dust adheres to the radiator surface, this may result in major faults in the thermal control system since it greatly enhances the absorption capacity of the radiator surface for visible and ultraviolet light. The relationship between the dust coverage rate and absorptivity is strongly nonlinear, when dust coverage rate reaches 11 %, absorptivity increases by 100 %.

The temperatures at 5 temperature measurement points on the Apollo 12 lunar module were about 38 °C higher than expected. As a result of performance reduction in the radiator, the battery temperature of the Apollo 15 lunar rover increased by 38–43 °C. The Apollo 16 and 17 also experienced various levels of overheating with their lunar rover batteries.

Seal Failure

Due to lunar dust, the seals in the space suits for astronauts of Apollo 12 were damaged, and the rate at which the pressure decreased within the space suits was more than expected. Commander Charles Conard's space suit was worn after the first walk on the moon and the leakage rate was about 1 kPa/min, which was up to 17 kPa/min after the second walk on the moon. In addition, due to lunar dust, seal failure occurred in every single vessel which had been used to store samples.

For manned moon landing projects, failures in the seal function of the space suits or the lunar module are an enormous threat both to the safety of the astronauts and to the success of the mission tasks as a whole.

Material Wear

Astronaut Pete Conrad once reported that his space suit was worn out only after 8 h of work on the surface of the moon. During the training on Earth, the space suit would be worn after 100 h of usage. However, he later found that the micrometeoroid protective layer around the boots of their space suits had been penetrated down to the Maylar fiber insulating layer. In completing the tasks of Apollo 16, astronauts cleaned the instrument dials on the lunar vehicle to which lunar dust had adhered with a brush. It turned out that several dials were seriously worn out and couldn't be read. The clarity of the spacesuit helmet visor of astronaut Harrison Schmitt became blurred as a result of abrasion by lunar dust, and he even could not see through his helmet from some angles.

Failure Mechanisms

Experience suggests that mechanisms in the space suit will immediately become jammed even if the astronauts only stop for just a moment in a place where lunar dust is raised from the surface forming a cloud. Every astronaut who has landed on the lunar surface had experienced this. In a few extreme cases, jamming in the space suit mechanisms has caused the emergency termination of walks on the moon and in some cases the mechanisms have become permanently jammed rendering them unusable.

Vision Shielding

The formation of lunar dust clouds makes it difficult to find the landing location, in turn making it more difficult to land on the moon and return to Earth. The astronauts of Apollo 11 once reported that as the lunar module descended, the visibility outside the lunar module constantly reduced and the minimum visibility went down to $<$100 ft. This problem was especially obvious when the Apollo 12 mission carried out its tasks. The astronauts could not see anything in the several seconds prior to landing, directly causing a support pole of the lunar module to fall into a pit. The following Apollo moon landing applied steeper descending trajectories for the landing of the lunar module. This resulted in an improved view during landing,

but the flying dust still had a great influence on visibility in the several seconds prior to touching down.

For our manned moon landing projects, the dust clouds raised during the landing of the lunar module may result in the astronauts being unable to clearly see the landform outside, thus affecting manual operation by the astronauts during landing. Furthermore, astronauts activities on the moon, while walking and working on the lunar surface, may cause lunar dust to lift from the surface and adhere to the masks of the astronauts, making them unable to see clearly and thus affecting the completion of the tasks on the lunar surface as well as their safety.

Electrostatic Effects

Lunar dust charging can affect the charge and discharge phenomena of the moon landing equipment and can affect electronic parts and components in the equipment. Electric charge accumulation of the electrophorus lunar dust may result in electric leakage and partial discharge of the solar cell array, and thus cause abnormality in, and even damage to, the solar cell arrays. Meanwhile, lunar dust electrification will strengthen the adsorption characteristics of lunar dust and aggravate contamination.

Johnson and others from George C. Marshall Space Flight Center calculated and analyzed the distribution characteristics of dust blown by the landing engine, including the calculation of the coverage degree of dust blown by the landing engine on surrounding instruments and equipment. They also analyzed the harm that lunar dust contamination can cause to the optical mirrors.

Lunar Dust Characteristics

Several of the most important physical properties of the dust are discussed below. These properties are: particle size distribution, density, chemical composition, abrasiveness, adhesion, and cohesion.

Particle Size Distribution

Extensive research has been conducted on samples of lunar dust collected during the Apollo missions. One typical set of data showed that the particle size distribution for lunar dust ranged from <0.2 μm to over 400 μm in diameter [3].

Density

The density of lunar dust ranges from approximately 1.0–2.0 gram per cubic centimeter (g/cm^3) [4]. The team assumed an average density of 1.5 g/cm^3.

Chemical Composition

The dust particles are composed of various oxides with silicon oxide, aluminum oxide, calcium oxide, iron oxide, and magnesium oxide accounting for more than ninety percent of the composition of the dust [5].

Abrasion

Hardness and the shape of the particles are the most important factors influencing abrasiveness. Since the oxides in lunar dust are very hard and the particles have many sharp edges, the dust is very abrasive.

Adhesion

The adhesion of lunar dust to a surface is mainly due to electrostatic forces. For large dust grains, these forces are due to an electrostatic dipole moment. The dipole moment creates an induced mirror charge on the surface to which the dust is adhered.

Cohesion

Cohesion of dust particles is also the result of electrostatic forces. Cohesion on the order of 1000 Newtons per square meter (N/m^2) was indicated from data collected on the Apollo15 mission.

Design of the Simulation System of Lunar Dust Suspension Caused by Lunar Rover Operation

Lunar dust is one of the extreme environmental conditions of lunar environment. Most of the lunar dust consists of particles in the micrometer scale and has strong absorption and permeability characteristics. Lunar dust particles have sharp edges

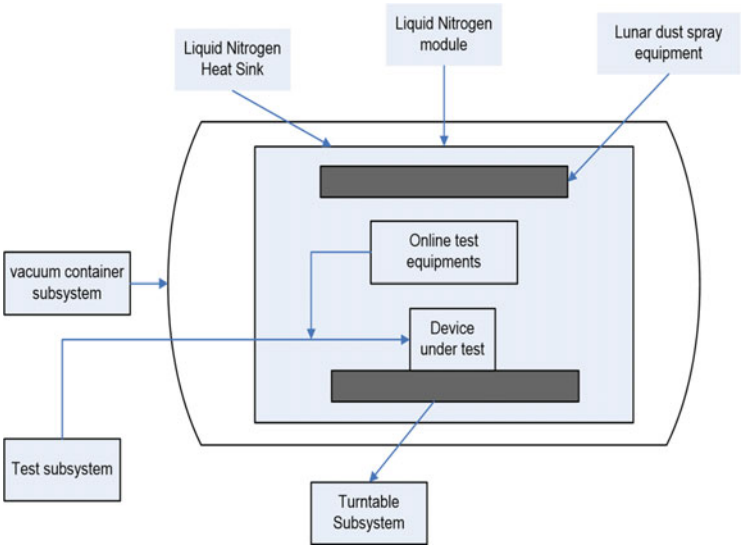

Fig. 1 The configuration of environmental simulation system

with a strong abrasive action. In vacuum radiation environment, lunar dust particles are also charged. Lunar Landers and lunar rover in lunar exploration phase will be inevitably affected by the lunar dust. All these factors affect the level of testing and validation of the equipment in ground testing before it can be confirmed that the equipment will survive the lunar dust environment adaptability and tolerance.

Based on the lunar environment surrounding a moving lunar rover, the environment simulation system is divided into three parts: the vacuum container subsystem, turntable subsystem and test subsystem. As shown in Fig. 1.

The Vacuum Container Subsystem

The vacuum container subsystem consists of vacuum container, vacuum tubes, heat sink and a liquid nitrogen module. Vacuum container and tubes are the main body of the environment simulation system providing a working vacuum not $<4 \times 10^{-3}$ Pa. The liquid nitrogen heat sink equipment will provide low temperature environment. The liquid nitrogen used in heat sink equipment will be provided by liquid nitrogen module. Crude pumping units and low temperature pumps will be used to obtain and maintain the required vacuum. Test subsystem will be connected with vacuum container subsystem to control the flow of liquid nitrogen module, temperature, vacuum measurement and control indicators.

Turntable Subsystem

The Turntable Subsystem is used for investigating the lunar dust suspension caused by lunar rover wheel operation. Temperature range of the working environment is from 0 to 120 °C. The Turntable Subsystem designed in the shape of a disk, 1200 mm in diameter and 150 mm high. Driven by a drive mechanism it can rotate in both directions in the horizontal plane. At the same time, the rotation of the lunar rover wheel in both directions can be conducted in the vertical plane. The turntable is vacuum sealed to keep the lunar dust interacting with the moving lunar rover wheel. A stress application system is used to simulate the weight of the lunar rover on the wheels. The driving mechanism consists of two parts, one for the operation of the turntable drive and the other for operating the rover wheel drive. The wheel drive can be used in two drive modes, i.e., one is rotating around its own bearings, and the other is contained in the dust turntable disk surrounding the central wheel axis. The center of the support structure can be locked, with the capability of working under low temperature in a vacuum.

Test Subsystem

The velocity field is evaluated through particle image velocimetry (PIV) measurements. Particle image velocimetry can be used for providing two-dimensional or three-dimensional velocity fields of the transient measurements. PIV system can observe the details of the flow field to obtain information on the spatial structure flow field.

According to the literature data, a single charge on dust particle can reach 10^{-14} C. So the precision of the power consumption meter has to be enough to record the 10^{-14} C charge. The evaluation of lunar dust charging is done by using a Faraday cup. The size of the Faraday cup must allow for easy measurement of charge of a single lunar dust particle, but at the same time has to meet the test chamber volume requirements. The power measurement device also has a communication interface with the terminal computer, so that it can automatically measure and collect data.

Focused beam reflectance measurement instrument (FBRM) probe is used for evaluation of particle's size and number. The FBRM can be used with particle flows of any density and viscosity. The probe, using a focused laser beam, scans the particles passing by the probe windows. FBRM can be highly sensitive and accurate measurement of particle size and particle number changes.

Conclusions

The study on lunar dust environment effects is one of the most important research directions of lunar exploration and lunar excursion all over the world and in China. The paper summarized the lunar dust characteristics, lunar dust environment effects and the conceptual design of the simulation system of lunar dust suspension caused by lunar rover operation. This study is still in the early stages of design in China and could provide the test platform for the design of lunar spacecrafts and lunar rovers.

References

1. Schmitt H (2005) The Apollo experience/problems encountered with lunar dust. Biological Effects of Lunar Dust Workshop, Sunnyvale, CA
2. Apollo 12 Technical Crew Debriefings (U) (1969) Manned Spacecraft Center, Houston TX, 1 December 1969
3. Heywood H (1971) Article and shape distribution for lunar fines sample 12057,72. In: Proceedings of the second lunar science conference, vol 3. The M. I. T. Press, pp 1989–2001
4. Mitchell JK, Houston WN, Scott RF, Costes NC, Carrier WDIII, Bromwell LG (1972) Mechanical properties of lunar soil; density, porosity, cohesion, and angle of internal friction. In: Proceedings of the third lunar science conference, vol 3. The M. I. T. Press, pp 3235–3253
5. Nava DF (1974) Chemical compositions of some soils and rock types from the Apollo 15, 16, and 17, lunar sites. In: Proceedings of the fifth lunar science conference, vol 2. Pergamon Press, pp 1087–1096

Qualification of High Temperature Platings and Corresponding Lessons Learned

Fabio Panin and Adrian Graham

Abstract BepiColombo is an ESA cornerstone mission for the exploration of the Mercury planet. The journey to Mercury is a 6 year long cruise that constitutes a challenge for the materials used because of the long exposure to the high intensity of Sun illumination.

Several metallic and organic materials will reach sustained high temperatures and undergo phenomena such as stress relaxation/creep, and degradation of thermal and mechanical properties. These aspects need to be considered upfront during material selection and evaluation. A specific logic has been for this, which considers the incremental detailed knowledge of the environment, the material use and the spacecraft configuration.

A number of high-temperature platings of titanium alloy substrate have been subject to development, namely the gold-plating of the Medium and High Gain Antenna Rotary Joints, and the silver-plating of the Low Gain Antenna. Their qualification testing has shown how process set up is crucial, to avoid plating degradation during thermal cycling at extreme temperatures. A number of lessons have been learned for the improvement of the processes used.

Keywords BepiColombo • High temperature • Plating • Gold • Silver • Lessons learned

Introduction

BepiColombo is an ESA cornerstone mission for the exploration of the Mercury planet, currently planned for launch in 2016 (Fig. 1). The journey to Mercury is a 6 year long cruise that constitutes a challenge for the materials used because of the long exposure to the high intensity of Sun illumination.

F. Panin (✉) • A. Graham
European Space Research and Technology Center, Keplerlaan 1, 2201 AZ Noordwijk, The Netherlands
e-mail: fabio.panin@esa.int

J. Kleiman (ed.), *Protection of Materials and Structures from the Space Environment*, Astrophysics and Space Science Proceedings 47,
DOI 10.1007/978-3-319-19309-0_25

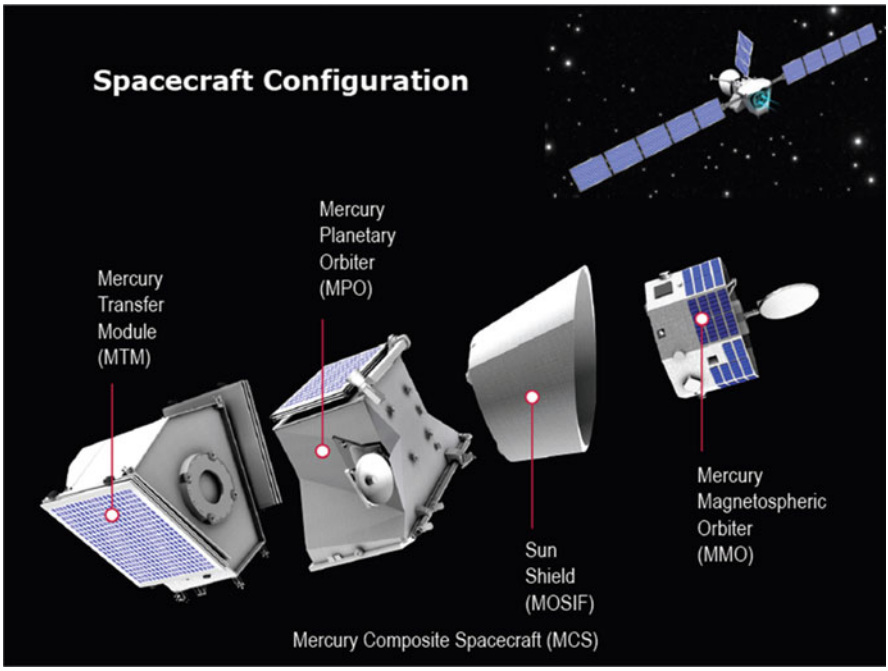

Fig. 1 The BepiColombo mercury composite spacecraft

Several metallic and organic materials therefore will reach sustained high temperatures and may undergo phenomena such as stress relaxation/creep, and degradation of thermal and mechanical properties. Such phenomena and degradation need to be considered upfront during material selection and evaluation. A specific logic has been devised for material selection and evaluation, which will be described, and considers the incremental detail knowledge of the environment, the material use and the spacecraft configuration.

In particular, a number of high-temperature platings of titanium alloy substrate have been subject to development, namely the gold-plating of the Medium and High Gain Antenna (MGA) Rotary Joints (up to 290 °C), and the silver-plating of the Low Gain Antenna (LGA), and MGA/LGA Wave Guide routing (up to 350 °C). Their qualification testing, that will be described, has shown how it is crucial to place great care in the set up of the processes used, to avoid plating degradation such as delamination and blistering during thermal cycling at extreme temperatures. A number of lessons have been learned and will be described, for the improvement of the processes used.

The BepiColombo Mission

The BepiColombo mission will be the first European mission to the planet Mercury, and is the 5th cornerstone in the Cosmic Vision Scientific Program of the European Space Agency (ESA). The BepiColombo mission will answer several questions on the planet itself, the exosphere as well as the magnetosphere and the interaction with solar wind. To fulfill all the scientific objectives, 16 instruments will be carried on two spacecraft orbiting around Mercury, one of them being provided by the Japan Aerospace Exploration Agency (JAXA).

The difficulty of reaching, surviving and operating in the harsh environment of a planet so close to the Sun makes BepiColombo one of the most challenging long-term planetary projects undertaken by ESA.

Following launch, the 4100 kg spacecraft will begin a 7.5-year journey towards Mercury. Eight planetary fly-bys will reduce the energy level required to reach Mercury. The delta-V still necessary will be achieved through an electric propulsion system and a complementary chemical propulsion system for navigation maneuvers and attitude control. Both propulsion systems are on board a dedicated transfer module, which will be separated from the orbiter shortly before capture at Mercury. When the Mercury orbit insertion is reached, the Japanese Mercury Magnetospheric Orbiter (MMO) will be released from the European Mercury Planetary Orbiter (MPO), by a spin and separation mechanism. Subsequently, the MMO protection sunshield (MOSIF) will be also released from the MPO. The primary science mission will commence in May 2024 and last for one Earth year with a potential extension until May 2026.

In order to cope with the challenging requirements (mostly constituted by the environmental conditions) and the mass constraint, a program of technology development was undertaken in preparation for the project implementation phase. Technology critical areas were:

- TT & C: Deep Space Transponder and High Power Amplifier.
- High Gain Antenna: Antenna Reflector (including thermal and RF coating), Antenna Pointing Mechanisms, Position Sensor, Rotary Joint, Low CTE Waveguides, High Temperature Feed, RF Compensated Phase-Stable Waveguide.
- Thermal: High Temperature MLI, MPO Radiator, High Temperature Cables.
- Power and Solar Arrays: High Temperature Solar Cells and Substrate, Shunt Diodes and Blocking Diodes.
- Mechanical: SADM (including Slip-Rings).
- AOCS: Star Tracker.
- Propulsion: Solar Electric Propulsion.

The wide perimeter of the above shows clearly the magnitude of the effort that was undertaken, namely through testing and evaluation of materials and components, both at constituent and unit level.

Material Evaluation Process

A first material overview shows that the externally exposed materials will see rather large thermal ranges. For example the MOSIF sunshield is expected to experience −180 to +280 °C. Thermal coatings such as Zirconia are used to protect sunshield materials against thermal radiation from the Sun.

Deployable thermal covers will see −50 to +250 °C. They will employ Multi Layer Insulation (MLI) for the shutter, a thermal coating, and Vespel SP1 has been used for the thermal spacer with the spacecraft that will reach 250 °C.

White paint is also used for those elements that, even if not exposed for the whole mission, will have extended exposure times e.g., 30–40 days and will experience high but not extreme temperature e.g., 150 °C.

There are also a number of exposed elements that after launch are required only to provide geometric stability with a low loading level (e.g., attitude maneuvers). For these, degradation of mechanical properties can be tolerated.

These considerations already show that a dedicated review and approval process is needed for this mission, to properly address the peculiarity of the environment, in relation to the materials used. A Materials and Process Control Board (MPCB) system has been organized at various levels to perform the systematic review of materials, processes and mechanical parts proposed by the project subcontractors. The first system-level MPCB was held in October 2009. Here, the criteria to be used to determine whether an MPCB meeting was necessary for a given unit, were established:

– New equipment or subcontractor;
– Critical equipment e.g., functions, environmental conditions;
– Procurement time.

which allowed to focus resources. It was also agreed to use the ESA PMP Tool [1]. For organic materials, due to the criticality of cleanliness and contamination control aspects to the mission, it was decided to request companies to indicate the date of the last outgassing test results that would have been claimed for material approval (to be noted that this information is not normally requested). The guideline to accept only outgassing test results not older than 10 years was established. Materials with older tests would have to be retested, especially where a mixing process is involved or the traceability to constituents of the suppliers is not available e.g., pottings, adhesives and paints.

In the following months, preliminary information was collected on material maximum expected temperature and exposure duration. This allowed a set of approximately 30 materials for outgassing test at 125 °C to be selected, and approximately 10 materials for dynamic outgassing test. In addition, it appeared that material assessment based on the information of temperature class, material class, etc. as per ECSS-Q-ST-70 was not sufficient. It was decided to establish a risk assessment flow (see Fig. 2) based on the incremental evaluation of the material properties vis-à-vis the expected environmental conditions. When the material was

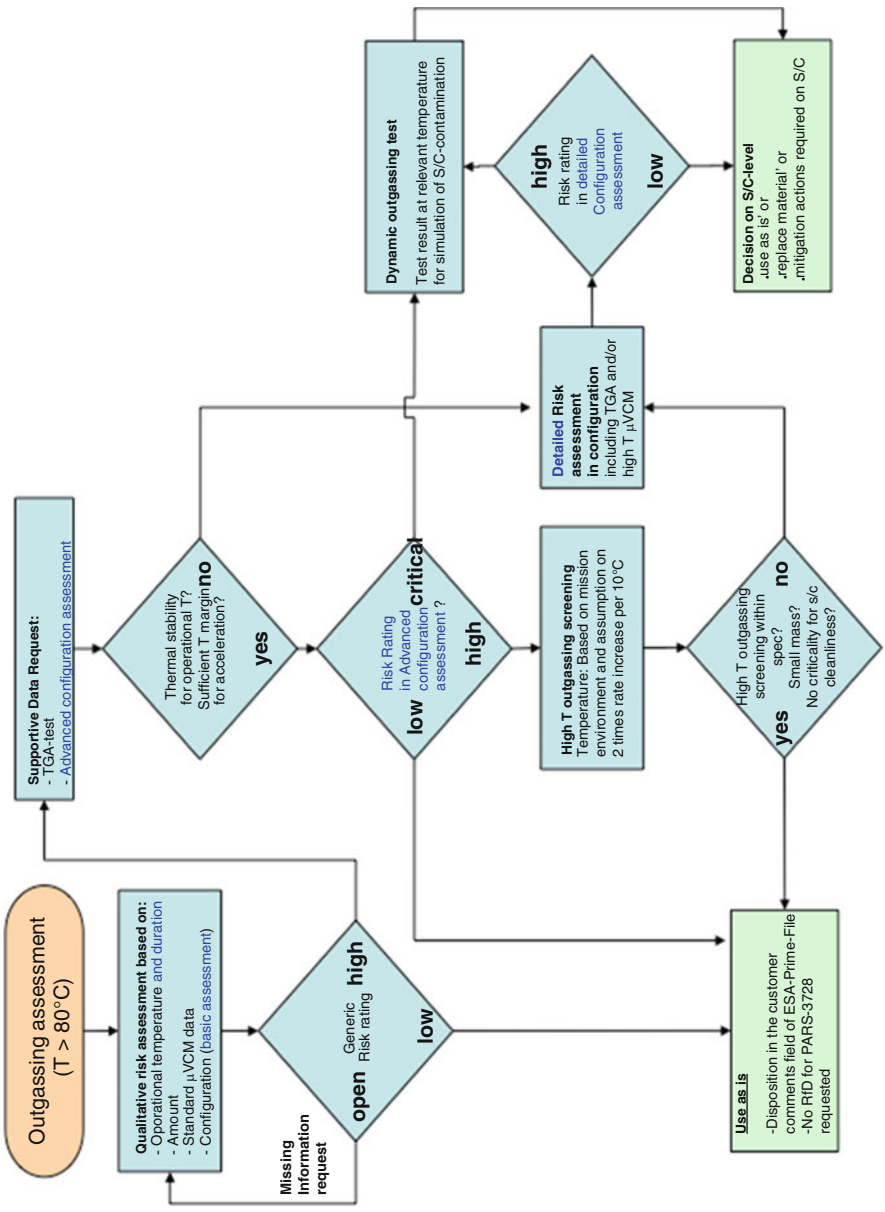

Fig. 2 High temperature organic materials assessment flow

to be used at high temperature (>80 °C), the expected maximum temp and duration exposure was needed, in addition to a detailed description of use, including material quantity and configuration. Depending on this first assessment, Thermal Gravimetric Analysis (TGA) results were considered to determine if any physical or chemical change (e.g., decomposition, sublimation) would occur which could affect the material function. If this risk could not be excluded, and thermal stability constituted a concern, a high temperature outgassing screening test had been performed. A final evaluation would consider detailed configuration aspects and potential impact on cleanliness and contamination. If deemed necessary, a dynamic outgassing test was performed that allowed information to be extracted as input to the spacecraft contamination simulation.

A similar process was put in place for metallic materials (Fig. 3) where the concerns were:

- Stress relaxation or creep;
- Loss of the mechanical properties achieved through heat treatment;
- Diffusion process taking place between different metals.

A first material assessment was based on examination of existing experience or heritage of use at high temperature.

The determination of the temperature level to be considered as safe was more involute than that for organic materials as it had to differentiate the various metals/alloys, and the various heat treatments within alloy family—all in conjunction with the expected use and state of stress.

For example, while AA1050 is mostly used for shims (hence the concern for creep) and can be safely used up to 250 °C, 7075 T73 shows a decrease of mechanical properties above 82 °C.

Solder materials have a specific use and their limits are:

- Sn63Pb37: extensive periods at +80 °C or short periods to a maximum of +120 °C.
- Sn96Ag4: extensive periods at +120 °C or short periods to a maximum of +150 °C.
- Sn60Pb40: extensive periods at +80 °C or short periods to a maximum of +120 °C.

The most critical materials, due to the combination of low safe temperature and application, are the aluminum alloys and solders. Stainless steels, titanium alloys, nickel alloys are less critical.

Metallic material assessment for extended exposure to high temperature was primarily based on the function to be provided by the element, and the material state of stress. Following temperature exposure, the questions that needed to be answered were:

- Which is the level of mechanical properties required for its function?
- Would stress relaxation or creep affect the function?

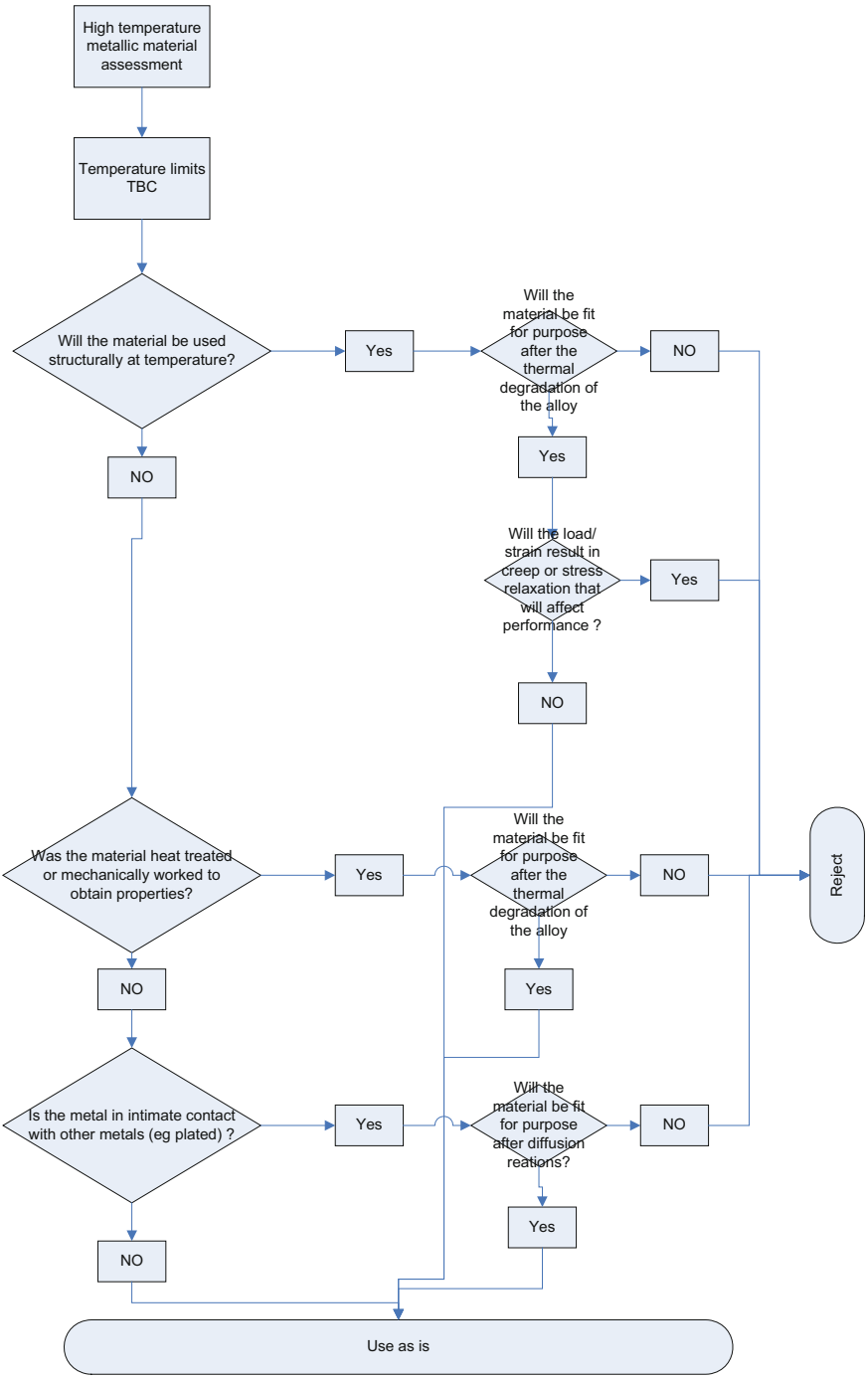

Fig. 3 High temperature metallic materials assessment flow

– If the metal is in contact with other metals, would diffusion occur, and if this does, would diffusion affect the needed performance?

The application of the above logic showed that indeed a number of aluminum alloys would pose no risk even after extended exposure to high temperatures, because the loading level at that stage of the mission would be extremely low—the driving design loads occurring at launch or during spacecraft separation (shock).

In other cases, an extreme temperature is related to failure cases only, and exposure times would be very short, therefore again not constituting a risk for the material use.

Following a number of iterations and research, the following safe temperature limits were been established:

– Aluminum alloys: 82 °C, when mechanical strength is required.
– Nickel alloys, titanium alloys, steels and stainless steels: 127 °C.

For filler metals used in brazing, welding, soldering, optical materials, and ceramics, it was impossible to establish generic safe temperature limits due to their nature and properties. On the other hand, due to the limited use of these materials, it was appropriate to assess them on a case-by-case basis.

The evaluation work described above resulted in the need for dedicated testing of some 70 materials and processes to verify their suitability to the mission environmental conditions. This represented a considerable effort for the industrial consortium and the project. The effort was both financial and sheer work, which sometime was of investigative nature as the demands placed on materials exceeded the known or "heritage" limits.

Overall, more than 3100 materials, 2200 processes, and 1040 mechanical parts have been subject of the evaluation process described above to achieve final approval. The ESA Request For Approval (RFA) process was implemented to control the implementation of qualification activities on materials and processes. This process includes a first step of review and approval of the proposed qualification test plan, followed by a second step of review of the obtained test results. Eventually, 70 RFAs were generated within the project, to cover, among others:

- Thermal coatings.
- RF platings.
- Solar array composite materials and processes, spacecraft interface harness.
- Low friction coating of separation mechanisms.
- VUV resistant rings for optics retention.
- Carbon/Silicon-carbide struts for High Gain Antenna.
- Materials exposed to fluids e.g., valve seals.
- Potting of the Solar Array Drive slip rings in addition to a number of bondings (e.g., heaters, tie-bases, thermistors), chemical conversion processes, coatings (e.g., Molycote), platings, and Surface Mount Technology (SMT) verifications.

In the following, two plating processes are discussed as examples.

Silver Plating of Titanium Substrate

The Low Gain Antenna (Fig. 4) is constructed with Ti6Al4V titanium alloy. To provide electrical performance, the titanium alloy is plated with silver [2]. Rymsa, Spain, was responsible for the procurement of the antenna, and performed the plating process. The antenna qualification temperature range was −150 to +350 °C. The plating process consisted of substrate cleaning, first nickel underplating, heat treatment, second nickel layer, silver plating (details of the process steps are proprietary and cannot be discussed).

The process qualification employed 28 flat, cubic and design-representative samples. The test flow was:

- Process quality and thermal/optical properties (flat samples)
  - Thickness measurement (X-ray spectrometry).
  - Adherence tests (peel, blister and bending tests).
  - Humidity test.
  - Thermal shock test.
  - Thermal/optical properties measurement.
- Process robustness against environment
  - Initial thickness measurement (X-ray spectrometry).
  - Humidity test.
  - Peel test.
  - SEM inspection.
  - Thermal shock test.
  - Peel test.
  - Diffusion test.
  - Surface roughness measurement.
  - Thickness measurement by micro-sectioning.

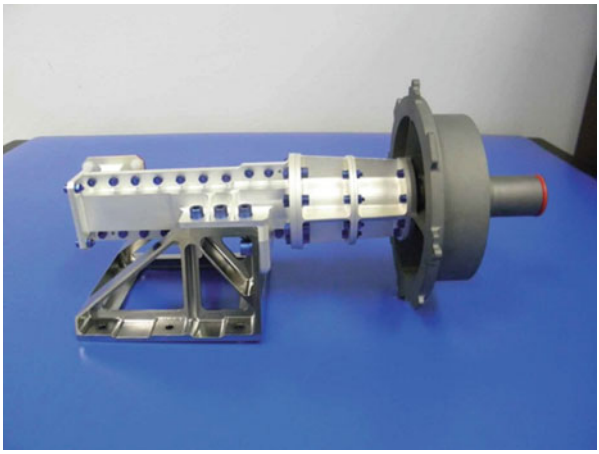

Fig. 4 Low gain antenna

- Verification of RF performance
  - Thickness measurement (X-ray spectrometry).
  - Blister tests.
  - RF performance test (on selected samples).
  - Humidity test.
  - Thermal shock test.

The peel, blister, and bending tests were according to ASTM-B571 and QQ-S-365.

The humidity test was an exposure to 95 % RH and 50 ± 5 °C for 96 h.

The thermal shock test was a thermal vacuum cycling between −150 and +350 °C with 200 °C/min rate and for 100 cycles, in accordance with MIL-STD-202F method 107G.

The diffusion evaluation was by SEM examination of microsections, and EDX analysis.

Adhesion problems after heat treatment were found during sample manufacturing. A number of changes were considered, that included abrasive blasting to improve the surface roughness, cleaning agent, and changes of current level. Experimentation showed that an extra cleaning before application of nickel strike, heat treatment and a second nickel layer solved the problem.

After the thermal shock test, two large plating detachments were found at the center of the inner walls of the waveguide, thus in a performance critical area (Fig. 5). The sample was cut, and the inspection showed that poor adhesion of the first nickel layer was the cause of the plating detachment. The stability and/or uniformity of the current was the suspected cause of the problem. Additional testing was performed on extra samples representing the waveguide cavity. Such testing included plating thickness measurement, peel test, hardness measurement before and after a thermal shock (−198 to +350 °C, five cycles). Three current levels were tried, and three different electrode positions. As a result, it was determined that while the position on the electrode internally to the waveguide has little or no effect, the current through the electrode may cause detachment if too low or too high. The investigation therefore allowed confirmation of the process set up and associated parameters, as well as their monitoring. Indirectly, this confirmed that the single-

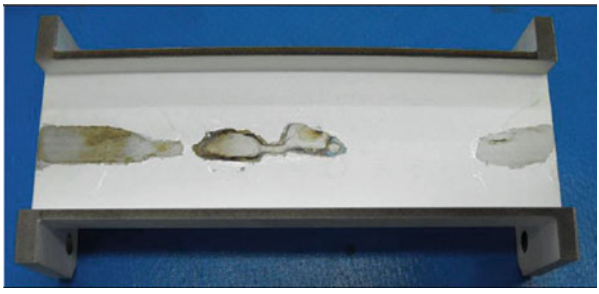

Fig. 5 After the thermal shock test: large plating detachment

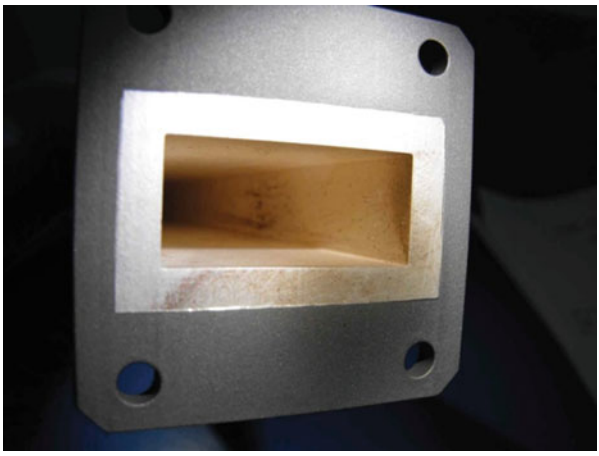

Fig. 6 After thermal vacuum test: brown stains, blisters and spots

piece waveguide design was feasible (the alternative being a more complex two halves design).

After thermal vacuum testing, brown stains, spots, and blisters were found (Fig. 6). Contamination was the suspected cause of stains and spots, and SEM inspection of the defect area was performed. This showed carbon on top of the silver layer, which could be deposited during compressed air drying after silver-plating, due to inevitable oil residues in the air stream. The preventive action was to replace compressed air drying with drying in low vacuum at 80 °C for 2 h.

To prevent blister formation due to bad nickel adhesion, the positioning of parts in the bath was changed to allow an easier hydrogen bubble evacuation, and thus lower its interference with nickel deposition. The effectiveness of all such actions was confirmed by additional testing.

Later on, during EQM Wave Guide manufacturing, sandblasting of silver-plated pieces following heat treatment caused their peeling, showing lack of nickel adhesion onto substrate. The first suspect was the correct oven temperature during heat treatment, but this did not show any deviation from normal profile. However, this enquiry showed that an oven leak had occurred which resulted in postponing the heat treatment to the following day, whereas this is usually performed during the first day, immediately after nickel plating (as per ASTM B481). Two sets of samples (one processes as per regular timeline, one with the delayed heat treatment) were tested, While the first set reproduced the failure, the second was acceptable. This showed that the time delay between nickel plating and heat treatment is a critical parameter that needs control.

The Medium Gain Antenna (manufactured by Rymsa, Spain) also needed silver plating for RF performance. For this application, however, qualification from −88 to +550 °C was necessary. The process qualification flow described above for the LGA was adopted, reducing the thermal vacuum test to 30 cycles at first (pre-qualification). At this stage, diffusion evaluation was paramount to determine

if the silver layer thickness was sufficient to guarantee end-of-life (EOL) performance. Diffusion evaluation (by SEM examination of micro sections) showed that this phenomenon took place among all three metals, despite the relatively short exposure to high temperature. Even if the overall silver thickness was maintained in this test, there was a concern over the expected lifetime. A high temperature storage test was devised to study diffusion over time, however the boundaries set by material properties implied a limitation on the acceleration factors that could be adopted. Eventually, a 3-week storage at 540 °C was performed, followed by 1-week storage at 600 °C (peel tests were performed at various stages to confirm good adhesion). In parallel, a re-design of the antenna with a larger size was performed and a maximum temperature of 350 °C, as a backup solution in case of a negative test outcome.

The results obtained with the storage test were used to derive the diffusion law and thus the EOL diffusion expected for 350 °C operation. The initial calculations showed that the planned mean plating thickness would be acceptable to maintain the antenna performance over the 2-year operational phase, but subsequent calculations showed that the possible error in this value was huge. A new method of analyzing the results was developed. This, in combination with published data, allowed the behavior of the coating system to be modeled over the predicted mission duration. The temperature experienced by the antenna will cover a range depending on the heat input from the sun and planet. The present coating would allow 2 years of continuous service at 420 °C without compromising data transmission rates.

Gold Plating

The High (Fig. 7a) and Medium (Fig. 7b) Gain Antenna Rotary Joints are constructed from Ti6Al4V titanium alloy. Sener, Spain, was responsible for the procurement. To provide electrical performance, the titanium alloy is plated with gold [3]. The plating system was performed by Epner Technologies Inc, USA, and consisted of a chemical cleaning/activation bath, followed by an Electroless-Nickel (EN) under-plate. After heat treatment, a second activation and EN layer was applied, before the final Electroless gold plating (details of the process steps are proprietary and cannot be discussed).

The process qualification flow was as follows:

- Initial surface roughness measurement.
- Plating.
- Thickness measurement (X-ray).
- Surface roughness measurement.
- RF performance test (on selected samples).
- Peel test.
- Thermal cycling.

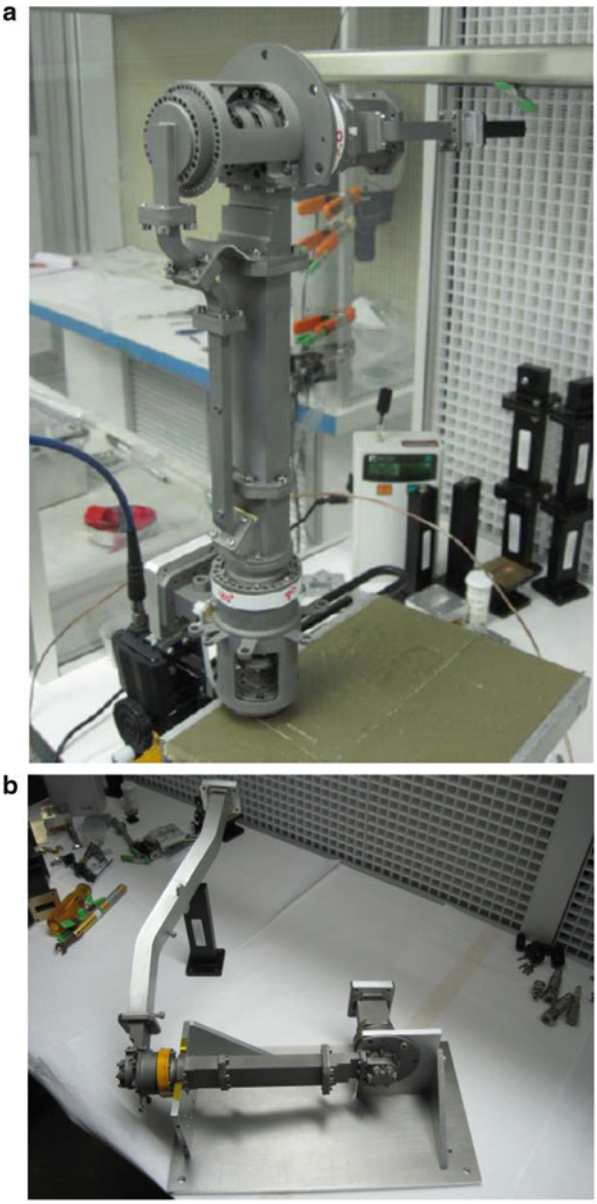

Fig. 7 (**a**) High gain antenna: antenna pointing mechanism rotary joint. (**b**) Medium gain antenna: mechanical assembly rotary joint

- Surface roughness measurement.
- RF performance test (on selected samples).
- Peel test.
- Cross sectioning.
- Peel test.

– Thickness measurement (X-ray).
– Microsectioning (to confirm X-ray measurement).

In total, 16 samples were used for the various tests. Both flat and complex shape samples were employed. Complex samples included representative cavities, holes and corners, and actual waveguide design. For the latter samples, plating of flanges and internal waveguide surfaces was performed and subject to inspection, hence the sectioning.

Thermal cycling was split in a cold step and a hot step:

– Cold cycling: −80 to 20 °C, 8 cycles, in atmosphere.
– Hot cycling: 20–290 °C, 100 cycles, in vacuum, 3′ dwell, 10 °C/min ramp.

and samples were removed at 5, 20, 40, 60 and 80 cycles for inspection.

For the application, the acceptance criteria did not include discoloration or tarnishing, as these would not affect electrical performance. Blistering, cracking or peeling were instead considered as a reason for rejection.

Following gold plating, four of the samples exhibited blistering (Fig. 8). The investigation showed that this was due an insufficient activation prior to the second nickel plating. The affected samples were stripped and re-plated. The remaining samples were thermally cycled to confirm the plating quality, however three showed blistering after only five cycles. Those not affected were further tested to 20 cycles and showed no problem.

The corrective action for this blistering issue eventually was an improvement of the workmanship to ensure a homogeneous wetting of all surfaces during activation.

After re-plating, some granularity was observed in six of the samples (Fig. 9). Granularity was found to be made of gold particles embedded in the gold plating. Even if this granularity was within the maximum acceptable roughness limit, it violated basic visual inspection criteria. Eventually the root cause was determined to lie with the masking tape that had been used and the orientation of the samples in

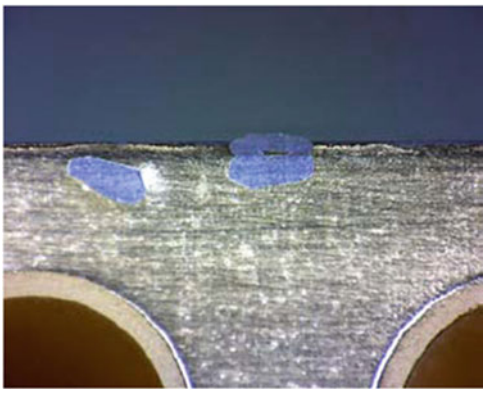

Fig. 8 RJ assembly blistering

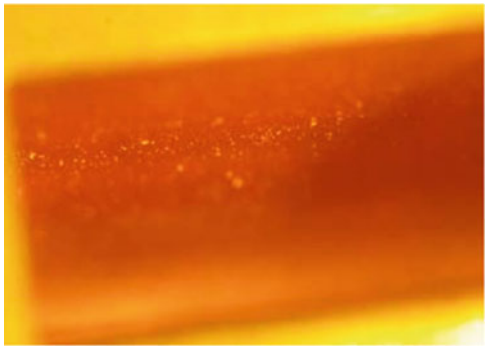

Fig. 9 RJ assembly granularity

the bath in relation to the flow. The affected samples were stripped and re-plated with changes to masking and raking.

Qualification testing performed on the seventeen samples showed the suitability of this RF plating for use in the high temperature space environment foreseen for the mission. The test samples showed no evidence of peeling or blistering and successfully passed adhesion and surface roughness tests. They also showed no evidence of metal diffusion when examined by scanning electron microscope.

The following is a summary of the findings:

- Surface roughness: this was measured three times on each sample (bare titanium, before and after thermal cycling) and passed the set criteria. Variation from sample to sample was observed which could be explained by a combination of factors: different measurement location, handling (for waveguide flange samples that were mounted for RF performance measurements), softness of pure gold layer;
- Plating thickness measurement: a discrepancy had been found between the results obtained through the X-ray fluorescence method and the SEM, which was determined to be caused by the insufficient accuracy of the X-ray equipment for the small thickness to be measured. Only SEM results have been retained and showed a thickness at least double than that specified.
- Diffusion: six samples were used to characterize any diffusion taking place at elevated temperatures. One of these samples was removed from thermal cycling at 5, 20, 40, 60, 80 and 100 cycles. The SEM images of micro-sections show no diffusion of gold into nickel, or inter-nickel diffusion.
- Surface patterning was observed on some of the samples. Plating, cleaning, or condensation during cold cycling could cause these patterns. The effect was only optical, and did not affect adhesion or performance.

Lessons Learned

As the discussion above has shown, the set up of plating processes for high temperature applications was not straightforward and had an iterative nature,

where the problems found needed investigation that in turn allowed increasing our experience for such applications.

A number of lessons have been learned that can be summarized as follows:

For Silver Plating

- A nickel under-layer with low thickness (flash or strike) improves the adhesion of the subsequent layers.
- For hollow pieces, the electrode current level is an important process parameters that needs set up and control.
- Drying in between baths may affect adhesion if performed too quickly with pressurized air, which can contain impurities.
- The timing between platings steps may affect adhesion and therefore needs control to ensure repeatability.
- Material degradation can have a direct impact on the efficiency of the spacecraft e.g., the correlation of diffusion with data bandwidth.
- For diffusion rate calculation, mean data can be useless if the possible errors affecting the results are not understood;
- Modification of how the available data is used can produce both meaningful and valuable results: the new analysis looked at the shape of the diffusion profile, rather than the depth of the diffusion wave front as normally it is done;

For Gold Plating

- Intermediate inspections during thermal cycling were invaluable in detecting problems as they arose (sometime, surprisingly at early phase of testing). Even if this implies a longer overall schedule and a higher number of samples, the return of information pays off as educated decisions can be made to adapt the test or process.
- A relatively low number of thermal cycles e.g., 5–10 is a good screening to identify major process weaknesses.
- It is inevitable that some process parameters e.g., strength of activation, need experimentation or confirmation.
- Due to the two points above, early trials on a limited number of samples allow confirmation of process or adjustment of such parameters. Such trials should be undertaken before formal qualification.

Conclusions

The high temperature requirements of the BepiColombo mission needed a dedicated material evaluation process. The process considered information such as: mission profile; time-temperature predictions; function and configuration. The potential effects of material degradation or contamination due to outgassing were

assessed. To support material evaluation, extensive material testing was necessary, both to provide valid input data to system level analysis (e.g., outgassing) and to confirm EOL performance within limits.

Two examples were discussed, of platings used for RF applications. The discussion of the problems encountered in the course of their qualification showed that processes needed great care both in their set up and the associated controls, in order to avoid poor quality e.g., low adhesion to substrate following exposure to high temperature.

A number of lessons were learned that have a general nature. The consolidation of processes involved a number of subsequent and incremental trials, and employed a relatively large number of samples of increasing complexity. It is therefore wise to initiate process qualification at an early stage of procurement, proceed step-wise, and foresee adequate resources for its completion.

Acknowledgements The authors wish to thanks all those who contributed to the work addressed here, and in particular the direct counterparts in industry:

- Andreas Leupolz (Astrium EADS).
- Daniela Formentin (Thales Alenia Space Italy).
- Isabel Santos Gutierrez (Rymsa).
- Jokin Zabala (Sener).
- Charlie Lisher, Paul Santos (Kevlin).
- David Epner (Epner).

References

1. BC-ASD-RP-00120, PMP synthesis report
2. BC-RYM-RA-10012, Silver plating of titanium substrate
3. BC-SEN-RA-10001, Gold plating process

Abrasion Research on Axle Materials with the Influence of Simulated Lunar Dust

Dongbo Tian, Man Li, Yu Bai, Zhihao Wang, Qiang Yu, and Yu Li

Abstract Using Lunar Dust Environment Simulator, the effects of friction and abrasion of lunar dust simulants in vacuum were investigated at the Beijing Institute of Spacecraft environment Engineering (BISEE). The abrasion characteristics of lunar dust on materials were studied, focusing on the CE-3 rover wheel axles. The sample coupons included aluminum alloy, Teflon and steel materials used on axle. The surface morphology of before-test and post-test samples were analyzed. The friction coefficient curves were acquired in vacuum dust environment. The mass losses of materials were analyzed.

In vacuum conditions without the application of lunar dust simulant, the abrasion degree of the friction pair was highest. The introduction of the lunar dust simulant can significantly change the friction–abrasion status. The abrasion of PTFE material was more serious than that of the aluminum alloy without the lunar dust conditions; while the abrasion of aluminum alloy exceeded that of the PTFE material with the participation of lunar dust particles.

Keywords Simulated lunar dust • Materials • Friction and abrasion

Introduction

Lunar dust having small particle size, sharp edges and high hardness, can be considered as a special "abrasive". These characteristics of lunar dust can cause scratches and damage to the surfaces in contact with it, especially when they are in relative motion. In particular, the surfaces, during reciprocating motion and rotational motion, will be abraded, with the surface coatings even stripped off. When the instrument panel on the inspection equipment of Apollo 16 was covered by lunar dust, after the astronauts removed the dust with a brush, certain instruments could not be read due to serious abrasion [1, 2]. After the two astronauts of Apollo 12 finished their moon walk, the window glass on the helmets of their space suits

D. Tian (✉) • M. Li • Y. Bai • Z. Wang • Q. Yu • Y. Li
Beijing Institute of Spacecraft Environment Engineering, Beijing 100094, China
e-mail: dongbotian@126.com

J. Kleiman (ed.), *Protection of Materials and Structures from the Space Environment*, Astrophysics and Space Science Proceedings 47,
DOI 10.1007/978-3-319-19309-0_26

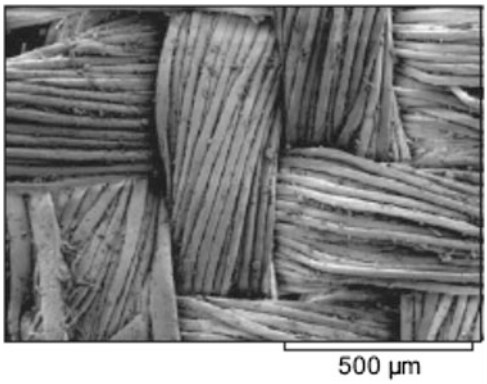

Fig. 1 Scanning electron microscopy image of the braided fabric on Space Suit from Apollo 12 worn by Alan Bean. Lunar dust particles are embedded in the fabric and abrasion can be seen on several of the individual fibers

became blurred because of scratches. Several layers of the laminated heat-insulated material were worn through. The electron microscopy image of a fragment of Apollo 12 astronaut Alan Bean's space suit, showed the damage resulting from this kind of abrasion (Fig. 1) [3]. Alan Bean wrote in his reports that "The space suit material on the lower part of the upper edge of the moon boots was seriously abraded, and several spots on the outer layer of space suit were worn through. These were all caused after less than three days of activity on the lunar surface. If we plan to carry out longer term activities on the lunar surface, we need to pay more attention to the abrasion effects [4]."

In the present paper the results of a study of abrasion effects of lunar dust simulant on metallic aluminum and PTEF materials conducted in a lunar dust environment simulator and using a vacuum lunar dust friction–abrasion testing machine are presented. The research results can provide strong support in understanding the abrasion effects caused by lunar dust particles to materials in China's lunar exploration program.

Testing Apparatus

The testing apparatus mainly includes the lunar dust environment simulator and the vacuum lunar dust friction–abrasion testing machine. The lunar dust environment simulator is a horizontal type vacuum chamber that provides a vacuum environment for the testing (Fig. 2). The size of the simulator is 800 mm in diameter and 1200 mm long. The vacuum system can create a vacuum environment with a pressure of 1×10^{-3} Pa inside the chamber. There is a dustproof system within the vacuum system. With the exterior being cylindrical, the vacuum lunar dust friction–abrasion testing machine includes the loading system, upper and lower test samples, sample rotation driving system, friction coefficient acquisition system, etc. By changing the test samples, a study on the changes in abrasion performance of different friction pairs was conducted. The control and data acquisition of the vacuum lunar dust friction–abrasion testing machine were set outside the lunar dust environment simulator. The build-in friction force data sampling system on the

Fig. 2 Lunar dust sediment and adsorption environment simulator

friction–abrasion testing machine was used for the real-time collection and recording of the friction force data during the test. The METTLER electronic balance with an accuracy of 10^{-5} g was used to weigh the samples and the dust-adding volume before and after the test.

The aluminum alloy material, the PTFE materials were prepared as friction samples, which were divided into upper test samples and lower test samples.

Results

Analysis on the Influence of Vacuum and Atmospheric Environmental Factors Without Use of Dust Particles

In this study the PTFE material was used to prepare the lower test sample, and the aluminum material was used to prepare the upper test sample. This friction pair was used to investigate the impact of the vacuum and atmospheric environmental factors on the friction pairs, without introducing the dust particles. The test conditions were as follows: the load applied to the friction pair $P = 3.85$ kg; the vacuum pressure $P_3 = 4.5 \times 10^{-3}$ Pa, the rotation speed of the corresponding friction pair in vacuum, $v_1 = 285$ rpm, and the rotation speed of the friction pair in the atmospheric conditions, $v_3 = 280$ rpm. See Fig. 3 for the surface appearance of the samples after the test. See Fig. 4 for the corresponding friction curves.

From the friction coefficient curves (see Fig. 4) we can see that the friction coefficient curve in the atmospheric conditions changed between 0.07 and 0.08, while the friction coefficient curve in the vacuum conditions changed between 0.25 and 0.3 with other conditions being equal.

The weight loss test results showed that the weight loss of PTFE sample in atmospheric condition was 0.02536 g, while the weight loss of PTFE sample in

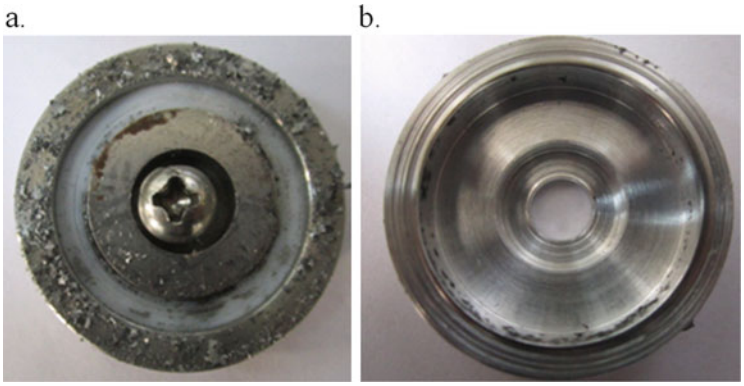

Fig. 3 Images of a friction PTFE/Aluminum pair after a test without the dust particles. (**a**) The appearance of the PTFE lower sample after test. (**b**) The appearance of the aluminum alloy upper sample after test

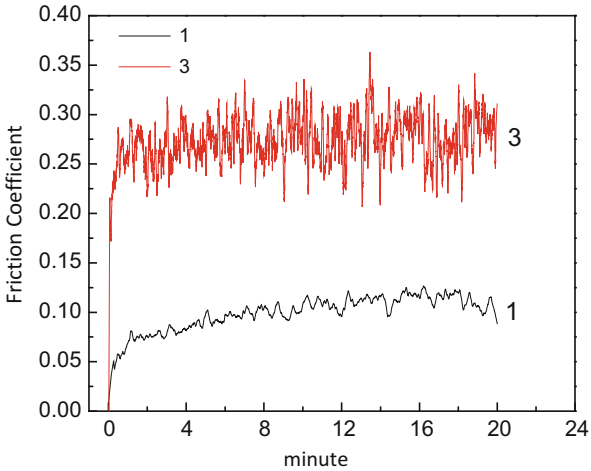

Fig. 4 Friction coefficient curves of samples in atmospheric and vacuum conditions without dust particles

vacuum conditions was 0.0379 g; the weight loss of aluminum alloy sample in atmospheric conditions was 0.00413 g, while weight loss of aluminum alloy sample in vacuum conditions was 0.00392 g.

Through data analysis, we can see that in the atmospheric conditions, the thin air film formed between the upper and lower samples significantly reduced the friction between the samples, and the damage of the lower sample was also reduced significantly, but its influence to the abrasion of the upper sample turned out to be small. In other words, the abrasion in vacuum conditions is much more serious than that in atmospheric conditions under the same operating conditions.

Analysis on the Influence of Vacuum and Atmospheric Environmental Factors with Participation of Dust Particles

In this study, the PTFE material was used to prepare the lower test sample, and the aluminum material was used to prepare the upper test sample. This friction pair was used to investigate the impact of the vacuum and atmospheric environmental factors on the friction pairs, with the dust particles. The test conditions: the load $P = 3.85$ kg; the pressure in vacuum is $P_4 = 4.3 \times 10^{-3}$ Pa, the rotating speed of the corresponding friction pair is $v_2 = 274$ rpm, and the rotating speed of the friction pair in the atmospheric conditions is $v_4 = 266$ rpm. Figure 5 shows the surface conditions of the samples after the test. Figure 6 presents the corresponding friction curves.

From the friction coefficient curves (see Fig. 6) we can see that the friction at atmospheric conditions was about 0.15, while the friction coefficient at vacuum conditions was about 0.25, with other conditions equal. The weight loss test results showed that the weight loss of PTFE sample in atmospheric condition was 0.02843 g, while the weight loss of PTFE sample in vacuum conditions was 0.02822 g; the weight loss of aluminum alloy sample in atmospheric conditions was 0.04346 g, while weight loss of aluminum alloy sample in vacuum conditions was 0.01219 g.

Through data analysis, we could find that in the atmospheric condition, the air film formed between the upper and lower samples also reduced the friction between the samples. The abrasion in vacuum conditions is much more serious than at atmospheric conditions under the same operating conditions with lunar dust.

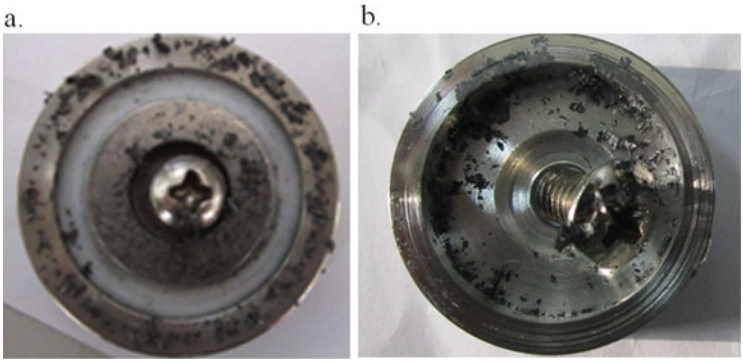

Fig. 5 Images of a friction PTFE/Aluminum pair after a test with the dust particles. (**a**) The appearance of PTFE lower sample after the test. (**b**) The appearance of aluminum alloy upper sample after the test

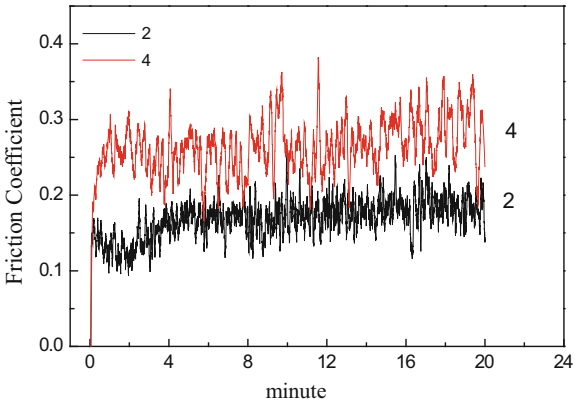

Fig. 6 Friction coefficients behavior of samples in atmospheric and vacuum conditions in experiment with dust particles

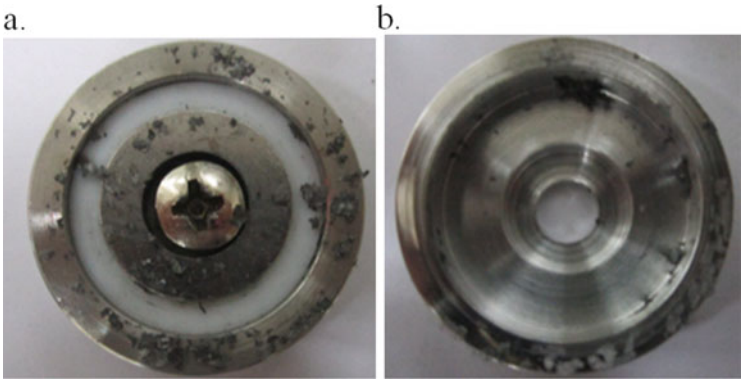

Fig. 7 Images of the PTFE and aluminum samples after a vacuum test with dust particles simulant. (**a**) The appearance of PTFE lower sample after a vacuum test with dust particles. (**b**) The appearance of the aluminum alloy upper sample after a vacuum test with dust particles

Analysis on Influence of Lunar Dust on the Degree of Abrasion in Vacuum Conditions

In this investigation, the PTFE material was used to prepare the lower test sample, and the aluminum material was used to prepare the upper test sample. The test conditions: the load $P = 3.85$ kg; the revolution velocity of the friction pair: $v_3 = 280$ rpm, $v_4 = 266$ rpm; the environmental pressure: $P_3 = 4.5 \times 10^{-3}$ Pa, $P_4 = 4.3 \times 10^{-3}$ Pa; there was no simulated lunar dust in test 3, and 0.01619 g of the dust was added in test #4.

The surface appearances of the upper and lower samples were evaluated before and after the test. Figure 7 presents the images of both surfaces after the test.

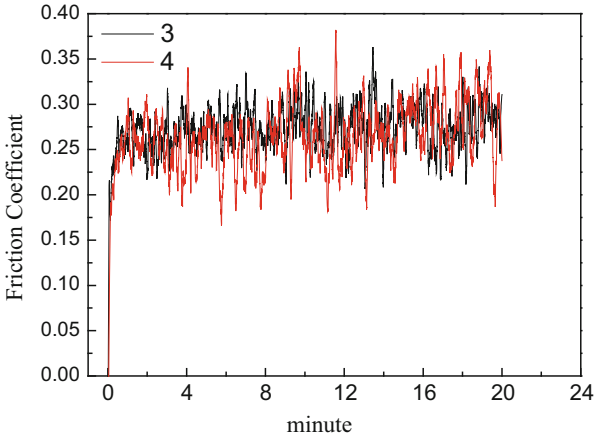

Fig. 8 Friction coefficients behavior of samples in experiments in vacuum conditions with dust particles

Figure 8 presents the friction coefficient curves. From the data analysis we can see that the influence of the lunar dust on the friction coefficient between the investigated PTFE-Aluminum friction pair was small in vacuum conditions. Through comparing the weight losses of friction pairs, we found that the weight loss of the PTFE lower sample without lunar dust is 0.0379 g, while the weight loss of the PTFE lower sample with lunar dust is 0.02822 g; the weight loss of the aluminum alloy upper sample without lunar dust is 0.00392 g, while the weight loss of the aluminum alloy upper sample with lunar dust is 0.01219 g. The data analysis showed that the damage to the PTFE material lower sample was significantly reduced in the lunar dust condition, but the damage to the aluminum alloy upper sample increased sharply at the same time.

Discussion

By comparing the results of the abrasion effects on the PTFE material and aluminum material in atmospheric, vacuum and lunar dust conditions, some preliminary results can be suggested.

Vacuum conditions have the most significant influence on abrasion. In vacuum conditions without the participation of lunar dust particles, the abrasion due to the friction was the highest. The addition of the lunar dust can significantly change the friction–abrasion status. For the PTFE material the abrasion was more serious than that of the aluminum alloy without the lunar dust; while the abrasion of aluminum alloy exceeded that of the PTFE material when the lunar dust was added.

The test results obtained in this study could provide useful reference information on abrasion patterns that may be caused by lunar dust to the inspection equipment, to the Lunar Lander on the lunar surface and to the moving parts and rotating parts of various scientific instruments. By adopting the vacuum friction–abrasion testing

method, this study can scientifically and effectively evaluate the influence of lunar dust particles on the abrasion of materials, providing stronger support for selecting the materials for moving parts of China's lunar exploration apparatus and equipment to withstand the effects of the lunar dust and reduce its influence from the stage of design to the stage of experimental verification.

References

1. Gaier JR (2005) The effects of lunar dust on EVA systems during the Apollo missions [R]. NASA/TM-2005-213610
2. Ronald CA (2005) The effects of lunar dust on advanced EVA systems: lessons from Apollo [R]. In: Lunar regolith simulant materials workshop. Marshall Space Flight Center, Madison
3. Rao NS, Wallace BE, Alabama H (1993) Considerations for the design of lunar rover structures and mechanisms for prolonged operation in the lunar environment [R]. AIAA 93-0993, AIAA
4. Gaier JR, Meador MA, Rogers KJ, Sheehy BH (2009) Abrasion of candidate spacesuit fabrics by simulated lunar dust. NASA/TM—2009-215800, 2009–01–2473

Effects Analysis and Simulation Technology of Dust Storm Environment on Mars

Lei Zhang, Jie Xu, and Shizeng Lv

Abstract The dust storm characteristics on Mars were analyzed. The material properties of thermal control coatings, windows and mirrors affected by such dust storm parameters like particle velocity, their density, size and hardness are discussed. Investigation directions and methods for studying the dust storm environmental effects are presented. By studying the Mars dust storm environments in ground simulators, the numerical simulation method of mixed flow of backfilled gas and dust particles has been developed and the analysis of the flow characteristics of Mars dust storm conditions with different scale parameters has been conducted. The Mars dust storm environment simulator concept is presented that allows providing technical support in simulating the dust storm environmental conditions testing.

Keywords Mars dust storm • Effect analysis • Mars environment simulator • Test method

Introduction

Dust storms on the surface of Mars are quite frequent, with the dust particles being highly invasive. In addition, friction between dust grains during such events will produce static discharges that may damage sensitive components of a Mars Probe and reduce its performance. So, dust storm environmental effects should be investigated and their influence on the parts and materials verified by studying them in ground simulators. This paper reports on a study carried on that included the following topics: (1) Analysis of the dust storm characteristics on Mars. Evaluation of the effects of such dust storm parameters as particle velocity, their density, size and hardness, on material properties of thermal control coatings, windows and mirrors. Investigation of the directions and methods for studying dust storm environmental effects. (2) Development of a numerical simulation method of mixed flow of backfilled gas and dust particles and analysis of the flow characteristics of

L. Zhang (✉) • J. Xu • S. Lv
Beijing Institute of Spacecraft Environment Engineering, Beijing 100094, China
e-mail: zhangleicast@126.com

J. Kleiman (ed.), *Protection of Materials and Structures from the Space Environment*, Astrophysics and Space Science Proceedings 47,
DOI 10.1007/978-3-319-19309-0_27

Mars dust storm conditions with different scale parameters. (3) Development of the Mars dust storm environment simulator concept that allows providing technical support in simulating the dust storm environmental conditions testing.

Mars Dust Storm Characteristics

The atmosphere of Mars is very thin, and 95 % of the atmosphere composition is carbon dioxide, whose density is only about 1 % of the Earth's. The atmosphere pressure at Mars' surface is 700–l000 Pa. Wind is a common weather condition on Mars, with the wind velocities being 10 times higher than those on Earth. The air density is 120 times lower than on Earth [1, 2].

The Martian atmosphere contains significant amounts of dust with dust densities reaching 10^{-7} kg/m^3. Due to the low atmospheric pressure conditions on Mars' surface and high levels of irradiation from the sun, it is easy to accelerate the dust particles forming strong dust storms that occur frequently on Mars' surface, with the average wind speed reaching 50 m/s or even 150 m/s and more [3].

Mars Dust Storm Environmental Effects

The research studies and investigations on Mars dust storms environmental effects are still in their infancy. Considering that the Mars dust and moon dust properties are similar, it is possible to study the Mars dust storms environmental effects drawing analogies to the lunar dust environmental effects. Similar to lunar dust, Mars dust storms environmental effects include shadowing effects, wear effects, retarding effects, deposition/adsorption effects and static discharge effects.

Shadowing Effects

The shadowing effects caused by Mars dust storms exhibit themselves mainly through the weakening of the sun light intensity reaching the surface of Mars and through changing the solar spectrum. The dust in the Martian atmosphere diminishes the sunlight intensity by scattering, absorption and other effects. The suspended dust caused by Mars dust storms can also change the solar spectrum. Due to lack of green light, the sunlight spectrum on Mars is dominated by red that has an impact on solar cells.

Wear Effects and Retarding Effects

The size of Martian dust particles is very small, usually in the micron range that would cause severe wear of moving parts. The very small, high hardness particles can be seen as a special "abrasive". Physical contact between the working surfaces of various parts that are in any relative movement on Mars with such particles would produce scratches, surface flaking and other wear effects that can also lead to seal failures. The interaction of the dust with moving parts can affect their relative movement causing jamming of the moving parts, namely retarding effects.

Deposition–Adsorption Effects

Due to the small size and irregular shapes of the Martian dust particles, they easily can get attached to surfaces. Also, since the Martian atmosphere is rarefied, and the airflow is weak, the dust can be deposited and stay on the surfaces of detectors and other equipment easily. An important consequence of such deposits on solar arrays that they would obscure the sunlight and reduce the output power of solar arrays.

Static Discharge Effects

The dust suspended in the Martian atmosphere during the dust storms for a long time through mutual friction between the particles can be charged. The rovers or other equipment on Mars through interaction with such charged clouds of dust can be charged to high potentials and, with these potentials reaching a certain threshold, produce discharge phenomena in the atmosphere of Mars. Electromagnetic interference and electronic noise associated with discharges will also have an impact on the on-board sensitive devices.

Simulation Technology of Mars Dust Storm

Wind Tunnel Structure Design

Wind tunnel structure design involves the following aspects:

a. Design of a stable and a contraction sections of the wind tunnel;
b. Use Pro/E software to establish the geometry model of the wind tunnel;
c. Design of the nozzle structure.

The curve equation of the contraction section using a quintic curve can be expresses as [4]:

$$\frac{H - H_2}{H_1 - H_2} = 1 - 10\left(\frac{x}{L}\right)^3 + 15\left(\frac{x}{L}\right)^4 - 6\left(\frac{x}{L}\right)^5 \quad (1)$$

Where H_1, H_2 are the height of the contraction section inlet and outlet, H is the height of contraction section at X point, L is length of the contraction section.

Stable section length is determined according to the following rules:

$$\begin{aligned} L_W &= (1.0 \sim 1.5)D_1 \quad \mathrm{m} < 5 \\ L_W &= (0.5 \sim 1.0)D_1 \quad \mathrm{m} > 5 \end{aligned} \quad (2)$$

where D_1 is stable segment equivalent diameter, m is the contraction ratio, $\mathrm{m} = \frac{H_2}{H_1}$.

In Pro/E modeling software's using the Cartesian coordinate system, according to the shrink segment curve equation and the shrink ratio, the 2-D geometric model of the wind tunnel is shown in Figs. 1 and 2. Two types of the nozzle structure were selected, i.e., a diverging type and a tapered type structure, as shown in Fig. 3.

Dust Transportation System

A pneumatic conveyor system was designed to generate the Martian dust storm conditions. The schematic plan of such system is shown in Fig. 4. In simulating the Martian dust storms, a number of parameters of the dust flow need to be controlled. Among them, the concentration of particles in the formed cloud, their speed, the pressure in the dust chamber, etc. The dust particles are mixed with the gases

Fig. 1 Contraction section

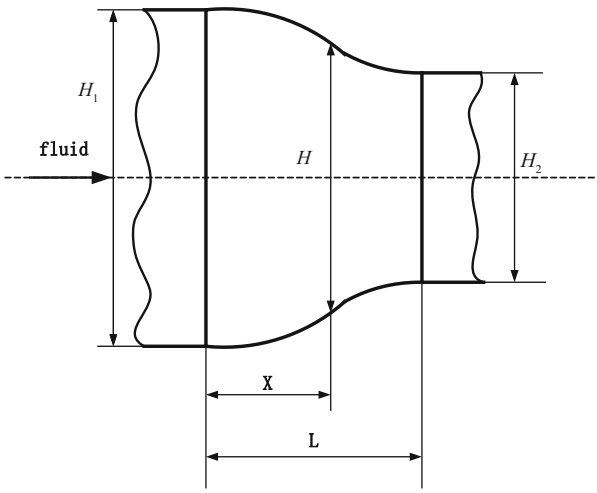

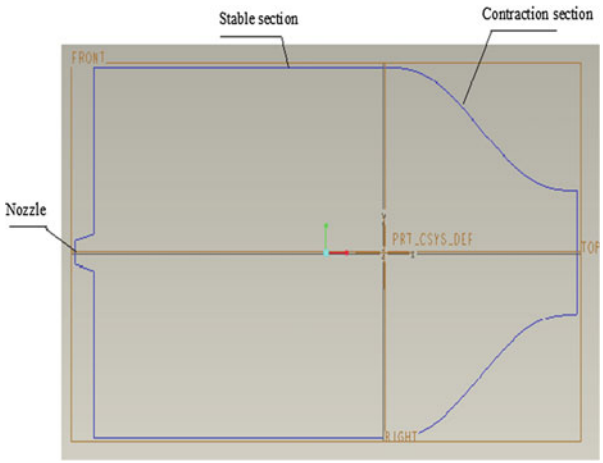

Fig. 2 2-D geometric model of the wind tunnel

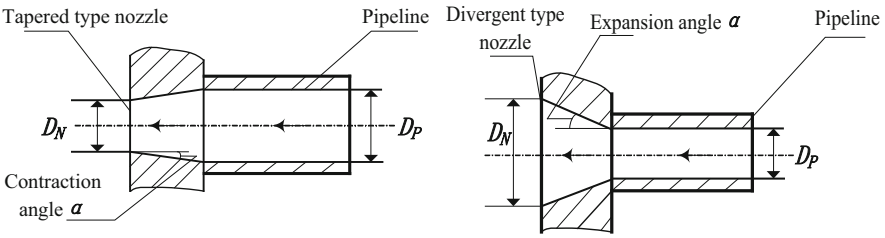

Fig. 3 Nozzle structure

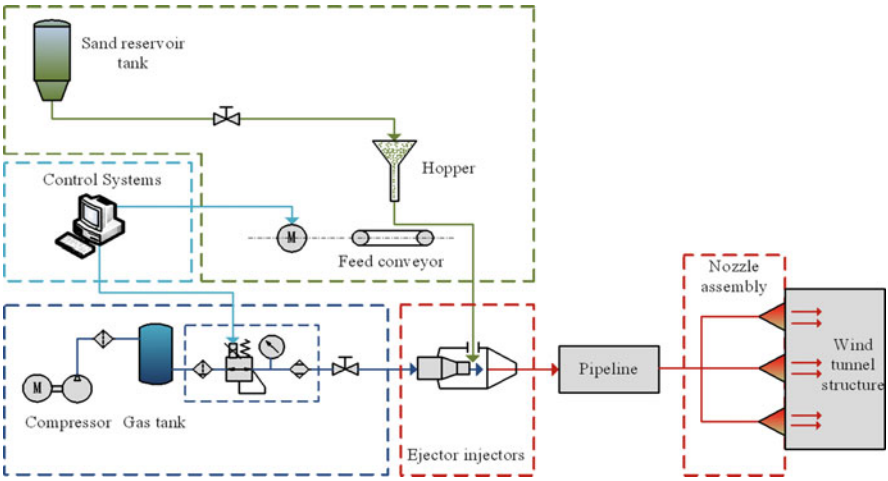

Fig. 4 Schematic of dust transportation to the wind tunnel

imitating the Martian atmospheric composition in the ejector to obtain the desired density of the particles in the mixture. Then the gas/particle mixture is sent through the pipeline into the dust chamber.

Numerical Simulation of Wind Tunnel Dust Storms

In the numerical simulation the meshing was done using ICEM software and the simulation using FLUENT software. Using Eulerian multiphase flow model, the gas processing was treated as the first phase; the solid particles are treated as second phase, The standard *k-e* model was selected for Mobile computing [5, 6].

Figure 5 shows the impact of the contraction ratio on flow distribution. As can be seen, wind tunnel with low contraction ratio has lower loss pressure and higher outlet speed. Wind tunnel with low contraction ratio has worse temperature uniformity.

Figure 6 shows the nozzle structure impact on flow distribution. As can be seen, tapered type nozzle outlet velocity can exceed the inlet velocity. Divergent type

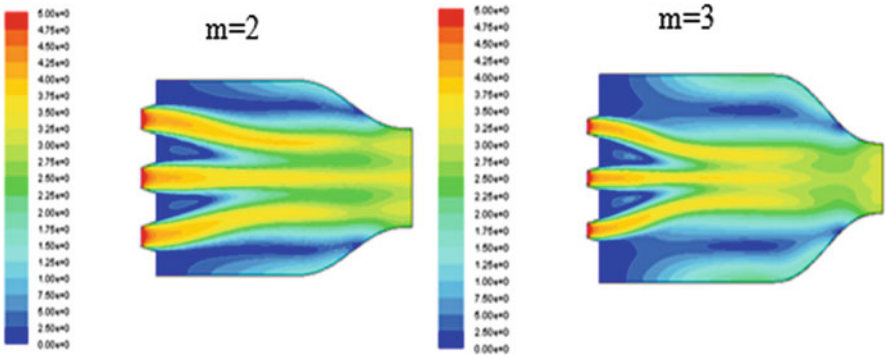

Fig. 5 Flow distribution of different contraction ratio

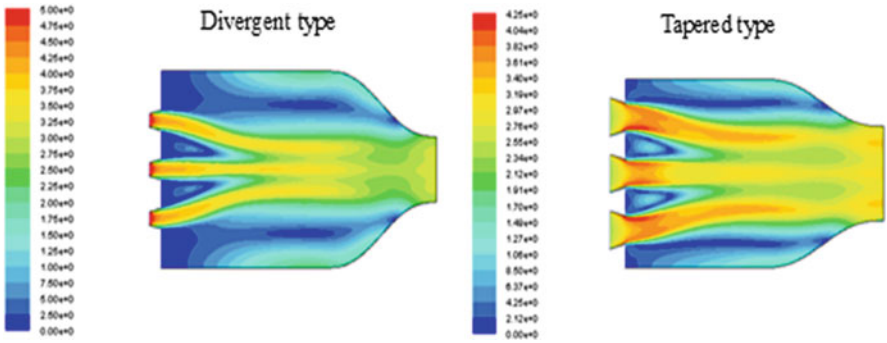

Fig. 6 Flow distribution of different nozzle structure

nozzle outlet velocity is less than the inlet velocity. Relative to the diverging type nozzle, the tapered type nozzle allow to achieve greater velocities.

Mars Dust Storm Simulator

Mars dust storm simulator includes a chamber, a vacuum system, a dust storm generator and a control system, as shown as Fig. 7. The technical parameters of the system are shown in Table 1.

The test chamber is placed horizontally, with the wind tunnel used for dust storm generation. A liquid carbon dioxide storage tank used as the gas source is set outside the chamber.

Firstly, the chamber is pumped using the vacuum pumps. Then, the flow of the dried CO_2 into the wind tunnel is initiated. By introducing the dust into the ejector where the dust particles are mixed with the gases, the airflow is generated and transferred under pressure to the main chamber. With the pressure of the chamber increasing, in order to maintain steady pressure, it is connected with another vertical chamber through a pipeline that is controlled by butterfly valve. When the pressure in the test chamber exceeds the requirements, the valve is opened and excess pressure is released, thus maintaining a relatively constant pressure in the main chamber.

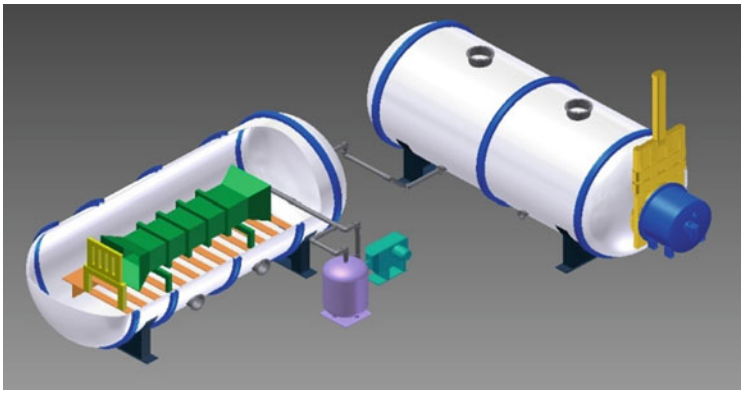

Fig. 7 Mars dust storm environmental simulator

Table 1 Summary of technical parameters of the Mars dust storm simulator

Property	Technical parameters
Atmospheric pressure	<1000 Pa
Simulated wind velocity	0–150 m/s
Dust density	0.01–1.24 kg/m^3
Size of dust particles	44–105 μm

References

1. Ouyang Z, Xiao F (2011) Major scientific issues involved in Mars exploration [J]. Spacecr Environ Eng 28(3):205–217
2. Ouyang Z, Xiao F (2012) The Mars and its environment [J]. Spacecra Environ Eng 29 (6):591–601
3. Hunt GE (1979) On the opacity of Martian dust storms derived by Viking IRTM spectral measurement [J]. J Geophys Res 84:8301–8310
4. Shih TH, Liou WW et al (1995) A new k-epsilon eddy-viscosity model for high Reynolds number turbulent flow model development and validation [J]. Comput Fluids 24(3):227–238
5. Samy M (2011) Hydrodynamic and thermal fields analysis in gas–solid two-phase flow [J]. Int J Heat Fluid Flow 34:740–754
6. Wang J, Xiao G, Ma B (2006) Numerical simulation of the gas-solid two-phase flows in a precalciner [J]. J Wuhan Univ Technol 27(4):177–179

Review of Atomic Oxygen Testing and Protection Methods in China

Jingyu Tong, Xiangpeng Liu, Haifu Jiang, Zhigang Shen, Meishuan Li, and Yiyong Wu

Abstract The developments in research conducted in China on atomic oxygen simulators, simulated space environment testing and methods for protection from space environment are reviewed. Principles and performance of atomic oxygen facilities in China (oxygen plasma ashing, directional oxygen plasma, energetic atomic oxygen with microwave or with laser), simulated space environment testing results, methods for protection from space environment that include the use of nano-particles, PVD, CVD and Sol–gel chemical modification processes are discussed. The preliminary results of atomic oxygen and its effects flight detection are described briefly. Future work in China in this area is suggested.

Keywords Atomic oxygen effects • Space environment simulation • Protection of space materials

Introduction

When the early shuttle missions returned from low Earth orbit (LEO) and materials' experiments flown on them and the ISS were returned to Earth and analyzed, it was discovered that many materials experienced extensive deterioration in their mechanical and physical properties. The surface morphology and chemical composition of many exposed materials changed, and some paints and coatings eroded away completely. Researchers determined that the space environment factors like atomic oxygen (AO), which exists in LEO, ultraviolet radiation, micrometeoroid

J. Tong (✉) • X. Liu • H. Jiang
Beijing Institute of Spacecraft Environment Engineering, Beijing, China
e-mail: tjyhjgcb@163.com

Z. Shen
Beijing University of Aeronautics and Astronautics, Beijing, China

M. Li
Institute of Metal, Chinese Academy of Sciences, Shenyang, China

Y. Wu
Harbin Institute of Technology, Harbin, China

J. Kleiman (ed.), *Protection of Materials and Structures from the Space Environment*, Astrophysics and Space Science Proceedings 47,
DOI 10.1007/978-3-319-19309-0_28

impacts had degraded these materials. This degradation has the potential to compromise the performance and lifetime of missions with significant time in LEO.

Since 1990's, China began to be interested in atomic oxygen and its effects. Beijing Institute of Spacecraft Environment Engineering [1], Lanzhou Institute of Vacuum Physics [2] and Beijing University of Aeronautics and Astronautics [3] developed three atomic oxygen simulators respectively and carried out a large number of atomic oxygen ground tests. Up to now, many institutes, university and companies of China are investigating the atomic oxygen effects and effective protection schemes from the atomic oxygen for Chinese manned spacecrafts and space station. This paper provides an overview of the efforts on development of atomic oxygen simulators, simulated space environment testing and methods for protection from space environment in China. Then the future work in these areas in China is suggested.

Atomic Oxygen Facilities

Energetic Atomic Oxygen with Microwave

The first energetic atomic oxygen facility of China was developed by Beijing Institute of Spacecraft Environment Engineering in 1996. The facility is based upon an advanced electron cyclotron resonance ions source driven by 1 kW RF at 2.45 GHz. A two plane-electrode is used as an extraction system. The energy of the extracted ion beam is 4000 eV. The beam is transported through a retarding mesh where the beam energy is reduced from 4000 to 6 eV. The beam is neutralized in a stainless steel cylinder through electron transfer during a grazing-incidence reflection from the inner surface of the cylinder. As ions exit the decelerating mesh, the effect of space charge in the beam results in the beam expanding radially as it runs through the cylinder and the ions are neutralized by electron pickup.

Two deuterium lamps are used to provide moderate intensity UV up to 1–3 suns between 115 and 400 nm. The lamps are used in combination with atomic oxygen source for performing synergistic studies.

The technical parameters of the facility are summarized below:

Atomic oxygen flux: 2.8×10^{15} AO/cm^2 s.
Beam energy: 5–6 eV.
UV wavelength: 115–400 nm.
UV intensity: 1–3 suns.

The schematic diagram of the facility is shown in Fig. 1.

The general view of the facility is presented in Fig. 2.

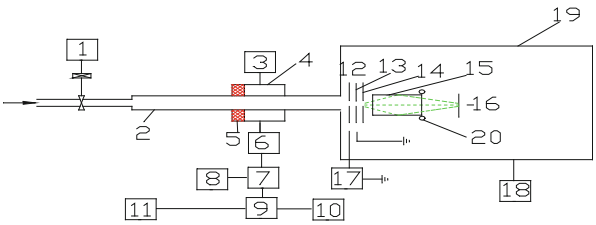

Fig. 1 Schematic diagram of atomic oxygen/VUV simulation facility. (**1**) Mass flow controller; (**2**) quartz tube; (**3**) short circuit piston; (**4**) discharge chamber; (**5**) permanent magnet; (**6**) stub tuner; (**7**) Directional coupler; (**8**) power meter; (**9**) circulator; (**10**) water load; (**11**) microwave source; (**12**) source pole; (**13**) accelerate pole; (**14**) decelerate mesh; (**15**) neutralizer; (**16**) sample stage; (**17**) high voltage source; (**18**) vacuum pump unit; (**19**) vacuum tank; (**20**) deuterium lamps

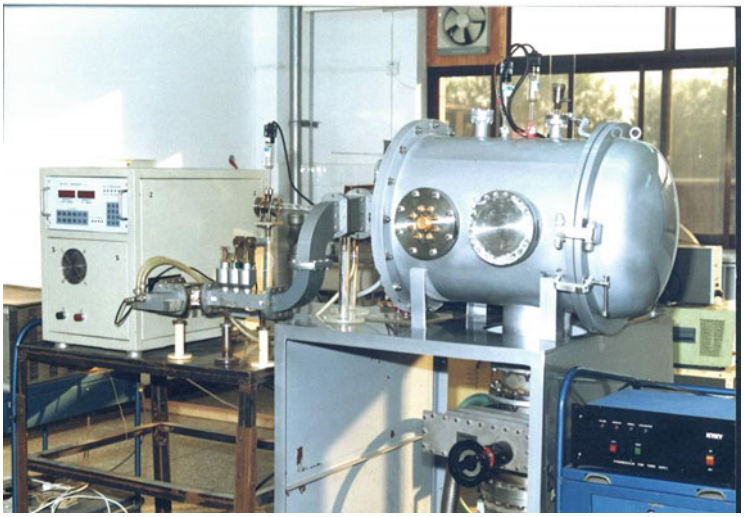

Fig. 2 Image of the atomic oxygen facility in the Beijing Institute of Spacecraft Environment Engineering

Directional Oxygen Plasma

The first directional oxygen plasma simulator in China was developed by Lanzhou Vacuum Physics in 1990's. The facility has a microwave oxygen plasma source with a sleeve antenna. The plasma beam, confined by a magnetic field, impacts on a molybdenum plate positioned at 45° to the incident beam. The plasma beam is neutralized and reflected to the sample holder.

The technical parameters of the facility are summarized below:

Atomic oxygen flux: 5.2×10^{15} AO/cm^2 s.
UV wavelength: 185–400 nm.
UV intensity: 2–4 suns.

Oxygen Plasma Ashing

The first oxygen plasma ashing simulator in China was developed by Beijing University of Aeronautics and Astronautics in 1990's. The facility has a thermal plasma source with a thermal cathode discharge. The walls of the plasma chamber are covered with 600 small permanent magnets to confine the plasma. The plasma density is $10^{10}/cm^3$. During a test, the sample is immersed in the plasma and is etched by it.

Energetic Atomic Oxygen with Laser

The first energetic atomic oxygen beam simulator using a detonation laser in China was imported from Canada by Harbin Institute of Technology. It was designed and developed by ITL. Inc., Canada [4]. The facility has a pulse laser and a hypervelocity nozzle. The laser beam is focused in the throat of nozzle, where O_2 is ionized to O^+. The O^+ beam is accelerated and neutralized forming an energetic neutral atomic oxygen beam with an average energy of 5 eV that corresponds to velocities of ~8 km/s.

Up to now, about 10 atomic oxygen beam facilities are operational in China. Except above-mentioned facilities, others are distributed in colleges, universities and institutes such as Shenyang Institute of Metals, Armored Corps College, Northwest Institute of Technology, Lanzhou Institute of Chemical Physics, Yanshan University, Dalian Institute of Chemical Physics, etc.

Atomic Oxygen Testing Activities

Since 1990's, a large number of tests in the atomic oxygen simulators have been carried out in China. The samples included paints, polyimide films, materials of various compositions, solar cells, seal materials, lubricant materials, etc.

Among the investigated materials great attention was given to the S781 white paint that is often used on surfaces of spacecrafts as thermal control material. Only AO and AO/UV simulation testing was conducted on the S781 paints with some results briefly discussed below.

Mass Loss

Figure 3 presents the mass loss curves of S781 white paint exposed to AO only and to AO + UV. The curves show that the increase in mass loss is linear as the AO

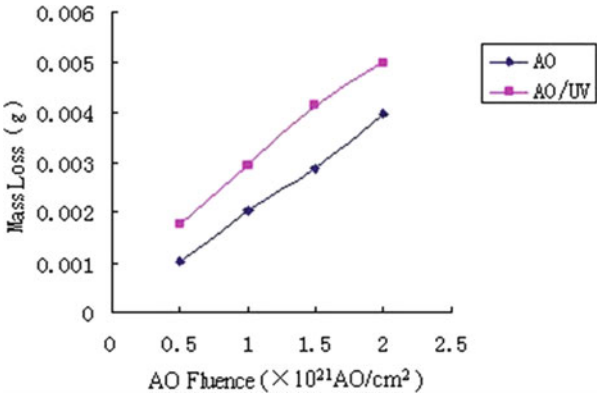

Fig. 3 Mass loss curves of S781 white paint without and with UV

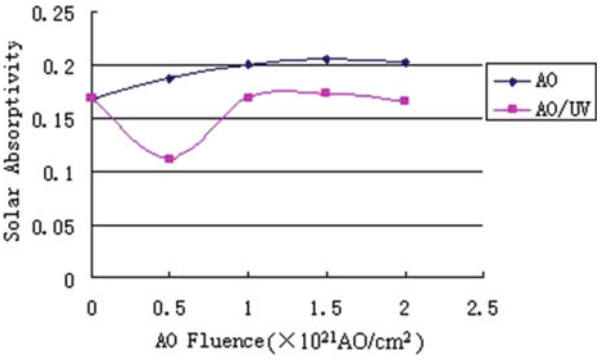

Fig. 4 Solar absorptivity of S781 white paint exposed to AO only and to AO + UV

fluence increases. They also tell us that there is a synergistic effect from exposure to a combined AO/UV flux, with a higher mass loss than in an AO exposure alone.

Solar Absorptivity

Figure 4 shows the dependence of solar absorptivity of S781 white paint on the total fluence of the AO without and with UV irradiation. As can be seen from Fig. 4, the solar absorptivity in the experiments with AO only increased in the early stages of AO exposure, stabilizing around AO fluencies reaching 1×10^{21} AO/cm^2. The total change in solar absorptivity is only 0.037. It is obvious that the solar absorptivity of S781 white paint is relative stable in AO environment.

In the AO/UV combined environment, the increase in solar absorptivity is smaller than in the experiments with AO only, because atomic oxygen may act to reverse some of degradation from UV. The data for AO/UV obtained at the fluence of 0.5×10^{21} seems to be abnormal and, possibly, due to a measuring error.

Table 1 XPS analysis of S781 paint

	Before exposure	After AO exposure	After AO/UV exposure
C	23.4	23.09	16.54
O	41.4	41.43	42.26
Si	10.3	5.73	7.47
Zn	24.8	28.84	33.73

Composition

The XPS analysis data of S781 white paint before and after the single and combined exposure to AO and AO + UV are shown in Table 1. The main composition of S781 paint includes C, O, Si and Zn. As can be seen from Table 1, a substantial reduction in C content happened after the combined AO + UV exposure. An increase in the Zn consternation on the surface after single AO and combined AO + UV exposure can be explained by erosion of the paint matrix and exposure of the Zn-based pigment particles. The chemical bonds of the binder matrix have been broken by AO attack with formation of volatiles like CO and CO_2.

Protection Methods Against Atomic Oxygen Erosion

During last 20 years, some protection methods against atomic oxygen erosion were developed in China that include the use of nano-SiO_2 particles fill, ion implantation and chemical processes. The materials modified with these processes show good stability against atomic oxygen.

1. Epoxy filled with nano SiO_2 particles.
   In this approach, an epoxy, a curing agent, a diluent and nano-SiO_2 particles are mixed and agitated sufficiently. The prepared mixture is cast and solidified providing for a modified epoxy material filled with nano-SiO_2 particles. In order to increase the compatibility between the epoxy and the nano-SiO_2 particles, the particles have been activated with via an aerogel process.
   The results of atomic oxygen simulation tests had shown that the higher the nano-SiO_2 percentage content in the modified epoxy material, the better the protection property of epoxy material against the atomic oxygen. For samples with the mass percentage of nano-SiO_2 particles of 5, 10 and 15 %, the erosion rate of modified epoxy material was found to reduce form 35 to 8 % and to 9 % of the original epoxy erosion rate correspondingly.
   The results of infrared analysis show that some new chemical bonds are formed, such as Si–O–C, Si–C on the surface of samples after exposure to atomic oxygen. The new chemical bonds may facilitate the protection ability of the epoxy material against atomic oxygen.

2. Ion implantation/deposition process:
   Using a multifunctional plasma treatment facility, firstly, silicon ions are implanted into the substrate surface, then the ion source is turned off and a SiO_2 film is deposited on the substrate surface in-situ using a PVD source. There is no clear interface between SiO_2 film and substrate surface with this process. The coating has a very good adhesion to the substrate and is not flaking off. If some pin-hole and crack defects are present in the coating, the AO will react with the silicon ions in the region below the defects and a new SiO_2 layer can be formed, providing a self-healing effect that should decrease substantially the "undercutting" damage of substrates by AO in such damaged regions. The results of ground-based tests of such samples show that this coating has a good AO resistance. The erosion rate is 10^{-25} cm^3/atom, i.e., 10 times lower than for the pristine substrate. The process does not significantly affect the thermo-optical properties of pristine substrate.
3. Sol–gel process.
   The ethyl orthosilicate (TEOS) is used to produce SiO_2 sol with Sol–gel process; Mixing SiO_2 sol up with polydimethylsiloxane as some rate to produce the mixture of organosilicon resin/SiO_2 sol; To increase the intersolubility of SiO_2 sol and polydimethylsiloxane, add some siloxane couplant to the mixture and stir the mixture sufficiently. The clear and achroic organosilicon resin/SiO_2 hybrid sol can be attained; The substrate surface is provided a hybrid sol coating and has a heating curing process in vacuum furnace. Then a clear and achroic organosilicon resin/SiO_2 hybrid coating can be formed on the substrate surface. Organosilicon resin/SiO_2 hybrid coating has both advantages of organosilicon resin and SiO_2. It is softer and tough and has less defects than SiO_2 coating produced with PVD and CVD. Meanwhile it has much better AO resistance than organosilicon resin. Sol–gel process is simple and cheap. It fits the protection of large and complex spacecraft surface against atomic oxygen.

Flight Experiments with Atomic Oxygen Detectors

In order to understand the atomic oxygen environment effects, to confirm and update predictive models for AO erosion of materials in LEO environment and to define the best techniques for ground-based experiments, it is necessary to develop reliable in flight experiments AO erosion detectors with collection of the erosion data.

Beijing Institute of Spacecraft Environment Engineering has been developing a small, low-cost sensor for evaluating the atomic oxygen erosion rates. The sensor is based on measuring the change in the electrical resistance of a film that is made of some susceptible to atomic oxygen erosion conductive materials. Presently, suitable atomic oxygen sensing conductive materials include silver, osmium and carbon. Silver has very high atomic oxygen reactivity that is non-linear. The carbon reactivity with atomic oxygen is medium and linear. But its electrical resistance has

a poor stability in the harsh space environment. Osmium electrical resistance is very stable in the space environment. Its atomic oxygen reactivity has good linearity.

So, osmium has been chosen as electrical resistance material in AO flux sensor. The sensor film has been prepared by electroplating and photo etching. It has a good stability and linear AO reactivity. Silver-based sensors were also evaluated. The silver sensors were prepared using PVD deposition. One of the Silver-based sensor advantages is its quick "switch" speed.

A combined detector with 2 AO flux sensors and 6 AO effect sensors has been developed. The detector has been evaluated and standardized in AO ground simulation tests. It passed also the radiation, thermal shock and vibration tests. Flight experiments are being planned on the Chinese space station with these detectors.

Conclusions

A large portion of space activities in the near future will be concentrated in the low Earth orbit. Spacecraft materials must be selected and assessed so that they can withstand the deleterious effects of low Earth orbit environment. Environmental factors in the low Earth orbit include atomic oxygen, ultraviolet, electrons, protons, micrometeoroids and orbital debris. It has been proven that atomic oxygen is one of the dominant factors in LEO that affect spacecraft materials.

Extensive work was conducted in China since 1990's to study the atomic oxygen effects on materials, simulating the atomic oxygen in ground facilities, develop AO sensors and protection methods to prevent the AO erosion.

In order to meet the development schedule of the Chinese space station and provide a unified approach to evaluating materials for LEO application a plan of action is proposed as follows:

1. All of the AO Facilities in China need to be standardized by an authoritative team of specialists, so that the tests results obtained form different facilities will be dealt with confidence.
2. Great attention should be given to the planning and conductance of flight experiments, so that the flight data would be of adequate value to be used in updating the existing predictive models both of the environment and the environmental effects on spacecraft, and in defining the best techniques for ground-based experiments.
3. In order to meet the requirements for effective protection of materials from the AO erosion for large and complex spacecraft surfaces, new protective methods that are efficient, simple in applications and cheap would be investigated continuously.

References

1. Duo S, Li M, Zhou Y, Tong J, Sun G (2003) Investigation of surface reaction and degradation mechanism of Kapton during atomic oxygen exposure. J Mater Sci Technol 19(6):535–539
2. Wang Y, Chen X, Li Z, Zheng K, Wang L, Feng Z, Yang S (2009) Atomic oxygen sensors based on nanograin ZnO films prepared by pulse laser deposition. In: Kleiman J (ed) Proceedings of the 9th international conference "Protection of materials and structures from space environment". AIP Conference Proceedings, vol 1087(1). AIP Conference Proceedings, pp 455–462, Torondo, Canada, 20–22 May 2008
3. Wang X, Zhao X, Wang M, Shen Z (2007) An experimental study on improving the atomic oxygen resistance of epoxy resin/silica nanocomposites. Polym Eng Sci 47(7):1156–1162, July
4. Kleiman J, Horodetsky S, Sergeyev V, Issoupov V, Ng R (2006) Critical review of the design of space environment simulators: lessons learnt. In: Proceedings of the 10th international symposium on "Materials in a space environment"/8th international conference on "Protection of materials and structure from the LEO space environment", Collioure, France, 19–23 June, 2006

Structural and Mechanical Properties Changes in Carbon and Boron Nitride Nanotubes Under the Impact of Atomic Oxygen

Ekaterina N. Voronina and Lev S. Novikov

Abstract This paper presents results of simulation of processes of the oxygen atom impact on carbon and boron nanotubes with *ab initio* (DFT) and semi-empirical (SCC DFTB) methods. Our calculations demonstrated that the impact of oxygen atoms may cause the nanotube elongation and unzipping. We performed DFTB simulations of the impact of hyperthermal oxygen atoms on graphene and carbon nanotubes of small diameter in the case of a low-coverage regime to obtain a detailed picture of the formation of different oxygen-containing groups on their surfaces.

Keywords Nanostructures • Carbon nanotubes • Boron nitride nanotubes • Graphene • Atomic oxygen • Computer simulation

Introduction

In the near future, various nanostructures: carbon and boron nitride nanotubes, graphene and sheet of hexagonal boron nitride (*h*-BN), nano-ribbons, etc., will be applied in spacecraft design both as fillers in nanocomposites and as stand-alone materials. In low-Earth orbits one of the main factors that cause the materials damage is atomic oxygen of the Earth's upper atmosphere. High relative kinetic energy of oxygen atoms (~5 eV) due to the spacecraft orbital velocity enhances their reactivity and opens additional pathways of their reaction with the matter [1]. AO impact leading to erosion and mass losses of materials is well studied for conventional bulk spacecraft materials but the data concerning the damage of nanostructures and nanomaterials under AO exposure are quite limited, and the computer simulation can become an efficient mean for its investigation.

E.N. Voronina • L.S. Novikov (✉)
Lomonosov Moscow State University, Skobeltsy Institute of Nuclear Physics, Moscow, Russia
e-mail: novikov@sinp.msu.run

J. Kleiman (ed.), *Protection of Materials and Structures from the Space Environment*, Astrophysics and Space Science Proceedings 47,
DOI 10.1007/978-3-319-19309-0_29

CNT-based nanocomposites can be applied as multifunctional spacecraft materials providing the protection against electrical discharges, thermo-cycling, hypervelocity impact, etc. Carried out experiments on CNT-based polymer nanocomposites allow to conclude that embedding CNTs into a polymer matrix improves its durability to AO. However, AO impact on carbon nanostructures can cause and significant changes in their properties and even their partial destruction. For example, oxidation is one of the most widely used methods for the purification of carbon nanostructures and tailoring their physical, chemical, and electronic properties [2], while high power oxygen plasma can inflict severe damage to the CNT structure [3].

Boron nitride nanotubes (BNNTs), structural analogues of CNTs but electrical insulators (bandgap of ~5 eV), attract much attention due to their excellent mechanical properties, high thermal stability and high resistance to oxidation [4].

Our calculations with DFT and DFTB methods demonstrated that the impact of oxygen atoms may cause the nanotube elongation and unzipping. Possible mechanisms of such interaction and its influence on the nanotubes structure and mechanical properties are discussed. The reported study was supported by the Supercomputing Center of Lomonosov Moscow State University [5].

Methodology

Our simulations are performed using density functional theory (DFT) and self-consistent charge density functional based tight-binding (SCC DFTB) method, implemented in DMol^3, CASTEP, and DFTB+ code (Accelrys Materials Studio 6.0 [6]). All-electron spin-polarized calculations are used within GGA approximation with PBE exchange-correlation functional and DNP basis set. For DFTB calculation we apply mio parameter set [7], molecular dynamics algorithms with time steps of 0.05–0.25 ps (total simulation time of 1.0–2.5 ps).

We consider armchair and zigzag single-walled CNTs and BNNTs with diameters of 0.4–2.1 nm. For nanotubes with diameter 0.4–1.1 our models are about 1.7 nm in length (sevenfold and fourfold periodicity for armchair and zigzag nanotubes, respectfully) and contain 84–224 atoms. For nanotubes of larger diameter, we use models with the length of 1.0 nm (fourfold and double periodicity). For graphene and *h*-BN sheets, the models with size of 7×7 unit cells are created. The periodic boundary conditions are applied, and the size of super-cells is $4.0 \times 4.0 \times 1.7$ nm for nanotubes and $1.7 \times 1.7 \times 2.0$ nm for graphene and *h*-BN. The Brillouin zone is sampled by $1 \times 1 \times 4$ and $1 \times 1 \times 8$ *k*-points using the Monkhorst–Pack scheme.

Adsorption energies are calculated by using the expression: $E_{ads} = E_{nanotube+O} - (E_{nanotube} + E_O)$, where $E_{nanotube}$, E_O and $E_{nanotube+O}$ is the total energy of the optimized nanotube, oxygen atom and nanotube + O system, respectively.

Results and Discussion

Preferential site for an O atom adsorption on the CNT surface is a bridge site over C–C bonds leading to formation of an epoxide (epoxy) or an ether group depending on the bond orientation with respect to the nanotubes axis [8]. The bonds of an armchair nanotube that lie at an angle of 90° with respect to the nanotube axis, are called "orthogonal", and the bonds that are at an angle of 30° are "slanted", or "longitudinal" (for an zigzag nanotube the angles are 60° and 0°, correspondingly). The formation of an ether over orthogonal bonds is energetically preferable in comparison with the epoxy formation over slanted ones, especially in the case of armchair nanotubes [e.g., for the (3,3) CNT $\Delta E_{ads} = 1.8$ eV]. This difference in adsorption energies for orthogonal and longitudinal bonds can be explained by the influence of the surface curvature, which becomes more apparent for armchair nanotubes of small (<1 nm) diameter [9]. Ether- and epoxy-like B–O–N structures form on the BNNT surface as a result of the O atom adsorption [10], although the energy differences are smaller.

Our calculations showed that the type of the forming group depends also on diameter of CNTs as well as of BNNTs [11]. With increasing nanotube diameter, the adsorption energy of oxygen atoms reduces, and the formation of epoxies on the CNT surface prevails (arrows mark the points where transition from ether to an epoxy occurs). Calculated dependences of bond opening ratio (BOR, the ratio of the distance between C or B and N atoms after the O adsorption to the bond length of the pristine nanotubes) and of the adsorption energies on the diameter of armchair and zigzag CNTs and BNNTs are presented in Fig. 1a, b. BOR of ~1.5 corresponds to the formation of an ether, and BOR of 1.1 corresponds to an epoxy. It should be

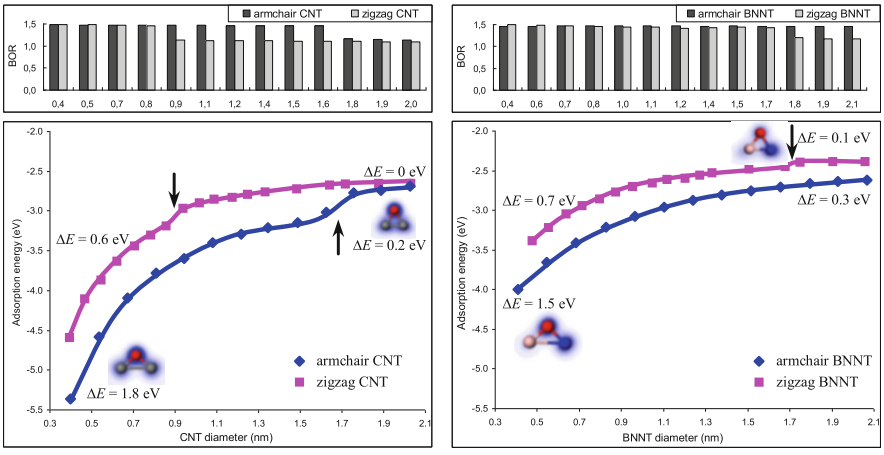

Fig. 1 BOR (*upper panel*) and adsorption energy (*lower panel*) in a bridge site over the orthogonal bonds versus CNT and BNNT diameter. ΔE_{ads} is the difference in adsorption energies for orthogonal and longitudinal bonds

noted that as the diameter increases the differences in the adsorption energy for orthogonal and longitudinal bonds decrease.

In general, the increase in the number of O atoms attacking a nanostructure leads to the enhancement of bond elongation and breaking [12, 13]. The adsorbed O atoms enhance the reactivity of adjacent bonds, and formed epoxy or ether groups can be more easily attacked by next O atoms. For nanotubes of small diameter the preferential site for the second O atom adsorption is the a bridge site over the orthogonal bond which is located in the same hexagonal cell and is parallel to the first O-containing group. As a result on the CNT surface two parallel ethers appear.

We calculated E_{ads} for the sequential adsorption of four O atoms on the surface of armchair and zigzag CNTs and BNNTs with diameters of 0.4–1.4 nm (Fig. 2).

The adsorption energy of the second O atom for almost all nanotubes lies lower than E_{ads} of the first one. This result indicates that the cooperative influence of two O atoms on neighboring bonds is more intensive in comparison with the case of independent adsorption when the distance between adsorbed atoms is large enough [12]. For armchair CNTs curves for 2–4 adsorbed atoms are almost parallel (except CNTs with diameter smaller than 0.5 nm), because there forms a chain of four parallel ethers on the CNT surface of all considered diameters. For zigzag CNTs there is a noticeable bend on the curve for two adsorbed atoms at ~0.9 nm. This bend is associated with the transition from ether to epoxy formation (Fig. 1a), leading to the increase in E_{ads} (in an absolute value). In the case of BNNTs, the curves for 2–4 atoms in the considered diameter range do not have any noticeable bendings and are almost parallel to each other.

To compare the atomic oxygen impact on bonds with different orientations with respect to nanotube axis, we performed similar calculations for the sequential adsorption of O atoms on the longitudinal bonds. As the number of adsorbed atoms rises, the groups situated in the middle of a forming epoxy chain may transform into ethers [12]. Such a transition is more typical to armchair nanotubes than to zigzag ones due to the fact that the distance between the formed epoxies is lesser. Because this distance depends also on the surface curvature, this effect intensifies with increasing the nanotube diameter (Fig. 3). The regularities described above are valid for BNNTs, too. Within the considered range of diameters, for armchair BNNTs the sequential adsorption of two and more O atoms over longitudinal bonds results in transforming all epoxy-like groups into ether-like ones, but for zigzag BNNTs such a transformation occurs only for groups situated in the center of epoxy chains consisting three or more atoms.

The sequential adsorption of several O atoms with formation of an ether chain can lead to noticeable changes in the nanotube geometry: CNTs and BNNTs with adsorbed O atoms have non-cylindrical geometry (their cross-section become ellipses), and the deviations are the most significant for armchair CNTs and BNNTs for adsorption over orthogonal bonds (a major/minor axis ratio reaches up to 1.2). Adsorption-induced elongation is more prominent for nanotubes with smaller diameter (~0.5 nm) and weakens with the diameter increasing. Figure 4 demonstrates the dependencies of relative elongation on diameter in the case of four adsorbed atoms. For adsorption over orthogonal bonds of armchair nanotubes strain

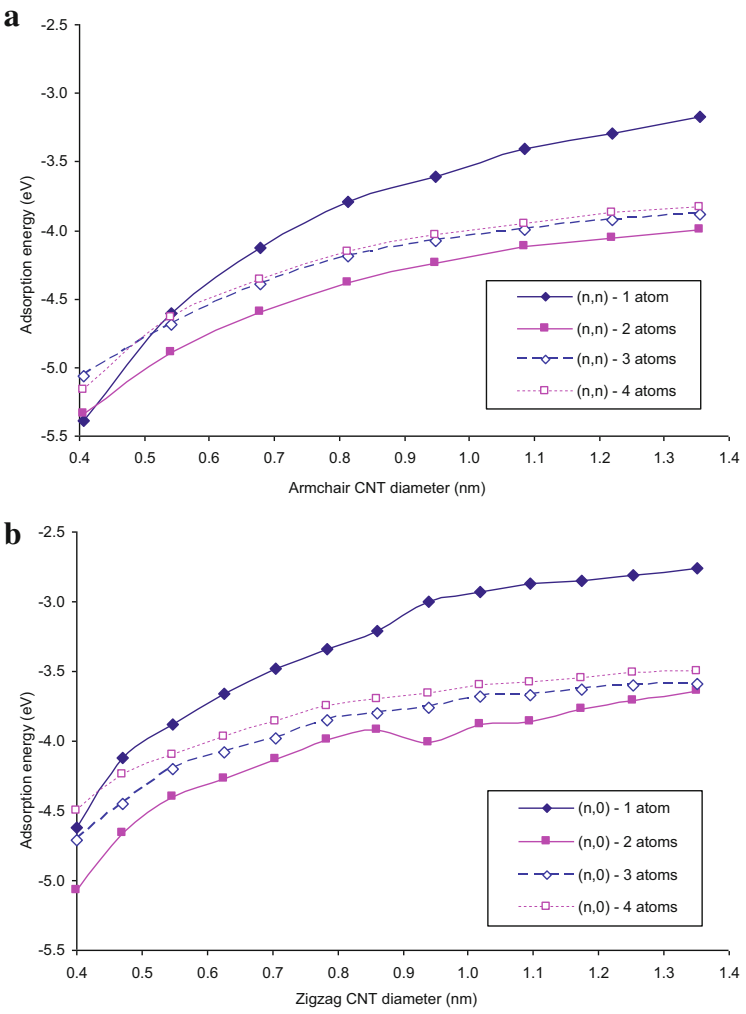

Fig. 2 Dependencies of E_{ads} for the sequential adsorption of four O atoms on diameter of armchair (**a**) and zigzag (**b**) CNTs (orthogonal bonds)

is small enough (no more than 0.5 %) whereas the similar process leads to more noticeable elongation of zigzag CNTs and BNNTs (up to 1–1.2 %). Such a difference can be explained by the fact that in zigzag nanotubes, orthogonal bonds are situated at an angle of 60° with respect to the axis, so bond breaking causes the more significant elongation for zigzag nanotubes than for armchair ones (for the latter orthogonal bonds are perpendicular to the axis).

For comparison, the relative CNT and BNNT elongation due the O atom adsorption over longitudinal bonds is presented in Fig. 4. Longitudinal bonds of armchair nanotubes are oriented at the angle of 60° with respect to the nanotube

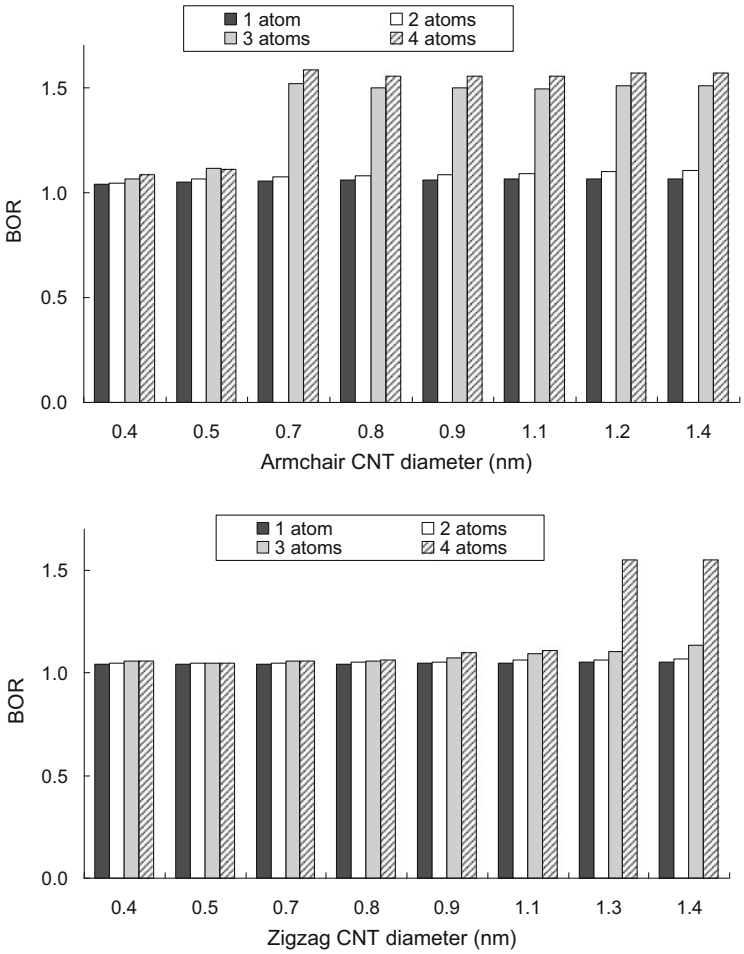

Fig. 3 BOR for sequential adsorption of four O atoms over longitudinal bonds on armchair (*upper figure*) and zigzag (*lower figure*) CNTs (in the case of 3 and 4 atoms, BOR is given for central atoms)

axis, and the formation of ethers over one or two longitudinal bonds (Fig. 3a) leads to a strain of ~1.4 % for a (4,4) CNT and ~2.1 % for a (4,4) BNNT, correspondingly [in the case of the epoxy formation, e.g., a (3,3) CNT, the elongation is only ~0.5 %]. For zigzag CNTs, the distance between forming epoxide groups is large enough, and breaking of longitudinal bonds upon the adsorption of several O atoms occurs only for nanotubes of large diameter (Fig. 3b), therefore the elongation for the given range of CNT diameters is small. In the case of zigzag BNNTs, the breaking of longitudinal B–N bond occurs at the adsorption of the second O atom (Fig. 3b), causing a noticeable (0.5–1 %) elongation of nanotubes.

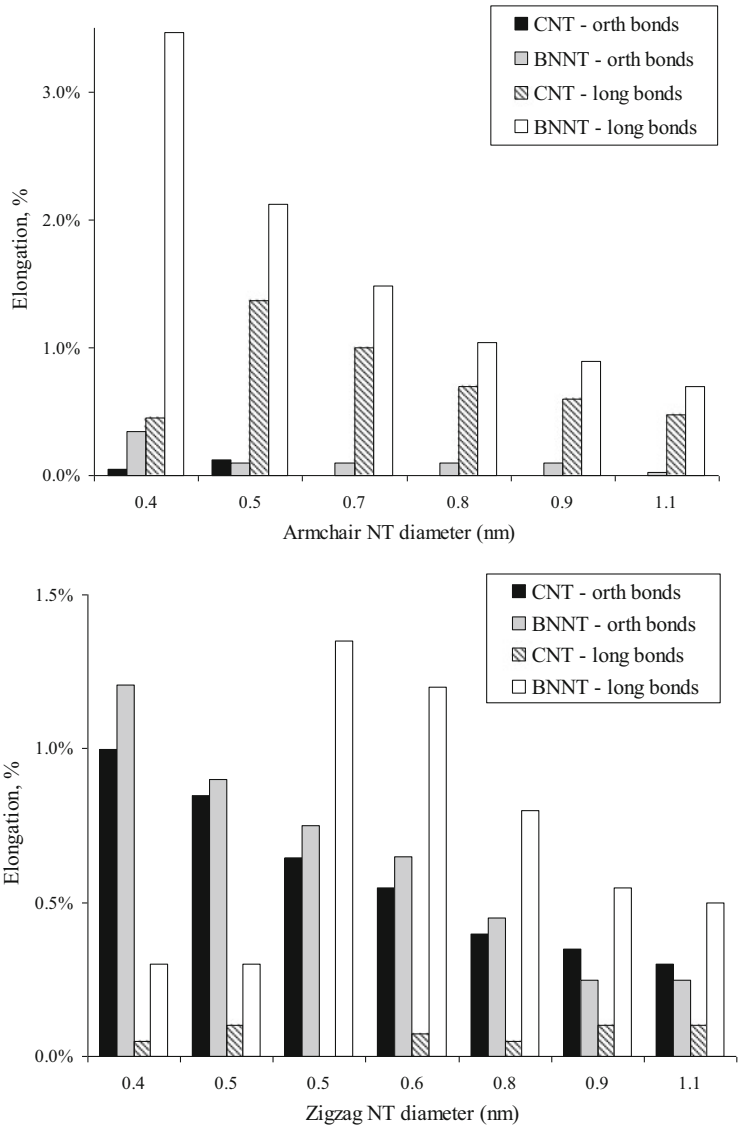

Fig. 4 CNT и BNNT elongation after the adsorption of four O atoms over orthogonal and longitudinal bonds versus nanotube diameter

To analyze changes of nanotube mechanical properties due to oxygen adsorption, we calculated Young's modulus. We used two approaches: via second derivative of strain energy with respect to the axial strain [14] with DMol^3 code and via stress with CASTEP software. Decrease in Young's modulus after adsorption of several (up to 4) O atoms, which formed an ether chain along the nanotube axis, is calculated to be about 5 %. However, if such an ether chain consists of 7 O atoms

(i.e., its length was almost equal to the length of our nanotube model which was 1.7 nm), Young's modulus reduces to ~15 %. Our calculations show that the destruction of armchair nanotubes occurs at larger strains in comparison with zigzag ones. For instance, failure strain of (4,4) CNT and BNNT are about 0.40 and 0.35, while for (7,0) nanotubes its value is significantly smaller (0.19 and 0.23, respectively). At some degree of tension applied to armchair (4,4) CNT (strain is ~0.14–0.16), ether groups transform into epoxides, however on the surface of zigzag (7,0) nanotube such groups remains longer, almost till the ultimate failure.

Under the attack of several O atoms, carbonyl (or semiquinone) pairs can form on CNTs surface, leading to CNT unzipping and breaking into graphene nanoribbons [15, 16]. The transformation of ether into a carbonyl pair as a result of the attack of a free O atom becomes more energetically preferable when there are two or more parallel ethers on the CNT surface, and the probability of such a process decreases for CNTs of larger diameter [17]. In the case of BNNTs, the similar process does not lead to the nanotube unzipping due to chemical bond formation between adsorbed O atoms. Moreover, for BNNTs with ether-like structures on their surface the attack of the free O atom may lead to desorption of O_2 molecule and almost complete recovery of the B–N bond.

As it was shown above, oxygen adsorption processes depend strongly on the surface curvature. Graphene can be considered as a limited case of CNT with infinitely large diameter. It can be expected that preferential sites for the second O atom adsorption for the armchair (4,4) CNT of small diameter (~0.5 nm) and a graphene sheet differ significantly. The relative energies of different configurations when the second O atom adsorbs in close vicinity of the first one, are given in Fig. 5. In the case of the (4,4) CNT, the lowest-energy configuration is two parallel ethers (CNT1) at the opposite ends of a hexagonal cell, whereas for graphene a pair of next nearest neighbor epoxies (Gr1) is energetically preferable [18] (although it should

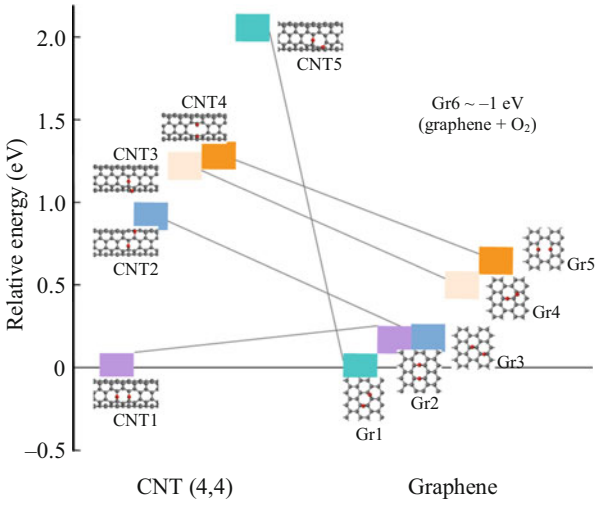

Fig. 5 Relative energies of configurations with two adsorbed O atoms for an armchair (4,4) CNT and a graphene sheet (when the second O atom adsorbs in the close vicinity of the first one)

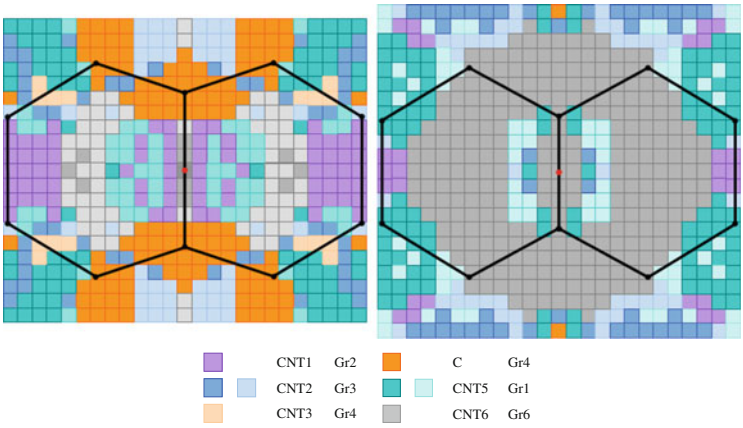

Fig. 6 Diagram of the O-containing group formation on the surface of (4,4) CNT (*left*) and graphene (*right*) with respect to the impact factor of incident O atom

be noted that the difference in energies of these configurations is small enough and reduces with increasing the size of a graphene sheet model). Moreover, when the second O atom is situated in the close vicinity of the first one, for graphene we observed the desorption of both atoms with formation of O_2 molecule, and the energy is the system "graphene sheet + O_2" (Gr6) is about 1 eV lower than that of structure Gr1. It should be emphasized that the presented energetic relations between different O-containing structures are valid only under condition of oxygen low-coverage regime.

The SCC DFTB simulation of the formation of O-containing groups on the surface of (4,4) CNT and graphene with one adsorbed O atom showed that the adsorption of the second O atom is governed also by its impact factor. The diagrams of the O-containing group formation with respect to the impact factor of the incident atom are presented in Fig. 6. It can be seen that for graphene the formation of O_2 molecule with subsequent desorption prevails [19] over the formation of structures Gr1–Gr3 whereas in the case of (4,4) CNT scattering and O_2 formation play a minor role, and the dominant process is the O atom adsorption over C–C bond (CNT1–CNT3, CNT5). When the incident O atom hits near C atoms in the close vicinity of the ether group on the CNT surface, we observe the formation of carbonyl or semiquinone pairs (CNT4) indicating CNT unzipping, but for graphene this event as well as the formation of two ethers is back enough.

Conclusions

1. The type of the oxygen-containing groups that form on the surface of carbon and boron nitride nanotubes as a result of oxygen atom adsorption depends not only on the bond orientation with respect to the nanotubes axis, but on nanotube diameter and chirality.

2. With increasing nanotube diameter, the adsorption energy of oxygen atoms reduces and the formation of epoxy groups prevails.
3. Results of SCC DFTB simulation of hyperthermal O atom impact on CNT of small diameter and graphene demonstrate that in the case of low coverage regime for graphene the dominant process is the formation of O_2 molecule and its subsequent desorption whereas for CNT the adsorption with formation ether and epoxy groups prevails.

References

1. Minton TK, Garton DJ (2001) Dynamics of atomic-oxygen-induced polymer degradation in low-Earth orbit. In: Dressler RA (ed) Chemical dynamics in extreme environments, vol 11, Advanced series in physical chemistry. World Scientific, Singapore, pp 420–489
2. Ajayan PM, Yakobson BI (2006) Oxygen breaks into carbon world. Nature 441:15
3. Felten A, Bittencourt C, Pireaux JJ et al (2005) Radio-frequency plasma functionalization of carbon nanotubes surface by O_2, NH_3 and CF_4 treatments. J Appl Phys 98:074308
4. Golberg D et al (2007) Boron nitride nanotubes. Adv Mater 19:2413–2432
5. Sadovnichy V, Tikhonravov A, Voevodin V et al (2013) "Lomonosov": supercomputing at Moscow State University. In: Contemporary high performance computing: from petascale toward exascale. CRC Press, Boca Raton, pp 283–307
6. Delley B (2000) From molecules to solids with the $DMol^3$ approach. J Chem Phys 113:7756
7. Elstner M et al (1998) Self-consistent-charge density-functional tight-binding method for simulations of complex materials properties. Phys Rev B 58:7260–7268
8. Dag S, Gulseren O, Yildirim T, Ciraci S (2003) Oxygenation of carbon nanotubes: atomic structure, energetics, and electronic structure. Phys Rev B 67:165424
9. Krueger A (2010) Carbon materials and nanotechnology. Wiley-VCH, Weinheim
10. Chen Y et al (2007) Theoretical study of O_2 adsorption and reactivity on single-walled boron nitride nanotubes. Chem Phys Lett 449:149
11. Voronina EN, Novikov LS, Chernik VN et al (2012) Mathematical and experimental simulation of impact of atomic oxygen of the Earth's upper atmosphere on nanostructures and polymer composites. Inorg Mater: Appl Res 3(2):95–101
12. Ashraf MK, Bruque NA, Pandey RR et al (2009) Effect of localized oxygen functionalization on the conductance of metallic carbon nanotubes. Phys Rev B 79:115428
13. Guo Y, Jiang L, Guo W (2010) Opening carbon nanotubes into zigzag graphene nanoribbons by energy-optimum oxidation. Phys Rev B 82:115440
14. Sanchez-Portal D, Artacho E, Soler JM (1999) *Ab initio* structural, elastic, and vibrational properties of carbon nanotubes. Phys Rev B 59(19):12678–12688
15. Kosynkin DV, Higginbotham AL, Sinitskii A et al (2009) Longitudinal unzipping of carbon nanotubes to form graphene nanoribbons. Nature 458:872–877
16. Rangel NL, Sotelo JC, Seminario JM (2009) Mechanism of carbon nanotubes unzipping into graphene ribbons. J Chem Phys 131:031105
17. Voronina EN, Novikov LS (2013) *Ab initio* study of unzipping processes in carbon and boron nitride nanotubes under atomic oxygen impact. RSC Adv 3(35):15362
18. Sun T, Fabris S (2012) Mechanisms for oxidative unzipping and cutting of graphene. Nano Lett 12:17
19. Paci JT, Upadhyaya HP, Zhang J, Schatz GC, Minton TK (2009) Theoretical and experimental studies of the reactions between hyperthermal $O(^3P)$ and graphite: graphene-based direct dynamics and beam-surface scattering approaches. J Phys Chem A 113:4677–4685

Effects of Atomic Oxygen Exposure on Tribological Property of Zirconium Alloy

Yong Liu, Zhuyu Ye, Jianqun Yang, Shangli Dong, and Zhengjun Zhang

Abstract ZrTiAlV alloy has potential applications in space mechanisms. The change of wear and the friction coefficient of the ZrTiAlV alloy subjected to atomic oxygen (AO) exposure were investigated aiming to evaluate the tribological properties influenced by the atomic oxygen (AO) environment of the low Earth orbit (LEO). The AO testing employing a 5 eV AO beam was performed under various AO fluencies. The mass loss and roughness of the exposed to AO surfaces were measured. The exposed surfaces and the worn surfaces were analyzed using scanning electron microscopy (SEM) and X-ray photoelectron spectrometry (XPS) to explore the mechanism of AO effect.

The results show that, the friction coefficient at the initial friction stage and the wear loss are increased after AO exposure. The exposure to energetic AO beam leads to mass loss and decrease in roughness, showing a polishing effect on the exposed surface. Comprehensive analysis indicated that the AO interaction with the exposed surface results in two simultaneously occurring phenomena, i.e., the growth of surface oxides and their spalling. The wear loss and friction coefficient exhibit a non monotonous variation with AO fluence under the competition of these two processes.

Keywords Atomic oxygen • Zirconium alloy • Friction • Wear • Oxidation

Introduction

Zirconium alloys have wide applications in chemical and nuclear industry due to their high specific strength and excellent resistance to corrosion and radiation [1, 2]. With the development of zirconium alloys, many new zirconium alloys are

Y. Liu (✉) • Z. Ye • J. Yang • S. Dong
School of Materials Science and Engineering, Harbin Institute of Technology, 92 Xidazhi Street, Harbin, China
e-mail: liuy@hit.edu.cn

Z. Zhang
School of Materials Science and Engineering, Tsinghua University, Beijing 100084, China

J. Kleiman (ed.), *Protection of Materials and Structures from the Space Environment*, Astrophysics and Space Science Proceedings 47,
DOI 10.1007/978-3-319-19309-0_30

emerging, such as ZrTiAlV alloy [3–8]. Some research pointed that Zr-alloys has low friction and wear in special gas atmosphere [9] that makes them ideal candidates as alternative materials for space applications. If a spacecraft is operating in the low Earth orbit (LEO), the atomic oxygen (AO) environment would be a challenging factor to the exposed materials [10]. The interaction of the energetic AO with high chemical activity with materials on the outside of spacecraft will result in degradation of these materials and in decrease in life and reliability of spacecraft [11].

The LEO flight tests showed that the AO interaction induced the formation of surface oxides on many foils made of pure metals, such as Ag, Os, Al, Ni, Pd, Ta, Ir, Cr, W, Mo, Ti, Nb, and Zr, et al. [12]. The silver is oxidized by AO forming layered oxide with high stress, leading to cracking and exfoliation of the oxide film [13]. The reaction between Zr and oxygen at high temperature has been widely investigated [14–17]. The simulation indicated that AO results in formation of oxide film with varied O/Zr ratio in the 300–600 K range [18]. The simulated AO exposure test showed that, surface oxidation and oxide spalling simultaneously exist during interaction between AO and ZrTiAlV alloy [19]. In general, the friction and wear of Zr-alloys are mainly controlled by adhesion, abrasion and delamination [20]. The AO induced oxide will affect the surface state and change the tribological behavior of Zr-alloys. The present work explored the effect of AO exposure on the friction coefficient and wear for ZrTiAlV alloy with aim to extend its application in space mechanisms.

Experimental

ZrTiAlV alloy was chosen as the test material, with the chemical composition listed in Table 1. The samples were spark cut from ZrTiAlV bar followed by mechanical polishing to Ra 3.2 μm. Figure 1 shows the shape and size of ZrTiAlV samples. Before AO exposure, all samples were ultrasonically in acetone for 10 min. The AO exposure tests were conducted in a RF microwave-induced AO simulator which is capable of providing AO beam with 5 eV energy and 5×10^{16} atoms cm^{-2} s^{-1} flux [21]. The ZrTiAlV samples were exposed to the energetic AO beam under different fluencies including 1×10^{20}, 2×10^{20}, 5×10^{20} and 1×10^{21} atoms/cm^2.

The friction and wear tests were performed in a pin-on-disk type tribometer under a dry sliding condition in vacuum of 1.3×10^{-4} Pa. The ZrTiAlV sample was installed into the pin holder sliding against the rotated disk of 52100 steel to form a friction couple. Normal load of 20 N and sliding velocity of 0.4 m/s were chosen as parameters for the tribological test. Friction coefficients of specimens subjected to AO exposure with different AO fluence were measured. The sliding distance in all

Table 1 Chemical composition of ZrTiAlV alloy (wt%)

Element	Zr	Ti	Al	V
Content	51.8	40.8	4.4	2.9

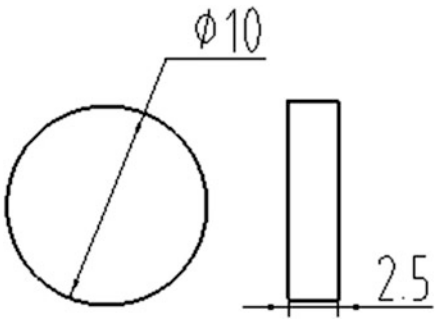

Fig. 1 Shape and size of samples for tribological test (all dimensions in mm)

tribological tests was 1000 m in order to obtain a stable friction. Each test data is calculated from the average of three samples under the same friction conditions.

The mass was measured on a MSC 21 type electronic balance with accuracy of 10^{-6} g before and after AO exposure respectively. The mass change was calculated by averaging three samples under the same AO fluence. X-ray photoelectron spectroscopy (XPS) was performed on a PHI 5700 ESCA System to determine chemical composition of the unexposed and the AO exposed surfaces, using an Al Kα source with energy of 1486.6 eV. All the tested surfaces were sputtered for 2 min before XPS analysis to avoid the influence of absorbed oxygen during analysis in air. The micro roughness of the AO exposed surface was measured using a Nanoscope IIIa type atomic force microscopy (AFM) (Fig. 1).

Results and Discussion

AO Interaction with Exposed Surface

The mass measurement after AO exposure indicates that interaction with AO leads to mass loss of ZrTiAlV alloy, as shown in Fig. 2. At fluencies $<5 \times 10^{20}$ atoms/cm^2, the mass loss is decreasing with increasing AO fluence. When the fluence exceeds 1×10^{21} atoms/cm^2, AO exposure results in relatively higher mass loss. The energy of the AO used in the present tests is ~5 eV that is not enough to knock out any metallic atom from ZrTiAlV alloy matrix. Thus, the AO interaction has little sputtering effect on the exposed surface. The mass loss would be induced by another process related to AO interaction with the surface of ZrTiAlV alloy.

The XPS analysis illustrates that the AO interaction with ZrTiAlV alloy results in formation of Zr and Ti oxides in the surface layer, as shown in Fig. 3. The surface oxidation by AO should result in mass gain of the exposed sample. However, the AO exposure leads to mass loss of the exposed samples. Therefore, it can be deduced that some oxides produced by AO are being detached from the exposed surface. Since the formation of Zr oxides and/or Ti oxides will generate high stress inside the oxides [22], there is a probability of some oxidized material cracking and

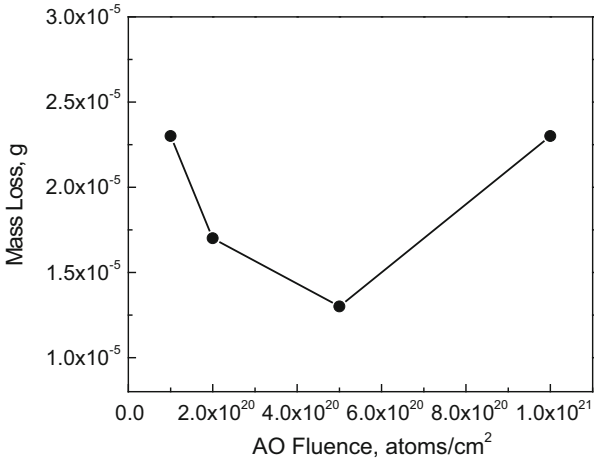

Fig. 2 Mass loss as a function of AO fluence

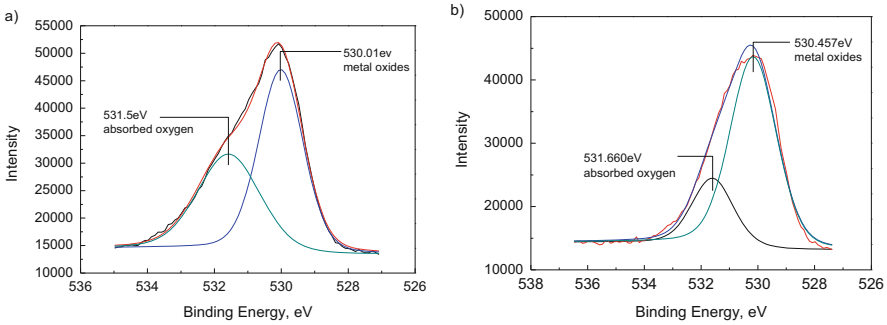

Fig. 3 XPS analysis on O element for (**a**) the unexposed and (**b**) the AO exposed to 1×10^{21} atoms/cm^2

spalling from the exposed surface if the inner stress accumulates to a certain level with the growth of AO induced oxides, leading to mass loss.

As the AO bombardment proceeds, the formed oxides will play a protective role, preventing the surface from the subsequent oxidation when interacting with the AO, which slows down the rate of mass loss. Thus, there are two competitive processes during AO bombardment. One is that oxides form and grow on the surface. The other is that the formed oxides break and spall off the surface. Basically, the removal of the oxides from the surface is the dominant factor leading to mass loss after AO exposure. According to Fig. 2, at AO fluencies $<5 \times 10^{20}$ atoms/cm^2, the domination of oxides spalling is weakened for the rate of mass loss is decreased. With fluencies exceeding 5×10^{20} atoms/cm^2, the oxides spalling mechanism dominates, leading to increase of mass loss.

Both mechanisms, i.e., the growth and the removal of oxides will change the surface micro topography, i.e., roughness. The AFM analysis of the surface

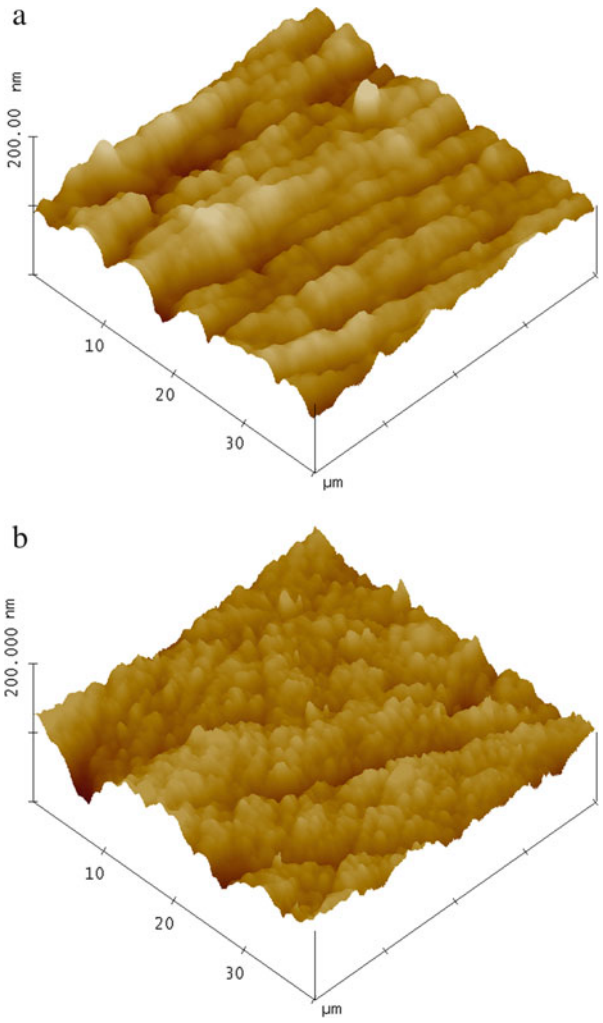

Fig. 4 AFM morphology for (**a**) the unexposed surface and (**b**) the exposed surface under 5×10^{20} atoms/cm^2

morphology (Fig. 4) shows the change in the surface geometry and roughness. Machining traces are found on the AFM images of the unexposed samples, as shown in Fig. 4a. The interaction of the surface with the AO flux makes the surface smoother, comparing to the unexposed surface, as shown in Fig. 4b. The final results of the AO interaction with the surface via the two competing mechanisms results in a "polishing effect" on the surface. The analysis of the AFM results indicates that the roughness is decreased after AO exposure, as shown in Fig. 5.

Moreover, Fig. 5 also illustrates that the variation of roughness with AO fluence corresponds to the relationship between the mass loss and the AO fluence. Under lower fluence ($<5 \times 10^{20}$ atoms/cm^2), the roughness is decreased with fluence. It implies that the formation and growth of AO induced oxides will smoothen the

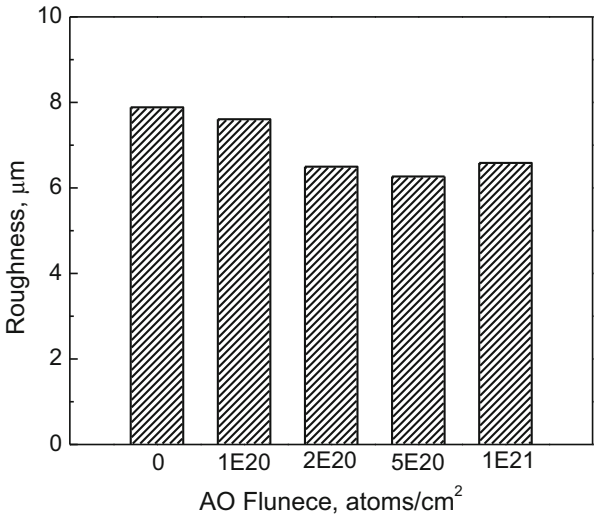

Fig. 5 Calculated roughness of the AO exposed surface under different AO fluence

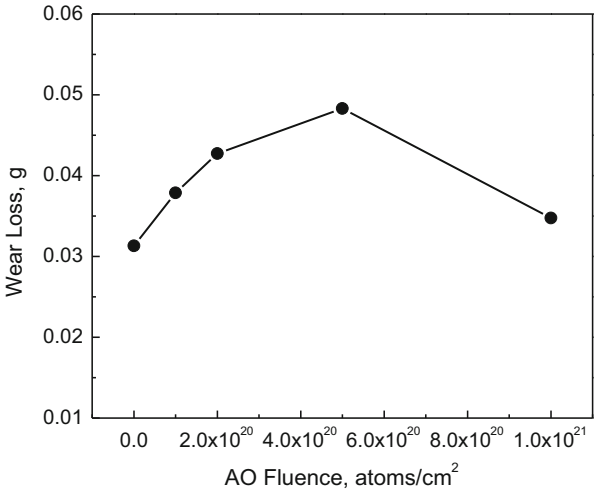

Fig. 6 Wear loss as a function of AO fluence

surface. The fracture and spalling of oxides on the contrary roughens the surface and increases its roughness.

Wear Loss

Figure 6 shows the wear loss as a function of AO fluence. All the AO exposed samples exhibit higher wear than the unexposed, indicating that the AO exposure

aggravates the wear behavior of ZrTiAlV alloy. Furthermore, with increasing AO fluence, the wear is increased. However, the AO effect on wear decreases at higher fluence of 1×10^{21} atoms/cm^2. Under the present test conditions, both the wear and the friction of ZrTiAlV alloy show a non-monotonous variation with AO fluence. Under higher AO fluence of 1×10^{21} atoms/cm^2, the monotonous increase of tribological property by AO is changed, which is similar to the relationship between mass loss and AO fluence. Therefore, AO interaction with the surface affects differently the exposed surface at this fluence. It also implies that the extent of AO effect on tribological property is related to the mass loss that induced by AO.

Worn Surfaces

The unexposed and the exposed samples show similar wear patterns on the surface, as illustrated in Fig. 7. The worn surface is mainly characterized by galling and local plastic deformation, indicating adhesion wear. In addition, there are some irregular fine scratches existing on the worn surface. These scratches are produced by abrasion with hard asperities on the counter surface or hard particles inside the friction interface. Therefore, the wear is dominated by a mixed mechanism of adhesion and abrasion for both the unexposed and the exposed ZrTiAlV alloy.

Generally, the existence of surface oxides will decrease the adhesion trend for the wear of metals and alloys. However, the present results show that the AO exposure increases the wear of ZrTiAlV alloy. The reason for that is associated with the effect of AO induced formation of oxides on the abrasive wear. During the process of friction and wear, some formed by AO oxides have a probability to be worn off by adhesion effect, forming wear debris and entering the friction interface.

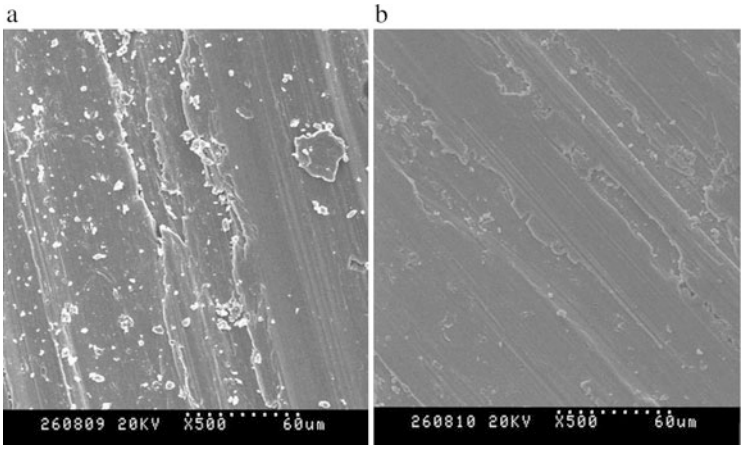

Fig. 7 SEM micrographs showing morphology of the worn surface; (**a**) unexposed, (**b**) exposed to a fluence of 5×10^{20} atoms/cm^2

The oxides in debris act as abrasive hard particles attributing to the increase of wear comparing to the unexposed sample. As mentioned above, formation and growth of oxides becomes more prevailed with increasing AO fluence to 5×10^{20} atoms/cm^2. It means that the amount of AO induced oxides is increased with AO fluence ($<5 \times 10^{20}$ atoms/cm^2). Thus, the abrasion from oxides particles is increased with AO fluence, leading to the increase of wear with AO fluence. When the spalling of oxides is enhanced under higher AO fluence (i.e., 1×10^{21} atoms/cm^2), the amount of remained surface oxides decreases, leading to weakening of abrasion attribution from oxides debris and decrease of wear, as shown in Fig. 6.

Friction Coefficient

The AO interaction with ZrTiAlV alloy results in different effects on friction coefficient within different sliding distance ranges, as shown in Fig. 8. During the initial 200 m, the exposure to AO increases the average friction coefficient. Furthermore, with increasing AO fluence, the average friction coefficient is firstly increased, and then slightly decreased when fluence exceeds 1×10^{21} atoms/cm^2. In contrast, the AO exposure has little effect on the average friction coefficient in 200–600 m range. Within the followed distance of 200–600 m, the average friction coefficient of the AO exposed sample is around 0.41–0.42, which is very close to that of the unexposed (about 0.413). The above results indicate that AO exposure only has a distinctive effect on friction coefficient in the initial stage of friction.

The friction coefficient depends on two factors, i.e., adhesion force and mechanical interaction between two counter surfaces. In a similar way, the formation of surface oxides will weaken the adhesive force between metals or alloys and

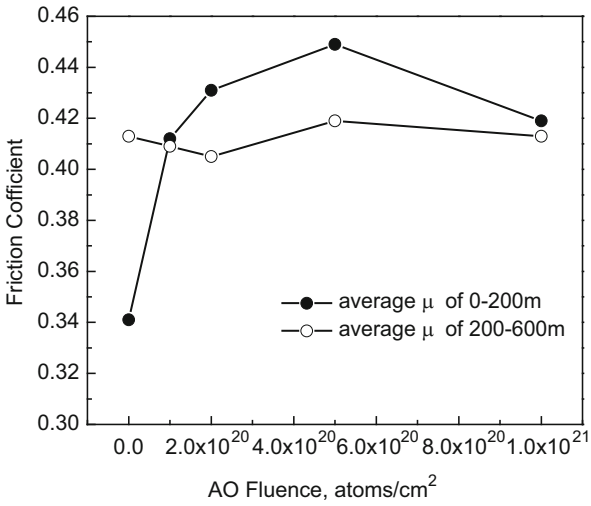

Fig. 8 Friction coefficient as a function of AO fluence

decrease the friction coefficient. In the present test, the friction coefficient is increased when the AO induced oxides remain on the surface. The reason for that is that the mechanical interaction becomes strong when the exposed surface is sliding against the counter surface. The enhancement of mechanical interaction between the friction surfaces comes from the increase of abrasive effect introduced by oxides particles in wear debris. Due to the higher hardness of oxides, they mechanically interact with asperities of both friction surfaces, resulting in formation of higher mechanical resistance force between surfaces against each other. When the sliding distance exceeds 200 m, the oxides produced by AO would completely wear off the surface, the above extra abrasion from oxides particles vanishes. In this case, the friction coefficient becomes similar to that of the unexposed.

Conclusions

The friction and wear test was performed on the ZrTiAlV alloy subjected to AO exposure. The results show that the energetic AO beam leads to the following effects on the exposed surface and its tribological properties.

1. The AO has a polishing effect on the surface of ZrTiAlV alloy resulting in mass loss and decrease of roughness.
2. The AO exposure increases the friction coefficient in the initial friction stage and the wear as well.
3. The AO interaction with the exposed surface induces two simultaneous and competitive processes of growth and spalling of surface oxides, which make the wear loss and friction coefficient varying non-monotonically with AO fluence.

Acknowledgement This study is supported by the National Basic Research Program of China (No. 2010CB731601).

References

1. Kritskii VG, Berezina IG, Motkova EA (2013) Simulating the corrosion of zirconium alloys in the water coolant of VVER reactors [J]. Therm Eng 60(7):457–464
2. Nikulina AV (2004) Zirconium alloys in nuclear power engineering [J]. Metal Sci Heat Treat 46(11):458–462
3. Savchenko AM, Rogova S, Vatulin AV, Morozov AV, Kulakov GV, Ershov SA, Laushkin AV, Maranchak SV, Konovalov YV, Malamanova EK (2012) Zirconium alloys matrix as innovative material for composite fuel [J]. Prog Nucl Energy 57:138–144
4. Liang SX, Ma MZ, Jing R, Zhang XY, Liu RP (2012) Microstructure and mechanical properties of hot-rolled ZrTiAlV alloys [J]. Mater Sci Eng A 532:1–5
5. Liang SX, Ma MZ, Jing R, Zhang XY, Liu RP (2012) Preparation of the ZrTiAlV alloy with ultra-high strength and good ductility [J]. Mater Sci Eng A 539:42–47

6. Liang SX, Yin LX, Che HW, Jing R, Zhou YK, Ma MZ, Liu RP (2013) Effects of Al content on structure and mechanical properties of hot-rolled ZrTiAlV alloys [J]. Mater Design 52:246–250
7. Tan YB, Liu WC, Yuan H, Liu RP, Zhang XY (2013) On the phenomenon of stress drop during hot deformation of ZrTiAlV alloy [J]. Metall Mater Trans A 44(12):5284–5288
8. Liang SX, Yin LX, Che HW, Tan CL, Jing R, Zhou YK, Ma MZ, Liu RP (2014) Existing forms and effects of carbon on the surface structure and hardness of ZrTiAlV alloys with various Zr contents [J]. Mater Design 55:864–868
9. Murakami T, Kaneda K, Mano H, Hata M, Sasaki S, Sugimura J (2010) Friction and wear properties of Zr and TiC-based cermet specimens in a hydrogen gas atmosphere [J]. Mater Sci Forum 638–642:3412–3417
10. Leger LJ (1982) Oxygen atom reaction with shuttle materials at orbital altitudes [R]. NASA Techical Memorandum 58246
11. Peters PN, Linton RC, Miller ER (1983) Reacts of apparent atomic oxygen reactions on Ag, C, and Os exposed during the shuttle STS-4 orbits [J]. Geophys Res Lett 10(7):569–571
12. Raja Reddy M (1995) Effect of low earth orbit atomic oxygen on spacecraft materials [J]. J Mater Sci 30(2):281–307
13. Li L, Yang JJ, Minton TK (2007) Morphological changes at a silver resulting from exposure to hyperthermal atomic oxygen [J]. J. Phys. Chem. C 111(18):6763–6771
14. Duriez C, Dupont T, Schmets B, Enoch F (2008) Zircaloy-4 and M5(R) high temperature oxidation and nitriding in air [J]. J Nucl Mater 380(1):30–45
15. Bolat G, Izquierdo J, Mareci D, Sutiman D, Souto RM (2013) Electrochemical characterization of ZrTi alloys for biomedical applications [J]. Electrochim Acta 88:447–456
16. Kurpaska L, Favergeon J, Lahoche L, Moulin G, Marssi ME, Roelandt J-M (2013) Zirconia layer formed by high temperature oxidation of pure zirconium: stress generated at the zirconium/zirconia interface [J]. Oxid Met 79(3):261–277
17. Malyi OI, Wu P, Kulish VV, Bai KW, Chen Z (2012) Formation and migration of oxygen and zirconium vacancies in cubic zirconia and zirconium oxysulfide [J]. Solid State Ion 212:117–122
18. Sankaranarayanan S, Ramanathan S (2008) On the low-temperature oxidation and ultrathin oxide growth on zirconium in the presence of atomic oxygen: a modeling study [J]. J Phys Chem C 112(46):17877–17882
19. Li LQ, Liu Y, Dong SL, Yang JQ (2012) Atomic oxygen effect of YZ-1 zirconium alloy [J]. Mater Sci Technol 20(6):67–71
20. Helmi Attia M (2006) On the fretting wear mechanism of Zr-alloys [J]. Tribol Int 39:1320–1326
21. Liu Y, Yang JQ, Ye ZY, Dong SL, Zhang L, Zhang ZJ (2013) Influence of atomic oxygen exposure on friction behavior of 321 stainless steel. Astrophysics and space science proceedings (C), Springer, Berlin, Heidelberg, 32:371–380
22. Zhang CS, Flinn BJ, Norton PR (1992) The kinetics of oxidation and oxide growth mechanisms on Zr (0001) [J]. Surf Sci 264(1):1–9

Effect of Atomic Oxygen Irradiation on the Properties and Structure of Spacecraft Composite Beta Cloth Film

Haifu Jiang, Tao Li, Lihua Chai, Xiangpeng Liu, Ruiqiong Zhai, and Xue Zhao

Abstract To study the effects of low Earth orbit environment on the surface properties of polymer matrix composite material, a black Beta cloth film was irradiated by atomic oxygen (AO) in ground-based simulation facility. The structure and properties, including morphology, mass loss, optical properties, and surface composition of the pristine and irradiated films were investigated using scanning electronic microscopy (SEM), high precision microbalance, energy disperse spectroscopy (EDS) and UV/VIS/NIR spectrophotometry. It was found that AO irradiation induced strong erosion of the Teflon resin on sample surface when AO fluence reached 1.85×10^{22} atoms/cm^2, as evidenced by SEM, EDS and XPS results. The real-time mass loss data show a non-linear relationship between etching and AO fluence. The variation of surface chemical structure and composition lead to bleached surface comparing to pristine black film. The optical properties show some variations of sample emissivity (ε_h) and a substantial decrease of solar absorptance (α_s) reaching a value of 0.20.

Keywords Low Earth orbit • Atomic oxygen • Beta cloth film • Surface morphology • Optical properties

H. Jiang (✉) • X. Liu • R. Zhai • X. Zhao
Beijing Institute of Spacecraft Environment Engineering, Beijing 100094, China
e-mail: haifujiang@163.com

T. Li
Science and Technology on Reliability and Environmental Engineering Laboratory, Beijing 100094, China

L. Chai
College of Materials Science and Engineering, Beijing University of Technology, Beijing 100124, China

J. Kleiman (ed.), *Protection of Materials and Structures from the Space Environment*, Astrophysics and Space Science Proceedings 47,
DOI 10.1007/978-3-319-19309-0_31

Introduction

A large variety of spacecrafts, such as spaceships, shuttles, space stations and application satellites are traveling in low Earth orbit (LEO). The space environmental factors in LEO include high vacuum, microgravity, neutral gas, constant thermal cycling, the full spectrum of solar radiation, micrometeoroid and space debris, etc. [1–4]. One of the most important factors that cause serious damage to many polymeric spacecraft materials is atomic oxygen (AO), which is the dominant neutral species in LEO and formed by photo-dissociation of molecular oxygen in the upper atmosphere with a concentration of 10^6–10^9 atoms/cm^3. Due to its high chemical reactivity and high impinging energy on material surface (approximately 5 eV, which is attributed to the high orbital velocity of spacecraft of 7–8 km/s), AO in LEO erodes many polymeric materials that are directly exposed to the space environment [5, 6].

Polymer matrix composite materials are widely used in space science due to their unique properties, such as low density, versatile electronic properties, high strength-to-weight ratios, low thermal expansion coefficients and manufacturing cost. However, it has been well established that polymer matrix composite materials may suffer accelerated erosion in low Earth orbit environment because of the presence of AO. Accordingly, it is very important both to evaluate material characteristics and to clarify the degradation mechanism in AO exposure [7, 8].

Flight experiments provide a significant opportunity for evaluating materials under a real space environment. Up to now, the National Aeronautics and Space Administration (NASA) has performed several flight experiments, such as short-term space flight experiment EOIMI-III, the Lockheed Space Flight Experiment (LSFE), Long Duration Exposure Facility (LDEF) and Material International Space Station Experiment (MISSE) [9–13]. Another method to examine material properties after AO exposure is ground-based simulation testing. Due to their lower cost and high efficiency, ground-based simulation experiment has been widely used in the field of space environment/spacecraft materials interactions.

In this work, a new type of composite material black flame retardant film, also known as Beta cloth was selected as a test subject exposed to a neutral AO beam produced by a microwave excited discharge of O_2 gas. After the experiment, the surface morphology, mass loss, surface composition and optical properties of the samples were investigated in order to evaluate its tolerance against AO erosion.

Experimental

Experimental Materials

The black Beta cloth film is an alternative material, which is used for installations around optical parts of spacecraft, such as optical lens, window glass and space docking mechanism, in order to reduce the reflected sunlight. This film was

produced by Shanghai Silicate Research Institute (Shanghai, China) and consisted of SiO_2 glass fiber and Teflon resin binder. For the sake of achieving high optical absorption, plenty of carbon was added to Teflon resin that ultimately resulted in a black sample surface. For this study, a black spacecraft flame retardant film sample, 200 μm thick and 4.0×4.0 cm^2 in surface area was cut from the larger film.

AO Simulation System

The AO irradiation experiments were performed using the LEO combined space environment test system. The test system is equipped with an AO source, an electron beam (EB) source and a vacuum ultraviolet (VUV) source. These sources can be used simultaneously or in any combination. The vacuum chamber is made of stainless steel and is 500 mm in diameter with a vacuum level of 10^{-5} Pa. A schematic view of the irradiation system is shown in Fig. 1. The AO generation in this system was based on the microwave detonation phenomenon. It utilized a microwave source to excite O_2 to oxygen plasma. A magnetic mirror field was provided in the discharge region by coils in order to increasing plasma density. The ions in the oxygen plasma were accelerated by an electric field resulting from negatively biased metal molybdenum plate in front of plasma. The accelerated oxygen ions collided with the metal molybdenum plate, and they were neutralized by the negative charges on the metallic molybdenum plate. The neutral AO rebounded to form particle beam with impingement kinetic energy, and eventually collided with the test sample fixed on a sample holder. The average energy of the AO produced by this system was about 5 eV and the sample temperature did not

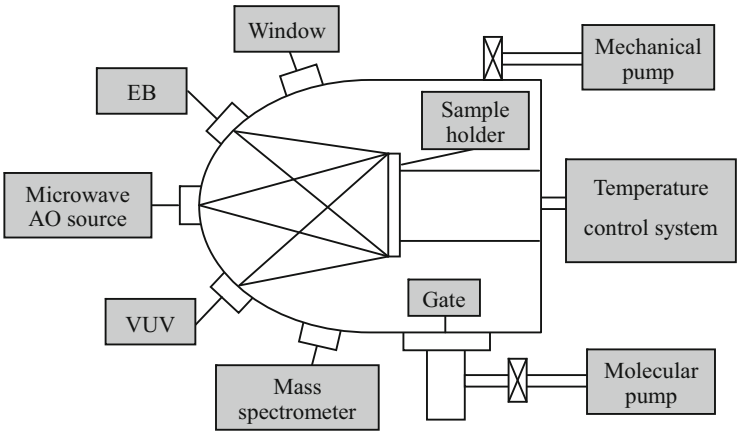

Fig. 1 Schematic view of the system used in simulation testing with three different space environment factors

exceed 40 °C by adjusting the temperature control of the combined space environment test system.

Experimental Details

In the experiment, the black Beta cloth film was affixed to the sample holder and oriented perpendicular to the exit of AO source which was 200 mm away. The equivalent AO flux was approximately 5.0×10^{15} atoms/(cm^2 s) in this position. The maximum AO fluence was 1.85×10^{22} atoms/cm^2, which was calculated to be equivalent to that of a 2 years exposure fluence at an orbit 350 km altitude and 42° inclination on the ram face of spacecraft. The fluence evaluation of each irradiation test was based on mass loss evaluations of a 25 μm thick Kapton HN film (DuPont, Inc.), assuming an erosion yield of 3×10^{-24} cm^3/atom [14]. The Kapton HN film, as well as the black flame retardant film, was installed on the sample holder. Before loading into the vacuum chamber, the samples were cleaned in an ultrasonic bath using alcohol for 2 min, and subsequently air-dried and conditioned in the vacuum chamber for 48 h in order to release the adsorbed gases completely. The purity of O_2 gas used in our experiments was 99.99 % and the working pressure was 5×10^{-2} Pa. The O_2 gas flow during experiment was 33 sccm and the microwave power was kept at 600 W.

Tests and Evaluation

The surface morphologies of samples were determined using SUPRA55 scanning electron microscope (SEM). An accelerating voltage of 15 keV was used for all sample observations, photographs of the samples were taken at magnifications of 100×. The mass loss of black Beta cloth film was obtained using a Sartorius ME235S microbalance with precision of 10^{-5} g and maximum load 210 g. Three measurements were taken to yield statistical averages for each sample. The laboratory temperature was 25 ± 2 °C and the relative humidity ranged from 30 to 40 %. In order to reduce the effect of moisture absorption in air, the mass loss measurements had to be accomplished within 5 min after taking samples from vacuum chamber. The changes in surface composition were evaluated using an energy dispersive spectroscopy (EDS) system attached to the SEM. The optical properties of the sample, including solar absorptance (α_s) and emissivity (ε_h), were evaluated using a Perkin-Elmer Lambda 9 UV/VIS/NIR spectrophotometer equipped with a barium sulfate coated integrating sphere. The precision of the measurement was ±0.003.

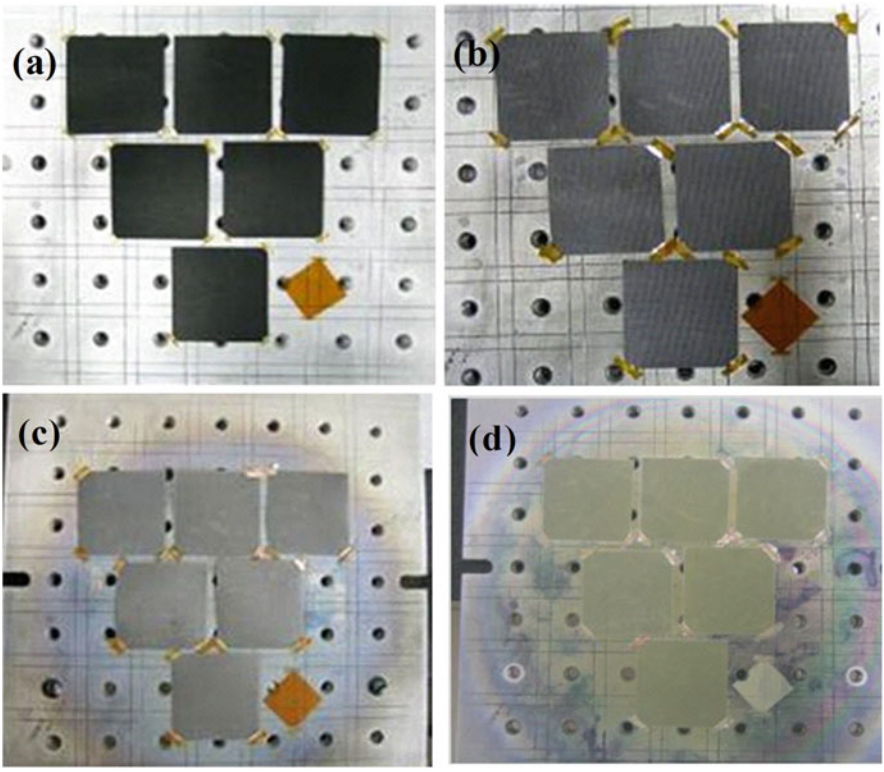

Fig. 2 Images of samples exposure to AO beams with different fluence: (**a**) $\Phi = 0$, (**b**) $\Phi = 1.2 \times 10^{21}$ atoms/cm^2, (**c**) $\Phi = 2.4 \times 10^{21}$ atoms/cm^2, and (**d**) $\Phi = 1.85 \times 10^{22}$ atoms/cm^2

Results and Discussion

Surface Morphology

The photographs of samples after AO exposure are shown in Fig. 2. Four corners of each sample are fixed to the aluminum holder by polyimide adhesive tape (3 M, Inc.).

Before AO exposure, the Beta cloth film exhibits a black surface because of a large carbon concentration added to the original material, but after AO exposure, it was observed that the surface dark color of samples gradually disappears with increasing AO fluence. This "bleaching effect" of AO on dark material's surface, was mentioned frequently in literature [15, 16].

Investigation of the surface morphology by SEM (Fig. 3) indicates that AO exposure results in considerable changes of sample surface structure. The pristine sample ($\Phi = 0$) appears to have a relatively smooth surface containing the SiO_2 fibers with $90^\circ \times 90^\circ$ fabric direction that are covered completely by Teflon resin

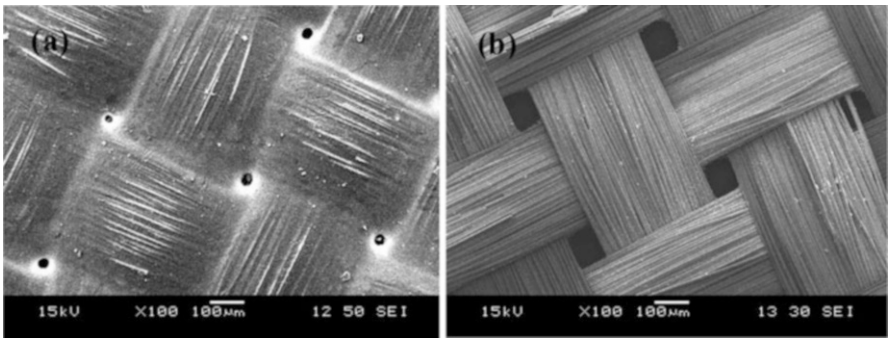

Fig. 3 SEM images of the samples before and after exposure to AO beam. (**a**) $\Phi = 0$, (**b**) $\Phi = 1.85 \times 10^{22}$ atoms/cm^2

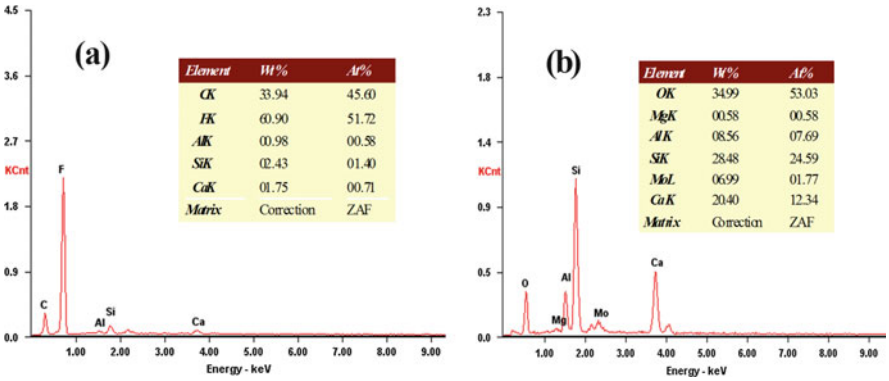

Fig. 4 Energy dispersive X-ray microanalysis results obtained from samples before and after AO exposure (**a**) $\Phi = 0$, (**b**) $\Phi = 1.85 \times 10^{22}$ atoms/cm^2

binder. In contrast, the surface of the sample exposed to an AO fluence of 1.85×10^{22} atoms/cm^2, is completely stripped of the carbon rich Teflon resin binder, leaving a surface that contains only the SiO_2 fiber bundles. This morphology difference of polymer matrix composite materials before and after AO exposure has been reported in flight experiment results [17, 18].

Surface Composition

Figure 4 illustrates the EDS spectra obtained from the sample surfaces before and after AO exposure. As shown in Fig. 4a, the surface of pristine sample ($\Phi = 0$) is mainly composed of carbon and fluorine elements, which indicates that Teflon resin is enriched with carbon in sample surface. But after AO exposure, the surface composition of the sample changes significantly, carbon and fluorine elements are

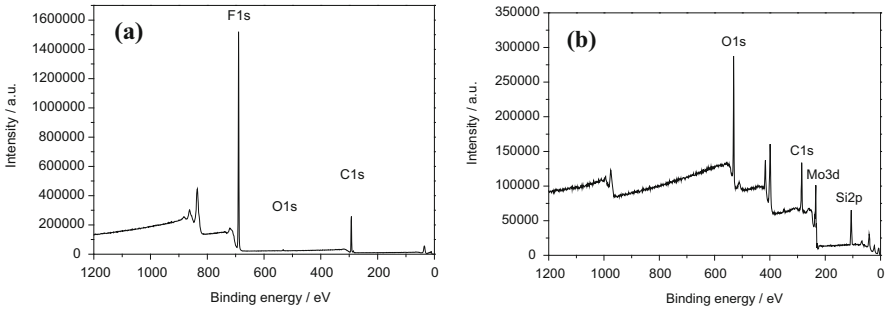

Fig. 5 XPS survey scan spectra of samples before and after AO exposure: (**a**) $\Phi = 0$, (**b**) $\Phi = 1.85 \times 10^{22}$ atoms/cm^2

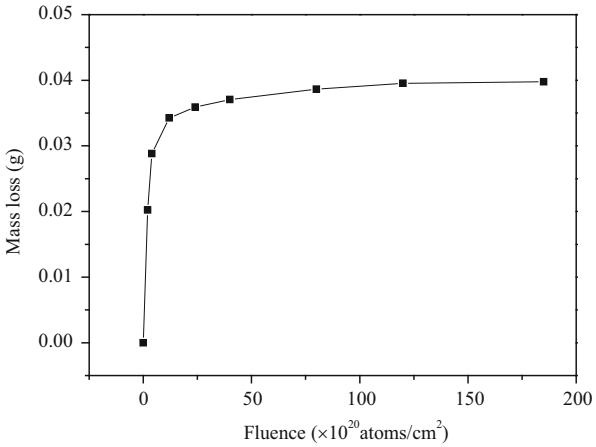

Fig. 6 The mass loss of samples versus AO fluence

replaced by oxygen and silicon elements, which validates that only SiO_2-based fibers are present on the sample surface. In addition, a minor peak of Mo is observed in Fig. 4b that is due to the Mo plate that was sputtered in the AO exposure process.

The X-ray photoelectron spectroscopy (XPS) analysis, as shown in Fig. 5 validates EDS result, and indicates at a serious erosion of the sample surface.

Mass Loss

Figure 6 presents the dependence of the mass loss of the sample after AO exposure on the total fluence of AO. As can be seen from Fig. 6 a non-linear trend between the mass loss and the AO fluence is observed. At the initial stage of AO exposure, the sample mass decreases sharply due to the intense impact of AO and extensive erosion of the F-C binder. With AO fluence continuing to increase (the second

stage), only a small change in mass (about 0.00016 g in mass loss) is observed with AO fluence increasing from 2.4×10^{21} to 1.85×10^{22} atoms/cm^2. The non-linear trend of mass loss is most probably due to the difference of erosion yield of the rich carbon Teflon resin binder (at the first stage of high mass loss) and the SiO_2 glass fiber (in the second stage of low mass loss) that are two basic component of film.

When oxidation reaction occurs between AO and the film, the surface layer of the Teflon resin binder is eroded firstly, leading to rapid increase of mass loss, but with increasing fluence, and the gradual exposure of the SiO_2 fibers, the erosion rate and the mass loss are reduced. For this flame retardant film, AO erosion yield can be calculated from the following expression [19]:

$$E_s = \frac{\Delta m_s}{\Phi \rho}, \tag{1}$$

where E_s is the AO erosion yield, Δm_s is the mass loss of test sample, Φ is equivalent fluence in experiment calculated from the mass change of witness Kapton HN, ρ is the density of test sample.

According to Eq. (1), the erosion yield of the flame retardant film is in the range 5.05×10^{-23}–1.07×10^{-24} cm^3/atom (the density of 1 g/cm^3 is used), which relates to the AO fluence. It is interesting that the erosion yield of black Beta cloth film at the initial stage of experiment is even higher than epoxy resin (1.7×10^{-24}–3.4×10^{-23} cm^3/atom) [20, 21] that is, most probably, associated with the carbon addition in materials.

Optical Properties

The black Beta cloth film is an anti-reflective material that has potential applications in use around optical observation equipment for providing high optical quality. The optical properties of the black Beta cloth film samples before and after AO irradiation experiment were measured and the results are shown in Figs. 7 and 8. Figure 7 presents the emissivity, ε_h value of samples after exposure to different AO fluencies. As can be seen from Fig. 7, after AO exposure, the ε_h values are steady around 0.88 and almost the same as that for the pristine sample ($\Phi = 0$).

In contrast, a substantial decrease of α_s is detected as shown in Fig. 8. The α_s decreases by approximately 0.19 when AO fluence changes from 0 to 2.4×10^{21} atoms/cm^2, but with increasing fluence, the change in α_s is only 0.01 until the end of experiment. The optical properties are associated with the surface structure and of the sample. When AO fluence does not exceed 2.4×10^{21} atoms/cm^2, the surface morphology is governed by strong erosion of the binder, which leads to the rapid decrease of α_s. But with continuous increase of AO fluence, the optical properties of the SiO_2 fibers that are exposed on the surface, become dominant. Because the SiO_2 fibers are little eroded by AO, the surface morphology does not change substantially at this stage, which eventually results in minor change in α_s.

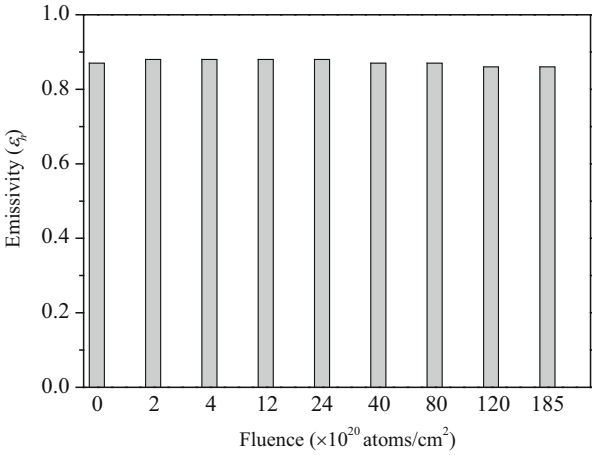

Fig. 7 The emissivity of samples after AO exposure versus the AO fluence

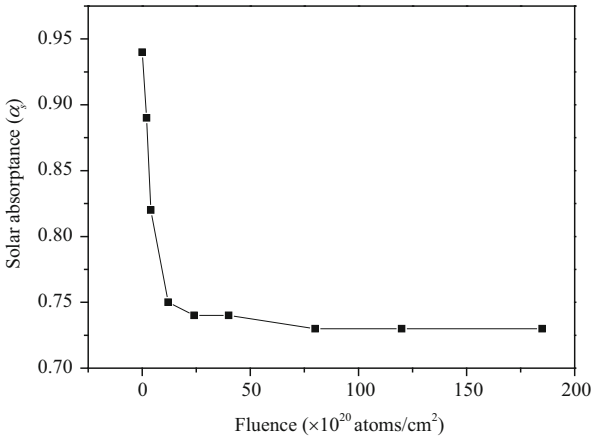

Fig. 8 The solar absorptance of samples after AO exposure with different fluence

The changes of α_s can be calculated using the following expression:

$$T = \frac{\Delta\alpha_s}{\alpha_{si}}(\%) = \frac{|\alpha_{sf} - \alpha_{si}|}{\alpha_{si}}(\%), \tag{2}$$

where T is the change in α_s, α_{sf}—is final value of α_s, α_{si}—is original value of α_s, $\Delta\alpha_s$ is the change of α_s. Using Eq. (2), the changes in α_s were estimated to exceed 20 %, implying that the application of black Beta cloth film in space mission has its limitations. Thus, it is obvious that for applications of black Beta cloth film on surfaces of spacecraft facing the ram direction and in long term operations in LEO space environment, the AO erosion would seriously affect the thermal optical performance of the film. While further improvements and optimization of the film properties should be considered for long term applications, for short term applications, in short term flight missions, this film may be a good choice.

Conclusions

AO testing was conducted on a black Beta cloth film in ground-based LEO simulation system. The sample surface was eroded seriously and the SiO_2 fibers were exposed with the F-based binder with carbon filler being eroded fully after AO exposure with fluence of 1.85×10^{22} atoms/cm^2. The mass loss and α_s of samples decrease distinctly with increasing AO fluence, but there is not obvious change in emissivity. These results suggest that the black Beta cloth film has a potential for use in space applications in short-term flight missions.

Acknowledgments The authors thank Mr. Liu Bingqing, China Academy of space technology, for his cooperation in supplying the black Beta cloth film for this evaluation. The authors also like to thank Mrs. Shu Qun, Beijing University of Technology, and Mrs. Yang Li, Beijing satellite manufacturing factory for their kind support on SEM and optical properties analysis.

References

1. Banks BA, Snyder A, Miller SK, de Groh KK, Demko R (2004) Atomic-oxygen undercutting of protected polymers in low earth orbit. J Spacecr Rockets 41(3):335–339
2. Lee C, Chen LW (2000) Reactive probability of AO with material surfaces in low earth orbit. J Space Rockets 37(2):252–257
3. Nakayama Y, Imagawa K, Tagashira M, Nakai M, Kudoh H, Sugimoto M, Kasai N, Seguchi T (2001) Evaluation and analysis of thermal control materials under ground simulation test for space environment effects. High Perform Polym 13:S433–S451
4. Shimanura H, Nakamura T (2009) Mechanical properties degradation of polymide films irradiated by atomic oxygen. Polym Degrad Stab 94:1389–1396
5. Yokota K, Ohmae N, Tagawa M (2004) Effect of relative intensity of 5 eV AO and 172 nm vacuum ultraviolet in the synergism of polyimide erosion. High Perform Polym 16:221–234
6. Tagawa M, Yokota K (2008) Atomic oxygen-induced polymer degradation phenomena in simulated LEO space environments: how do polymers react in a complicated space environment? Acta Astronaut 62:203–211
7. Milinchuk VK, Klinshpont ER, Shelukhov IP, Smirnova TN, Pasevich OF (2004) Degradation of polymer materials in low earth orbits. High Perform Polym 38(1):8–12
8. de Groh KK, Hall RL, Norris MJ, Espe MP, Cato DR (2000) Effects of heating on Teflon FEP thermal control material from the Hubble space telescope. NASA-TM-209085, NASA
9. Banks BA, de Groh KK, Miller SK, Waters DL (2008) Lessons learned from atomic oxygen interaction with spacecraft materials in low earth orbit. NASA-TM-215264, NASA
10. Dever J, Miller S, Messer R, Sechkar E, Tollis G (2001) Exposure of polymer film thermal control materials on the materials international space station experiment (MISSE). AIAA 4924
11. Clark LG, Kinar WH, Carter DJ, Jones JL (1984) The Long Duration Exposure Facility (LDEF), Mission 1 experiments. NASA SP-473, NASA
12. Koontz SL, Leger LJ, Visentine JT, Hunton DE, Cross JB, Hakes CL (1995) EOIM-III mass spectrometry and polymer chemistry: STS46 July–August 1992. J Spacecr Rockets 32 (3):483–495
13. Silverman EM (1996) Spacecraft environmental effects on spacecraft: LEO materials selection guide. NASA CR-4661, NASA

14. Miyazaki E, Tagawa M, Yomiko K, Yokota R, Kimoto Y, Ishizawa J (2010) Investigation into tolerance of polysiloxane-block-polyimide film against atomic oxygen. Acta Astronaut 66:922–928
15. Zhao XH, Shen ZG, Xing YS, Ma SL (2005) An experimental study of low earth orbit atomic oxygen and ultraviolet radiation effects on a spacecraft material-polytetrafluoroethylene. Polym Degrad Stab 88:275–285
16. Dever JA, Hasegawa MM, Reed CK (1998) Evaluation of low earth orbit environmental effects on international space station thermal control materials. NASA-TM-208500, NASA
17. Linton RC, Whitaker AF, Finckenor MM (1994) Space environment durability of Beta cloth in LDEF thermal blankets. NASA-31035, NASA
18. Whitaker AF, Little SA, Harwell RJ (1985) Orbital AO effect on control and optical materials: STS28 results. AIAA 852041514
19. de Groh KK, Banks BA, Hammerstrom AM, Youngstrom EE (2001) MISSE PEACE polymers: an international space station environmental exposure experiment. NASA-TM-211311, NASA
20. Reddy MR (1995) Review of low earth orbit atomic oxygen on spacecraft materials. J Mater Sci 30:281–307
21. Banks BA, Rutledge SK, Brady JA (1988) Proceedings of the 15th space simulation conference. NASA-CP-301551, NASA

The Study of the Effects of VUV/UV Radiation on the Thermal Control Coatings

Lingnan Wu, Yuzhi Zhang, Jia Meng, Xiaofu Yin, and Lixin Song

Abstract In recent years, extensive research has been conducted on long-term reliability of thermal control coatings (TCC) used in space. The properties of TCC's directly affect the internal temperature control of spacecraft and their normal performance. In this paper, optical properties of several typical TCC samples including the antistatic silvered cerium glass second reflectance mirror, KS-Z white coating, antistatic F46 film silvered second reflectance mirror were measured in situ in different VUV (115–200 nm) and UV (200–400 nm) ranges and radiation doses using a long-term ultraviolet radiation exposure facility. Data fitting was conducted to obtain the solar absorption ratio degradation curve of the thermal control coatings, and the ratio was extrapolated reasonably. The solar absorption ratio of the thermal control coatings tends stabilize after a certain amount of radiation, whether UV or VUV. Other parameters of the thermal control coatings before and after UV/VUV radiation, such as the surface microstructure and infrared emissivity were also measured and their degradation after UV/VUV radiation is discussed.

Keywords Thermal control coatings • Solar absorption ratio • UV/VUV radiation

Introduction

The effects of harsh space environment on spacecraft on different orbits vary. The low-orbit satellites are within the radiation belt, and the main effects are protons, atomic oxygen and vacuum ultraviolet radiation. The ultraviolet radiation consists of two parts: 200–400 nm (UV radiation) and 115–200 nm (VUV radiation). The direct result of deterioration of the thermal optical properties of thermal control coatings (TCC's) (caused by radiation and other factors) is poor control of surface temperatures of the spacecraft in the required range [1–3]. In the degradation of TCC's, the increase of the solar absorption ratio is the main factor affecting the

L. Wu (✉) • Y. Zhang • J. Meng • X. Yin • L. Song
Shanghai Institute of Ceramics, Chinese Academy of Sciences, Shanghai 200050, China
e-mail: wulingnan@mail.sic.ac.cn

J. Kleiman (ed.), *Protection of Materials and Structures from the Space Environment*, Astrophysics and Space Science Proceedings 47,
DOI 10.1007/978-3-319-19309-0_32

Fig. 1 Long-term ultraviolet radiation exposure facility

temperature of the spacecraft So the emphasis in this study was put on the solar absorption ratio changes in the UV/VUV irradiated TCC samples [4, 5].

In this paper, optical properties of several typical thermal control coating samples, including the antistatic silvered cerium glass second reflectance mirror, KS-Z white coating, antistatic F46 film silvered second reflectance mirror were measured in situ in different VUV (115–200 nm) and UV (200–400 nm) ranges and radiation doses using a long-term ultraviolet radiation exposure facility. Data fitting was conducted to obtain the solar absorption ratio degradation curve of the thermal control coatings, and the ratio was extrapolated reasonably.

Experiments

Experimental Samples

Antistatic silvered cerium glass second reflectance mirror (OSR), KS-Z white coating (KSZ), antistatic silvered F46 film second reflectance mirror (F46), and antistatic polyimide aluminized second reflectance mirror (PI-Al) were chosen as experimental samples. At least three samples were used of each type.

Experimental Process

The UV (200–400 nm) and the VUV (115–200 nm) vacuum radiation experiments were carried out in the long-term ultraviolet radiation exposure facility developed by our group (see Fig. 1). The facility consists of three major parts: ultraviolet

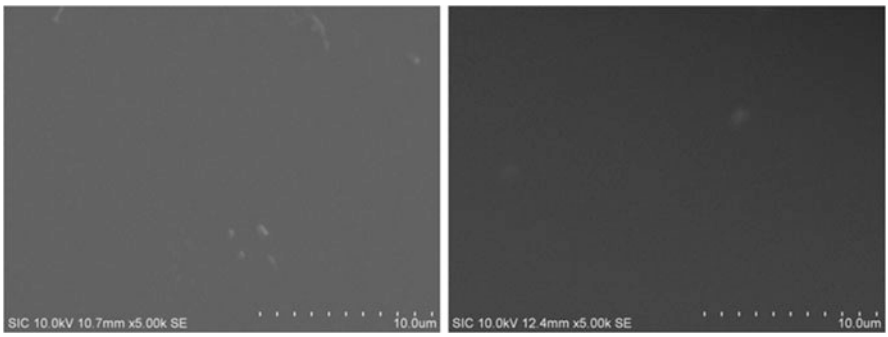

Fig. 2 SEM morphology of sample OSR before (*left*) and after (*right*) VUV radiation

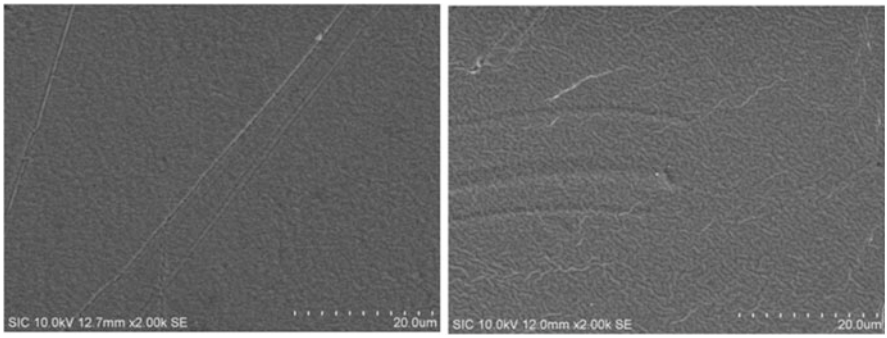

Fig. 3 SEM morphology of sample F46 before (*left*) and after (*right*) VUV radiation

radiation system, in-situ measurement system and automatic control system. As a source of UV (200–400 nm) radiation a high power Mercury Xenon lamp (5000 W) is used. The UV radiation intensity was 4 suns. As a source of VUV (115–200 nm) radiation a high power Deuterium lamp made in Japan was selected. The acceleration factor was 30–35. The vacuum in the irradiation chamber was kept at $<10^{-5}$ Pa.

Results and Discussion

Irradiation with VUV (115–200 nm)

SEM Morphology

Figures 2, 3, 4 and 5 present the results of SEM analysis of the four selected thermal control coatings before and after VUV radiation. The antistatic silvered F46 film second reflectance mirror sample exhibited some surface wrinkles (Fig. 3) due to its

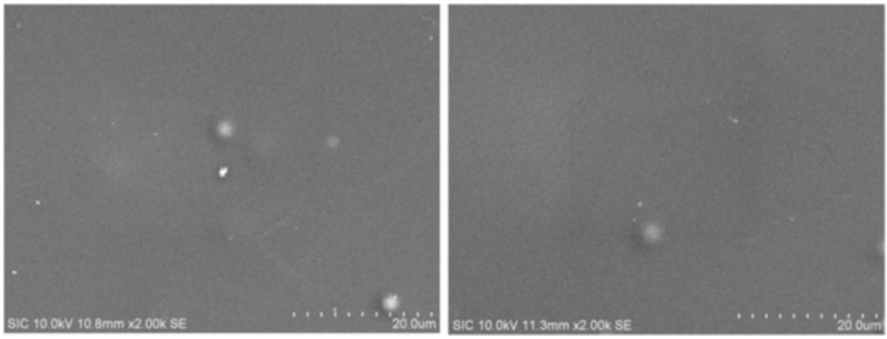

Fig. 4 SEM morphology of sample PI-Al before (*left*) and after (*right*) VUV radiation

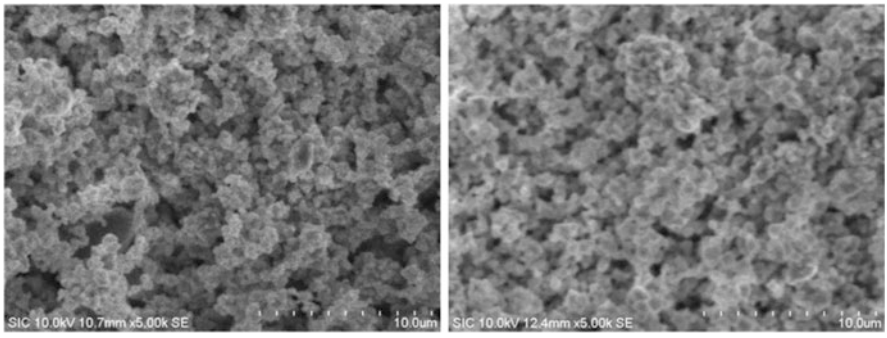

Fig. 5 SEM morphology of sample KSZ before (*left*) and after (*right*) VUV radiation

flexible nature. Otherwise, no apparent internal structure changes were noticed in the SEM images before and after VUV radiation of all samples, suggesting little influence of the VUV.

Data Fitting

The experimental data obtained for the solar absorption ratio was fitted by a power function regression. This form of power function regression equation can be expressed as

$$\alpha_s = \exp(a + b\ln(t)) \tag{1}$$

where α_s—the solar absorption ratio of the thermal control coatings, a, b—are undetermined coefficients and t—is the irradiation time.

The solar absorption ratio degradation curve of thermal control coating can be obtained through the experimental data.

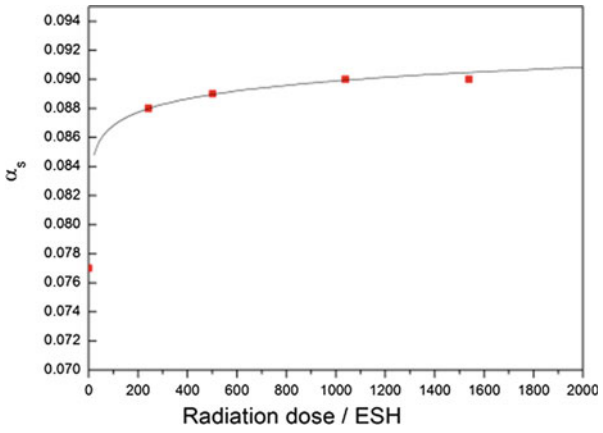

Fig. 6 The measured data and fitting curve of the solar absorption ratio of OSR

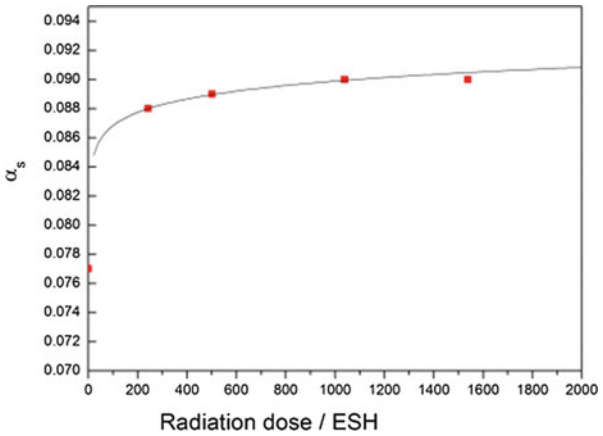

Fig. 7 The measured data and fitting curve of the solar absorption ratio of F46

Figures 6 through 9 present the results of the measurements (mean of 3 samples) and the fitting curves of the solar absorption ratio of OSR, F46, PI-Al and KSZ coatings. It can be seen from Figs. 6, 7, 8 and 9 that the solar absorption changed strongly in the beginning of the exposure, with the tendency for the data to stabilize after 500ESH of exposure. While some of the measured points deviated somewhat from the fitting curves, considering the test error of the solar absorption ratio measurement, the compliance between the data points and the fitting curves was good.

According to the fitting curves in Figs. 6, 7, 8 and 9, the experimental data could be extrapolated to assess the VUV radiation stability of the thermal control coatings. In Table 1, the measured values for the four coatings at 2000ESH and the extrapolated values of the solar absorption ratio to 5000ESH, 8000ESH and 12600ESH are shown. As can be seen from Table 1, the solar absorption ratio of

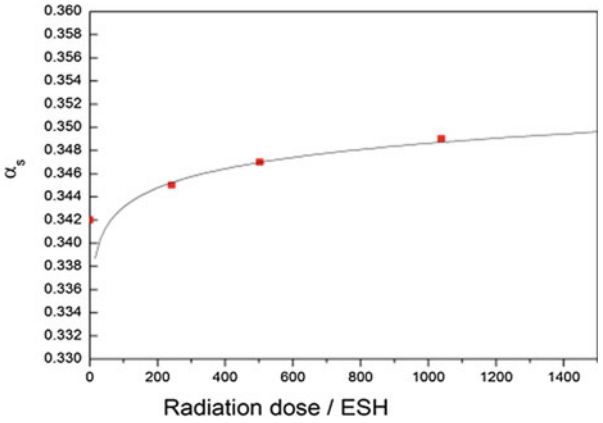

Fig. 8 The measured data and fitting curve of the solar absorption ratio of PI-Al

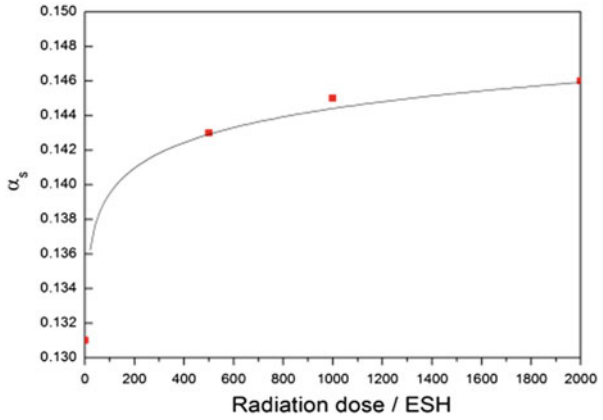

Fig. 9 The measured data and fitting curve of the solar absorption ratio of KSZ

Table 1 Summary of extrapolated solar absorption ratio changes of the thermal control coatings after VUV radiation

Radiation dose/ESH	OSR/$\Delta\alpha_s$	F46/$\Delta\alpha_s$	PI-Al/$\Delta\alpha_s$	KSZ/$\Delta\alpha_s$
2000	0.005	0.012	0.007	0.013
5000	0.009	0.015	0.011	0.017
8000	0.010	0.016	0.012	0.018
12,600	0.010	0.016	0.013	0.019

thermal control coatings remained relatively stable and within a reliable range even after prolonged exposures to UV.

Spectral Reflectance

Spectral reflectance of the thermal control coatings before and after VUV radiation was measured in order to better understand their solar absorption behavior.

Table 2 Infrared emissivity of thermal control coatings before/after 2000ESH VUV radiation

Sample	Infrared emissivity/ε_h		$\Delta\varepsilon_h$
	Before	After	
OSR	0.084	0.085	0.001
F46	0.729	0.719	−0.010
PI-Al	0.682	0.705	0.023
KSZ	0.940	0.946	0.006

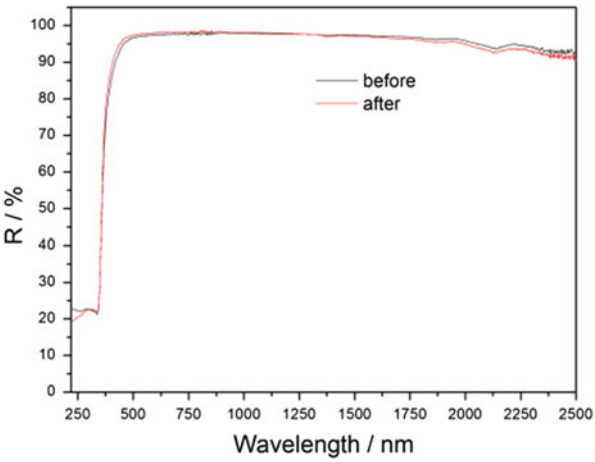

Fig. 10 Spectral reflectance of OSR before/after VUV radiation

After VUV irradiation, the solar absorption of OSR slightly increased. The trend for F46 after VUV irradiation was similar, however, change was much more pronounced, with the spectral reflectance in the near infrared region dropping significantly. The spectral reflectance change of PI-Al was basically similar to that of OSR, i.e., with a decrease in near infrared spectral reflectance. For the KSZ material a slight decrease in spectral reflectance was observed in the visible range. The observed spectral reflectance trends were consistent with vacuum VUV irradiation test results for thermal control coatings [6].

Infrared Emissivity

The results of the measurements of infrared emissivity of the tested thermal control coatings after 2000ESH VUV irradiation are listed in Table 2. It could be seen that the infrared emissivity of OSR and KSZ remained almost unchanged after VUV radiation that is consistent with the literature [7]. Certain change, however, occurred in the emissivity of F46 and PI-Al materials (Figs. 10, 11, 12 and 13).

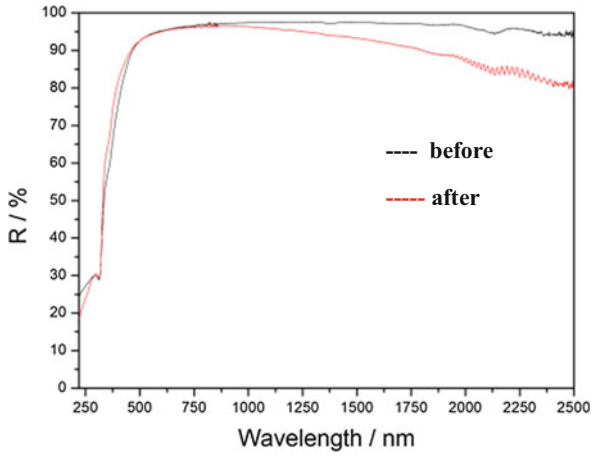

Fig. 11 Spectral reflectance of F46 before/after VUV radiation

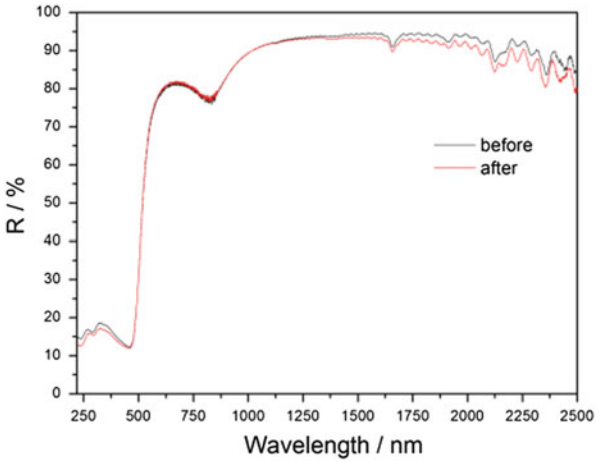

Fig. 12 Spectral reflectance of PI-Al before/after VUV radiation

UV (200–400 nm) Radiation

SEM Morphology

SEM analysis was conducted on OSR and KSZ thermal control coatings samples before and after UV radiation with the results shown in Figs. 14 and 15. As can be seen from Fig. 14, no evident surface morphology changes were found for the OSR sample after UV radiation. However, for the KSZ coating, significant spalling of the organic filler was observed after UV radiation (Fig. 15) that may have a negative impact on the optical performance of the coating.

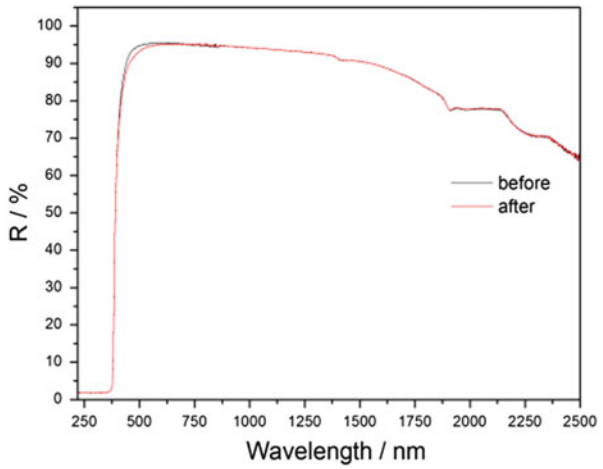

Fig. 13 Spectral reflectance of KSZ before/after VUV radiation

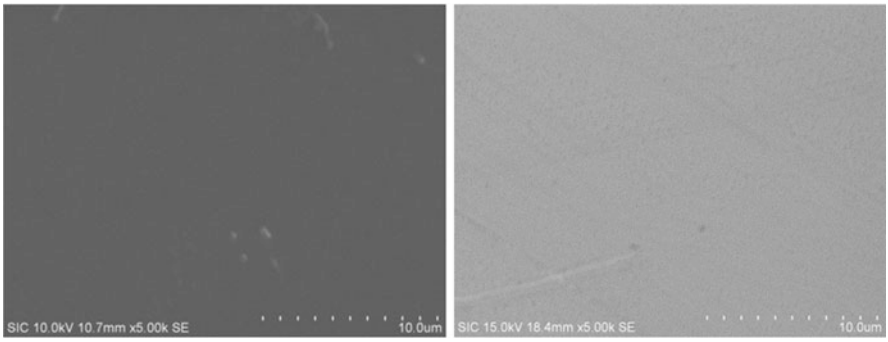

Fig. 14 SEM morphology of sample OSR before (*left*) and after (*right*) UV irradiation

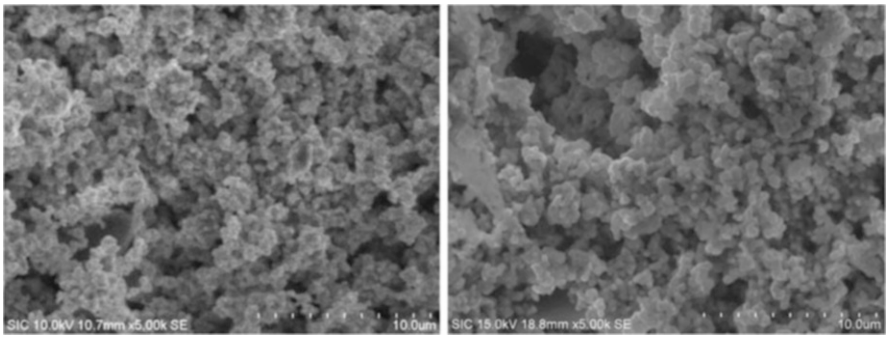

Fig. 15 SEM morphology of sample KSZ before (*left*) and after (*right*) UV irradiation

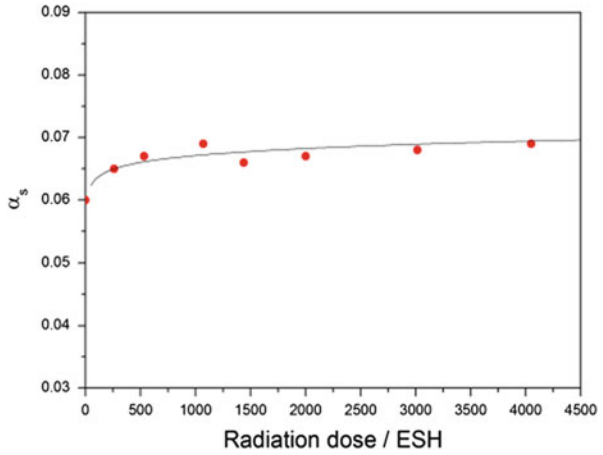

Fig. 16 The measured data and fitting curve of the solar absorption ratio of OSR

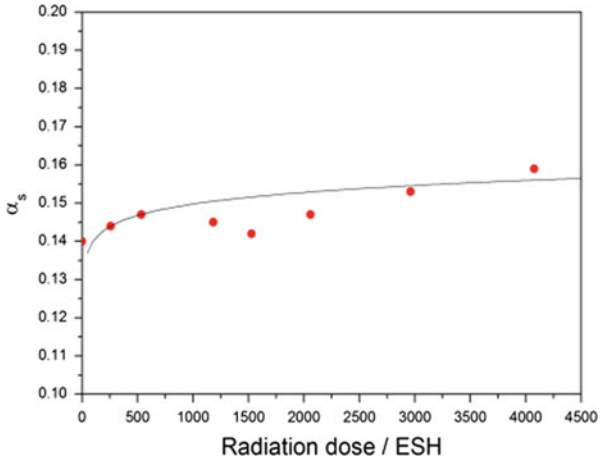

Fig. 17 The measured data and fitting curve of the solar absorption ratio of KSZ

Data Fitting

The experimental data obtained for the solar absorption of the OSR and the KSZ coatings were fitted by a power function regression using the Eq. (1). Figures 16 and 17 present the results of this data fitting.

Analyzing the data in Figs. 16 and 17, it can be suggested that deviations between the accumulated data and the fitting curves are larger in the beginning of the experiments with a much better fit occurring after ~3000ESH of exposure.

Table 3 The extrapolated solar absorption ratio changes in the value of OSR and KSZ after UV radiation

Radiation dose/ESH	OSR/$\Delta\alpha_s$	KSZ/$\Delta\alpha_s$
3000	0.009	0.015
5000	0.010	0.017
8000	0.011	0.019
12,600	0.011	0.021

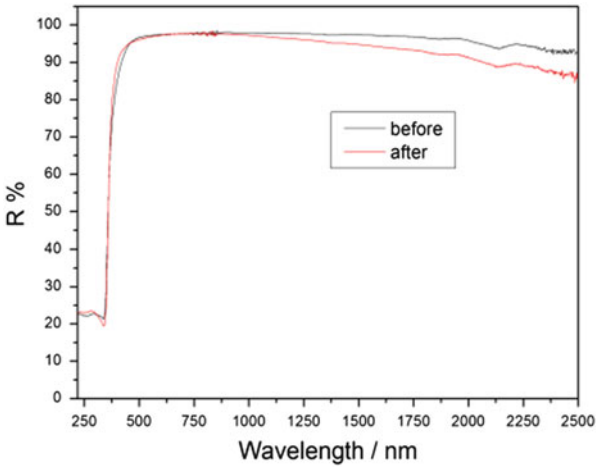

Fig. 18 Spectral reflectance of OSR before/after UV radiation

Using the fitting curves in Figs. 16 and 17, the experimental data could be extrapolated to assess the UV radiation stability of the thermal control coatings at higher exposures. Table 3, presents the results of such extrapolation. In the table the values of the solar absorption of OSR and KSZ coating samples at 3000ESH are given together with the extrapolated results for doses of 5000ESH, 8000ESH and 12600ESH.

As can be seen from Table 3, the extrapolated data for the solar absorption of OSR and KSZ coatings remained relatively stable at a value within the reliable range that was similar to results of thermal control coatings after VUV radiation.

Spectral Reflectance

Spectral reflectance of the OSR and KSZ thermal control coatings before and after UV radiation was measured in order to better understand their solar absorption behavior.

As shown in Fig. 18, the spectral reflectance of OSR coating rose slightly in the visible range, while decreasing significantly in the near-infrared region, which may be the main cause for the decrease of the solar absorption ratio. The spectral reflectance of the KSZ coating after UV radiation demonstrated a different behavior, decreasing in the 300–1300 nm range but increasing in the 1300–2500 nm

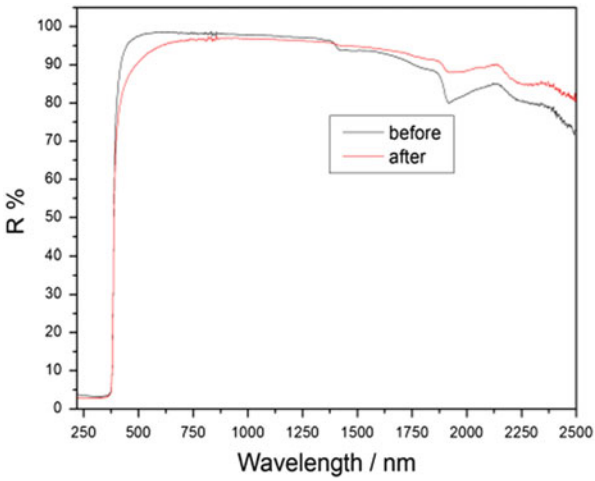

Fig. 19 Spectral reflectance of KSZ before/after UV radiation

range. Since the energy contribution in the sun spectrum in the 300–300 nm is much larger than in the 1300–2500 nm range, the solar absorption of KSZ after UV radiation experienced a greater decrease (Fig. 19).

Conclusions

The UV (200–400 nm) and the VUV (115–200 nm) irradiation experiments were carried out for a number of thermal control coatings, namely, OSR, KSZ, F46 and PI-Al in the long-term ultraviolet radiation exposure facility. The solar absorption was measured for these coatings in situ for a range of different irradiation doses. The solar absorption degradation curves were experimentally measured and fitted using a power function regression. By extrapolating the fitting curves, estimates were obtained for the solar absorption values of the thermal control coatings at high irradiation doses, which could provide reference data for designers.

The surface structure and infrared emissivity of the thermal control coatings before and after UV/VUV irradiation were also analyzed and measured and their degradation after UV/VUV radiation was discussed. The results showed that the VUV irradiation affected thermal control coatings to a lesser extend and the thermal control performances were stable. In contrast, UV radiation had a greater effect on the thermal control coatings, with the thermal performances, however, maintained a relatively stable range.

References

1. Bizhong C (1994) The combined effects of space environment on satellite. Environ Technol 38:60–132
2. Guangming CAI, Weidong YU (2008) Current status of research on flexible materials aging properties in space environment. J Text Res 29:131–136
3. Weixin J, Tian T (2007) Situation and prospects of the space environment research. Spacecraft Environ Eng 24:337–341
4. Weiquan F (2010) Evaluation and validation of spacecraft material in space environment. Spacecraft Environ Eng 27:139–143
5. Wan Z, Guangqiang F, Yuyan L et al (2009) Damage effects of thermo cycling and VUV radiation on Al/Kapton films. Mater Sci Technol 19:62–65
6. Yuzhi Z, Yunzhen C et al (2011) Ultraviolet irradiation tests of some thermal control coatings in vacuum. Spacecraft Environ Eng 28:126–131
7. Donald AJ, George CT, David TW et al (2008) Optieal properties of thermal control coatings after weathering, simulated ascen the ating, and simulated Paceradiationex Posure. NASA 2008–2152

Effect of Projectile Shape and Velocity on Crater Damage

Qiang Wei, Haorui Liu, Sam Zhang, and Yu Bai

Abstract The shape of the particles in ground simulations of space debris is mostly assumed as spherical particles. However, the number of flat particles in space debris is much higher than of spherical ones. Therefore, flat-shaped particles pose more danger to orbiting crafts. This paper describes a study that employs the laser-driven flyer technique to produce flat-shaped projectiles of different aspect ratio to impact on quartz glass (usually used as window in spacecraft) and studies the influence of the projectile boundary geometries on damage morphologies. The results show that the impact craters due to spherical particles and to flat ones are similar in shape but differ in depth of penetration and scatter. The equation for spherical debris was modified to describe the relationship between diameters of the crater and the flat projectile.

Keywords Space debris • Laser driven flyer • Boundary geometry • Hypervelocity impact • Impact equation • Aspect ratio • Penetration coefficient

Q. Wei (✉)
Tianjin Key Laboratory of Composite and Functional Materials, School of Materials Science and Engineering, Tianjin University, 92 Weijin Road, Tianjin, China

School of Mechanical & Aerospace Engineering, Nanyang Technological University, 50 Nanyang Avenue, Singapore 639798, Singapore
e-mail: spacematerials@163.com

H. Liu
Tianjin Key Laboratory of Composite and Functional Materials, School of Materials Science and Engineering, Tianjin University, 92 Weijin Road, Tianjin, China

S. Zhang
School of Mechanical & Aerospace Engineering, Nanyang Technological University, 50 Nanyang Avenue, Singapore 639798, Singapore

Y. Bai
Beijing Institute of spacecrafts Environment Engineering, Beijing 100094, China

J. Kleiman (ed.), *Protection of Materials and Structures from the Space Environment*, Astrophysics and Space Science Proceedings 47,
DOI 10.1007/978-3-319-19309-0_33

Introduction

With increasing human activities in space, the quantity of space debris is ever increasing. Micro debris has become one of the threatening factors to service life and reliability of the orbiting space vehicles [1]. Until now, ground simulation experiments often assume spherical projectiles [2, 3]. In space, however, the space debris are of different shapes and sizes with great differences in aspect ratio. As early as in 1995, NASA reported [4] that the spherical particle is not the main debris in space. The number of the flaky particles amounted to more than 13 % of the total space debris. As such, flakes pose more dangers because of their sheer number. In recent years, more studies of flaky projectiles appeared in the literature [5–7]. Until now, the emission of a group of particles was usually adopted in ground simulation, i.e., a "shotgun" effect: one single firing triggers many "shots". In group emission, scientists have to face a large distribution of particle velocities and sizes, thus it is difficult to pinpoint impact damage to a specific particle. The laser driven flyer (LDF) technique developed in early 2000's has great advantage to associate the flyer parameters with the specific impact result. In this paper, we use the LDF technique to generate projectiles of different aspect ratio to simulate flakes of different sizes and study the influence of debris boundary geometry on the hypervelocity impact damage morphology to describe the relationship between diameters of the crater and the flake projectile.

Figure 1 illustrates the damage morphologies induced by a spherical (a) and a flake particle (b).

In Fig. 1a mostly fragments of the target material are scattered around the impact crater, similar to eruption of a volcano [10]. In Fig. 1b, very few fragments of the window are seen but a large number of flyer residues is found around the impact crater.

In collision dynamics, hypervelocity impact creates a shock wave in the target material that leads to very high pressure and temperature. This leads to creation of an approximately hemispherical crater damage [11] induced by the interaction

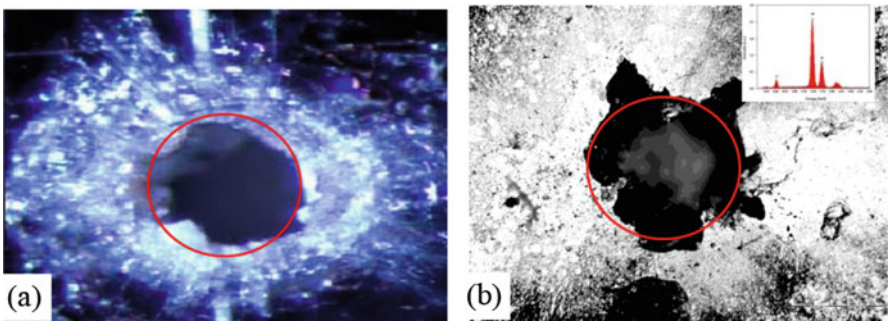

Fig. 1 A spherical projectile impact crater and flaky projectiles impact crater. (**a**) Spherical projectile hypervelocity impact crater [9]; (**b**) flake projectile hypervelocity impact crater [8]

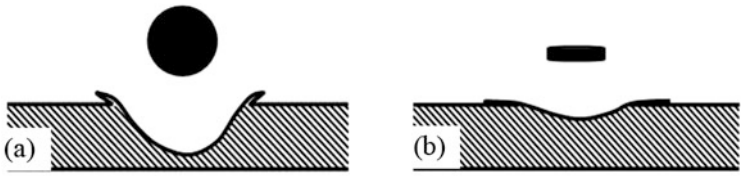

Fig. 2 Diagram of the produced craters for projectile particles with different shapes. (**a**) Spherical projectile impact model; (**b**) flake projectile impact model

between the compression wave and the reflection wave within the impact target. In addition, formation of micro cracks, ejecta and extrusion around the impact crater takes place.

The whole collision process includes creation of crater, penetration and extrusion, and reflective sputtering. The compression wave plays the leading role in the first two stages, the reflection wave in the last. This is true for crater formation by spherical projectile or by flake projectile, as illustrated in Fig. 2. However, in the case of impact by a flake particle, the time of penetration and extrusion is very short, which results in shallow crater and no extrusion (Fig. 2b). The shallower the crater becomes, the larger the scatter area results in. The difference in damage morphology originates from the penetration process, which, in fact, is largely affected by the projectile's boundary geometry, i.e., the aspect ratio of the projectile. The aspect ratio of a spherical particle is one, and that of a flake is much <1.

Experimental

In order to verify the influence of the aspect ratio on impact damage, particles of different aspect ratio (illustrated in Fig. 3) are created using different laser beam diameter. Table 1 tabulates the details.

A pulse solid laser Nimma-900 is used in the experiment. To accelerate a flyer, the laser beam 5–7 ns wide with a wavelength of 1064 nm is shot with a frequency of 1 Hz onto a composite flyer target 1 cm away and in 10^{-1}–10^{-4} Pa vacuum. The flyer target is made of a 16 μm thick aluminum foil glued with silicone oil onto a piece of quartz glass. The laser passes through the quartz onto the aluminum foil to ablate a small part of the aluminum foil at the foil/quartz interface to form plasma with high pressure and temperature that "launches" the residual foil towards an impact target. The impact target is a "quartz window", i.e., a quartz glass disk of 40 mm in diameter and 2 mm in thickness. The spot size and the energy density of the laser beam can be adjusted by changing the focal length to obtain flyers with different diameters to achieve different aspect ratio. The flyer velocity is measured by the polyimide piezoelectric films (PVDF) method [8]. The damage morphology of the impacted surface is examined under optical microscope and scanning electron microscope (SEM). The crater size is measured using Image-pro plus software.

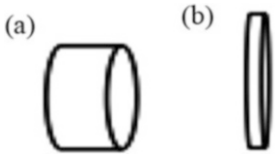

Fig. 3 Flyer diagrams with different aspect ratio. (**a**) The aspect ratio of flyer is 0.32; (**b**) the aspect ratio of flyer is 0.145

Table 1 Experimental parameters and data of flyer with different aspect ratio

Experiment No.	Velocity (km/s)	Diameter (μm)	Flyer thickness (μm)	Aspect ratio
1	1.4	50	16	0.32
2	1.4	110	16	0.145

Effect of Particle Shape on Damage Morphology

Figure 4 shows the damage morphology induced by projectiles of different aspect ratio. In Fig. 4a, the crater and volcano-like extrusion are observed, similar to that of spherical projectile. In Fig. 4b, along with an impact crater, large area is found contaminated around the crater due to ejecta by reflective sputtering.

Multi-Feature Damage Equation for Flaky Particles

In hypervelocity impact dynamics, the relationship between the diameter of the crater and that of the projectile is described by a dimensionless parameter D_c/d_p, projectile size effect in physical meaning. For spherical projectile, this equation is [12]:

$$\frac{D_{\mathrm{c}}}{d_p} = \Psi\left\{\frac{v_p}{\sqrt{Y_t/\rho_t}}, \frac{\rho_p}{t}, \frac{Y_p}{Y_t}\right\} \tag{1}$$

where, D_{c} is the crater diameter; d_p is the projectile particles diameter; ρ_p and ρ_t are the density of projectile particles and target materials, respectively and the Y_p and Y_t are the strength of projectile and target materials, respectively. The dimensionless velocity is introduced as

$$\frac{v_p}{\sqrt{Y_t/\rho_t}}$$

by using the target inertia ratio

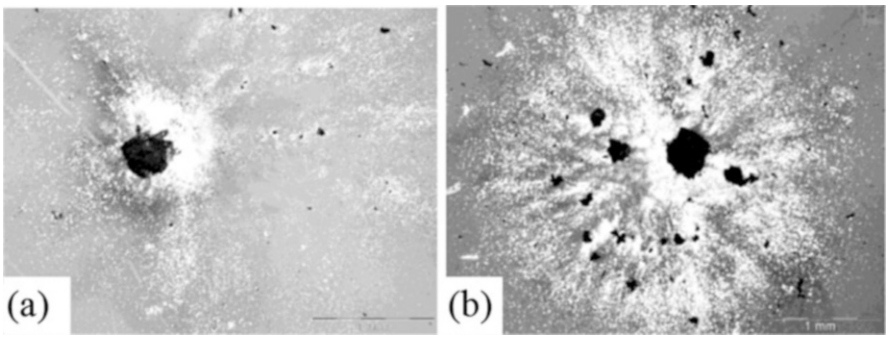

Fig. 4 Damage morphology induced by impactor with different aspect ratio: (**a**) 0.32, (**b**) 0.145

$$\sqrt{\frac{Y_t}{\rho_t}}.$$

To apply to flake projectiles, a parameter g representing penetration coefficient must be introduced. The penetration coefficient is related to penetration ability such as aspect ratio, and is different for different collision systems. With this consideration, Eq. (1) is modified as

$$\frac{D_c}{d_p} = \Psi\left\{g, \frac{v_p}{\sqrt{Y_t/\rho_t}}, \frac{\rho_p}{\rho_t}, \frac{Y_p}{Y_t}\right\} \tag{2}$$

According to the isotropic expansion theory in hypervelocity impact theory [12], D_c/d_p can be expressed as follows

$$\begin{aligned}\frac{D_c}{d_p} &= g*2\cdot\frac{p_c}{d_p} + A\left(\frac{\rho_p}{\rho_t}, \frac{Y_p}{Y_t}\right) \\ &= 0.54\bullet g\bullet\left(\frac{\rho_p}{\rho_t}\right)^{2/3}\bullet\left(\frac{v_p}{\sqrt{Y_t/\rho_t}}\right)^{2/3} + 1.4\cdot\left[1-\left(\frac{\rho_p}{\rho_t}\right)^{2/3}\cdot\left(\frac{Y_p}{Y_t}\right)^{1/3}\right]\end{aligned} \tag{3}$$

where, p_c is the crater depth, and it is only related to the material's parameters as follows.

$$\frac{p_c}{d_p} = 0.27\cdot\left(\frac{\rho_p}{\rho_t}\right)^{2/3}\bullet\left(\frac{v_p}{\sqrt{Y_t/\rho_t}}\right)^{2/3}. \tag{3a}$$

Table 2 The material parameters adopted in verification experiment

Parameters	Aluminum flyer	Quartz glass
Density	2.7 g/cm^3	2.2 g/cm^3
Strength	80 MPa	640 MPa
Diameter	50 μm	40 mm

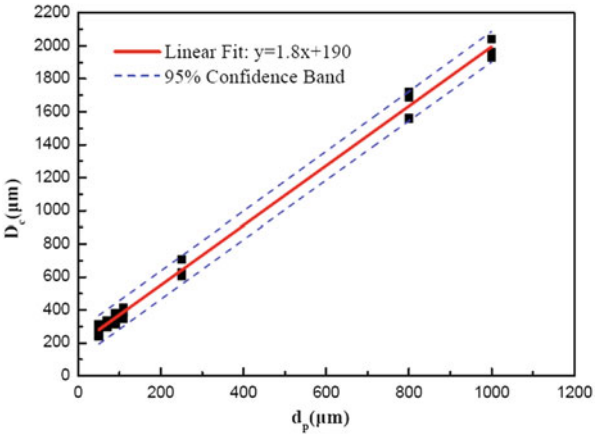

Fig. 5 The statistical relationship between the craters size D_c and debris size d_p at $v_p = 1.4$ km/s

$$A\left(\frac{\rho_p}{\rho_t}, \frac{Y_p}{Y_t}\right) = 1.4 \cdot \left[1 - \left(\frac{\rho_p}{\rho_t}\right)^{2/3} \cdot \left(\frac{Y_p}{Y_t}\right)^{1/3}\right]. \tag{3b}$$

Equation (3) is a dimensionless multi-parameter characteristic equation describing the relationship between the diameter of the crater and a flake projectile. Equation (3) has three different aspects of parameters: basic materials parameters such as density, strength of the projectile and impact target (ρ_p, ρ_t, Y_p and Y_t), the shape factor of the projectile or the penetration coefficient (g) and the impact velocity of the projectile (v_p). For a given projectile and impact target, D_c/d_p is a function of penetration coefficient g and impact velocity v_p.

Experimental Verification of the Multi-Parameter Characteristic Equation

To verify Eq. (3), the penetration coefficient g needs to be determined first. For this purpose, a series of impact tests was carried out with Aluminum flyers (c.f., Table 2) of different diameters at constant impact velocity $v_p = 1.4$ km/s.

Figure 5 plots the measured crater diameter as a function of projectile size. A straight line is obtained with a slope of 1.8. From Eq. (3), the slope contains g and the velocity used together with other materials constants, substitution of these values gives rise to coefficient $g = 1.5$.

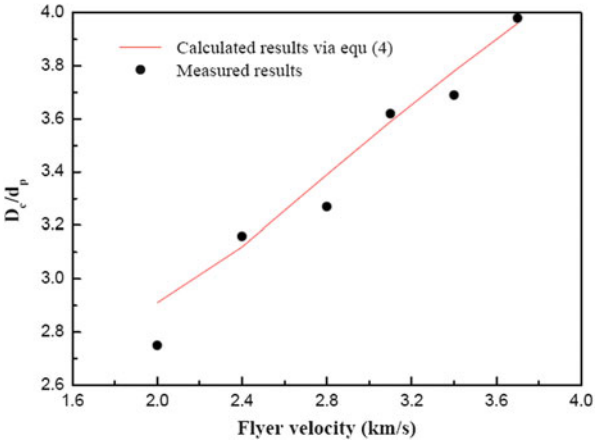

Fig. 6 The relationship between D_c/d_p and v_p in verification test

Equation (3) can be reduced to Eq. (4) as follows.

$$\frac{D_c}{d_p} = 0.93 \bullet \left(\frac{v_p}{539.36}\right)^{2/3} + 0.6 \tag{4}$$

Therefore, at a given flyer shape, the projectile size effect (D_c/d_p) is a function of velocity only. To verify this point, a series of impact tests with different velocities were conducted. Figure 6 plots D_c/d_p as a function of v_p according to Eq. (4). The experimental data points (solid dots) fit nicely the "theoretical prediction" (solid line), thus successfully validating Eq. (3).

Conclusions

1. The parameters of formed crater are related to the aspect ratio of a projectile. Flake flyers result in shallow craters with large spread of ejecta contamination.
2. The impact equation describing the relationship between diameters of the crater and flake projectiles is a function of the projectile velocity only for a given shape of the flyer material and impact target. In the case of an aluminum flyer being shot at a quartz window, this relationship becomes

$$\frac{D_c}{d_p} = 0.93 \bullet \left(\frac{v_p}{539.36}\right)^{2/3} + 0.6.$$

Acknowledgements Authors would like to acknowledge the funding of the National Natural Science Foundation of China (Grant no.41274191).

References

1. Liou JC, Johnson NL (2006) Planetary science. Risks in space from orbiting debris. Science 311(5759):340
2. Yan XJ, Zhang YZ, Nie JX (2002) Numerical simulation of the whipple shield under hypervelocity impact. J Astronaut (in Chinese) 23(5):81–84
3. Lamontagne CG, Manuelprojectileai GN, Kerr JH et al (2001) Projectile density, impact angle and energy effects on hypervelocity impact damage to carbon fibre/peek composites. Int J Impact Eng 26(1):381–398
4. McKnight D, Fudge M, Maher R (1995) Satellite orbital debris characterization impact test (SOCIT) series data collection report. NASA contract NAS 9-19215
5. Hu K, Schonberg WP (2003) Ballistic limit curves for non-spherical projectiles impacting dual-wall spacecraft systems. Int J Impact Eng 29(1):345–355
6. Schonberg WP, Williamsen JE (2006) RCS-based ballistic limit curves for non-spherical projectiles impacting dual-wall spacecraft systems. Int J Impact Eng 33(1):763–770
7. Williamsen JE, Evans SW (2006) Predicting orbital debris shape and orientation effects on spacecraft shield ballistic limits based on characteristic length. Int J Impact Eng 33(1):862–871
8. Song LH, Wei Q, Bai Y (2013) Impact effects on fused quartz glass by ground simulating hypervelocity space debris. Sci China Technol Sci 56(3):724–731
9. Li HW (2010) Research of small space debris impact effect. PhD Thesis, Beijing Center for Space Science and Applied Research Chinese Academy of Sciences (in Chinese), pp 45–72
10. Hernandez VS, Murr LE, Anchondo IA (2006) Experimental observations and computer simulations for metallic projectile fragmentation and impact crater development in thick metal targets. Int J Impact Eng 32(12):1981–1999
11. Ma XQ, Han F (1998) High speed impact dynamics. National Defense Industry Press (in Chinese), Beijing, pp 277–282
12. Zhang QM, Huang FL (2000) An introduction to hypervelocity impact dynamics. Science Press (in Chinese), Beijing, pp 87–100

The Study of Space Debris and Meteoroid Impact Effects on Spacecraft Solar Array

Dongsheng Jiang, Pei Zhang, and Yi Zhang

Abstract The debris impact may cause the degradation of solar cells because of the cumulative effect (Lei, Cumulative effects of micrometeoroid impacts on spacecraft, 2010), and even damage several strings of solar cells depending on the diameter of the debris. Hypervelocity impact event may excite plasma and by spreading the plasma can initiate discharges that are able to induce arcing on the solar circuits that will decrease the output power of solar arrays. The effect of impacts on wires and aluminum honeycomb is also discussed. The risk of impact on solar array of a GEO satellite will be analyzed, and the probability of impact will also be calculated by using the MASTER2005 flux model.

Keywords Solar array • Debris and meteoroid • Impact damage

Introduction

On June 12, 2011, the Y-axial solar array output current on a Chinese GEO satellite suddenly decreased, according to the telemetry signal, the shunt current dropped from the normal condition of 7.78–4.94 A. At the same time, the yaw angle of the satellite changed 0.1°, and after 3 min, the attitude and orbit control system stabilized the satellite. It was estimated that the satellite probably had been hit by space debris or meteoroids. In last 20 years, there were 8 impact events reported on satellites in orbit (see Table 1).

With the expansion of human activity in space, there has been a growing amount of objects whose secondary impact created a large amount of space debris left in orbit. The spacecraft also faces meteor shower threats from the comet and asteroid belt. Those debris and meteoroids are presenting a serious threat to spacecraft [1]. The meteoroid and orbital space debris environment in Earth orbits consists of hypervelocity particles of various mass, diameter, and velocity. Micrometeoroids have an average density and velocity of 0.5 g/cm^3 and 20 km/s respectively whereas

D. Jiang (✉) • P. Zhang • Y. Zhang
Beiijng Institute of Spacecraft System Engineering, Beijing, People's Republic of China
e-mail: jiang_dongsheng@sohu.com

J. Kleiman (ed.), *Protection of Materials and Structures from the Space Environment*, Astrophysics and Space Science Proceedings 47,
DOI 10.1007/978-3-319-19309-0_34

Table 1 Eight impact events reported on satellites, since 1993

Date	Satellite	Events
1993	Olympus	Hit by Perseids meteor shower; total loss
24 July 1996	Cerise	Hit by space debris (a fragment of Ariane V16)
19 Jan 2001	SO-35	Contact lost, possible collision with external object
21 Apr 2002	Kosmos 539	Hit by space debris or meteoroid
22 May 2007	Meteosat-8	Orbit change, likely hit by unknown object
10 Feb 2009	Iridium 33	Destroyed in accidental collision with defunct Russian milsat
22 May 2013	NEE-01 Pegaso	Hit by space debris, tumbling
22 May 2013	GOES-13	Unknown anomaly (possibly hit by micrometeorite); returned to service

space debris average density and velocity is 2.8 g/cm^3 and 9–10 km/s depending on the altitude [2]. According to NASA orbital debris program office's database (2009), there are currently about 19,000 objects with sizes larger than 10 cm, tens of millions particulates smaller than 1 cm and about 500,000 particles in between. As solar arrays have the largest exposed to the space area, their probability to be impacted by meteoroids or space debris is high. From the inspection of the retrieved HST array, for instance, the whole wing suffered between 5000 and 6000 micrometeoroid impacts in its 4-year life. The effects of these impacts range from slight grazing to puncture of cells and panels [3]. This paper studies the impact damage effects of space debris or meteoroids on spacecraft solar arrays.

Space Debris and Meteoroid Impact Damage on Solar Array

All spacecrafts in orbit have the impact risk from space debris and meteoroid. Practically, any spacecraft will suffer damage if it receives a hypervelocity impact from an object heavier than a few grams, with collisions with smaller objects causing serious surface erosion. The solar array surface area is the largest part of the total spacecraft surface area exposed directly to the space environment, so the space debris and meteoroid impacts have a particularly strong effect on it. Individual impacts on spacecraft solar array surfaces generally may not pose a threat to critical system functioning. However, the accumulation of impacts over the large area of the solar array would lead to a degradation of output power.

Structure of Solar Array

Typical solar array panels (Fig. 1) are built from aluminum honeycomb-type core supported with carbon fiber reinforcement. The solar cells are bonded to the array

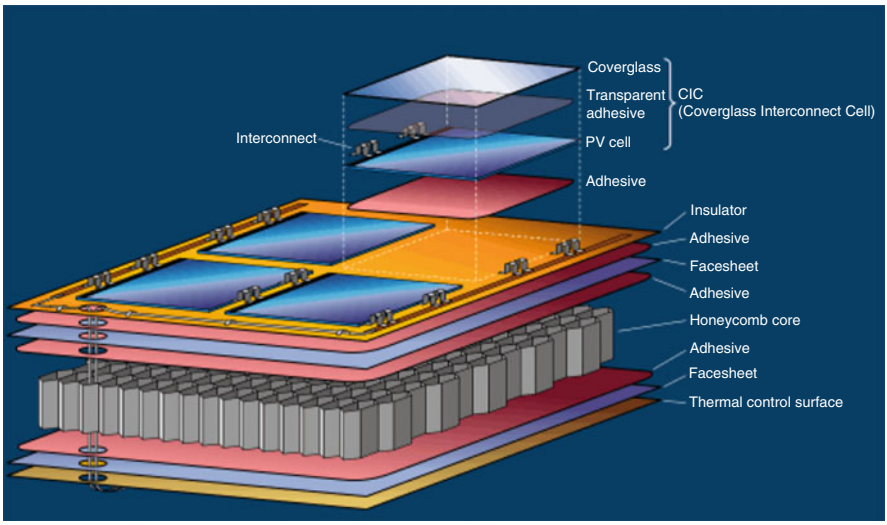

Fig. 1 A typical structure of a solar array panel

structure with silicon adhesive. Between the solar cells and solar panel, a layer of polyimide film is pasted to insulate the solar cell electrodes and conductive substrate. The cover glasses that are used to provide protection for the cells against radiation and microparticles impact damage are made usually of cerium-doped glass 0.01 cm thick. Multiple wires link the diode board and solar cells strings, and connectors link them between all panels, ensure the current transfer into the spacecraft.

The damage to the solar array from the impact by meteoroids or space debris includes creation of a small crater on the coverglass or even penetrating and leaving a hole in the solar array that depends on the velocity and size of the projectile. The hypervelocity impact of a meteoroid can form plasma on the solar array surface; the formed plasma can also trigger a discharge of solar circuit and even cause a short circuit with the potential consequence of losing output power from several strings of solar array.

Optical Degradation of Solar Cells

Optical degradation means incident light on solar cell is partially disperses and absorbs, so the amount of power converted into electrical is reduced. The damage that affects optical degradation typically happens mostly to the coverglass, with most of the damage not reaching the solar cell (Figs. 2 and 3). The erosion and mechanical destruction of the surface can happen upon impact by any type of particles. The effect of micro-particles 1–100 μm in size is mainly to reduce the

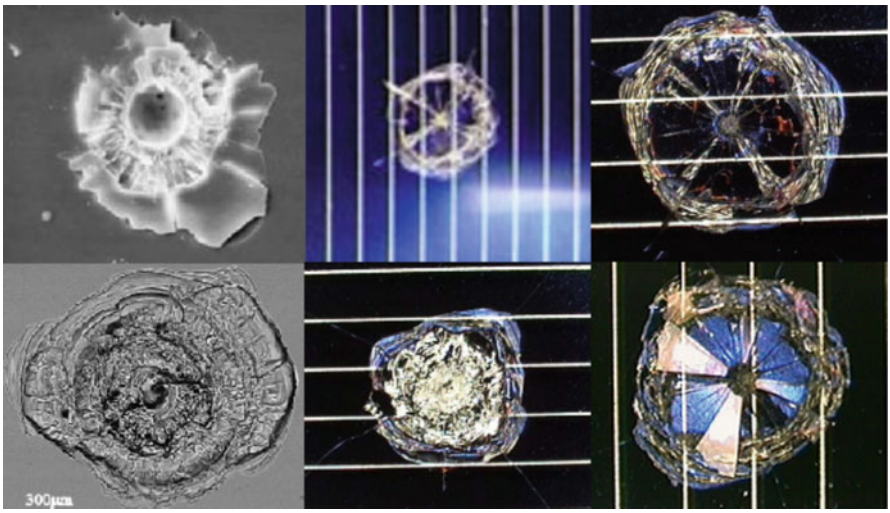

Fig. 2 Examples of craters formed on solar cell coverglasses

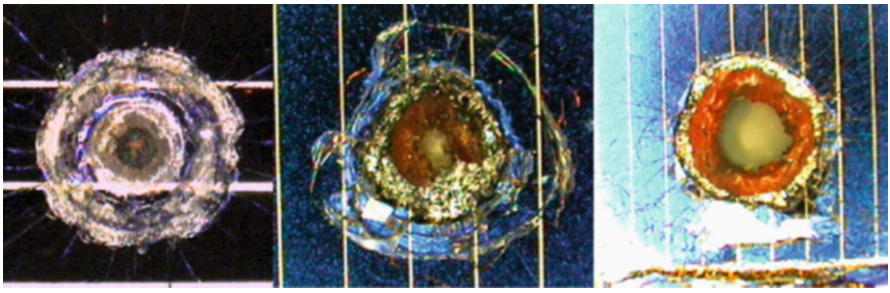

Fig. 3 Examples solar cell damage photo (from ESA HST)

amount of light reaching the cell. For particles over 1000 μm in size the optical losses are negligible, due to their relatively small numbers [4]. The optical degradation is induced by the surface damage of the coverglass where micro-cracks, scratches and craters are formed. The optical losses are determined by the amount of damaged area, i.e., the area of formed craters, and whether any dust remains in the craters or not.

Physical Damage of Solar Cell

The cover glasses can partly prevent the particle from hitting the cell itself. Under impact of particles with large sizes and high velocities, solar cells can be damaged as well, with the projectiles even penetrating and shunting the cells. Studies show

that the power losses under such impacts can be sufficiently greater than from the optical surface damage. Cells impacted by meteoroids and debris can exhibit two damage mechanisms: increase in series resistance due to grid damage, or decrease in shunt resistance due to junction damage. In both cases the output current in solar cells will decrease or will be totally lost.

Mechanical Damage on Solar Panel

As was discussed above, solar panels are generally built using aluminum honeycomb core covered on both sides with carbon fiber facesheets that form a sandwich panel (Fig. 1). Large sized particles travelling at high velocities can completely penetrate the solar panel and leave a clearly measureable hole. During such events, the formed fragments may propagate through the honeycomb core, eventually impacting on the rear facesheet. An increase in impact velocity will result in a larger damage to the honeycomb core structure a shown in Fig. 4 [5].

Plasma and Arcing

The space-debris impacts on solar array cause not only mechanical damage but also electrical damage such as solar-array arcing initiated by local high-density plasma created by hypervelocity impact. The formation of plasma can lead to arcing between the solar cells or the cell and the substrate on the solar array. In the worst case, the heating produced by arcing can carbonize the insulation layer and create a permanent short-circuit path [6].

It was shown in an experiment at Kyushu Institute of Technology that when the debris collided with the solar cell directly, the solar cell circuitry almost immediately was shortened onto the substrate [7].

Connectors and Cables

Cables that are gathered together into bundles together with connectors that are used between panels on the solar arrays are the major current carriers. Impact damage to the cables and connectors would have, therefore, more severe consequences. There are two kinds of failure modes of cables after impact. Firstly, the electrical continuity of cable is broken, which means that some of the output power from the solar array is lost; secondly, sustained arc occurs between two nearby cables. The heat generated by the burning arc can melt the insulator skin of a nearby

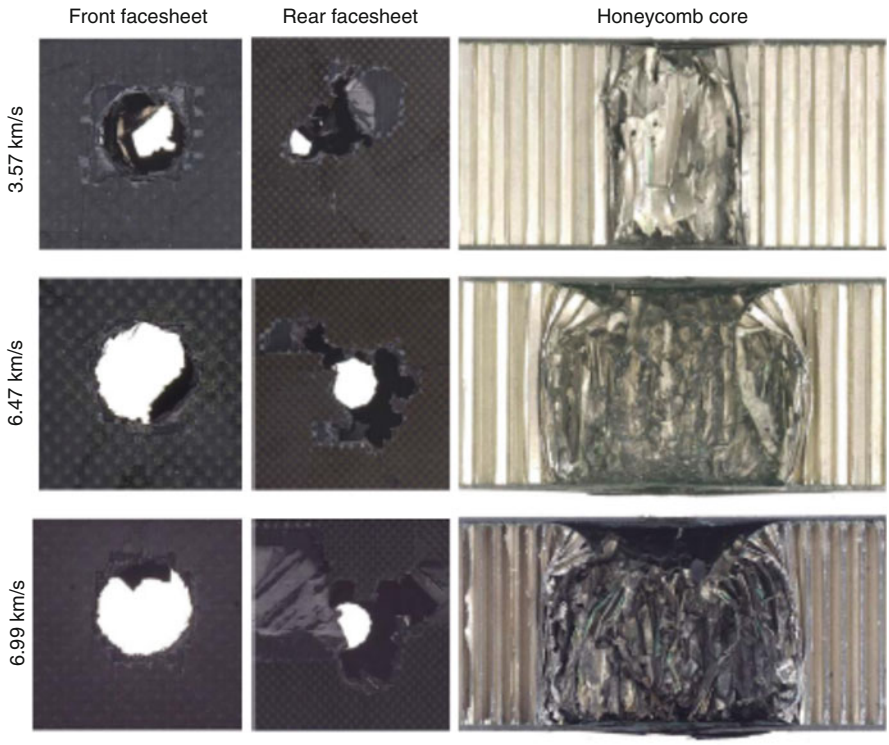

Fig. 4 Panel ground impact experiment photo (from RMIT University)

healthy cable, with the arc extending to another cable and so on, until the whole bundle can get affected (Figs. 5 and 6), causing a power loss from a whole solar array [8].

Impact Probability Between Solar Array and Particles

The probability of collision between meteoroids, space debris and a satellite solar array is proportional to the flux of meteoroids and space debris and also to the geometric projection area on cross flux direction of the solar array. The probability P of impact by a particle on a surface is given by

$$P = \int_{t}^{t+\Delta t} \mathrm{d}tF(t)A \tag{1}$$

where Δt is the duration of the exposure and $F(t)$ the normal component of the flux of particles [9].

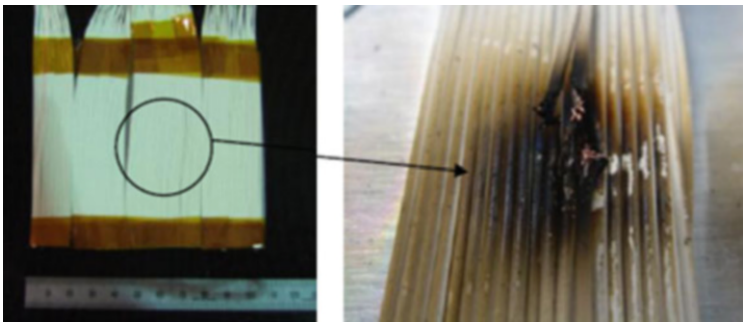

Fig. 5 A projectile impact onto a cable bundle triggers a short circuit in the cable

Fig. 6 Image of cable bundles destroyed by an impact

For one GEO satellite we talked earlier, the probability of its solar array impacted by space particles during its on orbit is studied. The meteoroids and debris flux for its orbit is obtained by using MASTER2005 flux models. Figure 7 shows the meteoroid and debris flux of this satellite orbit environment. For the particles with the diameter larger than 1 mm, the flux of meteoroid is 70 times as much as space debris; when they are larger than 5 mm, the flux of meteoroid will only be 9 times higher than space debris.

During the 8-year life in orbit, with a total area of 20 m^2 solar array, its probability hit by different size particles is shown in Fig. 8. As shown in the figure, the probability of the solar array hit by particles size <1 mm in diameter is highest, reaching 0.1.

With increasing particle size, the probability of collision between them and solar array will decrease rapidly. So in the design of solar array, it is more important to

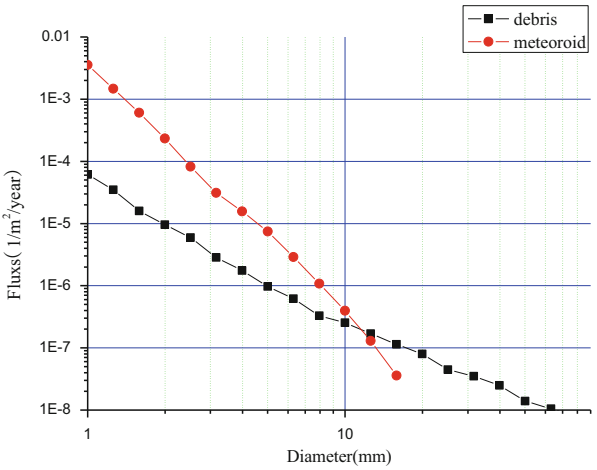

Fig. 7 Distribution of particles (by size) in the meteoroids and debris fluxes in orbit

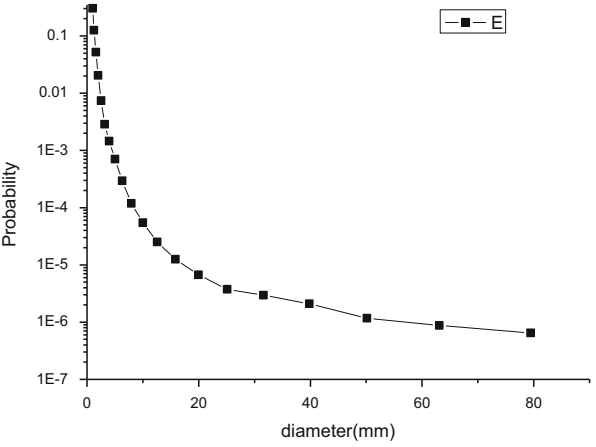

Fig. 8 Impact probability of a solar array by particles of different diameter

consider the impact effect from the small size particles than the larger one. The impact of small particles will cause mainly optical losses.

Summary

The risk of solar array from hypervelocity impacts should be considered for any spacecraft design. Common protective measures include additional shielding case or placing of sensitive component at safe and separate locations to reduce risk. For solar array, adding a proper extra area of solar cell for power degradation because of impact damage is the common solution. The cable and connector shall be carefully arranged and protect because of the severe consequence after impacting.

References

1. Lei Z (2010) Cumulative effects of micrometeoroid impacts on spacecraft. Master Thesis
2. Nahra HK (1989) Effect of micrometeoroid and space debris impacts on the space station freedom solar array surfaces. In: Spring meeting of the materials research society
3. Leach RD (1995) Spacecraft system failures and anomalies attributed to the natural space environment. In: AIAA space programs and technologies conference, Huntsville, AL, 26–28 September 1995. p 1812
4. Letin VA, Nadiradze AB (2005) Forecasting influence of solid microparticles on space craft solar array. In: Seventh European space power conference, Stresa, Italy, ESA SP-589, May
5. Ryan S (2008) Hypervelocity impact induced disturbances on composite sandwich panel spacecraft structures. Thesis of Doctor of Philosophy, RMIT University
6. Katz I (1998) Mechanism for spacecraft charging initiated destruction of solar arrays in GEO. In: Proceedings of AIAA 36th aerospace science meeting, Reno, NV, pp 98–1002
7. Harano T, Machida Y (2006) Preliminary study on sustained arc due to plasma excited by hypervelocity impact of space debris on the solar array coupon. Int J Impact Eng 33(1–12):326–334
8. Cho M (2005) Failure mechanisms and protection methods of spacecraft power system, vol 1. In: Electrical Insulating Materials (ISEIM 2005), pp 45–48
9. McNeil WJ (2002) Hazards of hypervelocity impacts on spacecraft. J Spacecr Rockets

Characteristic of Substrate Coloration Under Space Charged Particles

Hai Liu and Huicong Zhao

Abstract The radiation induced transmittance change of the lens with antireflection films of $MgF_2/ZrO_2/Al_2O_3$ on both surfaces was investigated under the 60–1000 keV electron and/or proton radiation on a space complex radiation simulator. The results show that the transmittance of lens is monotonously decreased with increasing radiation fluence. The major absorption band around 430 nm is caused by F_2 center, F^+ center and $V_{\bar{O}H}$ center in the antireflection films. The weak absorption band in 500–800 nm is related to the hole-type color center and the impurity-type color center under higher radiation fluence. Under the proton energy $<$100 keV, the radiation induced damage of antireflection films dominates the variation of transmittance, which is increased with increasing radiation energy. When the energy exceeds 100 keV, the energy loss in films is reduced and the substrate coloring becomes the main cause for the transmittance change. Under electron radiation, the change of transmittance increases with increasing energy while the energy loss in films dramatically decreases with increasing electron energy. In this case, the radiation induced effect on substrate is a dominant factor. The coloration of films also has certain contribution to transmittance change due to the scattering effect of electrons. In the near-Earth space, electron fluxes are higher than proton ones and the fluxes of low-energy charged particles are higher than high-energy charged particles. Therefore, for evaluation of radiation effects on the optical elements with films, the low-energy electron exposures are preferred, with the low-energy proton exposures being the second option.

Keywords Proton and electron radiation • Lens • Optical films • Spectral transmittance

H. Liu (✉) • H. Zhao
School of Materials Science and Engineering, Harbin Institute of Technology, Harbin 150001, People's Republic of China
e-mail: hitliuhai@163.com

J. Kleiman (ed.), *Protection of Materials and Structures from the Space Environment*, Astrophysics and Space Science Proceedings 47,
DOI 10.1007/978-3-319-19309-0_35

Introduction

The spacecrafts are irradiated by charged particles from Van Allen belt and cosmic ray during their flight [1]. According to the existing model for the radiation belt, the electrons energy is spread in 0.04–7 MeV interval while the protons energy ranges from 0.1 MeV to tens MeV and higher. The flux of these particles is decreased with increasing energy [2–4]. The irradiation by charged particles changes the structure and the properties of materials.

Optical systems that contain a series of optical elements are very often important payloads on spacecrafts. Optical transmission components such as lenses and filters have wide applications in optical systems. The light transmittance of an element is degraded after working in radiation environment for a period of time, thus, in many cases, affecting the functional performance of the whole system [5,6]. For these reasons much attention is paid worldwide to studies of radiation effects on optical materials and elements. Discoloration of optical materials caused by radiation induced color centers that absorb photons leading to decrease in the transmittance of certain wavelength is a major radiation effect on optical materials [7–10]. The radiation induced coloring effect on optical materials has been studied for decades. Although the classic theory of color centers is well developed, the mechanism for formation of complicated color centers is not clear from the present theory. Many types of compound centers with complicated structures are produced in complex material systems under higher radiation fluence. Their effect on optical properties needs further study.

For the transmission optical elements composed of a substrate and complex optical films, the type, evolution and distribution of their color centers are very complicated. The changes in optical properties of an element in such a structure are integrated into the overall change from all of its parts. Special glass can be selected as substrate to increase radiation resistance whereas the materials available for optical films are limited. In many cases, the damage to optical films is the dominant factor in degradation for optical element properties. The radiation induced damage of optical films not only depends on the species and energy of irradiation but also closely correlates with the structure of films [11, 12]. Presently, there is less detailed research in this area.

A lens with antireflective films was selected as the research subject in this work. The effects of particle type, their energy and fluence on the spectral transmittance of the selected lens were investigated through a series of irradiation tests with protons and/or electrons and the results are reported and the corresponding mechanisms discussed.

Experimental

A lens with both surfaces coated by antireflection film is chosen as the test sample. The substrate is a K208 type anti-radiation glass with a thickness of 3 mm. The substrate is coated using the PVD technique with a stack of antireflection films in the following sequence and thicknesses: 125 nm of Al_2O_3, 250 nm of ZrO_2, and 125 nm of MgF_2. The irradiation of the samples was conducted on three facilities, i.e., the space complex radiation simulator providing the 30–200 keV protons and/or electrons, with energies ranging from 0.5 to 1.2 MeV and the 0.5–4.5 MeV electrostatic proton accelerator. Spectral measurements were carried out on a Lambda950 type of spectrophotometer made by USA PE Company.

Results

Optical Spectra of Proton Irradiated Lens

The spectral transmittance data of the lens measured after 60 keV-proton irradiation tests under various energies and fluencies are shown in Fig. 1a. The change of spectral transmittance after proton radiation is also calculated as shown in Fig. 1b. It can be seen that the transmittance monotonously decreases in visible region. The maximum transmittance is obtained around 430 nm. The maximum moves slightly to the long-wave with increasing radiation fluence. The transmittance shows similar variation with energy but exhibiting different value of change. The obtained results indicate that proton irradiation has a significant effect on the lens.

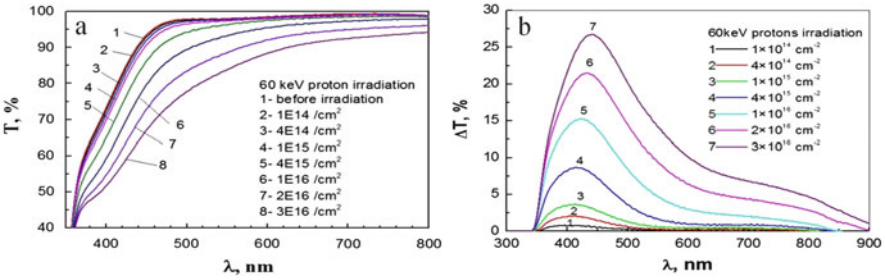

Fig. 1 Spectral transmittance of irradiated lens: (**a**) 60 keV proton radiation; (**b**) its change after radiation

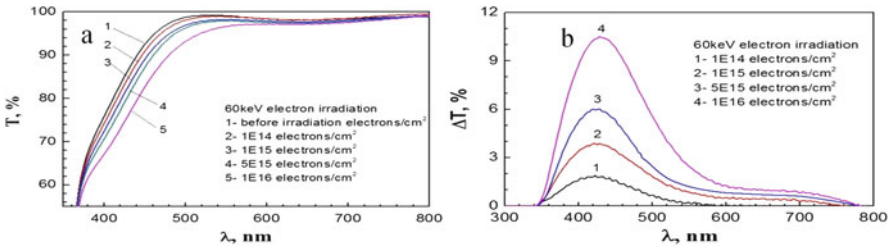

Fig. 2 Spectral transmittance of electron irradiated lens: (**a**) 60 keV electron irradiation; (**b**) transmittance change after radiation

Optical Spectra of Electron Irradiated Lens

Comparing the data from proton irradiation tests, the spectral transmittance after electron radiation shows similar behavior. The transmittance is also monotonously decreased with fluence within the wavelength of 350–800 nm, as shown in Fig. 2. Under the same energy and fluence, the electron induced changes of transmittance are relatively lower than those induced by protons.

Analysis of the Mechanism of Radiation Induced Damage in Optical Films

The color centers contributing to the absorption band of 350–500 nm are listed in Table 1 and are described in detail in ref. [9]. The weak absorption band of 500–800 nm is attributed to the hole-type color centers and the impurity-type color centers in films and substrate.

The wavelength where the optical spectrum possibly changes can be determined according to the data in Table 1. The change level depends on the color center concentration that is related to the absorbed dose of material. Figure 3 gives the calculated energy loss of protons dissipated in surface films. At lower energies, the protons lose their energy mainly in the surface layers, as shown in Fig. 3a. When the energy exceeds 100 keV, the energy loss in substrate is increased due to the increased shot range. Figure 3b gives detailed energy loss of protons in each of the three coatings. The energy loss is higher in ZrO_2 than in the other two films since ZrO_2 has a higher density and stopping power. The 80–200 keV protons have maximum energy loss in ZrO_2 film, as shown in Fig. 3b. The energy loss in MgF_2 and Al_2O_3 reaches a maximum at proton energies of 70 keV and 130 keV, respectively.

The above analysis implies that the energy losses in different films are not the same under single-energy proton irradiation, implying that the physical processes of proton interaction with the coated lens will be more complicated in interactions

Table 1 Main color centers and absorption band in films of lens

Material	Type of color center	Absorption band (nm)
MgF_2	F_2	370
ZrO_2	F^+	490
Al_2O_3	V_{OH} F_2^+	400 440–450

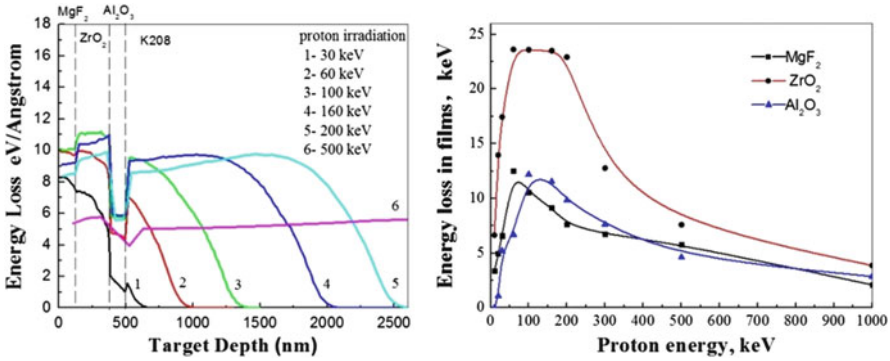

Fig. 3 Energy loss in lens as a function of penetrating depth and proton energy

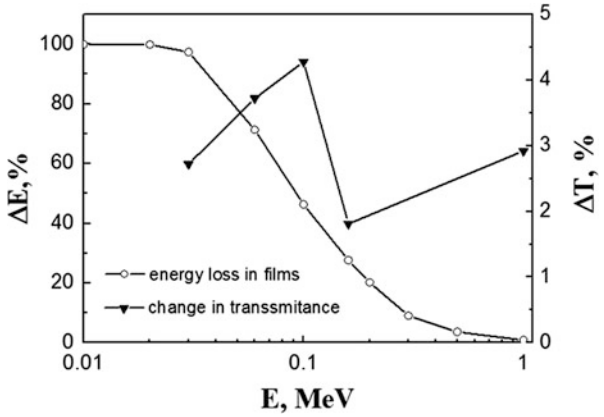

Fig. 4 Variation of energy losses in films and transmittance through lens versus proton energies

with the space charged particles having a broad energy distribution. Figure 4 gives the energy loss in films and the transmittance change through the lens versus the proton energy range under proton fluence of 1E15/cm^2. When proton energy is less than 30 keV, almost all of the energy loss occurs in films, affecting only the films. When proton energy exceeds 300 keV, it is deposited mainly in the substrate, having little effect on films. Within the proton energy range of 30–300 keV, the energy loss in films is monotonously decreased with increasing proton energy,

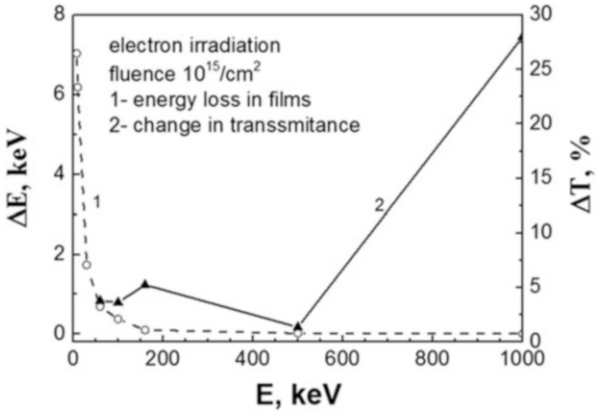

Fig. 5 Variation of energy loss in films and transmittance change under various electron energies

which complicates the spectral response of the lens. In the case of lower proton energy, although the proportion of energy loss in films is low, the total absorbed dose by films is increased with increasing proton energy resulting in increase of transmittance change.

When the proton energy is higher than 100 keV, the energy loss in films is reduced to below 40 %, leading to a distinct decrease of the absorbed dose by films and enhanced decrease in the transmittance. In this case, a part of proton's energy is delivered to the substrate. However, the shot range in anti-radiation substrate glass material is not enough to induce distinct coloring effects. Therefore, the 100–200 keV proton irradiation influences mainly the deposited films. Further increase in proton energy will thicken the colored layer in the substrate, resulting in transmittance decrease with increasing proton energy.

Due to the characteristic differences, the irradiation effects by electrons are different to those by protons. Firstly, the electron range is much higher than the thickness of the deposited optical films. If electron energy exceeds 10 keV, the energy loss mainly occurs in the substrate. Thus, the effect of electron irradiation should be taken into account. Secondly, electrons always lose a certain amount of energy in the films even having longer range due to their severe scattering in the target material.

Figure 5 shows the energy loss in films and the transmittance change of the lens versus the electron energy under electron radiation. It can be seen that the energy loss in films decreases dramatically with increasing electron energy whereas the transmittance change gradually increases with incident energy. This behavior implies that substrate coloration is a dominant process during electron irradiation. The analysis of absorption spectrum indicates that film coloration also has a certain contribution to spectral change which, however, is hard to quantify.

Above all, evaluating the anti-irradiation properties of a transmission element with deposited optical films, both the films and the substrate should be considered. The irradiation effect is related to many factors such as the type, the energy and the fluence of particles. Generally in the near-Earth space, electrons have higher fluxes than protons and low-energy particles have higher fluxes than high-energy particles.

Therefore, in ground testing, using low-energy electrons should be preferred to investigate the property of optical films under irradiation, and the low-energy protons should be used as the second choice.

Conclusions

1. The transmittance of lens is monotonously decreased with increasing fluence of protons or electrons in the ultraviolet and the visible bands. The major absorption band is located in the wavelength range 350–500 nm. A weak absorption band is found in the wavelength range 500–800 nm under high-fluence irradiation.
2. When the proton energy is <100 keV, the transmittance of the lens depends on the antireflection films. Substrate coloring becomes the dominate factor under proton energy higher than 100 keV.
3. Under certain radiation fluence, the transmittance change of the lens is increased with increasing electron energy. Substrate coloring is a major factor of electron radiation effect while the antireflection film structure has a certain effect on the transmittance changes.

References

1. Wu JG, Eliasson L, Lundstedt H, Hilgers A, Andersson L, Norberg O (2000) Space environment effects on geostationary spacecraft: analysis and prediction. Adv Space Res 26(1):31–36
2. Koshiishi H (2014) Space radiation environment in low Earth orbit during influences from solar and geomagnetic events in December 2006. Adv Space Res 53(2):233–236
3. Benton ER, Benton EV (2001) Space radiation dosimetry in low-Earth orbit and beyond. Nucl Instrum Methods Phys Res B 184:255–294
4. Koshiishin H, Matsumoto H (2013) Space radiation environment in low Earth orbit during solar-activity minimum period from 2006 through 2011. J Atmos Sol Terr Phys 99:129–133
5. Zhao X, Zhou Y, Liu H (2004) Research of space radiation design of optical system. J Harbin Inst Technol 03:406–409
6. Lu C, Zhao X, Zhou Y (2005) Analysis of the contamination affection on the space optical system. J Harbin Inst Technol 37(2):223
7. Piccinini M, Ambrosini F, Ampollini A, Carpanese M, Picardi L, Ronsivalle C, Bonfigli F, Libera S, Vincenti MA, Montereali RM (2014) Optical spectroscopy and imaging of colour centres in lithium fluoride crystals and thin films irradiated by 30 MeV proton beams. Nucl Instrum Methods Phys Res Sect B Beam Interac Mater Atoms 326:72–75
8. Kurobori T, Miyamoto Y, Maruyama Y, Yamamoto T, Sasaki T (2014) A comparative study of optical and radiative characteristics of X-ray-induced luminescent defects in Ag-doped glass and LiF thin films and their applications in 2-D imaging. Nucl Instrum Methods Phys Res Sect B Beam Interact Mater Atoms 326:76–80
9. Liu H, Liu G, Dong S, He S, Yang D (2011) Coloring effects of optical antireflective film irradiated by 60 keV protons. Thin Solid Films 519(15):5131–5134
10. Choi J, Heo J, Choi YG, Chung WJ (2012) Visible light emission from selenium color centers formed in silicate glasses. Opt Mater 34(7):1231–1234

11. Wei Q, Liu H, Wang D, Liu S-X (2011) Degradation in optical reflectance of Al film mirror induced by proton irradiation. Thin Solid Films 519(15):5046–5049
12. Di Sarcina I, Grilli ML, Menchini F, Piegari A, Scaglione S, Sytchkova A, Zola D (2014) Behavior of optical thin-film materials and coatings under proton and gamma irradiation. Appl Opt 53(4):314

Mass Loss of Spacecraft Polymeric Thermal Control Coatings Under Radiation

R.H. Khasanshin, A.V. Grigorevsky, and I.B. Vintaykin

Abstract Experimental results of influence of intensity and fluence of electrons, protons, and combined action of space environmental factors (vacuum, electrons, protons and electromagnetic radiation) on mass loss of a model polymeric composite are presented. Existence of threshold levels both for fluencies of electrons and protons at flux density of 10^{11} cm^{-2} s^{-1} and at flux densities of these particles corresponding to 10^{15} and 5×10^{14} cm^{-2} at fixed fluencies was established and a threshold level for combined action of protons and electrons was determined. It was shown that excess of threshold radiation modes makes a thermally stimulated mass loss of irradiated samples to reduce as compared with the source material.

Keywords Mass loss • Polymer composites • Thermal control coatings • Proton • Electron • Electromagnetic radiation • Combined irradiation

Introduction

An increase in spacecraft operational life imposes more severe requirements on reliability and quality to space environmental testing of materials. One of the factors able to disrupt the normal operation is the spacecraft outer atmosphere (SOA) that forms due to the mass loss of outer surface materials, gas leakage from internal compartments, emission from rocket fuel combustion products and other processes.

The most critical negative effect of SOA on existing and prospective satellites equipped with numerous high-sensitivity probes and scientific equipment is contamination of their surfaces by volatile products (VP) [1]. The severity of this problem is stipulated by widespread use of polymeric composites, for example, thermal control coatings (TCC), and by practical application of unpressurized

R.H. Khasanshin (✉) • A.V. Grigorevsky
JSC "Kompozit", 4 Pionerskay str., 141070 Korolev, Moscow, Russia
e-mail: rhkhas@mail.ru

I.B. Vintaykin
Bauman Moscow State Technical University, 5, 2-ay Baumanskay, Moscow, Russia

J. Kleiman (ed.), *Protection of Materials and Structures from the Space Environment*, Astrophysics and Space Science Proceedings 47,
DOI 10.1007/978-3-319-19309-0_36

modules in spacecraft design that create prerequisites for increasing SOA density and presence of high-molecular weight easily-condensable compounds in it.

Polymeric materials and based on them composites are used to create TCC's, structural components, vacuum-screen heat-insulations, sealants, adhesives, etc. It is known that absorbed doses of 10^5–10^6 Gy cause significant changes in their optical, mechanical, electro-physical and thermo-physical properties [2, 3].

To predict reliably the contamination levels of spacecraft functional surfaces we need physical–mathematical models describing processes of SOA formation, transfer in the vicinity of spacecraft and deposition of SOA products on sensitive surfaces. A whole range of problems exists, however, due to insufficient knowledge of the nature of such processes, among which we can name a few:

1. Lack of data concerning the influence of temperature and space radiation factors on mass loss of non-metallic materials and deposition of SOA products on spacecraft surfaces.
2. Lack of physical–mathematical models describing mass loss of polymeric composites that account for changes of their properties under radiation. Existing empirical models [2–4] have limited application and are mainly used to analyze results of laboratory experiments on mass loss of materials subjected to heat exposure in vacuum.
3. There are no data on dependence of mass loss rates of polymeric composites on energy, intensity and radiation type. There is no clear understanding on the synergistic effects of combined action of vacuum, temperature, UV, electron and proton radiations on these materials.

External coatings of geostationary orbit (GSO) satellites operating in space communications systems, radio- and television transmission are exposed to intense ionizing radiation. Estimated values of annual surface absorbed doses in this orbit are about 8.8×10^6 Gy [1]. The significant differences of dose distribution through thickness in various materials add to the difficulties in studying their mass loss. When carrying out radiation tests, electron and proton energies and flux densities are selected in such a way that distribution of total absorbed dose in material will approximately reproduce the space conditions.

Selecting the EKOM-1 paint, being applied as a spacecraft TCC, as the model polymeric composite, we show that dependence of properties of non-metallic materials on the absorbed dose and intensity of radiation should be taken into account to determine radiation induced mass loss. For this model material, the threshold values of flux density and fluencies of 40-keV electrons and protons were found and threshold level for the combined action (vacuum, EMR, protons and electrons) was defined.

Experimental Technique

Coupons, prepared from AMg6 aluminum alloy, 30 mm in diameter, were painted with the EKOM-1 paint. The EKOM-1 is a white enamel paint that is being used as thermal control coating with charge-dissipative properties. It consists of an acrylic copolymer with Ga-doped ZnO pigments. The weight of the samples was recorded before and after each experimental stage using the Shimadzu microbalance "AUW-220D" with an error of $\pm 10^{-5}$ g.

The effect of irradiation on mass loss of the model material was determined in two stages. In the first stage, the samples were irradiated in a vacuum chamber of the "UV-1/2" test facility. In the second stage, the dynamics of thermally induced mass loss of irradiated samples were evaluated using the "Vesy" radiation facility. Source material sample and witness samples were also tested in the same facility for comparison.

Beside the samples to be irradiated, witness samples protected from radiation were also fastened to the cooled sample stage of the UV-1/2 system. They were used to determine the mass loss by samples in vacuum chamber in the first stage.

To study the effect of space environment on mass loss of the model material, three series of irradiation tests have been carried out. All tests in these series had the following common conditions:

- Pressure in the chamber 1.0×10^{-4} Pa;
- Electron (E_e) and proton (E_p) energies were 40 keV.

In the first series, the samples were irradiated by different electron (Φ_e) and proton (Φ_p) fluencies with constant flux density of $\phi_e = \phi_p = 10^{11}$ cm^{-2} s^{-1}. The temperature of the sample holder to which the samples were attached with screws was 15 ± 1 °C.

In the second series, the samples were irradiated by different electron and proton flux densities to fluencies of $\Phi_e = 10^{15}$ cm^{-2} and $\Phi_p = 5 \times 10^{14}$ cm^{-2}, respectively. The temperature of the sample holder was kept at 15 ± 1 °C. Electron and proton fluencies were selected based on the results of the first series. Their values were not to exceed the threshold values of the fluencies found in the first series.

In the third series, the samples were irradiated using four different regimes given in Table 1. Solar electromagnetic radiation was defined by ESR and equivalent solar hours (ESH). In combined action, the flux densities of electrons and protons did not exceed the critical values established in the second series. Temperature of the sample holder for 1 ESR and 2 ESR was maintained at 30 ± 1 °C and 45 ± 1 °C respectively.

In the second stage, we obtained the dependencies of thermally induced mass loss on time, i.e., the kinetics (or dynamics) of mass loss. The mass changes were monitored on a microbalance using a 10.0-MHz temperature-controlled quartz piezoelectric resonator. In our experiments, the change of mass took place due to condensation of VP emitted by material sample.

Table 1 Summary of space environmental conditions in combined irradiation experiments

Level # of space environment conditions	$\phi_e \times 10^{-11}$, $cm^{-2}s^{-1}$	$\phi_p \times 10^{-10}$, $cm^{-2}s^{-1}$	$\Phi_e \times 10^{-15}$, cm^{-2}	$\Phi_p \times 10^{-14}$, cm^{-2}	Solar electromagnetic radiation	
					ESR	ESH
1	0	0	0	0	0	0
2	1.00	5.01	1.00	5.05	1 (2)	2.3 (5.6)
3	1.02	5.04	2.04	10.08	1 (2)	5.6 (11.2)
4	1.03	5.02	5.15	25.10	1 (2)	14 (28)
5	1.01	5.03	10.10	50.3	1 (2)	28 (56)

A sample of a material with an attached to it temperature sensor was placed on the heated sample holder of the "Vesy" facility and, while testing the calibration of measurement devices, it was kept for one hour in vacuum at 15 ± 1 °C. Then, the sample was heated up to 100 °C and the mass loss dynamics were recorded during a 24 h period (standard test period for determining the mass loss parameters of a heated material in vacuum conditions). The changes of the output frequencies of the microbalances were recorded every minute in the first 4 h, and every 20 min after that.

The thermally induced mass losses were measured in the following conditions:

- Vacuum 2×10^{-5} Pa;
- Material sample temperature 100 ± 1 °C;
- Temperature of piezoelectric resonator -187 ± 0.5 °C;
- Mass sensitivity of piezoelectric resonator 5×10^{-9} g/(cm^2 Hz).

The experimental set-up and the geometry between the sensitive element of microbalance and the sample was the same in all experiments.

Analysis of Results

To conduct a numerical analysis of obtained experimental data, a mathematical model was used that allows reducing the solution of the problem of mass loss of polymeric materials under irradiation in vacuum to a solution of a system of equations describing changes of VP concentrations in it, as follows:

$$\frac{\partial C_i(x,t)}{\partial t} = \frac{\partial}{\partial x}\left(D_i(x,t)\frac{\partial C_i(x,t)}{\partial x}\right) - \chi_i C_i(x,t) + S_i(x),$$

$$x \in (0, h - \upsilon \cdot t) \ , \quad t > 0, \qquad \upsilon \cdot t < h, \tag{1}$$

$$C_i(x,t)|_{t=0} = R_i(x), \qquad x \in [0,h], \tag{2}$$

$$D_i(x,t)\frac{\partial C_i(x,t)}{\partial x}\bigg|_{x=h-\upsilon\cdot t} + [k_i(t) + \upsilon]C_i(x,t)|_{x=h-\upsilon\cdot t}, \quad t > 0, \tag{3}$$

$$\frac{\partial C_i(x,t)}{\partial x}\bigg|_{x=0} = 0, \quad t > 0, \tag{4}$$

where $C_i(x,t)$—concentration of i-type VP in material; χ_i—chemical reaction rate with involvement of i-type VP, s^{-1}; $D_i(x,t)$—effective diffusion coefficient of i-type VP, μm^2/s; $R_i(x)$—concentration of i-type VP in material at the initial moment; $k_i(t)$—effective desorption coefficient of i-type VP, μm s^{-1}; h—thickness of sample, μm; υ—sublimation rate of material, μm/s; $S_i(x)$—a function of i-type VP source, dependent on type of material, spectrum, content and intensity of radiation. The shape of the source function, $S_i(x)$, repeats the distribution of absorbed energy.

The non-uniformity of propagation of the irradiation through the material thickness was taken into account by introducing a diffusion coefficient that increases with time $D_i(x,t) = D_{i0}[1 + \alpha(x)t]$, where $\alpha(x) \geq 0$—weight function proportional to $S_i(x)$; D_{i0}—effective diffusion coefficient of VP in source material.

The solution of Eqs. (1)–(4) has values that are functions of i-type VP concentration in the near-surface layer of material $C_i(h - \upsilon \cdot t, t)$. They are used to determine the mass loss rate from a unit surface:

$$\dot{M}_i(t) = m_i(k_i + \upsilon)C_i(h - \upsilon t, t), \tag{5}$$

where m_i—is the mass of i-type molecule.

Total mass loss from the unit surface of material M(t) for the time interval t can be calculated from the expression:

$$M(t) = \sum_{i=1}^{N} M_i(t) = \sum_{i=1}^{N} m_i \int_0^t \left(k_i + \upsilon\right) C_i(h - \upsilon\tau, \tau)d\tau. \tag{6}$$

Numerical calculations qualitatively reproducing the above-cited experiments were also made in two stages. The first one was concerned solving Eqs. (1)–(4) that describes VP concentration change in material under radiation. It had been considered that before irradiation VP's in material were distributed uniformly.

The same question was solved at the second step for thermal vacuum action when $S_i(x) = 0$ and $\upsilon = 0$. Distribution of diffusion coefficient and initial concentration were determined as $D(x,T) = D_0[1 + \alpha(x)T]$ and $R_i(x) = C_i(x,T)$ respectively where $C_i(x,T)$—is the VP distribution in the sample by the end of irradiation, T—is the irradiation time.

The non-linear regression analysis methods were used in processing data obtained at the second stage of experiment to determine accurately mathematical model parameters in Eqs. (1)–(6) [5].

Figure 1 shows some of the results from the first series of experiments in which the dependencies of thermally stimulated mass losses of model samples on fluencies of constant fluxes of 40-keV electrons and protons.

As can be seen from Fig. 1, both dependencies of mass loss of irradiated samples on fluencies of electrons and protons have pronounced peaks. They can be explained by the fact that irradiation triggers in material such simultaneous competitive processes like accumulation of radiolysis products, chemical reactions with these products and emission from material in vacuum of the VP's that were in it before irradiation and/or were generated under irradiation. The radiation-induced destruction and outgassing of the material increase its permeability that goes up together with the absorbed dose and accelerates the migration processes in material. Therefore, irradiation with fixed flux density increases mass loss rate of a sample and duration of the process in vacuum in line with fluence.

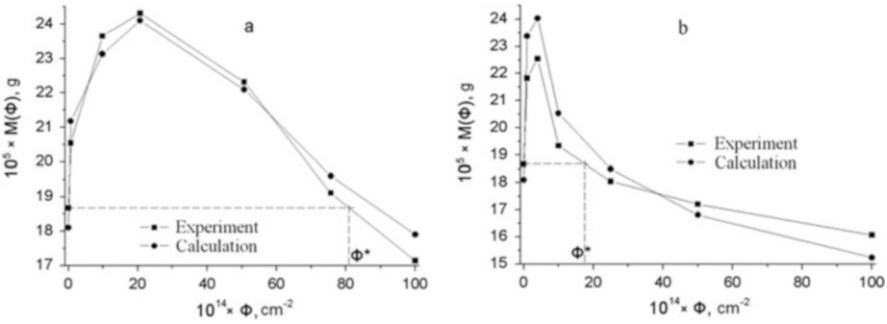

Fig. 1 Dependence of mass loss of irradiated samples on fluence of (**a**) electrons; (**b**) protons

Thus, the rate of VP generation in material sample exceeds the rate of their emission in vacuum if fluencies are below a threshold value Φ_e^*. Therefore, thermally stimulated mass loss of these samples is larger than the mass loss of the source material at the second stage of experiment. If the fluence exceeds Φ_e^*, the amount of VP being generated in the material does not compensate their loss due to chemical reactions and emission in vacuum. The following thermally stimulated mass loss of this sample is lower than that of the source sample.

Maximum penetration of 40-keV protons and electrons in model material are $R_\mathrm{p} \approx 0.8$ μm and $R_\mathrm{e} \approx 17$ μm. Consequently, under proton irradiation, their energy is released in a thin near-surface layer of the material and in that region the radiolysis takes place. Rates of formation of radiolysis products and increase of permeability of material are proportional to absorbed dose rate. Therefore, the threshold value for protons $\Phi_p^* \approx 1.7 \times 10^{15}$ cm^{-2} is less than that for electrons $\Phi_e^* \approx 8.2 \times 10^{15}$ cm^{-2}.

The weight results from samples before and after the first stage in all three series of experiments had shown that mass loss of each irradiated sample is greater than that of the witness sample. For example, these values differ by 1.4×10^{-4} and 3.6×10^{-4} g in the case of electrons with fluencies of 5×10^{15} cm^{-2} and 10^{16} cm^{-2}, respectively.

As an example, Fig. 2 shows the influence of the intensity of irradiation with fluence of electrons 10^{15} cm^{-2} on the dynamics of thermally induced mass loss of model samples.

With increasing, to a certain value, of electron flux density, the function $M(\varphi)$ is growing and, after reaching a maximum, is decreasing. When $\phi_e > \phi_e^* \approx 2.1 \times 10^{12}$ cm^{-2} s^{-1}, the mass loss of irradiated samples becomes smaller than that for source material samples. An analysis of the data in Fig. 3 that presents the dependence of mass loss of irradiated samples on radiation intensity of protons and electrons shows that in the case of proton irradiation, the threshold value of flux density is almost an order of magnitude smaller than for electron irradiation and is equal to $\phi_p^* \approx 2.6 \times 10^{11}$ cm^{-2} s^{-1}.

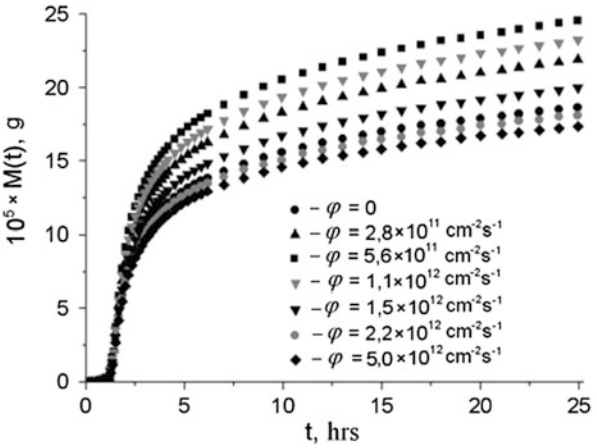

Fig. 2 The effect of flux density on mass loss of samples irradiated by electrons

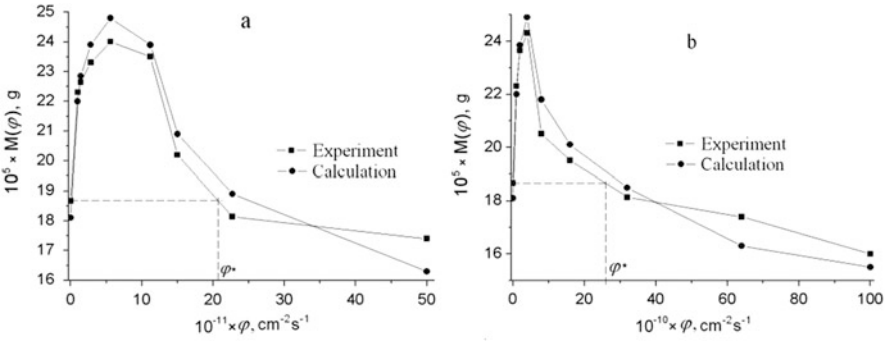

Fig. 3 Dependence of mass loss of irradiated samples on radiation intensity: (**a**) electrons; (**b**) protons

Figure 4 shows dependencies of thermally induced mass loss of model sample and samples irradiated in different space environmental conditions (see Table 1).

With an increase in the level of environmental impact, the dependence of mass loss of the samples on energy flux has the same character as in the scenario of irradiation by electrons and protons separately. With the intensity of irradiation at 2 ESR (see Fig. 4b) the mass losses for the irradiated samples after the first (2) and second (3) levels of environmental impact (as per Table 1) were greater, while after the third (4) and fourth (5) levels, they were lower than in a non-irradiated sample. With the intensity of irradiation at 1 ESR (see Fig. 4a), the mass loss was less than in the non-irradiated sample only after the fourth level of environmental conditions. The obtained results can be explained assuming that an increase in environmental impact level does not only lead to a growth in total absorbed energy in the material,

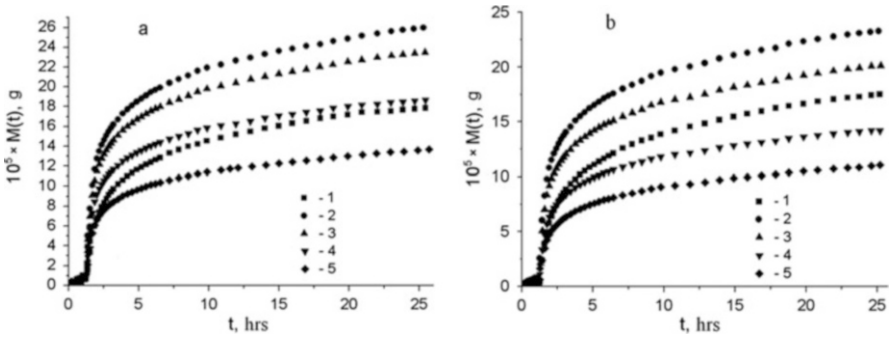

Fig. 4 Dynamics of mass loss of model samples (marked in the legends as—**1**), and samples exposed to different levels of space environment (marked in the legends as **2–5**): (**a**) 1 ESR; (**b**) 2 ESR

but also to a change in the penetration depth, allowing VP's to leave the material into the vacuum from deeper layers.

It should be noted that electron and proton fluencies were below the threshold values (Φ_e^* and Φ_p^*) obtained in the first series of experiments where influence of separate ionizing radiations on sample mass loss was investigated for all levels of combined action. Hence, the EMR was strong enough to cause the photolysis and to increase the sample temperature thus emitting existing VP's in addition to generated by combined radiation from material.

Conclusions

Based on the analysis of the experimental data and the results of computer modeling, threshold values for the fluencies and flux densities of electrons and protons were determined. If exceeded, a reduction of thermally induced mass loss of irradiated samples is observed in comparison with the source material. The threshold values depend on radiation type and energy.

The following threshold values were obtained for EKOM-1:

- Fluencies of 40-keV electrons and protons $\Phi_e^* \approx 8.2 \times 10^{15}$ cm^{-2} and $\Phi_p^* \approx 1.7 \times 10^{15}$ cm^{-2}, respectively at flux density of 10^{11} cm^{-2} s^{-1};
- Electron and proton flux densities $\phi_e^* \approx 2.1 \times 10^{12}$ cm^{-2} s^{-1} and $\phi_p^* \approx 2.6 \times 10^{11}$ cm^{-2} s^{-1} for fluencies 10^{15} cm^{-2} and 5×10^{14} cm^{-2}, respectively;

The similar threshold values have also been observed in testing of other polymer composites. The existence of such threshold parameters must be taken into consideration when selecting test modes of polymer composite materials to avoid making false conclusions regarding the impact of space environment on mass loss of material.

References

1. Model of space environment (2007) Scientific information publication. In: Vernov (ed) Influence of space medium on spacecraft materials and hardware, vol 2. KDU, p 1144
2. Milinchuk VK, Klinshpon ER, Tupikov VI (1994) Principle of radiation stability of organic materials. Energoatomizdat, p 256
3. Faye D (2000) Calculation approach for outgassing curves of PU1 paint and molecular contamination modeling: ground testing and computer simulation. In: 8th international symposium on materials in a space environment, Arcachon, France
4. Guillin J (1985) Evaluation of isothermal outgassing kinetics for some materials used in space. In: Proceedings of the third European symposium on spacecraft materials in space environment, ESA SP-232, The Netherlands. pp 35–38, October
5. Pomerantsev AL, Krotov AS, Radionova AE (2001) Computer system Fitter for regression analysis of experimental data, study guide. P.H. AGU, Barnaul

Numerical Simulations of Spacecraft Wake Charging

Cheng-xuan Zhao, De-tian Li, Sheng-sheng Yang, Xiao-gang Qin, Jun Wang, Yi-feng Chen, Dao-tan Tang, and Liang Shi

Abstract The outer region of the Earth's ionosphere, where the earth's magnetic field controls the motion of charged particles is called magnetosphere. Generally, the plasma properties in the magnetosphere are described by particle density and energy temperature. The plasma properties in the magnetosphere region are affected significantly by changes in latitude and altitude. The plasma environment in the orbits such as Low Earth Orbit (LEO) and Polar Earth Orbit (PEO) is characterized by high density (10^{10}–10^{12} m^{-3}) and low energy temperature (0.1–0.3 eV), because of the high energy auroral electron (1–10 keV) injection that leads to spacecraft wake charging effects.

A wake area where electrons and ions currents are different will be formed behind a spacecraft in LEO cold, dense plasma environment. The electrons, due to high spacecraft velocity, could accumulate in the wake area of spacecraft to form a high negative potential barrier. The wake effect will develop differential charging on the surface of a spacecraft. The surface potential mainly depends on the collection of the electrons and ion fluxes. Surface charging formed by the wake effect affects the safe operation of the low and middle orbit, especially polar orbit, satellites. In this paper the physical mechanism of wake charging effect is analyzed, Three-dimensional spacecraft computing model based on Particle In Cell (PIC) methods is established by using of Fontheim distribution model of hot electrons and taking account of the effects of the secondary electrons and photoelectrons. The wake charging potential distribution and its variation in time are also discussed.

Keywords Wake charging • PIC (particle in cell) • Numerical simulations

C.-x. Zhao (✉) • D.-t. Li • S.-s. Yang • X.-g. Qin • J. Wang • Y.-f. Chen • D.-t. Tang • L. Shi
Science and Technology on Vacuum and Cryogenics Technology and Physics Laboratory, Lanzhou Institute of Physics, 97 Weiyuan Road., Lanzhou, China
e-mail: zhaocx2000@sina.com

J. Kleiman (ed.), *Protection of Materials and Structures from the Space Environment*, Astrophysics and Space Science Proceedings 47,
DOI 10.1007/978-3-319-19309-0_37

Introduction

Spacecraft–plasma interaction and the charging problems associated with it has been an attractive field of research since 1970s [1, 2]. Generally, spacecraft charging is usually associated with high energy electrons in the magnetosphere causing formation of high potentials on geosynchronous satellites. Spacecraft charging at low altitudes is not regarded as a problem, because typical ambient electron has a temperature of 0.1 eV, so that the charging potential of a spacecraft in the ionosphere is about the same temperature order. However, the high energy (1–10 keV) auroral electron injection in polar Earth orbit (PEO) environment will lead to spacecraft wake charging effects. And, in fact, spacecraft charging has been frequently observed on low-altitude, polar-orbiting spacecraft. The data from the Defense Meteorological Satellite Program (DMSP) have shown that charging in the auroral oval occurs hundreds of times per year [3].

The particle-in-cell (PIC) method has become in the last few decades an efficient numerical computational tool to study the complicated behavior of plasmas, as well as plasmas in space [4, 5]. It provides a kinetic description of the plasma by following the trajectories of charged macroparticles in self-consistent electromagnetic fields computed on meshing [6]. When spacecraft interacts with the PEO plasma, the electrons and ions will move to and deposit on the surface of the spacecraft and will result in electrostatic potential on the surface. The electrons could accumulate in the wake area of spacecraft to form a high negative potential barrier. The wake effect will develop a differential charging on the surface of a spacecraft.

So far, several spacecraft charging three-dimensional modeling tools have been developed and incorporated, which can be used for spacecraft wake charging simulation, such as POLAR software of NASA, SPIS of ESA and Japan's MUSCAT, and the simulation results of the tools are consistent with data of space monitoring according to the published data.

Model of Spacecraft–Plasma Interaction

Spacecraft charging problem at low polar orbit is commonly represented by a moving large scale spacecraft immersed in dense and cool ionosphere plasma as well as in hot auroral electrons. The effects of secondary electrons and photoelectrons should be taken account in the numerical simulations as well. In order to simply the problem, it is assumed that the plasma is in thermal equilibrium and the geomagnetic field is neglected in PEO environment. In order to investigate the potential or the electric field of the disturbed plasma around the spacecraft it is necessary to solve the coupling Poisson and Vlasov equations as follows:

$$\begin{cases} \nabla^2 \varphi = -\dfrac{\rho}{\varepsilon_0} = \dfrac{e}{\varepsilon_0}\left(n_i - n_e + n_{se} + n_{pe}\right) \\ \boldsymbol{v} \cdot \nabla f + \boldsymbol{a} \cdot \nabla_v f = 0 \end{cases} \tag{1}$$

where f is the particle distribution function, ν is the velocity, a is the acceleration, n_i, n_e, n_{se} and n_{pe} are the number densities of the ions, electrons, secondary electrons and photoelectrons. Because of the difficulty of obtaining the analytic solution for the above Eq. (1), we can simulate the charging process by using the classic motion equation of macroparticles based on PIC method.

Spacecraft Structure Modeling

The first step in developing the polar orbit simulation is to build a model of a spacecraft with a large scale paraboloid antenna and a solar array attached to it. The main body of the spacecraft is modeled as a cube with a rib length of 1 m. The length, width and thickness of the solar array are 3 m by 1 m by 0.1 m, respectively. The radius of the paraboloid antenna is 3 m, and the thickness is 0.1 m. The simulated surrounding plasma area is a sphere with a radius of 8 m, as shown in Fig. 1. The set of surface materials on the spacecraft is selected as follows: the main body of the spacecraft and ion-ram side of paraboloid antenna are coated with ITO, the back surfaces of the solar array and the back of paraboloid antenna are covered with dielectric material Kapton, which is usually more conductive under space

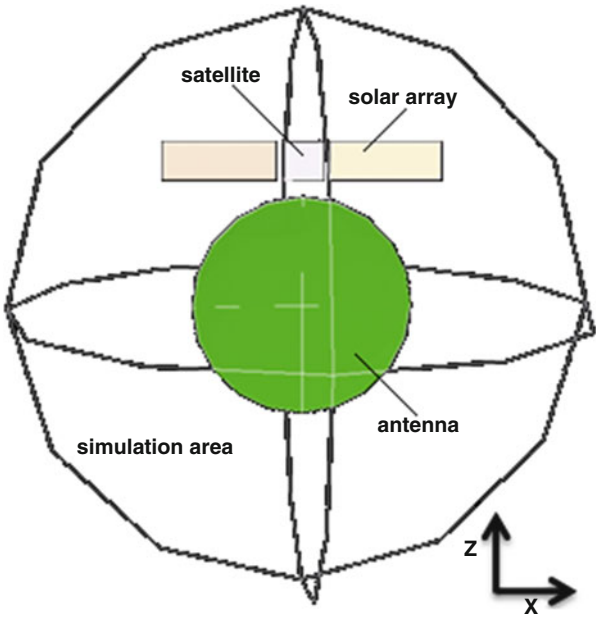

Fig. 1 Modeling of the spacecraft and the ambient plasma region

Table 1 Properties of the selected spacecraft surface materials

Material (Ω)	Thickness (m)	Relative permittivity	Surface resistivity
ITO	1.0×10^{-5}	1.0	~0
CERS	1.0×10^{-5}	3.8	1.0×10^{15}
Kapton	2.5×10^{-5}	3.0	1.0×10^{15}

irradiation. The sunlit surface of the solar array is CERS (Cerium doped silicon with MgF2 coating). The initial and boundary conditions are selected such that the spacecraft moves in the Y direction and the initial potential of the spacecraft is zero volts. The sunlight comes from the Z axis direction. The surface properties of the selected materials are listed in Table 1.

Auroral Electron Environment Fitting

Unlike geosynchronous environment, polar orbit spacecraft will fly through a region of background plasma of high density (10^9 m^{-3}) and low energy (0.1 eV) that is described by a Maxwellian distribution. Besides the background plasma, it is very important to fit the real auroral electron spectra due to the important role it played in the process of spacecraft wake charging. An auroral electron spectra observed by the DMSP F13 satellite has been given by Cooke [7] and is shown in Fig. 2 where it is also fitted with the Fontheim distribution function.

The high auroral electron environment is described in our simulation by a Fontheim distribution [8] that has three components, specified by the net current in each component. The Maxwellian component describes the low and high energy flux plasma environment, the Gaussian component describes the electrons flux intensified by aurora, and the Power Law component describes the secondary and backscattered electrons from interactions between the Gaussian beam and the rest of the plasma. The electron differential flux formation of Fontheim distribution function is as follows:

$$Flux(E) = \sqrt{\frac{e}{2\pi m_e}} n \frac{E}{\theta^{\frac{3}{2}}} e^{-\frac{E}{\theta}} + A_G E e^{-\left(\frac{E-E_0}{\Delta}\right)^2} + A_p E^{-\alpha},\ E_{PL} < E < E_{PH} \qquad (2)$$

where, in most circumstances, the parameters are set as follows:

$$\begin{aligned} &A_p = 3 \cdot 10^{11} m^{-3},\ \alpha = 1.1,\ E_{PL} = 50\,eV,\ E_{PH} = 1.6 \cdot 10^6 eV, \\ &n = 6 \cdot 10^5 m^{-3},\ \theta = 8\,keV, A_G = 4 \cdot 10^4 m^{-3}, \\ &E_0 = 24\,keV,\ \Delta = 16\,keV \end{aligned}$$

The logarithm of Fontheim distribution is shown in Fig. 3.

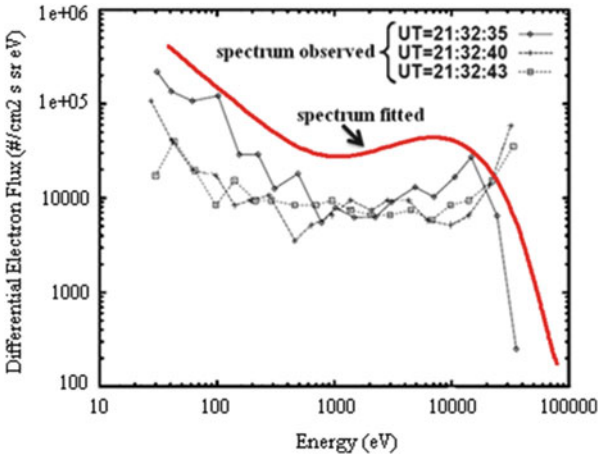

Fig. 2 The Fontheim fit electron spectrum compared with the spectrum observed by DMSP [7]

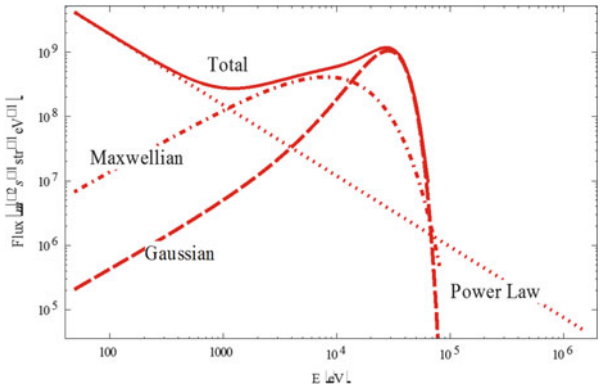

Fig. 3 The Fontheim electron spectrum logarithm distribution

Calculation of Ram Ions and Secondary Electrons

The dense ram ions should be considered in the spacecraft wake charging, and their moving direction relative to the spacecraft must be taken into account in initial conditions. Suppose the spacecraft in the simulation area is resting, and the ions are impacting on the surface of the spacecraft at a velocity of the spacecraft's orbital speed. In the simulation, we think that there will be ions injection at certain energy at the boundary of the simulation area every time step, as shown in Fig. 4. The ions spectrum is shown in Fig. 5.

The surface emission of secondary electrons comes from both ion impact and electron impact. The secondary yields vary with different materials, which is difficult to predict. The emission efficiencies depend on the energy of the impacting particles. To calculate the contribution of the secondary electrons, one must determine the secondary yield as a function of energy, with the incident electron energy typically peaking between 100 and 1000 eV. The spectrum of secondary electrons

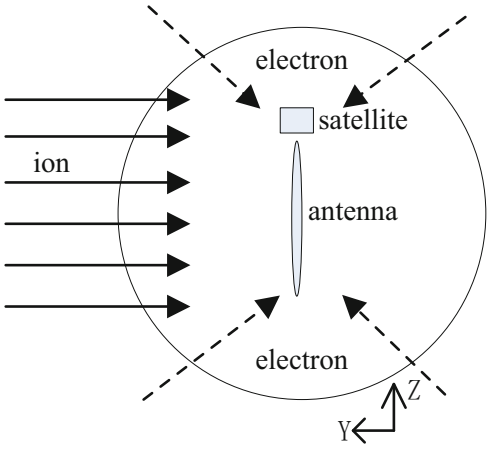

Fig. 4 Illustration of the geometry between the ram ions and the moving spacecraft

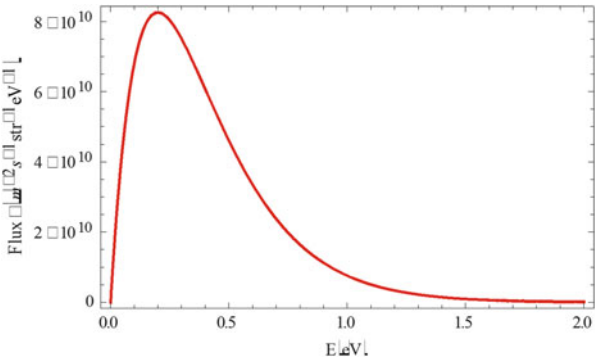

Fig. 5 Spectral energy distribution of the ram ions spectra

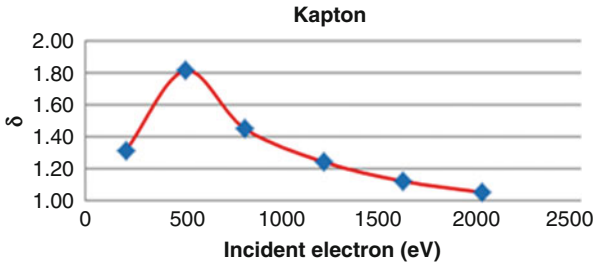

Fig. 6 Yield energy of the secondary electrons in Kapton as a function of incident electron energy

typically has a characteristic energy of 2 eV. Figure 6 shows the yield energy of the secondary electrons as a function of incident electron energy for Kapton. As for the photoelectrons, their initial current can be set to 10^{-5}A m^{-2}, and their characteristic energy to 2 eV.

Results and Discussion

As was described above, the direction of plasma flow is from +y to −y at a velocity of 7000 m/s. When the net current through the surface of the spacecraft equals zero, the sum of all currents coming in equals to the sum of all currents going out, which means that the spacecraft comes to a charging equilibrium. Figure 7 shows the charging potential distribution in Kapton in the wake side of the spacecraft. As can be seen from Fig. 7, the dielectric material Kapton at the back of paraboloid antenna has been charged to −811 V, and in the wake zone the potential varies sharply due to the absence of the ion neutralizing process. The surface potential of Kapton versus time is shown in Fig. 8 that presents data from 100 data points. When charging equilibrium is reached, the surface potential of Kapton is −811 V. While the total simulation time was 4 s, as can be seen from Fig. 7, the surface potential after t = 0.3 s stabilized around −811 V. Compared to the typical charging equilibrium times of tens of minutes, the charging time in PEO environment is very short, implying that charging mitigation measures must be taken when designing the spacecraft for PEO operations.

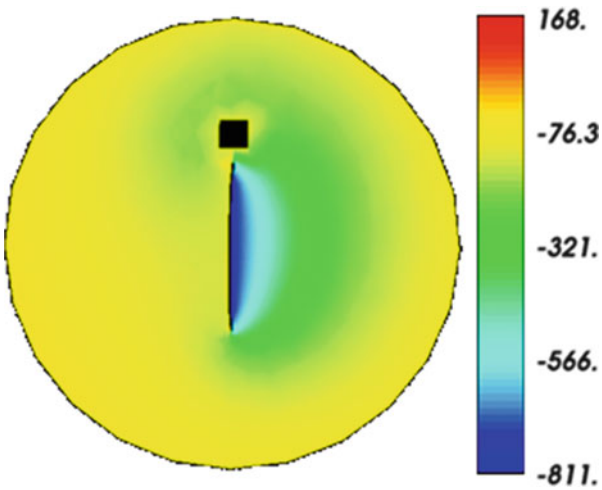

Fig. 7 Charging potential distribution of the Kapton on the back of the antenna (in the wake side)

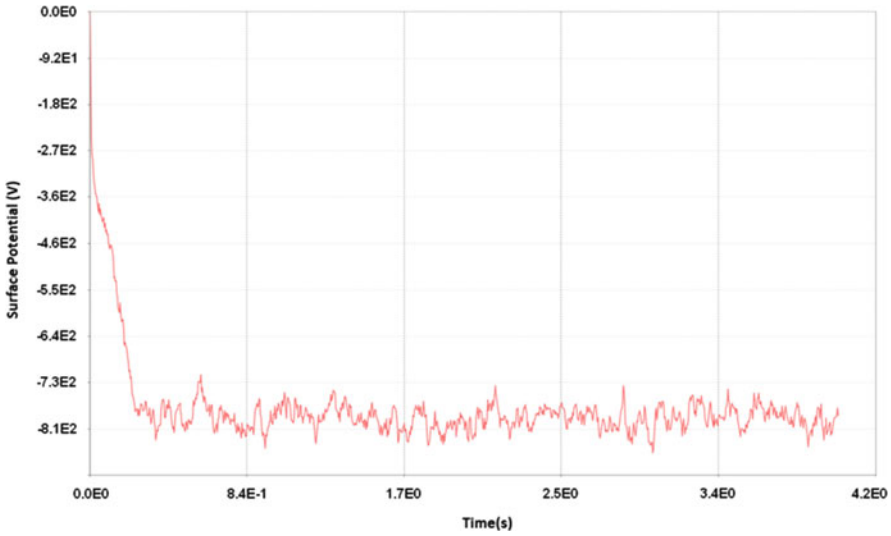

Fig. 8 Surface potential variation of Kapton with time in wake of the spacecraft

Conclusions

In conclusion, the wake charging effects of spacecraft in PEO environment were studied using the PIC method in this work. Three-dimensional spacecraft computing model was established by using of Fontheim distribution model of hot electrons and taking into account the effects of the secondary electrons and photoelectrons. It is shown that a zone exhibiting severe charging exists in the wake of a large scale antenna under the auroral-electron condition. The potential of the dielectric material Kapton in the wake side can reach −811 V in polar auroral plasma environment and the time scale to reach charging equilibrium can be as short as 0.3 s.

Some payloads such as electric field or plasma density detecting instruments must be placed out of the near wake charging zone due to avoid the strongly changing potential gradients. Wake charging may have significant implications for polar satellites such as some meteorological satellites and earth observation satellites.

References

1. Garrett HB, Whittlesey AC (2000) Spacecraft charging, an update. IEEE Trans Plasma Phys 28 (6):2017–2028
2. Garrett HB (1981) The charging of spacecraft surfaces. Rev Geophys Space Phys 19 (4):577–616

3. Cooke DL, Adrian T et al (2009) Simulation of auroral charging in the DMSP environment. In: 47the AIAA aerospace sciences meeting including the new horizons forum and aerospace exposition, Orlando, Florida, 5–8 January 2009
4. Forest J, Eliasson L, Hilgers A et al (2001) A new spacecraft plasma interactions simulation software, PICUP3D/SPIS. In: 7th proceedings of the spacecraft charging technology conference
5. Wang J, Leung P et al (1994) Multibody-plasma interactions charging in the wake. J Spacecr Rockets 31(5):889–894, September–October
6. Birdsall CK, Landon AB (1991) Plasma physics via computer simulation. Institute of Physics Publishing, London
7. Cooke DL (2000) Simulation of an auroral charging anomaly on the DMSP satellite. In: 6th spacecraft charging technology conference, AFRL-VS-TR-20001578, 1 September
8. Fontheim EG, Stasiewicz K, Chandler MO et al (1982) Statistical study of precipitating electrons. JGR 87:3469

Synergistic Effects of LEO Space Environment and Their Influence on Space Station

Zicai Shen and Dekui Yan

Abstract Space station, during its projected extended stay in LEO, will encounter many environmental factors including energetic particles, ultraviolet radiation, atomic oxygen, and space debris and meteoroids, together with some induced environments such as contamination and discharging. Firstly, the synergistic effects of the above environments on space station are briefed in pairs. Then the synergistic effects from extravehicular space environments are studied one by one, including the interactions between energetic particles and solar electromagnetic irradiation, between atomic oxygen and ultraviolet radiation, between space debris and atomic oxygen, as well as the contamination induced by space factors and discharging. Thirdly, the synergistic effects inside the space station between microbes, temperature, humidity and gas circulation, micro vibration, residual radiation, space radiation and microgravity and so on are analyzed. Lastly, some recommendations and countermeasures against synergistic effects are proposed for improving the mechanism's analysis, the simulation studies, the test methods, the forecasting techniques and the protection of space station.

Keywords Space environment • Synergistic effects • Space station • Manned spacecraft • Countermeasures

Introduction

Space station, that usually is orbiting the Earth at an altitude of about 300–500 km will encounter many LEO environmental factors such as energetic particles, ultraviolet radiation, atomic oxygen, meteoroids and space debris, and some induced environments such as contamination [1, 2], as illustrated in Fig. 1. In addition, there

Zicai Shen (1980) Doctor, major in space radiation environment engineering and deep space exploration. Project supported by National Natural Science Foundation of China (Grant No. 41174166).

Z. Shen (✉) • D. Yan
Beijing Institute of Spacecraft Environment Engineering, Beijing 100094, China
e-mail: zicaishen@163.com; kuikui@139.com

J. Kleiman (ed.), *Protection of Materials and Structures from the Space Environment*, Astrophysics and Space Science Proceedings 47,
DOI 10.1007/978-3-319-19309-0_38

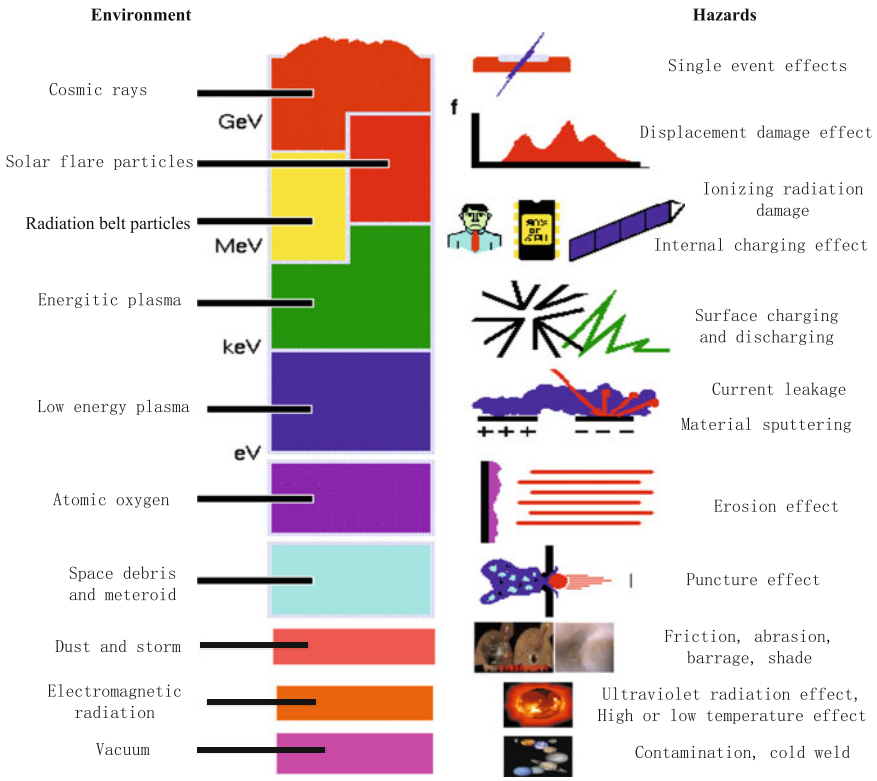

Fig. 1 Space environmental factors and their hazards to spacecrafts

are some special environments inside the space station such as micro biological environment, residual radiation, temperature, humidity and gas circulation, etc. Some of the space environmental factors are influenced by solar activity, especially in the region of the South Atlantic Abnormality. The space environmental effects will results in the degradation and deterioration of spacecraft materials or devices, and can threaten the reliability and life of space station.

In recent years, more experiments and studies were conducted on the effects of single environmental factors on the spacecraft materials and devices, but the results from ground simulation tests do not always agree with the data collected in space. These discrepancies may be caused, among other things, by synergistic effects of space environmental factors.

For example, the decrease in transmittance of solar cells contaminated by small space debris and their impact products is larger than from only the impact products [3]. Besides, it is conceivable to assume that interaction between many types of energetic particles, electromagnetic radiation, atomic oxygen, etc. will have a synergistic effect on solar cells and other space station materials. So, it is essential to study the synergistic effects between various space environmental factors and provide guidance for design of ground simulation tests and failure analysis of space materials and components on space station.

Table 1 Summary of possible synergistic effects between space environmental factors

Space environments	Energetic particle	Ultraviolet	Atomic oxygen	Space debris	Plasma	Contamination
Energetic particle	1[a]	2	2	2	1	2
Ultraviolet	2	1[b]	3	2	1	2
Atomic oxygen	2	3	0	3	1	3
Space debris	2	2	3	0	1	3
Plasma	1	1	1	1	0	2
Contamination	2	2	3	3	2	0

Degree of interaction: 0-none, 1-micro, 2-common, 3-obvious
[a]There are synergistic effects between electron, proton and heavy ions
[b]There are synergistic effects between near ultraviolet and far ultraviolet

In this paper, the synergistic effects between the environmental factors affecting the space station are introduced firstly, and then the synergistic effects from extravehicular space environments or inside the spacecraft are analyzed. At last, recommendations and countermeasures preventing the synergistic effects on mechanisms, simulation techniques, test methods, forecasting techniques and protection methods are proposed.

Synergistic Effects Between Space Environmental Factors

The space environmental factors around and inside the space station are complex and they may interact synergistically with the space materials and components. The interactive synergistic effects between some space environmental factors are listed in Table 1.

For space environment containing such factors as electrons, protons, ultraviolet radiation, debris, atomic oxygen, etc. it is conceivable to expect that some of them will interact synergistically, affecting the spacecraft and/or influencing each other's effects. In order to increase the effectiveness and the efficiency of ground simulation testing and error analysis, the synergistic effects between space environmental factors should be taken into account.

Synergistic Effects of Open Space Environments

Synergistic Effect Between Energetic Particles and Electromagnetic Radiation

Surface materials of space station will encounter radiation damage not only by energetic particles but also by ultraviolet radiation. For thermal control coatings

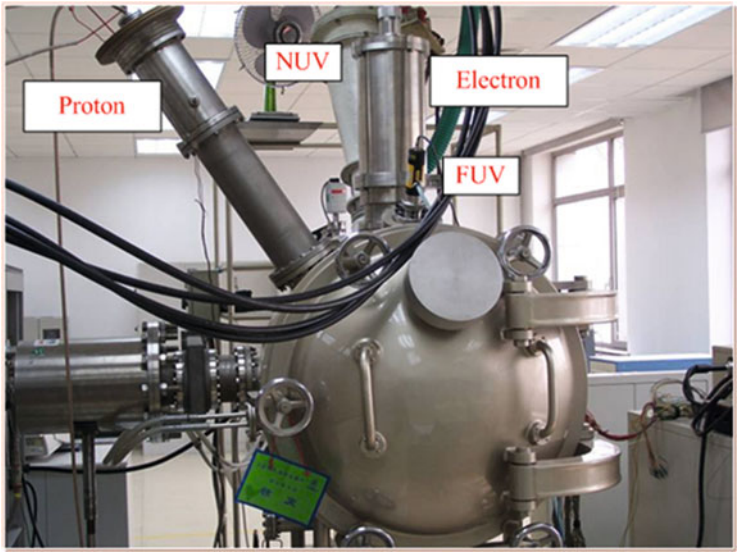

Fig. 2 Combined radiation environment simulator in BISEE

such as thermal control white paints or optical components, energetic particles not only damage the chemical bonds of organic materials, but also bring ionizing effect and displacement effect to them. Ultraviolet can bring chemical bond break effect or ionizing effect, but also increase the damage or get some repair from it. So many aerospace countries or companies built space combined radiation facilities which includes electron, proton, ultraviolet and so on, just as combined radiation facility in Beijing Institute of Spacecraft Environment Engineering (BISEE), as shown in Fig. 2 [4].

Synergistic Effect Between Atomic Oxygen and Ultraviolet Radiation

Atomic oxygen and ultraviolet are the major space environments of spacecraft in LEO. From lots of flight test and ground simulation test, it is can be concluded that surface degradation of low earth orbit spacecraft is mainly caused by atomic oxygen, ultraviolet and their synergistic effect [5].

The Bleaching Effect of Atomic Oxygen on the Ultraviolet Radiation

Spacecraft surface material such as thermal control coating can be damaged by ultraviolet radiation and results in the dark of material's color and increase of solar absorption. But atomic oxygen has some bleaching effect on the ultraviolet

radiation, and results in some recovery of optical property of materials. Therefore, both space environmental affects to the performance of the optical parameters of the thermostat paint mutually offset.

This is because there are many color centers produced in the pigment particles of the material irradiated by UV radiation. Metal oxide in materials absorb photon from UV radiation and then results in the appearance of electron transition and the formation of the hole—electron pairs, which led to the increase in the absorption rate. Color center of the metal oxide pigment particles will disappear after exposure to oxygen environment, resulting in "bleaching" or "recovery" effect.

Enhancement of Ultraviolet Radiation on the Erosion Effect by Atomic Oxygen

Synergistic effect of atomic oxygen and ultraviolet will exacerbate surface erosion of thermal control paint. For UV radiation can cause cross-linking of the molecular chain and valence bond breaking in the thermal control coating or organic polymer, which results in the material surface softening or fragmentation, providing channel to the atomic oxygen erosion [6, 7].

Synergistic Effect Between Space Debris and Atomic Oxygen

The synergistic effect of space debris and atomic oxygen will greatly exacerbate the extent of space material erosion.

Space debris <1 mm usually can not cause catastrophic damage to the spacecraft, but due to the large number and high collision probability with spacecraft, the surface long-term cumulative effect caused by multiple impacts is obvious. Despite difficult to find, micro debris impact will generate many pinholes or cracks in space functionality protective film, and these defects will provide channel into the base material to atomic oxygen, resulting in the "hidden loss" and emptied under the protective layer by atomic oxygen, causing tearing and shedding of the protective layer, which led to the failure of protective measures, especially to large area of the plate-shaped structure array antenna and solar array [8].

Discharge Induced by Space Debris and Meteoroids

Solar panel is an important energy systems of the spacecraft and its working state directly affect the operating conditions and service life of the spacecraft. Because of huge area, and exposed to the space debris environment, it has a very high probability of being struck by space debris.

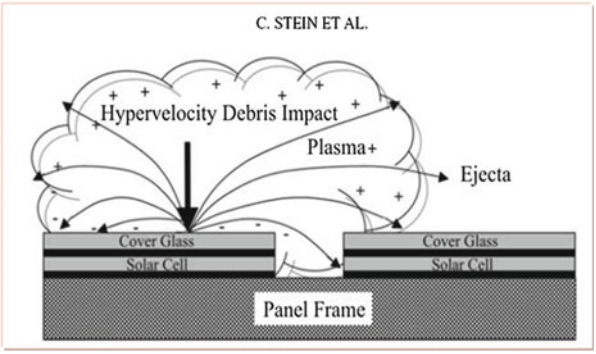

Fig. 3 Discharge of solar panel induced by space debris

The continuing the secondary arc can be generated in the high voltage battery plate by electrostatic discharge, and it's usually occur at the edges, for example, between the solar cell sheet where exists a bias and a dielectric material. However, the secondary arc in high-voltage solar array can be easily induced by the ejection from hypervelocity debris and contamination, which has been the support for the work of the Crawford and Schultz et al., the study found that plasma splashing with high conductivity near the point of impact provide a convenient channel for discharge, as illustrated in Fig. 3 [9].

Contamination Induced by Space Environments

Contamination Induced by Space Debris and Micrometeoroid [10]

Spacecraft may impact by space debris and micrometeoroids and cause damage to spacecraft, the type and extent of the damage depends on the size of the spacecraft configuration, working hours and micro-meteoroid mass, density, speed characteristics. The impact damage includes rupture of the pressure vessel, the degradation of the porthole, spallation of the thermal control coatings, thermal protection performance degradation and damage of the antenna system.

Besides from natural pollution and the spacecraft itself volatile, pollution also from spacecraft impact by ultra-high space debris and micro-meteoroids. When spacecraft surface materials and devices impact by the ultra-high-speed movement of space debris, the impacting particle will be hinder by the spacecraft materials and devices and generate high temperature and pressure, which knocked a hole in the material near the point of impact and high temperature melting occurs splash. The splashing will scattered near the crater and form pollution, as illustrated in Fig. 4. For example, the pollution from the impaction by hypervelocity debris to a large area of solar panel, it can absorption and scatter electromagnetic radiation in a specific wavelength range. The pollution caused by hypervelocity impact can lead

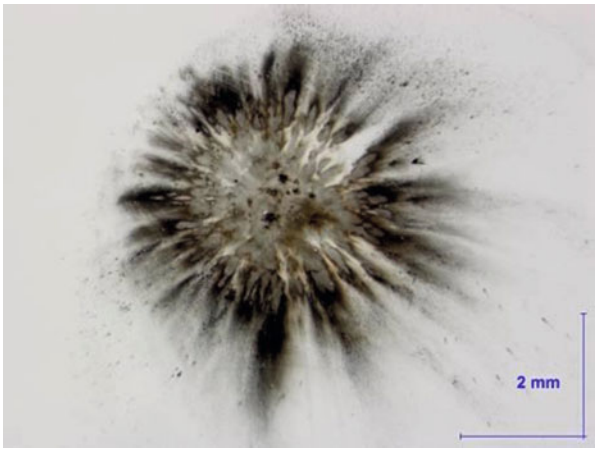

Fig. 4 K9 glass impacted by micro debris (diameter 1 mm, thickness 7 μm, velocity 5.5 km/s)

to degradation of solar transmittance of the transparent cover glass material up to 15 %.

Synergistic Effects Between Ultraviolet, Atomic Oxygen and Contamination

Outgases of spacecraft material can be caused by the ultraviolet radiation and atomic oxygen erosion. The contamination deposited on the surface of the spacecraft and then pollutes the sensitive materials and devices of spacecraft, resulting in the decrease of transmittance of the optical devices and the performance degradation of thermal control coatings.

However, the pollution mechanism induced by ultraviolet radiation and atomic oxygen on spacecraft materials is complex. Firstly, when the spacecraft surface material radiated by ultraviolet, valence bond breakage of organic material will occurs and the desorption of the adsorbed molecules and the material component, resulting in the occurrence of the outlet and pollution effects; Secondly, the undercutting of the atomic oxygen and its sputtering and chemical reaction to the surface material will cause surrounding diffusion deposition of the material molecules or components, resulting in contamination of the spacecraft; Thirdly, pollutants generated by atomic oxygen erosion and sputtering of atomic oxygen to spacecraft materials will deposited on the surface, and then it will be radiated by UV and solidified on the surface of the spacecraft, exacerbated the pollution on the spacecraft; Fourthly, contamination on the surface of the spacecraft will be sputtered and chemical reacted by the atomic oxygen, and it will reduce the pollution and play a role of slowing down.

Therefore, ultraviolet radiation, atomic oxygen and their induced pollution effect mechanism is related with spacecraft surface material composition, structure closely.

Surface Charge to Enhancement of Pollution Effect

The spacecraft charging on the surface by charged particles generate charged particle adsorption, and then increase the surface contamination, which is due to the low energy ion group from spacecraft out-gassing or sputtered neutral atoms ionized by photovoltaic or charge exchange with other ions. These ions will be attracted to the negatively charged surface, and results in the change of surface optical performance changes, increase temperature and the absorption coefficient, decrease the transmittance and the surface conductivity. The satellite surface contamination can also cause the changes of the number of incident electrons and secondary electron, causing the change of the optical performance, decreases the surface conductivity, increases surface charge and discharge. Charged Surface will also cause the plasma measurement error in the space environment.

Synergistic Effect Between Charged Particle and Contamination

Spacecraft materials or devices radiated by charged particle can cause outgas of the material, and then increasing the pollution of the spacecraft sensitive materials or devices, causing the optical performance degradation. For thermal control materials, the sun absorption rate will rise and threat the safety of the spacecraft thermal control.

Besides, space high vacuum, high and low temperature alternating, atomic oxygen, radiation and other environments will have synergistic effects too, and give a threat to the spacecraft orbit performance and reliability.

Synergistic Effects Inside Space Station

Synergistic Effect Between Microbiology and Micro Vibration

During the course of its lifetime, some processing such as deployment of solar arrays, movement of manipulators and so on will results in the appearance of micro vibration, which difficult attenuation gradually by itself, and some stress fatigue in structural material or functional material will generate. At the same time, micro biology will erode metal materials too. Under the synergistic effect of micro biology and micro vibration, oxidation film on the surface of metal material will be corrupted and the floor metal will appear. The naked metal surface and the oxidation coating becomes anode and cathode separately, and results in the appearance of electrochemistry erosion. Furthermore, crack may generate in the erosion site gradually. All of this will accelerate the corruption of metal surface and its function invalidation.

Synergistic effect between micro biology, temperature, humidity and gas circulation.

Temperature and humidity give a good chance of propagation to micro biology, and the activities of cosmonaut and flow of gas bring the micro biology to everywhere place of space station.

Some organic from protection coating can be eat off by micro biology, and the metabolize production of micro biology has erosion effect to protection coating too. As the propagation of micro biology in gas and water, the micro biology and its secretion, erosion production and so on may bring jam to water or gas circulation system, and influence the operation of life support system in space station.

Synergistic Effect Between Microbiology and Residual Radiation

There is residual radiation inside space station, which may not kill the microbiology but improve their activity in some extent.

Comparing with flight tests and ground test, some micro biology has apparently enhancement in reproductive ability under space condition, and their growth rate increase and morphological differentiation advance. For example, Russian smoke detector is space station were Fungal-contaminated severely, as shown in Fig. 5 [11].

Synergistic Effect Between Space Radiation and Microgravity

Genetic variation of biology is mainly induced by space radiation and micro gravity in space station. There are cell damage and genetic variation induced by space radiation, and micro gravity can give some recovery from macrocosm and cell

Fig. 5 Fungal-contaminated Russian smoke detector

level. The influence of space radiation and micro gravity to biology is dependent, and their synergistic effect on biology brings large variety contrast to ground environment.

Research Situation and Countermeasures

After decades of development, the world have initially capability to carry out ground simulation test evaluation of synergistic effect between multi space environmental factors and carried out a series of ground simulation test study. But compared with the actual in-orbit environment, there are still need to be given further efforts and improvements.

Firstly, improve ground simulation capability of the space environments and effects.

Now, the space powers have ground simulation capabilities of synergistic effect between space charged particles and solar electromagnetic radiation, atomic oxygen and ultraviolet, plasma discharging induced by space debris, but not yet implemented all these space environment simulation in the same device, and cannot in the ground simulation equipment to carry out in situ testing of material composition, microstructure defects.

So, multi-functional ground simulation facilities with multi factor space environments and their synergistic effects, in situ testing of material composition, microstructure defects should be built [12].

Secondly, synergistic mechanism between space environmental factors should be given further study.

While scientists and engineers engaged in the spacecraft space environment effect have recognized the importance of the synergistic effect between space environments and carried out some ground simulation test and mechanism research, but it is still in its infancy, and further study should be given.

Thirdly, establish and improve the space factor synergies test methods.

Some efforts have given to the experimental studies of the synergistic effect between some environmental factors, but the space ground simulation test method for multi-factor environmental effects has not established.

Fourthly, develop space environmental synergistic effect software and tool.

At present, the world has not yet carried out a simulation study of synergies evaluation of the spacecraft materials and devices between space environments. So the performance degradation indicates and the simulation model should be studied and established on the basis of spacecraft performance degradation mechanism and test analysis.

Conclusions

With the increasing on-orbit life of spacecrafts, the synergistic effect of multi space environments may pose larger threat onto the performance and reliability of spacecraft. Therefore, in the design, development and selection process of spacecraft materials and devices, the related synergistic effect should be paid more attention to, and the work of space environment tailoring, the synergistic test method, the degradation mechanism and indicates and so on should be strengthened to improve the reliability of operating spacecraft and to meet the requirements of new generation space missions.

References

1. Huang BC (1993) Space environment engineering [M]. Aerospace Press, Beijing
2. Huang BC, Ma YL (1993) Spacecraft environment test technology. National Defense Industry Press, Beijing
3. Stein C, King TR, Wilson WG, Robertson R (1998) Spacecraft contamination: active cleaning and control. In: Proceedings of SPIE—the international society for optical engineering, optical systems contamination and degradation, 3427-006. pp 56–64
4. Feng WQ, Ding YG, Yan DK (2005) Study on space electron, proton and ultraviolet combined irradiation simulation test [J]. Spacecr Environ Eng 22(2):69–72
5. Stein C, Roybal R, Tlomak P, Wilson W (2000) A review of hypervelocity debris testing at the air force research laboratory [J]. Space Debris 2:331–356
6. Townsend JA, Park G (1996) A comparison of atomic oxygen degradation in low earth orbit and in a plasma etcher. In: 19th space simulation conference: cost effective testing for the 21st century. Baltimore, Maryland. NASA CP-3341, X-28103, 29–31 October 1996. pp 295–304
7. Verker R, Grossman E, Gouzman I et al (2006) Synergistic effect of simulated hypervelocity space debris and atomic oxygen on durability of poss-polyimide nanocomposite. In: 10th international symposium on materials in a space environment and the 8th international conference on protection of materials and structures in a space environment, Collioure, France
8. Schultz PH, Crawford DA (1998) Electromagnetic properties of impact-generated plasma, vapor and debris [C]. In: Hypervelocity impact symposium, Huntsville, AL, 16–19 November 1998
9. Tong JY, Liu XP, Sun G et al (2006) Simulation of combined environment of atomic oxygen and ultraviolet and development of protection technologies [J]. Chin J Vac Sci Technol 26 (4):263–267
10. Stiegman AE, Brinza DE, Anderson MS et al (1993) An investigation of the degradation of Fluorinated ethylene propylene (FEP) copolymer thermal blanketing materials aboard LDEF and in the laboratory [J]. NASA CR-192824, N93-25078. pp 1–18
11. Macatangay AV (2010) Impacts of microbial growth on the air quality of the international space station. AIAA, 2010-6069
12. Kleiman J, Horodetsky S, Issoupov V (2009) Concept of a new multifunctional space simulator for accelerated ground-based testing in modern space exploration era. In: Proceedings of the 9th international conference: Protection of materials and structures from space environment, vol 1087. AIP Conference Proceeding, pp 432–452

Effects of Thermal Cycling on Atomic Oxygen Interaction with Graphite/Cyanate Composite

Ruiqiong Zhai, Yuming Liu, Dongbo Tian, Haifu Jiang, and Yuting Li

Abstract In the Low Earth Orbit (LEO) environment where some of the spacecraft would be located, surfaces will be exposed to potentially damaging environmental conditions including atomic oxygen (AO), solar ultraviolet (UV) radiation, charged particles, thermal cycling, and so on. It is necessary to utilize ground-based tests to determine how these environmental conditions would affect the properties of candidate spacecraft materials. Differences between the results of ground-based and on-orbit materials tests are generally not reproduced in the ground test. While some progress had been made for AO reactions in the presence of UV, or energetic-electron bombardment; little has been done to study AO reactions combined with thermal cycling. It was to remedy this deficiency that the work in the paper was undertaken.

Keywords Composite material • Atomic oxygen • Thermal cycling • Space environment

Introduction

Due to its high specific strength and specific modulus, excellent dimensional stability and many other advantages, and well-developed manufacturing process, thermosetting resin matrix composite enhanced by carbon fiber has been broadly employed in the aerospace manufacturing industry [1, 2]. Since the early 1990s, support barrels of horn antenna, despun frame, and folded rigid solar cell array made by carbon/epoxy composite materials have first been introduced in domestic DFH-2 broadcasting satellites and FY-1 meteorological satellites. After 20 years, high-performance fiber-enhanced resin matrix composite materials have been increasingly applied in satellites structures [3].

R. Zhai (✉) • Y. Liu • D. Tian • H. Jiang
Beijing Institution of Space Environment Engineering, Beijing 100094, China
e-mail: lingid_83@163.com

Y. Li
Ohio University, Athens, OH, USA

J. Kleiman (ed.), *Protection of Materials and Structures from the Space Environment*, Astrophysics and Space Science Proceedings 47,
DOI 10.1007/978-3-319-19309-0_39

For the orbiting spacecraft, its exterior structure will be remarkably impacted by various spatial environment factors. Atomic oxygen, which is a strong oxidizing agent and the key component in the low earth orbit (LEO) atmosphere, gives rise to one of the major environment factors in the LEO [4]. When the spacecraft orbits at 7–8 km/s, the atomic oxygen strikes its surface at high speed, leading to the oxidation corrosion of surface material and mass loss, which will eventually give rise to the degradation in optical and mechanical properties [5–8]. On the other hand, since spacecraft experiences low temperature environment during orbiting, there will be alternate changes in ambient temperature when it's entering or leaving the Earth's shadow area.

Currently, the interactions between atomic oxygen and resin matrix composite materials have been extensively studied internationally. However, the influences due to thermo circulation on the interactions between atomic oxygen and resin matrix composite materials have rarely been explored. To study the resistivity of resin matrix composite materials against oxidation due to atomic oxygen under the alternating hot and cold condition, this paper mainly focuses on two materials: cyanate ester composites enhanced by carbon fibers M40/DFA-1, and epoxy resin composites enhanced by carbon fibers M40/AG-80. In the following sections, by carefully measuring and analyzing the reaction rate of atomic oxygen, observing the surface optical topography, testing the shearing properties between different layers, and analyzing the X-ray photoelectron spectroscopy (XPS), the effect of single atomic oxygen environment factor and the sequential effect due to both thermo circulation and atomic oxygen environment factors are compared. And the mechanism of increment in resistivity of resin matrix composites against atomic oxygen due to thermo circulation is proposed.

Experimental Procedure

Experiment Materials

Cyanate ester composites enhanced by carbon fibers M40/DFA-1, and epoxy resin composites enhanced by carbon fibers M40/AG-80 are tested in the experiments respectively.

M40/DFA-1 materials are divided into two groups, marked as A and B. The materials in A group are employed in atomic oxygen experiment directly. The materials in B have experienced two hundred times of thermo circulations prior to the atomic oxygen experiment. Similar procedures have been repeated for M40/AG-80 materials.

Experiment Instruments and Methods

The atomic oxygen experiments of both materials are simulated on atomic oxygen simulation facilities at Beijing Satellite Environment Engineering Research Institute. The experimental parameters are shown in Table 1.

The F-10 (chamber B) thermo cycle test chamber at Beijing Satellite Environment Engineering Research Institute has been employed for the thermo circulation experiments. Its performance indexes are given in Table 2.

To avoid the impact of microcracks on the mechanical properties of testing materials during thermo circulations, the temperature ranges of thermo circulations are chosen as −150 to +150 °C according to other related studies [9, 10]. Two hundred thermo cycles have been performed, with a typical one cycle temperature curve illustrated in Fig. 1.

The mass loss of samples is measured by German MiroSatorius precision electronic balance, the measuring accuracy is 10^{-5}. The mass of samples prior to and after the experiments have been recorded respectively. Three trials have been performed for every experiment, and means are calculated. The reaction rates of atomic oxygen are calculated based on the mass loss method of Kapton membrane [11]. Calculation details are shown as following:

$$R_e = \frac{\Delta m/\rho}{f_k t \cdot A} = \frac{\Delta m \cdot V}{f_k t \cdot A \cdot m} = \frac{\Delta m \cdot d}{f_k t \cdot m} = \frac{\Delta m \cdot d}{F \cdot m} \tag{1}$$

Where, R_e is the atomic oxygen interaction rate of the specimen, cm^3/atom; F is the atomic oxygen flux (atoms/cm^2); Δm is the mass loss of the specimen, m is the mass of the specimen, d is the thickness of the specimen, cm

The surface optical topographies of samples are observed by Olympus GX-51 optical microscope at Beijing Institution of Space Environment Engineering. The shear strengths between different layers are tested based on GB3357-82 standard by applying the three-point short beam shear test. These experiments were performed by universal material testing machine MTS with loading rate as 1.3 mm/min. The surface XPS of all samples were analyzed by VGDSCALABMK II XPS instrument at Tianjin Polytechnic University.

Experimental Results and Analysis

Surface Optical Topography

Atomic oxygen irradiation experiments with or without thermo circulation have been performed respectively for M40/DFA-1 and M40/AG-80 materials. After the

Table 1 Experiment parameters of atomic oxygen experiments

Vacuum degree	Fluence impact area	Fluence energy	Atomic oxygen flux
5×10^{-2} Pa	>φ150	3–10 eV	1.5×10^{20} atoms/cm^2

Table 2 Performance indexes of thermal-cycling-test chamber

Chamber capacity	Range of flexible temperature	Temperature increasing rate	Temperature decreasing rate
0.3 m^3	−150 to +180 °C	>30 °C/min	>10 °C/min

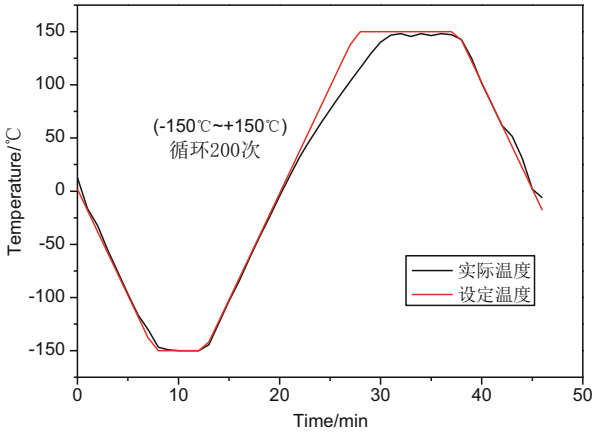

Fig. 1 Thermal cycling test parameters

experiments, the surface optical topographies due to both methods are observed by optical microscope, as shown in Figs. 2 and 3. With the influence of atomic oxygen, various degrees of denudations are shown on the surface of resin composite materials, exposing the carbon fiber near the surface. By contrast, the samples exposed to atomic oxygen are corroded more seriously as illustrated in Figs. 2b and 3b, the structures and trends of exposed carbon fibers are pretty obvious. Moreover, after exposing to atomic oxygen, the color resin residue left on the surface darkens, due to the oxidation of the epoxy resin and cyanate ester resin by atomic oxygen. The long molecule chains are broken in to micro molecules due to atomic oxygen. The optical index of each molecules are different, influence the optical permeability, leading to the darkening of material color.

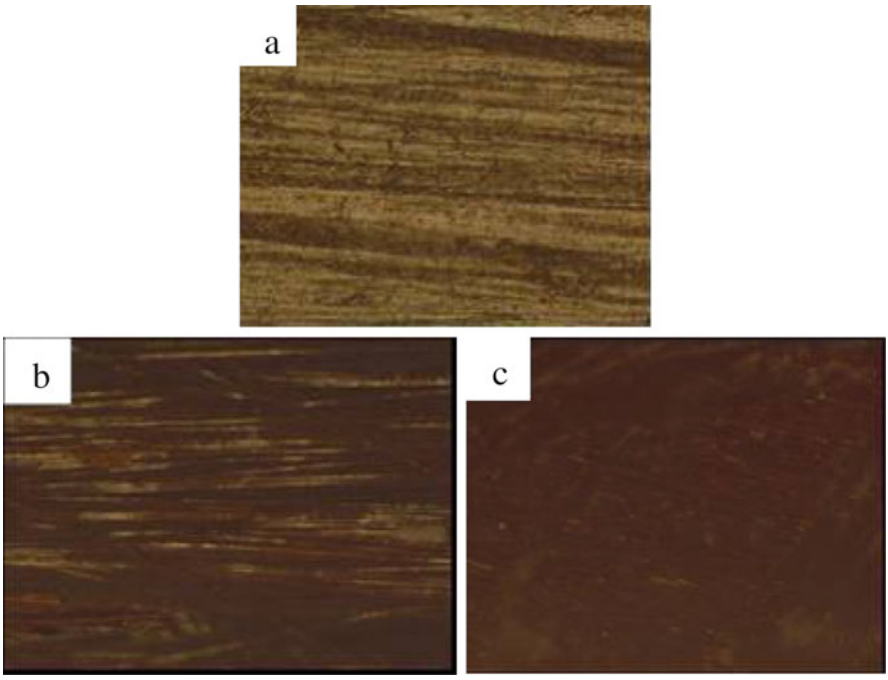

Fig. 2 Surface of M40/DFA-1 specimen before/after space environment test. (**a**) Original; (**b**) after AO erosion; (**c**) after TC + AO erosion

Reaction Rate of Atomic Oxygen

Using the data obtained from mass loss measurements, the reaction rates of atomic oxygen for two kinds of materials are calculated using Eq. (1), the results are listed in Table 3.

Comparing the reaction rage of atomic oxygen for these two materials under two different environmental conditions, it appears that the atomic oxygen reaction rates decline after thermo circulations for both composite materials. In another word, the thermo circulations weaken the corrosion due to atomic oxygen. The reason could be that the thermo circulations lead to curing reaction of resin matrix, increasing the intermolecular crossing links, and more closely packed, which originates the increment in resistivity against corrosion due to atomic oxygen. Within these two materials, the changing rage of M40/AG-80 is relatively big, and the changes could hardly be observed for M40/DFA-1. The reason is that cross-linking groups in epoxy resin are soft segments, which have better movement ability during thermal treatments than cyanate ester resin. Then after thermo circulations, it would be easier for epoxy resin to undergo cross-link reaction and its molecular chains would arrange more orderly, which gives rise to the more enormous effect of thermo circulation on epoxy composite matrix than the one on cyanate resin composite.

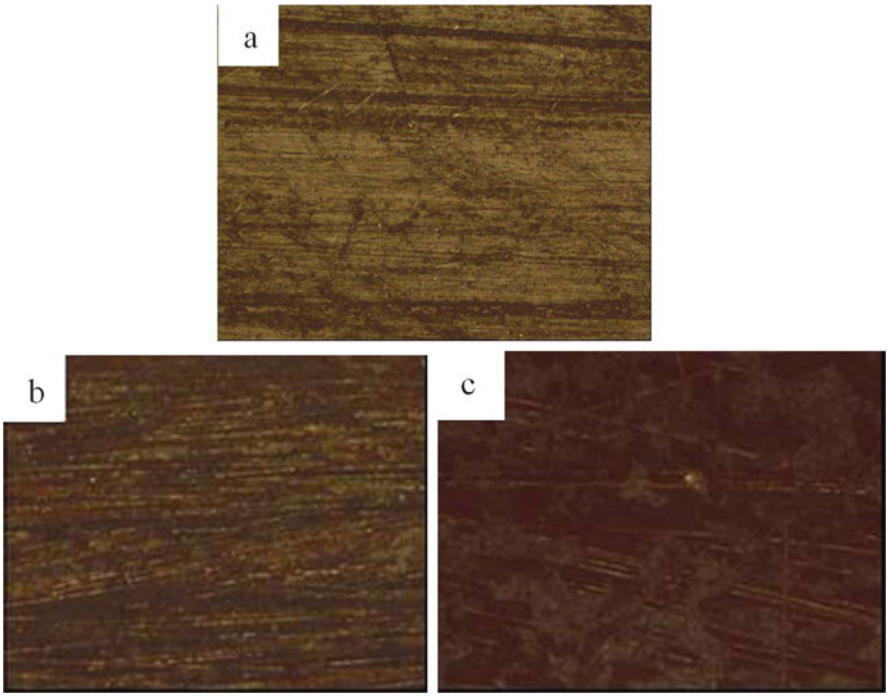

Fig. 3 Surface of M40/AG-80 specimen before/after space environment test. (**a**) Original; (**b**) after AO erosion; (**c**) after TC + AO erosion

Table 3 Comparison of the atomic oxygen reaction rate under different condition

Status of the specimen	AO interaction rate before thermal cycling $(\times 10^{-24})/cm^3\ atom^{-1}$	AO interaction rate after thermal cycling $(\times 10^{-24})/cm^3\ atom^{-1}$
M40/DFA-1	2.37	2.33
M40/AG-80	4.63	3.95

Shearing Strength Between Layers

The testing results of shear mechanics between different layers are presented in Fig. 4. The shearing strengths of both materials decline at certain degree. M40/DFA-1 decreases by 4.47 %, and M40/AG-80 is reduced by 1.75 %. Whereas, after applying TC + AO, it appears for shearing strength there are increments at certain degree for both samples, MD40/DFA-1 increases by 1 %, and for M40/AG-80 the number rises by 4.57 %. It appears that thermo circulations increase the mechanical properties of both composite materials, which could compensate the decline due to atomic oxygen corrosion.

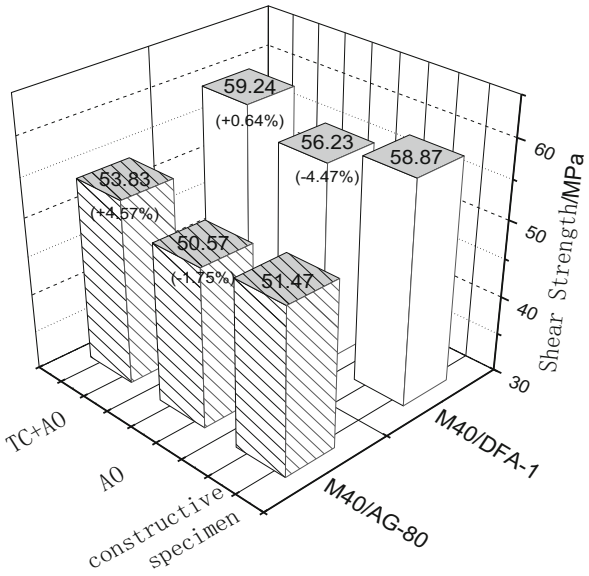

Fig. 4 Comparison of interlaminar shear strength under different condition

Generally speaking, the effects due to thermo circulation on composite materials can be categorized into two aspects [12–14]: (1) at the beginning of thermo circulation, curing reactions of resin matrix take place, increasing the intermolecular crosslink and improving the mechanical properties. (2) After thermo circulations achieve certain times and temperature, the difference of thermal expansion coefficients between fibers and resin matrix leads to stress concentration. When it exceeds the interfacial strength, the debonding between fibers and resin matrix would occur, leading to decline in mechanic properties. According to the experimental result, the thermo circulation conditions applied in this experiment have little impact on the interfacial strength between fibers and resin matrix. Instead of causing decline in mechanical properties after thermo circulations, the curing reactions due to thermo circulation make the molecular chains packed more ordered and closely, which significantly improves the mechanic properties of composite materials.

Analysis of Surface XPS

The detail analysis of C1s peaks in XPS of M40/DFA-1 before and after the spatial environment experiments are shown in Fig. 5. The peak for carbon in organic compounds usually can be found around 285 eV (C–C bond), 286.5 eV (C–O–C bond), 287.6 eV (CHO bond) and 288.6 eV (COOH bond). The peak positions for samples before spatial experiments are shown as Fig. 5a. After the oxidation of atomic oxygen, the strength of the C_c peak at 285 eV (C–C bond) reduces significantly. Whereas the C_b peak at 286.5 eV (C–O bond) shows enormous

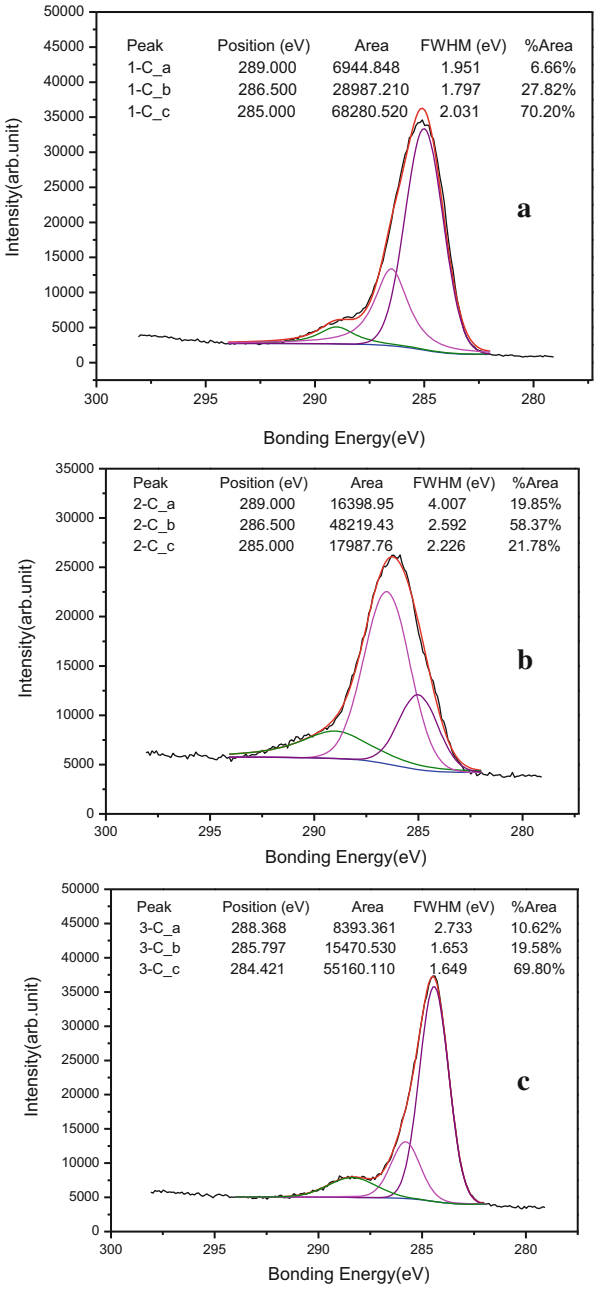

Fig. 5 XPS spectrum of M40/DFA-1sample surface before/after space environment test; (**a**) original; (**b**) after AO erosion; (**c**) after TC + AO erosion

increment in its strength, and the peak strength for C_a peak at 289 eV (C=O bond) also increases slightly, as shown in Fig. 5b. It could be due to the reaction between oxygen and C–C bond, giving rise to new C–O bonds, which leads to the rising of

peak strength at 286.5 eV. The bonding energy of C–C bond is 3.60 eV, which should be broken by O first. The carbon atom within a C–O single bond also connects with two other hydrogen atoms with bonding energy 4.28 eV, which should oxidized further by atomic oxygen, forming C=O bonds, leading the increment in corresponding peak strength. With the increasing number of C–O bonds in the materials, the rate of intermolecular cross-linking raises correspondingly, which gives rise to the fragility of material and harm the mechanical strength. These observations are in great agreement with the testing results of shearing properties between layers.

For the M40.DFA-1 which undergoes thermo circulations prior to the reactions of atomic oxygen, all three peaks shift to the low-energy region by 0.6–0.8 eV. It suggests that certain changes in bonding condition occur during experiment, which could be due to the curing reaction of resin matrix composite during thermo circulation. Also the molecular chains are packed more orderly in composite matrix, increasing the resistivity against corrosion of atomic oxygen. However, the changing ranges are smaller than the results in experiments which only undergo atomic oxygen oxidation without thermal circulation, which means the thermo circulations weaken the interaction between atomic oxygen and materials. At certain level, it could be concluded that thermo circulations enhance the resistivity of materials against oxidation of atomic oxygen.

The Cls fine spectrums of M40/AG-80 before and after applying atomic oxygen are illustrated in Fig. 6. Before applying atomic oxygen, there are three peaks in Cls spectrum, which are at 284.5, 286.3 and 287.3 eV. The peak at 284.5 eV corresponds with the carbon atoms within the benzene ring which do not bond with N and O atoms (C–C bond on benzene). The area ratio of this peak is around 35.62 %. The peak at 286.3 eV correlates with C–O bonds, and 287.3 eV relates with CHO functional groups. After the oxidation of atomic oxygen, the strength of original peak 4-C_b and 4-C_c decrease enormously and shift to high-energy range. A new peak appears at 289 eV as shown in Fig. 6b, which is due to C=O functional group. This indicates during the reactions between atomic oxygen and M40/AG-80, the C–C bonds are broken by oxygen, forming new C–O bonds, which can be further oxidized to C=O bonds.

For the samples which undergo thermo circulation prior to the reaction of atomic oxygen, the C–C peaks strengthen exceptionally. This indicates that new C–C bonds are formed during thermo circulation, leading to more closely packed molecular chains. The influence on molecular chains due to corrosion of atomic oxygen decreases, which is in good agreement with the observation for M40/DFA-1 composites. Thermo circulations weaken the interaction between atomic oxygen and M40/AG-80 (or M40/DFA-1). In other words, the resistivity against corrosion due to atomic oxygen of both two materials has been enhanced.

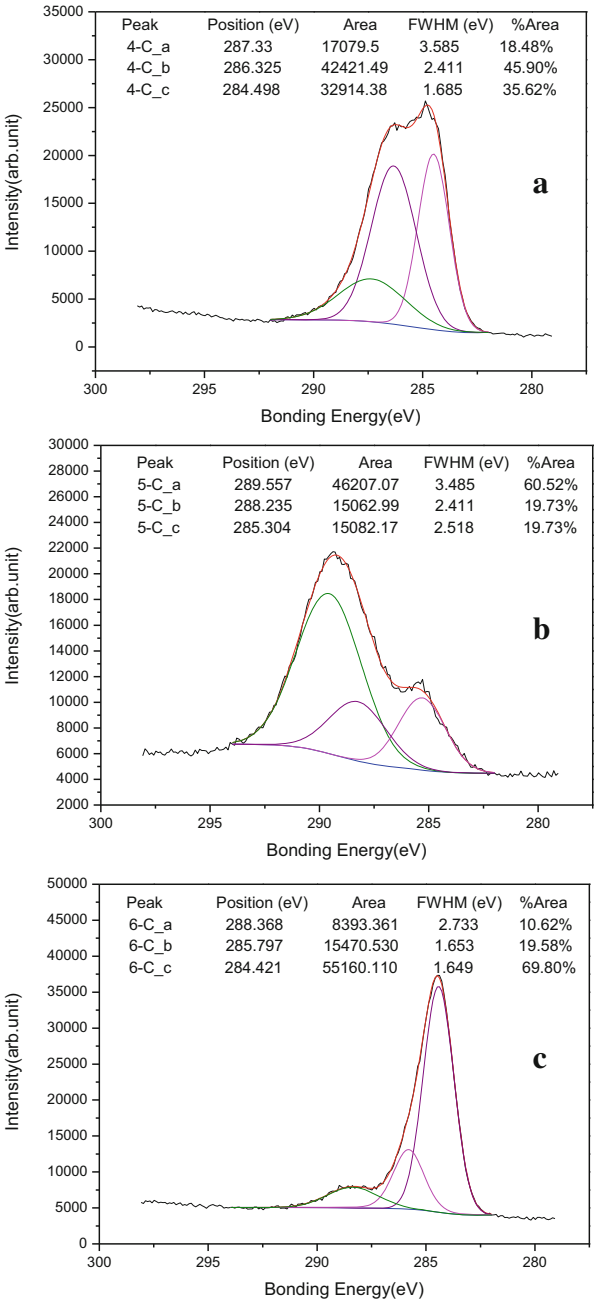

Fig. 6 XPS spectrum of M40/AG-80 sample surface before/after space environment test. (**a**) Original; (**b**) after AO erosion; (**c**) after TC + AO erosion

Conclusions

Generally speaking, our results can be summarized as following:

1. The impacts of atomic oxygen on the surface of composite materials lead to severe corrosion on the resin matrix near the surface, exposing the carbon fibers. According to the analysis of surface composition, the effects due to atomic oxygen are not only limited to physical corrosion, but also chemical interactions with materials.
2. The major reactions between atomic oxygen and surface of materials appear to break the C–C bond, and add an oxygen atom between these two carbon atoms, forming an ester. The increments in the ratio of ester functional groups lead to higher branching levels of polymers, decreasing the intermolecular crosslink, and further weakening the mechanical strength.
3. Thermo circulations lead to curing reaction of resin matrix in polymers, changing the bonding conditions, which makes the atoms more closely packed. Consequently, the reactions between atomic oxygen and materials are weakened. From certain point of view, thermo circulation strengthens the resistivity of materials against corrosions due to atomic oxygen.
4. The oxidative denudations of polymers due to atomic oxygen harm the mechanic properties. However, in this experiment, the samples, which undergo thermo circulations prior to exposing to atomic oxygen, have shown slight increment in mechanic properties. There are two factors contributing to this observation: First, the curing reactions of resin matrix during thermo circulations increase the mechanic properties. Secondly, the thermo circulations weaken the interaction between atomic oxygen and samples, which leading less damage on the mechanic properties. This can be concluded by comparing the reaction ratio between atomic oxygen and samples.

In a word, the thermo circulations will influence the reaction between atomic oxygen and resin matrix composites at certain level. For M40-DFA-a and M40/AG-80 tested in this experiment, thermo circulations weaken the interaction between atomic oxygen and samples, leading to higher resistivity against corrosion of atomic oxygen. Thus it can be concluded that, since various environment factors present at the same time in spatial environment, the interactions between each factor and materials may compensate with each other. In certain cases, the declines in material properties in simulated atomic oxygen experiments on the ground would exceed the real level for orbiting spacecraft. Therefore, for simulated experiments about spacecraft structures and spatial environments, the compensation effect between various environment factors should be taken into consideration.

References

1. Jiang L, He S, Yang S et al (2001) Application of carbon (graphite) fiber/epoxy composites in the spacecraft and the research on their behavior [J]. J Mater Eng 9:39–43
2. Silverman EM (1996) Space environment effects on spacecraft: LEO materials selection guide. NASA contractor report 4661 [R]
3. Tang J (2010) Review of studies of carbon fiber resin matrix composites [J]. Spacecr Environ Eng 27(3):269–2804
4. Huang B, Tong J (2010) Space environment engineering [M]. China Science and Technology Press, Beijing, pp 3–8
5. Zhao S, Shen Z, Xing Y et al (2002) Experimental investigations of atomic oxygen effects on a carbon fiber/epoxy resin composite material [J]. J Beijing Univ Aeronaut Astronaut 28 (6):668–670
6. Li T, Jiang L, Feng W et al (2009) The effects of space atomic oxygen erosion on epoxy and silicone adhesives in LEO spacecraft [J]. Spacecr Environ Eng 26(3):222–224
7. Jiang L, Li T, Feng W et al (2008) FTIR and mass loss analysis of polymer materials in magnetic torque after atomic oxygen exposure [J]. Spacecr Environ Eng 25(6):542–545
8. Tong J, Liu X, Zhang C et al (2009) The space atomic oxygen environment erosion on spacecraft. Environ Eng 26(1):1–4
9. Banks BA, Miller SK, de Groh KK (2003) Atomic oxygen effects on spacecraft materials. NASA/TM-2003-212484
10. Tompkins S, Williams SL (1984) Effects of thermal cycling on mechanical properties of graphite polyimide. J Spacecr Rockets 21(3):274–280
11. Gao Y, Yang D, He S (2004) Effect of vacuum thermo-cycling on mechanical properties of M40J/epoxy composites [J]. Chin J Mater Res 18(5):529–536
12. Li T (2008) Simulation method of atomic oxygen effects in the space [J]. Spacecr Environ Eng 25(2):134–137
13. Liu Y, Jiang L, Feng W et al (2009) The effects of electron irradiation on ITO/Kapton/Al films [J]. Spacecr Environ Eng 26(5):411–414
14. Dever JA, Bruckner EJ, Rodriguez E (1992) Synergistic effects of ultraviolet radiation, thermal cycling and atomic oxygen on altered and coated Kapton surfaces. AIAA 92-0794 [R]

Atomic Oxygen Monitor Based on Resistance Film

Xiangpeng Liu, Jingyu Tong, Dingyigang, Liuyuming, Haifu Jiang, and Jia Zheng

Abstract Atomic oxygen (AO) monitor based on resistance film had been developed for the detection of flux of AO impinging on the surface of the spacecraft in low earth orbit (LEO) and AO erosion effects. The monitor is comprised of electrical resistance film which is made of some AO susceptible conductive materials. The electrical resistance will change as monitor is eroded by AO attack. The AO flux and the erosion rate of flight samples can be deduced by measuring electrical resistance changes in-situ.

An osmium-based AO sensor had been prepared by plating, UV-light etching and metal etching micro processing techniques for AO flux detection. The AO effects sensor consist of silver film and test samples film deposited onto a quartz substrate successively. The material film becomes thinner and thinner by AO attack. When the material film is eroded away completely, exposed silver film would be oxidized quickly and its electrical resistance will become large. By the variation of Ag film electrical resistance, we can determine the erosion time of experiment material film and the material AO erosion rate. The results of ground simulation test of atomic oxygen monitor revealed that the measured resistance increases of AO sensor was agreed with the theoretical values well.

Keywords Atomic oxygen sensors • Silver-based Atox sensors • Low Earth Orbit • Osmium-based Atox sensors • Ground-based testing

Introduction

Spacecraft in LEO operate in a hostile environment, which can significantly affect their operational capability or mission duration. Atomic oxygen (AO) is the most abundant atmospheric species over most of this altitude range. Orbital AO is

X. Liu (✉) • J. Tong • Dingyigang • Liuyuming • H. Jiang
Beijing Institute of Spacecraft Environment Engineering, Beijing, China
e-mail: tjyhjgcb@163.com

J. Zheng
Harbin Institute of Technology, Harbin 150001, China

J. Kleiman (ed.), *Protection of Materials and Structures from the Space Environment*, Astrophysics and Space Science Proceedings 47,
DOI 10.1007/978-3-319-19309-0_40

formed by the breakup of molecular oxygen under short wavelength solar UV irradiation and is the most dominant atmospheric species at altitudes of between 200 and 700 km. The exact AO density distribution is highly variable and depends on the level of solar irradiation and, hence, the local time, local season, and the 11 year solar cycle. Commonly the F10.7 index is used as an indicator for solar activity and, by calculation, the number density of AO in the upper atmosphere [1].

The orbital velocities give rise to AO impact energies about 5 eV. The energy is much higher than the thermal energy of the AO, which is less than 0.5 eV. Consequently, satellite surfaces receive large fluxes of chemically reactive, high energy AO. Hence, it is thought that AO is one of the most dangerous environment in LEO [1]. It is found that some of the materials used to fabricate satellites are eroded, or otherwise degraded, by the action of this chemically reactive AO. A limited range of non-polymeric materials are also affected: silver, carbon, and osmium are the most vulnerable. In each case, AO erosion causes chemical and morphological alteration of these materials that, in general, leads to changes in material properties.

Several remote instruments have been used to monitor thermospheric AO before. Mass spectrometers, carbon-coated quartz crystal microbalance have been used in orbit [2]. However, their size and mass, power prevent the use of microsatellite. Another technique, that of the witness sample, has also been used but this requires the retrieval of the experiment making its use expensive [3].

In this paper we concentrate on techniques used to measure the concentration of AO in the Earth's atmosphere. Actinometers are sensors which experience a change in electrical resistance when an electrically conductive element is exposed to AO. The changes in resistance are caused either by erosion of the conductive element and/or conversion to a non-conducting oxide, or by changes to the element's electronic structure. Knowledge of the element's electrical characteristics and its response to AO attack provide a means for converting resistance measurements into AO flux/fluence [4]. Actinometers also can be used for testing the AO response of coatings. Actinometers have the advantage of small, light, cheap, simple and small amounts of power.

Sensor Construction

Osmium-Based AO Sensor

The initial criteria for selecting the element of the sensor was that conductive material can react with AO. There are three materials, silver, carbon and osmium, which are suited for resistance AO sensor. They react efficiently with AO and undergo significant mass loss when exposed to the space environment. Table 1 shows their properties.

Sliver has a very rapid reaction yield with AO. However, it has the drawback that it reacts too rapidly for much information to be gathered in low LEO. The formation of a brittle oxide layer prevents the reliable regeneration of the sensors so AO erosion rate of silver is non-linear which would result in measurement error.

Table 1 Properties of silver, carbon and osmium

Property	Silver	Carbon	Osmium
Atomic oxygen erosion rate ($\times 10^{-24}$cm^3/AO)	10.5	0.3 ~ 1.1	0.03
Resistivity ($\times 10^{-8}\Omega$.m)	1.587	8.2	8.8

Carbon has a medium erosion yield. Volatile CO, CO_2 would be produced as the carbon is oxidized by AO. Carbon oxide is vapor and does not retard fresh carbon to be oxidized by AO, so its AO erosion rate is linear. But temperature sensitivity of carbon sensor and several structures, such as graphite, vitreous carbon and adamantine etc, may cause significant problems in its calibration.

Osmium is known to react efficiently with AO and to undergo significant mass loss when exposed to the space environment. The mass loss is due to the formation of OsO_4, which is volatilizable. As the osmium metal surface reacts with AO, under the low-pressure conditions existing in orbit, the oxidized metal sublimes away from the surface and continually exposes fresh metal to the environment. Osmium is the elemental metal and its structure has good stability in space environment, so osmium resistance sensor has high measurement accuracy.

Osmium-based sensor is used for AO flux measurements. The principle is as follows: Osmium resistance film is deposited on insulating substrate of sensor. After exposed in AO environment, the resistance film becomes thin as it is eroded by AO and the resistance increases. The mass loss can be computed according to the resistance change. As the erosion rate of resistance film, exposure interval is known, AO flux can be determined.

Osmium sensor is deposited onto fused silica substrates with dimensions 30 mm $\times$ 20 mm $\times$ 1.5 mm. Electrochemical method of deposition is used to deposit osmium film. Before deposition, the glass substrates are thoroughly cleaned to remove foreign matter from the surface. First a very thin layer of chromium is deposited to improve adhesion followed by 100 A of gold film. Chromium film and gold film are manufactured using a vacuum evaporation coater. Then osmium is deposited by plating. A perfect film with 0.3 μm thickness has been prepared successfully, by optimizing the plating bath PH, temperature and current efficiency.

The film was etched by UV-light etching and metal etching technique, after osmium film deposited. It was produced to a resistance line with 340 mm in length and 0.2 mm in width. The bonding pad is then formed by a thick gold deposition to provide continuity for the resistance line (Fig. 1).

Silver-Based Resistance Sensor

Silver-based sensor is used for AO effect measurements. AO effect sensor principle is as follows: a space material film is deposited on the resistance film of above-mentioned sensor. After exposed in AO environment, the resistance keeps constant as it is protected from AO by space material film. But when the space material film

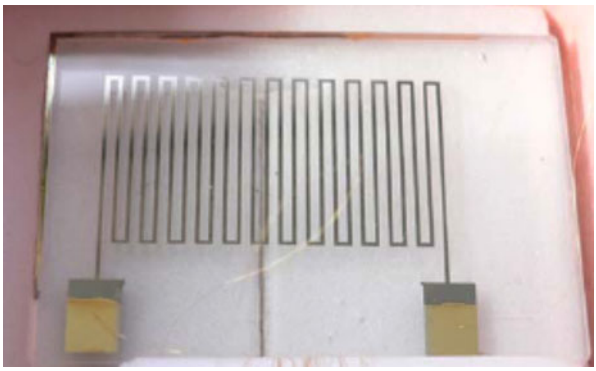

Fig. 1 Photo of the Osmium-based sensor

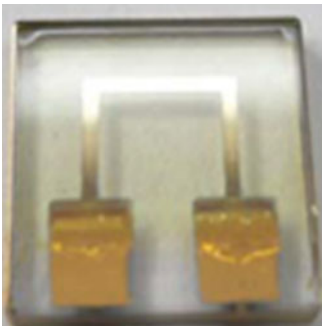

Fig. 2 Photo of the Silver-based sensor

is eroded away completely, exposed resistance film would be oxidized quickly and its electrical resistance would become large. Then, the eroded time of material film could be determined and the material eroded rate by AO could be computed easily.

There are materials, Kapton, polythene and epoxy resins, which are most used spacecraft outer material. They are used for AO erosion experiment of coatings.

The silver film sensors are manufactured using physical vapor deposition (PVD). The resistance line of Ag is direct deposited on the glass substrate through a mask, followed by 100 A of gold pad. Then the testing coating is covered on the silver resistant line. After finishing the sensors are solidified and dehydrated. Figure 2 is the schematic diagram and photo.

Experimental

AO test is conducted in the AOBISEE. AO is generated using an Electron Cyclotron Resonance (ECR) plasma source and electrically biased metal surfaces. Neutralization apparatus is a molybdenum plate. Within the exposure chamber, the

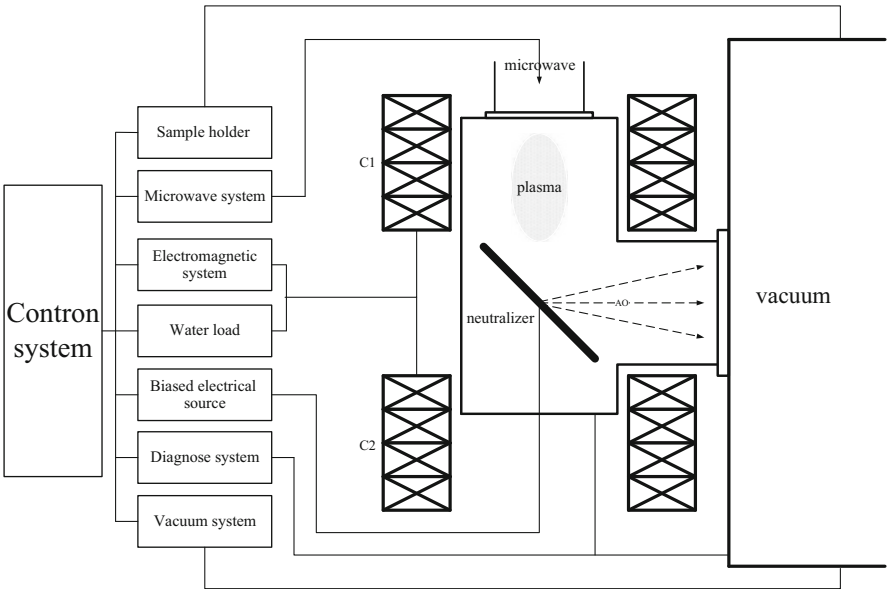

Fig. 3 Schematic diagram of atomic oxygen simulation facility

Fig. 4 Photo of atomic oxygen simulation facility

sensors are mounted upon a sample holder. The effective fluence of the AO exposure facility is based on the mass loss of the witness samples Kapton H (Figs. 3 and 4).

Test Parameters

The AO flux at different distance from the neutralizer is calibrated before the test. The test parameters are determined from the calibration results. The AO fluence is 10^{20}atoms/cm^2 and its flux is 10^{15}atoms/(cm$^2 \cdot$ s). The test samples include the Osmium resistance sensor and three types of materials AO effect sensor. The sample temperature during the test is below 40 °C.

Results of Calibration Test

The Osmium Resistance Sensor Calibration Test

Test Principle

The resistive film is eroded in the AO environment. The ratio of the resistance after erosion to the original resistance of the film can be express as following:

$$\frac{R_0}{R} = \frac{\rho\frac{L}{A_0}}{\rho\frac{L}{A}} \tag{1}$$

Where:

R_0 Original resistance, Ω
R Resistance after erosion, Ω
A_0 Original section, cm^2
A Section after erosion, cm^2
L Length of the film resistive path, cm
ρ Resistivity of film, Ω cm

It is assumed that the cross section of the resistive path is a rectangle and the resistivity is constant, then Eq. (1) can be changed as follows:

$$\frac{R_0}{R} = \frac{A}{A_0} = \frac{\tau W}{\tau_0 W} = \frac{\tau}{\tau_0} \tag{2}$$

Where:

τ_0 Original thickness, cm
τ Thickness after erosion, cm
W The width of the resistive path, cm

By estimating the eroded volume from:

$$\Delta V = WL\left(\tau_0 - \frac{R_0\tau_0}{R}\right) \tag{3}$$

Where $\Delta V =$ Volume change due to erosion (cm^3). It can be shown that the erosion yield is given by:

$$Y = \frac{\Delta V}{FWL} \tag{4}$$

Where F is AO fluence ($atoms/cm^2$) and Y is the erosion yield ($cm^3/atom$).

From the above equations, we can express the AO fluence as that:

$$F = -\frac{\tau_0}{Y}\frac{R_0}{R} + \frac{\tau_0}{Y} \tag{5}$$

The AO fluence can be expressed from flux as:

$$F = ft \tag{6}$$

Where f is AO flux ($atoms/cm^2/s$) and t is exposure time(s).

Assuming the flux and erosion yield remains constant throughout the exposure, normalized resistance can be plotted against time as a straight line, as shown in Fig. 5 below. From Eq. (5), it is shown that the sensitivity and life of the resistance sensor is correlated with the ratio of original thickness and erosion yield [5].

AO Exposure Test Results of the Resistance Sensor

The Osmium thickness is 300 nm. After $1 \times 10^{20} atoms/cm^2$ AO exposure, the normalized resistance curve against time is shown in Fig. 5. From this figure it can be found that R_0/R is linearity to time approximately and its response is accorded with the ideal sensor (Fig. 6).

AO Effect Sensors Calibration Test

Silver-based sensor can be also used for AO flux measurements. A space material film is deposited on the resistance film of above-mentioned sensor. During exposure in AO environment, the resistance of the sensor is constant since it is protected from AO by the deposited on top of it space material film. When the space material film is eroded away completely, the resistance film would be oxidized quickly and its electrical resistance would change. Then, AO exposure fluence could be determined from the time it took to erode the sample material film and the material AO erosion

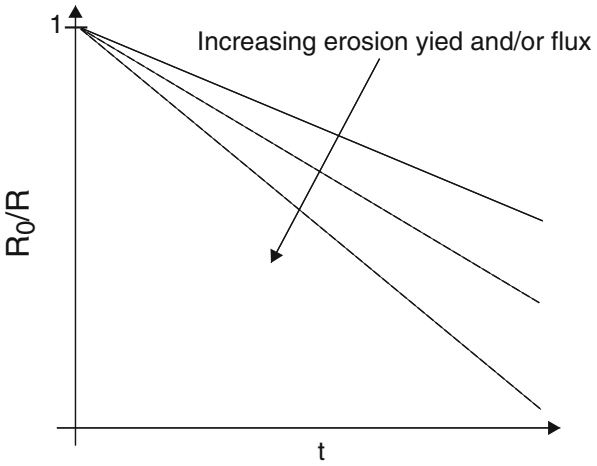

Fig. 5 Ideal sensor response

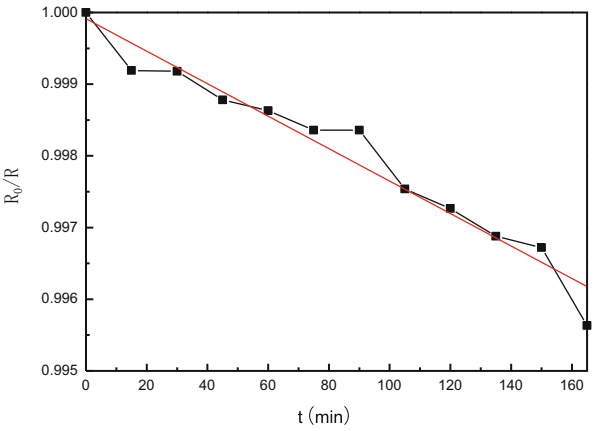

Fig. 6 The Osmium film resistance change vs. exposure time

Table 2 Results of sensor's exposure to AO

Sample	Exposure fluence ($\times 10^{19}$ atoms/cm^2)	Erosion yield measurements (10^{-24}cm^3/at)	Erosion yield flight results (10^{-24}cm^3/at)
Kapton/Ag	6.8	4.3	3
polyethylene /Ag	13	2.7	(3.3–3.7)
Epoxy/Ag	0.76	2.1	1.7

rate could be computed easily. The results of AO effect sensors calibration test are listed in Table 2. It is clear that the measurement of AO erosion yield is the same magnitude as the flight test results.

Discussion of Test Results

It is shown that the Osmium film sensors have a linear response to low fluence AO exposure. The stability of Osmium film sensors should be verified in high fluence AO exposure experiments. The calibration tests of Ag film sensors demonstrated that their response is in accord with the flight test results.

Summary

The study of Os resistance sensor and Ag resistance AO effect sensors is performed in BISEE. The preparation processes of these two types of sensors are investigated and the prototype device of resistance AO detector is developed. The ground simulation test showed that the results of Os resistance sensor and Ag resistance AO effect sensors are well in accord with the ideal values. In the future our efforts will focus on the further engineering implementation of sensor preparation.

References

1. Ryden KA, Fearn DG, Alexander SH (1993) Update on space technology research vehicle. In: Proceedings of the Conference Small-satellite technology and applications III, Orlando, FL, April 14 and 15, 1993, ed. Bellingham, WA, Society of Photo-Optical Instrumentation Engineers (SPIE-1940), pp 194–205
2. Galica GE, Green BD, Joshi PB, Nakamura T, Kobayashi AM (2006) Atomic oxygen monitor based on carbon actinometers. Proceedings of the 10th ISMSE & the 8th ICPMSE, Collioure, France, 19–23 June 2006
3. Osborne JJ, Roberts GT, Chambers AR, Gabriel SB (1999) Initial results from ground-based testing of an atomic oxygen sensor designed for use in Earth orbit. Rev Instrum 70 (5):2500–2506
4. Harris LL, Chamber AR (1997) A low cost microsatellite instrument for the in situ measurement of orbital atomic oxygen effects. Rev Instrum G8(8):3220–3228
5. White CB, Rao J, Roberts GT (2003) The development of carbon-based sensors for the measurement of atomic oxygen. Proceedings of the 9th International symposium on materials in a space environment Noordwijk, The Netherlands, 16–20 June 2003

Effects of Thermal-Mechanical Cycling on Tension Properties of AZ31 Magnesium Alloy

Shangli Dong, Hao Wang, Libo Fu, Gang Lv, and Shiyu He

Abstract Effects of thermal-mechanical cycling on tension properties of an extruded AZ31 alloy are studied. The results show that the strength of the examined AZ31 alloy samples varies with thermal cycles, increasing from non-cycle to 50 cycles and then decreasing to 380 cycles. The plastic elongation exhibits out of steps tendency which has maximum at 100 cycles and decreases after that. Microstructure development indicates that dislocation and twinning induced by accumulated internal stress vary with thermal cycling. And the tension fracture surface of the thermal cycled samples shows that fracture of cycled samples transits from cleavages and facets into dimple and second phase crack dominated feature. It is believed that dislocation and twinning evolution during thermal cycling are responsible for the observed tension deformation and fracture behaviors.

Keywords Thermal-mechanical cycling • Magnesium alloy • Mechanical property • Tension

Introduction

Magnesium alloys are widely used in transportation industry and aero-industry due to the excellent properties such as low density, high specific strength, fatigue strength and good cutting performance [1–3]. Numerous studies about the deformation mechanism of magnesium single crystal and polycrystalline have been established in the past half century [4–8].

Compared to other light metals such as aluminum and titanium, the deformation complexity, steming from dislocation and twinning interaction under temperature, texture and strain rate influences, prevents expanding the use of magnesium alloys. The lack of suitable slip system is the main reason for its poor plastic capability in room temperature (RT) and low temperature, but magnesium alloy can be ductile at higher temperature and moderate strain rate [6, 9].

S. Dong • H. Wang (✉) • L. Fu • G. Lv • S. He
School of Materials Science and Engineering, Harbin Institute of Technology, Harbin, China
e-mail: wewhl7r@gmail.com

J. Kleiman (ed.), *Protection of Materials and Structures from the Space Environment*, Astrophysics and Space Science Proceedings 47,
DOI 10.1007/978-3-319-19309-0_41

Basal dislocation in magnesium has the smallest critical resolved shear stress (CRSS) and the greatest mobility under loading, but limited contribution to deformation compatibility especially in c-lattice direction [10]. Prismatic **a** dislocation is often activated in tension along rolled direction in rolled sheet which is also short of supporting **c**-direction deformation [7, 9]. Pyramidal **c** + **a** dislocation with highest CRSS gains more attention with the satisfaction in Taylor criterion of free deformation, and have been considered as important source to maintain deformation from 77 K to 300 K [6, 9, 11].

On the other hand, deformation twinning in magnesium is also taken as additional source to support deformation with the effect that reorient hard slip plane to easy one. And, twinning as sub-grain structure can reduce dislocation slip free path length to cause stress increasing in Hall-Petch-like way [12, 13]. Under cycling loading condition, twinning and de-twinning would lead to Bauschinger effect [14]. There are two kinds of deformation twin in magnesium, tension twin and compression twin, which are activated by elongation and contraction stress along c-axis with different CRSS. Therefore, different strain path would show different mechanical behavior such as tension-compression asymmetry [15–17].

For service on spacecraft, thermal cycling effect on the loading parts is regarded as the reason for early failure and deformation misfits of structure parts. Temperature variation of 240 K between exposing in sun and in the shadow of the earth may cause thermal stress discrepancy between matrix and additive of composite material [18], and ageing effect to alloy microstructure change. Experiments on composite material and alloy have been done considerably [19, 20]. But thermal mechanical loading on magnesium is far less understood. For polycrystalline magnesium, the internal stress rising from temperature cycling and external loading has direct influence on microstructure change and would vary subsequent deformation behavior to impact the service life.

In this paper, extruded AZ31 alloy was chosen to perform tension test in order to reveal thermal mechanical loading effects on mechanical properties. By optical observation, microstructure changes after different cycling were examined.

Materials and Experiments

A commercial extruded AZ31 alloy was used to perform thermal mechanical loading and tension test, with average grain size of 15 μm and extruded fiber texture that basal plane parallel to extrusion direction (ED). The specimens were cut along ED and annealed at 673 K for 4 h to remove twinning and homogenize microstructure. The set-up of thermal mechanical loading is shown in Fig. 1. Direct current was used to heat sample during heating stage, and liquid nitrogen was used for cooling. Temperature data were acquiring during whole thermal cycling by the sensors fixed in three positions, and process in LabView programmer to control heating and cooling parts.

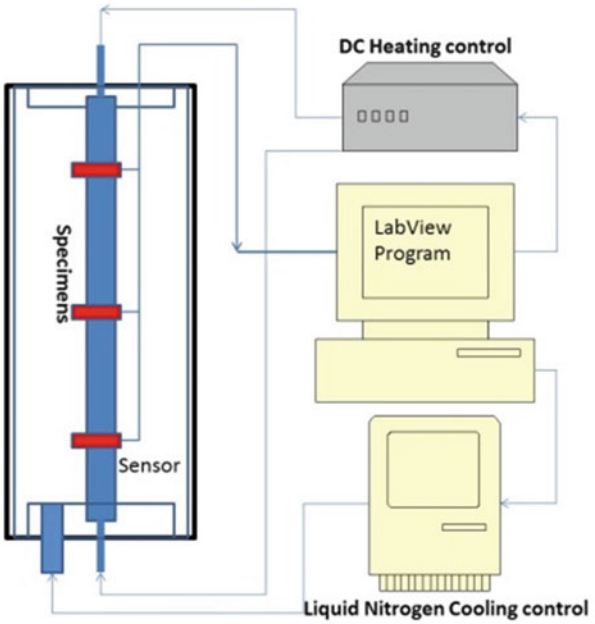

Fig. 1 Set up of thermal mechanical loading experiment

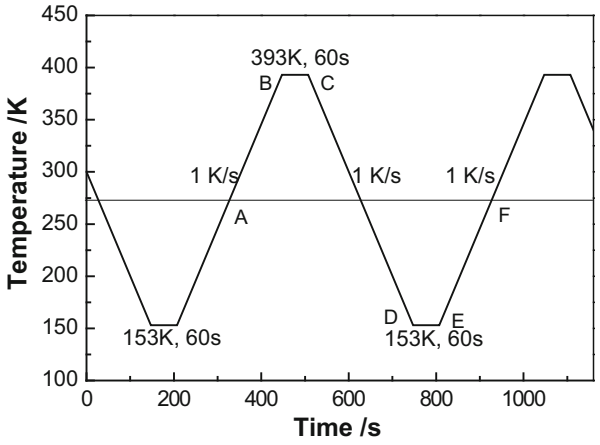

Fig. 2 Thermal cycling procedure. The curve between letters A and F indicates a full cycle

Thermal procedure is shown in Fig. 2, which illustrates four stages of one cycle, heating stage and cooling stage with temperature change rate of 1 K/s and two temperature stabilization stages with dwell time of 60 s each.

The loading part took 120 Kg weight as external stress on the specimens during the thermal cycling. The microstructures of cycled specimens were polished, etched with picric acid ethanol solution, and then observed with Olympus GX5 optical microscope.

After thermal mechanical cycling, tension test was carried out on universal test system under the deformation rate of 1 mm/min. The fracture surfaces were examined by HITACHI S-4700 scan electron microscope.

Results

Microstructure of Cycled AZ31 Alloy

The specimens were examined after different cycling times using optical microscopy to evaluate cycling effects on grain size and twinning nucleation, with the observations shown in Fig. 3.

The grain sizes of all cycled specimens were calculated and are shown in Fig. 4. With cycling time increasing, the tendency of grain size change has a trend of increasing from 17 μm to 31 μm. The grain enlargement can be divided into three stages, i.e. during 10–20 cycles, during 20–100 cycles and during 100–380 cycles. In the first and the last stage, grain size changes little with cycled times, but changes dramatically in the second stage. Grain growth takes place during the period of 20–100 cycles.

Besides the grain size change, twinning nucleation was also noticed with the number of cycles increasing. The initial grain structure, before cycling started, did not have twins, due to the anneal process. However, with number of cycles increasing, the twinning process increased, from a single twin in one grain to multiple twinning in one grain. The morphology of twinning shown in the cycled grain is consistent with contraction twins that have thin lamellar. And during the loading thermal coupling, the stress along loading direction would accumulate and activate contraction twin. The increase in twin volume fraction with number of cycles is indicative that during thermal cycling and loading the internal stress is enough to activate twinning and thus mechanical properties would vary with cycling times.

Tension Results of Cycled Magnesium

Tension tests at deformation rate of 1 mm/min at room temperature were carried out on the cycled specimens. Tension test results are shown in Fig. 5a in true strain—true stress format. Tension properties versus the number of cycles are shown in Fig. 5b. The insert in Fig. 5a presents a magnified portion of the true strain graph, between 0.015 and 0.035, to show the effect of cycling on the yield initiation behavior. The yield stress increases to maximum after 100 cycles to 179 MPa and ultimate strength has the peak value of 271 MPa at 50 cycles. Elongation is increasing abruptly at 100 cycles. The general tendency in tension properties

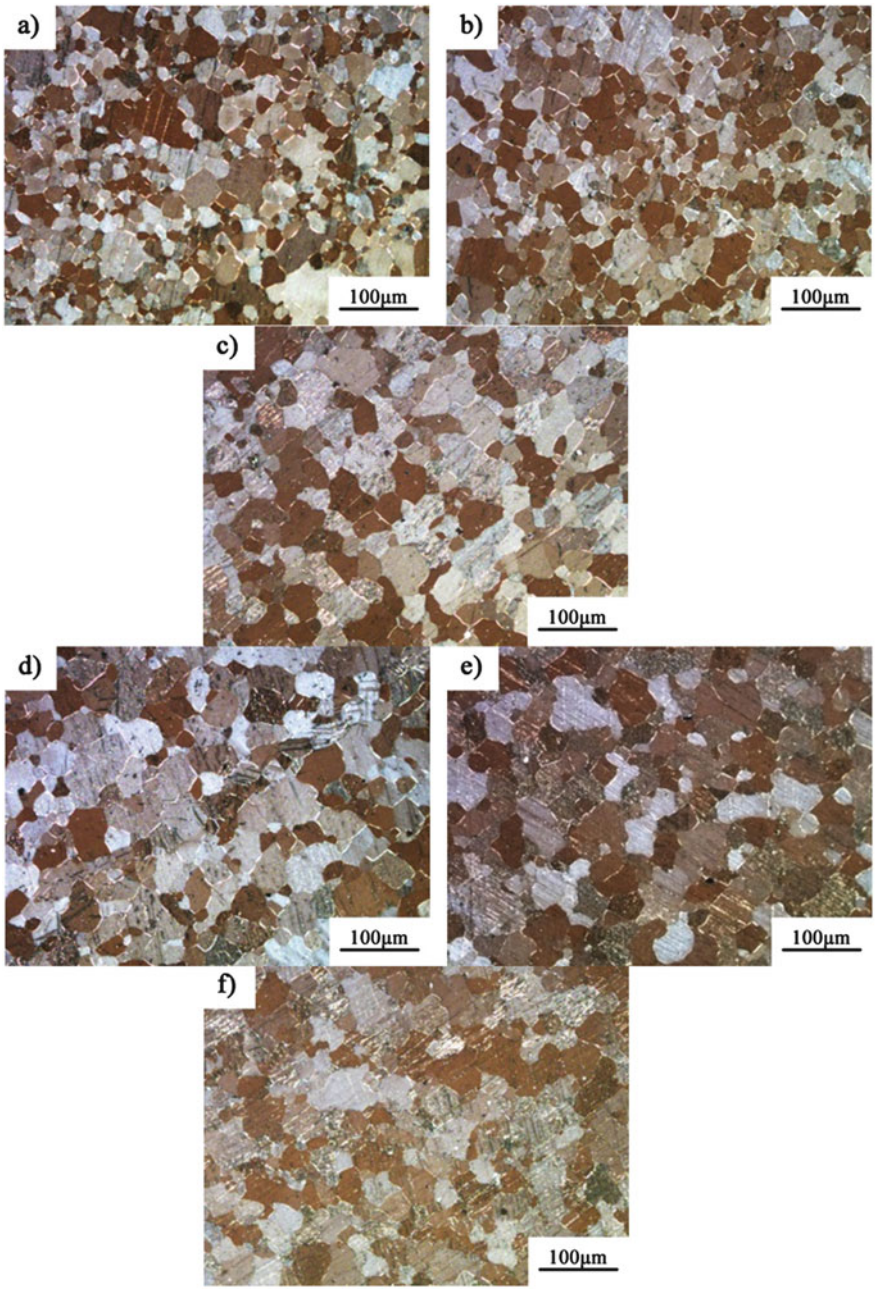

Fig. 3 Optical microstructure observation of specimens cycled for different times. (**a**) 10 cycles; (**b**) 20 cycles; (**c**) 50 cycles; (**d**) 100 cycles; (**e**) 200 cycles; (**f**) 380 cycles

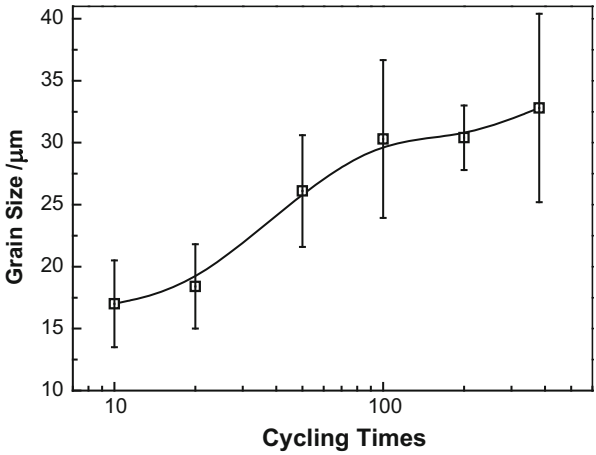

Fig. 4 Average grain size variation with number of cycles

changes is, firstly, to increase with cycled time and then to decrease after reaching the peak value, at around 50–100 cycles.

Since microstructure changed with cycling time, the yield initiation behavior varies accordingly, as shown in the insert of Fig. 5a. The yield stress increases from 170 MPa after 10 cycles to 179 MPa after 100 cycles and then decreases to 171 MPa after 380 cycles. The hardening behavior after yield also differs, as the slops of true strain—true strain change with different cycled times. Hardening rates ($\theta = d\sigma/d\varepsilon$) of test specimen after different cycling times are calculated and shown in Fig. 6. Two regions, with respect to the initial microstructure, that are formed after yielding to 0.035 strain and, later, after 0.035 strain, i.e. can be distinguished, with the former one affected by the initial microstructure and the latter one not. During the initial microstructure affect region, hardening rates at 0.02 strain were calculated. As can be seen from Fig. 6b, the hardening behavior changes, with two peaks present at 50 and 200 cycles, respectively. When strain is over 0.035, a uniform behavior in hardening is exhibited.

Fractographs

According to optical observation of specimens after different number of cycles, initial microstructures vary from twin-free to twinned, which would cause different fracture behavior. The fractographs corresponding to specimens after 10, 20, 50, 100, 200 and 380 cycles were analyzed using scanning electron microscopy at 500 times magnification and are shown in Figs. 7a–f. The dominating features in the fractographs are cleavages and facets, with dimples present on a small scale, which presents localized ductile and integral brittle fracture patterns. Figure 7a shows a large number of cleavages and facets separated by shallow dimples. The facets have a special lattice orientation, and, in the surface of the facets, deformation traces can

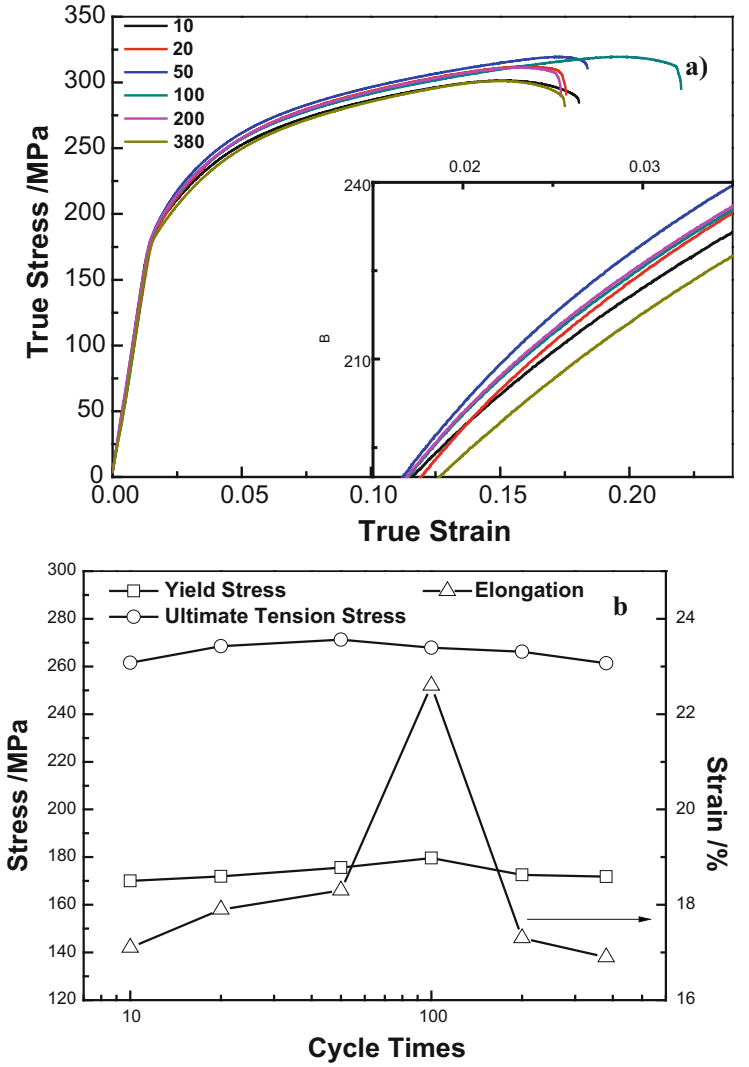

Fig. 5 (**a**) True strain-true stress curve of different cycled specimens, amplified insert graph shows strain of 0.015–0.035. (**b**) Tension properties variation with cycling times

be found, which suggests that the effect of suppressing the non-basal slip left straightforward deformation mode. Copious dimples segregated between cleavages prove that the extrude AZ31 alloy has better localized ductility. The facets formed at the fracture surface would also come from twinning effects that sudden oriented lattice of grain releases the stress concentration by localized plastic deformation, and dimples are formed at these localized sites with crack grown along twinning planes. With increasing cycled times, fracture surfaces have more cleavages, facets

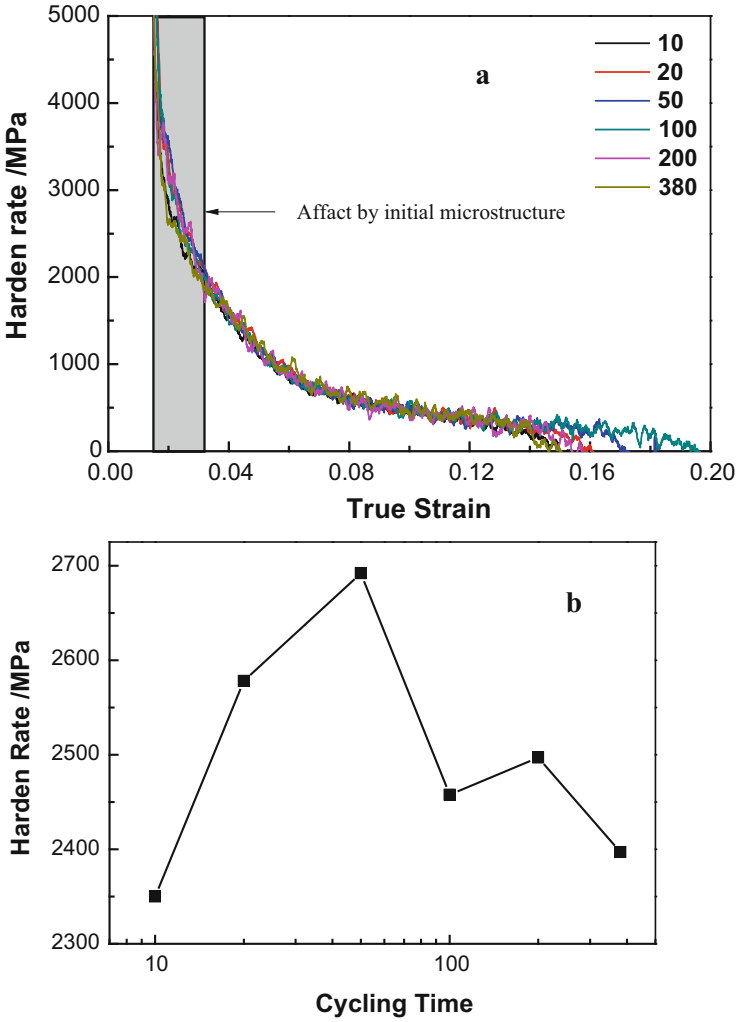

Fig. 6 Hardening behavior of specimens in cycling experiments. (**a**) Hardening rates in different cycled specimens. (**b**) Hardening rate at 0.02 true strain variation with cycled times

and steps until 100 cycles, after which more dimples are presented with secondary phase at the bottom. This tendency is consistent with mechanical properties change. Fractographs of test specimens reveal quite many features of inter-granular morphology as marked in Fig. 7c, but not in the same proportions. As cycling times increase, the effect of thermal ageing on the microstructure appears, with secondary phase formed as shown on the postmortem fractographs. After 50 cycles, dimples (in Fig. 7 d, e, f) on the fracture surface have secondary phase in the center. The microcracks induced by the secondary phase contribute to the origin of voids and crack coalescence. This transition indicates dominated fracture mechanism change

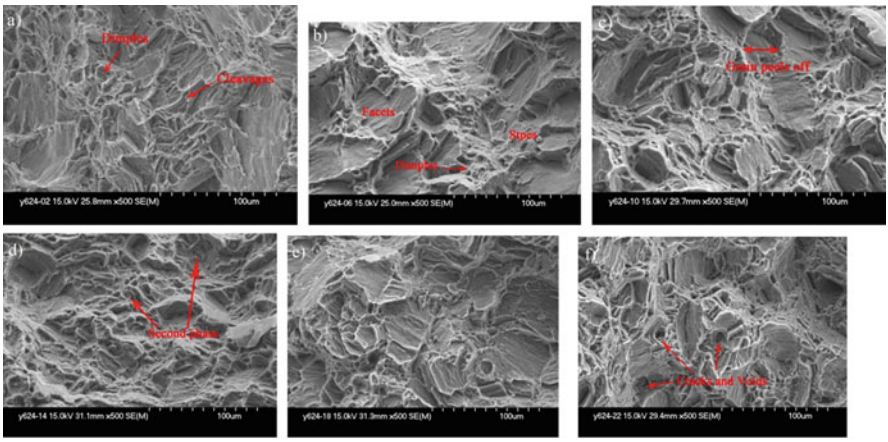

Fig. 7 Fractographs of fracture surfaces of differently cycled specimens. (**a**) after 10 cycles; (**b**) after 20 cycles; (**c**) after 50 cycles; (**d**) after 100 cycles; (**e**) after 200 cycles; (**f**) after 380 cycles

from twin-induced dominated fracture to micro-void coalescence dominated fracture.

Discussion

In this study, the microstructure evolution in specimens after thermal mechanical loading testing, involved dislocation density/structure changes, thermal ageing and twinning formation. The effects of thermal mechanical loading can be reflected on the initiation yielding behavior and fracture behavior, and discussed from the perspective of dislocation and twinning changes. The thermal stress induced by the heating-cooling cycles acts as asymmetrical cycling stress adding up to the constant loading that would cause fatigue-like damage such as microcracks generation from weak phase boundaries and twinning-detwinning progress. Besides, thermal effects combined with external loading on the microstructure would cause ageing and grain growth.

For dislocation related yielding, yield stress can be written as function of dislocation density as shown in Eq. (1) [21],

$$\tau_y = \tau_0 + \tau_{\text{forest}}\left(\sqrt{\rho_{\text{forest}}}\right) + \tau_{\text{deb}}\left(\sqrt{\rho_{\text{deb}}}\right) + \tau_{\text{HP}}\left(\frac{1}{\sqrt{d_{\text{eff}}}}\right) \quad (1)$$

where τ_y is the yield stress, τ_0 is a materials constant for the starting stress for dislocation movement (or the resistance of the lattice to dislocation motion), ρ_{forest} and ρ_{deb} are density of forest dislocation and dislocation debris. τ_{forest} and τ_{deb} is

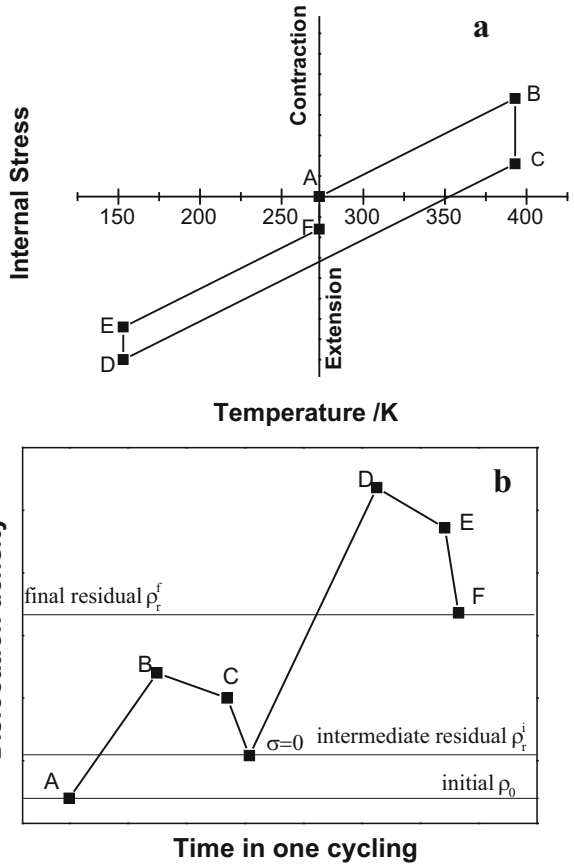

Fig. 8 (**a**) Schematic diagram of stress change during a full cycling period. (**b**) Schematic diagram of dislocation density change during a whole cycling

stress related to forest dislocation and dislocation debris, d_{eff} is the effective grain size altered with dislocation structure and twinning.

During thermal mechanical loading, the stress concentration would increase after each cycle, as illustrated in Fig. 8a. During the cycling sequence A–F shown in Fig. 2, the stress concentration would increase during AB heating, for the reason of deformation compatibility among grains with different orientation. To coordinate the discrepancy of each grain's expansion, dislocations are formed at the stress concentration sites. And the dislocation density increases with an increase in cycling temperature during the AB heating part. When specimens are going through the dwell time BC, dislocation annihilate under assistance of stress and temperature, causing a decrease in stress, leaving behind dislocations with the same Burger vector (forest dislocation, ρ_{forest}) and dislocation debris (ρ_{deb}) that are immobilized. Dislocation annihilation would continue until the stress reduces to the point that it is not sufficient to maintain this progress. During the cooling part, dislocation density will reach the intermediate residual density values that means when loading is off, dislocation density would not change. The residual dislocations would exist in the

form of a forest structure, sub-cell and debris. The stress during the cooling part CD decreases to zero and increases reversely to cause stress state convert from contraction to extension at the stress concentration sites. Dislocation density increases as well to mediate strain compatibility. Compared to the high temperature dwell situation, the dislocation annihilation is much less at 153 K dwell time, neither does the stress decrease. After a full cycling period until reaching the F point, stress in the concentration sites would have extension pattern $\Delta\sigma_e$ and residual dislocation density increases to final residual density ρ_r^f.

For a certain times cycling, concentration stress $\Delta\sigma$ is equal to $N\Delta\sigma_e$, and dislocation density is $N\rho_r^f$. The micro-structure will alter when stress and dislocation density reach critical stress and density denoted as σ_c^i and ρ_c^i to form sub-cell structure, support grain growth and twin, where i represents sub cell structure (sc), grain growth (g) and twinning (t).

Combined with optical microscope observation, the correlation of cycling times and microstructure evolution can be illustrated as below:

N(≤20): During these stage, dislocation density accumulate with cycling times as expressed in $N\rho_r^f$. The increasing dislocation density has two parts contribution on both ρ_{forest} and ρ_{deb}, which are increasements in portion of forest dislocation and dislocation debris. The overall effects of cycling times on this stage is the accumulation of dislocation in the form of forest dislocation and debris that forest dislocation would increase the yield stress after and debris has contribution on hardening. The influence of forest dislocation and dislocation debris on initial harden rate of yielding can be expressed in Eq. (2):

$$\theta_{ini} = \frac{d\sigma_\rho}{d\varepsilon}\Big|_{\varepsilon=0.002} = \frac{\partial\sigma_\rho}{\partial\rho_{forest}} * \frac{d\rho_{forest}}{d\varepsilon}\Big|_{\varepsilon=0.002} + \frac{\partial\sigma_\rho}{\partial\rho_{deb}} * \frac{d\rho_{deb}}{d\varepsilon}\Big|_{\varepsilon=0.002} \quad (2)$$

The contribution of forest dislocation and debris dislocation vary with their density variation on stress. From the calculation results of Fig. 6b, the initiation hardening rate increase solely with cycling times in this stage. But the yielding stress of these stage changes indicate that dislocation density has limited effect on stress at this stage due to the localized generation in stress concentration sites near the grain boundary that barely change the dislocation free mean path as known in d_{eff}. While dislocation density reaching to ρ_c^s and stress reaching to σ_c^s, sub-cell structure can be formed localized near the grain boundary which are essential to next steps grain growth.

N(20 ~ 100): Microstructure evolution during this stage has two remarkable features, grain growth and twinning nucleation. These two processes have a common effect of reducing the density of dislocation in the way of dislocation annihilation under the thermal annealing effect and releasing stress concentration by twins rather than dislocation generation. Once the sub-cell structure of dislocation formed near the grain boundary that dislocation density reach to ρ_c^g, thermal cycling at the elevated temperature range with external and internal stress helping that σ_c^g is reached, recovery would take place that dislocation annihilate and small size

grain cluster intend to converge into bigger size grain. This is the reason that initial hardening rate decreases dramatically after 50 times cycled according to Eq. (2). Meanwhile, the large size grain intends to twin within the grain where stress concentration reaches to σ_c^t, because large size grain facilitates twinning nucleation compared to small size grain. Yield stress during this stage still keeps increasing and reaches to the maxima of all test results. Since dislocation decreasing, the yield stress of Eq. (1) may dominate by the twin's behavior in the form of Hall-Petch-like equation as in Eq. (3),

$$\tau = \tau_0 + k d_{eff}^{-1/2} \tag{3}$$

where k is the strengthening coefficient (a constant unique to each material). The newly formed twin in grain reduces d_{eff}, and the yield stress increases accordingly.

N(>100): When cycling times is over 100 times, the microstructure evolution is dominated by the twinning. In this stage twinning continue nucleating and will be forming net structure as illustrated in Fig. 9.

As we see in Fig. 9, at the beginning of this stage (cycled 100 times), specimen only has single twin nucleated within some grain, these first generation twins often

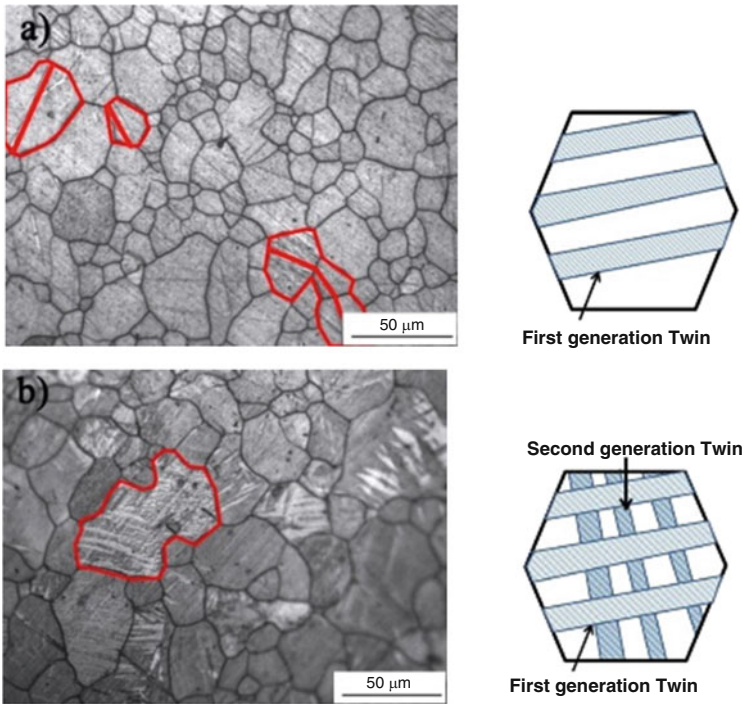

Fig. 9 Optical microscopy analysis of specimens after 100 cycles (**a**) and 380 cycles (**b**) with schematic figures of first generation and second generation twins. The *red* zones in the figures indicate the twinned grains

keep their thin morphology across the entire grain. After 380 times cycled, specimen has multiple twins within a single grain, that second generation twin insert with first generation twin to form net twinning structure as shown in Fig 9b. With the help of twinning, stress concentration releasing would no longer need generating dislocation, the density of forest dislocation and dislocation debris stop increasing. On the contrary, due to the twinning growth, dislocation debris immobilized with **c** direction character is consumed to participating twin boundary expanding. But the harden effect of twinning is still in playing until the volume of twinning is reaching its maximum in the grain. So the initial harden rate has a peak in the range of 100–380 times cycling.

The effects of thermal mechanical loading impacts the evolution of microstructure and further more influences the tension properties later. Before the twinning formation, the fracture surface observation shows the dominated feature of cleavage and facets as in Fig. 7 a–c, dislocation slip is the mainly source of deformation especially the basal slip. The cleavages and facets with uniform deformation trace indicate the single deformation mechanism is activated and non-basal dislocation deformation is suppressed. After twinning formed, cleavages and facets in the fracture surface are replaced by shallow dimples partially as shown in Fig. 7d, and the elongations of tension test increase dramatically. By introducing twinning, the plasticity of extrude AZ31 alloy is improved. The dimples of the fracture are most localized which indicate the role of local softening by the twins for its reorientation of hard slip system. The condition of non-basal slip is also improved when the tension test was carried on to maintain the plasticity compatibility. When the twinning net structure formed, tension loading will enhance the stress concentration to the intersection sites to nucleate micro-cracks and cause failure.

The ageing effect of thermal mechanical loading would also incline to promote second phase to nucleation at grain boundary, which are shown in Fig. 7 d–e. The incompatibility of two phase would also lead to the early failure due to the cracks formed in the phase boundary or by the second phase splintering.

Conclusions

The effect of thermal mechanical loading with cycling times on tension properties and microstructure of an extruded AZ31 magnesium alloy are evaluated in current study, and following conclusions are obtained:

(1) The tension yielding stress and ultimate strength increase with increasing cycling times first and drop after reaching to a maximum. The fracture strain also increases firstly and then decreases with increasing cycling times.
(2) The microstructure development with thermal mechanical loading cycling is a dynamic process, including sub-cell dislocation structure formation, grain growth and twinning formation in this sequence with increasing cycling times.

(3) The discrepancy in tension yielding of different cycled specimen is the result of microstructure variation during the cycling. Up to 100 cycles, the dominating mechanism is controlled by dislocation behavior as sub-cell structure formation and grain growth. After 100 cycles, the mechanism inclines to be controlled by twinning.
(4) Fracture behavior of AZ31 magnesium alloy also inherits the microstructure discrepancy due to thermal cycling, and varies from cleavages and facets into dimple and second phase crack dominated feature with increasing cycling cycles.

Acknowledgements The support from the Key Laboratory Opening Funding of National Key Lab for Space Materials Behavior and Evaluation as well as from the National Defense Basic Research Foundation is greatly appreciated.

References

1. Lou XL, Li M, Boger RK, Agnew SR, Wagoner RH (2007) Int J Plast 23:44
2. Máthis K, Trojanová Z, Lukáč P (2002) Mater Sci Eng A 324:141
3. Wagoner RH, Lou XY, Li M, Agnew SR (2006) J Mater Process Technol 177:483
4. Reed-Hill RE, Robertson WD (1957) Trans TMS-AIME 220:496
5. Lavrentev FF, Salita OP, Luká P (1982) Acta Univ Carolinae Mat Phys 23:33
6. Obara T, Yoshinga H, Morozumi S (1973) Acta Metall 21:845
7. Tonda H, Ando S (2002) Metall Mater Trans A 33:831
8. Sulkowski B, Mikulowski B (2012) Acta Phys Pol A 122:528
9. Agnew SR, Duygulu O (2005) Int J Plast 21:1161
10. Reed-Hill RE, Abbaschian R (1994) Physical metallurgy principles, 3rd edn. PWS Publishing, Boston, MA
11. Bhattacharya B (2006) PhD Thesis, McMaster University
12. Knezevic M, Levinsom A, Harris R, Mishra RK, Doherty RD, Kalidindi SR (2010) Acta Mater 58:6230
13. Ma Q, El Kadiri H, Oppedal AL, Baird JC, Li B, Horstemeyer MF, Vogel SC (2012) Int J Plast 29:60
14. Hama T, Kitamura N, Takuda H (2013) Mater Sci Eng A583:232
15. Lou XY, Li M, Boger RK, Agnew SR, Wagoner RH (2007) Int J Plast 23:44
16. Knezevic M, Levinson A, Harris R, Mishra RK, Doherty RD, Kalidindi SR (2010) Acta Mater 58:623
17. Yin SM, Wang CH, Diao YD, Wu SD, Li SX (2011) J Mater Sci Technol 27:29
18. Mei H, Cheng L, Zhang L (2006) Scripta Mater 54:163
19. Fukunaga H, Chou TW, Peters P, Schulte K (1984) J Comp Mater 18:339
20. Nairn JA (1989) J Comp Mater 23:1106
21. Beyerlein IJ, Tomé CN (2008) Int J Plast 24:867

Self-Assembly Structures in $ZnFe_xMn_{(2-x)}O_4$ Ceramics and Effect on Thermal Properties

Bin Wang, Jilong Dai, and Chaobo Liu

Abstract Thermoelectric technology has been regarded as a perfect energy source on spacecraft thanks to its advantages such as no moving part, zero emission and high stability in harsh environment. $ZnFe_xMn_{(2-x)}O_4$ ceramics were fabricated and self-assembly structures were observed in the sample of some compositions, which may be of benefit to the thermoelectric performance. In this paper, the applications of thermoelectric technology on spacecraft were briefly reviewed. The synthesis method and crystal structures of $ZnFe_xMn_{(2-x)}O_4$ ceramics were also introduced. Furthermore, the phase transitions in the system were carefully studied by SEM technique. Finally, the heat capacities and thermal diffusivities, which were key parameters of thermoelectric performance, were measured.

Keywords Thermoelectricity • Ceramics • Phase separation • XRD • SEM • Thermal properties

Introduction

Thanks to the developments in nanotechnology and advanced material preparation techniques, thermoelectric technology experienced a boom in the last 20 years. By far, thermoelectric devices have been commercially used as cooler, waste heat generator, aircraft power supplier and so on [1–42]. In 2006, the size of thermoelectric market was over $200 million and customers were widely spread in areas such as consumer marketing, telecom, automotive, etc [2].

Thermoelectric technology has many advantages such as no moving parts, zero emission, quiet and high stability in harsh environment. However, there is a fatal disadvantage, low efficiency, which is a big barrier for extensive application. As a result, most researchers in this field are struggling to enhance the thermoelectric figure of merit (zT) which is used to evaluate the quality of the material.

B. Wang (✉) • J. Dai • C. Liu
Beijing Institute of Spacecraft Environment Engineering, Beijing, China
e-mail: wangbin1983@hotmail.com

J. Kleiman (ed.), *Protection of Materials and Structures from the Space Environment*, Astrophysics and Space Science Proceedings 47,
DOI 10.1007/978-3-319-19309-0_42

The peak zT values of different materials emerge at different temperatures that opens up a problem of temperature adaptability. Since the traditional alloy thermoelectric materials usually cannot endure a temperature higher than 800 °C, oxide materials are developed for thermoelectric applications at high temperature. Furthermore, the top zT value of oxide materials has been about 1 which is competitive [32].

However, no matter what kinds of materials are being studied, the key point could be consistent. Disalvo [10] theoretically predicted the existence of a new material, whose zT value can be over 4, and he pointed out that the material should be of particular structure to lower the lattice thermal conductivity, hopefully without increasing the resistivity. This description was in agreement with the candidate material described by Slack [11], a narrow-bandgap semiconductor with high-mobility carriers which he called a "phonon glass and electron crystal". Furthermore, Nolas [5] summarized the recent developments in bulk thermoelectric materials such as "rattlers" in cage structures and mixed-lattice atoms and got a conclusion that the ability to manipulate the thermal conductivity was essential point to get a remarkable thermoelectric property.

Experiment

The samples of $ZnFe_xMn_{2-x}O_4$ were produced by a solid-state synthesis method. The mixed powder was ball milled and pressed into compacts of 3–5 g. The compacts were sintered at 1300 °C for 4 h and then cooled down at two cooling rates (either 180 °C/h or 6 °C/h). The flow chart of preparation process is shown in Fig. 1.

According to the phase diagram shown in Fig. 2, $ZnFe_xMn_{(2-x)}O_4$ ceramics are not single phase when $0.2 < x < 1.4$. To research the structural transformation and properties of the whole system, five kinds of samples of compositions in different regions were prepared. Two compositions ($x = 1.6$, 1.4) were in the single phase region and three others were in the 2-phase region. In addition, $ZnFe_2O_4$ and $ZnMn_2O_4$ were also prepared.

XRD Data

Based on the information from $ZnFe_2O_4$ and $ZnMn_2O_4$, samples were indexed with their relevant space group, respectively. The patterns of two Fe-rich samples ($x = 1.6$, $x = 1.4$) were indexed with an Fd-3 m space group like $ZnFe_2O_4$ as shown in Fig. 3.

According to the patterns, no matter with which cooling rate, the Fe-rich samples ($ZnFe_{1.6}Mn_{0.4}O_4$, $ZnFe_{1.4}Mn_{0.6}O_4$) are of a cubic structure similar to $ZnFe_2O_4$ in general. However, little peak shoulders can be detected on the (3 1 1), (4 0 0) and (5 1 1) peaks in $ZnFe_{1.4}Mn_{0.6}O_4$ which are more pronounced in the low cooling rate.

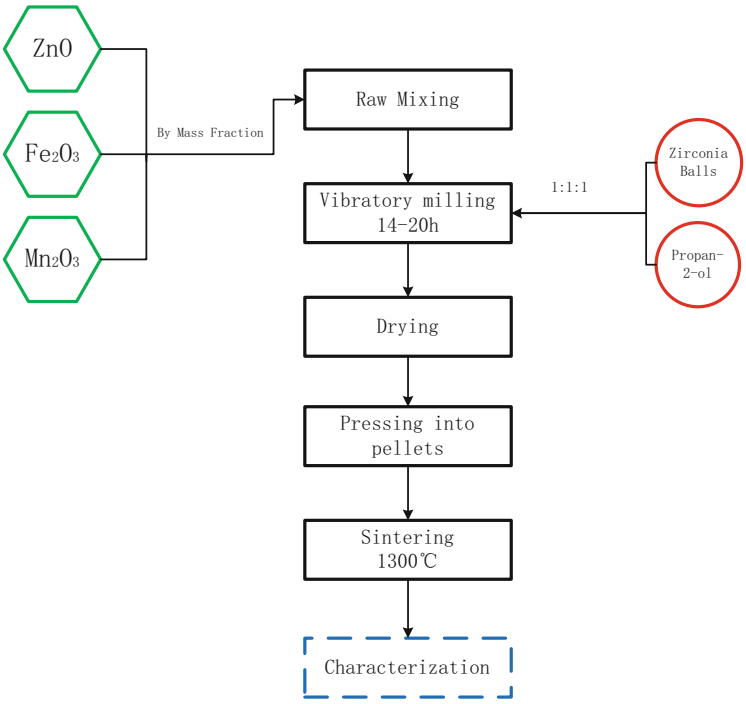

Fig. 1 Flow chart illustrating the process of sample preparation

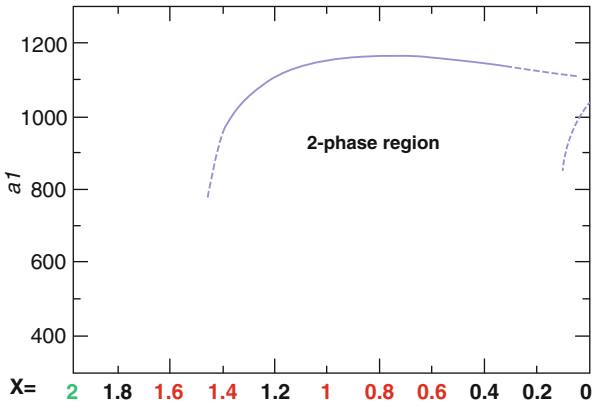

Fig. 2 Phase diagram of $ZnFe_xMn_{(2-x)}O_4$ system [42]

Considering the phase diagram, because composition of $x = 1.4$ has been on the boundary of two different phases, the peak splitting in $ZnFe_{1.4}Mn_{0.6}O_4$ could indicate a starting point of phase transformation. Furthermore, a more significant phenomenon in the low cooling rate sample could demonstrate that the low cooling rate may be beneficial to this transformation.

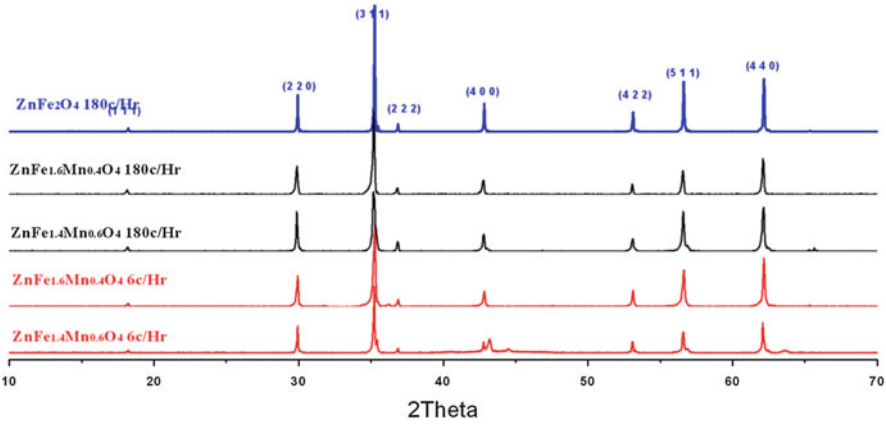

Fig. 3 XRD patterns of Fe-rich samples indexed with cubic structure (Fd-3 m space group)

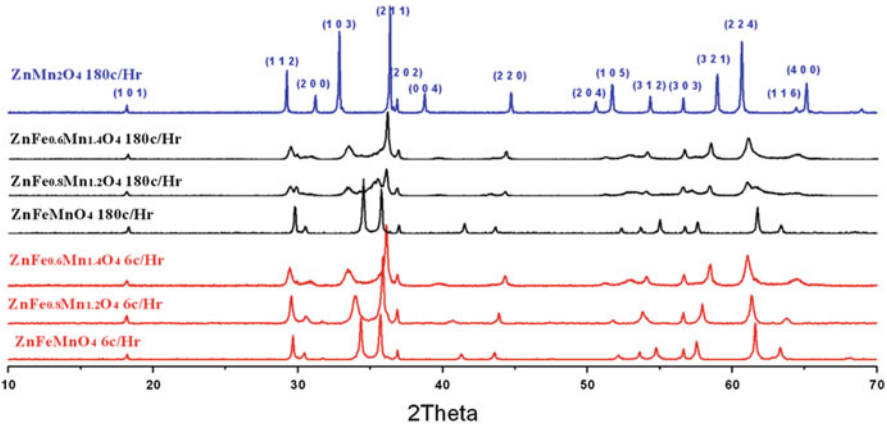

Fig. 4 XRD patterns of Mn-rich samples indexed with a tetragonal structure (I41/amd space group)

The patterns of Mn-rich ($ZnFe_{0.6}Mn_{1.4}O_4$, $ZnFe_{0.8}Mn_{1.2}O_4$, $ZnFeMnO_4$) samples were indexed with an I41/amd space group like $ZnMn_2O_4$ as shown in Fig. 4.

Compared with the pattern of $ZnMn_2O_4$, the peaks can be generally indexed but displacements and shape transformations are obvious. The peak displacements could indicate lattice distortions due to the substitution of Mn ions by Fe ions. The width of peaks in the patterns is obviously broadened which decreases with increasing Fe content. According to the theory of XRD profile, this phenomenon could imply a nanostructure.

Phase Separation

The phase and structure analysis were based on the SEM images of polished surface in BSE mode. In Mn-rich samples, ordered stripes (Fig. 5) inside grains are observed on the SEM images. Since contrast of BSE image reflects the Z number of atoms in the material or different crystal orientations, these stripes may indicate an ordered phase separations or an ordered crystal orientation distribution in the samples.

In order to identify these stripes, the formation and scale should be firstly studied. The widths of these stripes are between 0.5 μm and 2 μm and they

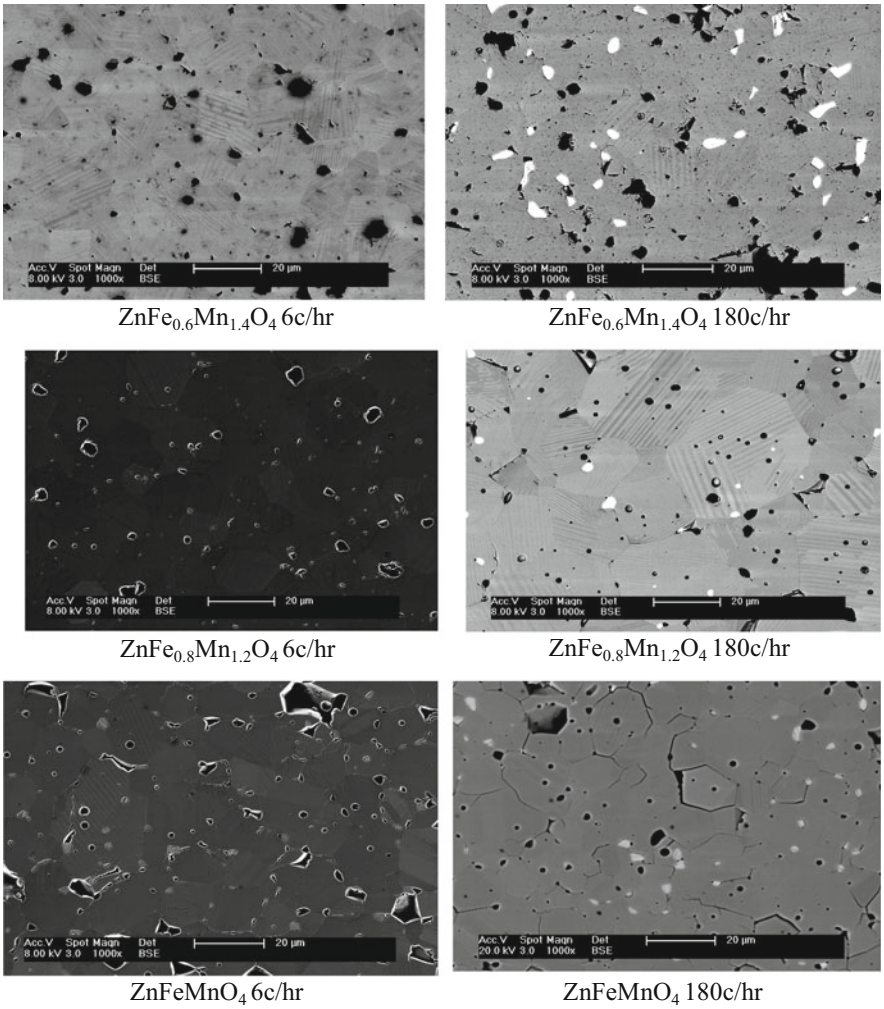

Fig. 5 SEM (BSE) images of Mn-rich samples

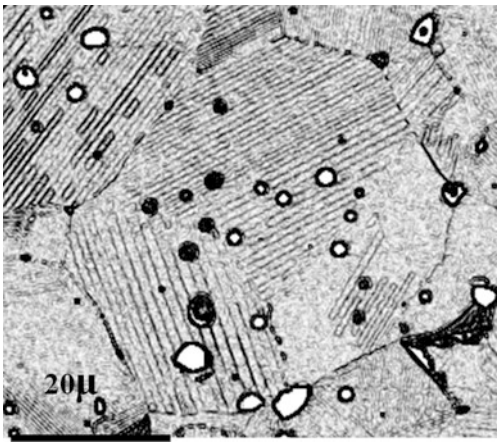

Fig. 6 Processed SEM image for formation and scale analysis

constitute a parallel lines formation as shown in Fig. 6. In a ceramic system, contrast difference in such a big scale has little chance to be attributed to atom separation. So, it more possibly implies a crystal orientation distribution.

Thermal Properties

The temperature dependent thermal diffusivities of low cooling rate samples are shown in Fig. 7. The legends in the diagram are marked with the ratio of Fe and Mn in the composition.

As shown in the figure, the diffusivities of all the samples decrease with increasing temperature. Furthermore, diffusivities of the Mn-rich compositions (Fe3Mn7, Fe4Mn6, Fe5Mn5) with tetragonal structure have higher rate of decrease than those of Fe-rich ones (Fe7Mn3, Fe8Mn2) with cubic structure.

The temperature dependent heat capacities of low cooling rate samples are measured and a 3 order polynomial fit was undertaken to highlight the trend of the curves, as shown in Fig. 8. The legends in the diagram are also marked with the ratio of Fe and Mn in the composition.

Based on these fitted curves, Fe-rich samples have higher heat capacity than Mn-rich samples in most of the temperature range. Moreover, the trend of Mn-rich curves show an accelerated growth instead of uniform growth of Fe-rich curves.

Based on thermal diffusivity and heat capacity data, the temperature dependent thermal conductivity was calculated as shown in Fig. 9. The legends in the diagram are also marked with the ratio of Fe and Mn in the composition.

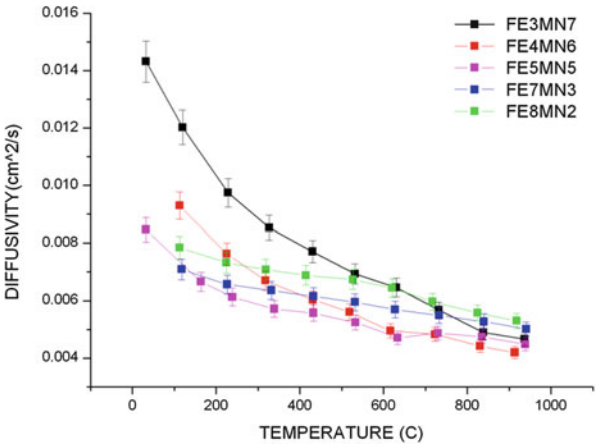

Fig. 7 Thermal diffusivities of the 6 °C/h samples vs. temperature

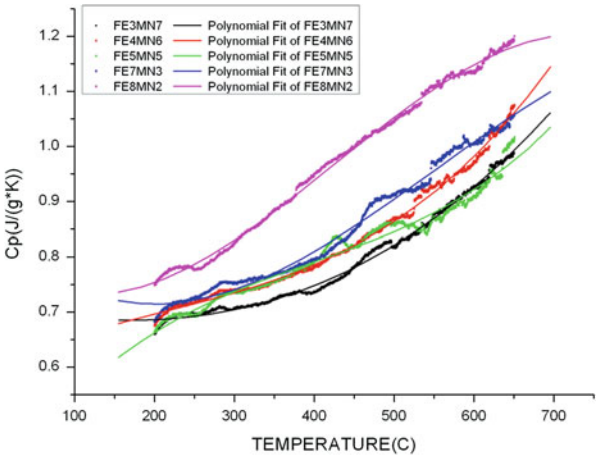

Fig. 8 Heat capacities of the 6 °C/h cooling rate samples vs. temperature

The trend and magnitude of thermal conductivity show a dependence on the structure of the samples. The thermal conductivity rises with increasing temperature in Fe-rich samples without any sub-grain structure. However, a slight temperature-dependent decrease occurs in Mn-rich samples with sub-grain structures. Furthermore, in Fe_5Mn_5 sample the thermal conductivity increases in a relatively low temperature range but decreases at higher temperature. The lowest thermal conductivity emerges in the Fe_5Mn_5 sample. Besides, in both Fe-rich and Mn-rich group, the farther the composition of the middle point (Fe_5Mn_5), the higher the thermal conductivity magnitude.

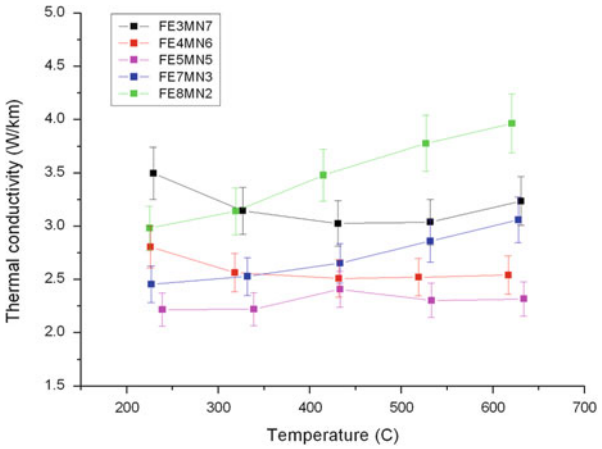

Fig. 9 Thermal conductivity of the 6 °C/h samples vs. temperature

Conclusions

A self-assembly ordered sub-grain structures can be detected on SEM images of tetragonal samples. These sub-grain structures display as parallel stripes with a width of 0.5–2 μm on BSE images. Based on a similar research [42] of the $ZnGaMnO_4$ ceramic and considering the peak shape variation on XRD patterns, an ordered orientation distribution of fine domains may be the nature of this phenomenon.

Thermal conductivities of the samples are relevant to their structure. Thermal conductivity rises with increasing temperature in cubic samples. However, a slight temperature-dependent decrease occurs in the $x = 0.6$ and $x = 0.8$ samples with the sub-grain structure. Furthermore, in the $x = 1$ sample thermal conductivity increases in the low temperature range but decreases at higher temperature. The lowest thermal conductivity emerges in the $x = 1$ sample. Besides, in both tetragonal and cubic group, the farther the composition of the middle point ($x = 1$), the higher the thermal conductivity magnitude. All in all, the sub-grain structure in the material can affect the thermal conductivity behavior and these effects can be employed to improve the performance of the thermoelectric materials.

References

1. Vining CB, Rowe DM, Stockholm J, Rao KR (2006) History of the International Thermoelectric Society. In: *Thermoelectrics handbook–macro to nano*, D. M. Rowe, CRC Taylor & Francis Group, Appendix 1–8
2. Gould CA, Shammas NYA, Grainger S, Taylor I (2008) A comprehensive review of thermoelectric technology, micro-electrical and power generation properties. 26th International Conference on Microelectronics, Vol. 1 and 2, Proceedings, IEEE, New York, pp 329–332

3. Tritt TM, Subramanian MA (2006) Thermoelectric materials, phenomena, and applications: a bird's eye view. MRs Bull 31(3):188–194
4. Ohtaki M (2011) Recent aspects of oxide thermoelectric materials for power generation from mid-to-high temperature heat source. J Ceram Soc Japan 119(1395):770–775
5. Nolas GS, Poon J, Kanatzidis M (2006) Recent developments in bulk thermoelectric materials. MRs Bull 31(3):199–205
6. Goldsmid HJ (2009) Introduction to thermoelectricity. Springer, Berlin
7. Riffat SB, Ma X (2003) Thermoelectrics: a review of present and potential applications. Appl Therm Eng 23(8):913–935
8. Yang J (2005) Potential applications of thermoelectric waste heat recovery in the automotive industry Thermoelectrics, ICT 2005. 24th International Conference, pp 170–174
9. LaLonde AD, Pei Y, Wang H, Snyder GJ (2011) Lead telluride alloy thermoelectrics. Mater Today 14(11):526–532
10. DiSalvo FJ (1999) Thermoelectric cooling and power generation. Science 285(5428):703–706
11. Slack GA (1997) Design concepts for improved thermoelectric materials. Thermoelectric Mat—New Directions and Approaches 478:47–54
12. Terasaki I, Sasago Y, Uchinokura K (1997) Large thermoelectric power in NaCo2O4 single crystals. Phys Rev B 56(20):12685–12687
13. Smith GE, Wolfe R (1962) Thermoelectric properties of bismuth-antimony alloys. J Appl Phys 33(3):841
14. Yim WM, Amith A (1972) Bi-Sb Alloys for magneto-thermoelectric and thermomagnetic cooling. Solid State Electron 15(10):1141
15. Goldsmid HJ (1958) The electrical conductivity and thermoelectric power of bismuth telluride. Proc Phys Soc Lond 71(460):633–646
16. Wright DA (1958) Thermoelectric properties of bismuth telluride and its alloys. Nature 181 (4612):834–834
17. Goldsmid HJ, Giutronich JE, Kaila MM (1980) Solar thermoelectric generation using bismuth telluride alloys. Sol Energy 24(5):435–440
18. Wyrick R, Levinstein H (1950) Thermoelectric voltage in lead telluride. Phys Rev 78 (3):304–305
19. Lambrecht A, Bottner H, Nurnus J (2004) Thermoelectric energy conversion—overview of a TPV alternative. Thermophotovoltaic Generation of Electricity. A. C. T. J. L. J. Gopinath, Vol. 738, pp 24–32
20. Snyder GJ, Toberer ES (2008) Complex thermoelectric materials. Nat Mater 7(2):105–114
21. Mandel N, Donohue J (1971) Refinement of crystal structure of skutterudite $CoAs_3$. Acta Crystallogr Sect B Struct Crystallogr Cryst Chem B27(15):2288
22. Sales BC, Mandrus D, Chakoumakos BC, Keppens V, Thompson JR (1997) Filled skutterudite antimonides: electron crystals and phonon glasses. Phys Rev B 56(23):15081–15089
23. Macnicol DD, McKendrick JJ, Wilson DR (1978) Clathrates and molecular inclusion phenomena. Chem Soc Rev 7(1):65–87
24. Kuznetsov VL, Kuznetsova LA, Kaliazin AE, Rowe DM (2000) Preparation and thermoelectric properties of A(8)(II)B(16)(III)B(30)(IV) clathrate compounds. J Appl Phys 87 (11):7871–7875
25. Hicks LD, Dresselhaus MS (1993) Effect of quantum-well structures on the thermoelectric figure of merit. Phys Rev B 47(19):12727–12731
26. Hicks LD, Dresselhaus MS (1993) Thermoelectric figure of merit of a one-dimensional conductor. Phys Rev B 47(24):16631–16634
27. Venkatasubramanian R, Siivola E, Colpitts T, O'Quinn B (2001) Thin-film thermoelectric devices with high room-temperature figures of merit. Nature 413(6856):597–602
28. Harman TC, Taylor PJ, Walsh MP, LaForge BE (2002) Quantum dot superlattice thermoelectric materials and devices. Science 297(5590):2229–2232
29. Koh YK, Vineis CJ, Calawa SD, Walsh MP, Cahill DG (2009) Lattice thermal conductivity of nanostructured thermoelectric materials based on PbTe. Appl Phys Lett 94(15):153101. doi: 10.1063/1.3117228

30. Boukai AI, Bunimovich Y, Tahir-Kheli J, Yu JK, Goddard WA, Heath JR (2008) Silicon nanowires as efficient thermoelectric materials. Nature 451(7175):168–171
31. Masset AC, Michel C, Maignan A, Hervieu M, Toulemonde O, Studer F, Raveau B, Hejtmanek J (2000) Misfit-layered cobaltite with an anisotropic giant magnetoresistance: Ca3Co4O9. Phys Rev B 62(1):166–175
32. Shikano M, Funahashi R (2003) Electrical and thermal properties of single-crystalline $(Ca_2CoO_3)(0.7)CoO_2$ with a $Ca_3Co_4O_9$ structure. Appl Phys Lett 82(12):1851–1853
33. Okuda T, Nakanishi K, Miyasaka S, Tokura Y (2001) Large thermoelectric response of metallic perovskites: Sr1-xLaxTiO3 ($0 <= x <= 0.1$). Phys Rev B 63(11), 113104
34. Koumoto K, Terasaki I, Funahashi R (2006) Complex oxide materials for potential thermoelectric applications. MRs Bull 31(3):206–210
35. Funahashi R, Urata S, Mizuno K, Kouuchi T, Mikami M (2004) Ca2.7Bi0.3Co4O9/La0.9Bi0.1NiO3 thermoelectric devices with high output power density. Appl Phys Lett 85 (6):1036–1038
36. Funahashi R, Mihara T, Mikami M, Urata S, Ando N (2005) Power generation of thermoelectric oxide modules. ICT: 2005 24th International Conference on Thermoelectrics, pp 295–302
37. Ji X, Zhang B, Tritt TM, Kolis JW, Umbhar A (2007) Solution-chemical syntheses of nanostructured Bi2Te3 and PbTe thermoelectric materials. J Electron Mater 36(7):721–726
38. Zhang YH, Xu GY, Han F, Wang Z, Ge CC (2010) Preparation and thermoelectric properties of nanoporous Bi2Te3-based alloys. J Electron Mater 39(9):1741–1745
39. Whitesides GM, Grzybowski B (2002) Self-assembly at all scales. Science 295 (5564):2418–2421
40. De Rosa C, Park C, Thomas EL, Lotz B (2000) Microdomain patterns from directional eutectic solidification and epitaxy. Nature 405(6785):433–437
41. Ikeda TL, Collins A, Ravi VA, Gascoin FS, Haile SM, Snyder GJ (2007) Self-assembled nanometer lamellae of thermoelectric PbTe and Sb2Te3 with epitaxy-like interfaces. Chem Mater 19(4):763–767
42. Yeo S, Horibe Y, Mori S, Tseng CM, Chen CH, Khachaturyan AG, Zhang CL, Cheong SW (2006) Solid state self-assembly of nanocheckerboards. Appl Phys Lett 89(23):233120. doi: 10.1063/1.2402115

Preparation and Space Environmental Stability of a Nano-Materials Modified Thermal Control Coating

Zhou Bo, Liu Gang, Cao Kangli, and Chen Weimin

Abstract As an essential part of the spacecraft thermal control system, thermal control coatings are widely used. In this paper, nanometer modification technology for spacecraft thermal control coatings is studied. Sol-Gel technology is used to add nano-SiO_2 into thermal control coating system, where TEOS is used as the precursor of SiO_2, in order to modify the binder and the filler of the coating system. The thermal control coatings were characterized by FTIR, PL and optical properties testing, both before and after proton irradiation, which has a significant applied background in engineering and theoretical research importance. The test results prove that the nano modified coating has well established optical properties ($\alpha_s \leq 0.2$) and radiation stability. After 90 keV proton irradiation, $\Delta\alpha_s$ of the nano modified coating is reduced to 0.12. The stability improves almost 50 % as compared to ordinary ZnO white paint. The main reason why the performance of nano modified coating degrades is that defects are formed in ZnO during the irradiation, according to the analysis. Modified ZnO powder can effectively eliminate the variations and quantities of irradiation defects, such as oxygen vacancies. This not only improves the proton irradiation stability of ZnO powder, but also effectively reduces the absorbed oxygen content in the coating system, thereby, lowering the damage to chemical bonds in the adhesives.

Keywords Thermal control coating • Nano-SiO_2 • Proton irradiation • Spacecraft

Z. Bo (✉) • L. Gang • C. Kangli
Shanghai Institute of Spacecraft Equipment, Shanghai 200240, China

Shanghai Space Environment Simulation & Verification Engineering Technology Research Center, Shanghai 200240, China
e-mail: sast_casc_8122@126.com

C. Weimin
Shanghai Institute of Spacecraft Equipment, Shanghai 200240, China

J. Kleiman (ed.), *Protection of Materials and Structures from the Space Environment*, Astrophysics and Space Science Proceedings 47,
DOI 10.1007/978-3-319-19309-0_43

Introduction

Thermal control system is one of the most important subsystems in spacecraft, similar to the importance of keeping the constant temperature control in a human body. The thermal control of subsystems in a spacecraft is a prerequisite to ensure the internal parts of the spacecraft instruments and structures to function properly and to provide protection for the spacecraft normal operation in orbit [1, 2]. Thermal control coatings are special coatings applied on spacecraft surface to adjust the optical thermal properties to maintain the thermal control.

White organic thermal control coating is widely used as outer surface thermal control material for geostationary spacecraft [3]. Its optical properties will be degraded under the influence of space environment effects, consequently, worsening the reliability and stability of spacecraft thermal control system. Nano-SiO_2 powders have excellent properties that include quantum size effect, small size effect, surface effect and macroscopic quantum tunneling effect, as well as an excellent stability. The stability of coatings can be effectively improved if the nano-SiO_2 is added to the coating system.

This article introduces the use of the Sol-Gel method combined with heat treatment technology to uniformly coat the nano-SiO_2 on the surface, forming a layer of $ZnSiO_4$ core-shell structure. Meanwhile, SiO_2 sol is added into the silicone resin system, and the SiO_2-silicone binder is formed by the Graft copolymerization technology. Thermal control coating is made from modified ZnO filler and modified silicone binder by dispersing and blending. The irradiation experiment of the coating is carried out using the proton with energy less than 200 keV, to study the variation of modified coating performance before and after radiation.

Experiment

Materials

Silicone resin, Tetraethoxysilane, KH550, Aqueous ammonia, Polyethyleneglycol, Ethyl acetate, Butyl acetate, Acetone, Xylene, Ethanol, Distilled water, ZnO powder.

Modification Methods for ZnO Filler

Sol-Gel method: Coating SiO_2 membrane with particles by the hydrolysis-condensation principle reaction of Tetraethoxysilane, then drying TEOS and ZnO pigment before the organic components are removed by calcination, finally obtaining the modified ZnO pigment.

The TEOS hydrolysis-condensation reaction is conducted in three steps. The reaction equations are as follows:

The first step: hydrolysis reaction:

$$\mathrm{Si(OR)_4 + H_2O \rightarrow HO\text{-}Si(OR)_3 + ROH} \tag{1}$$

$$\mathrm{HO\text{-}Si(OR)_3 + H_2O \Leftrightarrow (HO)_2Si(OR)_2 + ROH} \tag{2}$$

$$\mathrm{(HO_3)Si(OR)_2 + H_2O \Leftrightarrow (HO)_3Si(OR) + ROH} \tag{3}$$

$$\mathrm{(HO)_3Si(OR) + H_2O \Leftrightarrow (HO)_3Si(OR) + ROH} \tag{4}$$

The second step: condensation reaction:

$$\equiv \mathrm{Si - OR + HO - Si} \equiv \Leftarrow\Rightarrow \equiv \mathrm{Si - O - Si} \equiv + \mathrm{ROH} \tag{5}$$

The third step: Polymerization:

$$\mathrm{X(Si - O - Si) \rightarrow (-Si - O - Si)_X} \tag{7}$$

The Sol-Gel method modified ZnO process is shown in Fig. 1.

Method for Modified Silicone Resin Binder

Blending the TEOS sol with the organic silicone resin, the hydrolysis mechanism of TEOS as shown in formula Eq. (8):

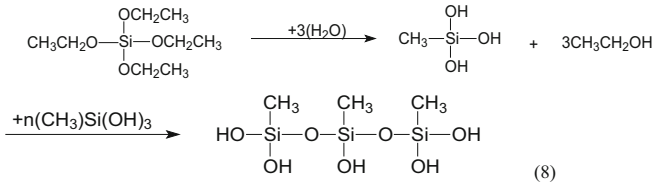

(8)

The Method for modifying the silicone resin is shown in Fig. 2.

Parameters of Proton Irradiation Experiment

The parameters of proton irradiation experiment were selected as follows: the proton irradiation flux is $\varphi_p = 5 \times 10^{11}$ cm^{-2}·s^{-1}, the energy of proton irradiation is 90 keV, specimen temperature is 298 K, the vacuum is 1×10^{-4} Pa, the total irradiation fluencies were selected at 5×10^{14} cm^{-2}, 1×10^{15} cm^{-2}, 2×10^{15} cm^{-2}, 3×10^{15} cm^{-2} and 5×10^{15} cm^{-2}.

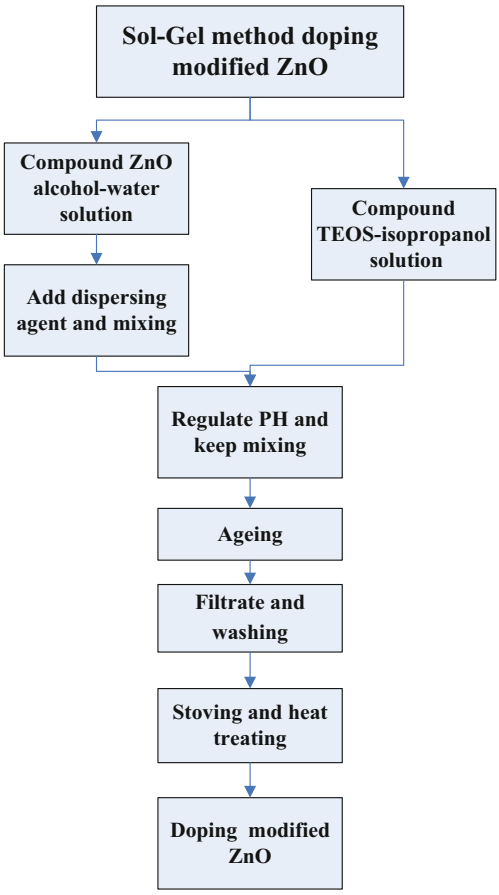

Fig. 1 Sol-Gel process doping modified ZnO

Result and Discussion

Surface Morphology Analysis

Figure 3 shows the surface morphology of the samples before and after irradiation. As can be seen from the presented photographs, with the increases of radiation fluence, the color of specimen turns dark, in other words, its optical performance is decreased. Thus, it is necessary to measure the optical performance of the thermal control coating after irradiation with different fluencies.

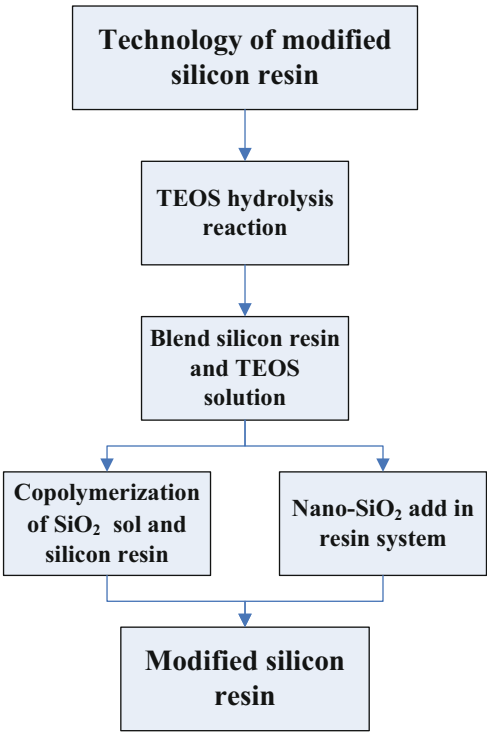

Fig. 2 Modification process of the organic silicone

Fig. 3 Surface morphology of the samples before and after irradiation

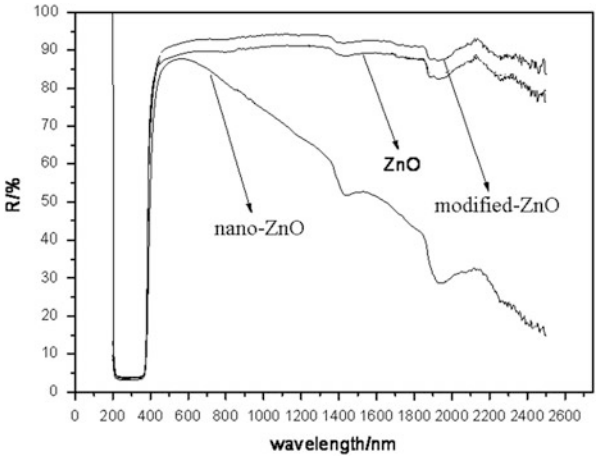

Fig. 4 The spectral reflectance spectrum of three types of ZnO

Optical Performance Test

Filler ZnO

Figure 4 shows the spectral reflectance spectrum of three types of ZnO. This figure shows that in the wavelength range from 460 nm to 2500 nm the spectral reflectance of modified ZnO is higher. In the wavelength range from 460 nm to 2500 nm, the optical performance of nano-ZnO is not good, and its spectral reflectance drops to sharply with wavelength.

Thermal Control Coating System

In order to study the proton irradiation stability of the modified thermal coating, the specimens are tested with 90 keV protons at different radiation fluencies of 5×10^{14} cm^{-2}, 1×10^{15} cm^{-2}, 2×10^{15} cm^{-2}, 3×10^{15} cm^{-2} and 5×10^{15} cm^{-2}. Figure 5 shows the spectral reflectance spectrum of specimens after irradiation with five different radiation fluencies.

If one will plot the change in spectral reflectance as a function of the proton fluence it can be shown (Fig. 6) that the change is largest at the wavelength of 400 nm, and the peak is getting higher with higher proton fluencies. It is known that the composition of thermal control coatings under proton irradiation is deteriorated [4–7], forming many absorption regions. As the total radiation fluence increases, the degree of composition break up is increasing and the optical performance is dropping.

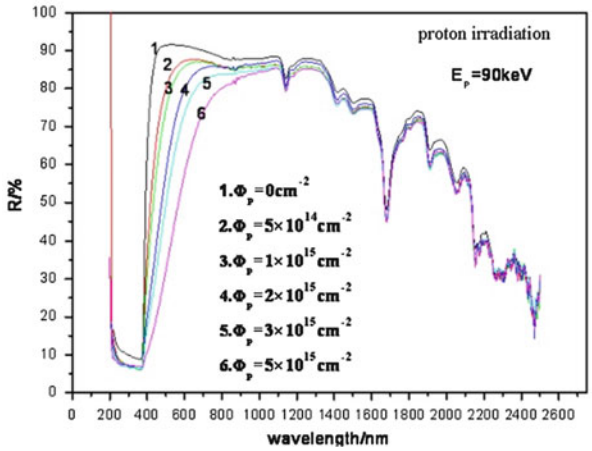

Fig. 5 Spectral reflectance of modified thermal coating samples exposed to different proton fluencies

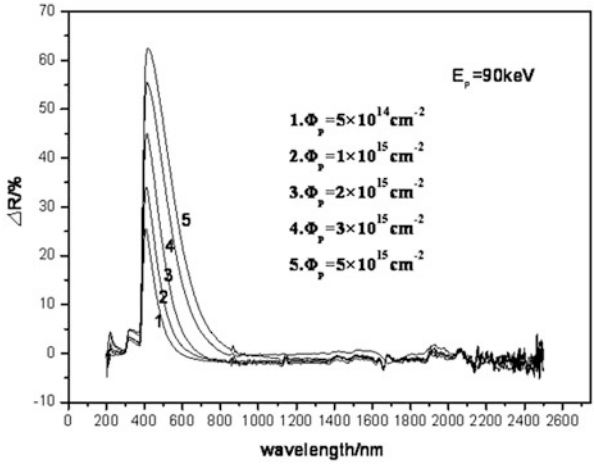

Fig. 6 Variation of spectral reflectance spectrum

FTIR Analysis

Figure 7 shows the influence of the total radiation fluence on the infrared spectra. The changes in the phenyl peak intensity are small that indicates the damage to the phenyl groups in the silicon resin is small. As the proton fluence increases, the peak of Si-O-Si is changed, the peak at 1130 cm^{-1} disappeared and the peak at 1050 cm^{-1} widened. This effect proves that the Si-O bond is damaged under proton irradiation.

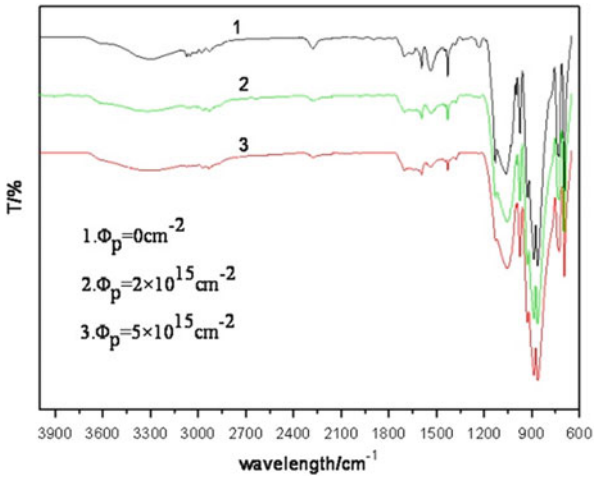

Fig. 7 FTIR for thermal control coating

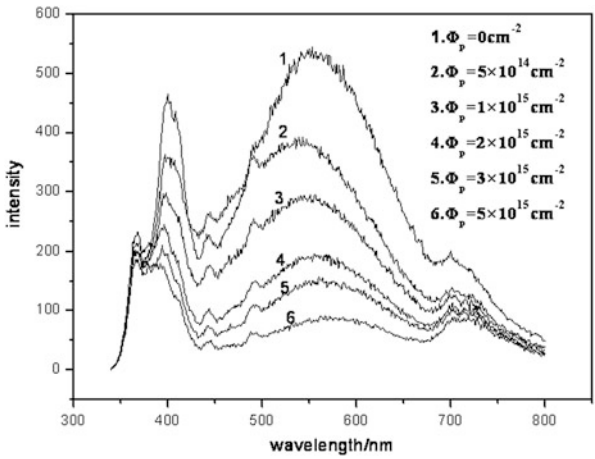

Fig. 8 PL for thermal control coating

PL Analysis

As shown in Fig. 8, the shape and location of the fluorescence spectrum peak at 380 nm do not change with proton fluence. The peak at 510 nm is getting weaker as the proton fluence increases but even at the strongest fluence it is still present.

Conclusions

Modified ZnO powder can effectively eliminate the variations and quantities of irradiation defects, such as oxygen vacancies. This not only improves the proton irradiation stability of ZnO powder, but also effectively reduces the absorbed oxygen content in the coating system, consequently lowering damage to chemical bonds in the adhesives. The reason why the performance of nano modified coating degrades is because deterioration of ZnO occurs under irradiation, as was found from the analyses.

References

1. Guirong M, Shun G (1998) Thermal control of spacecraft. Science Publishing, Beijing, pp 94–99
2. Jiang J (1993) Thermal control coating. Aerospace Materials & Technology, pp 1–7
3. Shailesh K, Dhoke RB, Khanna AS (2009) Effect of nano-ZnO addition on the silicone-modified alkyd-based waterborne coatings on its mechanical and heat-resistance properties. Prog Org Coat 64:39–64
4. Xiao H, Sun M, Li C et al (2008) Formation and evolution of oxygen vacancies in ZnO white paint during proton exposure [J]. Nucl Inst Methods Phys Res B 266:3275–3280
5. Rejsek-Riba V, Inguimbert V, Duzellier S et al (2011) Spectrometers results of material exposure and degradation experiment onboard international space station. J Spacecr Rockets 48:38–44
6. Chuang F (2008) Thermal degradation of poly (siloxane-urethane) copolymers. Polym Degrade Stab 93(10):1753–1761
7. Xiao H, Li C, Yang D et al (2006) A study on damage effects of 200 keV protons on ZnO/silicone white paint. Mater Res 12:3022–3028

Analysis of the Effect of Space Environment Parameters on the Solar Radiation Pressure Model for IGSO Satellite

Qiuli Chen, Zhonggui Chen, and Haihong Wang

Abstract This paper analyzes the mechanism of solar radiation which causes the perturbation acceleration. After that, a solar radiation pressure perturbation model is developed for the Inclining Geostationary Synchronized Orbit (IGSO) satellite using the finite element approach. The effect of space environment parameters on the solar radiation pressure model is analyzed. These parameters include solar radiation intensity, optical property parameter of satellite surface, temperature difference of thermal radiation, and Earth infrared radiation intensity. The results show that, because of solar radiation pressure perturbation is a non-conservative force caused by interaction between the space environment and the satellite surface, the model precision would decline to different level varying with the space environment parameters mentioned. The error of the solar radiation pressure model caused by the solar radiation pressure and optical property parameter of satellite surface is crucial, whereas the effect of temperature difference of thermal radiation and Earth infrared radiation intensity could be ignored. The precision declining of the solar radiation pressure model due to space environment change should be concerned during orbit determination and correction for the solar radiation pressure model should be made on the basis of space environment parameters change given by other observation means.

Keywords IGSO satellite • Solar radiation pressure model • Environment parameter • Precision declining

Introduction

Solar radiation pressure (SRP) is converted from energy transformation of the reflected or absorbed photons while acting on the satellite body and solar panels. The most important perturbation source according to this mechanism is the direct solar radiation. Besides, satellite thermal radiation pressure (TRP) and Earth

Q. Chen (✉) • Z. Chen • H. Wang
Beijing Institute of Spacecraft System Engineering, Beijing 100094, China
e-mail: cql_hong@163.com

J. Kleiman (ed.), *Protection of Materials and Structures from the Space Environment*, Astrophysics and Space Science Proceedings 47,
DOI 10.1007/978-3-319-19309-0_44

radiation pressure (ERP) [1] are also included. For medium and high orbit navigation satellites, SRP is the most difficult pressure force to be accurately modeled. It's also the most important error source in modeling the orbital dynamics for satellite navigation [2]. SRP models are generally divided into analytical models based on pre-launch physical information, and empirical models built on the basis of a large number of observed orbital data [3–9]. For the beginning orbit or a pre-launch satellite, the research on modeling method on the basis of physical properties is the only effective way.

In this paper, a research on modeling method of SRP is proposed and a parameterized model of SRP is constructed based on the mechanism, using the engineering parameters and attitude control mode of a Beidou inclining geostationary synchronized orbit (IGSO) satellite. On the basis of the model, the key influence factors are analyzed. Specifically, the influences of optical properties aging of the surface, variation of solar radiation intensity, surface thermal radiation and infrared radiation intensity are analyzed. These offer a theoretical analysis reference for further improvements on the precision and stability of the SRP model.

Modeling for IGSO Satellite SRP

Mechanism Analysis of SRP

Starting from the energy, mass, and momentum relationships given by Einstein's special theory of relativity, the radiation pressure caused by incident solar radiation is:

$$\text{Fincident} = \text{E}/\text{c} \tag{1}$$

where E is the radiation intensity and c is the speed of light.

The incident light at the surface is divided into specular reflection and diffuse reflection. The proportional coefficient of the specular reflection of photons is μv, with v being the reflectivity of the surface material and μ the coefficient of the mirror surface of the material. The number of diffuse reflection photons is $v(1-\mu)$. Diffuse light scatters at Lambert hemisphere of the object surface element, which is in line with Lambert law.

The normal component and tangential component of direct SRP on the surface are:

$$F_{\hat{n}} = -(AE\cos\theta/c_{EM})\left[(1+v\mu)\cos\theta + \frac{2}{3}v(1-\mu)\right] \tag{2}$$

$$F_{\hat{s}} = (AE\cos\theta/c_{EM})(1-v\mu)\sin\theta \tag{3}$$

Modeling Method for Direct SRP

The navigation satellite nominal attitude at any time is determined by the satellite navigation task requirement, such as to center the field of the geocentrically pointing navigation antenna, to send navigation signals, to hold solar panels always perpendicular to the Sun vector in order to get enough energy, etc. Therefore, the satellite body fixed coordinate system (BFCS) is defined as follows: the satellite center of mass is defined as the origin, the Z-coordinate is the center axis of the antenna field, the Y-coordinate is in the solar panel beam direction, and the X-coordinate completes the right-hand system, as shown in Fig. 1 [10]. The BFCS is chosen as the reference coordinate system for the direct SRP model.

Under normal circumstances, continuous yaw-steering is taken by the IGSO satellite attitude control system. Sun vector moves in the XOZ plane in BFCS, which is expressed by the angle between Sun rays and +Z axis of BFCS, denoted as θ_{eps}. When the sun elevation is small, yaw-fixed was chosen by the attitude control system. Sun vector is decomposed into the projection in the XOZ plane and the Y component. θ_{eps} is defined as the angle of projection in the XOZ plane and +Z axis. θ_{eps} is an argument of the SRP model.

Because the distance between Sun and the satellite is far enough, sunlight could be equivalent to a beam of parallel light. A pixel array which is vertical to the line between the sun and the satellite is used to simulate the Sun light. A number of points with vertical ray emanating from the center of each pixel spaced by 1 mm express the sunlight as shown in Fig. 2 [11].

The geometry relationship between all surface components of the satellite and the Sun vector is calculated in each satellite attitude control modes. The SRP of each surface component is calculated using optical tracking function. The linear equation of light simulation was calculated in the BFCS using the Sun vector.

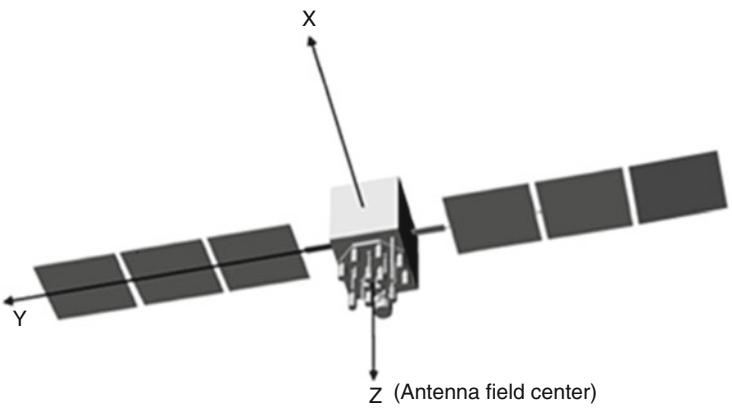

Fig. 1 Body-fixed coordinate system of IGSO satellite

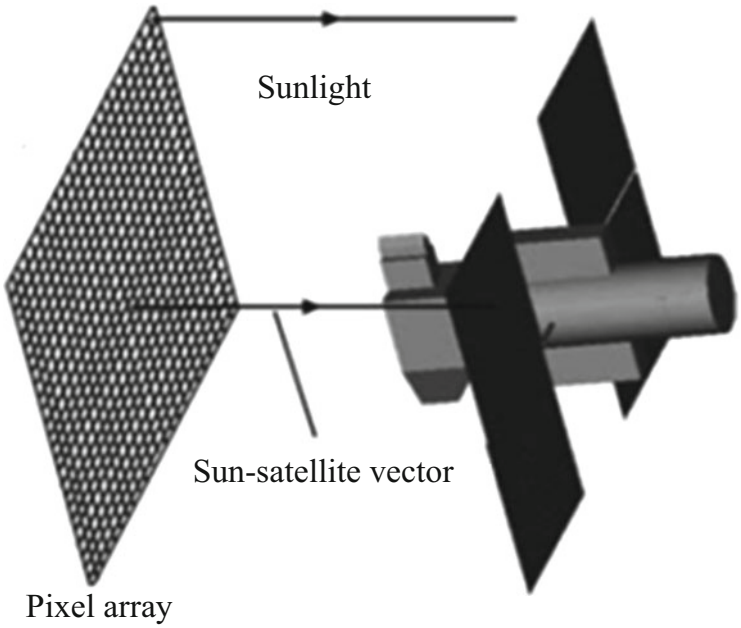

Fig. 2 Pixel array perpendicular to the vector between Sun and satellite

Taking into account that space is curved, equations have been developed for surface components and edge of the parts determined by the area of intersections of rays and the surface. The part at a shortest distance between the intersection and the center pixel is actually radiated. Thus, the effective radiated area is calculated. According to Eqs. (2) and (3), the direct SRP of surface parts are calculated. The SRP of a whole star is obtained by combining all surface perturbations.

SRP Model

The SRP of the IGSO satellite is modeled using the above method in this section. A complex 3D view of the IGSO satellite is presented in Fig. 3.

During yaw-steering regime, the variation of X component and Z component of the SRP model with θ_{eps} is shown in Figs. 4 and 5, respectively. The Y component was 0.

During yaw-fixed regime, the variation of X component, Y component and Z component of the SRP model with θ_{eps} are shown in Fig. 6, Figures 7 and 8, respectively. The results show that the Y weight has perfect regularity with solar elevation.

In order to verify the precision of simulation calculation, the above models were used for precise orbit determination for 3 days. The results are compared with the

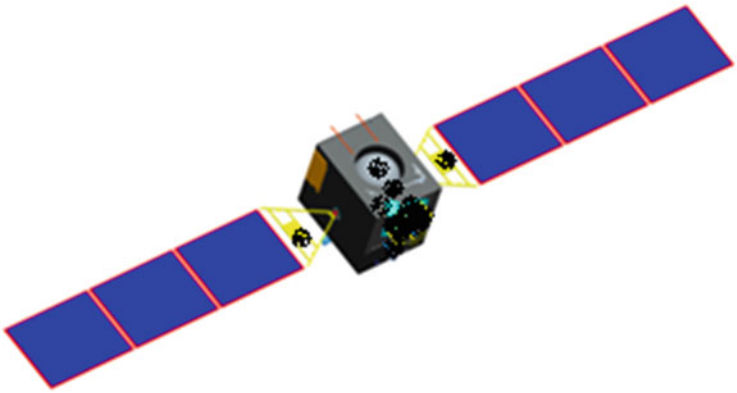

Fig. 3 A complex 3D view of the IGSO satellite

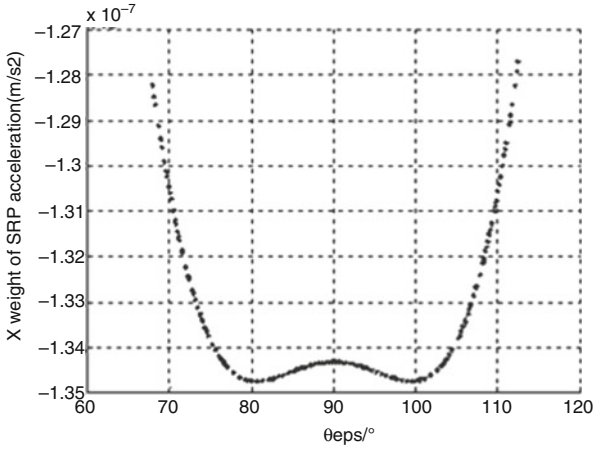

Fig. 4 X weight of SRP acceleration during yaw-steering regime

precise ephemeris published by Wuhan University. The position fitting error was 1.5 m. The fitting error of STW directions is shown in Fig. 9.

Analysis of the Key Factors Effect

Many space environment parameters are used in modeling the SRP. Some of them would inevitably change the model error, including the surface optical parameter, solar radiation intensity, thermal radiation temperature, Earth albedo intensity, and so on.

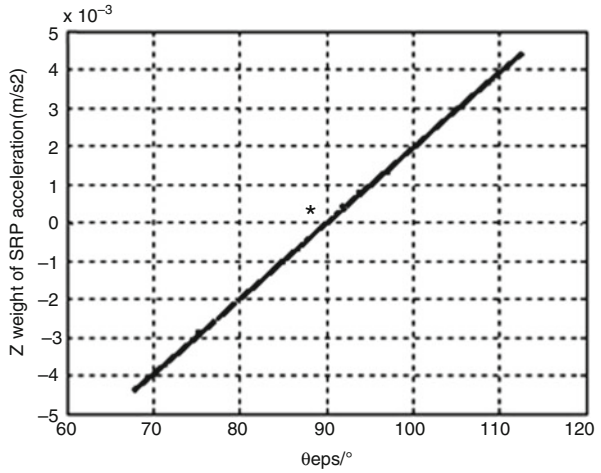

Fig. 5 Z weight of SRP acceleration during yaw-steering regime

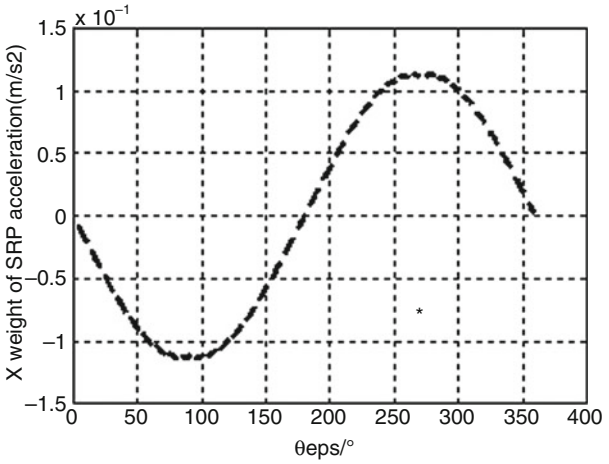

Fig. 6 X weight of SRP acceleration during yaw-fixed regime

Surface Optical Parameter Aging

The Geosynchronous Earth Orbit (GEO) has a large number of low-energy electrophorus particles which affect significantly the satellite surface. Hence, solar absorptivity of the satellite surface would degrade with time [12]. Along with accumulation of in-orbit time, solar absorptivity of the satellite surface degenerates, this is expressed by absorptivity increased and reflectivity decreased.

The difference from the initial values of the telophase optical parameter predicted by the SRP model is shown in Figs. 10 and 11.

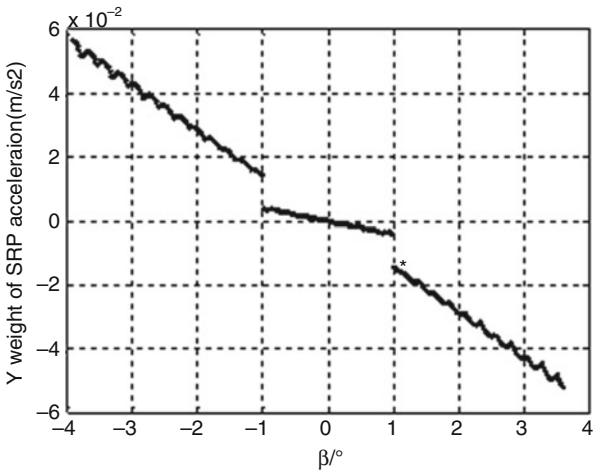

Fig. 7 Y weight of SRP acceleration during yaw-fixed regime

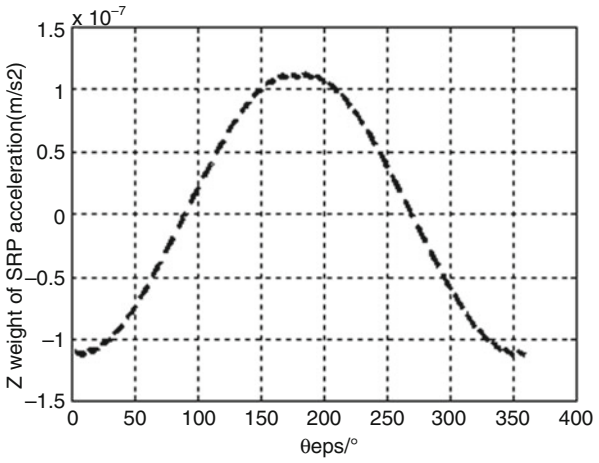

Fig. 8 Z weight of SRP acceleration during yaw-fixed regime

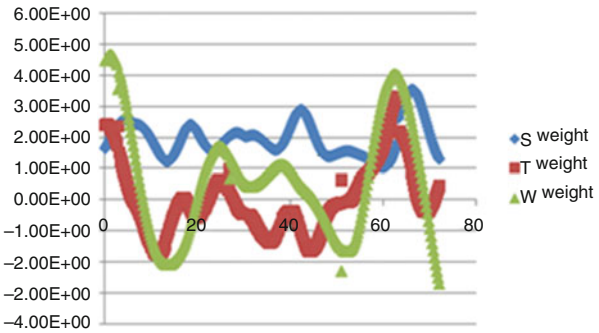

Fig. 9 SRP model fitting error of STW directions

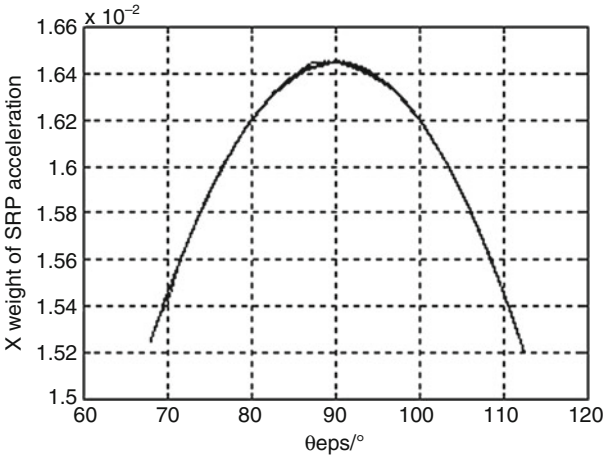

Fig. 10 X component error of the SRP model caused by optical parameter aging

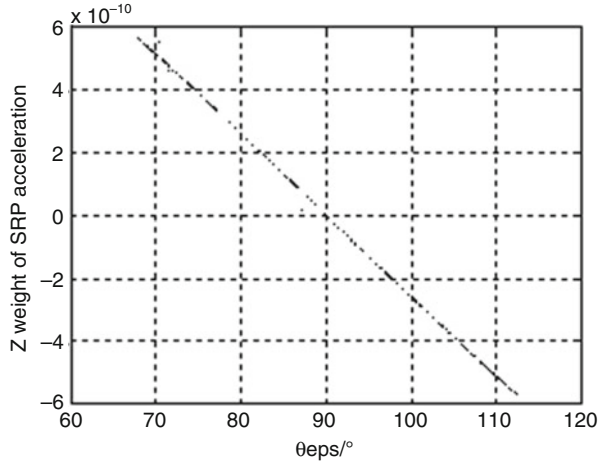

Fig. 11 Z component error of the SRP model caused by optical parameter aging

Figures 10 and 11 show that the errors for the X component and the Z component of the SRP model are 1.21 % and 1.2 %, respectively, and they are caused by decreasing reflectivity.

Solar Radiation Intensity Change

The direct solar radiation intensity is 1367 W/m^2 as determined by the international standard. The Sun-Earth factor would change with season change. The minimum is

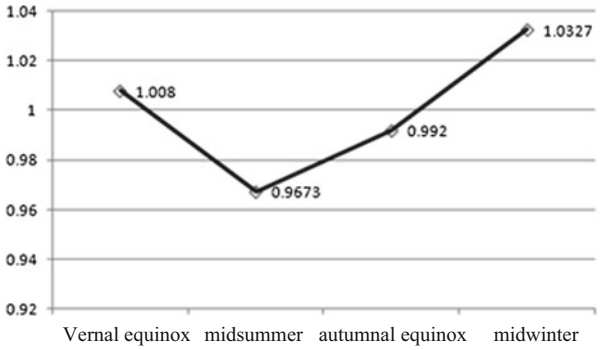

Fig. 12 The Sun-Earth factor change with season changes

Table 1 The SRP error caused by nominal attitude warp

Error source	Xweight	Yweight	Zweight
Midsummer intensity	2.67 % decrease	/	3 % decrease
Midwinter intensity	2.7 % increase	/	3 % increase

0.9673 at midsummer. The maximum is 1.0327 at midwinter. It is 1.008 and 0.992, respectively, for the vernal equinox and for the autumnal equinox [13]. The Sun-Earth factor change is represented in Fig. 12.

From data shown in Fig. 12, the deviation of the intensity in midsummer and midwinter are the most important. The radiation intensity is 1322.299 W/m^2 and 1411.7009 W/m^2, respectively, in midsummer and in midwinter. Compared with the standard intensity, the SPR model error caused by intensity change is offered in Table 1.

Instead of using the standard intensity, the radiation intensity at midsummer and at midwinter were used in the SRP model for precise orbit determination. As a result, the RMS decreased from 1.384 m to 1.998 m and 4.977 m.

Thermal Radiation Temperature Error

When the equivalent temperature of the south and north surface are the same, the Y weight of TRP acceleration is 0, since the TRP on these surfaces compensate each other. If there is a temperature difference, the thermal radiation imbalance would affect the Y weight of TRP. The relationship between the Y weight of TRP and temperature difference Δt is shown in Fig. 13.

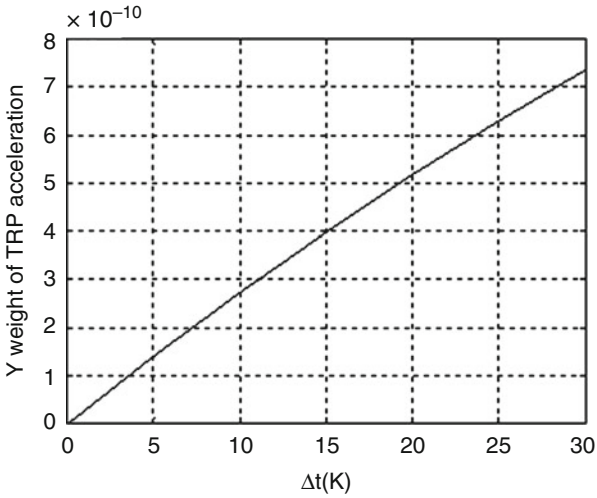

Fig. 13 Y weight of TRP acceleration caused by temperature difference of the south and north surfaces

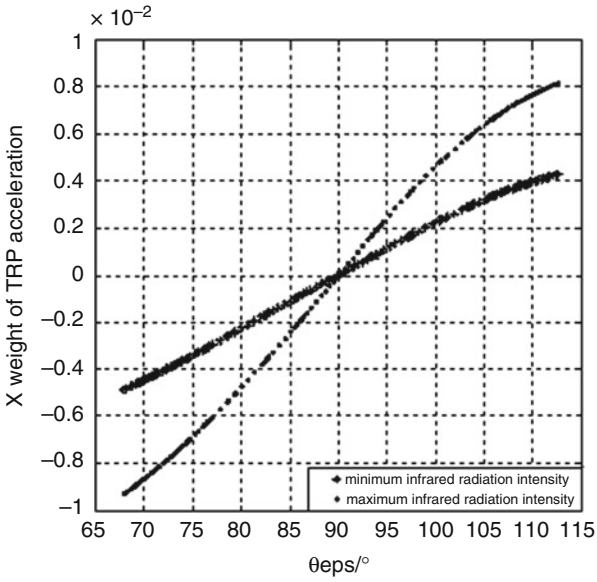

Fig. 14 X weight acceleration of different infrared radiation intensity

Infrared Radiation Intensity

The intensity of infrared radiation is related to orbital altitude and clouds change. Taking the orbital altitude of IGSO navigation satellite as an example, infrared radiation intensity is 21.486–49 W/m^2. In the BFCS, the ERP model has only the X weight and the Z weight. The ERP model results for the maximum and minimum infrared radiation intensity are shown in Figs. 14 and 15.

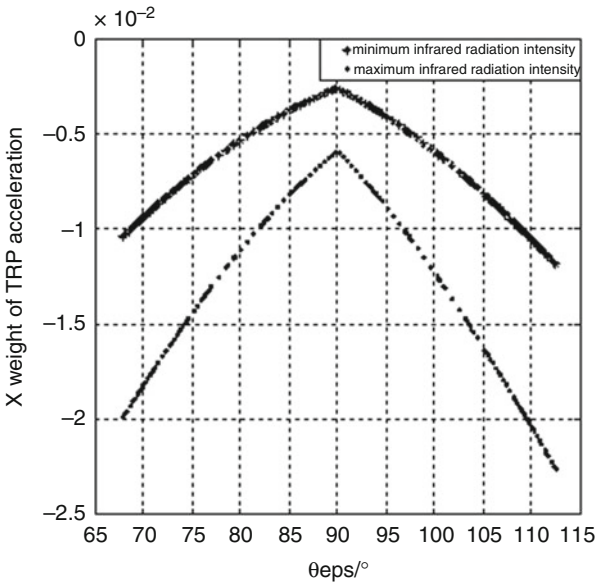

Fig. 15 Z weight acceleration of different infrared radiation intensity

When the infrared radiation intensity is minimum, the X weight acceleration of ERP is 0.531 % based on the direct SRP model, the Z weight acceleration of ERP is 2.86 %. When the infrared radiation intensity is maximum, the X weight acceleration of ERP is 0.796 % based on the direct SRP model, the Z weight acceleration of ERP is 5.24 %.

Conclusion

The IGSO satellite is chosen as the object of study in this paper. The SRP model has been developed. Based on the SRP model, the influence factors of SRP model were analyzed. The results are as follows:

(1) The attitude control modes are the foundation of SRP. The movement law of the Sun vector in the BFCS would change with different attitude control modes, which leads to variation of the satellite surface radiation. There are corresponding SRP models for different attitude control modes.
(2) The satellite surface material aging, solar radiation intensity error, thermal radiation temperature error, and infrared radiation intensity change would cause a different level error of the SRP model. Therefore, improving the accuracy of space environment parameters or compensating the error caused by the environment parameters are important to improve the SRP model accuracy.

References

1. Ziebart M, Cross P, Adhya S (2002) Modeling photon pressure the key to high-precision GPS satellite orbits. GPS World 13(1):43–50
2. Kaplan ED, Hegarty C (2005) Understanding GPS principles and applications. London Artech House, London
3. Froideval LO (2009) A study of solar radiation pressure acting on GPS satellites. The University of Texas, Austin, TX
4. Springer TA (1999) Modeling and validating orbits and clocks using the global positioning system. University of Bern, Astronomical Institute, Bern
5. Springer TA, Beutler G, Rothacher M (1999) A new solar radiation pressure model for the GPS. Adv Space Res 23(23):673–674
6. Qinghai Z, Nan L (2011) The determination of partial derivative for solar perturbation model of T20, CSNC 2011. CSNC, Beijing (in Chinese)
7. Rodriguez-Solano C, Hugentobler U, Steigenberger P (2012) Adjustable box-wing model for solar radiation pressure impacting GPS satellites. SciVerse Science Direct 49:1113–1128
8. Fligel HF, Gallini TE, Swift ER (1992) Global positioning system radial force model for geodetic applications. J Geophys Res 97(z1):559–568
9. Springer TA, Beutler G, Rothacher M (1999) A new solar radiation pressure model for GPS satellites. GPS Solutions 2(3):50–62
10. Marek Z (2004) Generalized analytical solar radiation pressure modeling algorithm for spacecraft of complex shape. J Spacecr Rockets 41(5):841–845
11. Ziebart M, Dare P (2011) Analytical solar radiation pressure modeling for GLONASS using a pixel array. J Geod 75:587–599
12. Weiquan F, Yigang D (2005) Study on long-term degradation of solar absorptance properties of geostationary satellite thermal control coatings. Chin Space Sci Technol 2:34–37 (in Chinese)
13. Cook DG (2001) Solar radiation pressure modeling issues for high altitude satellites. Air Force Institute of Technology, Wright-Patterson AFB, OH

3-Dimensional Characteristic of Electric Field and Potential Induced by Internal Charging Effects in Typical PCB

Xiao-Jin Tang, Zhong Yi, Chao Zhang, Ye-Nan Liu, Zhi-Hao Wang, Li-Fei Meng, and Jian-Guo Huang

Abstract To assess satellite internal charging effects more accurately, a 3-D computation method is developed to study the internal charging problems with realistic geometry and grounding configuration. The method includes two steps: 3-D electron transport simulation and internal electric field computation. The transport simulation is carried out by a self-developed software based on GEANT4. And 3-D internal electric field is calculated through solving a set of electrostatic equations by COMSOL Multiphysics. In this work, the 3-D characteristics of electric field and potential in a typical PCB irradiated by an electron beam through an aluminum shield are demonstrated. This PCB is partially grounded by a rectangular circuit and the electron beam uses the GEO space-like spectrum with flux in the worst case. According to these conditions, the 3-D field and potential distributions in charging stationary state can be computed. Finally, the following conclusions are drawn: distributions of dose and charge deposition rate have remarkable edge effects. Severe distortion of electric field can arise around edges of partial grounding, especially at corners. The degree of field distortion decreases significantly with the increase of the distance from the grounding surface.

Keywords 3-Dimensional simulation • Internal charging • Internal electric field • GEANT4

X.-J. Tang (✉) • Y.-N. Liu • Z.-H. Wang • Li-Fei Meng
Beijing Institute of Spacecraft Environment Engineering, Beijing, China
e-mail: aiveidy@126.com

Z. Yi
Beijing Institute of Spacecraft Environment Engineering, Beijing, China

The Science and Technology on Reliability and Environmental Engineering Laboratory, Beijing, China

C. Zhang • J.-G. Huang
The Science and Technology on Reliability and Environmental Engineering Laboratory, Beijing, China

J. Kleiman (ed.), *Protection of Materials and Structures from the Space Environment*, Astrophysics and Space Science Proceedings 47,
DOI 10.1007/978-3-319-19309-0_45

Introduction

Internal charging, induced by space high-energy (0.1–10 MeV) electron radiation, generally arise in spacecraft dielectric components, such as printed circuit board (PCB) and cable insulation. If the conductivity is very low and the grounding is poorly designed, the charge accumulation may increase continuously to discharge. It can be damaging to the local circuit or subsystem. So high-energy electrons are a great threat to spacecraft, and internal charging is one of the major causes of satellite anomalies [1, 2].

In order to resolve the problem of internal charging and discharging, a substantial research effort has been undertaken. In this connection, numerical simulation is an important means used for revealing the mechanism of internal charging, assessing the discharging risk and promoting the defensive design for spacecraft dielectrics.

There exist several software tools which enable spacecraft designers to predict the sensitivity of spacecraft structures to internal charging effects, such as DICTAT [1, 3], NUMIT [4] and ATICS (Assessment Tool of Internal Charging for Satellite) [6, 7]. Their common points are that they are able to compute the 1-D electric field distribution for planar or cylindrical dielectric and assess discharge risk by means of comparing between the maximum electric field and breakdown threshold. This 1-D computation makes them impossible to tackle real problems with 3-D feature, such as PCB with partial grounding. So some researchers, including us, have already set out to study 3-D simulation method used to deal with realistic internal charging problems. C. L. Lemon et al. [12] construct a 3-D internal charging model with parallel electric field solver for complex geometries and arbitrary source particle distributions. However, the model excludes the charge dissipation process and cannot solve problems with complex boundary conditions. Ira Katz and Wousik Kim [13] develop a 3-D internal charging model for single PCB with two or more circuit traces. The model includes the time-dependent charge dissipation process and can resolve problems with floating and fixed potential boundary conditions. Also, we study a method for computation of 3-D internal charging field and potential in arbitrary structure dielectric with multiple boundary conditions using the self-developed software ATICS and COMSOL Multiphysics [15]. The basis on mature software and classic theories provides our method with powerful modeling capability and good reliability. In this paper, the charging of a typical PCB is simulated by the 3-D method and the 3-D characteristics of the computed electric field and potential are discussed in detail.

Simulation Approach

In this paper, we use ATICS to calculate electron and energy deposition. ATICS is developed to tackle the problem of the electron transport and internal charging process in spacecraft immersed in high-energy electrons. It is based on GEANT4 which is an open source code package and can be used to accurately simulate the transport process of particles through matter. ATICS has a 3-D geometry modeling capability and two geometry design modes. Simple geometry, such as a slab, cylinder and combination of them, can be directly constructed via ATICS. Complex geometry can be designed in CAD software, transformed into GDML (Geometry Description Markup Language [16]) file, and then imported into ATICS. As for transport process model, standard electromagnetic physics, which includes ionization, bremsstrahlung, multiple scattering and secondary gamma effects, such as Compton scattering, photoelectric effect and gamma conversion, is built in. ATICS has the modeling capability of space electron radiation environment and several special sources like point, beam, plane, surface and volume sources through embedment of the GPS (General Particle Source) model of GEANT4.

The research object is a typical PCB (10 mm × 14 mm × 3 mm) with a 2-mm-thickness-aluminum shield slab. The PCB is composed of epoxy (shown in Fig. 1). A rectangular circuit trace (3 mm × 7 mm) is printed on the front surface (plane z = 3, on the upper surface in the view of Fig. 1). All the corners on the PCB are transformed into rounded corner of 0.2-mm curvature radius.

In the transport simulation, a multi-energy electron beam with an exponential spectrum (shown in Eq. (1)) perpendicularly irradiates the shield-PCB structure (shown in Fig. 1) from the plane z = 10 mm. The spectrum can be described by the formula [7]:

$$flux(>E) = flux(>2\text{MeV}) \cdot exp\left(\frac{2-E}{E_0}\right) \tag{1}$$

where E is energy [MeV], E_0 is e-folding energy [MeV], which depends on *flux* (>2 MeV). In this work, the GEO-Worst-Case flux ($flux(>2\text{MeV}) = 1\times10^9\ \text{m}^{-2}.\text{s}^{-1}.\text{sr}^{-1}$) is adopted, then E_0 can be computed (0.5209). In the ATICS simulation, the minimum energy is 0.6 MeV, then the integral flux (>0.6 MeV) of the beam is $1.85 \times 10^7\ \text{cm}^{-2}.\text{s}^{-1}$.

Then 3-D meshes (50 × 70 × 15) in x-y-z dimension can be made. The threshold cut of transport particle is set to 0.1 mm.

Electric field is built in dielectric with electron accumulation. Under electric field, electrons can migrate along with the excited holes despite the low conductivity. Then a current, namely leakage current, can be generated inside the dielectric and conducted through grounding. Consequently, field, electron accumulation and charge dissipation process are inter-coupled. This is a negative feedback process and final equilibrium state can be reached.

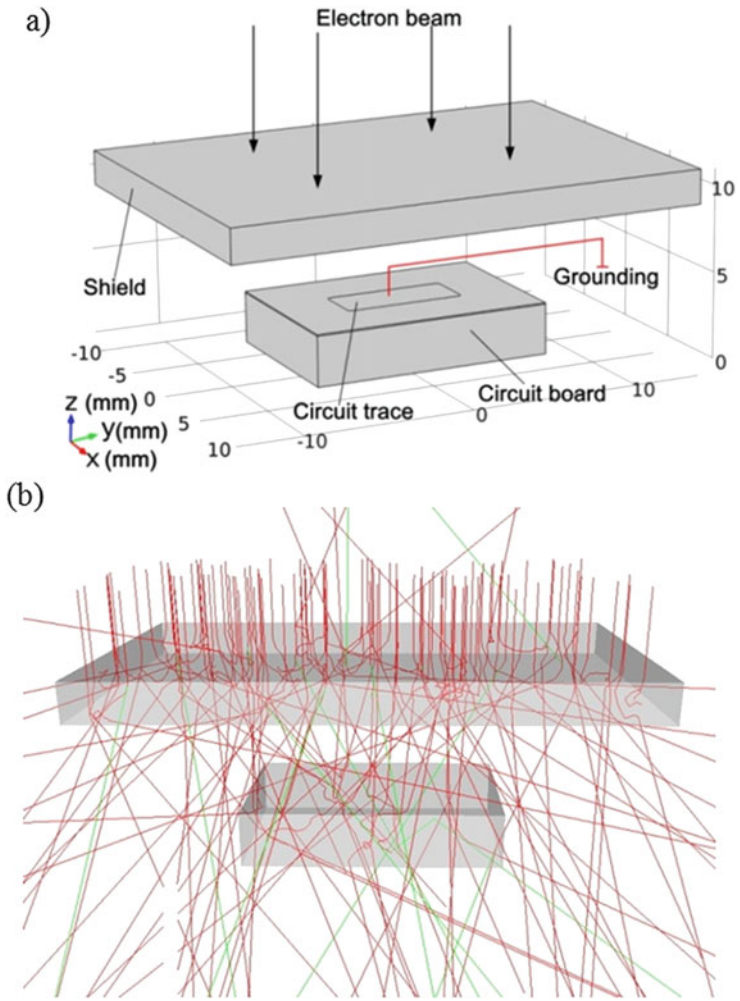

Fig. 1 The 3-D shield-PCB structure (a) and its simulation effect of electron transport (b)

According to Gauss' law, the magnitude of the field is determined by the net quantity of the deposited charge. Thus the field in dielectric is determined by the rates of electron deposition and leakage. The electron deposition rate can be obtained by transport simulation, whereas the leakage current is related to the conductivity and field. The greatest complexity in the charging process comes from the varying conductivity of the dielectrics, which is affected by several variables, such as temperature, electric field, dielectric properties, and dose rate. So stationary equations used to determine electric field can be established via above charging physics model [5].

$$\nabla \cdot \vec{J}(x,y,z) = Q_J(x,y,z) \tag{2}$$

$$\vec{J}(x,y,z) = \sigma(x,y,z)\vec{E}(x,y,z) \tag{3}$$

$$\vec{E}(x,y,z) = -\nabla u(x,y,z) \tag{4}$$

$$\sigma(x,y,z) = \sigma_r(x,y,z) + \sigma_{ET}(x,y,z) \tag{5}$$

$$\sigma_r(x,y,z) = k_p \dot{D}(x,y,z)^{\Delta} \tag{6}$$

$$\sigma_{ET}(x,y,z) = \frac{\sigma_T sinh(\alpha\gamma)}{3\alpha\gamma} \times \left[2 + cosh\left(\alpha\sqrt{\beta E(x,y,z)}\right)\right] \tag{7}$$

$$\sigma_T = \frac{\sigma_0 T_0}{T} exp\left[\frac{E_a}{k}\left(\frac{1}{T_0} - \frac{1}{T}\right)\right] \tag{8}$$

Where

$\vec{E}(x,y,z)$	The electric field vector	σ_0	The dark conductivity
$E(x,y,z)$	$\lvert\vec{E}(x,y,z)\rvert$	T_0	The temperature in σ_0 test
$\vec{J}(x,y,z)$	The total current density vector	α	$1/2kT$
$Q_J(x,y,z)$	The volume current density	β	$e^3/\pi\varepsilon_r\varepsilon_0$
$u(x,y,z)$	The electric potential	γ	$e\delta E(x,y,z)$
$\sigma(x,y,z)$	The total conductivity	e	The charge of a electron
$\sigma_r(x,y,z)$	The RIC (Radiation Induced Conductivity)	δ	The jump distance (fixed at 1 nm)
$\sigma_{ET}(x,y,z)$	The field-temperature conductivity	T	The temperature of PCB
k_p	The material-dependant co-efficient of RIC	k	Boltzmann's constant
Δ	The dimensionless material-dependent exponent ($\Delta<1$)	ε_r	The relative dielectric constant
$\dot{D}(x,y,z)$	The radiation dose rate	ε_0	The dielectric constant of vacuum
σ_T	the temperature conductivity	E_a	the activation energy

Equation (2) is charge conservation equation. The divergence of $\vec{J}(x,y,z)$ means the decrease of current in point (x,y,z). $Q_J(x,y,z)$ ($A \cdot m^{-3} = C \cdot m^{-3} \cdot s^{-1}$) equals the density of deposited electrons divided by the simulation time and can be obtained directly by ATICS. Equation (3) is Ohm's Law. Equations (2) and (3) mean that the newly injected charges per unit time will leak away entirely by conduction current and the charge density holds steady in equilibrium state. Equation (4) shows the relation between the field and potential. Equation (5) is conductivity mode [1, 7–11]. Equation (6) denotes that RIC rises with dose rate converted from energy deposition, which is computed directly by ATICS. Equations (7) and (8) show that the field and temperature have significant effects on conductivity.

After the transport simulation and the physics modeling of electron dissipating process, the other modeling work can be implemented in COMSOL Multiphysics. It has flexible physics modeling interface, and the above equations can be embedded in via PDE (Partial Differential Equation) solver. Complex geometry can be

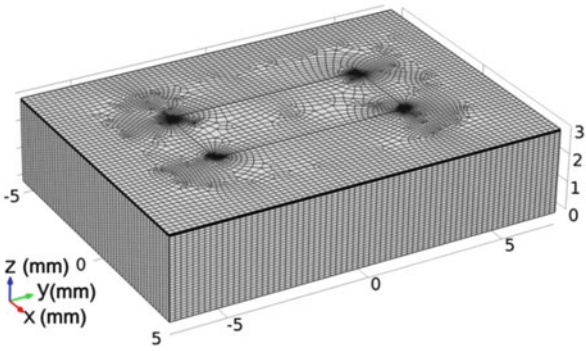

Fig. 2 The mesh figure of the PCB

Table 1 Parameters of PCB dielectric material used in the computation

$\rho(\ g/cm^3)$	$\sigma_0(s/m)$	E_a(eV)	ε_r	$k_p(s.\Omega^{-1}.m^{-1}.rad^{-1})$	Δ
1.5	2.5×10^{-15}	1	3.6	6.5×10^{-14}	1

constructed in COMSOL and multiple boundary conditions can be modeled according to the shape. In the computation, the geometry is built as shown in Fig. 1. The rectangular circuit trace is fixed at zero potential (grounding). The other surfaces are set to free and electric insulation boundary condition.

Meshing the PCB is an important work in field computation. Figure 2 shows the mesh grid figure of the PCB by COMSOL. The PCB is meshed with dense hexahedral elements, especially in circuit edges and corners.

As for the conjunction between transport simulation and electric field computation, it is performed through the importation of electron deposition and dose rate distribution data sheet, which are assigned to variable $Q_J(x, y, z)$ and $\dot{D}\ (x, y, z)$.

Table 1 [1] shows the parameters of PCB dielectric used in the computation.

Results and Analysis

According to the above conditions, electron transport simulation is carried out by ATICS. As a result, electron deposition and dose rate distributions are obtained.

The dose and electron deposition distributions of cut plane z = 3 mm are shown in Figs. 3 and 4. They indicate remarkable edge effects that energy and electron deposition in the middle region is larger than edge region. Figures 5 and 6 show the dose and electron deposition profiles along the 3 cut lines which are parallel to the *z*-axis. Line1 locates at the center. Line2 is at the center of one shorter edge and Line3 is just at one corner. From these figures, in general, the dose and electron deposition decrease linearly with the depth, and the edge effects are still remarkable in deeper depth. The linear characteristic is different from that in literature [5, 14], in which there is no adopted shield and mono-energy electron beam. The edge effects can be

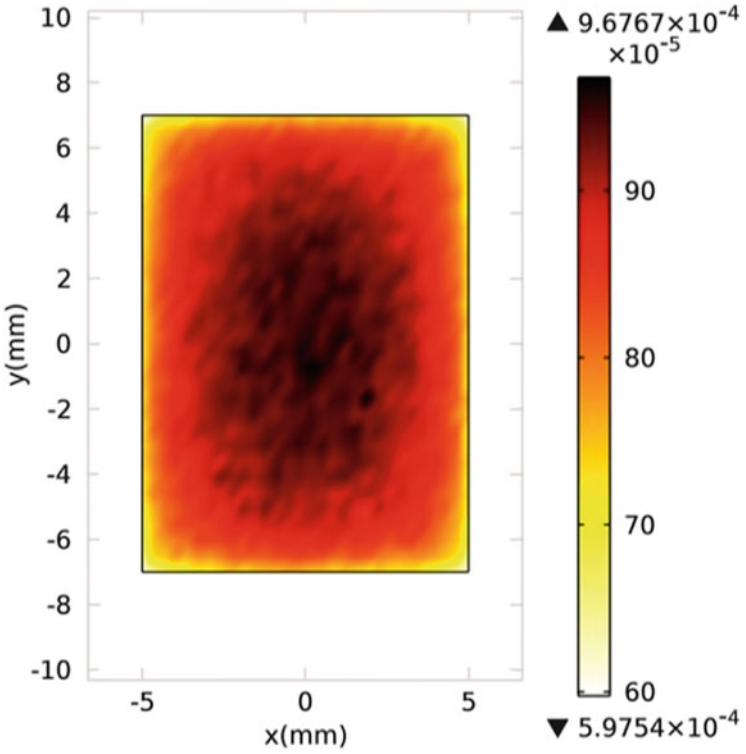

Fig. 3 The dose rate of cut plane z = 3 mm

explained by the fact that the probability of energy and electron deposition in the middle region is larger than that in the edge region.

The 3-D computation of charging electric field is carried out through solving Eqs. (2)–(8) by COMSOL with the above conditions and transport result. Then 3-D internal electric field and potential distribution in charging equilibrium state are obtained (as shown in Figs. 7, 8, 9, 10, 11, 12, 13, and 14). In this paper, the electric filed and potential are considered as absolute value, and the sign is ignored.

From these 3-D results of field distribution, the maximum electric field in the PCB is 2.8×10^7 V/m and it occurs at the circuit trace corners (as shown in Fig. 7). According to the classification of predicted fields in literature [1], this electric field is definitely hazardous. It indicates that discharge may occur despite 2-mm-thickness shield and grounding in the front surface.

For better presentation of the 3-D field distribution, we can illustrate the results through height plots of several typical cut-planes. The electric field height plot of plane z = 3 mm, z = 2.98 mm, z = 2.8 mm, z = 2 mm and z = 0 are shown in Fig. 7 through Fig. 11.

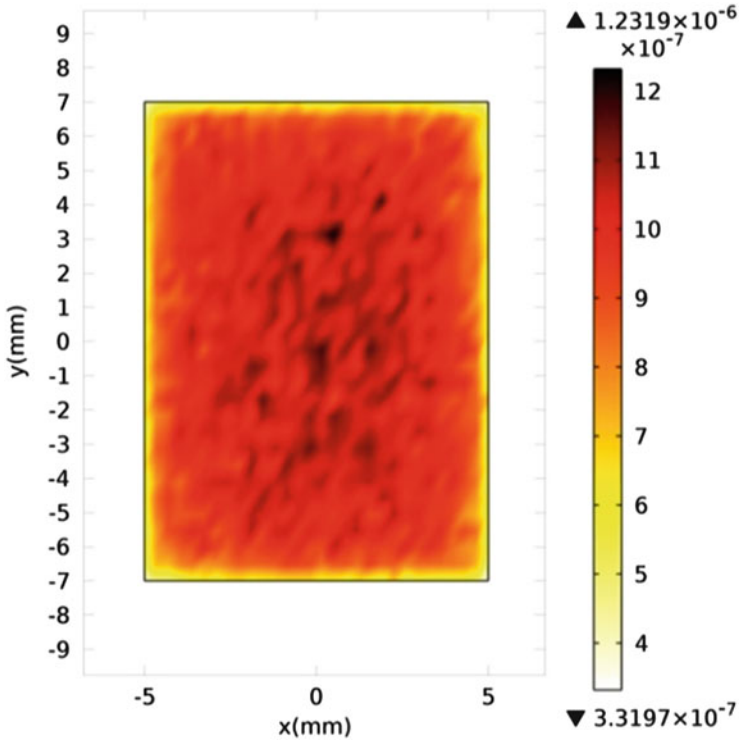

Fig. 4 The electron deposition rate of cut plane z = 3 mm

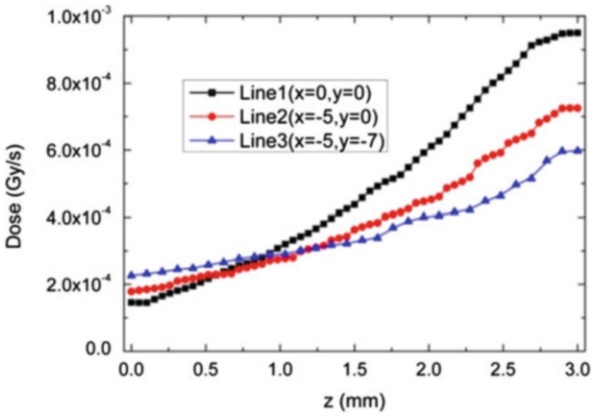

Fig. 5 The dose rate of the 3 cut lines

The common points between the three figures (Figs. 7, 8, and 9) are that similar distortion of electric field distribution arises around the four edges of rectangular circuit trace, and the distortion is especially severe around the four corners.

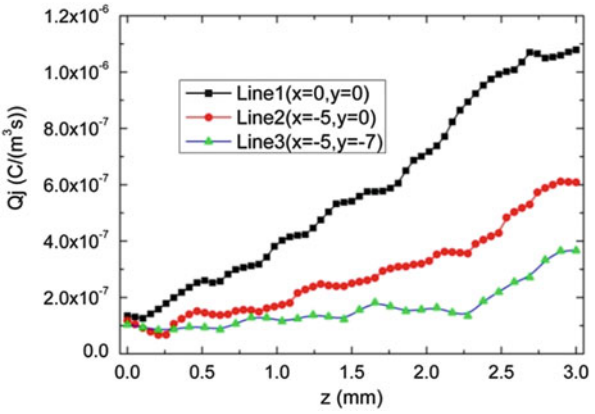

Fig. 6 The electron deposition rate of the 3 cut lines

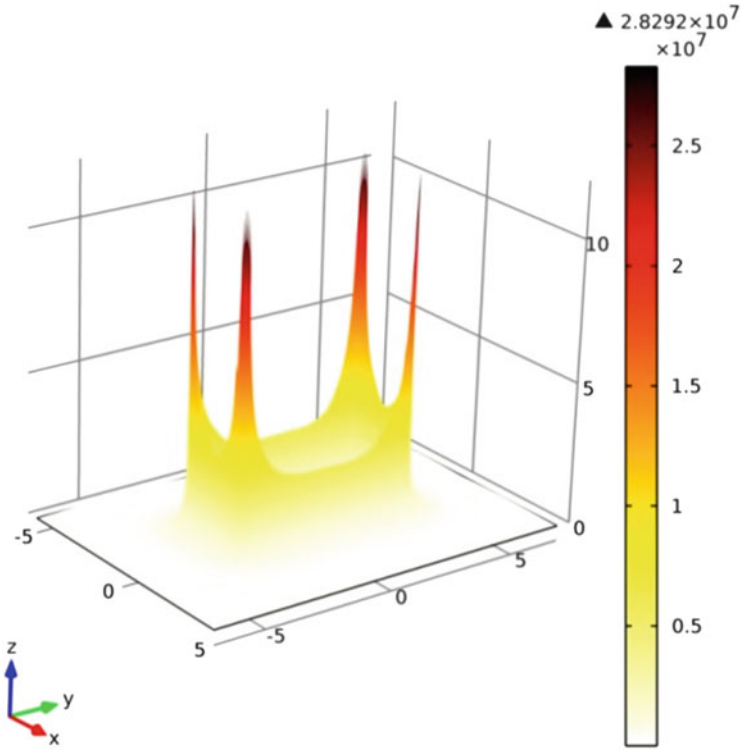

Fig. 7 The electric field of the plane z = 3 mm

Considering that electrons driven by field migrate most likely towards grounding through the shortest path, we can make a deduction that the internal current density around grounding, especially in the circuit edges and corners, is generally the

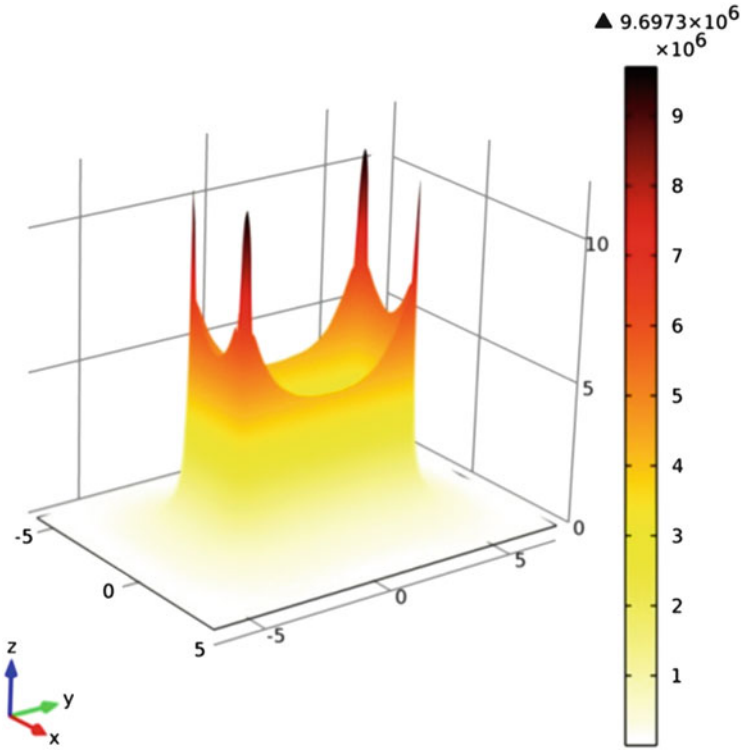

Fig. 8 The electric field of the plane z = 2.98 mm

largest in the PCB. And it isn't hard to understand that the current density around the corners is larger than that around the edges for the convergence effects in different geometric feature. According to Eq. (3), the electric field is certainly the largest around the corners than around the edges and the least in the other ungrounded district. This phenomenon is very obvious in Fig. 12, which shows the electric field of the 3 cut lines which are parallel to the *z*-axis. Line1 locates at the center of the circuit trace. Line2 is just at one corner of the trace and Line3 is at the center of one shorter edge of the trace.

The different points between Figs. 7, 8, and 9 are that the field decreases generally with the increase of the distance from the plane z = 3 mm, and the degree of the field distortion goes down as well, especially in Figs. 10 and 11. It is can be explained by considering that the closer distance from the grounded circuit, the more current converges.

In addition, the interval between plane z = 3 mm and z = 2.98 mm is merely 0.02 mm, but the maximum field of the former is about 3 times of the later. The great change of electric field can be explained by the effects of current convergence at boundary corners. It indicates that any tiny distinction may result in a great change of electric field in dielectric.

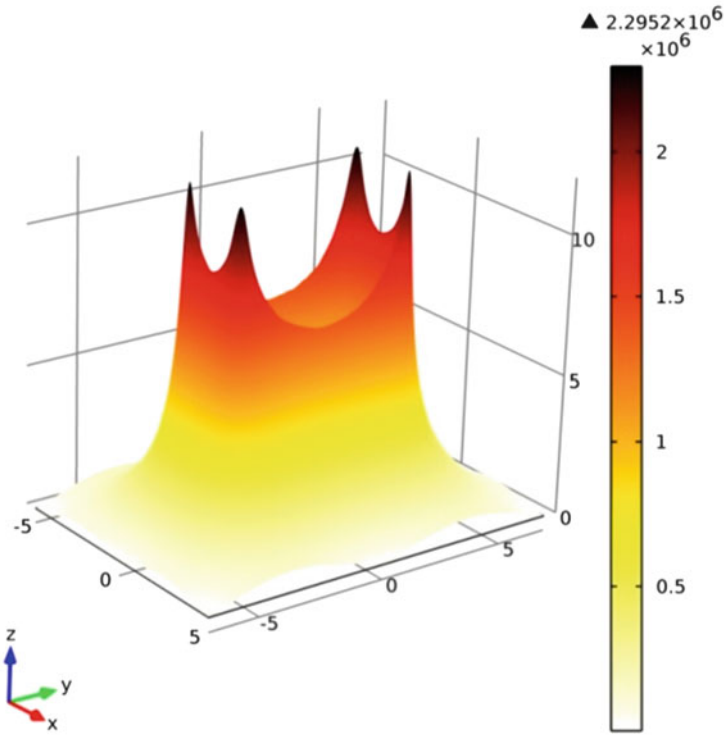

Fig. 9 The electric field of the plane z = 2.8 mm

Figures 13 and 14 are electric potential height plot of plane z = 3 mm and z = 2 mm. As shown in these two figures, the profiles are similar to a potential well. The rectangular circuit trace just locates at the bottom. It makes that the current flows from the ungrounded district with higher potential to the grounding circuit with the least potential. This can prove the above analysis about current density. Besides, there is steep drop in the potential of plane z = 3 mm around the circuit edges. In view of Eq. (3), it agrees with the field distribution around the edges. The more gradual potential change of plane z = 2 mm denotes that the field in closer distance from the grounded circuit is generally larger than that in the other district. This can indicate the quantity relation from Figs. 7, 8, 9, 10, and 11.

Conclusions

In this paper, our new 3-D simulation algorithm of internal charging is used to compute the 3-D field and potential distribution of a typical PCB. Only by a 3-D method in the real sense, the field distortion within a real object can be quantified

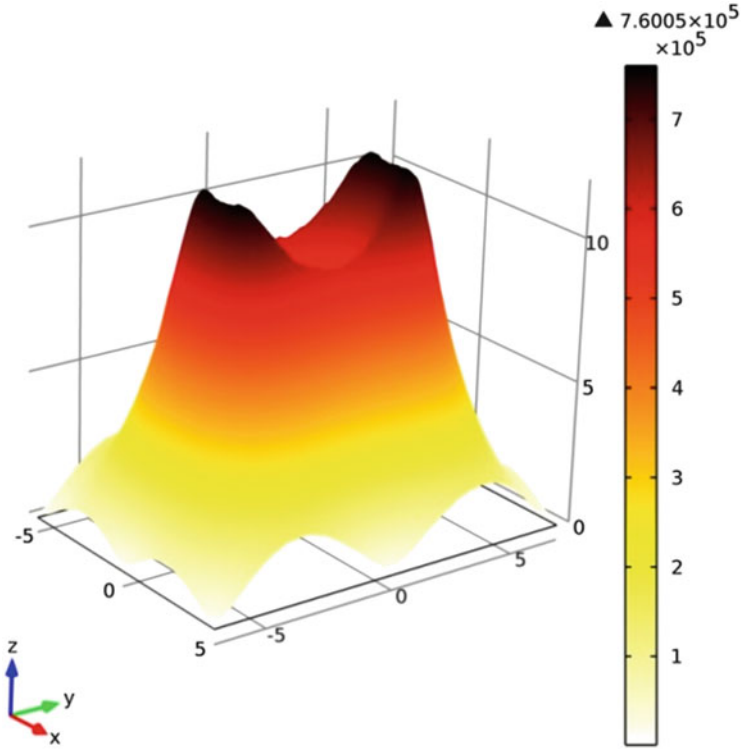

Fig. 10 The electric field of the plane z = 2 mm

well. On the basis of these accurate results, the root causes of field formation and distribution are discussed in detail. This may be useful in defensive design to internal charging effects.

According to the above calculation results and analyses, achieved conclusions and defensive design suggestions are as follows:

- Distributions of dose and charge deposition rate have remarkable edge effects.
- Severe distortion of electric field can arise around the edges of partial grounding, especially at the corners.
- The electric field distribution is mainly caused by the effects of current convergence at the boundaries.
- The degree of field distortion decreases significantly with the increase of the distance from the grounding surface.

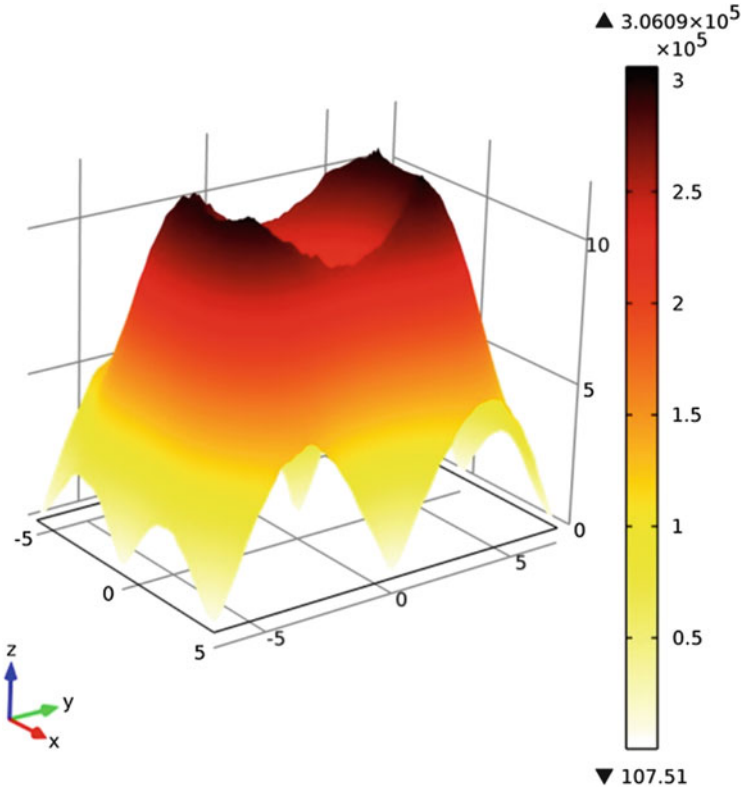

Fig. 11 The electric field of the plane z = 0 mm

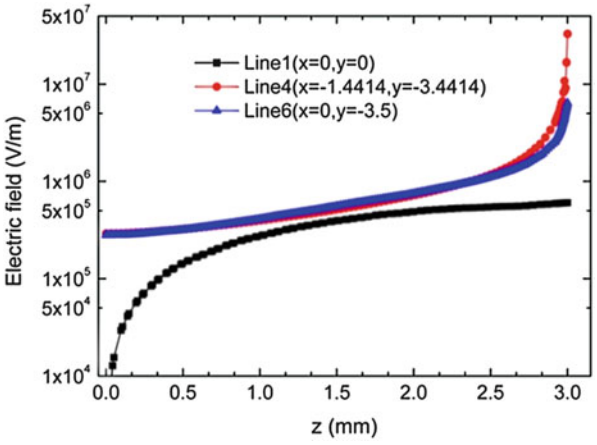

Fig. 12 The electric field of the 3 cut lines

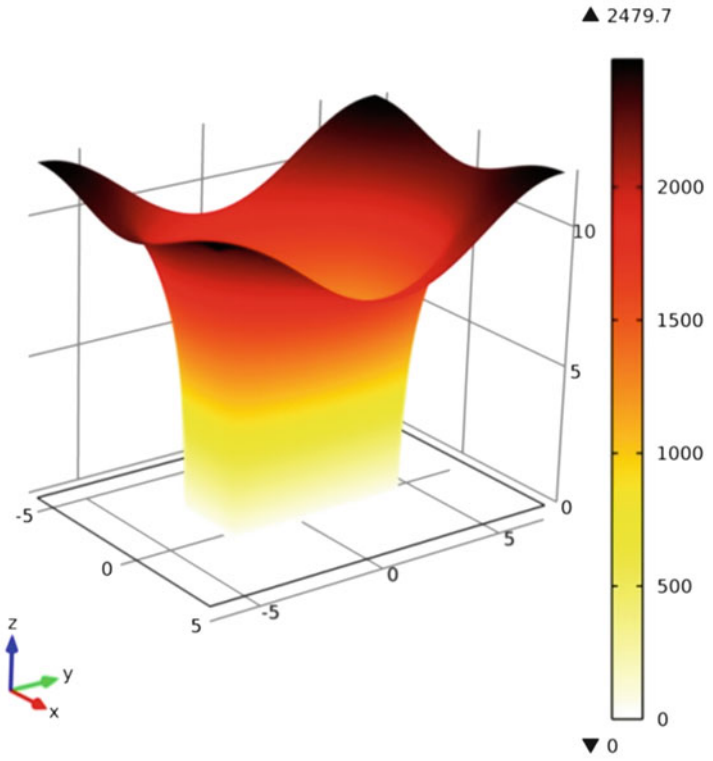

Fig. 13 The electric potential of the plane z = 3 mm

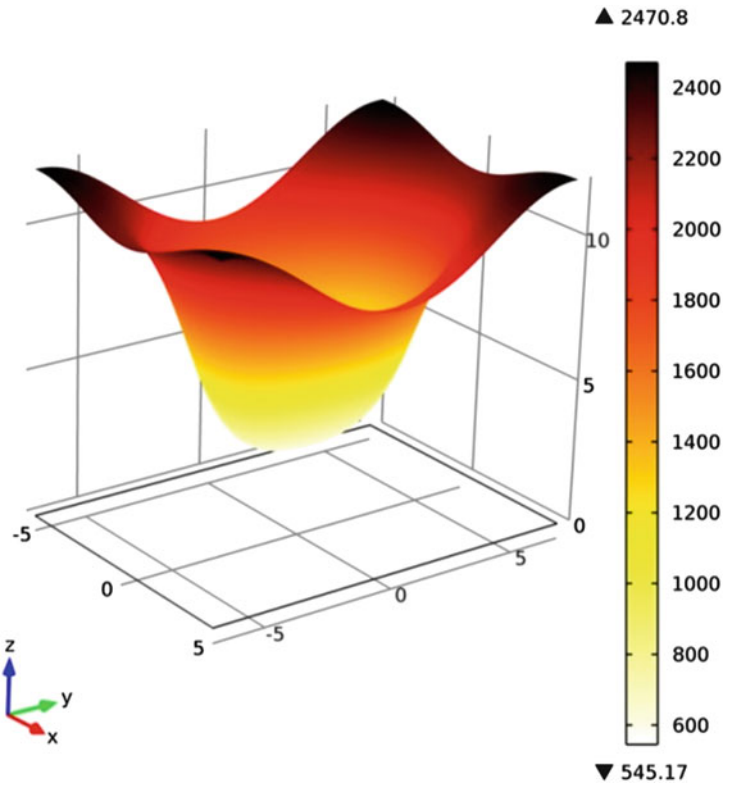

Fig. 14 The electric potential of the plane z = 2 mm

References

1. Rodgers DJ, Ryden KA, Lathem PM, Wrenn GL, Levy L, Panabiere G (1999) "Engineering tools for internal charging," ESA, Paris, France, Final Report DERA/CIS(CIS2) /7/3/36/2/4/ FINAL, January
2. Huang JG, Chen D (2004) A study of deep dielectric charging on satellites by computer simulation. Chin J Geoph 47(3):442–447
3. Sorensen J, Rodgers DJ, Ryden KA, Latham PM, Wrenn GL, Levy L, Panabiere G (2000) ESA's tools for internal charging. IEEE Trans Nucl Sci 47(3):491–497
4. Insoo J, Garrett HB, Wousik K, Minow JI (2008) Review of an internal charging code, NUMIT. IEEE Trans Plasma Sci 36(5):2467–2472
5. Tang XJ, Yi Z, Meng LF et al (2013) 3-D Internal charging simulation on typical printed circuit board. IEEE Trans Plasma Sci 41(12):3448–3452
6. Yi Z, Tang XJ, Meng LF (2007) Calculation of internal charging for spacecraft. In: Proceedings 10th Spacecraft charging technology conference
7. Tang XJ, Zhang C, Yi Z (2007) Study on internal charging of GEO satellite by computer simulation. In: Proceedings 11th International space conference pacific basin societies
8. Fowler JF (1956) Analytic expression for electrons transmission in dielectrics. Proc R Soc Conf 236:464–475

9. Adamec V, Calderwood JH (1975) Electric conduction in dielectrics at high fields. J Phys D Appl Phys 8(5):551
10. Dissado LA, Forthergill JC (1992) Polymers as wide band-gap insulators. In: Proceedings electrical degradation breakdown polymers, pp 24–48
11. Bielby RM, Morris PA, Ryden KA, Rodgers DJ, Sorensen J (2004) Determination of conductivity parameters of dielectric used in space application. In: Proceedings International conference solid dielectrics, July, pp 936–939
12. Lemon CL, Roeder JL, Looper MD et al (2010) A 3-D model of the internal charging of spacecraft dielectric materials. In: Proceedings 11th spacecraft charging technology conference, September
13. Katz I, Kim W (2010) A 3-D model of circuit board internal electro static charging. In: Proceedings 11th spacecraft charging technology conference, September
14. Seltzer SM, Berger MJ (1982) Procedure for calculating the radiation stopping power for electrons. Int J Appl Radiat Isot 33(11):1219–1226
15. http://www.comsol.com/
16. http://gdml.web.cern.ch/GDML

Investigation of the Radiation Environment in Deep Space and Its Effect on Spacecraft Materials Properties

Yigang Ding and Zicai Shen

Abstract In the deep space exploration activities, the spacecraft would travel through the interplanetary space and arrive at other planets. The vehicles would be exposed to the harmful space environments during traveling or while orbiting the planet. The radiation environment is one of the most important environmental factors that would affect the spacecraft performance. The radiation environment in the interplanetary space, as well as on Jupiter, Saturn and Mars is described in this paper. Radiation in the interplanetary space consists of galactic cosmic rays and solar protons. Because Jupiter has the strongest magnetic field in the Solar system, the particle energy in its radiation belt is ten times that of the Earth's radiation belt and its flux is a few orders of magnitude larger than at the Earth. In this harmful radiation environment, many of the materials used in the vehicle design would suffer significant properties degradation or failure. Also the effects of these severe radiation environments on vehicle materials are analyzed in this paper.

Keywords Deep space • Radiation environment • Spacecraft material • Effect • Mars • Jupiter • Saturn

Introduction

The deep space exploration has never been stopped. So far, the exploration activities conducted on the solar celestial bodies beyond the moon have exceeded 200 [1, 2]. When the deep space exploration spacecraft is travelling to the target celestial body or orbit around the target, it will encounter the harsh space radiation environment. One of the main features of deep space beyond the Earth's magnetosphere is a radiation field of energetic particles. The radiation environment experienced by a deep space explorer can be divided into three stages: first, the radiation environment during the journey from the Earth to other planets, its main source of radiation is solar particle events and galactic cosmic rays (GCR). Second, the

Y. Ding • Z. Shen (✉)
Beijing Institute of spacecraft Environment Engineering, Beijing 100094, China
e-mail: zicaishen@163.com

J. Kleiman (ed.), *Protection of Materials and Structures from the Space Environment*, Astrophysics and Space Science Proceedings 47,
DOI 10.1007/978-3-319-19309-0_46

radiation environment during landing on the target planet, its main source of radiation is energetic particles trapped by the planet magnetic field; third, the surface radiation environment of deep space planets, it is mainly from the second radiation due to the interaction of the planet body and the cosmic rays. These radiation environments are mainly composed of energetic particles.

This radiation environment will cause the sensitive materials and devices onboard the vehicle a more serious degradation than in the Earth's orbit. In the long term exposure to a deep space environment, the vehicle materials, such as thermal control materials, solar cells, optical materials, insulating materials, sealing materials and alike, encounter a severe degradation, including deterioration of optical properties, electrical properties and mechanical properties, as well as degradation of insulating performance and sealing performance.

This paper reviews the investigation of the planet's radiation environments and their models during deep space exploration activities, and provides a preliminary analysis on the degradation effects of deep space environment on spacecraft materials.

Deep Space Radiation Environment

Interplanetary Space Radiation Environment

The radiation environment in the interplanetary space is mainly composed of solar particle events and galactic cosmic rays. The galactic cosmic rays are charged particles from outside of the solar system, their main component are high energy protons, alpha particles and heavy nuclei with an atomic number greater than 2 [2]. The occurrence and intensity of solar particle events related to the solar activity cycle, consisting mainly of high energy protons, in addition to a small amount of alpha particles and heavy nuclei.

Radiation Environment at Mars

Martian surface radiation environment mainly includes galactic cosmic rays, occasional solar proton events and secondary neutrons. The galactic cosmic rays reaching Mars' surface is one of the main sources of radiation. Figure 1 shows the absorbed dose in solar maximum (1990) and solar minimum (1977) under different shielding materials and thickness. The Mars surface radiation environment by Marsgram atmosphere model during solar maximum (1990) and solar minimum (1977) activities is shown in Fig. 2.

Mars surface also is affected by the solar particle event (SPE). However, due to attenuation in the Mars atmosphere, the SPE dose reaching Mars' surface decreases approximately one order of magnitude compared to the SPE dose in space. Figure 3

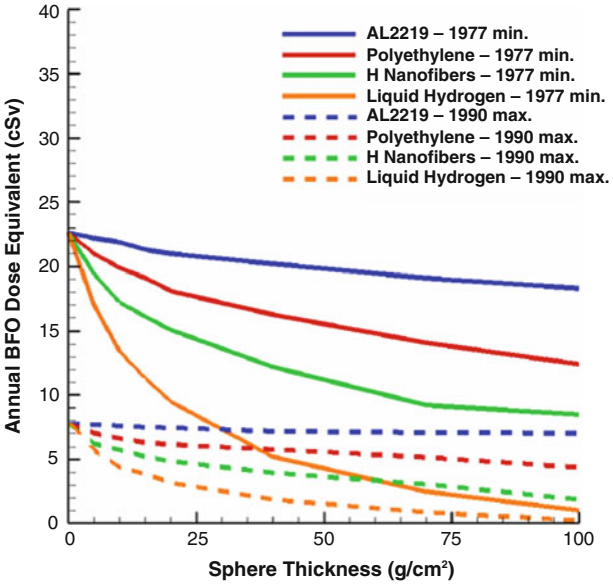

Fig. 1 Martian GCR surface exposures for various shielding materials for solar min and max activities

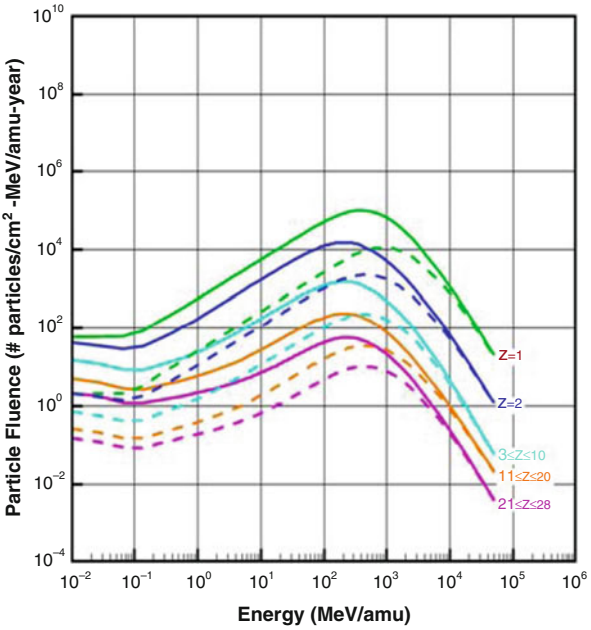

Fig. 2 Galactic cosmic ray spectra at the 1997 solar minimum (*solid lines*) and 1990 solar maximum (*dashed lines*) activities

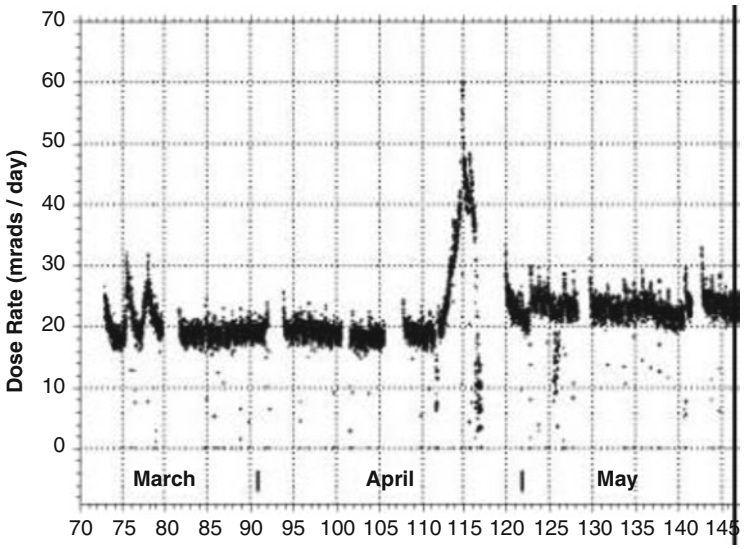

Fig. 3 MARIE absorbed dose measurements showing the peak doses from the SPEs of March 16 and 18, Apr 23 and 30, and May 22 and 27 in 2002 [3]

shows the SPE dose rate at Mars' surface measured by the Marie detector and its variation with orbit time, with the peak dose rate of 60 mrad/day [3].

Galactic cosmic rays and solar energetic particle will interact with Mars' atmosphere and low energy charged particles will be absorbed, changing the particle distribution on the surface of Mars. Meanwhile, the particles interact with the Mars' surface materials and produce secondary neutron radiation reflected back into the atmosphere. The secondary neutron component is closely related to the surface of Mars. On the regolith and bedrock, neutrons with energy below 20 MeV diffused into atmosphere from the surface is in absolute dominance in the Mars' surface neutron environment. Thus, the flux and energy of surface neutrons vary for different surface and different atmospheric conditions.

Radiation Environment on Jupiter

Jupiter is located on an orbit in 5.2 AU from Sun. It has at least 60 satellites, four main satellites are Io, Europa, Ganymede and Callisto. Jupiter has a more powerful magnetic field than Earth. Its core magnetic field is 17,500 times stronger than the Earth's core. On the surface of Jupiter, the magnetic field strength becomes smaller, but it is still more than ten times stronger than the Earth's surface magnetic field. Jupiter's magnetic moment is 1.55×10^{20} Tm^3, approximately 20,000 times higher than the Earth's magnetic moment.

Because Jupiter has the strongest magnetic field in the solar system, its energy density and number of trapped particles is much higher than on other planets. The energy of trapped particles in Jupiter's radiation belt is ten times higher than the energy of particles in the Earth's radiation belt, and its number density is several orders of magnitude more than the Earth's radiation belt. Now it is considered that most of the radiation belt particles are mainly from Jupiter's moon Io. Therefore, the most intensive part of the magnetosphere is located in the torus between 5.5 and 8 R_J. The results from the Energetic Particles Detector (EPD) in Galileo shows that the proton number and energy density in the range of 20–25 R_J is higher than those of other particles. The results from Ulysses show that the equatorial omnidirectional proton flux has an exponentially decaying distribution with the distance from the magnetic equator and approximately vertical symmetry. The two-dimensional image of synchrotron radiation from the radio telescope shows that there are two different distributions of high energy electrons (1–100 MeV) in the inner radiation belt. First, radiation intensity at the magnetic equator, with the maximum density at 1–1.5 R_J. Second, the electron density has a wide angular distribution and produces radiation over a wide range of magnetic longitudes. The distribution of energetic electrons is limited by absorption in Jupiter's ring and by its satellites.

Jupiter's radiation belt is composed of electrons, protons and heavy ions. The first model of the belt was built in late 1950s and in early 1960s, shortly after the discovery of Jupiter's radiation belt. This model is based on the theory of Earth radiation belt and ground observation results of Jupiter synchrotron radiation. Later, based on the observation of Pioneer and Voyager vehicles, the first comprehensive model of Jupiter trapped radiation was developed in 1980s and 1990s. Recently, the model of high-energy electron and heavy ions was improved on the basis of observation data by Galileo spacecraft. Figure 4 shows the predicted synchrotron emissions at 1.4 GHz and CML 200 for the modified DM electron radiation distributions for $E > 1$ MeV. Also during this period, the understanding of Jupiter magnetosphere trapped particles was improved based on a physical model developed in Europe.

Radiation Environment at Saturn

Saturn is located at 9.54 AU from the Sun and has an equatorial radius (RS) of 60,268 km. Saturn was first visited by NASA's Pioneer 11 in 1979 and later by Voyager 1 and 2. Cassini (a joint NASA/ESA project) arrived on July 1, 2004 and orbited Saturn for at least 4 years.

Saturn's magnetic field is mainly composed of three parts; the first part is the intrinsic dipole magnetic field, the second is the toroidal plasma magnetic field around the Saturn, the third part is from the contribution of solar wind on the magnetosphere.

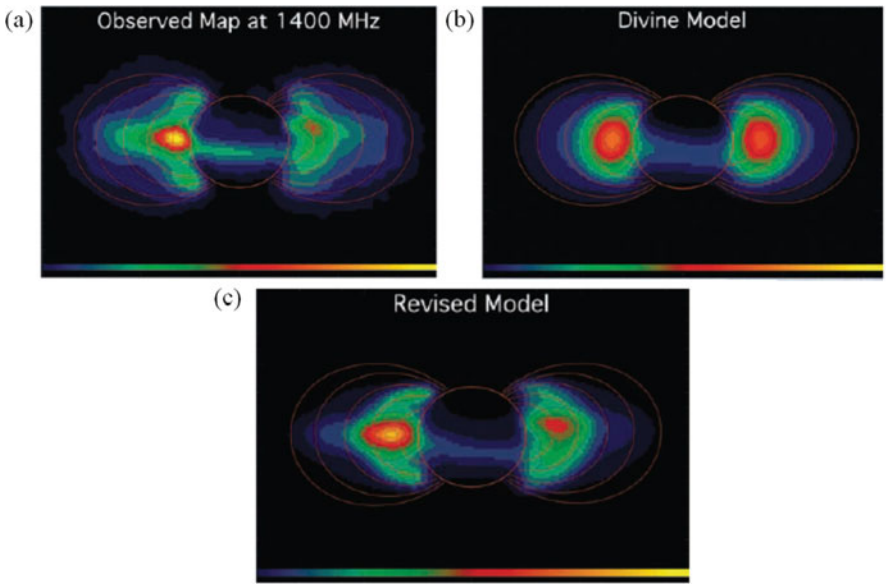

Fig. 4 Predicted synchrotron emissions at 1.4 GHz and CML 200 for the modified DM electron radiation distributions for E > 1 MeV. (**a**) observation results; (**b**) old model; (**c**) revised model

The former two parts are called inner source field and they have axis symmetry and equatorial symmetry. In the South and North Polar Regions of Saturn, the magnetic field strength is about 0.7 Gauss and 0.6 Gauss, respectively.

Due to the presence at Saturn of a strong magnetic field, a trapped particle radiation belt is formed around this planet. Saturn's radiation belt was first observed by the instruments on Pioneer 11 in September 1979. These results gave evidence that the observed trapped radiation is absorbed by the satellite and by the Saturn rings.

The Saturnian radiation belts did not receive as much attention as the Jovian radiation belts because they are not nearly as intense, the famous Saturnian particle rings tend to deplete the belts near where their peak would occur. As a result, there was no systematic development of engineering models of the Saturnian radiation environment for mission design.

A primary exception is that of Divine (1990) [4]. That study used published data from several charged particle experiments aboard the Pioneer 11, Voyager 1, and Voyager 2 spacecraft during their flybys at Saturn to generate numerical models for the electron and proton radiation belts between 2.3 and 13 Saturn radii. The Divine Saturn radiation model described the electron distributions at energies between 0.04 and 10 MeV and the proton distributions at energies between 0.14 and 80 MeV. The model was intended to predict particle intensity, flux, and fluence for the Cassini orbiter. Divine carried out hand calculations using the model but never formally developed a computer program that could be used for general mission analyses (Fig. 5).

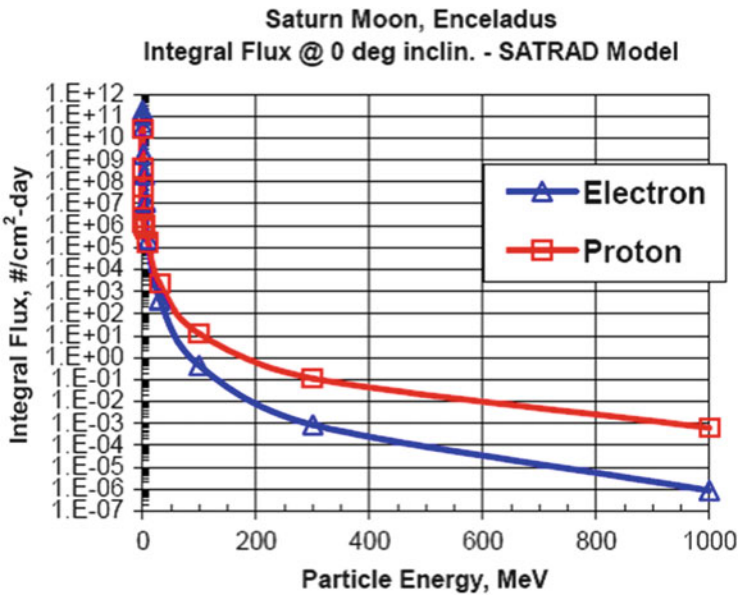

Fig. 5 Enceladus integral proton and electron spectra at 0° inclination using the SATRAD model

The Effects of Deep Space Radiation Environment on Materials

Radiation Effects on Spacecraft Materials

Thermal control materials are an important component of the spacecraft thermal control subsystem. The commonly used thermal control materials include thermal control paints, second surface mirrors, polymer films, and so on. Thermal control paints are generally composed of pigments and organic or inorganic matrices. These components will degrade under the radiation environment and their properties will change, thus leading to an increase in the solar absorptance.

Polymer materials are widely used on spacecraft. The effect of radiation environment on polymer materials will lead to cross-linking, degradation, change in the unsaturated bond content and free radical production. This will cause the degradation of physical properties and mechanical properties of polymer materials.

Optical materials in the optical systems will suffer degradation of optical properties under the action of radiation environment. Optical materials will experience the following effects when exposed to electrons or protons: (1) Coloration effects. Many optical glasses and crystals will generate some additional spectral absorptance, i.e. a coloration phenomenon. Materials coloration can lead to a transmittance decrease. (2) Surface erosion. Particles with energies of tens of keV can cause the atoms in the materials composition to be sputtered, leading to surface

sputter erosion of materials. In addition to direct sputtering effect, the effect of radiation can also cause foaming at the surface of optical materials, i.e. the optical surface erosion. (3) Charging and discharging effects, energetic charged particles can cause significant surface non-uniform charging, causing the breakdown of glass lenses.

The Effect of Deep Space Radiation Environment on Materials

Due to different deep space exploration missions, spacecraft experience different radiation environments. For more harsh radiation environments of Jupiter and Saturn, we must pay attention to choice of candidate materials. The particle flux of Jupiter's radiation belt is several orders of magnitude higher than the Earth's belt. In medium or high Earth's orbits, the average dose absorbed by surface materials is about 109 rad, thereby we can estimate that the surfaces of materials on spacecraft flying in Jupiter's radiation belt will absorb a dose more than 10^{10} rad. Due to such a dose, many polymer materials, such as polypropylene, POM, PTFE, etc., will experience strong performance degradation. Most of optical glasses will be unusable after exposure to 10^6–10^8 rad. Thus, we must carry out a detailed analysis of radiation environments met in deep space exploration missions, to determine the candidate materials tolerant to radiation.

Summary

Radiation in the interplanetary space consists of galactic cosmic rays and solar protons. The Martian surface radiation environment mainly includes galactic cosmic rays, occasional solar proton events and secondary neutrons. Because Jupiter has the strongest magnetic field in the Solar system, the particle energy in its radiation belt is ten times higher than that of the Earth's radiation belt and its flux is a few orders of magnitude larger than the radiation flux on Earth. In this harmful radiation environment, many of the materials used in the vehicle design would suffer significant properties degradation or failure. Thus, we must carry out a detailed analysis of radiation environments met in deep space exploration missions, to determine the candidate materials tolerant to radiation.

References

1. Atwell W (2007) Radiation environments for deep-space missions and exposure estimates. In: AIAA SPACE 2007 conference & exposition, 18–20 Sept, Long Beach, CA

2. Tripathi RK, Nealy JE (2007) Mars radiation risk assessment and shielding design for long-term exposure to ionizing space radiation. Nov 23
3. Atwell W (2003) Solar Proton event observations at Mars with MARIE: an update. Space. 23–25 Sept, Long Beach, CA
4. Garrett HB, Levin SM and Bolton SJ (2005) A revised model of Jupiter's inner electron belts: updating the divine radiation model. Geophys Res lett 32: L04104. doi: 10.1029/2004, GL021986

Mechanism and Kinetic Characterization of the Electron Irradiation Induced Degradation of Dgeba/Dicy

Gang Liu, Lixin Zhang, and Jian Jiang

Abstract The diglycidyl ether of bisphenol A/dicyandimide (DGEBA/DICY) films were tested using 160 keV electron irradiation simulation facility. The degradation mechanism of the irradiated DGEBA/DICY was analyzed using EPR, FT-IR, and XPS. The kinetic process of irradiation induced degradation of DGEBA/DICY was expressed quantitatively based on the data from FT-IR and XPS. The relationship between the micro-mechanism and the macro-property was proposed that allowed describing the property variation of DGEBA/DICY with electron irradiation fluence.

Keywords Electron irradiation • Epoxy resin • Degradation • Exponential recession

Introduction

With the development of space technology, epoxy resins have found wide applications in coating, composites materials and adhesives [1], and, gradually, are becoming an important spacecraft structural material. Under the irradiation of electrons and protons during the space flight in orbit, the properties of epoxy resins will be degraded, consequently, resulting in potential serious spacecraft malfunctioning. Therefore, study of the mechanism and the kinetic process of the irradiation induced degradation is a new demand in the application field of high-molecular materials [3–6].

Under ionizing radiation environment, a series of complex physical and chemical changes will arise in the polymer materials, generally exhibiting two effects of

G. Liu (✉) • L. Zhang
Shanghai Institute of Spacecraft Equipment, Shanghai 200240, China

Shanghai Space Environment Simulation and Verification Engineering Technology Research Center, Shanghai 200240, China
e-mail: sast_casc_8122@126.com

J. Jiang
Shanghai Institute of Spacecraft Equipment, Shanghai 200240, China

J. Kleiman (ed.), *Protection of Materials and Structures from the Space Environment*, Astrophysics and Space Science Proceedings 47,
DOI 10.1007/978-3-319-19309-0_47

cross-linking and scission. Most efforts in the field of radiation chemistry is focused on radiation processing and modification of polymer materials [7, 8]. However, relatively less study was carried out on the mechanism and kinetics of irradiation induced degradation. The degradation and change in the performance of epoxy resin under condition of electron irradiation were studied in literatures [9–11], where a few useful results were reported. However, there is a lack of refining the common law due to a difference in the materials and the experimental conditions chosen by different researchers.

There are various methods to analyze the microstructure of polymers, such as Fourier Infrared Spectroscopy (FT-IR), X-ray photoelectron spectroscopy (XPS), and electron paramagnetic resonance spectroscopy (EPR) [12–14]. Benedicte Mailhot obtained the variation in stiffness as a function of film thickness and gave degradation profiles for polymers using a combination of AFM nano-indentation and micro-FTIR, named as depth profiling. Their results connected the mechanical properties and the aging mechanism of irradiated polymers, providing a new way to explore degrading mechanism of irradiated polymers [15].

Aiming at space applications, a study was conducted of the degradation mechanism of DGEBA/DICY films irradiated with 160 keV electrons and the irradiation induced degradation kinetics of DGEBA were characterized quantitatively by combining several common analytical methods.

Experiment

The specimens are Diglycidyl Ether of Bisphenol A (DGEBA) solid films with a thickness of 0.35 mm and an epoxy value of about 0.5. The molecular structure is shown in Fig. 1. The curing conditions for the specimens are as follows: using dicyandimide (DICY) as curing agent, firstly heated to 125 °C with a rate of 3 °C/min, and maintaining for 3.5 h, then followed by cooling in air to room temperature.

The irradiation test was performed in a complex radiation simulation facility at Harbin Institute of Technology. The specimens were placed in a vacuum chamber maintained at 1×10^{-4} Pa and irradiated with 160 keV energy electrons at a maximum fluence of $4 \times 10^{16}/\text{cm}^2$.

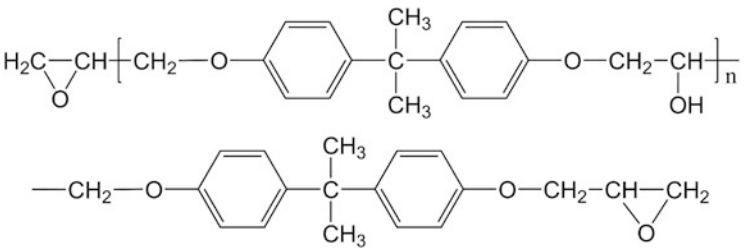

Fig. 1 Molecular structure of DGEBA

Before and after irradiation, tensile fracture strength of the specimens was measured on the Э-71 type universal testing machine made in Ukraine. The EPR, FTIR and XPS analyses were carried out using the German Brook A200 electronic paramagnetic resonance spectrometer, Magna IR560 (Nicolet) Fourier transform infrared spectroscopy, and K-Alpha X-ray photoelectron spectroscopy made by Scientific & Technical Corporation, respectively.

Degradation Mechanism Induced by Electron Irradiation

As shown in Fig. 2, when the electron fluence exceeds 5×10^{15} cm^{-2}, EPR analysis detected the distinct signal of free radicals, giving evidence that electron irradiation induced degradation of DGEBA/DICY is controlled by a free radical mechanism. On the other hand, the g value of the paramagnetic spectrum remains unchanged during the irradiation, indicating the type of the formed free radicals does not change with increasing irradiation fluence.

Figure 3 shows the results of FT-IR analysis which shows that the benzene ring is stable during the irradiation. The extension of vibration absorption peak of the C-N bond (1292 cm^{-1}) in the curing structure and that of the aliphatic C-O bond (1036 cm^{-1}) in the main chain are decreased with increasing irradiation fluence, indicating that the major mechanism of irradiation induced degradation are the damage of the curing structure and the breaking of aliphatic C-O bond in the

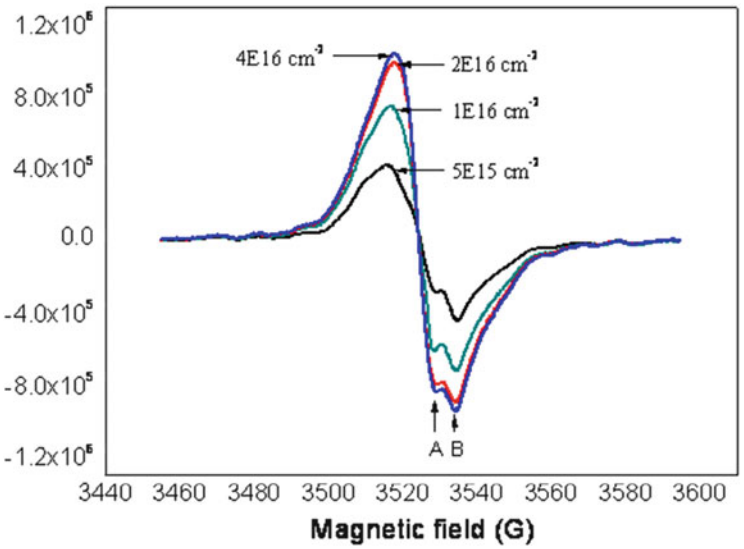

Fig. 2 EPR spectra of DGEBA/DICY electron irradiated with various fluence

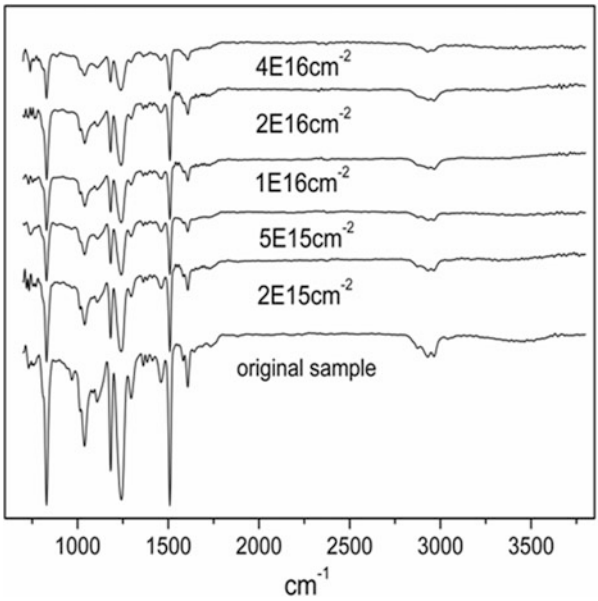

Fig. 3 ATR-FTIR spectra of DGEBA/DICY after 160 keV electrons irradiation vs. fluence

backbone structure of DGENA/DICY. The two disappeared peaks at 1382 and 1362 cm^{-1} suggest that there was also isopropylidene cleavage under electron irradiation.

Figure 4 presents the results of XPS analysis which shows that the binding energy of the feature peak (532.3 eV) corresponding to the C-O ether bond is decreased with increased electron irradiation fluence, which further confirms the bond breaking mechanism of ether C-O. By contrast, the binding energy of the feature peak attributed to carbonyl C = O (531.5 eV) shows an opposite variation comparing to that of the ether C-O bond, indicating that the generated carbonyl C = O is transformed from the broken ether C-O bond.

The degradation reaction of the C-N and C-O bonds is shown schematically in Figs. 5 and 6.

Degradation Kinetics of the Irradiated DGENA/DICY

The irradiation induced degradation causes a decrease in the fracture strength of the specimens with an increase of irradiation fluence. According to the above analysis, the major degradation mechanism is bond breaking of the C-N and C-O bonds in the DGENA/DICY's curing structure and in the backbone structure, respectively. Thus, the data from tensile test and the FTIR and XPS analyses were normalized. The normalized property degradation and the bond breaking yield refer to the percentage of decrease in the fracture strength for DGENA/DICY, and of the broken C-N

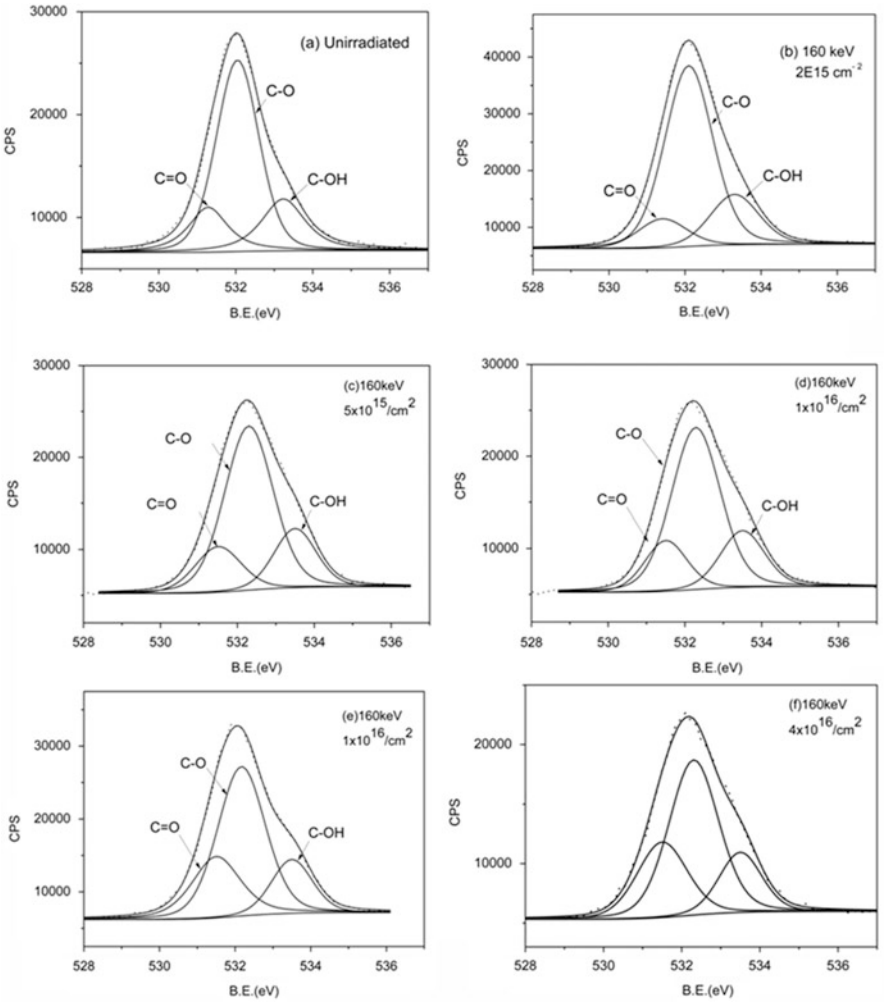

Fig. 4 High resolution O1s XPS spectra of DGEBA/DICY irradiated with 160 keV electrons with various fluencies

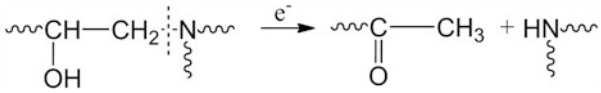

Fig. 5 Degradation reaction of the C-N bond

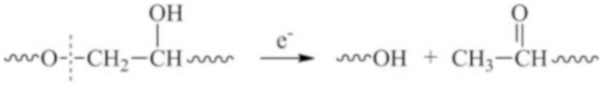

Fig. 6 Degradation reaction of the C-O bond

and/or C-O bonds comparing to un-irradiated specimens. The mathematical fitting on the normalized data demonstrates that both normalized decrease in the fracture strength and the yield of broken C-N or C-O bond can be expressed by the same equation form, which represents an exponential variation with irradiation fluence, as shown by Eq. (1).

$$y = y_0 + A_1 \exp\left(-\frac{\phi}{t_1}\right) \tag{1}$$

where y represents the normalized decrease in the fracture strength of DGENA/DICY or the bond breaking yield; y_0 represents the maximum value of electron irradiation induced damage; A_1 is a constant related to the property and structure of the material; Φ is fluence of electron irradiation; and t_1 is the ratio constant of irradiation induced degradation.

Table 1 gives the mathematical fitting of the parameters in Eq. (1) calculated for the normalized decrease in the fracture strength of the specimens and the bond breaking yield of C-N and C-O. We tried to explore the quantitative relationship between the variation in macro properties of the material and the degrading process induced by irradiation, in order to set up the equation characterizing the dynamic degrading process of DGEBA/DICY under electron irradiation. It can be seen from Table 1 that the t_1 values for normalized decrease in the fracture strength and bond breaking yields of C-N and C-O bonds are almost the same. The y_0 and/or A_1 of DGENA/DICY, which characterize the fracture strength of DGENA/DICY, is equal to the sum of the corresponding y_0 and/or A_1 of the normalized broken C-N and C-O bonds, demonstrating there is an interrelationship between the change in the fracture strength and the breaking of the two bonds.

Plotting the above three fitting curves together allows to see that the curve of the normalized decrease in the fracture strength closely conforms to the curve for the C-N bond plus that of the C-O bond, as shown in Fig. 7. This result further proves that the intrinsic mechanism of the change in the fracture strength of DGEBA/DICY under electron irradiation is the breaking of the C-N and C-O bonds. Although there is also cleavage of the isopropylidene group, its effect on mechanical properties variation can be neglected.

Thus, this study allows establishing the internal relationship between the mechanical properties and irradiation induced degradation and shows that Eq. (1) is able to characterize and evaluate quantitatively the kinetics of DGEBA/DICY's degrading evolution under electron irradiation conditions.

Table 1 Fitting of the parameters in Eq. (1)

Fitting parameters	y_0	A	t
y_σ	78.35	−76.03	12.90
$y_{C\text{-}N}$	26.11	−24.86	12.79
$y_{C\text{-}O}$	50.69	−45.26	12.78

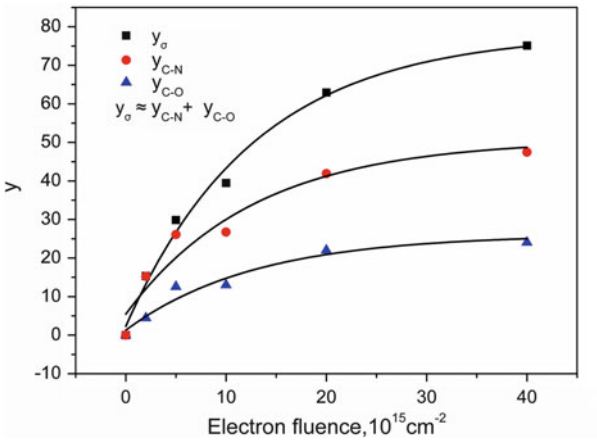

Fig. 7 Fitting curves of the normalized decrease in the tensile fracture strength of DGEBA/DICY and breaking bond yields of the C-N and C-O bonds vs. electron fluence

Conclusions

The results of EPR, FTIR and XPS analysis show that DGEBA/DICY is degraded under electron irradiation by a free radical mechanism. The degradation is characterized by damage of the C-N bond in the curing structure and by damage of the C-O bond in the backbone structure, as well as in the isopropylidene structure. Normalization and mathematic fitting of the test data prove that breaking of the C-N and C-O bonds is the major factor that leads to the decrease in the fracture strength of DGEBA/DICY. An equation of the $y = y_0 + A_1\exp(\Phi/t_1)$ form is established to characterize and evaluate quantitatively the kinetic process of property evolution under electron irradiation for DGEBA/DICY, demonstrating the existence of an interrelationship between the change in the fracture strength and breaking of the two bonds.

References

1. Wang D (2001) Production and application of epoxy resin, 1st edn. Chemical Industry Press, Beijing, p 10
2. Grossman E, Gouzman I (2003) Space environment effects on polymers in low Earth orbit. Nucl Inst Methods Phys Res B 208:48
3. Gao Y, Jiang S, Yang D, He S, Xiao J, Li Z (2005) A study on radiation effect of <200keV protons on M40J/epoxy composites. Nucl Inst Methods Phys Res B 229:261

4. Longieras N, Sebban M, Palmas P, Rivaton A, Gardette JL (2007) Degradation of epoxy resins under high energy electron beam irradiation: radio-oxidation. Polym Degrad Stab 92:2190
5. Vignoud L, David L, Sixou B, Vigier G, Stevenson I (2001) Effect of electron irradiation on the mechanical properties of DGEBA/DDM epoxy resins. Nucl Instrum Methods B 185:336–340
6. Vignoud L, David L, Sixou B, Vigier G (2001) Influence of electron irradiation on the mobility and on the mechanical properties of DGEBA/TETA epoxy resins. Polymer 42:4657–4665
7. Phil HK, Jong SP, Young CN (2002) Effect of electron beam and γ-ray irradiation on the curing of epoxy resin. Macromol Res 10:332
8. Li F, Jianwenb B, Chen X, Bao H, Wang H (2002) Factors influencing EB curing of epoxy matrix. Radiat Phys Chem 63:557
9. Benard F, Campistron I, Laguerre A, Laval F (2006) Influence of silica fillers during the electron irradiations of DGEBA/TETA epoxy resins, part I: study of the chemical modification on model compounds. Polym Degrad Stab 91:2110
10. Benard F, Campistron I, Laguerre A, Vigier G, Laval F (2006) Influence of silica fillers during the electron irradiation of DGEBA/TETA epoxy resins, Part II: study of the thermomechanical properties. Polym Degrad Stab 91:2119
11. Benard F, Buzaré JY, Campistron I, Laguerre A, Laval F (2007) Influence of silica fillers during the electron irradiation of DGEBA/TETA epoxy resins, part III: solid state NMR investigations. Polym Degrad Stab 92:785
12. Wang T-L, Huang F-J (1999) XPS and ATR surface studies of block copolyurethanes based on 1,2-ethylene bis(4-phenyl isocyanate). Macromol Rapid Commun 20:497
13. Mailhot B, Morlat-Therias S, Ouahioune M, Gardette JL (2005) Study of the degradation of an epoxy/amine resin 1: photo- and thermo-chemical mechanisms. Macromol Chem Phys 206:575
14. Mailhot B, Morlat-Therias S, Bussiere PO, Gardette JL (2005) Study of the degradation of an epoxy/amine resin 2: kinetics and depth-profiles. Macromol Chem Phys 206:585
15. Mailhot B, Bussiere PO, Rivaton A, Morlat-Therias S, Gardette JL (2004) Depth profiling by AFM nanoindentations and micro-FTIR spectroscopy for the study of polymer ageing. Macromol Rapid Commun 25:436

Effectiveness Analysis of Ground Simulation Space Environmental Tests and Their Effects on Spacecraft

Zicai Shen and Xiaoyi Zhai

Abstract Space environments and their effects have threatened the reliability and lifetime of spacecraft materials and structures. Besides flight tests, ground simulation tests are essential to evaluate the property degradation of spacecraft materials and structures. However, restricted by the technology, ground simulation cannot reproduce totally the space environments. Space environments and their effects are introduced firstly in this paper, and then a study on the effectiveness of ground simulation testing for spacecraft to imitate space environmental effects is reported, and some key problems and key technologies are analyzed. At last, some advices to improve the effectiveness of ground simulation testing are proposed.

Keywords Space environments • Ground simulation testing • Effectiveness

Introduction

During the preparation, launch, in-orbit fly and reentry, spacecraft will encounter ground environments, launch environments, in-orbit environments and reentry environments. All the environments will result in degradation or damage of spacecraft materials and structures, so flight tests, ground simulation tests and numerical simulations are used to evaluate the change in their properties. Because of low cost and convenience of use, the ground simulation testing is widely used as acceptance testing and evaluation testing of spacecraft materials and structures. Because of uncertainties between the space environments and their models, difficulties in

Zicai Shen (1980–), Doctor, major in space radiation environment engineering and deep space exploration. Project supported by National Natural Science Foundation of China. (Grant No. 41174166)

Z. Shen (✉)
Beijing Institute of Spacecraft Environment Engineering, Beijing 100094, China
e-mail: zicaishen@163.com

X. Zhai
Institute of Manned Space System Engineering, China Academy of Space Technology, Beijing 100094, China

J. Kleiman (ed.), *Protection of Materials and Structures from the Space Environment*, Astrophysics and Space Science Proceedings 47,
DOI 10.1007/978-3-319-19309-0_48

reproducing the parameters of the effects, the inconsistency of simulation sources or in test methods, added complexity due to packaging or structure of samples, questions of reproducibility of results on different systems, etc. there are errors or mistakes in the ground simulation testing. So it is very important to pay attention to effectiveness analysis of ground simulation testing imitating the space environments and their effects [1–3].

In this paper, space environments and their effects are introduced firstly, and then uncertainties between the space environments and models, test methods, samples, etc. are analyzed. Thirdly, the effectiveness analyses of ground simulation testing are made for both accidental and systemic factors. At last, some countermeasures are proposed to decrease the errors and to improve the effectiveness of ground simulation testing.

Space Environments and Effects

Space Environments

During the course of space missions, spacecraft will operate in different orbits such as LEO, GEO, HEO, SSO or deep space. Spacecraft in different orbit will encounter different environments such as solar cosmic rays, galactic cosmic rays, atomic oxygen, space debris and meteoroids, induced radiation belts, dust, etc. Some space environment factors should be given special attention when concerning particular orbits of operation. For example, fast atomic oxygen (AO) and AO/UV (ultraviolet) in LEO, or intensive space radiation in MEO consisting of keV to MeV protons and electrons, are critically important factors for some sensitive materials, as listed in Table 1 [4]. So spacecraft materials should be tested and evaluated according to their operation orbit and their location on spacecraft.

Space environments are complex and dynamic. The energies, densities, and constituents of orbital environmental factors vary with position (such as attitude, latitude, and longitude), local time, season and solar activity. Furthermore, the presence and activities of space systems modify many of the natural environments, such as the neutral particles and plasma environments, induced contamination, etc. A summary of the near- and interplanetary space environmental factors that need to be included in the evaluation of spacecraft materials is given in Table 1.

We should consider that space environmental factors may affect spacecraft materials and structures simultaneously, and that space environmental factors may influence spacecraft materials synergistically. Being concerned only with one environmental factor may result in inadequate or incorrect conclusion while evaluating the degradation of spacecraft materials properties.

Table 1 Summary of near-/interplanetary space environmental factors to be included into evaluation of spacecraft materials [4]

Factors		LEO	MEO GEO NEO	Near-planetary environments						
				Moon	Mars	Venus	Jupiter	Saturn	Pluto	Uranus
Temperature range (°C)		−125/ +125	−30/+400	−125/ +225	−140/ +150	−80/ +270	−150/ +230	−175/ +130	−130/ +150	−130/ +270
Atmosphere	Pressure (bar)	$10^{-4} \sim 10^{-5}$	$>> 10^{-5}$	10^{-5}	8×10^{-3}	92	>>100	>>100	3×10^{-6}	>>100
	Composition	H 10^{13} m^{-3} He 10^{15} m^{-3} O 10^{16} m^{-3} N_2 0^{16} m^{-3} O_2 10^{16} m^{-3} Ar 10^{16} m^{-3}	–	Radon –	95 % CO2 3 % N2 2 % Ar	95 % CO2 3 % N2 OH	90 % H_2 10 % He	96 % H_2 3 % He	?% CH_4 ?% N_2 ice	83 % H_2 15 % He 2 % CH_4
UV (W/m^2)	100–400 nm	118	2360–9800	2600	50	225	23	16	49	8
Protons (P/cm^2s	0.1–0.4 MeV	10^8	10^{10}	10^8	5×10^7	2×108	3.7×10^5	10^6	6×10^4	2×10^6
Electrons (e/cm^2s)	0.1–0.4 MeV	10^8	10^{10}	10^8	5×10^7	2×108	3.7×10^5	10^6	6×10^4	2×10^6
Micro meteoroid velocity	Km/s	0.5–12	2–30	1.5–23	0.65–15	1.2–30	2.4–40	1.5–30	2–16	3–30

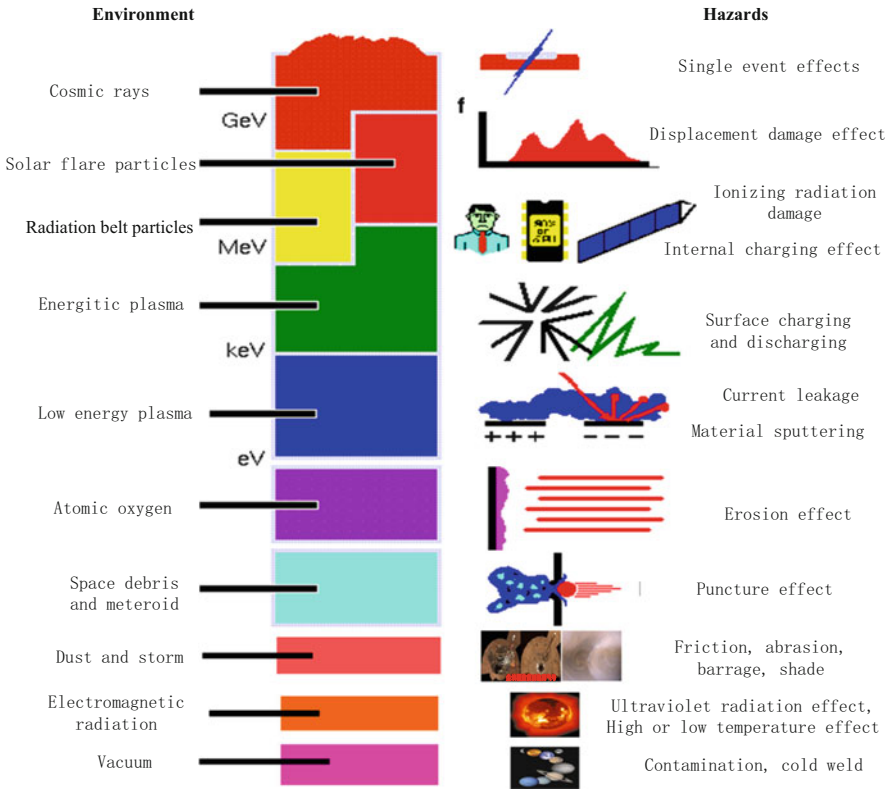

Fig. 1 Space environments and their hazards for spacecraft [5]

Space Environmental Effects

Space environment comprises many factors which can produce important effects on the spacecraft systems, subsystems, structures, and materials. The impact of these interactions must be assessed to ensure successful design and operation of spacecraft. Environment effects on the materials and structures play a key role in determining the system's operation, reliability and lifetime.

Figure 1 illustrates the environmental factors and their effects. Many of the effects are materials related. Table 1 summarizes the near-/interplanetary space environmental factors on spacecraft materials to be included into evaluation [4].

The effects of the main space environmental factors on spacecraft materials and possible consequences for the materials' properties are listed in Table 2 [4], the outcomes of some environmental effects such as energetic particles radiation, space debris impact, atomic oxygen erosion, and plasma discharge are shown in Figs. 2, 3, 4 and 5 [5, 6].

Table 2 Effects of the primary space environmental factors on materials [4]

Space environments	Effects	Possible consequences
Vacuum	Outgassing	Dimensional changes Mechanical properties variation Contamination Surface morphology variation
Temperature	Thermal cycling	Modification of residual stresses Warping of surfaces Micro cracking Outgassing and contamination
UV	Photo chemical reactions	Degradation of outside surfaces Free radical formation Surface morphology degradation Chain destruction and mechanical property degradation
Energetic particles	Ionization and excitation Cross linking Polymeric chains destruction	Surface morphology degradation Degradation across the thickness, includes optical, electrical and mechanical properties
Atomic oxygen	Oxidation	Chemical erosion on the surfaces Mass loss Contamination
Space debris and meteoroids	Impaction	Contamination Mechanical damage

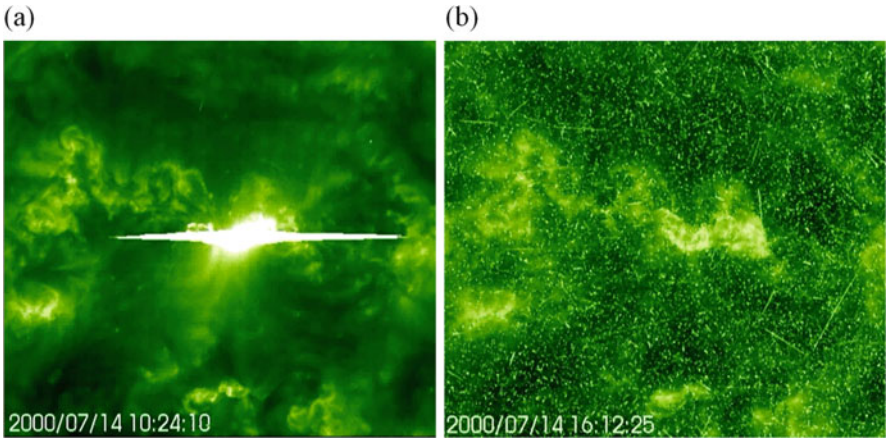

Fig. 2 Solar flare effect on an optical material [5]. (**a**) Solar flare breakout (**b**) After solar flare radiation

Fig. 3 Space debris impact on optical glass

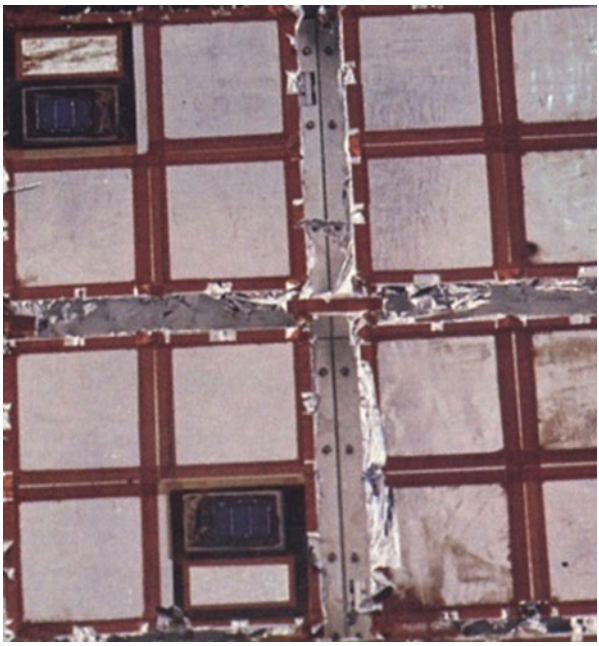

Fig. 4 Atomic oxygen erosion of polymer

Uncertainty Analyses

Environment Uncertainty

Space environmental models used in ground simulation testing are based on satellite data. But the models are inaccurate due to uncertainties in these measurements associated with instrument calibration and characterization difficulties, extrapolation and interpolation procedures employed in constructing the models,

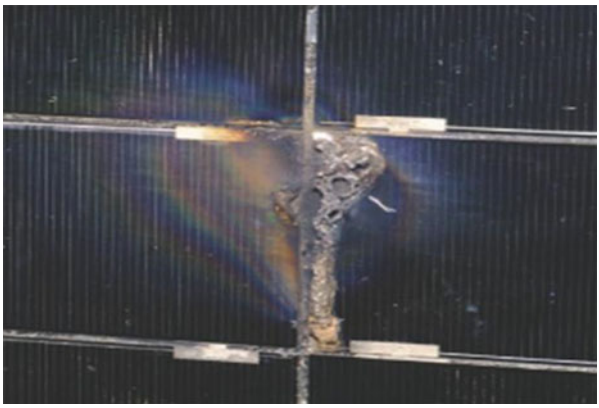

Fig. 5 Plasma discharge on solar array [6]

representation of measured periods, etc. For example, the space radiation environmental model AE-8/AP-8 is accurate within a factor 2, which means that the uncertainty factor of the AE-8/AP-8 model is 2 [7, 8].

In order to improve the precision of space environmental models, "confidence level" is introduced to evaluate the reliability of the models. For example, the AE-9//AP-9 models can provide the space radiation data with different confidence levels for ground simulation testing and analysis.

Effects of the Parameters Uncertainty

During the tests, reliability of parameters from instruments will influence the test results for the spacecraft materials and structures in the ground simulation environments. Instrumental errors and instability will bring some uncertainty to the test results.

Testing-Related Uncertainties

Ground simulation testing has uncertainties related to systematic and random errors which come from simulation sources of space environments, preparation of devices or samples, measurement of the effects and test facility parameters, etc.

Uncertainty from Simulation Sources

For particle beam sources, some important parameters, including particle energy, energy spread, particle flux, beam uniformity, particle beam composition and their precision, have influence on the reliability of ground simulation testing.

For radioactive sources such as ^{60}Co, which is commonly used for total dose testing, dose variation and emission composition should be considered.

In addition to the main emission of alpha particles, the ^{252}Cf source also emits low energy neutrons and a range of ions. It is usually used for single event effects simulation in a rough vacuum, to ensure a sufficient particle range.

Uncertainty from the Packaging or Structure of Samples

The packaging of electronic components should be considered as it can modify the source environment. To ensure that low energy particles can reach the sensitive zones of a device, the lid is often removed. Though, the lid removal is often difficult and residual layers can still obstruct the sensitive device regions.

Besides the packaging problem, penetration of particles into materials usually results in decreasing the velocity and energy of particles in LETs and NIELs, or in decreasing the dose profiles.

The profile of deposited dose depends on the energy distribution and particle type of the radiation. While the surface dose may be the same, using a different energy spectrum or different type of particles would lead to such a result that the dose profile in the material can be different from that in space. Especially for optical materials, such as solar cells or optical devices, the color center distribution can be unrepresentative.

Uncertainty from Test Methods

Considering the complexity of space environments and long duration orbiting of spacecraft, accelerated testing and effect equivalency considerations are usually used in ground simulation testing to reduce the test time and cost. Therefore, the energies or type of particles used in ground simulation testing often do not correspond to the space conditions. For example, the direct ionization single event effect is assumed to be characterized by the particle's LET, independent of the particle type and energy. However, different ion species possessing the same LET can give rise to different effects because of the details of ionization track structure.

Dose rate adopted in the accelerated testing is another key parameter that can result in the uncertainty of simulation testing. As some devices show the apparent dose rate effect, the response can be different to low and high dose rates.

Procurement Process and Device Reproducibility

The materials or devices flown in orbit should be as identical as possible to the ones tested. But this is difficult to achieve since the structural materials or devices may

come from different countries with different manufacturing processes involved in their design and production.

The stability of preparation environments or parameters is another reason for the uncertainty of materials properties. The reproducibility of devices also depends on the skills and experience of the manufacturing engineers and properties of the raw and processed materials.

Effectiveness Analysis of Ground Simulation Testing

According to the above uncertainty analysis and historical testing data analysis, we can suggest a ground simulation testing effectiveness analysis as follows:

Firstly, the uncertainty factors can be divided into accidental factors and systematic factors.

Secondly, the influence of uncertainty on the test results can be divided into different ranges, such as slight, common, and severe. The slight range has a little influence on the test results, the common range has some influence on the results, and severe range has high influence on the test results, as shown in Table 3.

Thirdly, according to their probability and frequency, the uncertainty factors can be also divided into three effect groups like little, common and often, as shown in Table 4.

And lastly, a combined evaluation allows considering the influence of uncertainty factors on the effectiveness of ground simulation of space environmental effects, as shown in Table 5.

According to the combined influence of uncertainty factors on the effectiveness of ground simulation testing, further study is required to conduct a mathematical evaluation. A concept of "confidence level" should be used to evaluate the reliability of ground simulation testing, and this is our future work.

Considering the uncertainties in the ground simulation testing, we can do a critical analysis and give a design margin showing how the test results can be

Table 3 Influence of the grade of uncertainty factors on ground simulation testing

Effect Range	Influence
Slight	There is little influence to ground simulation testing
Medium	There is some deviation to ground simulation testing
Severe	There is severe influence to ground simulation testing and may lead to mistakes in the test results

Table 4 Probability (P) of uncertainty factors in the ground simulation testing

Effect group	Probability
Little	Seldom, such as $0.1\,\% \leq P < 1\,\%$
Common	Possible, such as $1\,\% \leq P < 10\,\%$
Often	Often, such as $P \geq 10\,\%$

Table 5 Combined evaluation of uncertainty factors in ground simulation testing

Combined effect	Probability
I	Common, severe
	Often, severe
II	Often, medium
	Common, medium
	Little, severe
	Little, medium
	Often, slight
III	Common, slight
	Little, slight

used in the design of spacecraft. For different missions, the design margin can vary from 1 to 2 to even more depending on the mission reliability requirements. And further work on the design margin will be done in the future.

Countermeasures

From the above discussion, the following countermeasures should be considered in the ground simulation testing to improve the effectiveness and reliability of the tests.

As for the combined effect I, especially in case of a systematic error, the ground simulation methods should be improved to increase the reliability of ground simulation testing.

As for the combined effect II, especially in case of a random error, ground simulation facilities with high reliability and stability should be developed, the test environments should be kept clean, and the samples for ground simulation testing should have stable properties.

As for the combined effect III, a scientific operation criterion should be established and be carried on to decrease the uncertainty of ground simulation testing.

Besides, research and studies should be continued on the synergistic effects of space environmental factors.

Conclusions

The space environments are complex, they actually represent dynamic environments, and these environments have important effects on spacecraft systems, subsystems, structures and materials.

In the ground simulation testing, the uncertainties related to the environmental models, effects parameters, simulation sources, preparation of devices or samples,

measurement instruments, facility parameters, and procurement processes and device reproducibility can bring the problem of the effectiveness of the ground simulation testing.

By dividing the uncertainty factors into systematic and random and giving them a combined evaluation, some countermeasures, such as improving the ground simulation methods, using ground simulation facilities with high reliability and stability, establishing scientific operation criterion, etc., should be adopted to improve the effectiveness of ground simulation testing.

At last, further research and studies should be done on the synergistic effects between space environments.

References

1. Bencheng H (1993) Space environment engineering. Aerospace press, Beijing
2. Huang B, Ma Y (1993) Spacecraft environment test technology. National Defense Industry press, Beijing
3. Shen Z, Qiu J, Ding Y et al (2012) Space environment synergistic effect on spacecraft. Chin Space Sci Technol 32(5):54–60
4. Kleiman J, Horodetsky S, Issoupov V (2008) Concept of a new multifunctional space simulator for accelerated ground-based testing in modern space exploration era. Proceedings of the 9th international conference: protection of materials and structures from space environment. AIP Conf Proc 1087:432–452
5. Daly E, Evans H (2010) ESA space environments and effects. The role of Spenvis & some perspectives. ESA space environments and effects section. SPENVIS User's Workshop 2010 Mechelen, Belgium, 7–9 Jun
6. Ferguson DC, Hillard GB (2003) Low Earth orbit spacecraft charging design guidelines. NASA/TP-2003-21228, pp 24–26
7. ECSS-E-HB-10-12A (2010) Space engineering-calculation of radiation and its effects and margin policy handbook. 17 Dec
8. ECSS-E-ST-10-12C (2008) Space engineering-methods for the calculation of radiation received and its effects, and a policy for design margins. 15 Nov

Research on Vacuum Outgassing of a Cable Material for Spacecraft Applications

Jialong Dai, Dongsheng Yang, Xiaoxue Yuan, Zhong Yi, Lifei Meng, Weiguo Zang, Yu Bai, and Qian Yu

Abstract Degradation of parts in thermal vacuum testing may happen through contamination by outgassed products. Vacuum outgassing tests for a cable material were systemically conducted and two parameters of the cable material, namely the TML and the CVCM were measured at three temperatures after outgassing tests in vacuum environment. CVCM curves at various times at 65 °C were evaluated and the components of the cable material at three temperatures were tested. The results from these tests provided the condition and criterion of the end of vacuum bakeout test.

Keywords Vacuum outgassing • TML • CVCM

Introduction

With the extensive development of spacecraft, during long term flights, the spacecraft are facing serious contamination problems that may jeopardize the mission goals. Spacecraft operate in hostile environments that may include sunlight, charged particles, debris and micrometeoroids, and self-contamination. These environments adversely affect thermal and optical properties of spacecraft surfaces. Operational experience had shown that performance of radiators, solar power arrays and optical elements of sensors are degraded by contamination. As mission durations increase, along with increased requirements for spacecraft design and operation, contamination becomes a substantial problem.

Degradation of a number of parts was studied in a thermal vacuum test. This report describes the results of a study of performance degradation of parts occurred during a thermal vacuum test through contamination. A series of vacuum

J. Dai (✉) • X. Yuan • W. Zang • Q. Yu
Beijing Institute of Spacecraft Environment Engineering, Beijing 100094, China
e-mail: daijialong@163.com

D. Yang • Z. Yi • L. Meng • Y. Bai
Science and Technology on Reliability and Environmental Engineering Laboratory, Beijing 100094, China

J. Kleiman (ed.), *Protection of Materials and Structures from the Space Environment*, Astrophysics and Space Science Proceedings 47,
DOI 10.1007/978-3-319-19309-0_49

outgassing tests for a cable material were performed, with two parameters of the cable material, namely the TML and the CVCM, being measured at three temperatures after outgassing tests in vacuum environment. CVCM curves at various times at 65 °C were evaluated and the components of the cable material at three temperatures were tested. The results from these tests provided the condition and criterion of the end of vacuum bakeout test.

Effect of Molecular Contamination

Spacecraft contamination can generally be divided into two categories: molecular contamination and particulate contamination. The former category means that the contaminants form a single molecular film layer. Some volatiles and condensable substances have already accumulated on the surface before the spacecraft launch. Under vacuum environment, the volatile condensable materials (VCM) come out of non-metallic materials and can be transported to anywhere on the spacecraft. If VCM are deposited onto the surface of solar arrays, the output power of solar arrays is reduced. In general, the effects of contamination can be summarized as follows:

1. Functional performance of surfaces will degrade due to the deposition of contaminants. For example, emissivity of thermal control surfaces is impacted by contaminant deposition that, in turn, may lead to temperature increases of such contaminated surfaces.
2. The contaminants may accumulate in certain areas leading to corona discharge events in such situations.
3. Organic contamination deposited on optical systems can degrade the signal through reflection, scattering, interference and absorption.
4. The deposited contamination films upon irradiation by solar vacuum ultraviolet (VUV) may darken, changing further the optical and thermal optical properties of the functional surfaces.

Vacuum Outgassing of Cable Materials for Spacecraft

Sheaths of electrical cables that are used widely on satellites were selected for this study. The sheath samples were cut to 3 cm long segments and thermally tested between −55 and +150 °C. Phthalate and siloxane were identified as the main contaminants in the satellite thermal vacuum tests and solar array thermal vacuum tests. A possible source of methylphenylsiloxane in the solar array thermal vacuum test is that it may come from the solar cell adhesive.

The main accent in this research program was put on the following:

1. TML and CVCM were measured of the cable sheath material at three different temperatures.

2. CVCM of the material and its variation in time were measured.
3. The outgassing components of the material at three different temperatures were identified.

The Vacuum Test of Material Volatile

Molecular contaminants can degrade the performance of spacecraft systems by changing the optical properties of optical materials and thermal control surfaces. Some systems of the satellite were shut down during the thermal vacuum test. Upon completion of the thermal vacuum test, the outgassing test was conducted.

The outgassing vacuum test facility in our department was used to obtain the material's TML and CVCM at different. The sample holder includes nine cells to accommodate specimens. The cells temperature can be maintained from 35 to 125 °C. Most of the outgassing tests of materials were carried out using this equipment.

The time-dependent curve of the CVCM was measured. The QCM sensor was used to collect essentially the outgassed species.

A gas chromatograph-mass spectrometer (GC-MS) was used to analyze the components of the CVCM. The contaminants were collected on the specimen collectors.

Test Results and Analysis

Vacuum Test Results of Material Volatile

Tables 1, 2, 3, 4 and 5 present the results of the conducted testing.

According to data in the above tables, the TML change vs. test time at different temperatures was plotted and is presented in Fig. 1.

Summarizing the data in Fig. 1, the following conclusions can be drawn:

1. During the outgassing test for 24 h in vacuum, the mass of cable material is decreased.

   When the outgassing temperature is 65 °C, the TML is 1.2 % and the CVCM is 0.02 %.

   When the outgassing temperature is 85 °C, the TML is 1.33 % and the CVCM is 0.02 %.

   When the outgassing temperature is 105 °C, the TML is 1.64 % and the CVCM is 0.16 %.

2. The outgassing rate increases with temperature but this increase is non-linear.

Table 1 Weight at different temperature and test time

Test time	Weight (g) at		
	65 °C	85 °C	105 °C
0 h	3.54879	3.58362	3.49919
24 h	3.50628	3.53592	3.44164
46 h	3.50469	3.53411	3.43924
68 h	3.50375	3.53245	3.43801

Table 2 TML at 65 °C

Test time	Change of mass (g)	TML (%)
24 h	0.04252	1.20
46 h	0.04411	1.24
68 h	0.04504	1.27

Table 3 TML at 85 °C

Test time	Change of mass (g)	TML (%)
24 h	0.04771	1.33
46 h	0.04951	1.38
68 h	0.05118	1.43

Table 4 TML at 105 °C

Test time	Change of mass (g)	TML (%)
24 h	0.05754	1.64
46 h	0.05995	1.71
68 h	0.06118	1.75

Table 5 Collector weight at different temperature after 24 h

	Initial weight (g)	Post-test weight (g)	Mass change (g)	CVCM (%)
65 °C	8.54722	8.54744	0.00022	0.02
85 °C	8.73077	8.73095	0.00018	0.02
105 °C	8.39533	8.39714	0.00181	0.16

Components of the CVCM

A QCM sensor was used to measure the CVCM kinetics at a constant temperature. With the QCM temperature set to 25 °C the QCM frequency remained constant in time after a 4 h exposure, implying that contaminants did not deposit on the crystal surface. This result confirmed that data of the QCM at 25 °C could not be used to provide the criterion for the end of the vacuum bakeout test.

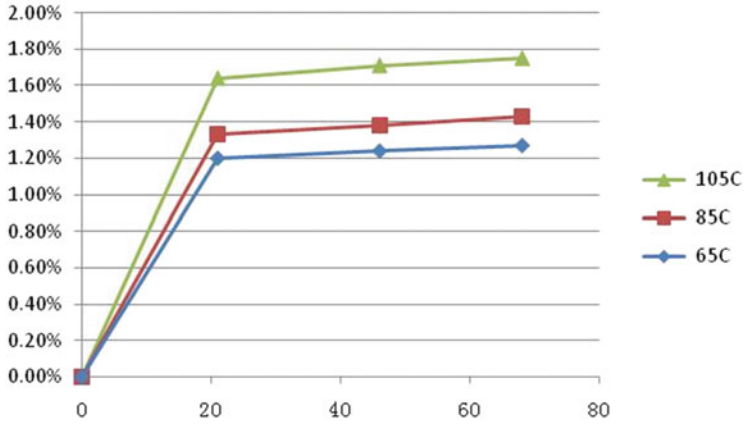

Fig. 1 TML vs. test time for the cable sheath at different temperatures

Ion Chromatography Analysis of Contaminants of the Cable Sheath at Various Temperatures

The byproducts of the outgassing testing after 65, 85 and 125 °C were analyzed on the MS-GC system, with the results presented in Figs. 2, 3 and 4. Analyzing the data in Figs. 2, 3 and 4, it is clear that the outgassing deposits are not the same at various temperatures. Thus at 65 °C, the deposits are mainly phthalic acid esters (PAEs) and some siloxane groups. At 125 °C while the types of deposits are the same as at 65 °C, their amount are different, with the amounts collected at 125 °C being higher than at 65 °C.

PAEs are often found in the contaminants during the vacuum thermal testing of satellites and solar arrays. They are widely used in cables and plastics. PAEs are harmful for transmittance of the optical test equipment. Because they are extensively used, it is difficult to control or eliminate the contamination by PAEs in space.

Siloxane is another main contaminant in this test. It is widely used in adhesives and thermal control paints. The deposition rate of siloxane is increased if vacuum ultraviolet radiation is also present. The contaminant film deposited on sensitive surfaces has a dark appearance.

Conclusions

A vacuum outgassing test of a cable material was conducted. The TML and CVCM of the cable material were measured at three temperatures after the outgassing tests in vacuum environment. Based on the collected data, the following conclusions could be drawn for the bakeout conditions of the cables:

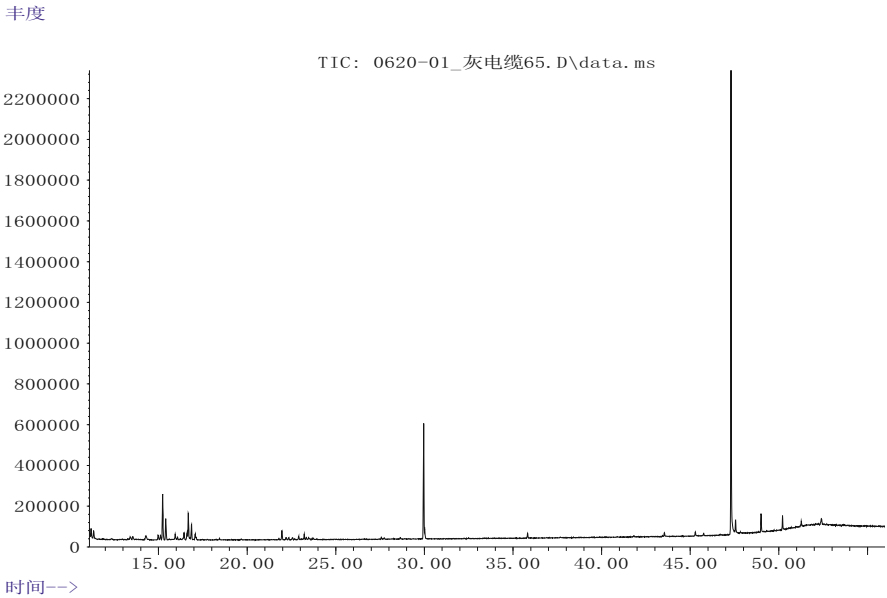

Fig. 2 Chromatography analysis of the contaminants from the cable sheath at 65 °C

Fig. 3 Chromatography analysis of the contaminants from the cable sheath at 85 °C

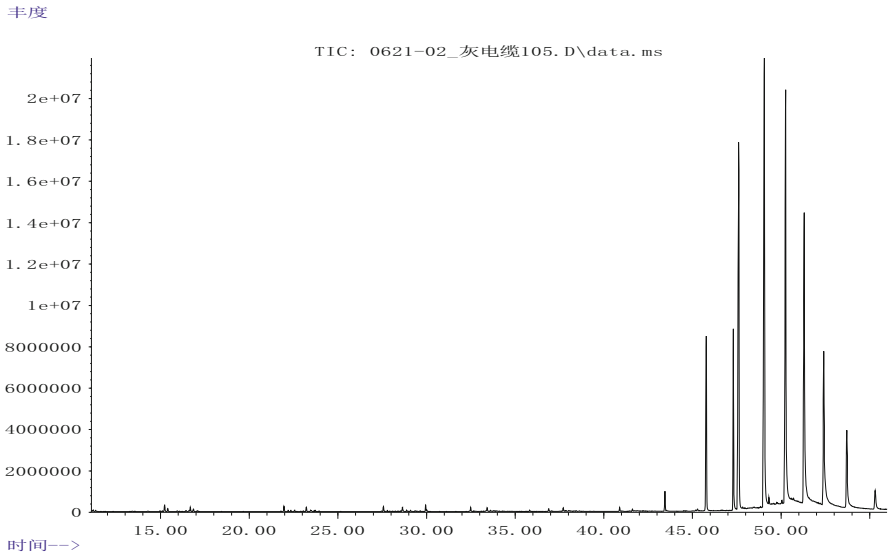

Fig. 4 Chromatography analysis of the contaminants from the cable sheath at 125 °C

1. It is save to set the bakeout temperature to 65 °C because siloxane volatiles come out at 85–125 °C
2. The contaminants evaporated at 65 °C do not deposit on the QCM crystal at 25 °C
3. The QCM data measured at 25 °C cannot be used to provide the criterion for the end of the vacuum bakeout test.
4. After the 24 h bakeout test at 65 °C, the outgassing rate of the cable material is close to saturation. This time and temperature provide the condition and criterion for the vacuum bakeout test.

References

1. ASTM standard test method for total mass loss and collected volatile condensable Materials from outgassing in a vacuum environment. ASTM E595-15
2. Knopf PW, Lee AL (1995) Application of temperature-dependent venting simulation for early orbit operation. In: 33rd aerospace sciences meeting and exhibit, Jan 9–12, Reno, NV
3. Lee AL, Glassford AP, Knopf PW (1993) Prediction and test correlation of venting from a satellite enclosure with temperature-dependent out-gassing. In: AIAA 28th thermophysics conference Jul 6–9, Orlando, FL
4. Jiao Z (2010) The simulation method for spacecraft molecular contamination. Spacecr Environ Eng 4:181

A Method for Locating Space Debris Impact Source Based on PVDF Films

Zhenhao Liu, Jianmin Wang, Fanjin Kong, Wugang Liu, and Haibo Li

Abstract With the continuing development of space activities, the total number of space debris is increasing at an alarming rate, which greatly threatens the orbiting spacecraft. Confirming the location of space debris impact on a spacecraft is important to efficiently repair the damage and increase the life of the spacecraft on orbit. Polyvinylidene fluoride (PVDF) is a permanently polarized piezoelectric polymer material with a high molecular weight. A charge signal will be generated when a pressure load is applied to the surface of the PVDF film. In addition, a high-velocity projectile impacting the PVDF film will produce very rapid irreversible local depolarization in the foil volume destroyed by the projectile. It will also generate a large charge signal. The PVDF film can be applied in space for detection of impacts due its excellent characteristics like high piezoelectric efficiency, stable temperature characteristics, good radiation resistance capacity, wide frequency range, to name a few.

Presently, research is being conducted on position-sensing PVDF sensors aimed at detection of cosmic dust impacts. In this paper, based on the related research in the world, a method for locating the space debris impact is proposed. In this method, a number of narrow aluminum foil strip electrodes are plated orthogonally on the positive and negative surfaces of the PVDF film. A gap exists between two strips on the same side of the PVDF film. Each strip electrode on the PVDF film is a channel and the electrical charge is extracted by a conductive wire. The response amplitudes of the generated signals and the impact occurrence times detected from the channels located at the impact site are different from the signals from other channels in the developed matrix. The electric charge signal is translated to voltage signal via a demodulation circuit and the output signal of each channel is collected by the data acquisition system. The data from the impacted channels is acquired and the intersection of the affected channels identifies the location of the impact. The method provides a theoretical basis on PVDF position sensing and on-orbit space debris detection.

Z. Liu (✉) • J. Wang • F. Kong • W. Liu • H. Li
Science and Technology on Reliability and Environment Engineering Laboratory, Beijing Institute of Structure and Environment Engineering, Beijing 100076, China
e-mail: liuzhenhao1985@126.com

J. Kleiman (ed.), *Protection of Materials and Structures from the Space Environment*, Astrophysics and Space Science Proceedings 47,
DOI 10.1007/978-3-319-19309-0_50

Keywords PVDF • Films • Space debris • Impact location

Introduction

With the continuing development of space activities, the total number of space debris is increasing at an alarming rate, which greatly threatens the orbiting spacecraft. Being able to pinpoint accurately the space debris impact site on a spacecraft is an effective method to ensure the security of the spacecraft and astronauts. If such accidents can be found quickly by the ground control center, emergency measures can be applied in an efficient way. To deal with the threats of space debris, a number of on-orbit monitoring technologies are developed, such as acoustic emission, acceleration signal detection, thermal imaging detection, fiber optic sensor, ferroelectric thin films, etc. [1]. The acoustic emission technology has a good potential for application in the space debris on-orbit sensing field because of its insensitivity to the structure shape and good environmental adaptability. However, some factors associated with the installation and protection of the acoustic emission sensors may impose some restrictions in their application.

Polyvinylidene fluoride (PVDF), a high molecular weight polymer, is a permanently polarized piezoelectric material. The PVDF film can be applied in space debris impact detection due to the advantages of high piezoelectric efficiency, stable temperature characteristic, good radiation resistance capacity, wide frequency range, and so on. A high-velocity projectile impacting the PVDF film will produce very rapid irreversible local depolarization in the foil volume destroyed by the projectile and generate a large charge signal. Thus, the impact information could be acquired by using this characteristic. NASA had used the PVDF for detecting the position of cosmic dust impacts and developed a concept of two-dimensional PVDF [1–3]. Based on this concept, a method for location of high-velocity impacts of space debris is researched in this paper to provide more theoretical basis on PVDF position-sensing and on-orbit space debris detection.

Typical PVDF Detector

SPADUS Detector

NASA and Chicago University developed a Space Dust Experiment (Spadus) for measurement of the distribution of man-made and natural dust in the near-earth space for flight on the P91-1 Advanced Research and Global Observation Satellite (ARGOS) shown in Fig. 1. Sixteen pieces of PVDF film were put on the surface of the detector as a piezoelectric sensor. The thickness of each film was 6 μm and the area was 36 cm^2. The impulse signal was generated with the depolarization effect when the PVDF film was penetrated by dust particle. In SPADUS, the impact

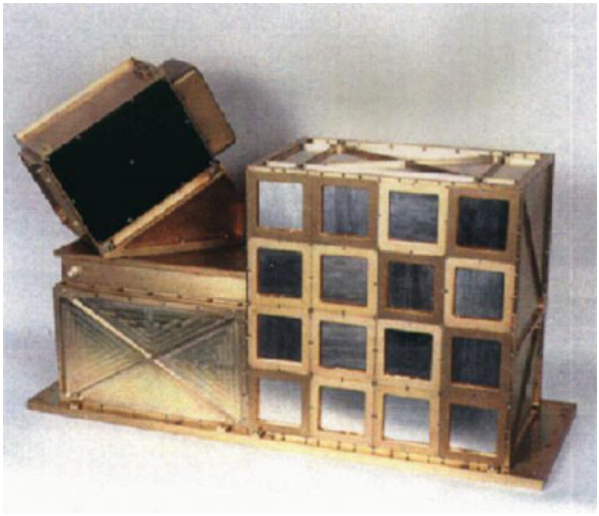

Fig. 1 SPADUS detector

velocity of a dust particle could be acquired by measuring the time interval of two impulse signals generated by a particle penetrating two pieces of PVDF film successively, that is why the method was called Time of Flight (TOF). In addition, the mass of the impact particle could be acquired by analyzing the shape of the hole. In 739 days of on-orbit operation, SPADUS has detected 368 impact accidents, including 35 impacts on the matrix of PVDF detector, and allowed 19 particle's impact velocity calculations [2, 3].

PINDROP Detector

After the accident of the Columbia space shuttle, NASA developed a LAD-C project and explored a space detector named PINDROP shown in Fig. 2. This detector was based on the principle of acoustic emission technology but the sensor array consisted of PVDF film sensors. Corsaro [4] designed ten types of different PVDF sensors and used a number of materials like aluminum alloy, Kevlar, PET film, et al. The space debris impact signals were collected successfully by these sensors. After termination of the LAD-C project [5], PINDROP was improved by NASA, by adding a thin film resistant to micro debris. At present, the research on this detector is in progress.

DUCMA Detector

DUCMA detector, which had flown on Vega-1 and Vega-2, was used for taking count of dust impacts and mass analysis from the comet Halley [6]. The thickness of

Fig. 2 PINDROP detector

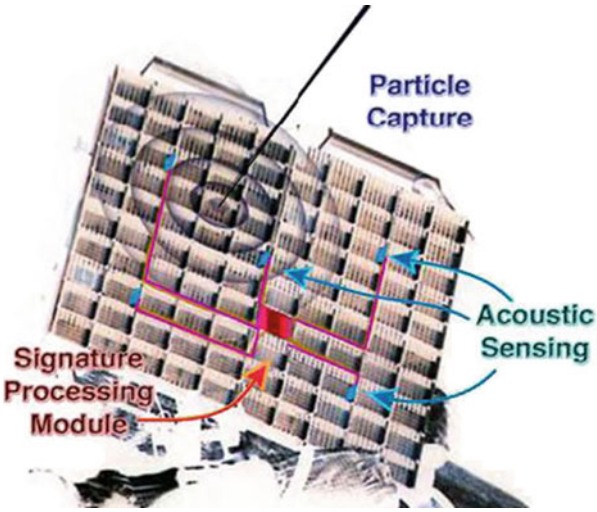

Fig. 3 DUCMA detector

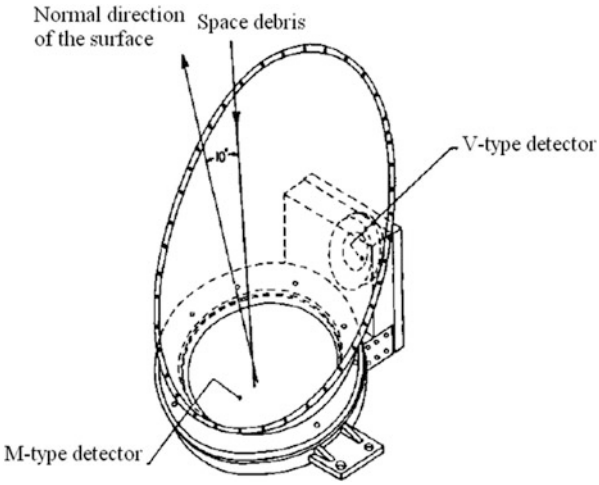

the PVDF films selected for DUCMA was 28 μm, including a 75 cm^2 M-type detector and a 3.8 cm^2 V-type detector shown in Fig. 3. The M-type was used for space debris detection and the V-type was used for acquiring the noise signal. The event when the M-type detector got a signal and V-type detector didn't, was the real impact signal from space debris and it was considered as a detection. When the two detectors generated two signals at the same time, it would be a noise from mechanical vibration and this event was deleted.

Detecting Principle of PVDF Film

PVDF films have an extensive potential for space detection. The advantages of PVDF are described below:

- Good manufacturing ability. The thickness could be 5 μm–1 mm;
- A wide frequency range (10^{-5}–10^{-9} Hz at room temperature);
- High impact strength to measure the shock wave;
- Relative permittivity is low but piezoelectric constant d_{33} is high;
- Soft and diligent. It is 30 times softer than the piezoelectric ceramics PZT and lots of complex shapes could be made;

Based on these advantages, PVDF films have been used commonly in a lot of fields.

PVDF sensor has a volume polarization P, taking 5 μC/cm^2 as an average value. The approximate connection between the area of the center hole A and signal amplitude of electronic charges N is:

$$N(\mathrm{e}) = 3.1 \times 10^5 A, \tag{1}$$

Based on abundant testing, the relation between N, particle velocity v, and mass m is:

$$N(\mathrm{e}) = k \cdot m(\mathrm{g})^a \cdot v(\mathrm{km/s})^b, \tag{2}$$

where k, a, b are constants. They could be determined from calibration tests. Chicago University had finished calibration tests with iron particles on 28 μm PVDF films. The electronic charge N was described as:

$$N(28\mu\mathrm{m}) = 6.94 \times 10^{14} m(\mathrm{g})^{0.9} v(\mathrm{km/s})^{1.05}. \tag{3}$$

This equation is commonly used in engineering calculations of PVDF detection [7].

Locating Method Based on PVDF Films

NASA developed position-sensing PVDF dust detectors named two-dimensional PVDF films in 1986, which are successfully used for detecting cosmic dust [3]. The sensor is shown in Fig. 4.

We modified this method [8] and developed a method for high-velocity space debris location that is described in this paper. Narrow strips of aluminum foil electrodes are plated on the positive and negative sides of the PVDF film. Small distances are kept between the electrodes. All the electrodes on each side of PVDF film are in the same direction and the angle of the electrodes between the two sides is

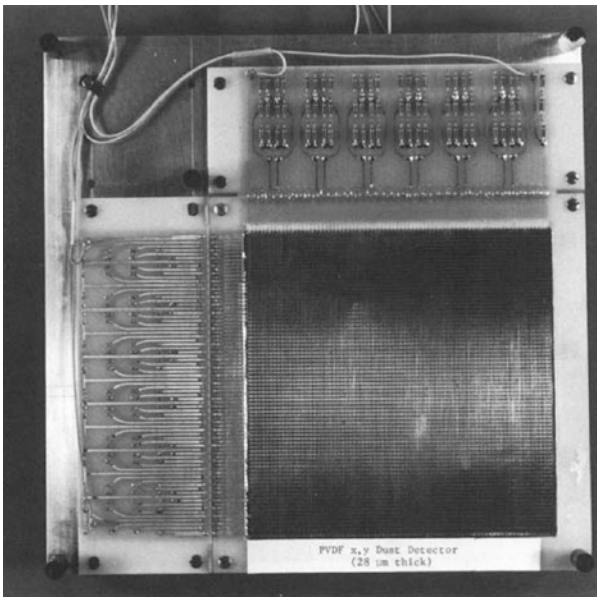

Fig. 4 Position-sensing PVDF dust detector

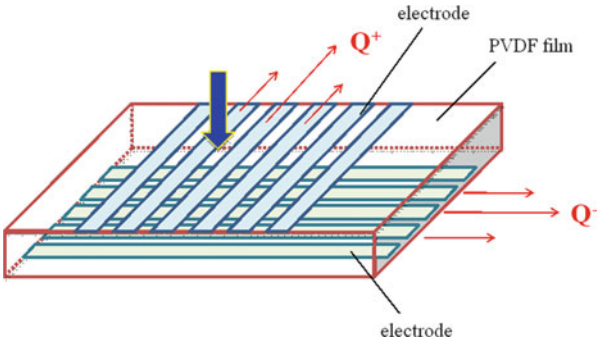

Fig. 5 Principle of PVDF film based sensor for impact location

90°. When a pressure load is created in a region of the surface with the electrodes, a positive electric charge is generated on the positive side and negative electric charge is generated on the other side [9, 10]. All electrodes are connected to individual channels and the output signal of each channel could be acquired due to a demodulation circuit thus providing information on the location of the impact in the generated electrode matrix. When the space debris is large, multiple channels are affected. Therefore, the channels affected by the impact of a particle on both sides of the PVDF film, could be identified by reading the response signal of each channel. The center location of the impacted channels is the impact location. The principle is shown in Fig. 5 and a PVDF film sensor sample was developed based on this principle.

Conclusions

In summary, we investigated the use of typical PVDF detectors, for detection of large size space debris by modifying the design of the PVDF film detector. While the PVDF films, based on the piezoelectric effect they exhibit, are commonly used in meteoroid and space dust detection, for space debris larger than 1 mm they need to be modified. The two-dimensional PVDF films used for cosmic dust location could be extended to detect space debris of large diameters. A signal acquisition circuit and related experiments will be explored later to understand the response from such structures. This research could provide more theoretical basis on PVDF position-sensing and on-orbit space debris detection.

References

1. Wang Q (2012) Research on sensing technologies of space debris in orbit based on PVDF. Harbin Institute of Technology, Harbin
2. Tuzzolino AJ, McKibben RB, Simpson JA et al (2001) The Space Dust (SPADUS) instrument aboard the Earth-orbiting ARGOS spacecraft: I—instrument description. Planet Space Sci 49:689–703
3. Tuzzolino AJ, McKibben RB, Simpson JA et al (2001) The Space Dust (SPADUS) instrument aboard the Earth-orbiting ARGOS spacecraft: II- results from the first 16 months of flight. Planet Space Sci 49:705–729
4. Corsaro R, Giovane F, Tsou P et al (2004) PINDROP an acoustic particle impact detector. Orbital Debris Q News 03:3–4
5. Liou JC, Burchell M, Corsaro R et al (2009) In situ measurement activities at the NASA Orbital Debris Program Office, Darmstadt
6. Cao G (2007) Development of Space-micro-debris detector. The Chinese Academy of Science, Beijing
7. Yuan Q (2005) Research of space debris detector. The Chinese Academy of Science, Beijing
8. Liu W, Pang B, Wang Z et al (2008) Technique advances about space debris in-situ impact-sensing-system. Struct Environ Eng 01:57–64
9. Simpson JA, Rabinowitz D, Tuzzolino AJ (1989) Cosmic dust investigations: I. PVDF detector signal dependence on mass and velocity for penetrating particles. Nucl Inst Methods Phys Res 03:611–624
10. Simpson JA, Tuzzolino AJ (1989) Cosmic dust investigations II. Instruments for measurement of particle trajectory, velocity and mass. Nucl Inst Methods Phys Res 03:625–639

"Meteor" Sensors Mounted on a Small Spacecraft AIST

M. Telegin, N.D. Semkin, and L.S. Novikov

Abstract At present, developers of space technology are paying great attention to small spacecraft. These satellites can be used for testing various technical solutions, as well as for scientific research. One of these satellites is a small satellite AIST. The major payload on the AIST satellite consists of scientific equipment METEOR that represents a set of six parametric sensors with a primary purpose to measure high-velocity micro-particles in the near-Earth space. The study of high-velocity micro-particles, i.e. the particles of space debris and micro-meteoroids, is a vital objective due to the consequences of their impact on the spacecraft. Micron-size particles having a velocity of several km/s may impair significant damage on the spacecraft equipment. If one knows the distribution of the high-velocity micro-particles in the Earth orbit, their collisions with the spacecraft can be simulated and the negative effects from the impacts minimized. Our results were obtained by measuring the surface temperature of the spacecraft which is the initial data on the micro-meteoroid environment in the Earth orbit.

Keywords Spacecraft • Space debris • Micrometeoroid • Sensor • Satellite

Introduction

During the time in orbit, the spacecraft (SC) are exposed to streams of dust particles. The following effects are observed during the interaction of the particles with materials and structural elements: surface erosion, spacecraft surface contamination by the precipitating particles generated by own outer atmosphere (OOA), increased light background in the vicinity of SC due to the scattering of light by OOA particles and luminescence, leakage current increase of open high-voltage devices and decline in their electric strength [1].

M. Telegin (✉) • N.D. Semkin
SSAU, Moskovskoye shosse 34, Samara 443086, Russia
e-mail: talex85@mail.ru

L.S. Novikov
MSU SINP, Leninskie gory, GSP-1, 1(2), Moscow 119234, Russia

J. Kleiman (ed.), *Protection of Materials and Structures from the Space Environment*, Astrophysics and Space Science Proceedings 47,
DOI 10.1007/978-3-319-19309-0_51

Recently, there has been a trend of an increasing concentration of man-made high-velocity debris in the low Earth orbit space [1–3]. Given the increasing demands on the reliability and durability of spacecraft, as well as the emergence of many new materials, further development of the research into the interaction mechanisms of small particles with material elements of spacecraft is essential [3, 4]. To determine the parameters of micrometeoroids and space debris, we need sensors that are able to convert shock impact into electrical signals.

Based on the articles and reviews describing experiments with high-velocity particle detectors of various designs in laboratory and in field conditions and theoretical studies of physical phenomena underlying the operation of such transducers, all physical phenomena used in the instrumental measurement methods can be classified as follows: physical phenomena associated with the mechanical motion of the object under investigation; physical phenomena associated with the properties of the object as a material particle; physical phenomena associated with the properties of the electric charge in the object of study.

There are a number of ways and based on them methods and systems for detection of dust particles. Thus, methods based on particle interaction with the device are divided into contact and contactless. Methods using convertors are characterized by having one informative output dependence or more. Methods using the speed and the duration as parameters differ according to generated output pulse signals.

In practice, the ionization method is the most sensitive to the effects of interaction of micro-meteoroids with surfaces of the spacecraft.

Description of the Experiment

In 2013, two small "AIST" satellites were launched into the Earth orbit [5]. Each one of them (Fig. 1) was equipped with a scientific instrument METEOR, equipped with six multi-parameter sensors, the primary purpose of which was to register high-velocity micro-particles in the near-Earth space.

Each of the multi-parameter sensors on METEOR has a temperature sensor, an ion gauge for high-speed dust particles, a solar sensor, and an electrification sensor (Fig. 2).

Figure 3 shows the structure of the ionization sensor, the key elements of which are the target 4 with effective yield of ions and the collecting electrodes 4.

In laboratory, several series of experiments with the ionization sensor using an electro-dynamic accelerator system were conducted (Fig. 4). The characteristic ionization pulse induced on the collecting electrodes is shown in Fig. 5.

A generally adopted characteristic curve for the ionization sensor is a curve displaying the ratio of ionic charge to particle mass vs. particle velocity. This curve for the above-mentioned sensor is shown in Fig. 6.

During the experiment, the position of the METEOR instrument was changing every 45 min between the sunny and the shade sides of the Earth. The position of

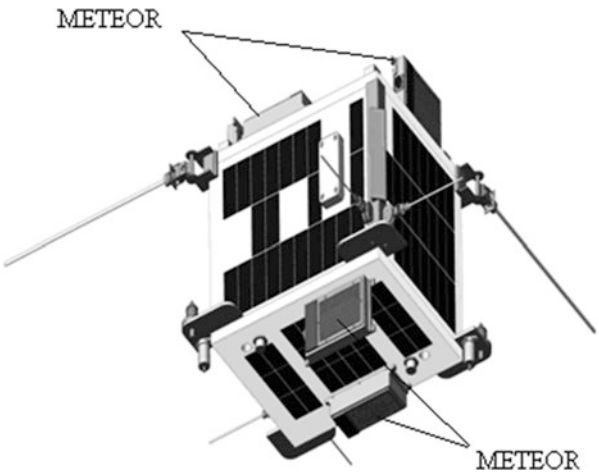

Fig. 1 The model of small "AIST" satellite with the METEOR scientific instrument locations marked on it

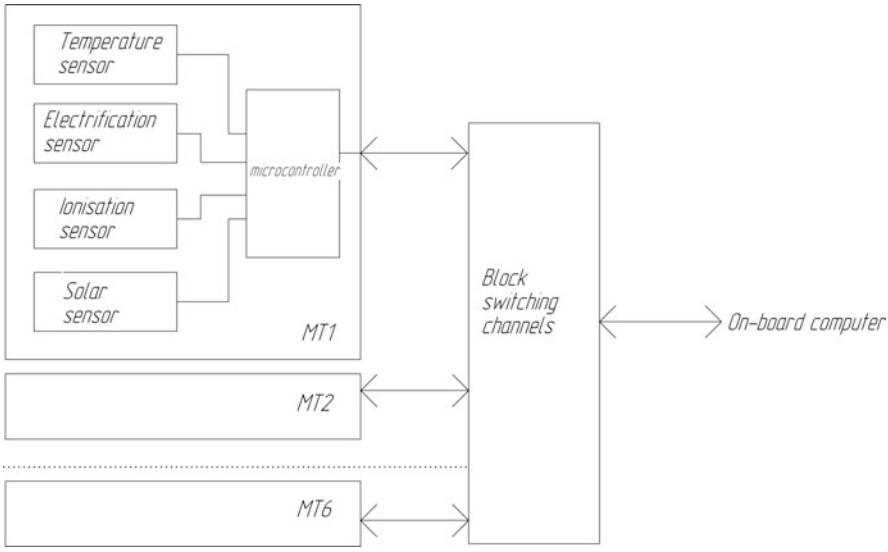

Fig. 2 Block diagram of the apparatus METEOR

the sensor at each moment of time can be estimated by the appropriate temperature and solar sensors.

According to the temperature sensors, the maximum temperature was 47 °C and the minimum temperature was 10 °C. Data measured by the temperature sensors has a periodic character ("shadow-light") depending on the flight time of the

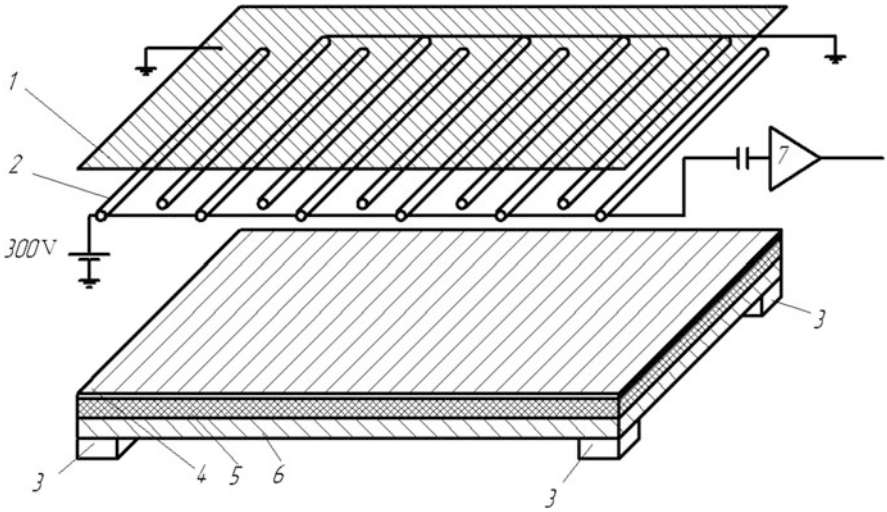

Fig. 3 Block-diagram of the ionization sensor. *1* grounded grid, *2* ionization sensor electrodes, *3* attachment of the target, *4* target (steel), *5* insulator, *6* aluminum, *7* amplifier with an ionization sensor

Fig. 4 Accelerator system for simulation of hypervelocity particles [6]. Key Features: Effective accelerating voltage: ~735 kV; Particles velocity 15 km/s; particles mass: 10^{-12}–10^{-15} g

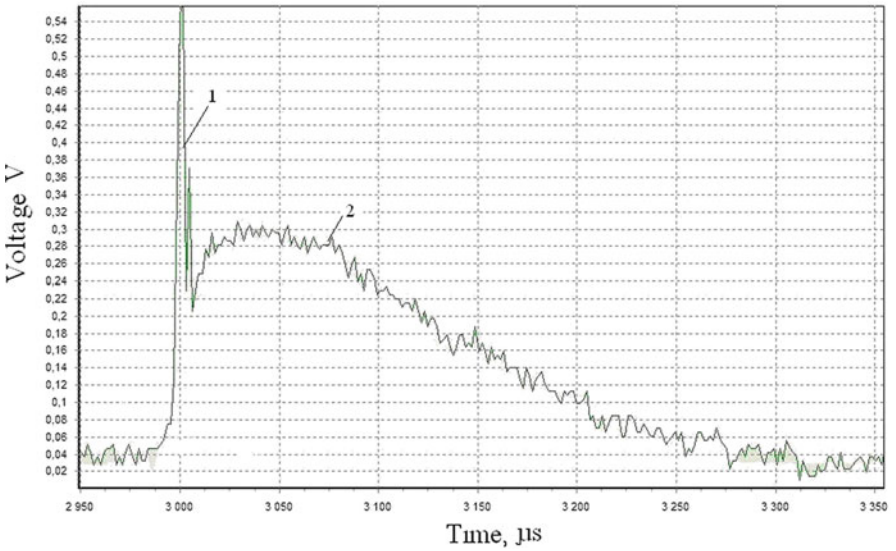

Fig. 5 Ion pulse: *1* component of the charge, *2* ion constituent

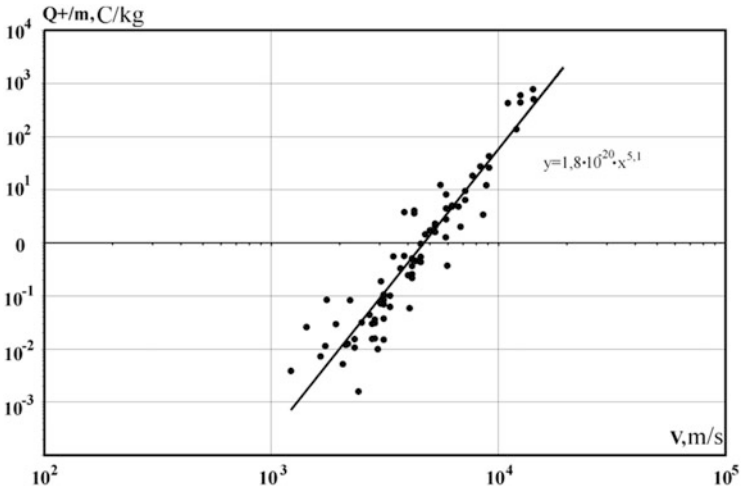

Fig. 6 Dependence of Q^+/m vs. particle velocity

satellite. The local maxima of the temperature data correspond to exposure of SC to the Sun.

The electrification sensor is a condenser transducer; its top plate is exposed to the charged particles in space. The area of the electrifying plate is 22.75 cm^2. Converting the capacity per 1 m^2, one can get about 6 kV potential for AIST. These experimental results are in good agreement with the results obtained by simulation.

Because of a lack of power onboard the SC AIST, sensors operate continuously only for 2 h in a 2–3 day span operation. The rest of the time AIST fulfills other scientific and housekeeping tasks. As a result of operation of the METEOR equipment within this specified time, several events were recorded, about 15 of which can be classified as high-velocity micro-particles impact.

Conclusions

By monitoring the multi-parameter sensors consisting of a temperature sensor, an ion gauge for high-speed dust particles, a solar sensor, and an electrification sensor on the METEOR instrument flown on the AIST microsatellite in Earth orbit important information on the microparticle impacts and the surrounding conditions was collected.

A linear relationship was found between the ratios of ionic charge to particle mass vs. particle velocity. A number of events were recorded during the operation of the METEOR equipment within the specified observation time, with about 15 of which could be classified as high-velocity micro-particles impact. According to the temperature sensors, the maximum measured temperature was +47 °C and the minimum temperature was +10 °C. The data from the electrification sensor suggested that the formed potential from the impacts is around 6 kV that is in good agreement with the results obtained by simulation.

References

1. Novikov LS (ed) (2006) Interaction of spacecraft with surrounding plasma. University Book, p 120
2. Vernov SN (ed) (1983) Space simulation, 7th edn. Moscow State University Press, T.Z., Moscow, pp 281–311
3. Semkin ND, Piyakov AV, Kalaev MP, Telegin AM, Izyumov MV (2009) Degradation of optical materials under the impact of micrometeoroids and space debris flow. In: 3rd International Scientific and Technical Conference Metal Physics, mechanics of materials, nanostructures and deformation processes. "Metallodeform 2009". Proceedings of the International Conference, 2009, Samara, p 303
4. Semkin ND (2005) Registration of dust and gas particles in the laboratory and space conditions. In: Semkin ND, Voronov KE, Novikov LS (eds). Samara State Aerospace University, Samara, p 470
5. http://www.n2yo.com/satellite/?s=39133
6. Semkin ND (2009) Imitation of micrometeoroids using electro-dynamic accelerator. In: Semkin ND, Voronov KE, Piyakov IV, Piyakov AV (eds) PTE-2009, vol 4. pp 159–165

Hypervelocity Impact Response of Al-Sc and Al-Ti Targets

Peiji Li, Weigui Zhang, Liangju He, and L.S. Novikov

Abstract Al-Sc and Al-Ti semi-infinite targets were impacted by stainless steel projectiles with velocity range of 0.6–1.9 km/s. It was found that the Al-Sc targets demonstrated a much better ability to resist hypervelocity impact. It is concluded that different microstructures of Al-Sc and Al-Ti alloys, including different grain sizes and secondary particles precipitated in the matrix, result in their greatly different abilities to resist impact.

Furthermore, the effect of the size range of nanoscale Al_3Sc precipitates in Al-Sc target on the resistance of hypervelocity impact was investigated. Simultaneously, the response of Al_3Sc precipitates on shock wave propagation generated by hypervelocity impact was analyzed.

Keywords Hypervelocity impact • Al-Sc target • Al-Ti target • Al_3Sc particle

Introduction

Aluminum (Al) alloys are widely used as structural materials for airplanes and space vehicles, due to their low density, high specific strength and high specific modulus. Because of the importance of Al alloys in spacecraft and the inevitability of hypervelocity impacts between spacecraft and micrometeoroids or space debris, the studies of hypervelocity impact behavior of Al alloys has always been carried out [1, 2]. Al alloys containing Sc represent a new generation of high-performance alloys that display numerous advantages over high strength Al alloys [3]. These Sc-containing Al alloys have been proved to be attractive materials for applications in the aerospace industry. However, until now, little is known about the

P. Li (✉) • W. Zhang
Department of Mechanical Engineering, Tsinghua University, Beijing 100084, China
e-mail: peiji@tsinghua.edu.cn

L. He
School of Aerospace, Tsinghua University, Beijing 100084, China

L.S. Novikov
Skobeltsyn Institute of Nuclear Physics, Moscow State University, Moscow 119992, Russia

J. Kleiman (ed.), *Protection of Materials and Structures from the Space Environment*, Astrophysics and Space Science Proceedings 47,
DOI 10.1007/978-3-319-19309-0_52

hypervelocity impact response of the Al-Sc alloy. Only in recent studies, the impact deformation behavior of several kinds of Al-Sc alloys was studied by employing the compression split Hopkinson pressure bar (SHPB) [4–6]. Impact deformation behavior and microstructural evolution were investigated and the constitutive equations of Al-Sc alloys were elaborated in their works. However, the SHPB test cannot substitute the hypervelocity impact test. Lately, the residual microstructures and impact responses of Al-Sc alloys have been investigated and compared with Al-Ti alloys using the hypervelocity impact test [7, 8]. Nevertheless, the influence of the size range of nanoscale Al_3Sc particles on the hypervelocity impact was not involved. In addition, the response of Al_3Sc particles on the shock wave propagation was not analyzed as well.

The present study is aimed at studying the hypervelocity impact response of the Al-Sc target by comparing the results to those from the Al-Ti target. Also, the effect of material microstructures on the impact characteristics will be illustrated.

Experimental Procedures and Simulation Methods

Samples of Al-1.0wt.%Sc alloy and Al-1.0wt.%Ti alloy (referred to as Al-Sc and Al-Ti, respectively, in the following) were obtained by adding master alloys Al-2.12wt.%Sc and Al-2.15wt.%Ti to pure Al (99.99 %), respectively, with annealing for 1 h at 450 °C after finishing the solution treatment for 3 h at 600 °C. The projectiles were carefully selected stainless steel spheres with a density of 7.9 g/cm^3 and a diameter of 0.8 mm, which is a typical size of space debris in the near Earth space. These projectiles were launched from a two stage light gas gun with impact velocities from 0.5 to 6 km/s.

The samples were carefully cut and polished through the middle of the formed craters. The crater geometries were measured from these sections. Metallographic observations and analysis was performed using NEOPHOT 32 microscope system. Thin foils for transmission electron microscopy (TEM) examination were prepared by grinding sections of samples, punching out 3 mm diameter discs and electropolishing them in a solution of 30 vol.% nitric acid in methanol at −30 °C and 16 V. The foils were examined in a 2011 TEM at 200 kV. Vickers microhardness was obtained using THV-30S microhardness tester. The load of 10 gf and a dwell time of 15 s were employed during microhardness measurements.

Results and Discussion

Figure 1 shows cross-sections of the Al-Sc and Al-Ti targets impacted by the stainless steel projectiles with velocities of 0.8, 1.0, 1.2 and 1.5 km/s. Consistent with reported results [9], there is a protuberance around the crater of the target. If the projectile is hard and has a comparatively high melting temperature while the target is comparatively soft, a whole projectile can be found in the crater after the

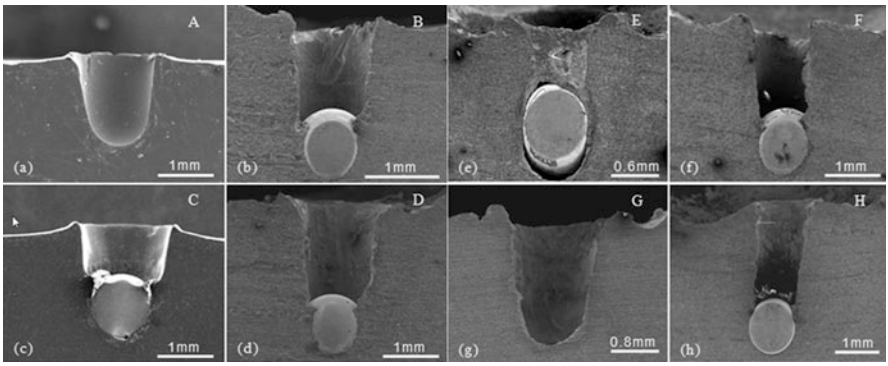

Fig. 1 Cross-sectional optical images of impact craters in the Al-Sc and Al-Ti targets impacted by 0.8 mm diameter stainless steel projectiles. (**a**) sample A, Al-Sc, 0.8 km/s (**b**) sample B, Al-Ti, 0.8 km/s (**c**) sample C, Al-Sc, 1.0 km/s (**d**) sample D, Al-Ti, 1.0 km/s (**e**) sample E, Al-Sc, 1.2 km/s (**f**) sample F, Al-Ti, 1.2 km/s (**g**) sample G, Al-Sc, 1.5 km/s (**h**) sample H, Al-Ti, 1.5 km/s

impact with a comparatively low velocity of ~1 km/s. The projectile was used to impact the Al alloy in this research with the impact velocity lower than 2 km/s. Therefore, the projectile was found in the crater in most of the experiments. The absence of projectiles in Fig. 1a, g is due to fact that they fell out during the sample preparation procedures. Actually, after high-speed impact, these two samples contained projectile in their craters.

The parameters of the craters of the samples were measured according to definition of reference [7] and the relationship between the crater depth and the impact velocity was obtained (see Fig. 2). As shown in Figs. 1 and 2, the crater depth of the Al-Sc target is smaller than that of the Al-Ti target at the same impact velocity. And as the impact velocity increases, the increment of the crater depth for the Al-Sc target is smaller than that for the Al-Ti target. Therefore, it is concluded that the resistant ability to high-speed impact of the Al-Sc target is higher than that of the Al-Ti target in this experiment.

A great deal of experimental work on examinations of impact crater shapes has been reported. These studies usually adapt metallic projectiles as impact bodies and Al alloy as targets which have practical consequences in structural materials in space. Correspondingly, a wide range of empirical cratering equations has also been developed (largely based on Al targets). Among the formulas, Eq. (1) is a typical one [10]:

$$p_c/d_p = c_1\left(\rho_p/\rho_t\right)^{a_1}\left(v_p/\sqrt{H_t/\rho_t}\right)^{a_2} \tag{1}$$

where p_c is the crater depth, d_p is the projectile diameter, ρ_p is the density of the projectile, ρ_t is the density of the target, v_p is the velocity of the projectile, H_t is the hardness of the target, and a_1, a_2 and c_1 are constants.

According to Eq. (1), the hardness of the target (H_t) plays a more important role to influence the ability to resist high-speed impact. Reference [11] summarized the

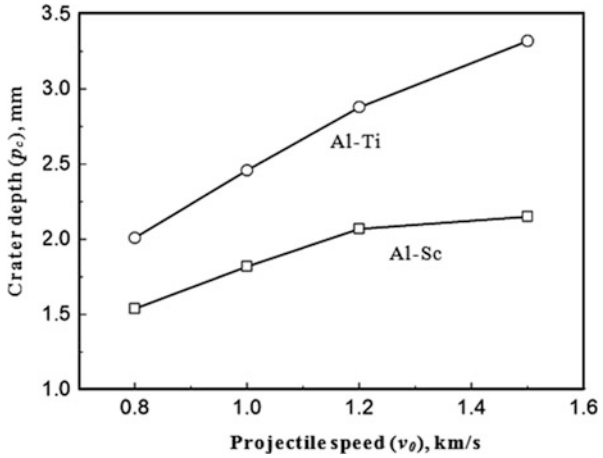

Fig. 2 Dependence between crater depth (p_c) and impact velocity (v_0)

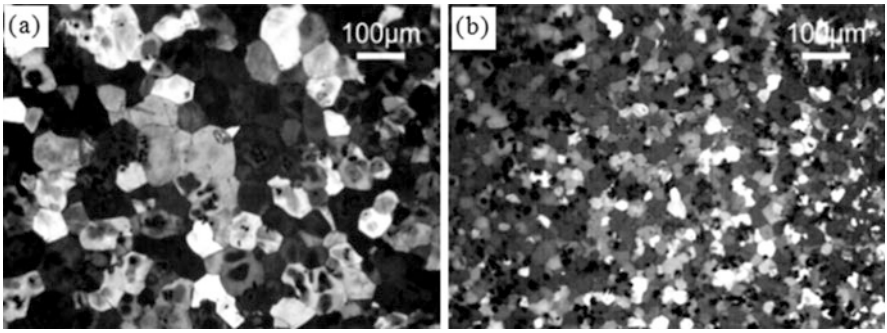

Fig. 3 Grain structure of original samples: Al-Ti (**a**) and Al-Sc (**b**)

depth of cavities and craters of many projectile/target systems, indicating that p_c/d_p depends on the target strength (H_t). It is suggested that there are two main factors leading to the notable difference in strength between the Al-Sc and Al-Ti targets, which will be discussed later.

Typically, as the size of the grains in the material decreases, the number of grain boundaries which prevent glide increases and the strength and hardness of the material is enhanced, correspondingly. The general relationship between hardness and grain size is as follows:

$$\mathrm{HV} = A + Bd^{-1/4} \tag{2}$$

where HV is Vickers hardness, A and B are constants and d is average grain diameter. Obviously, the alloy hardness depends on grain size.

The microstructures of the Al-Ti and Al-Sc samples are shown in Fig. 3. As can be seen from Fig. 3, there is a dramatic difference in the grain sizes between these

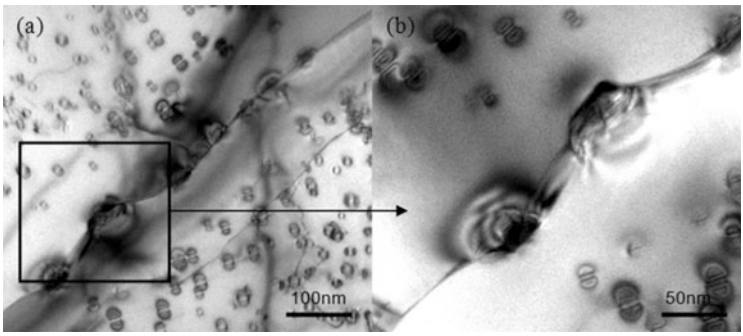

Fig. 4 TEM photos of microstructures in Al-Sc target before impact

two alloys. The average grain sizes of the Al-Ti and Al-Sc targets are 85 μm and 25 μm, respectively. The grain size of the Al-Sc target is much finer than that of the Al-Ti target that results in a higher hardness value compared with the Al-Ti target.

The TEM micrograph of the Al-1.0wt.%Sc alloy annealed at 450 °C for 1 h (before impact) shows that there is a great deal of fine second-phase particles in the Al-Sc matrix (Fig. 4). Though, no such particles were found in the Al-Ti target. The particles in the Al-Sc target were proved to be secondary Al_3Sc, which was also confirmed in our previous studies [7]. Due to the similarity between the crystal lattices of the Al matrix and the Al_3Sc phase in terms of structure and dimension, the Al_3Sc particles precipitate homogeneously with a very high density as stable spherical particles fully coherent with the matrix that provides a considerable increase in strength to Al alloys. It can be seen from Fig. 4 that secondary Al_3Sc particles are distributed uniformly in the Al matrix after annealing. The Vickers hardness of the Al-Sc and Al-Ti targets before impact is HV67 and HV30, respectively.

Based on the law of dynamic behavior of materials, it is inferred that the microstructure of a material has a significant effect on the penetration of projectiles in the target. In order to investigate the relationship between microstructure of the material and impact behavior, comparative impact tests of Al-Sc targets under different heat treatment conditions were carried out. Then the effect of the grain sizes and the secondary phase particles were examined. The results of the impact experiments were plotted in the coordinates by making the dimensionless ballistic velocity as the X-axis and the crater shape factor as the Y-axis (see Fig. 5a). By carefully examining the results, several conclusions can be obtained:

1. The Al-Sc target which was not subjected to heat treatment and the Al-Ti alloy, which was either subjected to heat treatment or not, are all close to the fitted curve 1. Though, the Al-Sc alloy which was subjected to heat treatment is close to the fitted curve 2. It is obvious that curve 2 represents higher resistive ability to hypervelocity impact.
2. The samples corresponding to data points near curve 1 do not have secondary phase particles, the differences between which are the grain sizes. The hardness

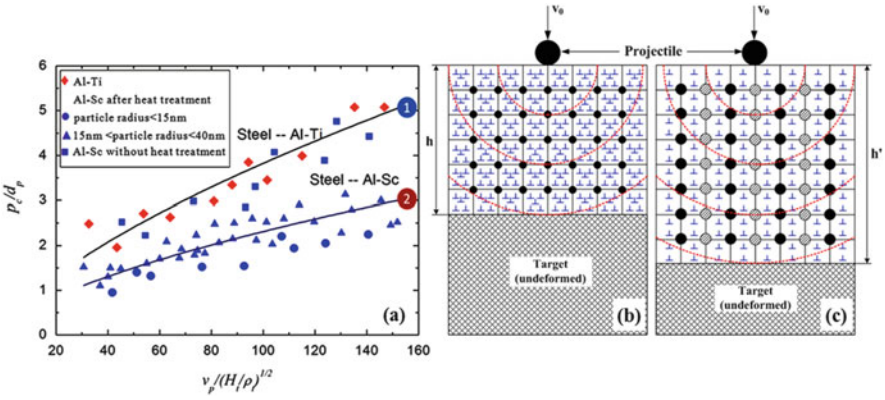

Fig. 5 Dependence between dimensionless crater depth (p_c/d_p) and dimensionless impact velocity ($v_p/(H_t/\rho_t)^{1/2}$) (**a**) and the effect of different particle state on shock wave propagation (**b**, **c**)

differences resulted from different grains sizes are shown in the X-axis. This demonstrates that the grain sizes show no direct influence on the penetration depth of the crater produced in the impact process.

(3) The samples corresponding to data points near curve 2 are all heat treated Al-Sc alloys, which shows a common obvious characteristic of secondary Al_3Sc precipitation reinforcement. Curve 2 is under curve 1, which demonstrates that the precipitation of the secondary Al_3Sc particle shows more influence on enhancing the resistive abilities of the alloys than just on the hardness of the alloys, because the hardness effect has been shown in the X-axis. The data points close to curve 2 can be divided into 2 regions. The data from samples with secondary Al_3Sc particles having their radii in the range 15–40 nm are scattered above or on both sides of the curve, and there are more data points above the curve than under the curve. Most of the data points corresponding to the grains with radii smaller than 15 nm are under the curve. According to reference [12], the secondary Al_3Sc particles with radii within the 15–40 nm range are transition particles. It means that among these particles, some just began to lose their coherency with the matrix and some have lost their coherency completely and turned into semi-coherent particles. The secondary Al_3Sc particles with radii smaller than 15 nm are all coherent with the matrix.

In this experiment, as the size of second phase particles decreases, the degree of dispersed precipitation increases, demonstrating the gradually improving resistive ability to impact. The effect of different particle state on shockwave propagation is illustrated in Fig. 5b, c. It is concluded that the secondary Al_3Sc particles play a predominant role on the hypervelocity impact process in addition to the grain size. The secondary Al_3Sc particles have two effects: (1) stabilizing the matrix structure, and (2) acting as a source of dislocations, which reduces the deformation range and improves the alloy hardening in the Al-Sc target. As a result, the ability of the alloy to resist hypervelocity projectile impact is enhanced.

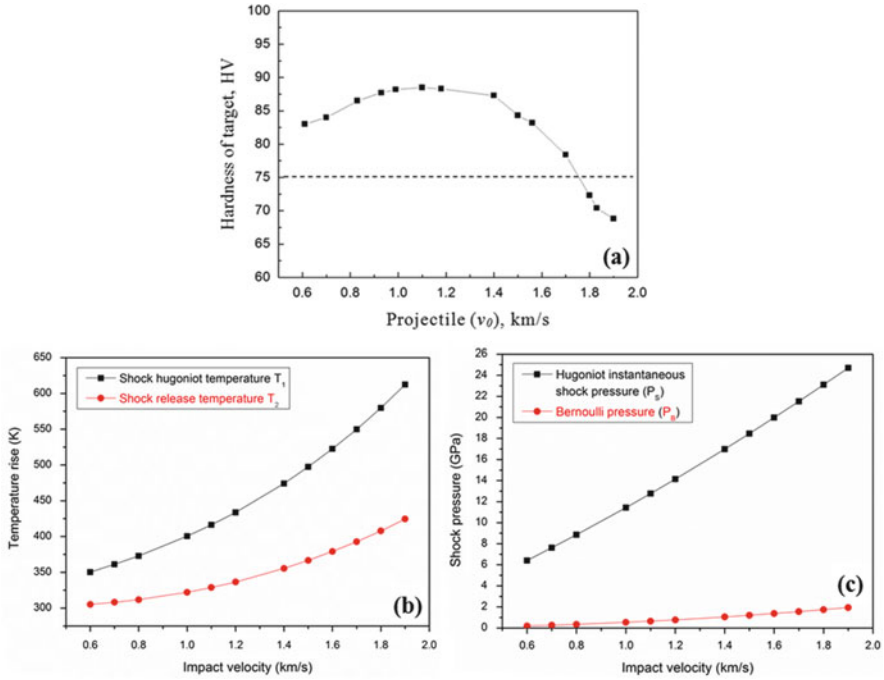

Fig. 6 Relationship between the projectile impact velocity and hardness of the target after impact (**a**), shock temperature (**b**) and shock pressure (**c**) rise at different impact velocity

To further investigate the response of secondary Al_3Sc particles on shock wave propagation, a hypervelocity impact test of Al-0.7wt.%Sc target annealed at 450 °C for 30 min was carried out. Fig. 6a shows the relationship between the projectile velocity (0.6–1.9 km/s) and the Vickers hardness of the target. The dotted line in Fig. 6a is the original hardness before impact. As can be seen, hardness increases first and then decreases when impact velocity increases. Hardness achieves the maximum when the velocity is 1.1 km/s. When the impact velocity is less than 1.7 km/s, hardness is greater than the original hardness of the target. As impact velocity increased and shockwave enhanced, the coherency between Al_3Sc particles and Al matrix is destroyed, leading to a decrease in the precipitation strengthening of Al_3Sc particles. Thus, the second phase particles have excellent resistance to shockwave propagation in a certain velocity range; however, strengthening of the second phase particles is reduced when impact velocity exceeds a critical value. Figure 6a, b show the calculated shock pressure and temperature rise during the hypervelocity impact process. The shock Hugoniot temperature rises from 350 K to 620 K when impact velocity increases and the temperature increment is 347 K, which promotes the detachment of Al_3Sc particles from the Al matrix.

Conclusions

Al-Sc and Al-Ti targets were impacted by hypervelocity projectiles with a velocity in the range of 0.6–1.9 km/s. The results show that the Al-Sc targets demonstrate a better ability to resist to hypervelocity impact than the Al-Ti targets. It is concluded that different microstructures of the Al-Sc and Al-Ti alloys, including different grain sizes and secondary particles precipitated in the matrix, result in having greatly different abilities to resist impact. For the Al-Sc targets, the Al-Sc alloy containing Al_3Sc particles with size smaller than 15 nm exhibits the best ability of resisting high-speed impact. Besides, the Al_3Sc particles have excellent resistance to shockwave propagation at a certain speed range; while, strengthening of particles is reduced when impact velocity exceeds a critical value.

References

1. Nishida M, Hayashi K, Nakagawa J, Ito Y (2012) Influence of temperature on crater and ejecta size following hypervelocity impact of aluminum alloy spheres on thick aluminum alloy targets. Int J Impact Eng 42:37–47
2. Liang XP, Li HZ (2012) Microstructural evolution of 2519-T87 aluminum alloy obliquely impacted by projectile with velocity of 816 m/s. Trans Nonferrous Metals Soc China 22:1270–1279
3. Lathabai S, Lioyd PG (2002) The effect of scandium on the microstructure, mechanical properties and weldability of a cast Al-Mg alloy. Acta Mater 50(17):4275–4292
4. Lee WS, Chen TH (2008) Dynamic deformation behavior and microstructural evolution of high-strength weldable aluminum scandium (Al-Sc) alloy. Mater Trans 49(6):1284–1293
5. Lee WS, Chen TH (2009) Comparative study of dynamic impact properties and microstructures of weldable and unweldable aluminium-scandium (Al-Sc) alloys. Mater Sci Technol 25 (6):711–724
6. Lee WS, Chen TH (2010) Impact deformation behaviour and dislocation substructure of Al-Sc alloy. J Alloys and Compd 2493(1–2):580–589
7. Ye YC, Li PJ (2010) Comparison of residual microstructures associated with impact craters in Al-Sc and Al-Ti alloys. Acta Mater 58(7):2520–2526
8. Zhang WG, Ye YC (2013) Dynamic response and microstructure control of Al-Sc binary alloy under high-speed impact. Mater Sci Eng A 578:35–45
9. Murr LE, Quinones SA (1998) The low-velocity-to-hypervelocity penetration transition for impact craters in metal targets. Mater Sci Eng A 256(1–2):166–182
10. Herrmann W, Wibeck JS (1987) Review of hypervelocity penetration theories. Int J Impact Eng 5(1–4):307–322
11. Kadono T, Fujiwara A (2005) Cavity and crater depth in hypervelocity impact. Int J Impact Eng 31(1):309–1317
12. Iwamura S, Miura Y (2004) Loss in coherency and coarsening behavior of Al_3Sc precipitates. Acta Mater 52(3):591–600

Thermal Control and Shield Design for the Instrumental Module of the X-Ray Pulsar Navigation Sensor

Fuchang Zuo, Loulou Deng, Liansheng Li, Chunyu Wang, and Yanan Mo

Abstract The X-ray pulsar navigation sensor represents a focal plane detector with a controllable operation environment, meeting the operation requirements of the detector and electronics. The focal plane detector must operate at about −55 °C. The heat generated by devices with a high heat consumption of the electronics, may result in performance degradation or even a failure of key devices. The background radiation of the X-ray detector mainly consists of charged particles (electrons, protons, ions, etc.) and dispersed cosmic rays (X-ray, γ-ray, etc.), which will result in a background noise of the detector, lowering the detector sensitivity, deteriorating performance of the detector and electronics, thus even leading to damages and a failure.

The instrumental module, consisting of the detector, the preamplifier, the collimator, the thermo electric coolers (TECs), the housing and the shielding layer, is the critical module of the X-ray pulsar navigation sensor. A good thermal control and shield design must therefore be provided for the instrumental module to improve the sensitivity and ensure normal operation of the detector, as well as to provide shielding from stray light, contamination, and background noise.

Firstly, the initial structure of the instrumental module was designed; on this basis thermal design and thermal analysis were implemented. The temperature gradient and temperature distribution in the detector instrument and electronics were obtained. The thermal control measures and materials were selected, which helped to provide a controllable thermal environment for the detector and electronics. Secondly, shield design was developed in order to reduce the effects of space background radiation on the detector. The shielding measures for electrons, protons, ions, and high-energy cosmic X-rays were proposed and appropriate materials and their thicknesses were selected. Finally, the effectiveness of thermal control was verified through computer simulation, providing guide lines for the design of the X-ray pulsar navigation sensor.

Keywords Instrument module • Thermal control • Shield • Background • Focal plane detector

F. Zuo (✉) • L. Deng • L. Li • C. Wang • Y. Mo
Beijing Institute of Control Engineering, Beijing 100190, China
e-mail: zfch-2004@163.com

J. Kleiman (ed.), *Protection of Materials and Structures from the Space Environment*, Astrophysics and Space Science Proceedings 47,
DOI 10.1007/978-3-319-19309-0_53

Introduction

The thermal control system is one of the important subsystems. Its function is to control the temperatures of various electronic instruments and mechanical equipment of the spacecraft in the required range, in order to ensure the normal on-orbit operation of the spacecraft. The modern spacecraft thermal control subsystems usually adopt the design schemes of passive thermal control and electric heating active thermal control [1]. The thermal control subsystem is the key to ensure normal operation of spacecraft in specific space thermal environments including high vacuum, darkness, low temperature and various types of radiation [2].

The purpose of thermal control design is to release the adverse heat in the equipment as much as possible, so the temperature of equipment is kept in a specified range in its operating environment, ensuring the reliable and safe operation of the equipment, through optimizing the design of heat flow path, reducing the thermal resistance between the equipment and the radiation environment, adopting an effective cooler, as well as a radiator [3].

Thermal control technology includes passive thermal control and active thermal control. The passive thermal control technology is an open loop control, in which temperature of the object has no feedback. The structural material, surface coating, thermal insulation material, phase change material and heat pipe are generally adopted for the passive thermal control, which is simple and reliable technology, with a long service life and good economical efficiency. The active thermal control technology is a closed loop control, in which temperature of the object provides a feedback for the thermal control mechanism. The shutter, heat pipe, electric heater and switches are generally used for the active thermal control. This technology can adjust the heat transfer characteristics of the controlled object in real time. Its temperature regulation accuracy is high, but the service life and reliability are restricted.

The focal plane surface detector must operate at about −55 °C. The devices with high thermal power consumption in the electronics design produce high amounts of heat. The accumulation of heat will result in performance degradation or even a failure of key devices. Therefore, thermal control is necessary.

The space background radiation for the X-ray detector consists mainly of charged particles (electrons, protons, and ions) and dispersed cosmic radiation (X-ray, γ-ray) that will cause increased levels of background noise of the detector, reduce the detector sensitivity, degrade the performance of the detector and electronics, and even lead to damages and a failure. Therefore, to improve the detection sensitivity, the effect of background radiation must be reduced. The shield is an important component of the instrumental module of the X-ray pulsar navigation sensor.

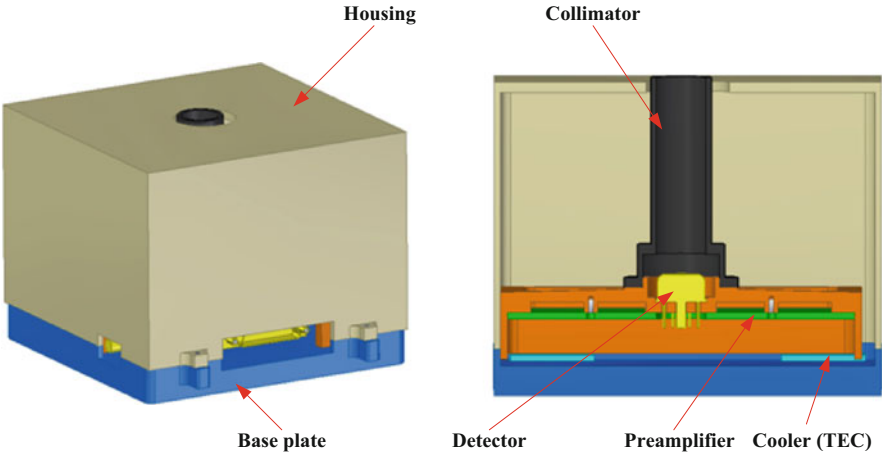

Fig. 1 Instrumental module

Instrumental Module Design

The instrumental module of the X-ray pulsar navigation sensor consists of the detector, the preamplifier, the collimator, the thermal electric cooler, the base plate, and the housing, as shown in Fig. 1.

Configuration

The focal length of the X-ray pulsar navigation sensor is 1200 mm. The focal plane detector is placed on a support, as required by the distance to the optics. In a short distance from the front of the detector, a collimator is mounted to shield the detector from the radiation background. The preamplifier electronics boards are attached to the reverse side of the detector support at a minimum distance for direct electrical connection with the detector. The base plate is mounted below the detector support separated by four 2-stage thermo electric coolers (TECs), and it plays the role of heat conduction and radiation background shield at the same time. The TECs cool the detector support, so that the temperature meets the requirements of detector operation. The key requirements of the FPA are to provide a radiation, contamination, thermal and stray light shield for the FPAs. This is accomplished by a 5 mm thick housing which completely surrounds the detector [4, 5].

Collimator

The paraboloid-type grazing incidence X-ray optics can reflect X-rays effectively in their FOV and focus them on the detector which is mounted on the focal plane. However, in practice, it can also reflect X-rays out of their FOV to the focal plane, which will then hit the structures and serve as a background noise for the detector.

The collimator having a tube shape mounted in front of the detector can reduce the effect of non-FOV X-rays, thus improving the detection sensitivity.

Detector Support

The detector is mounted on the support within an aluminum housing. The support, made of aluminum, is placed on four 2-stage coolers to cool the detector to its operation temperature. Material with high conductivity is added between the detector and its support to better conduct the produced heat.

The optimum operation temperature of the detector with respect to radiation damage in space was determined to be about −55 °C. Measures have been taken to minimize the power consumption on the detector board and to thermally separate it from the warmer environment. Accordingly, a thermal design has been developed to achieve nearly the optimum detector temperature, with a minimized active heat load of 0.8 W on the detector board.

Preamplifier Electronics

The detector has its dedicated preamplifier electronics. The preamplifier electronics comprise one printed circuit board (PCB) accommodated in an aluminum housing. In addition, the drive electronics for the TECs are also supplied on the same PCB.

The detector is connected via its 12 pin connector to the preamplifier electronics board inside the electronics box. This board provides in addition the electrical interfaces to other electronic subsystems for signal processing.

Thermal Control Design

The X-ray pulsar navigation sensor being developed includes a detector, which needs to operate at a temperature below −55 °C in order to avoid the unacceptable heat noise. This cooling is achieved through a sophisticated thermal design which cools the detector with a combination of TECs [6].

This section will describe in detail the thermal design necessary to maintain the detector at its cold operation temperature while providing the means to reject the heat generated by the TECs. It will focus on optimized techniques developed to manage the parasitic loads, including material selection, surface finishes and thermal insulation. This section will also address analytical techniques developed to characterize the TEC performance. Finally, thermal simulation and analysis results will provide the temperature of the key parts.

Thermal design of the focal plane assembly is the research focus due to the important requirement for the operation temperature of the detector. To cool the detector to the desired level, an appropriate cooling design is needed. According to the above environmental characteristics, only passive cooling and active cooling methods are needed to achieve the cooling demands. TECs are miniaturized solid-state heat pumps capable of providing localized cooling to devices that require cold temperatures for proper operation. Throughout the 1990s, TECs have become relatively common devices in low noise amplifiers, star trackers, and IR (infrared) sensors.

TECs provide cooling via the Peltier effect, which is cooling that results from the flow of an electrical current through a junction formed by dissimilar metals. The Peltier effect is the inverse of the Seebeck effect, the basis for the common thermocouples. The simplest TEC consists of two semiconductors, one p-type and one n-type, connected by a metallic conductor. For space application, TECs have the advantages of simplicity, reliability, compactness, low weight, noiseless, and absence of vibration. Unlike common heat pumps, these devices have no moving parts. Their use in space is limited by their relatively low coefficient of performance, particularly with large hot-to-cold-side temperature differences. Because of their limited efficiency, they are best suited to situations with modest heat loads, providing a cold temperature not lower than 150 K, and hot-to-cold-side temperature differences lower than 100 °C.

Heat Pumped Requirements

Based on the given thermal boundaries of the detector, the quantity of heat pumped is analyzed. The heat mainly consists of three parts. The first part is the power dissipation of devices in the preamplifier electronics, $Q1 = 140\,\text{mW}$.

The second part is thermal radiation from the package of the focal plane assembly to the detector,

$$Q2 = \varepsilon \sigma A(Tp - Tdetector) \tag{1}$$

where ε is the infrared emissivity of the detector surface; Tp is temperature of the package; $\varepsilon = 0.5$; $Tp = 293\,\text{K}$; $Tccd = 218\,\text{K}$; $Q2 = 430\,\text{mW}$.

The third part is active power dissipation of the detector, including the detector power and the internal cooler power, $Q3 = 3.7\,\text{mW} + 1.225\,\text{W} = 1.229\,\text{W}$.

The total heat pumped requirements is the sum of Q1, Q2 and Q3:

$$\Sigma Q = Q1 + Q2 + Q3 = 1.235\ \text{W}.$$

Because radiation is the fourth part of heat pumped, reducing the temperature of the package is crucial to minimize the parasitic loads. A cold shield should be used as the package to provide for cold environment.

Thermal Control System Design

As shown in Fig. 2, the telescope uses two distinct combined cooling methods to maintain the detector below its required operation temperature in the environment describe above. The cooling parts include an active cooling system and a heat rejection system. Active cooling is achieved by some TECs and relevant control circuits. The TECs are attached directly to the bottom surface of the detector mounting structure to lower the temperature. The heat generated by these devices is removed from the detector housing by a heat rejection system which consists of a TEC base plate, flexible heat pipes, and radiators. As shown in Fig. 2, the telescope uses two distinct combined cooling methods to maintain the detector below its required operation temperature in the environment describe above.

The cooling parts include an active cooling system and a heat rejection system. Active cooling is achieved by some TECs and relevant control circuits. The TECs are attached directly to the bottom surface of the detector mounting structure to lower the temperature. The heat generated by these devices is removed from the detector housing by a heat rejection system which consists of a TEC base plate,

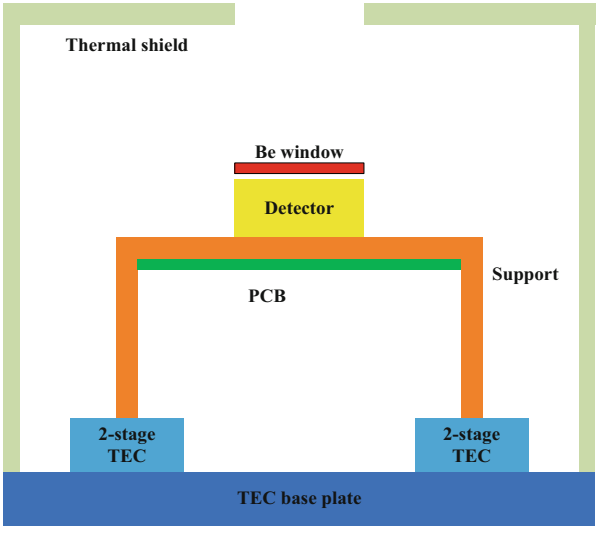

Fig. 2 Schematic of detector thermal control system

flexible heat pipes, and radiators. The TEC base plate supports the TECs and serves as an interface plate between the hot sides of the TECs and the flexible heat pipes. The flexible heat pipes transport the heat to a dedicated external radiator that is utilized to reject the heat to space. Thermal resistance from the TECs hot sides to the radiator is minimized to ensure the sufficient design margin. A cold shield is needed to be used to provide for colder environment and it will be cooled to a temperature lower than the housing temperature, with gold finished shield surfaces to reduce heat radiation to the detector.

Active Cooling System

To improve reliability and to ensure the mechanical stability of the detector, four TECs are utilized to actively cool the aluminum support of the detector. The heat pumped requirements is 0.8 W for the detector cooled to −55 °C when the housing temperature is 20 °C. Based on the loaded performance analysis, the TECs type was selected. The TECs surface is made from the AlN material which has high thermal conductivity and a good CTE match with the detector support. Figure 3 shows the cut view of the detector assembly.

To improve the efficiency of the TECs, thermal resistance should be reduced, the thermal transfer structure should be optimized, and thermal conductivity of materials should be improved.

Heat Reject System Design

To reject the waste heat of the TECs, a heat reject system is designed. The system consists of one base plate, two flexible heat pipes, and one radiator for one set of the

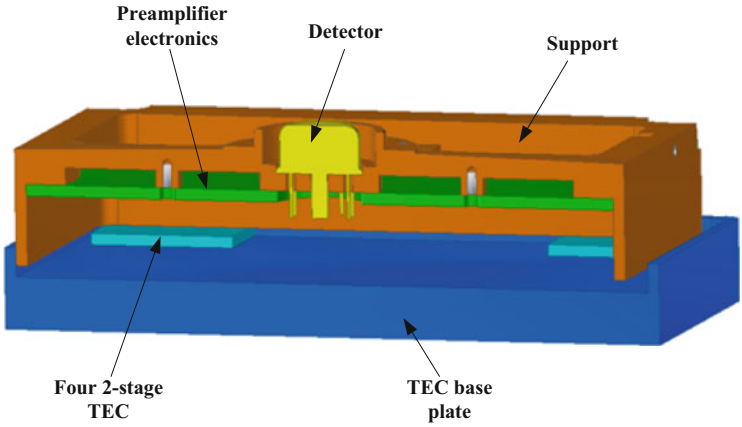

Fig. 3 Cut view of detector assembly

focal plane assembly. To reduce thermal resistance, the base plate is made of molybdenum which has a high thermal conductivity and can match the coefficient of thermal expansion (CTE) of the detector support and the TEC side ceramics. Flexible heat pipes are utilized to transfer heat from the base plate to the radiator. To minimize a mechanical load to the focal plane assembly due to vibration during launch or in orbit, the heat pipes should be flexible. Two heat pipes are utilized to achieve this design and to improve the reliability. The thermal resistance from the hot side of the TEC to the radiator is about 0.8 K/W. The radiator is fixed outside the instrument module. To minimize the absorbed space heat flux, thermal coating with a low absorption and a high emissivity is adopted. The radiator is made of aluminum honey-comb materials.

Thermal Insulation Design

To minimize the parasitic heat load to the focal plane, thermal insulation between the detector and the housing and the electronics module must be optimized. To reduce heat radiation from the housing to the detector, the inner surfaces of the housing are gold-coated to reduce the surface emissivity. The focal electronics such as the preamplifier and drive modules are placed under the detector support to reduce radiation from the electronics to the detector. To minimize heat conduction, a material with low conductivity is added between the electronics and the support. To minimize the parasitic heat load from the hotter environment to the heat rejection system which consists of heat pipes and radiators, a multi-layer-insulation (MLI) is applied on their surface, except for the contact surface and the outer radiator surface. Furthermore, thermal isolation spacers and screws made of low thermal conductivity materials are utilized.

Thermal Analysis

The efficiency improvement of the TEC mainly depends on the heat dissipation, heat transfer, and good structure design.

According to the operation requirements for the detector, the detector support needs to be cooled to about 20 °C. The overall temperature of the instrument module can be simulated based on the heat powers of the detector and the preamplifier. In addition, based on the cooling target temperature and different hot side temperatures, power consumption of the TECs can be simulated by a FEM software.

The simulated temperature distribution of the instrument module with the TEC cold side temperature of 10 °C and hot side temperature of 50 °C is shown in Fig. 4.

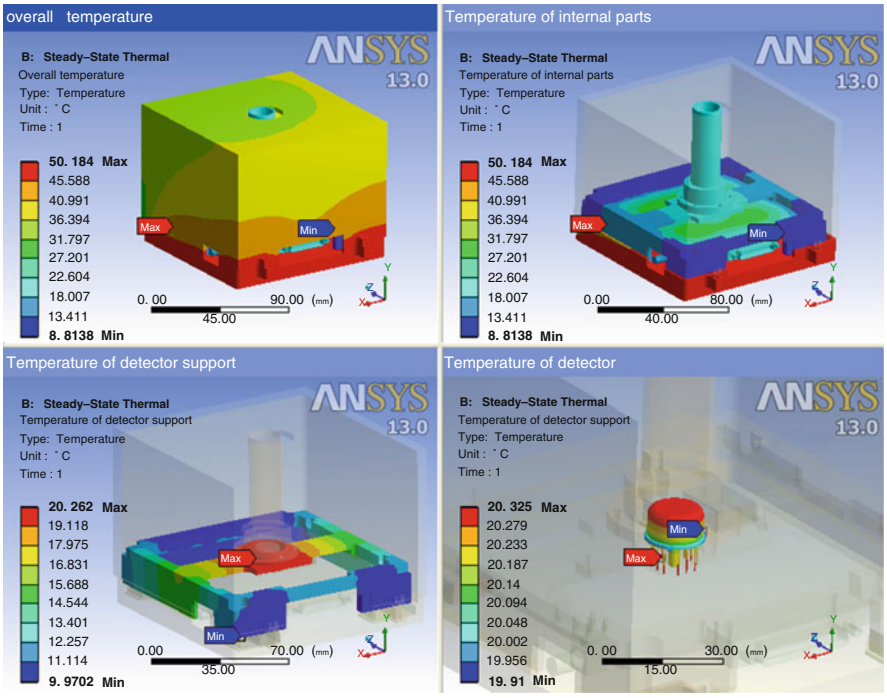

Fig. 4 Temperature distribution in the instrument module

Table 1 Power estimation of the TECs

Hot side temperature (°C)	TECs power (W)	TECs efficiency (%)
50	21.07	37.5
40	19.87	44.5
30	18.68	50.8
20	17.47	56.3
11	16.39	60.9

Figure 4 shows that the cold side temperature of 10 °C can meet the operation requirements of the detector. However, assuming this temperature, the TECs power and efficiency at different hot side temperatures are different, as shown in Table 1.

Table 1 shows that as the hot side temperature decreases, the TECs power is reduced, but the TECs efficiency is improved. When it continues to decrease, it is not necessary to keep the TECs working and only the cooler operating inside the detector module can ensure the temperature requirements.

Radiation Shield Design

The detector used in the instrument module is a photon-counting detector with low internal noise. Made of a low-radioactivity Si, the detector has an intrinsic internal noise of only 0.04 counts cm^{-2} s^{-1} in the range of 2–150 keV. To benefit from the low internal noise of these detectors, it is required to suppress other sources of background radiation, such as stray UV and visible light, diffused X-rays and γ-rays, particle-induced photons and charged particles. While relatively light-weight baffle systems can control the non-penetrating radiation, suppressing the penetrating radiation can require a significant mass in shielding. Furthermore, adding more mass in shields, although effective in reducing the direct photon contribution, can increase the induced background due to an extra amount of material producing more particle interactions, cascades, and activation.

The detector has a small energy resolution and a non-negligible efficiency to radiation more energetic than 10 keV. Preliminary estimates of the contribution of diffused cosmic X radiation to the detector counting background showed that it is necessary to shield against X-rays up to nearly 100 keV, in order to ensure that the diffused X-ray background and bright sources would not exceed that of the Si material intrinsic to the detector. For such hard X-rays, much of the instrument module structure is transparent. Hence, the instrument module incorporates X-ray baffles and a shielding collimator. In most instances, the X-ray baffles and shield are nominally tantalum layers of 125 μm, as shown in Fig. 5. The inactive shield only shields against background sources out of the light way of the optics. The

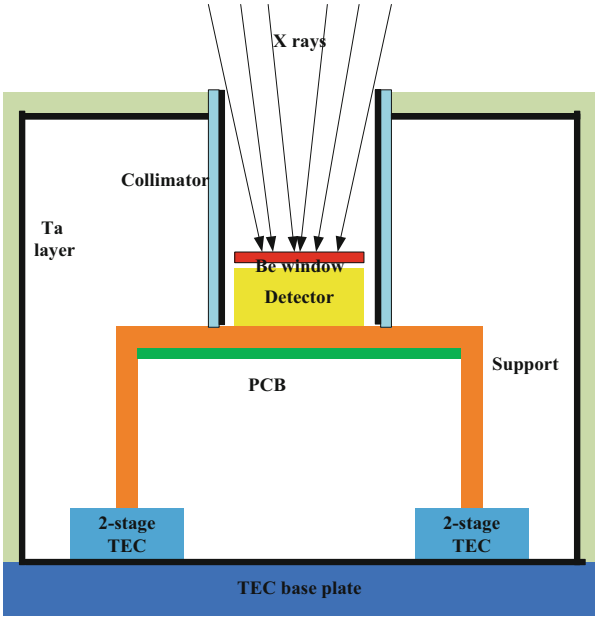

Fig. 5 Schematics of detector radiation shield system

background radiation passing through the mirror by reflection is suppressed by a magnetic diverter, which would be discussed in our future works.

Conclusions

According to the operation requirements for the instrumental module of the X-ray pulsar navigation sensor, the initial structure of the instrumental module, including the detector, the preamplifier, the collimator, the TECs, the housing and the shielding layer, is designed. We focused on the thermal design and the radiation shield design at the same time. The thermal control measures and materials are selected, providing a controllable thermal environment for the detector and electronics. Thermal analysis is implemented to obtain the temperature gradient and distribution in the detector, electronics and other structures. In addition, a shield design is developed, in order to reduce the effects of space background radiation on the detector. The shielding measures for electrons, protons, ions and high-energy cosmic X-rays are proposed and the appropriate materials and their thicknesses are selected. The effectiveness of thermal control is verified through computer simulation, providing guide lines for the design of the X-ray pulsar navigation sensor instrument module.

References

1. Yin Z, Wang Y et al (2010) Design of high performance temperature controlling system based on TEC. Comput Meas Control 18(6):1296–1297
2. Li P (2007) Study on thermal network theory and application in thermal control design of spacecraft. Dissertation for doctor degree, Shanghai Jiaotong University
3. Chen L, Wu Q et al (2009) Design for thermal control system of electronic equipment in space camera. Opt Precis Eng 17(9):2145–2152
4. Meidinger N, Andritschke R et al (2012) Design and performance of the eROSITA focal plane instrumentation, high energy, optical, and infrared detectors for astronomy V. Proc SPIE 8453:84530P
5. Little D, Jacoby M, Casco E (2011) Design, build, and test of the NIRCam focal plane array housing, cryogenic optical systems and instruments XIII. Proc SPIE 8150:81500G. doi:10.1117/12.896488
6. Yang W, Wang Y et al (2012) Thermal management for detector performance of one space telescope. In: 6th international symposium on advanced optical manufacturing and testing technologies: optical system technologies for manufacturing and testing. Proc SPIE 8420

Design and Simulation of a Magnetic Diverter Structure for the X-Ray Detecting System

Liansheng Li, Chunyu Wang, Loulou Deng, Fuchang Zuo, Zhiwu Mei, and Zhengxin Lv

Abstract Minimization of the charged particle background in the x-ray detecting system is an important issue. Generally, there are four possible sources of damaging radiation for x-ray detecting systems, namely: geomagnetically trapped electrons, galactic cosmic ray particles, solar flare events, and onboard radiation sources that always cause noise and damage to the performance of the payload of a spacecraft. In order to alleviate the background noise of the x-ray detecting system, a magnetic diverter is proposed to shield the electrons. The main idea of this method is, using the Monte Carlo method, to follow the tracks of all the electrons and determine whether the electrons collide with the x-ray tube, how they collide, and other parameters of this collision. The number of deflected electrons can be obtained by computing all the physical parameters of electrons. As a result, the shielding efficiency of background noise can be calculated.

Firstly, the electron motion can be classified into the following three types: (1) electrons hit the detector directly, (2) electrons hit the rest of the area of the detector plane except for the active area of the detector, and (3) electrons hit the inner wall of the x-ray detecting system tube. In addition, in accordance with the relativity principle, the velocity of different electrons with different energies can be obtained. In order to mimic the actual motion of electrons, the incidence direction, incidence position and energy of electrons are assumed random.

Secondly, the whole simulation process is divided into two steps. One step is to simulate the motion of electrons in the x-ray detection system without a magnetic diverter, obtaining the number of electrons that arrive to the detector plane, except for the active detector area, and to the inner tube, respectively. The other step is to simulate the motion of electrons in the x-ray detecting system with a magnetic diverter and the initial magnetic parameters, calculating the number of electrons which arrive to the active area of the detector, to the detector plane except for the active area of the detector, and to the inner tube, respectively. As a result, the total shielding efficiency can be obtained.

L. Li (✉) • C. Wang • L. Deng • F. Zuo • Z. Mei • Z. Lv
Beijing Institute of Control Engineering, Beijing 100190, China
e-mail: ililiansheng1981@163.com

J. Kleiman (ed.), *Protection of Materials and Structures from the Space Environment*, Astrophysics and Space Science Proceedings 47,
DOI 10.1007/978-3-319-19309-0_54

Finally, in order to reduce the weight of the x-ray detecting system, the structure of the magnetic diverter has been designed and optimized based on the simulation results.

Keywords X-ray detection • Background noise • Monte Carlo • Magnetic diverter

Introduction

The space background shielding techniques play an important role in the spacecraft design. The charged particles (protons, electrons, and heavier ions), X-rays and γ-rays, naturally present in the cosmic environment, constitute an important background source for detectors in X-ray detecting systems, when they collide with the X-ray detector. Similar problems have been encountered in the Chandra, Newton-XMM, Swift-XRT and SIMBOL-X spacecrafts.

In 1999, soon after the launch of Chandra X-ray Observatory, an increase of the Charge Transfer Inefficiency was observed on the Advanced CCD Imaging Spectrometer, which was caused by a reservoir of high-energy charged particles. It is proven that the range of soft protons in silicon (0.92 μm for 100 keV protons [1]) is sufficient for them to traverse the top layers of the CCD and create charge traps in the sensitive region, which leads to an energy sensitivity degradation. Therefore, some approaches are adopted in the Chandra to prevent the CCD from a quick damage. For example, the ACIS is moved out of the focal plane when the particle flux becomes high. The detector field is obstructed with a transmission grating when the ACIS is not in use [2, 3], etc. In addition, the Newton-XMM [4, 5] is also affected by soft protons although it is partially obstructed by the RGS gratings and the CCDs are coated with protective layers (aluminum, polypropylene and tin for the EPIC-MOS camera onboard XMM).

To protect the X-ray detector from charged particles, a magnetic diverter for electrons is used on the Newton-XMM and Swift-XRT. The successful flight and excellent performance have proven that the employed magnetic fields are able to shield effectively the detector from the electrons. Specially formed magnetic fields should be produced according to the design requirements of different spacecraft. For the Newton-XMM, the electron diverter is composed of permanent magnets fixed at 12 spider spokes of the mirror module, while the magnetic dipoles are oriented in the spider plane to produce an azimuthally-directed magnetic induction. However, the magnets on the swift telescope are bars of 15 mm × 5 mm × 70 mm, which produce a magnetic field from 110 G in the mid-plane to 30 G at 2 cm from the mid-plane. It was shown that such systems can effectively shield electrons in a broad energy range. Of course, the efficiency will decrease gradually with the increase of the electron kinetic energy, because the magnetic field intensity is restricted by the size of the magnetic diverter.

It is essential to determine the background radiation of an X-ray astronomy instrument prior to producing the detailed design of the payload and to assess the

scientific performance of the experiment. As for the X-ray detecting system, it is aimed at detecting soft X-rays in the universe and should be exposed to the radiation belts. The X-rays, high electrons, protons and other particles will exert on or collide with the X-ray detector. Therefore, they will constitute the major background sources for the X-ray detector having a sensitivity of up to 150 eV.

In this paper, we describe a magnetic diverter designed to deflect the high-energy electrons thus decreasing the background radiation of the X-ray detector and improving its Signal-to-Noise ratio. In order to simulate the relationship between the magnetic field intensity and shielding efficiency, a new simulation algorithm based on the Monte Carlo method is proposed. In addition, the simulation results allowed to optimize the structure of the magnetic diverter. In section "Monte Carlo-Based Simulation Algorithm", a Monte Carlo-based simulation algorithm is proposed. Both the structure design and simulation of the magnetic diverter are implemented and addressed in section "Structural Design and Simulation of the Magnetic Diverter". The results and conclusion are summarized in section "Conclusion".

Monte Carlo-Based Simulation Algorithm

Simulation Model

In order to simulate the actual collision process, it is necessary to classify the high-energy electrons coming from all directions into the following three types: (a) electrons that hit the detector directly, (b) electrons that hit the rest area of the plane except for the active area of detector, and (c) electrons that hit the inner wall of the x-ray detecting system tube. The trajectories of the electrons and the simulation model are shown in Fig. 1.

In this paper, the orbital simulation parameters are taken from Chandra [6,7] and only electrons ($\leq$3 MeV) are considered. During simulation, five simulation parameters, namely the incidence energy ($E\in$[0–3 MeV]), the incidence position ($\Phi\in$[0–48 mm]), the angle between the incidence point and the X axis ($\theta\in$[0–2π]), the incidence angle ($\alpha\in$[0–π]), and the angle between the projection of the

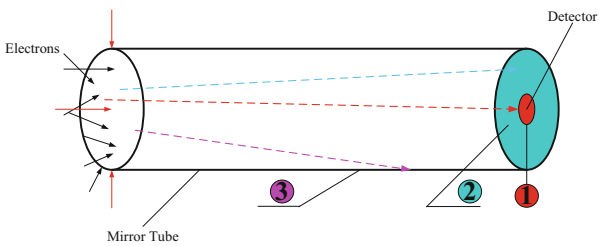

Fig. 1 Trajectories of the electrons and the simulation model

incidence angle and the X axis ($\beta \in [0–2\pi]$) are random parameters and should be determined.

Proposed Simulation Algorithm

Generally, the whole simulation process is divided into two steps.

Step 1: Without a magnetic diverter structure. Generate 10^5 electrons randomly; simulate the motion of the electrons in the x-ray detecting system without magnetic diverter to obtain the number of electrons which arrive to the detector, to the rest of the detector plane area except for the active detector area, and to the inner tube, respectively. Meanwhile, diffusion of space electrons can be computed.

Step 2: With a magnetic diverter structure. To simulate the motion of the electrons in the x-ray detecting system with initial magnetic parameters, calculating the number of electrons which arrive to the detectors, to the rest of the detector plane area, except for the active detector area, and to the inner tube, respectively. As a result, the total shielding efficiency can be obtained. In addition, the magnetic structure can be optimized according to the simulation results.

For a single electron, the trajectory in the XDS can be described as shown in Fig. 2. The initial position, velocity and other parameters are stored and the actual trajectory is divided into 1000 steps. We capture the position and velocity of each electron in time. Meanwhile, the calculations in three dimensions are made and compared with the boundary conditions to verify whether the electrons fly out of the magnetic field or collide with the mirror tube. The procedure of this algorithm is shown in Fig. 3.

Step 1: Initiation. Setting all the simulation parameters and generate 10^5 electrons randomly.

Step 2: Marking the initial positions $(x_0 = R\cos\theta, y_0 = R\sin\theta, z_0 = 0)$ and initial velocity $(v_x = V\cos\alpha\cos\beta, v_y = V\cos\alpha\sin\beta, v_z = V\sin\alpha)$.

Step 3: Compute the flight time of each electron.

Case 1: arriving at the detector, the flight time is $t_1 = 1.0\ \text{m}/v_z$.

Case 2: arriving at the inner wall of the tube, the flight time t_2 can be obtained from the following equation:

$$(x_0 + v_x t_2)^2 + (y_0 + v_y t_2)^2 = R^2 \tag{1}$$

Step 4: Calculate the final position of each electron.

Case1: arriving at the detector and its plane

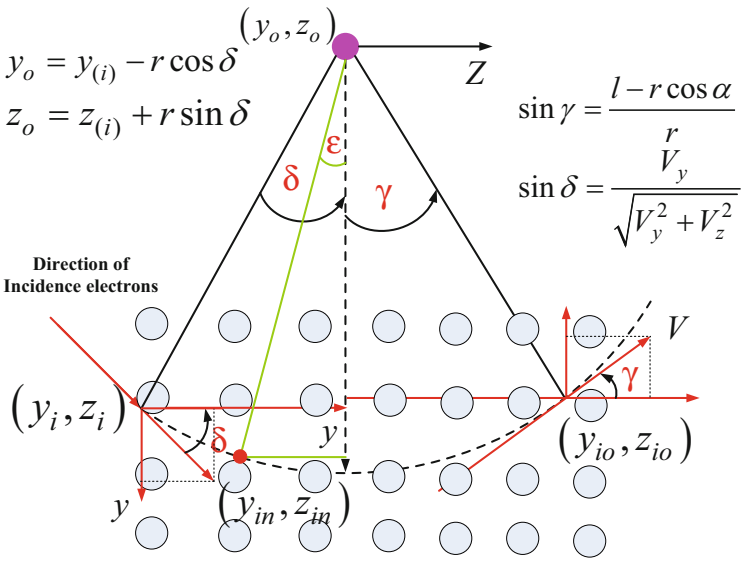

Fig. 2 The trajectory of electrons in the magnetic field

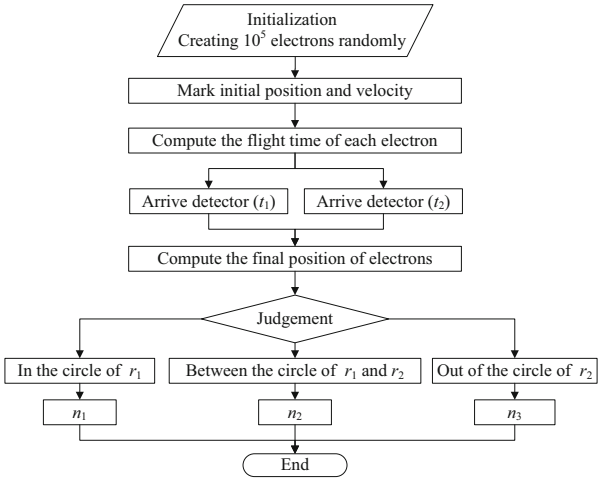

Fig. 3 Flowchart of the proposed approach

$$x_f = x_0 + v_x{*}t_1,\ y_f = y_0 + v_y{*}t_1,\ z_f = 1.0\ \text{m} \tag{2}$$

Case2: arriving at the inner wall of the tube

$$x_f = x_0 + v_x{*}t_2,\ y_f = y_0 + v_y{*}t_2,\ z_f = z_0 + v_z{*}t_2 \tag{3}$$

Step 5: Verification.

Case1: arriving at the detector

$$x_t^2 + y_t^2 \leq 6.25e(-6)\mathrm{m}^2 \tag{4}$$

Case2: arriving at the plane that fixing the detector

$$6.25e(-6)\mathrm{m}^2\mathrm{m}^2 \leq x_t^2 + y_t^2 \leq 0.002304\mathrm{m}^2 \tag{5}$$

Case3: arriving at the inner wall of the tube

$$x_t^2 + y_t^2 \geq 0.002304\mathrm{m}^2 \tag{6}$$

Step 6: Calculate the number of electrons in Step 5, respectively.

Structural Design and Simulation of the Magnetic Diverter

Structural Design

Actually, the background of the detector caused by X-rays from other directions can be avoided by adding a collimator in front of the grazing-incidence mirror. The related collimator techniques have been proposed and studied for many years, which is a much matured technique. However, few researches have been putting an effort to design and simulate a structure to shield the high-energy electrons efficiently. As a result, we focus on the high-energy electrons and propose an optimized magnetic diverter to alleviate the background of the detector.

The idea of a magnetic diverter is a hollow cylinder which is made of permanent magnetic material, the direction of magnetization varies gradually along the circumferential direction. All the magnetic force lines are circled between the cavity and the permanent magnetic material, the cavity is a uniform magnetic field. The magnetic field intensity [8] can be described by Eq. (7).

$$B = B_r \cdot \ln\left(\frac{r_2}{r_1}\right) \tag{7}$$

where B_r is the remanence, r_2 and r_1 are the inner and outer radius of the magnetic diverter, respectively.

However, the practical and feasible way to keep the direction of magnetic force lines varying continuously is to divide the diverter into a number of small parts which keep the original variation law. Therefore, the magnetic field intensity can be reformulated by Eq. (8).

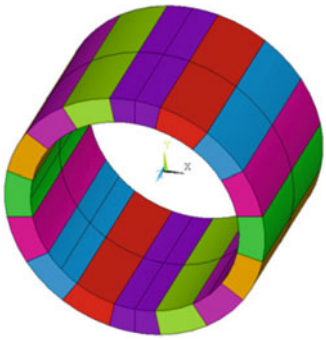

Fig. 4 The designed magnetic diverter structure

$$B = B_r \cdot \left(\frac{\sin(2\pi/n)}{2\pi/n} \right) \cdot \ln\left(\frac{r_2}{r_1} \right) \tag{8}$$

where n is the number of discrete parts of the magnetic diverter. The Nd-Fe-B is chosen as the material for the magnetic diverter. According to [8] and Eq. (2), we can see that an increase of the length L and the ratio r_2/r_1 will enlarge the magnetic field intensity. Theoretically, the magnetic field intensity of the discrete magnetic diverter is 90, 97.4 and 99.4 % of the original magnetic diverter when it is divided into 8, 16 and 32 parts, respectively. In this paper, the designed magnetic diverter is divided into 16 parts (see Fig. 4). A specific dimension optimization will be discussed and the shielding efficiency of this structure will be simulated in the next section.

Simulation and Analysis

Based on the formulated simulation model and algorithm, the shielding efficiency of the designed magnetic diverter was simulated. Fig. 5 is the trajectory simulation of electrons in the XDS with the magnetic field. The number of electrons arrived to the detector under different magnetic field strength is shown in Fig. 6. The total simulation data is listed in Table 1. We can see from above figures and table that the number of high energy electrons arrived to the detector and to the focal plane has decreased dramatically, especially with an increase of the length of the magnetic diverter.

Specifically, without the magnetic diverter, the number of: (1) electrons that hit the detector directly, (2) electrons that hit the rest area of the plane except for the area of detector, and (3) electrons that hit the inner wall of the x-ray detecting system tube are 9,2548, and 97,443, respectively. When the magnetic diverter is added to the tube, only one electron collides with the focal plane and 0 electrons arrive at the detector. Obviously, the probability of high energy electrons that arrive to the detector under the magnetic field is 0.0001, only one tenth of that without any

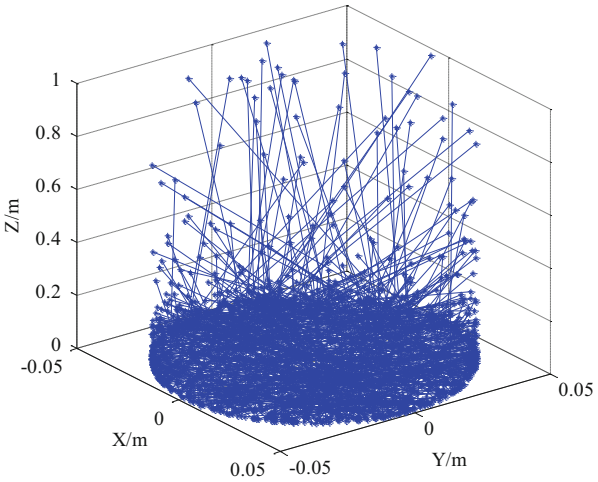

Fig. 5 Trajectory simulation of high energy electrons in the magnetic diverter

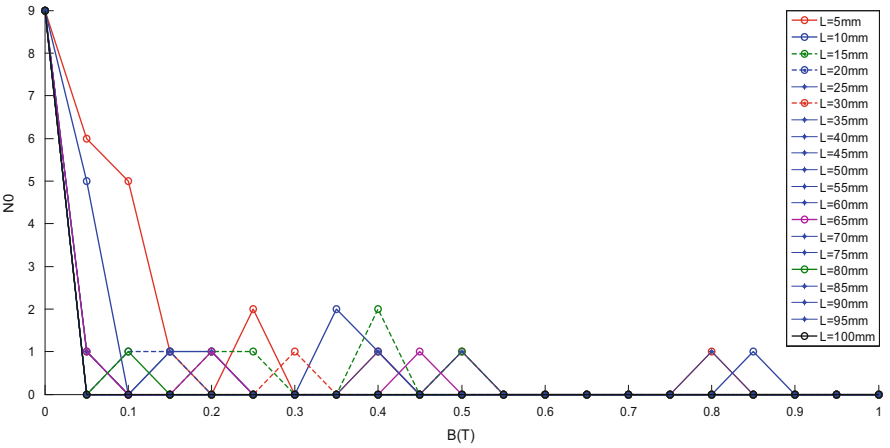

Fig. 6 The number of electrons arrived to the detector under different magnetic field strength

Table 1 Monte-Carlo simulations of high energy electrons (N = 10^5)

	No. of electrons		
Magnetic diverter	N_0	N_1	N_2
No	9	2548	97,443
Yes	0	1	99,999

magnetic diverter. The simulation results show that the magnetic diverter can shield effectively the background noise caused by high energy electrons.

Figure 6 also shows that shielding efficiency becomes higher with the increase of the length and the thickness of the magnetic diverter. However, the weight of the magnetic diverter will become more important with the increase of its dimensions. In fact, both shielding efficiency and weight are conflicted design targets. Therefore, the magnetic diverter structure should be optimized during the design process according to the design requirements and all existing constraints.

In order to determine the relationships between the magnetic field strength (T), length of the magnetic diverter (L), and shielding efficiency (η), we designed an experiment based on the above simulations. The design and simulation parameters are as follows:

$B(T) \in [0.05 : 0.05 : 1] \in L(m) \in [0.005 : 0.005 : 0.1]$, the number of high energy electrons is $n = 10^5$. The relationships between the magnetic field strength, length of the magnetic diverter, and shielding efficiency is shown in Fig. 7. One can see that electrons arrived to the detector decrease with an increase of the length of the magnetic diverter when B is a constant. Also, when the length is constant, the shielding efficiency has the same variation law with an increase of the magnetic field strength. Fig. 8 is the relationship between the weight, magnetic field strength, and length of the magnetic diverter. Obviously, the weight of the magnetic diverter increases gradually when the length and field strength become higher. Assuming the weight of the designed structure, shielding efficiency, and design requirements ($W_{\text{total}} < 3.0$ kg), we choose $B = 0.15\,T$, $L = 80$ mm as the final design parameters. The total weight of the magnetic diverter would be 2.7 kg, the inner radius would be 60 mm, and the outer radius would be 70.55 mm.

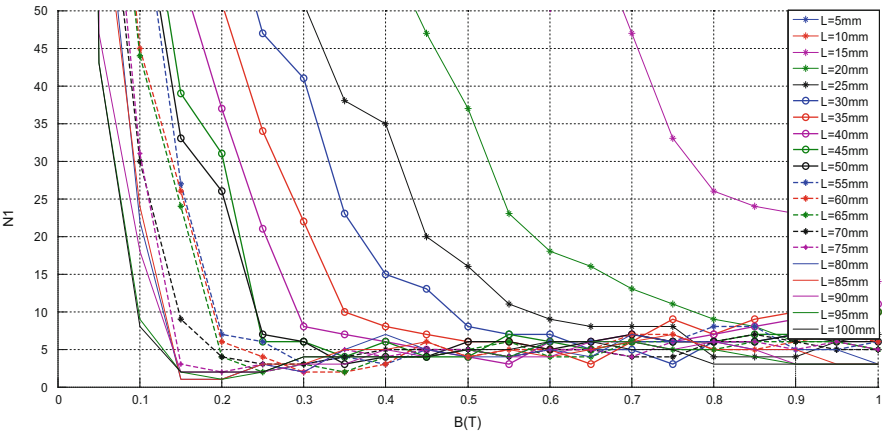

Fig. 7 The relationship between $B(T)$, L(mm), and η

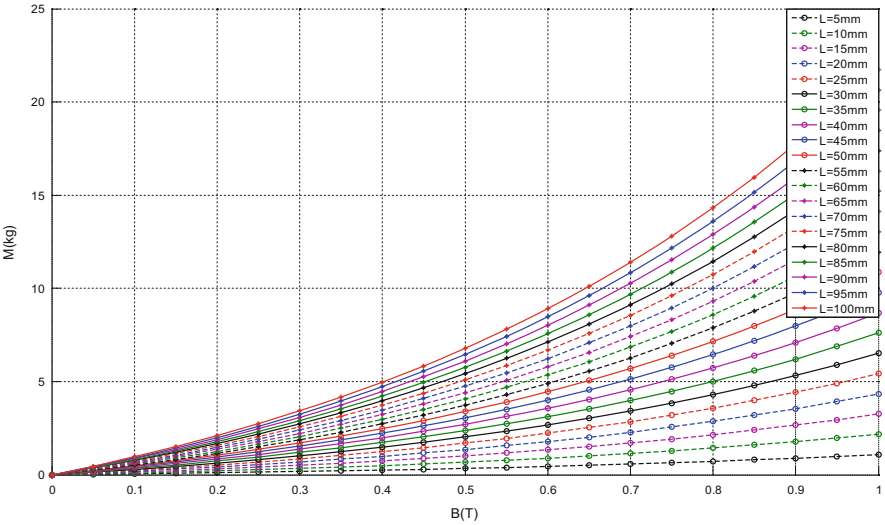

Fig. 8 The relationship between the weight, magnetic field strength, and length of the magnetic diverter

Conclusions

For geomagnetically trapped electrons, galactic cosmic ray particles, solar flare events, and onboard radiation sources that may cause serious damage to the XDS, a magnetic diverter is proposed to shield the high energy electrons. Firstly, a simulation model that tracks the trajectories of all electrons during the detection process is formulated. Thereafter, based on the Monte Carlo method, a simulation approach is proposed, with both the initial simulation parameters and procedures addressed in detail. The whole simulation process is divided into two steps. The number of electrons which arrives to the detector, to the rest area of the plane except for the detector, and to the inner tube are obtained, respectively. As a result, the total shielding efficiency can be obtained. Finally, taking into consideration the shielding efficiency, the weight, and other design requirements, the whole structure has been designed and optimized based on the simulation results. Simulation results show that the designed magnetic diverter can shield the high energy electrons effectively, which reduces the damage on the XDS caused by the space background noise.

References

1. Lo DH, Srour JR (2003) Modeling of proton-induced CCD degradation in the Chandra X-ray observatory. IEEE Trans Nucl Sci 50:2018–2023
2. Kołodziejczak JJ, Elsner RF, Austin RA, O'Dell SL (2000) Ion transmission to the focal plane of the Chandra X-ray observatory. SPIE Proc 4140:135–143

3. Carter JA, Read AM (2007) The XMM-Newton EPIC background and the production of background blank sky event files. Astron Astrophys 464:1155–1166
4. Willingale R (2000) An electron diverter for the Swift Telescope. XRA study note RT-LUX-RE-011/1, University of Leicester
5. Abele MG (1993) Structures of permanent magnets. Wiley, New York
6. Wattes JW Jr, Wright JJ (1976) Charged particle radiation environment for the Spacelab and other missions in low Earth orbit, revision A. NASA Technical Memorandum, TMX-73358, 29 Nov
7. Spiga D et al (2008) A magnetic diverter for charged particle background rejection in the SIMBOL-X telescope. In: Proceedings of SPIE. Space Telescopes and Instrumentation: Ultraviolet to Gamma Ray, vol 7011, p 70112Y. doi:10.1117/12.789917
8. Winkler CE, Dailey CC, Cumings NP (1991) Advanced X-ray astrophysics facility science instruments. In: Proceedings of SPIE, Space Astronomical Telescopes and Instruments, pp 301–311

Design and Implementation of an On-orbit Maintenance Method for the Interior Decoration Materials in a Manned Spacecraft Habitation Module

Zhe Li, Chuanfeng Wei, Xi Qu, and Hao Zheng

Abstract Maintainability is one of the primary characteristics that a manned spacecraft should possess. There are lots of interior decoration materials in the manned spacecraft habitation module. Realization of on-orbit maintenance on interior decoration materials with the help of astronauts can improve the work efficiency and life conditions of astronauts significantly, which is very important for construction of the space station. In this paper, a method of on-orbit maintenance on interior decoration materials in a manned spacecraft habitation module is proposed and practically applied to an on-orbit maintenance program on interior decoration materials. After sufficient verification on the ground, the program was carried out by astronauts in a manned spacecraft, and it showed that the method is correct and effective. The method can provide an important reference for the design of on-orbit maintenance in manned spacecraft.

Keywords On-orbit maintenance • Interior decoration materials • Manned spacecraft • Habitation module

Introduction

Realization of on-orbit maintenance allows one to simplify the design, improve the reliability and safety, extend the life-span and reduce the development costs of manned spacecraft. The Russian and American programs accumulated extensive experience regarding on-orbit maintenance. For example, the designed life-span of the Russian Mir Space Station was only 5 years, but through the on-orbit maintenance by cosmonauts, its actual life-span was extended to 15 years [1–4]. China has fully recognized the importance of on-orbit maintenance and completed a lot of maintenance design work in the ground development phase of manned spacecraft [5–7].

Z. Li (✉) • C. Wei • X. Qu • H. Zheng
China Academy of Space Technology, Beijing, China
e-mail: lzxoyo@163.com

J. Kleiman (ed.), *Protection of Materials and Structures from the Space Environment*, Astrophysics and Space Science Proceedings 47,
DOI 10.1007/978-3-319-19309-0_55

There is a large number of interior decorative materials in the manned spacecraft habitation module that provide a comfortable working and living environment for astronauts. The design of interior decorative materials should meet among other things the ergonomic requirements. In cases when astronaut's feedback is indicative that the interior in an orbiting manned spacecraft has flaws in design or material selection, carrying out the on-orbit maintenance of the interior decorative materials is particularly important. In this paper, a method for on-orbit maintenance on interior decorative materials in a manned spacecraft habitation module is proposed. According to this method, an on-orbit maintenance project on interior decorative materials was designed. After ground tests, this project was carried out by astronauts in an actual manned spacecraft environment. The results proved that the method was correct and effective.

General Requirements of On-orbit Maintenance on Interior Decorative Materials

According to the characteristics of human activity in a zero gravity environment, general requirements of on-orbit maintenance on interior decorative materials include the following six aspects.

1. The interior decorative materials should be of high strength and resistance.
2. The interior decorative materials must meet the flame retardant test requirements; the combustion products test requirements, and the harmful gases test requirements.
3. The interior decorative materials should meet the ergonomics requirements.
4. The interior decorative materials should facilitate the on-orbit operation of astronauts and the maintenance of other platform devices.
5. The necessary limit measures should be provided to astronauts during the maintenance process; the operating point of the equipment should be reached by astronauts; every astronaut's operation should be provided with an adequate space.
6. The maintenance tools should be convenient and the maintenance project should not affect the normal daily routines of astronauts.

Implementation Method of On-orbit Maintenance on Interior Decorative Materials

Design of the Maintenance Procedure

The on-orbit maintenance procedure on interior decorative materials generally includes: checking the installation interface in the habitation module by astronauts,

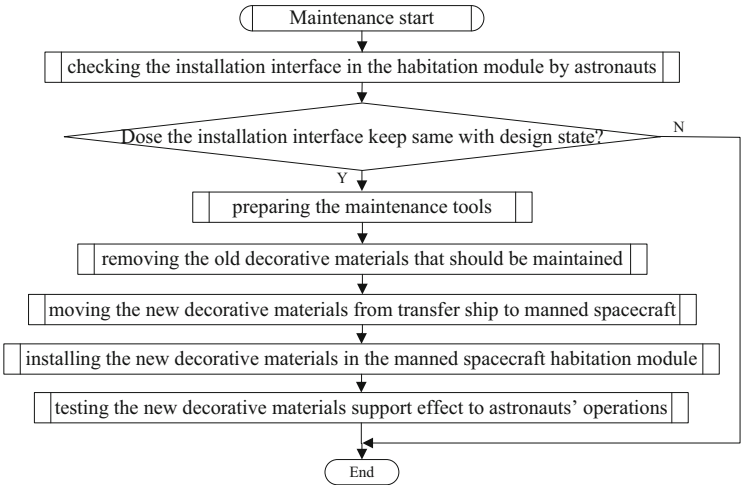

Fig. 1 Schematic diagram of equipment maintenance process

preparing the maintenance tools, removing the old decorative materials, moving the new decorative materials from the transfer ship into the manned spacecraft, installing the new decorative materials, testing the support effect of new decorative materials to operations of astronauts. Figure 1 shows the flow chart of a maintenance process.

Design of the Maintenance Ergonomics

The bodies of astronauts are in the neutral position in a zero gravity environment. According to the body parameter data for 90 Chinese fighter pilots and considering the range of astronaut's movements, an 170 cm × 70 cm × 70 cm space is required for one astronaut when he is in the neutral position. The neutral position is shown in Fig. 2. In the habitation module with limited space, astronauts should keep the activities restricted when carrying out the maintenance operations.

During the maintenance process, old decorative materials should be cut off, and there are no foot limit blocks or handrails for the astronauts when they install the new decorative materials, therefore, waist binding belts should be used. A waist binding belt consists of one waistband and two binding belts (Fig. 3). The waistband is tied on astronaut's waist, and the binding belts tie the waistband to the poles or beams around the astronauts. Thus the bodies of the astronauts are fixed and both hands could be used to carry out the maintenance operations.

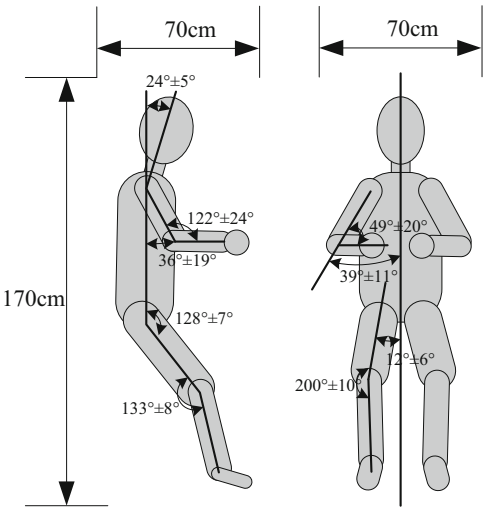

Fig. 2 Neutral position of an astronaut

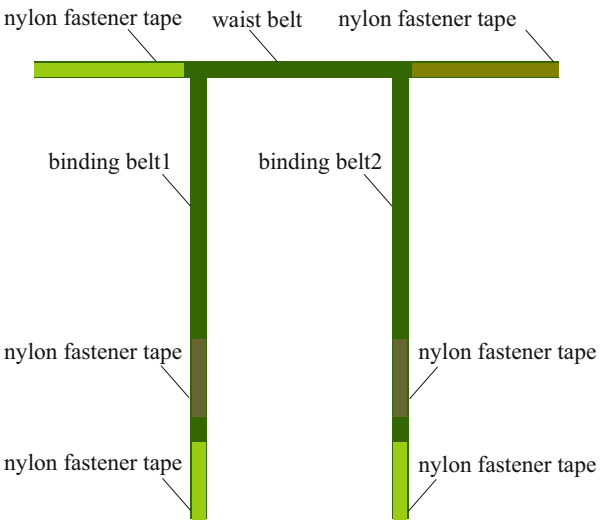

Fig. 3 Schematic view of an astronaut's binding belt system

Design of Interior Decorative Materials

Material Selection

According to the experience of astronauts, rigid decorative materials and rigid handrails give better support effect to the activities of astronauts. The selection of rigid decorative materials should be considered in the following three aspects: (1) the weight of the decorative materials should be as low as possible to save transport resources of the transfer ship; (2) decorative materials should have high

tensile strength and no plastic deformation; (3) decorative materials must meet the flame retardant test requirements, the combustion products test requirements, and the outgassing requirements.

The interior decorative materials in manned spacecraft can be selected as the materials which have been widely used on commercial aircraft, such as the paper honeycomb board.

Design of Installation Interface

The design of new interior decorative materials installation interface is the most important part of the maintenance project. Because the manned spacecraft has been flying in orbit and it would be impossible to adopt a new installation interface, there are only two types of installation interfaces that could be used, ones are those that have been adopted originally but were not used, the others are those left when the old interior decorative materials were cut off. Special adapter brackets should be developed in the ground development phase in order to fix the newly decorative materials on the spacecraft installation interface.

Design of Support Measures

In order to create a comfortable ambience, the new interior decorative materials should have warm colors, such as white or beige. Foot limit blocks and handrails should be arranged to reach the body limits of astronauts. The design of new interior decorative materials laid on the equipment and requiring frequent operation should be removable or retractable to facilitate the operations.

Design of Maintenance Tools and Estimation of Maintenance Time

General maintenance operations on interior decorative materials include: removing the mounting fasteners of new decoration materials in the transfer ship, temporary lashing of new decorative materials, cutting off the old decorative materials, protecting the cut interface, installing the mounting fasteners for new decorative materials in the manned spacecraft. The function of maintenance tools include mechanical installation and disassembly, cladding, cutting, pasting, etc. In order to reduce the amount and the weight of the tools, the maintenance tools should be selected among the universal tools which are taken along by manned spacecraft. The universal tools of manned spacecraft are listed in Table 1.

To ensure the daily routines of astronauts, a quantitative estimation of the time required from astronauts for the maintenance operations is very important.

Table 1 General tools used in a manned spacecraft

No.	Type of tools	Name	Function
1	Enginery tools	Ratchet spanner	Mount and dismount inner hexagon bolt
2		Inner Hexagon spanner	Mount and dismount inner hexagon screw
3		Flathead screwdriver	Mount and dismount slotted screw
4		Opening spanner	Mount and dismount nut
5		Pliers	Clamp object
6		Multi-tool	Cut material, mount and dismount screw
7	Electrostatic protection tool	Anti-static wrist strap	Electrostatic protection
8	Binding tools	Band	Bind or fix object
		3M adhesive tape	Paste object

According to the statistical results, when the same operation is carried out by astronauts on the ground and on-orbit, the time required on-orbit is about 1.5–2 times longer than the time required on the ground [8].

Ground Test of On-orbit Maintenance

Test Conditions

The test site was arranged in a spacecraft on the ground according with the spacecraft that needs to be maintained in orbit. The interior decorative materials which needed to be taken into the spacecraft were fixed in the transfer ship. The test was carried out by four spacecraft engineers, two were in the spacecraft, and two were in the transfer ship. Spacecraft engineers have the same body proportions as the astronauts, and had plenty of operation experience in a manned spacecraft habitation module. During the test, the ergonomics evaluation was carried out by the Astronauts System synchronously.

Test Results

Spacecraft engineers completed the on-orbit maintenance operations according to the maintenance procedure. The installation interface between the interior decorative materials and the manned spacecraft was matched.

Spacecraft engineers were fixed in the spacecraft with waist binding belts, so maintenance operations could be carried out using both hands. The limit measures were effective.

The visibility and accessibility of maintenance operations were good, and the operation space was ample. The conclusion about the ergonomics evaluation from the Astronaut System was qualified.

Spacecraft engineers simulated the routine operation work in spacecraft, and the results showed that the newly installed decorative materials supported the activities of the engineers effectively.

The tools configuration was reasonable, and its interface was well matched with the interior decorative materials. The maintenance operations took about 2.5 h on the ground, so the on-orbit maintenance operations are expected to take 3.75~5 h.

It could be concluded that the method for on-orbit maintenance on interior decorative materials was correct and it could be implemented on orbit.

On-orbit Implementation

The on-orbit project on maintenance of interior decorative materials was carried out in a manned spacecraft as follows. With the support from ground engineers, two astronauts completed the on-orbit maintenance work in 3.8 h that is consistent with the estimated time. The ground engineers judged that the installation interface between the interior decorative materials and the manned spacecraft was well matched as determined by the astronauts. The feedback from the astronauts showed that the ergonomics of the interior decorative materials were perfect, which supported the operations of astronauts effectively and eased their living and working conditions. The on-orbit maintenance project on interior decorative materials was a success.

Conclusions

A method of on-orbit maintenance on interior decoration materials in the manned spacecraft habitation module is proposed and elaborated in four aspects: Design of maintenance procedures; Design of maintenance ergonomics; Design of interior decorative materials; Design of maintenance tools and estimation of maintenance time. After sufficient verification on the ground, the maintenance program was carried out by astronauts in a manned spacecraft, it showed that the method is correct and effective.

References

1. Zhao H, Zhang Y (2007) Statistical analysis of DFH-3 serial satellites failure. Spacecr Eng 16 (1):33–37
2. Mak T (2007) A study of on orbit spacecraft failures, Hyderabad, India. In: the 58th International Astronautical Congress, pp 195–204
3. Landis GA, Bailey SG, Tischler R (2006) Causes of power related satellite failures, Waikoloa, Hawaii. Conference record of the 2006 I.E. 4th world conference on photovoltaic energy conversion, pp 1943–1945
4. Tan C, Hu T, Wang D et al (2011) Analysis on foreign spacecraft in-orbit failures. Spacecr Eng 20(4):130–136
5. Wei P (2008) Research of maintainability technology in manned spacecraft. Spacecr Eng 17 (6):68–72
6. Wang D, Tan C, Zhang B (2010) On-orbit maintainability system design for manned spacecraft. Chin Space Sci Technol 10(5):16–21
7. Xu H, LV C (2003) Space environment effect on the maintainability design of space systems. Aerosp Shanghai 5:38–41
8. Nie C, Zhu X, He Y (2005) Maintenance-flow-diagram-based maintenance time simulation. Comput Simul 22(3):41–47

Leak Detection and Location of Seals in Spacecraft Structures Based on a Multi-sensor Data Fusion Method

Ping Hao, Dong-Yong Jia, and Zhao Yin

Abstract During manned long-term missions in orbit, sealed structures have to meet the challenges of the space environment, such as meteoroids and space debris impacts, charged particles radiation, temperature cycling, vacuum environment, etc. Sealed structures and rubber sealing may be damaged by these factors. A sealed module faces the risk of leaks that can affect the pressure inside the module and even threaten the safety of the astronauts. Therefore, when performing leak-proof welding, it is an important precondition to know how to repair the failed structure and how to detect and locate the leak rapidly.

General leak monitoring methods were surveyed and analyzed and it was demonstrated that any method, when used alone, can't be used effectively for rapid detection and location of leaks in a sealed structure. A multi-sensor data fusion method is presented that allows diagnosing the leaks and the leakage rate thus allowing for effective leak detection and location in sealed spacecraft structures. The leak detection and location system consists of two subsystems: pressure leak monitor and meteoroid and space debris impact monitor. These two subsystems work continuously to monitor the spacecraft leakage rate and impact damage, respectively. In addition, an information interface, estimation strategy, and transfer flow of five subsystems were designed. This method is substantiated by a ground experiment to confirm that the sealed structure leak reason, location and leakage rate can be detected accurately and can be applied in welding operations directly.

Keywords Leak detection and location • Structure health estimation • Manned spacecraft • Seal structure • Multi-sensor data fusion • Structure protection

P. Hao (✉) • D.-Y. Jia • Z. Yin
Institute of Manned Space System Engineering, CAST, Beijing 10094, China
e-mail: haoping1977@hotmail.com

J. Kleiman (ed.), *Protection of Materials and Structures from the Space Environment*, Astrophysics and Space Science Proceedings 47,
DOI 10.1007/978-3-319-19309-0_56

Introduction

Since thousands of years ago, it is always a wonderful dream for human beings to fly off the Earth to develop the outer space peacefully and legitimately. In order to achieve this dream, many countries have designed the ISS (International Space Station), which can be used to conduct long term space experiments in orbit. However, the ISS has to meet the harsh space environment and it is possible that sealed modules start leaking because on an impact of meteoroids and space debris. Furthermore, the factors, such as structural deformation, surface oxidation, corrosion and irradiation will accelerate structural aging and lead to formation of brittle zones. Besides, the phenomenon of vacuum outgassing will also embrittle, harden, and crack the sealing materials. Sealing structures of the ISS have to face the rising risk of leakage by all these factors. For example, the US space shuttle needs replacing 1–2 portholes after each flight, with a total number of 80 since 2001 [1]. In 1996, the French electronic reconnaissance satellite "CERISE" was hit by Ariane rocket debris and the satellite altitude was affected due to the damaged gravity gradient pole [2]. In 2009, many hypervelocity impact holes were found on the multilayer thermal insulations of Hubble Space Telescope [3].

Therefore, it is necessary that a leakage monitor operates in real time in sealed structures in orbit to determine the leak points and the leak causes. The methods to repair the leak points are proposed from the analysis of monitored data to guarantee the astronaut's health and spacecraft safety [4].

Research Overview

Many technical solutions for the space debris sensing, such as the accelerometers, thermal imagers, calorimeters, fiber impact, resistive film, electromagnetic emission, optical camera, acoustic emission technics, etc., are proposed based on the long life manned spacecraft. The acoustic emission is recognized as the most effective means in the leakage monitor technology in orbit for the reason that it has the characteristics of a passive, real time, mature technology, with lower resource occupancy rate, environmental adaptability, and insensitive to structural damage, etc.

In the 1970s, people began to research the acoustic emission technology for space applications. Several groups investigated the acoustic emission wave source of high-speed impact, propagation characteristics, source location and damage pattern recognition. After the explosion of the space shuttle Columbia, NASA has accelerated the study of the acoustic emission technology and completed several experiments in the space shuttle. ESA also has completed the low-temperature and high-speed impact experiment on the ground to simulate the sense signal of the debris impact event. The research results showed that the relationship between the impact acoustic signal and the impact damage mode has a lack of quantitation.

NASA developed a variety of leak detectors used to locate gas leak sources for international space station, which can detect and pinpoint the leak sources by monitoring a fluctuation signal caused by gas leak in the cabin air and from a structural impact. The typical detectors based on this technology are the handheld ultrasonic detection system [5] and the wireless ultrasonic detection system [6, 7]. However, the effect of these detectors is not ideal because they are unable to locate the leak source effectively in practice [8]. Russia has developed a handheld extravehicular leak detector and carried out scientific experiments on "MIR" space station. Then, in 1998, Russia applied the handheld leak monitor to detect the leak location on "MIR" space station after an impact event. But at present, the efficiency of monitoring and location of leak sources is low. It always takes several weeks or even months to confirm the leak point [9].

Now, the mass spectrometer and passive ultrasonic leak detection method are mature technologies and they have been applied on the space station. Moreover, the acoustic emission leak detection method has been tested in a ground test experiment, instead of its application in space. All these leak detection methods are relatively independent and effective in case of a single leak. However, the leak signal and collected information could not be fused together to allow the evaluation of the structural health comprehensively.

Leak Monitor System Design

The leak monitor system of orbiting spacecraft is designed as two subsystems: the leak monitor module and the debris impact sensing module. The pressure and temperature of the pressure module is monitored by the leak monitor module. Then, the accurate leak rate is calculated based on the pressure variation which can be obtained by weighted compensation of related factors in data processing. The leak information is transferred to host computer and is displayed on the instrument board to remind the astronaut to locate the leak zone and to repair it. The interaction between the blocks of the system hardware is shown schematically in Fig. 1.

System Working Mode of Each Module

The working modes of two modules of the leak monitor system are shown in Table 1. The leak monitor module and the debris impact sensing module work in real time. The data obtained by these modules is fused together to calculate the leak rate and the impact signal. For the reason that the reaction time of the debris module is faster than the reaction time of the leak monitor module, the impact result should be judged and confirmed firstly based on the impact signal obtained by the debris impact module. Thus, when the sealed structure is impacted by high speed debris,

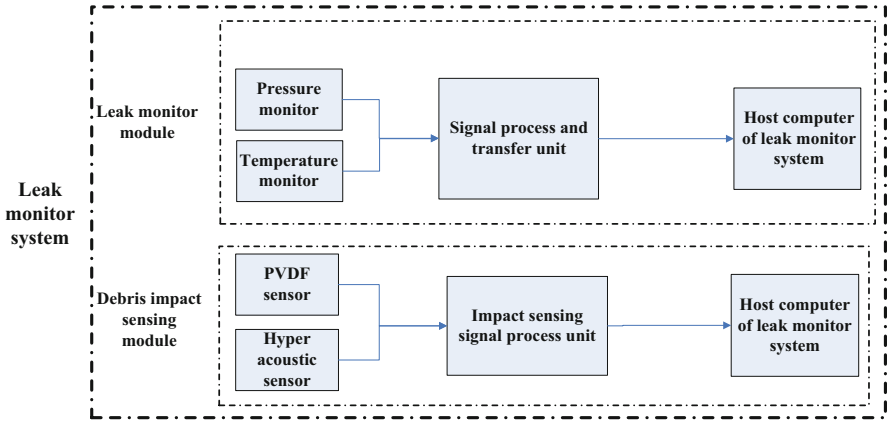

Fig. 1 Schematic presentation of the leak monitoring system hardware

Table 1 Module function and working mode

Module	Regime	Function	Operation mode	Remark
Leak monitor	Real time	Pressure leak monitor and alarm	Working in real time automatically	
Debris impact sensing	Real time	Space debris impact signal sensing and location	Working in real time automatically	Alarm for large leak rate of breakdown hole

the structure damage can be detected according to the frequency and amplitude of the signal obtained by the debris impact module. Then, the damage is calculated and confirmed again by the pressure variation signal obtained from the leak monitor module.

Experiment of Leak Detection Module

In order to validate the method of fusion and processing of information from the two leak detection modules, a comprehensive test of a sealed spacecraft capsule was simulated. Two types of tests are simulated, including the static leak test without a wind field and the dynamic leak test with a wind field, as well as two working conditions, "2–1" and "1–0". The "2–1" condition refers to inflation of 0.2 MPa, which means that the entry of the leak hole is at the 0.2MPa side and the exit hole is at the atmospheric condition side.

The condition of "1–0" means that a leak at the atmospheric conditions and vacuum outside. Five leak holes at different leak rates were opened to simulate a capsule leak in this comprehensive leak detection test.

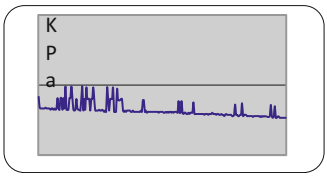

Fig. 2 Pressure curve of nominal leak rate of 0.94×10^{-2} Pa.m^3/s

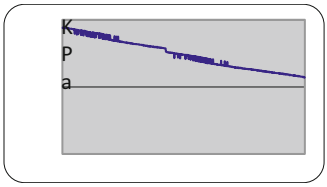

Fig. 3 Pressure curve of nominal leak rate of 1.0×10^{-1} Pa.m^3/s

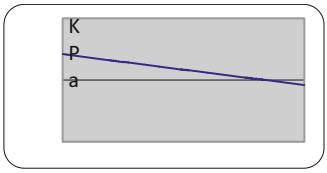

Fig. 4 Pressure curve of nominal leak rate of 5.4×10^{-1} Pa.m^3/s

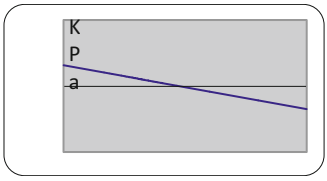

Fig. 5 Pressure curve of nominal leak rate of 1.01 Pa.m^3/s

Synthetic atmospheric air at 2 atm pressure (absolute pressure of 200.3 kPa) was injected into the sealed cabin of spacecraft, and five different leak holes of 0.94×10^{-2} Pa.m^3/s, 1.0×10^{-1} Pa.m^3/s, 5.4×10^{-1} Pa.m^3/s, and 1.01 Pa.m^3/s were opened in the sealed cabin to simulate different leak types of the sealed cabin and to test the alarm functioning and the performance of the leak detection and the alarm system. The accuracy of calculating the leak rates can be analyzed by comparing the rates of standard leak holes.

Figs. 2, 3, 4, 5, 6 and 7 show the leak curves of leak holes with nominal values of 0.94×10^{-2} Pa.m^3/s, 1.0×10^{-1} Pa.m^3/s, 5.4×10^{-1} Pa.m^3/s and 1.01 Pa.m^3/s and the time intervals for representing the curves were randomly selected.

(a) As can be seen from the pressure curve in Fig. 4 with the nominal leak rate of Pa.m^3/s, the system error of measuring pressure is quite large, therefore the difference between the maximum and minimum is 8–9 Pa and the error is distributed by a certain law. Theoretical analysis shows that the leak of 0.94×10^{-2} Pa.m^3/s is close to the minimum leakage rate, which is the

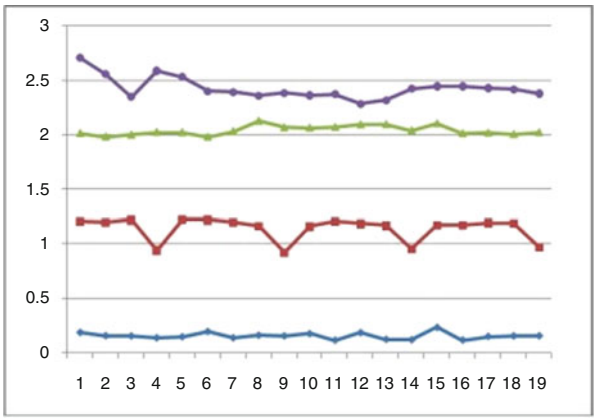

Fig. 6 Leak rate curves of leak holes with different nominal leak

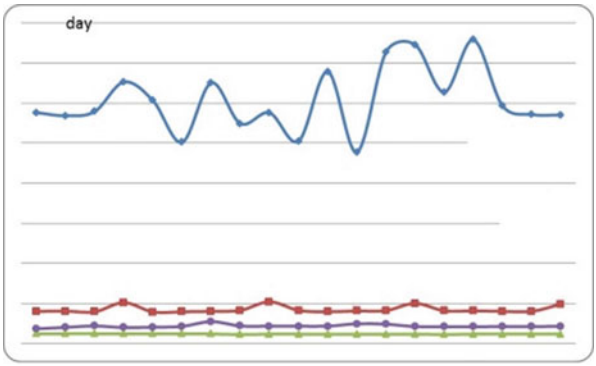

Fig. 7 Removal of a fault time curve of different leak holes

sensitivity of this method. According to the error theory, the closer the error approaches the detection sensitivity, the lower the accuracy of the test results.

(b) As can be seen from the pressure curve in Fig. 5 with the nominal leak rate of 1×10^{-1} Pa.m^3/s, the leak trend can be attained, but still there are errors distributed by a certain law. As can be seen from Figs. 6 and 7, pressure curves of higher leak rates are much more clear and obvious, and the error is much lower, and the testing results demonstrate that the system software meets the requirements.

(c) At the beginning of the experiment, the accuracy parameter is set to 6 by the system software, which means that the initial pressure and the final pressure for calculating the leak rate differ by 6σ. When the amount of leaking is little (the volume of the cabin is about 9.4 m^3 and the nominal leak rate of the leak hole is 0.94×10^{-2} Pa.m^3/s), the base pressure caused by environmental temperature may be higher than the difference between the initial pressure and the final pressure to allow the calculation of the leak rate. Therefore, the leak rate is calculated by the software with large variations, which cannot reflect the actual leak rate. Thus, appropriate parameters need to be set once more to distinguish the baseline noise and the actual leak rate.

(d) It can be seen from the test data and analysis results in the "1-0" test condition that leak rates of ~10^{-1} Pa.m^3/s and above 10^{-1} Pa.m^3/s can be detected by the leak detection system in orbit with an accuracy below 10 %. For the leak rates of ~10^{-2} Pa.m^3/s and above 10^{-2} Pa.m^3/s, the accuracy is higher than 10 %.

Experiment of Debris Impact Perception and Location

The accuracy of the layout of sensors and the location method was verified in this experiment by testing the impact location technology which was discussed above.

The hypervelocity impact event is simulated by launching a projectile on the sealed cabin to produce acoustic emission signals, which are detected by three broadband sensors located on the sealed cabin structure of spacecraft. Sensors are connected to NI data sampling equipment and are designated to record the acoustic emission signals.

The experiment parameter and position of the sensors and the impact location are shown in Figs. 8 and 9. The first annular weld at the bottom of the cabin and a vertical annular weld can be considered as a reference line and the crossover point of two annular welds can be considered as the original point. Two sensors are positioned on each side of the reference line, 1600 mm away from the original point, and another sensor is positioned on the reference line in the cabin height direction. The initial position starts from the bottom reference line, and nine lines parallel to the reference line in the cabin height direction and eight lines parallel to the reference line on each side of the cabin are made. There are 73 crossover points crossed by parallel lines in the area fenced by these three sensors, and the crossover points are set to be the impact points and the coordinates of these impact points are shown in Table 2. Acoustic emission signals are produced by launching the projectile five times onto the impact points. There are 73 groups of acoustic signals, and each group contains the experimental data collected in five tests.

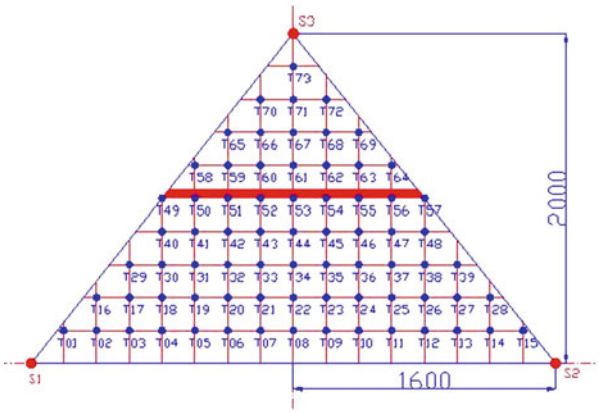

Fig. 8 Theoretical location of the module position experiment

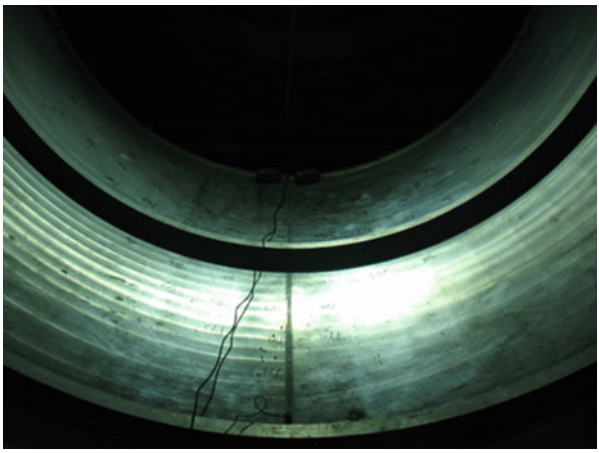

Fig. 9 Photograph of the module position experiment

Table 2 Impact point coordinates

	Impact point			Impact point			Impact point			Impact point	
No.	X	Y	No.	X	Y	No.	X	Y	No.	X	Y
1	−1400	200	19	−600	400	37	600	600	55	400	1000
2	−1200	200	20	−400	400	38	800	600	56	600	1000
3	−1000	200	21	−200	400	39	1000	600	57	800	1000
4	−800	200	22	0	400	40	−800	800	58	−600	1200
5	−600	200	23	200	400	41	−600	800	59	−400	1200
6	−400	200	24	400	400	42	−400	800	60	−200	1200
7	−200	200	25	600	400	43	−200	800	61	0	1200
8	0	200	26	800	400	44	0	800	62	200	1200
9	200	200	27	1000	400	45	200	800	63	400	1200
10	400	200	28	1200	400	46	400	800	64	600	1200
11	600	200	29	−1000	600	47	600	800	65	−400	1400
12	800	200	30	−800	600	48	800	800	66	−200	1400
13	1000	200	31	−600	600	49	−800	1000	67	0	1400
14	1200	200	32	−400	600	50	−600	1000	68	200	1400
15	1400	200	33	−200	600	51	−400	1000	69	400	1400
16	−1200	400	34	0	600	52	−200	1000	70	−200	1600
17	−1000	400	35	200	600	53	0	1000	71	0	1600
18	−800	400	36	400	600	54	200	1000	72	200	1600

Thus, a location experiment was carried out in the sealed cabin of manned spacecraft and the method of impact location was validated in this experiment. The conclusions are as follows:

1. The speed of acoustic emission signals in the sealed cabin can be considered as a certain value and it does not change with the movement direction. An appropriate wave speed can be chosen to meet the location requirement.

2. The virtual wave front method can be applied to locate the acoustic emission source. The average accuracy of location was quite good in the experiment carried out to determine the projectile location in the sealed cabin. This stable method can meet the requirements of location accuracy and stability.

In summary, when a hypervelocity impact on the pressurized cabin of manned spacecraft occurs, the layout of sensors and the location method can be applied to locate the position of the impact of space debris.

Conclusions

The leak monitoring technology was successfully validated in a ground experiment and the following conclusions can be drawn:

1. The leak rate obtained by the leak monitor in this experiment is consistent with the theoretical data. The system hardware and software can work and match correctly and reliably, thus satisfying the requirements.
2. The acoustics emission signal velocity in a typical sealed structure can be considered as a fixed value which doesn't vary with the direction of propagation. It can satisfy the requirement of source location if the appropriate velocity is chosen. Furthermore, the virtual wave front method can be applied in engineering and generalized to the acoustic emission source location in a typical sealed structure. This is because this method provides a high position precision and reliability and it was validated in a shooting location experiment on spacecraft.
3. The leak rate and debris impact signal can be obtained by fusing and processing the data from the leak monitor module and the debris impact module. Because the response time of the debris impact module is faster than that of the leak monitor module, the impact result should be first determined preliminarily from the degree of the signal strength provided by the debris impact module.

References

1. Bai Y, Pang HW, Gong ZZ (2009) Research progress of spacecraft window damage caused by small space debris. Spacecr Environ Eng 26(5):7–411
2. Alby F, Lansard E, Michal T (1997) Collision of cerise with space debris. In: 2nd European Conference on Space Debris, Darmstadt, Germany
3. Liou JC (2010) MMOD inspection of the HST Bay 5 multi-layer insulation panel. Orbital Debris Q News 14(2):2
4. Dou H, Liu J (2002) Manned space flight and space debris. Aerosp China 2:18–23
5. George S (2002) Ultrasonic detectors in space. Johnson Space Center, Houston, pp 1–3
6. Champaigne K, Krug K (2002) Wireless instrumentation system for plasma measurements on the international space station. In: 40-th Aerospace Sciences Meeting and Exhibit, Nevada

7. Champaigne KE, Sumners J (2005) Wireless impact and leak detection and location systems for the ISS and shuttle wing leading edge. In: Aerospace conference 2005 IEEE, 5–12 Mar, pp 1–8
8. Stephen D, Roberts R, Chimenti D et al (2005) Two-sensor ultrasonic spacecraft leak detection using structure-borne noise. Acoust Soc Am 6(2):63–68
9. Wilson W, Coffey N, Madaras E (2008) Leak detection and location technology assessment for aerospace applications. Langley Research Center, Hampton, pp 3–10

Simulation Technology for Tissue Dose Ionizing Radiation in the Manned Spacecraft Pressurized Cabin

Biao Yang, Dongsheng Yang, and Chuanfeng Wei

Abstract The pressurized cabin of the manned spacecraft provides the places of working and living for astronauts. It is critical to analyze the tissue dose in the pressurized cabin, in order to predict quantitatively the hazard for the astronauts due to the space ionizing radiation. This paper introduces a technical approach to calculate the tissue dose in a pressurized cabin of manned spacecraft. For a medium-term-resident manned spacecraft, a three-dimensional simulation model is established to achieve the magnitude distribution of tissue dose in the pressurized cabin. The simulation results can be used for the systematic design on radiation protection of astronauts in a space flight.

Keywords Manned spacecraft • Tissue dose • Radiation

Introduction

Astronauts in the spacecraft flying in the low-Earth orbit will inevitably encounter space ionizing radiation, mainly arising from charged particles of the radiation belt, solar particle events, as well as galactic cosmic radiation [1]. These charged particles with high energy can penetrate the panel of the manned spacecraft and interact with the tissue of astronauts, causing tissue damage and even inducing cancer [2–4]. The pressurized cabin of the manned spacecraft provides the places of working and living for astronauts, in which radiation dose absorbed by human tissue (named 'tissue dose') should be below the Radiation Dose Limits [5]. Therefore, it is critical to analyze the tissue dose in the pressurized cabin, in order to

B. Yang (✉) • C. Wei
Beijing Institute of Manned Space System Engineering, China Academy of Space Technology, Beijing 100094, China
e-mail: yangbiao228@gmail.com

D. Yang
Beijing Institute of Spacecraft Environment Engineering, Beijing 100094, China

Science and Technology on Reliability and Environmental Engineering Laboratory, Beijing 100094, China

J. Kleiman (ed.), *Protection of Materials and Structures from the Space Environment*, Astrophysics and Space Science Proceedings 47,
DOI 10.1007/978-3-319-19309-0_57

predict quantitatively the hazard for the astronauts due to the space ionizing radiation.

Three-dimensional radiation dose analysis has been used in satellite engineering, providing significant data to improve the systematic design on radiation protection of electronic equipment and materials onboard satellite [6]. However, it is rare to apply the three-dimensional radiation dose analysis approach on manned spacecraft for radiation protection of astronauts in China. In the traditional systematic design, one-dimensional analysis approach based on the solid sphere shielding model is applied to estimate the tissue dose of astronauts roughly.

The configuration and structure of manned spacecraft is usually complex. In this regard, the mass shielding in different directions is not uniform. The tissue dose derived from the solid sphere shielding model could not effectively guide the systematic design on radiation protection. China is developing long-term-resident spacecraft. The radiation harm to the astronauts is potentially severe. It is significant to develop a three-dimensional simulative technology to calculate the tissue dose for the astronauts. The result is supposed to help optimize the mass shielding of spacecraft and provide effectively radiation protection for the astronauts.

In this paper, firstly, a three-dimensional simulation model is developed to calculate the tissue does in pressurized cabin of manned spacecraft. Then, a medium-term-resident manned spacecraft is taken as an example. The magnitude distribution of tissue does is obtained from the simulation model. Finally, it is shown how to use the result to optimize the systematic design on radiation protection.

Simulation Model

The flow chart to calculate the three-dimensional tissue dose in a pressurized cabin is shown in Fig. 1. The steps are summarized below:

(a) Calculate the position of spacecraft expressed in the geomagnetic coordinates as a function of time based on the orbital elements.

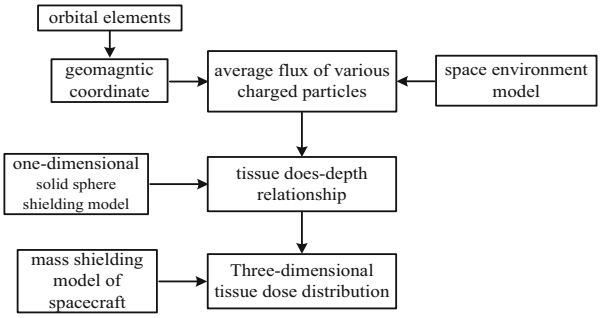

Fig. 1 The flow chart of three-dimensional tissue dose calculation

(b) Use the space environment model (radiation belt model, solar particle event model, and galactic cosmic ray model) to obtain the average fluxes of various charged particles along the orbit.
(c) Get the relationship between the tissue dose and the shielding thickness (i.e. the tissue dose-depth relationship) based on the one-dimensional solid sphere shielding model.
(d) Establish the three-dimensional geometry model of mass shielding.
(e) Calculate the magnitude of tissue dose in different directions and obtain the tissue dose distribution.

Given a medium-term-resident manned spacecraft flying in the low-Earth orbit at a 340 km altitude and 40° inclination, the simulation model was applied to calculate the tissue dose. The resident time for the astronauts in the spacecraft is supposed to be not longer than 30 days. The radiation effect is mainly attributed to charged particles in the radiation belt. The radiation belt models AP-8 and AE-8 [9–11] were used during the solar minimum to calculate the mean particle fluxes along the orbit.

The SHIELDOSE-2 [7] method utilizing the one-dimensional solid sphere shielding model was used to get the radiation dose vs. depth relationship. The typical tissue dose in a human is then obtained by multiplying the radiation dose by the radiation weight factor [8]. The tissue dose vs. depth relationship obtained from the SHIELDOSE-2 model is shown in Fig. 2. The depth indicates the equivalent aluminum thickness. The tissue dose represents the radiation dose accumulated during 30 days and absorbed by human's tissue.

The spacecraft comprises a pressurized cabin, a transient segment, and a propulsion cabin. The pressurized cabin consists of a port, a font cone, a cylindrical section, and a spherical back part. The geometry model is shown in Fig. 3. In the spacecraft geometry coordinates, the x axis is along the symmetric axes of the spacecraft, the y and z axes are in the cross section of the spacecraft. Four points in the pressurized cabin marked as A1, A2, A3, and A4 along the x axis are selected to calculate the three-dimensional tissue dose. For simplification, the shielding effect

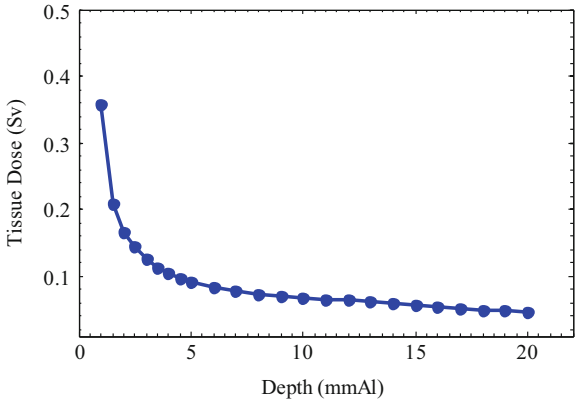

Fig. 2 The organ dose as a function of the aluminum thickness

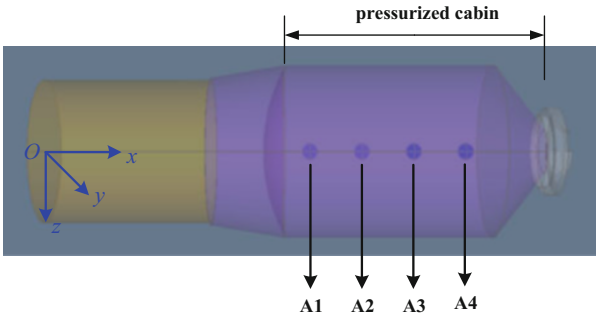

Fig. 3 The geometry of the manned spacecraft

Table 1 The equivalent aluminum thickness of the panel and port

Spacecraft		Equivalent aluminum thickness (mm)
Pressurized cabin	Port	3.0
	Front cone	3.0
	Cylindrical section	2.5
	Back spherical part	3.5
Transient cabin		1.5
Propulsion cabin		3.0

only of the panel and port is considered. The equivalent aluminum thickness of the panel and port are shown in Table 1.

Result and Discussion

The simulation results for the tissue dose accumulated during 30 days in four analysis points are shown in Table 2, including the dose components along each axis, as well as the total dose. It can be seen that the magnitude of tissue dose is different in different points. The dose component in different directions of a particular point is also different. It is remarkably that the component in the $+x$ direction is larger than that in the $-x$ direction, and smaller than those in the y and z directions. Since the mass shielding model is symmetrical along the x axis, the component in the y direction is equal to the one in the z direction. The simulation results can evidently reflect the inhomogeneities of mass shielding of the spacecraft.

Three types of graphs can be obtained from the simulation results, as shown in Figs. 4, 5 and 6, representing the magnitude distribution of tissue dose in each direction (graph Type I), the tissue dose component in each direction (graph Type II), and the total tissue dose in each analysis point (graph Type III), respectively.

The three-dimensional simulation result is very significant to support the systematic design on radiation protection. Firstly, from the Type III graph, the total tissue dose in a particular point is compared to the Radiation Dose Limits for the

Table 2 Simulation results of the tissue dose in four analysis points

	30 days accumulated tissue dose						
	Component dose (Sv)						
Analysis point	$+x$	$+y$	$+z$	$-x$	$-y$	$-z$	Total dose (Sv)
A1	1.99×10^{-2}	2.38×10^{-2}	2.38×10^{-2}	1.45×10^{-2}	2.38×10^{-2}	2.38×10^{-2}	1.30×10^{-1}
A2	2.07×10^{-2}	2.62×10^{-2}	2.62×10^{-2}	1.61×10^{-2}	2.62×10^{-2}	2.62×10^{-2}	1.42×10^{-1}
A3	2.09×10^{-2}	2.62×10^{-2}	2.62×10^{-2}	1.81×10^{-2}	2.62×10^{-2}	2.62×10^{-2}	1.44×10^{-1}
A4	2.08×10^{-2}	2.46×10^{-2}	2.46×10^{-2}	1.83×10^{-2}	2.46×10^{-2}	2.46×10^{-2}	1.38×10^{-1}

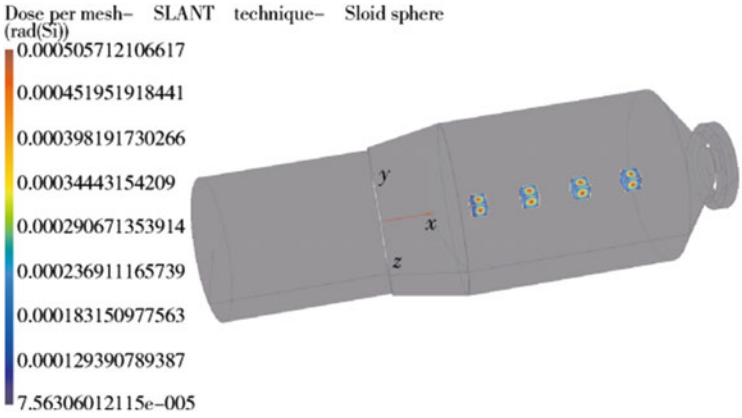

Fig. 4 Graph I: the tissue dose distribution in each direction

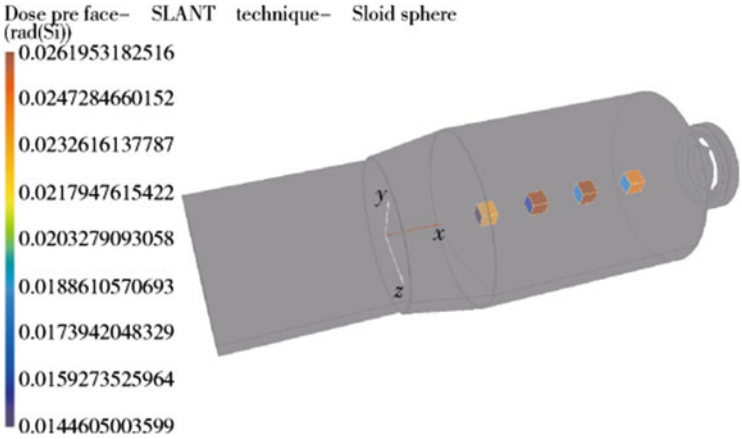

Fig. 5 Graph II: the tissue dose component in each direction

astronauts. A position can be found where the magnitude is larger than the Radiation Dose Limits. Then, the direction can be distinguished where the tissue dose component is visibly larger than the others from the Type II and Type I graphs. Finally, optimized design on mass shielding can be conducted efficiently. One point is that the layout of spacecraft can be adjusted to enhance the intensity of mass shielding in the direction with a high tissue dose component, without increasing the total weight of the spacecraft. Another point, materials can be added in the position of weak mass shielding, if the total tissue dose is still higher than the Radiation Dose Limits after several rounds of layout optimization.

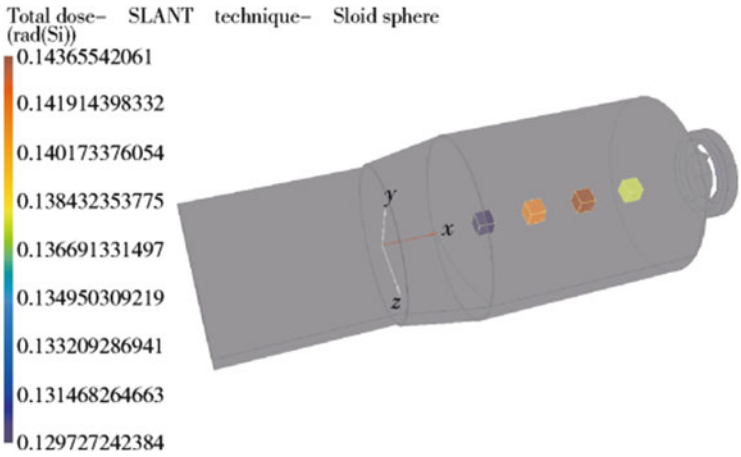

Fig. 6 Graph III: the total tissue dose in each analysis point

Summary

A three-dimensional simulation technology was developed to calculate the tissue dose in the pressurized cabin of manned spacecraft. Taken a medium-term-resident manned spacecraft as an example, the magnitude distribution of tissue dose was obtained from the simulation model. The simulation results showed that the layout and configuration of the spacecraft can be improved to achieve the optimal mass shielding, making the magnitude of the tissue dose lower than the Radiation Dose Limits for a pressurized cabin. The simulation approach proposed in this paper is valuable to optimize the systematic design on radiation protection for astronauts in a space flight.

References

1. Qi Z (2003) Radiation protection and monitoring for manned spaceflight. National Defense Industry Press, Beijing, pp 12–15
2. Cucinotta FA, Manuel FK, Johns J et al (2001) Space radiation and cataracts in astronauts. Radiat Res 156(5):460–466
3. Letaw JR, Silberberg R, Tsao CH (1989) Radiational hazards on space missions outside the magnetosphere. Adv Space Res 9(10):285–291
4. Todd P (1983) Unique biological aspects of radiation hazards: an overview. Adv Space Res 3 (8):187–194
5. Zhu W (2008) Study on radiation does limits absorbed by astronaut in space activities. Spacecr Eng 17(1):48–52
6. Cai Z, Lin G, Chen G et al (2002) The 3D radiation does analysis for satellite. In: 53rd International Astronautical Congress. The World Space Congress, Huston, TX, pp 1–5

7. Seltzer SM (1994) Updated calculations for routine space- shielding radiation dose estimates: SHIELDOSE-2, NISTIR 5477. NIST Publication, Gaithersburg, MD
8. GJB 4018-2000. Radiation protection requirement for spacecraft crew module
9. Sawyer DM, Vette JI (1976) AP-8 trapped proton environment for solar maximum and solar minimum. NSSDC/WDC-A-R&S, 76-06. NASA/Goddard Space Flight Center
10. Vette JI (1991) The NASA/National space science data center trapped radiation environment model program (1964–1991). NSSDC 91-29. NASA/Goddard Space Flight Center
11. Gaffey JD, Bilitza D (1994) NASA/National Space Science Data Center trapped radiation models. J Spacecr Rocket 31(2):172–176

A Study on Control Methods for Thermally Induced Disturbances of Large Space Structures

Yanqiang Bi, Xinming Su, Jing Wang, Xiyuan Li, and Dianfu Qie

Abstract Thermally induced structural disturbances are known to affect the altitude dynamics and pointing performance of satellites during eclipse transitions. In this study the thermally induced disturbances of spacecraft structures and accessories are analyzed by Finite Element Method based on dynamics and heat-transfer theory. Passive control methods of thermally induced disturbances presently include the optimization of surface solar absorptivity, material thermal conductivity and elasticity in order to make the Boley non-dimensional parameter be far from 1. The methods are reliable, convenient and low-cost, and they have demonstrated their applicability in numerical simulations. The study will be significant to analyze a large space structure design.

Keywords Large space structures • Thermally induced disturbances • Control methods

Introduction

With the development of aerospace technology, large space structures are used more and more extensively. The large space structures mainly refer to a solar array, large antenna reflector, long truss, and so on. As the large space structures are exposed outside of the spacecraft, they will be extensively impacted by the space environment including solar radiation, radiation to space, radiation reflected from the Earth, and infrared energy emitted by the Earth [1]. When the temperature field of a large space structure varies radically, a thermally induced disturbance may take place under some conditions. Such spacecraft accidents have happened several

Y. Bi (✉) • X. Su • X. Li
Beijing Institute of Spacecraft Environment Engineering, Beijing 100094, China
e-mail: yangbiao228@gmail.com

J. Wang • D. Qie
Beijing Institute of Spacecraft Environment Engineering, Beijing 100094, China

Science and Technology on Reliability and Environmental Engineering Laboratory, Beijing 100094, China

J. Kleiman (ed.), *Protection of Materials and Structures from the Space Environment*, Astrophysics and Space Science Proceedings 47,
DOI 10.1007/978-3-319-19309-0_58

times, among which the most severe one was a Hubble Space Telescope accident. The metal braced structures of the Hubble Space Telescope vibrated in space that impacted the normal operation, causing substantial losses. Thus, the research on methods to countermeasure the thermally induced disturbance is of great importance. The first theoretical predictions of thermal disturbances were made back in Boley's study [2, 3].

Geometrical Model

Thermally induced vibration of a thin-wall tube is calculated to analyze the effect of application of the thermal control method to vibration. In this analysis the inner diameter of the tube is 20 mm and the external diameter is 21 mm. The length of the tube is 18 m. We assume that the tube can bend in the x–y plane only. The geometry of the tube is shown in Fig. 1.

Calculation Model

Coupled Thermal-Structure Dynamics Equation

Based on the differential equation of small deflection, the equilibrium equation of the tube can be written as [4, 5]:

$$EI\frac{\partial^2 \upsilon}{\partial x^2} + m\frac{\partial^2 \upsilon}{\partial x^2}(l-x) + M_T(x,t) = 0 \tag{1}$$

where $I = \pi R^3 h$, m is the mass load on the edge of the tube and can be looked at as the load of satellite, E is the modulus of elasticity of the material, l is the length of tube, M_T is the equivalent load by thermal effect.

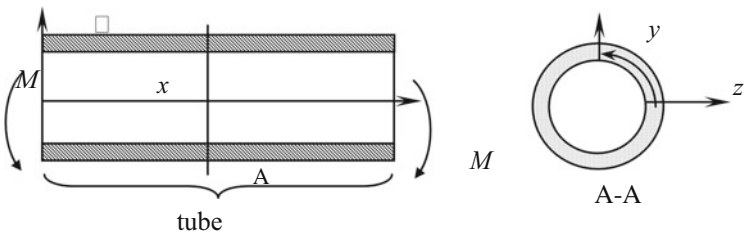

Fig. 1 The geometry of the tube adapted in the calculations

Equivalent Load of Thermal Effect

If thermal deformation is considered, the strain of any point of the tube can be expressed as:

$$\varepsilon_x = \frac{\sigma_x}{E} + \alpha(T - T_0) \tag{2}$$

where α is the thermal coefficient of expansion, T is temperature of any point, T_0 is the initial temperature. The integral that shows the stress caused by thermal effect along the cross section and the thermal moment can be obtained as:

$$M_T(x,t) = \int_A \alpha E[T(x,\phi,t) - T(x,\phi,t_0)]ydA \tag{3}$$

Temperature Calculation Model

Because the wall of the tube is very thin, temperature gradients across the tube can be ignored and temperature is considered uniform in the diameter direction. Temperature field inside the tube has a two directional distribution and can be expressed as $T = T(y,z,t)$. The temperature governing equation is:

$$\rho c\frac{\partial T}{\partial t} - k\frac{\partial}{R^2\partial\phi}\left(\frac{\partial T}{\partial\phi}\right) - \frac{\partial}{\partial x}\left(k\frac{\partial T}{\partial x}\right) + \frac{\varepsilon\sigma}{H_s}\left(T^4 - T_C^4\right) - \frac{\alpha_s}{H_s}\bar{q}(x,y,z,t) = 0 \tag{4}$$

where t is time, H_s is thickness of the wall, c is thermal capacity, ρ is density, k is thermal conductivity, ε is emission, α_s is solar heat flux absorptance coefficient, σ is the black body radiation constant, $\bar{q}(x,y,z,t)$ is the heat flux directed normally to the wall of the tube, T_c is space temperature at around 4 K.

The solar heat flux is constant but it can be changed with the movement of the tube, so the temperature could change. This temperature change would cause deformation of the tube, and this deformation would cause a change too, so coupling of temperature and movement effects may cause vibration.

Boundary Condition and Initial Condition

The boundary condition is:

$$v(0,t) = \frac{\partial v}{\partial x}(0,t) = 0$$

The initial condition is:

$$v(x,0) = \frac{\partial v}{\partial x}(x,0) = 0$$
$$T(x,0) = T_0$$

Calculation Results and Discussion

Thermal Conductivity Effect on Thermal Vibration

The thermal conductivity effect on thermal vibration is shown in Fig. 2. The amplitude of thermal vibration would decrease if thermal conductivity is increased, and the load effect will be reduced by this thermal effect. While thermal control is designed, high thermal conductivity materials can be used to reduce thermal vibration.

Thermal Absorptivity Effect on Thermal Vibration

The thermal absorbance effect on thermal vibration is shown in Fig. 3. The amplitude of thermal vibration will decrease greatly if thermal absorbance is decreased. So reducing the thermal absorbance is an efficient method to reduce possible thermal vibration. While thermal control is designed, the space structure cannot be covered with any heat insulation material, instead a coating should be applied, such as white paint with a low thermal absorbance.

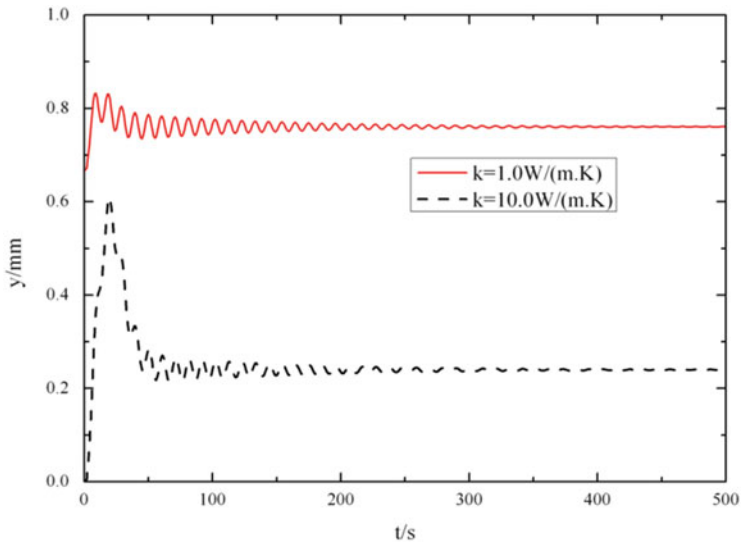

Fig. 2 Thermal vibration at different thermal conductivity

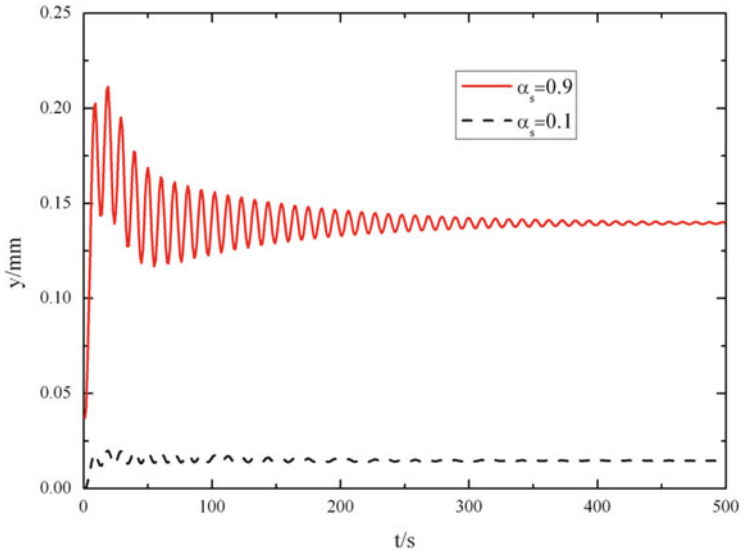

Fig. 3 Thermal vibration at different thermal absorptivity

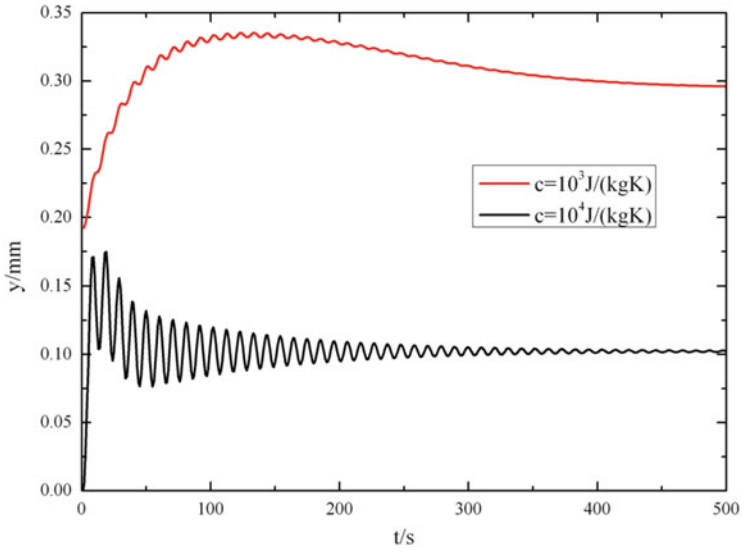

Fig. 4 Thermal vibration at different thermal capacity

Thermal Capacity Effect on Thermal Vibration

The thermal capacity effect on thermal vibration is shown in Fig. 4. As thermal capacity increases, thermal deformation becomes smaller, while vibration becomes

larger. If thermal capacity becomes smaller, the initial vibration will be larger and thermal deformation will be also larger.

Conclusions

The thermal control method effect on thermal vibration is analyzed by numerical calculation and a conclusion could be drawn as follows: by increasing thermal conductivity, reducing solar absorbance, and increasing thermal capacity, thermal vibration can be made smaller. Among these methods, reducing solar absorbance is a simple and efficient method.

References

1. Gilmore DG (2002) Spacecraft thermal control handbook. The Aerospace Press, EI Segundo, CA
2. Boley BA (1956) Thermally induced vibrations of beams. J Aeronaut Sci 23:179–181
3. Boley BA, Weiner JH (1960) Theory of thermal stresses. Wiley, New York
4. Xue MD, Ding Y (2003) Two kinds of tube elements for transient thermal-structural analysis of large space structures. Int J Numer Methods Eng 59:1335–1353
5. Song O, Yoon I, Librescu L (2003) Thermally induced bending vibration of composite spacecraft booms subjected to solar heating. J Therm Stresses 26:829–843

A New Method to Evaluate the Adaptability of Initiating Explosive Used in the Aro-Pyrotechnic Device in Deep Space

Yaokun Ye, Feng Ding, Jianfeng Man, Nan Yan, and Weituo Li

Abstract In order to find a solution for continuous testing of the physically varying process of pyrotechnic material decomposition with temperature change, a method is proposed based on using digital cameras and differential scanning calorimetry (DSC). A small amount of loose or compacted pyrotechnic material is placed in the crucible of a DSC system that can continuously heat and cool the sample from room temperature at a certain heating or cooling rate. Pictures are taken by a high-definition digital camera to record the physical appearance of the samples that allows monitoring the physical properties of pyrotechnic samples continuously as a function of temperature. This method is not only simple, universal and safe to operate, but also provides a new way to analyze the stability of the pyrotechnic composition.

Keywords Pyrotechnic composition • Physical properties • Continuous testing method • Temperature adaptability

Introduction

Pyrotechnic composition is a dedicated, special energetic material for pyrotechnic devices, the role of which is to release combustion, deflagration or explosion energy after rapid chemical reaction by accepting weak stimulation energy from a pyrotechnic transducer element [1–3]. The released energy helps achieve ignition, pass fire, initiation, booster, extension, for the power and fireworks effects in pyrotechnic devices and, therefore, the pyrotechnic materials are widely used for altitude control, isolation and unlocking, pressing and releasing, as well as in other mechanisms of satellites and spacecraft.

Compared to other energetic materials, ignition powder that is one of the most sensitive energetic materials with very special functions has unique explosion and

Y. Ye (✉) • F. Ding • J. Man • W. Li
Beijing Institute of Spacecraft System Engineering, Beijing 100094, China
e-mail: yeyaokun@163.com

N. Yan
Beijing Institute of Technology, Beijing 100081, China

J. Kleiman (ed.), *Protection of Materials and Structures from the Space Environment*, Astrophysics and Space Science Proceedings 47,
DOI 10.1007/978-3-319-19309-0_59

combustion characteristics. Usually, there are three types of chemical reaction energy outputs: the detonation type, the combustion type, and the pneumatic force power type. Ignition powder is the most sensitive explosive with high energy density, excellent self-activating and self-oxidizing system. It belongs to metastable materials, which can lead to explosive reaction even if the outside stimulation is by low energy.

In the past, the ignition powder devices experienced temperatures in the range of 60 °C. With the rapid development of space technology, deep space probes begin to face conditions with over 100 °C ambient temperature, requiring higher environmental adaptability for the ignition powder power devices. For the burning powder devices, the physical and chemical properties of ignition powder are equally important when varying with the process temperature, because any change in the ignition powder effects significantly the success of the detectors' task.

At present, a variety of ignition powder chemical properties depending on temperature can be tested by Differential Scanning Calorimetry (DSC) or by other methods, but they do not allow evaluating the change of physical properties, mainly due to the unique explosion and combustion characteristics of the powder, which may be dangerous to test personnel. Thus, it becomes a technical difficulty, as well as an urgent problem to be solved how to test the variety of ignition powder's physical properties in a safe, simple, and effective way.

Analysis of Existing Test Methods

The existing continuous testing methods are mainly based on the Differential Scanning Calorimetry (DSC) methods used to continuously detect the decomposition reactions of ignition powder taking place with temperature change [4–9]. As can be seen from Fig. 1, a DSC cell is composed of a lid, a crucible, a heating block and thermocouples. The test procedure is as follows: weight a small amount of the sample material and the reference material, place them in the crucibles and cover the lid, then start the DSC test, while the heating block heats or cools the test sample and the reference at a pre-set temperature rate of 5 °C/min. The thermocouples monitor the temperature of the sample and the reference and it is displayed in the DSC's terminal interface, which can continuously monitor the decomposition reactions of the samples with the change of temperature.

The fundamental principle of the existing method is that it measures the relation between power difference and temperature of the sample and the reference based on the pre-set heating or cooling process of DSC. When there is temperature difference between the sample and the reference, it does not record temperature directly, but it records the compensation power required to compensate for the temperature difference of the test sample and the reference, meanwhile, the heat flow rate versus temperature of the test sample is displayed on the terminal screen of the DSC instrument. The rate of heat flow indicates the absorption and heat release rate of the sample, which can supervise the initial decomposition temperature, initial

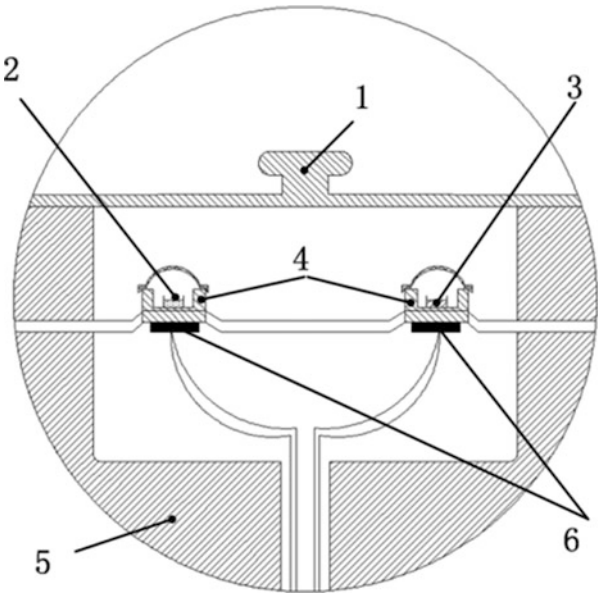

Fig. 1 DSC method to test the pyrotechnic powder decomposition with temperature. *1* lid; *2* sample; *3* reference; *4* crucible; *5* heating block; *6* thermocouples

decomposition time, maximum decomposition temperature, peak temperature time, and other chemical properties versus temperature change.

This method is primarily used to test the chemical properties of a variety of pyrotechnic compositions with temperature change. For the pyrotechnic composition power devices of deep space probes, it is required not only to assess the chemical properties of the pyrotechnic composition with temperature change, but also to evaluate the physical properties, however, the DSC method can only reflect the chemical properties change with temperature.

Design of New Test Method

In order to test the change of pyrotechnic composition with temperature from the physical morphology changes point of view, this study suggests a design for a new method. The schematic of the new method is shown in Fig. 2.

According to the proposed method, the lid of the DSC instrument is removed when the samples are placed in the crucible and pictures of the sample appearance are taken by a high-definition digital camera, thus, the appearance change is followed when the sample is continuously heated or cooled at a certain temperature rate in the DSC instrument that is also continuously testing the physical changes of the pyrotechnic composition under different temperature conditions.

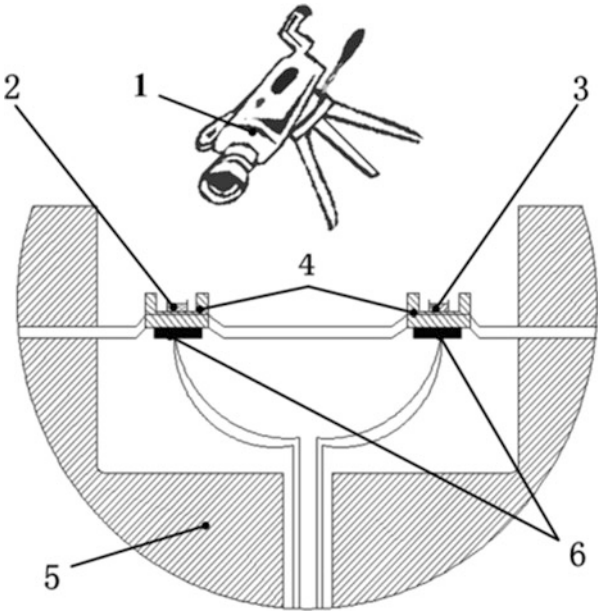

Fig. 2 New method to test the physical changes of pyrotechnic composition. *1* high-definition digital camera; *2* sample; *3* reference; *4* crucible; *5* heating block; *6* thermocouples

The procedure of the new method can be described as follows:

1. Before experiment: Open the lid of the DSC instrument, weight up to 0.5 mg of the pyrotechnic sample and the reference in two uncovered crucibles that allows taking pictures of the sample and the reference by a high-definition digital camera, and in the same thermal environment as well, therefore, it won't affect accuracy of the test data, like the initial decomposition temperature, initial decomposition time, maximum resolution temperature, time peak, and others, that the DSC instrument can accurately test. Place a high-definition digital camera in a confined space environment of the DSC instrument, without ventilation, to ensure the thermal environment of the sample and the reference in strictly at the heating or cooling rate preset by the DSC instrument. It is important that the maximum heating temperature is set at least 30 °C lower than the flash point to guarantee the safety of the personnel, but with no minimum temperature limitation.
2. Preparing an experiment: There are two kinds of pyrotechnic composition states, the loose state and the compacted state. From the observation of loose samples, obtain the properties of pyrotechnic composition changing with temperature, and discover the reaction of the pyrotechnic device under continuously changing temperature from testing a simulated explosive device with compacted pyrotechnic composition. The optimal weight of the loose sample is 0.5 mg, while the optimal weight and charge method of the compacted sample should be based on the type of the pyrotechnic device. In this method, it can accurately test the physical properties of pyrotechnic composition varying with temperature on one hand, and test its physical properties inside the pyrotechnic device on the other hand.

3. Beginning of experiment: Set the heating or cooling rate of the DSC at 5 °C/min to heat or cool the sample and the reference from the initial temperature. The 5 °C/min preset temperature rate of the heating block is optimal at uniform heating for the sample and the reference, and also it offers enough time for the high-definition digital camera operators to take pictures. The temperature of the samples is displayed on the terminal interface of the DSC, which should be matched with the relevant pictures in order to compare the difference.
4. Take a picture of the pyrotechnic sample every 10 °C with the high-definition digital camera and record the temperature on the DSC terminal interface, to ensure that the taken photographs are in correspondence with the temperature. Besides, when photographing the sample and the reference, it is important to achieve the high-definition digital camera precise focus and to keep the focus and the camera position unchanged, to ensure the photographs would be comparable.
5. Compare the photographs taken by the digital camera to analyze the variation in color, volume, particle size, and other physical performance of the pyrotechnic composition, which can provide the properties change of the pyrotechnic composition under difference temperature conditions from the physical point of view.

   In conclusion, the new method which just needs a high-definition digital camera and the DSC instrument is easy and simple to operate. The test results are based on physical properties testing and supplemented by chemical testing.

Case Studies

A test was carried out on the primary explosive of an aerospace pyrotechnic device using the above testing method. The typical test results are as follows:

1. Figure 3 presents the pictures of loose primary explosive physical properties during a continuous heating process, from which it can be seen that the color changes little below 110 °C, but it begins to get lighter at 110 °C and a small part turns brown at 160 °C, then the most part becomes brown at 180 °C, finally the whole sample turns brown at 200 °C. Therefore, the physical properties of the loose primary explosive and the change dynamics can be obtained during the heating process.
2. Figure 4 presents the pictures of compacted primary explosive physical properties during a continuous heating process. It can be noticed that the color has no changes below 110 °C, but it starts to change at 110 °C and the surface color turns light brown at 160 °C, then turns dark brown at 180 °C, accompanied by some volume expansion, swelling and cracking. As a result, it shows the physical properties change of the compacted primary explosive in terms of the color, charge density, appearance, and other physical parameters, which is related indirectly to difference status of the pyrotechnic device explosive with temperature change.

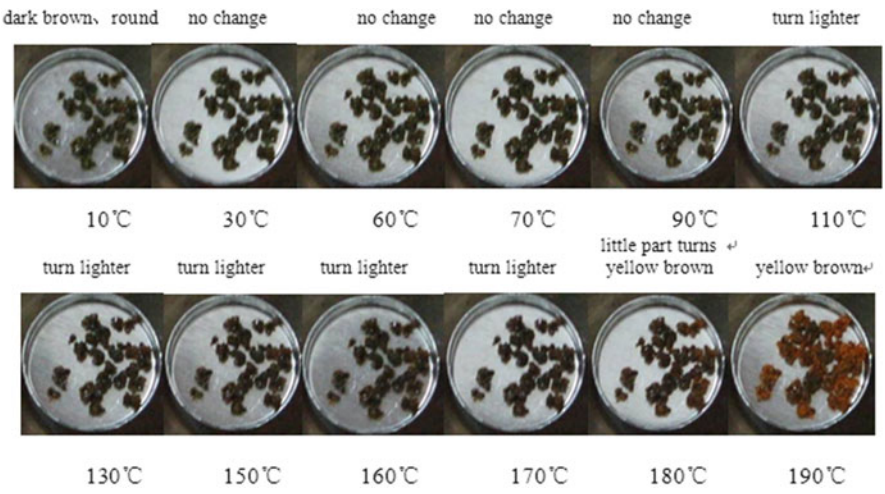

Fig. 3 Appearance change of a loose primary explosive during continuous heating

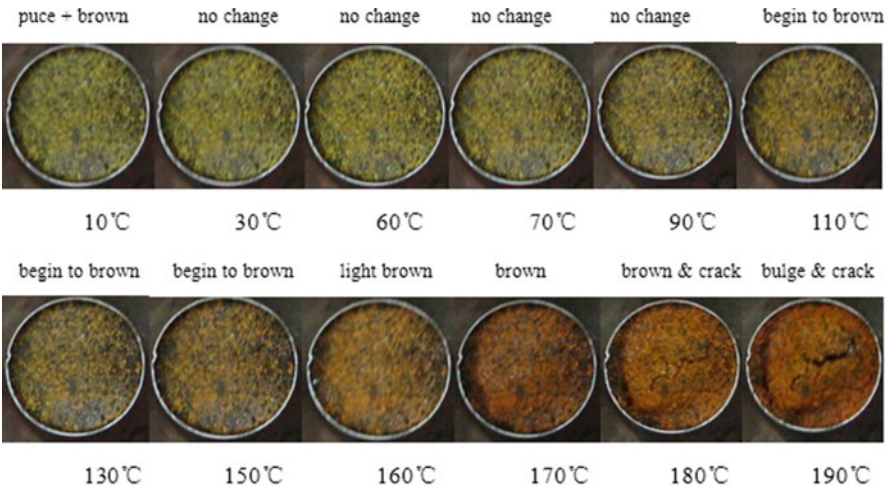

Fig. 4 Appearance change of a compacted primary explosive during continuous heating

3. Figure 5 is the typical test result of the primary explosive chemical properties change after a continuous heating process based on the new method. It is obvious that heating of the primary explosive starts at 110 °C and reaches an endothermic peak between 160 and 180 °C, which suggests that chemical reaction in the primary explosive begins, and the first chemical reaction rate peak appears between 160 and 180 °C. These results allow to discuss the evolution of the thermodynamic parameters of primary explosive during continuous heating, like the decomposition temperature, the initial decomposition time, the maximum decomposition temperature, and the peak temperature time. The chemical

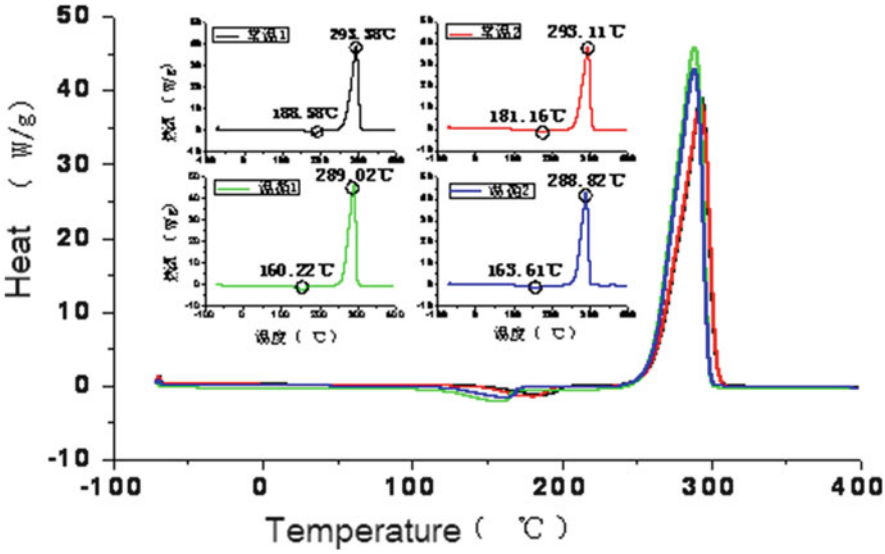

Fig. 5 Test results for the chemical properties of a primary explosive during continuous heating

properties change of the primary explosive with different temperature can also be discussed from the chemical point of view.

Conclusions

This paper presents a new method which represents a combination of the Differential Scanning Calorimetry with a high-definition digital camera for testing the physical properties change of the pyrotechnic composition with temperature. The new method was applied for testing of a primary explosive and allowed to successfully obtain the continuous change of its properties for the loose and compacted samples.

The results of the experiment showed that this method allows to evaluate the physical properties change with temperature in an easy, universal, and safe way, which offers a new method for a stationary analysis of the pyrotechnic composition.

References

1. GJB 772A-1997 (1997) Explosive test method
2. Urbanski T (1964) Chemistry and technology of explosives, vol 1. Pergamon Press, New York
3. Joseph FK (1977) Bridgeport Conn. Method of forming lead styphnate ammunition priming mixture [P]. USP 4029530

4. Dilhan D (2004) Laser ignition systems for space applications. In: 31st International Pyrotechnics Seminar, Fort-Collins, CO, July
5. Lao YL (1997) Primary explosive chemistry and technology [M]. Beijing Institute of Technology Press, Beijing
6. GJB737.1-1989 (1989) Pyrotechnics pharmacy vacuum stability test methods
7. GJB 5383.11-2005 (2005) Pyrotechnic stability and compatibility tests: differential thermal analysis and differential scanning calorimetry
8. GJB 737.12-1993 (1993) Pyrotechnics pharmaceutical test methods: determination of primary explosive lead content
9. Lao YL, Sheng D (2011) Explosive pharmacy [M]. Beijing Institute of Technology Press, Beijing

Re-entry Aerothermal Environment Simulation of the TPS of Hypersonic Flight Vehicles

Xinyan Ji, Jing Wang, and Yirong Wang

Abstract The thermal performance, structural integrity, reusability and aerodynamic stability are important parameters of hypersonic flight vehicles. A simulation test for the re-entry aerothermal environment is required to verify the thermal protection system (TPS). The TPS is exposed to an aggressive aerothermal environment during the atmospheric re-entry of hypersonic flight vehicles, especially because temperature of the hot-structure control surface can reach more than 1800 °C. This paper describes an approach to simulate the aerothermal environment of the actual flight trajectory by testing in a ground-based facility, including a test setup, aerodynamic heating calculation, heater layout design, thermal boundary conditions control and temperature measurement methods. The simulation results meet the desired temperature distribution on the TPS during re-entry. The effectiveness analysis of test conditions and instrumentation is also discussed in this paper. The study will be significant for TPS materials and structure design of hypersonic flight vehicles.

Keywords Re-entry • Aerothermal environment • Thermal protection system

Introduction

Simulation of the atmospheric re-entry of hypersonic flight vehicles, by testing in a ground-based facility, needs to carry out aerodynamic heating modeling of a hot structure and to use the predicted aerodynamic heating to calculate the transient temperature response of the test article. The heating system design goal [1] is to design a test setup to simulate the desired temperature distribution. Before testing, a

X. Ji (✉) • Y. Wang
Beijing Institute of Spacecraft Environment Engineering, Beijing 100094, China
e-mail: wtsjtu@126.com

J. Wang
Beijing Institute of Spacecraft Environment Engineering, Beijing 100094, China

Science and Technology on Reliability and Environmental Engineering Laboratory, Beijing 100094, China

J. Kleiman (ed.), *Protection of Materials and Structures from the Space Environment*, Astrophysics and Space Science Proceedings 47,
DOI 10.1007/978-3-319-19309-0_60

test condition analysis must be performed using the actual boundary conditions, for example, providing more representative pre-test predictions and better correlation between the test data and analysis. Finally, it is required to provide valid strain and temperature data to support the validation of the finite element modeling techniques and thermal structural analysis.

Hot-Structure Physical Modeling and Thermal Modeling

The C/SiC Ruddervator (RSTA) [2–5] is a hot-structure control surface of the Reusable Launch Vehicle (RLV) that was designed for thermal analysis and studying of the test method but it was never tested under the real RLV program. The RSTA is a truncated version of the full-scale RLV control surface but it incorporates all major full-scale features, including the metallic spindle, five major C/SiC quasi-isotropic lay-up components fastened together with, mainly, C/SiC fasteners, and the face sheets that serve as access panels for the RSTA assembly. The RSTA surface temperature is in excess of 1800 °C.

Figure 1 shows the C/SiC ruddervator subcomponent test article (RSTA). The test article is the flight-weight truncated full-scale RLV RSTA and includes five C/SiC boxes spared with C/SiC fasteners. There is an inconel 718 spindle with C/SiC torque boxes spared with inconel 718 bolts mounted at 25″ from the center. Access panels are mounted with Rene 41 screws.

Figure 2 shows the C/SiC RSTA geometry for thermal modeling created in the thermal analysis software named The Thermal Desktop. The Thermal Desktop is

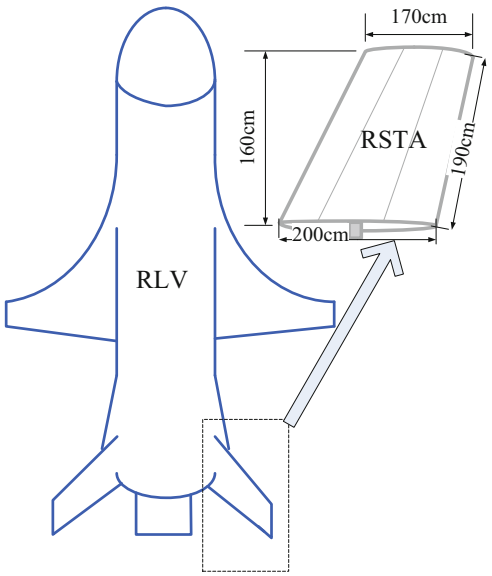

Fig. 1 Location of the RSTA on an imaginary RLV

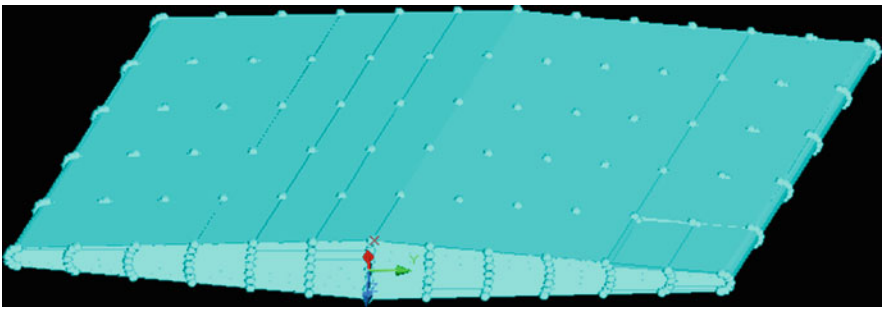

Fig. 2 The C/SiC RSTA geometry for thermal modeling

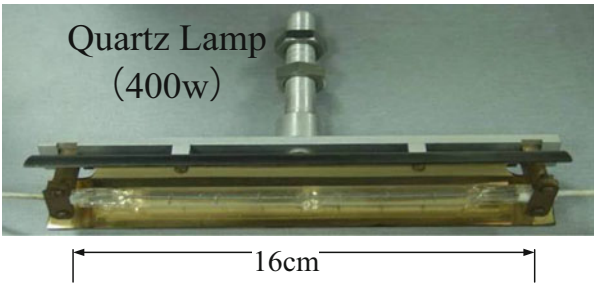

Fig. 3 The quartz lamp

able to import and analyze FEM models directly, without the typical ad-hoc "element centroid" conversion process.

Heater (Quartz Lamp) Physical Modeling and Thermal Modeling

A quartz lamp and/or graphite heaters are selected depending on temperature and heat flux requirements. A typical quartz lamp is shown in Fig. 3 and the thermal modeling for this lamp is shown in Fig. 4. In order to achieve a longer heating time and higher temperature, a multi-zone quartz-lamp heater setup was designed, with polished aluminum reflectors increasing the heat flux and water (gas) cooled pipes decreasing the wall temperature of quartz lamps. The maximum temperature of the typical multi-zone quartz lamp heater is 1430 °C. The modular quartz-lamp heater is shown in Fig. 5.

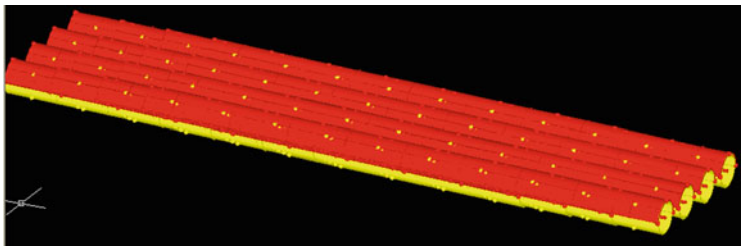

Fig. 4 Quartz lamp thermal modeling

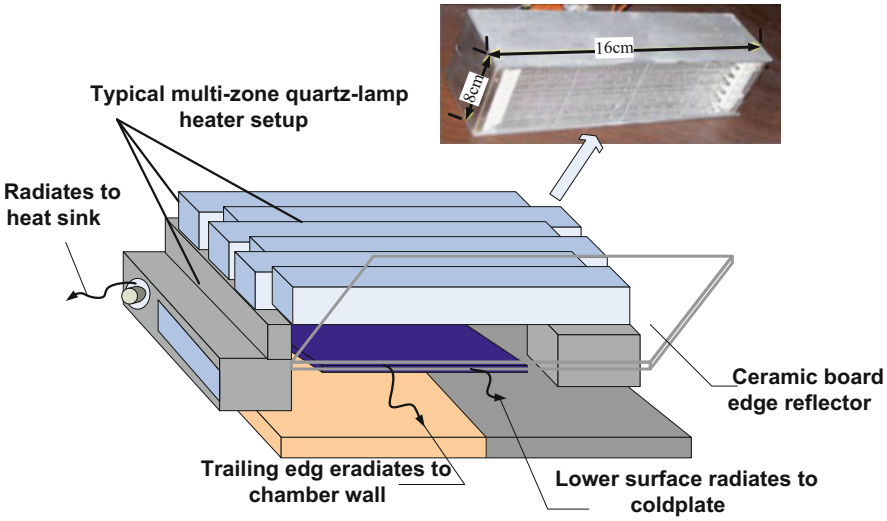

Fig. 5 Modular quartz lamp heater

Thermal Boundary Conditions

Thermal simulation is carried out in a nitrogen-purged atmosphere. Figure 5 shows the radiative exchange between the test article and test equipment. The edges of this modular quartz lamp heater radiate to the chamber wall, the lower surface radiates to the cold-plate. The heater is able to heat efficiently the front surface, the edges, as well as the inboard/outboard surfaces.

The test setup allows testing in a controlled temperature environment which includes a heat exchanger, a cold-plate and the heaters. The temperature control equipment also includes heat sinks and insulated surfaces.

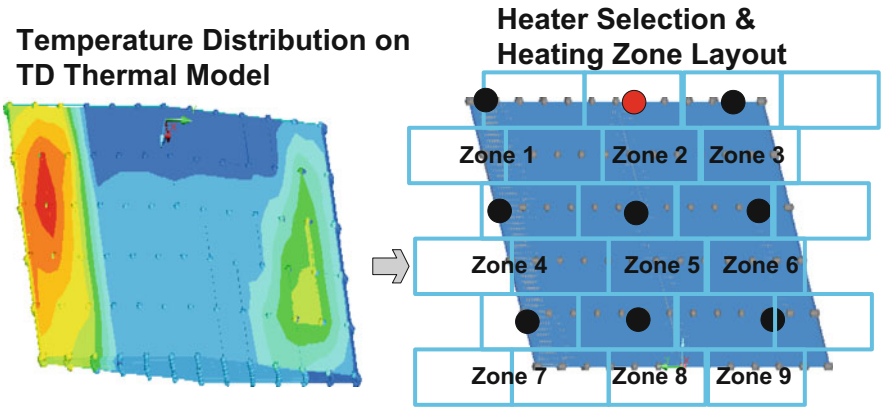

Fig. 6 Typical temperature control zones

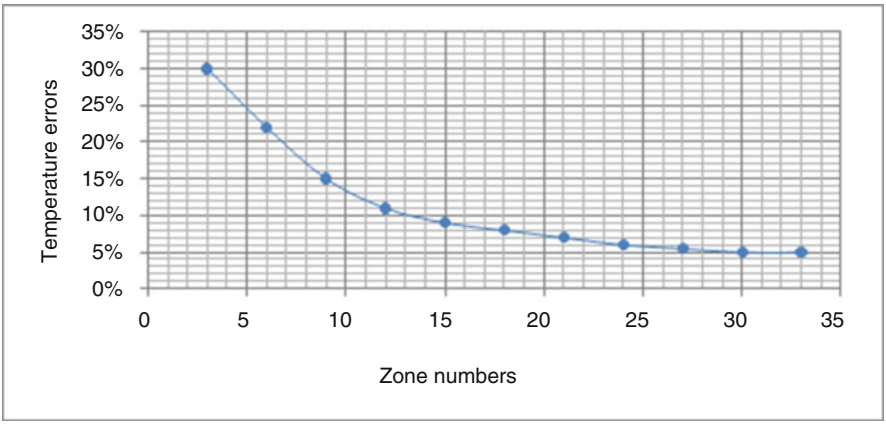

Fig. 7 The number of temperature control zones vs. temperature errors

The Multi-zone Quartz-Lamp Heater Simulation

The heating layout was planned out and heaters were arranged in zones in the created multi-zone quartz-lamp heater, simulating the heating process of the ruddervator subcomponent test article. The heaters were grouped as required to simulate the modeled and predicted aerodynamic heating distribution. The modeling results were used to determine the number of temperature control zones and the temperature error as a function of the number of temperature control zones, as shown in Figs. 6 and 7.

Suggestions for Improved Heaters Design

1. Heaters should be arranged in zones
   - Group heaters as required to simulate the predicted aerodynamic heating distribution
   - Extend heaters past the edges of the test article to minimize end effects
   - Bake out the heaters to minimize the lamp effects end thermal losses
   - Custom heater designs are often required for unique heating applications
   - Structures with heat sinks or complex shapes may require tailored lamp spacing, lamp lengths, and/or voltage requirements
2. Specific heat boundary conditions should be created
   - Separate zones with radiation barriers to minimize the "cross-talk" effect
   - Use barriers around heaters to minimize the edge effects and to reduce natural and forced convection
   - Use reflective plates, ceramic boards, etc.
   - Use reflectors to provide heating extended past the test article edges

References

1. Glass DE, Merrigan MA, Sena JT, Reid RS (1998) Fabrication and testing of a leading-edge-shaped heat pipe [R]. NASA CR-1998-208720, October
2. Glass DE, Merrigan MA, Sena JT (1998) Fabrication and testing of mo-re heat pipes Embedded in carbon/carbon [R]. NASA CR-1998-207642, March
3. Glass DE, Merrigan MA, Sena JT, Reid RS (1998) Fabrication and testing of a leading-edge-shaped heat pipe [R]. NASA CR-1998-208720, October
4. Glass DE, Camarda CJ (1992) Preliminary thermal/structural analysis of a carbon/carbon refractory- metal heat-pipe-cooled wing leading edge [M]. Thermal structures and materials for high-speed Flight. In: Thornton EA (ed) Progress in astronautics and aeronautics. AIAA, New York, pp 301–322
5. Curry DM (1993) Space shuttle orbiter thermal protection system design and flight experience [C]. In: 1st ESA/ESTEC workshop on thermal protection systems, ESA/ESTEC

Index

J. Kleiman (ed.), *Protection of Materials and Structures from the Space Environment*, Astrophysics and Space Science Proceedings 47,
DOI 10.1007/978-3-319-19309-0